Reaction kinetics and rheological characteristics of ultra-thin P-based triboreactive films

Abdel Kader Y.A. Dorgham

School of Mechanical Engineering
University of Leeds

Submitted in accordance with the requirements for the degree of
Doctor of Philosophy

December 2017

To my loving parents who saw my first step, taught me my first word and looked after me their whole life ...

Declaration

The candidate confirms that the work submitted is his own, except where work which has formed part of jointly-authored publications has been included. The contribution of the candidate and the other authors to this work has been explicitly indicated below. The candidate confirms that appropriate credit has been given within the thesis where reference has been made to the work of others.

In all papers listed below, the primary author performed all the experimental work, data analysis and preparation of publications. All other authors contributed to proof reading of the articles prior to publication.

Papers contributing to this thesis:

- A. Dorgham, A. Neville, K. Ignatyev, F. Mosselmans and A. Morina "An in-situ synchrotron XAS methodology for surface analysis under high temperature, pressure and shear" Review of Scientific Instruments, 88(1), 015101 (2017).
- A. Dorgham, A. Morina and A. Neville, "Tribochemistry and morphology of ZDDP antiwear films" Chapter 10, Triboanalytics: Modern analytical and numerical tools in Tribology, Springer (2017)

Acknowledgements

I would like to express my sincere appreciation and gratitude to my supervisors Anne Neville and Ardian Morina for giving me the opportunity to work with them over the last few years on challenging ideas, and for their invaluable guidance, support and positive attitude throughout the PhD endeavour. Many thanks also to Dr. Chun Wang for all her support, encouragement and good discussions. I would also like to thank all the members of IFS (Leeds) and SMaRT (Leuven) especially Bruke Jofore, Ashwin Sankaran, Tom Verwijlen, Ruth Cardinaels, Thawhid Khan, Pourya Parsaeian, Erfan Esfahani and Abdullah Azam, for the good time we had along our PhD odyssey.

Abdel Dorgham.

Abstract

To access the evolving tribochemistry at the contacting asperities, a miniature pin-on-disc tribological apparatus was developed and combined with synchrotron X-ray Absorption Spectroscopy (XAS). The new apparatus makes it possible to study in-situ the transient decomposition reactions of various oil additives on different surfaces under a wide range of realistic operating conditions. The results suggest that the decomposition of ZDDP starts by forming intermediate sulphate species on the steel surface, which are readily reduced to sulphides of discontinuous clusters. The clusters can play different vital roles including binding the subsequently formed phosphate layers with the steel surface. Initially, the phosphate layers consist of short chains due to excess concentration of metal oxides on the steel surface. As the oxides' concentration decreases in the subsequent layers, the short chains start to polymerise into longer ones. The polymerisation reaction appeared to follow first-order reaction kinetics with two distinctive phases. The first is a fast transient burst phase near the metal surface, whereas the second phase dominates the formation of the layers away from the metal surface and is characterized by slow kinetics.

To better understand the origin of the superior antiwear properties of the P-rich tribofilms, an Atomic Force Microscope (AFM) liquid cell was designed to form tribofilms in-situ while examining their textural and rheological properties over time. The obtained results indicate that the tribofilms behave as a molten glass with an average viscosity of 1×10^{12} Pa.s. This suggests that their superior antiwear properties originate from their intrinsic rheological properties that allow them to flow while formed, which was clear from their ability to maintain local order on the nanoscale through the motion, rearrangement and local reconfiguration of single and multiple patches of the formed tribofilm at the interface. This seems to effectively mitigate the smearing and wearing of the contacting asperities resulting in less wear. The findings of this study open future opportunities for quantitatively analysing the interfacial rheology and reaction kinetics governing a broad range of additives and substrates, which can help build mechanistic models capable of better predicting wear.

Table of contents

List of figures xix

List of tables xxxvii

Nomenclature xxxix

1 Introduction 1

1.1 Background . . . 1

1.2 Motivation . . . 2

1.3 Research objectives . . . 5

1.4 Thesis outline . . . 5

2 Basics of tribology, rheology and contact mechanics 7

2.1 Tribology: from macro- to nanoscale . . . 7

2.1.1 Friction . . . 8

2.1.2 Wear . . . 11

2.2 Rheology: basics and models . . . 13

2.2.1 Small Amplitude Oscillatory Shear (SAOS) . . . 14

2.2.2 Creep–Recovery . . . 15

2.2.3 Stress relaxation . . . 16

2.3 Contact mechanics . . . 17

2.3.1 Elastic deformation theories . . . 17

2.3.2 Plastic deformation theories . . . 24

2.4 Summary and concluding remarks . . . 26

3 Literature review **27**

3.1 Introduction . . . 27

3.2 Chemical nature of ZDDP and DDP . . . 29

3.3 Reactions of ZDDP and DDP . . . 31

3.3.1 Ligand exchange . . . 31

3.3.2 Decomposition of peroxides and peroxy-radicals . . . 32

3.3.3 Formation of tribo- and thermal films . . . 32

3.3.3.1 Thermal decomposition . . . 33

3.3.3.2 Thermo-oxidative decomposition . . . 35

3.3.3.3 Hydrolytic decomposition . . . 38

3.4 Composition of antiwear films . . . 39

3.4.1 Phosphorus, zinc and iron species . . . 40

3.4.2 Sulphur species . . . 42

3.4.3 Factors affecting the tribofilms' composition and formation 45

3.4.3.1 Material of counterbodies . . . 45

3.4.3.2 Type of base oil . . . 51

3.4.3.3 Duration of rubbing and heating . . . 53

3.4.3.4 Concentration of additive . . . 56

3.4.3.5 Temperature and load . . . 56

3.4.3.6 Sliding and rolling speeds . . . 58

3.5 Mechanical properties of antiwear films . . . 59

3.5.1 Structure . . . 59

3.5.2 Hardness and elastic modulus . . . 64

3.5.3 Tenacity and durability . . . 68

3.6 Rheological properties of antiwear films . . . 69

3.7 Tribological properties of antiwear films . . . 71

3.7.1 Friction mechanism . . . 71

3.7.2 Antiwear mechanism . . . 74

3.8 Antiwear films in humid environments . . . 76

3.8.1 Effect of water on the composition of tribofilms 77
3.8.2 Effect of water on the tribological properties of tribofilms . 78
3.9 Summary 79
3.9.1 Knowledge gaps 79
3.9.1.1 Decomposition mechanisms of antiwear additives 79
3.9.1.2 Composition of antiwear tribofilms 80
3.9.1.3 Reaction kinetics of the tribofilms formation . . . 81
3.9.1.4 Effect of water on antiwear tribofilms 82
3.9.1.5 Role of cations in tribofilms formation 83
3.9.1.6 Rheological properties of antiwear tribofilms . . . 84
3.9.1.7 In-situ evaluation of tribofilms evolution 85
3.9.2 Concluding remarks 88

4 Materials and methods 91

4.1 Materials 91
4.1.1 Oils and additives 91
4.1.2 Standard phosphate glasses 93
4.1.3 Standard sulphur samples 94
4.2 Experimental methods 95
4.2.1 Tribological characterisation techniques 95
4.2.1.1 Mini-Traction Machine (MTM) 95
4.2.1.2 Development of a new AFM liquid cell 99
4.2.1.3 Development of a new in-situ XAS tribometer . . 102
4.2.2 Mechanical characterisation 109
4.2.3 Rheological characterisation 110
4.2.4 Surface analysis techniques 112
4.2.4.1 Raman spectroscopy 112
4.2.4.2 X-ray Photoelectron Spectroscopy (XPS) 113
4.2.4.3 X-ray Absorption Spectroscopy (XAS) 116
4.2.4.4 Focused Ion Beam (FIB) 118

4.2.4.5 Transmission Electron Microscope (TEM)/Energy-Dispersive X-ray spectroscopy (EDX) 119
4.2.4.6 White light interferometry 120
4.3 Summary 120

5 Reaction kinetics of ZDDP tribofilms using ex-situ techniques 123
5.1 Tribological tests 123
5.2 Surface analysis 127
5.2.1 TEM/EDX cross-section analysis 130
5.2.2 XPS concentration evolution 132
5.2.3 XPS depth analysis 135
5.3 Kinetics of ZDDP decomposition reaction 136
5.4 Summary and concluding remarks 142

6 Morphology of ZDDP and DDP tribofilms using in-situ XAS 145
6.1 Friction and wear performance 146
6.2 XAS analysis of standard samples 148
6.2.1 P k-edge spectra of synthesised phosphate glasses 148
6.2.2 S k-edge spectra of sulphur samples 150
6.3 XAS analysis of ZDDP thermal and tribofilms 151
6.3.1 ZDDP thermal films formed at 80°C 151
6.3.1.1 Characterisation of P k-edge spectra 151
6.3.1.2 Characterisation of S k-edge spectra 155
6.3.2 ZDDP tribofilms formed at 80°C and 1.0 GPa 159
6.3.2.1 Characterisation of P k-edge spectra 159
6.3.2.2 Characterisation of S k-edge spectra 161
6.3.3 ZDDP tribofilms formed at 25°C and 1.0 GPa 163
6.3.3.1 Characterisation of P k-edge spectra 163
6.3.3.2 Characterisation of S k-edge spectra 166
6.3.4 ZDDP tribofilms formed at 80°C and 1.0 GPa: DLC coated counter-surfaces 168

6.3.4.1 Characterisation of P k-edge spectra 168
6.3.4.2 Characterisation of S k-edge spectra 171
6.3.5 ZDDP tribofilms formed at 80°C and 2.2 GPa 173
6.3.5.1 Characterisation of P k-edge spectra 173
6.3.5.2 Characterisation of S k-edge spectra 176
6.4 Overall comparison between ZDDP tribo- and thermal films . . . 178
6.5 XAS analysis of DDP-1 tribofilms 181
6.5.1 DDP-1 tribofilms formed at 80°C and 1 GPa 181
6.5.1.1 Characterisation of P k-edge spectra 181
6.5.1.2 Characterisation of S k-edge spectra 183
6.6 XAS analysis of DDP-2 tribofilms 186
6.6.1 DDP-2 tribofilms formed at 80°C and 1 GPa 186
6.6.1.1 Characterisation of P k-edge spectra 186
6.6.1.2 Characterisation of S k-edge spectra 188
6.7 Summary and concluding remarks 190

7 Structure and rheology of ZDDP and DDP tribofilms using in-situ AFM 193
7.1 Results of ZDDP tribofilms 193
7.1.1 Local occupancy of the tribofilm's pads 193
7.1.1.1 Case I: 128 scanning lines 194
7.1.1.2 Case II: 64 scanning lines 196
7.1.1.3 Case III: 32 scanning lines 196
7.1.1.4 Case VI: 16 scanning lines 197
7.1.1.5 Case V: 8 scanning lines 199
7.1.1.6 Case VI: 4 scanning lines 200
7.1.1.7 Case VII: 1 scanning line 201
7.1.2 Tribofilm durability and tenacity 201
7.1.3 Tribofilm growth hysteresis 203
7.1.3.1 Case I: growth at 2.7 GPa 203

7.1.3.2 Case II: growth at 4.5 GPa 205
7.1.3.3 Case III: growth at 5.7 GPa 206
7.1.3.4 Comparison: growth at different contact pressures 208
7.1.4 Tribofilm reaction kinetics 210
7.1.4.1 Effect of contact pressure 210
7.1.4.2 Effect of temperature 212
7.1.4.3 Combined effect of temperature and contact pressure 213
7.1.5 Effect of substrate (H-DLC) 214
7.2 Results of DDP tribofilms 215
7.2.1 Local occupancy of the tribofilm pads 215
7.2.1.1 Case I: 64 scanning lines 216
7.2.1.2 Case II: 16 scanning lines 217
7.2.1.3 Case III: 8 scanning lines 219
7.2.1.4 Case IV: 4 scanning lines 220
7.2.1.5 Case V: 1 scanning line 222
7.2.2 Tribofilm durability and tenacity 223
7.2.3 Effect of substrate 225
7.2.4 Tribofilm growth hysteresis 226
7.2.5 Tribofilm reaction kinetics 227
7.2.5.1 Effect of contact pressure 227
7.2.5.2 Effect of temperature 228
7.2.5.3 Combined effect of temperature and contact pressure 229
7.3 Summary 230

8 Overall discussion 233

8.1 ZDDP decomposition mechanisms 233
8.1.1 Induction period and base layer composition 233
8.1.2 Tribofilm composition 237
8.1.3 Effect of water 240
8.1.3.1 Composition of base sulphur layer 241

8.1.3.2 Composition of phosphate bulk layers 242
8.1.3.3 Length of phosphate chains 244
8.2 DDP decomposition mechanisms 247
8.3 Tribofilm formation/removal cycles 248
8.4 Effect of countersurfaces 249
8.4.1 ZDDP additive 249
8.4.2 DDP additive 250
8.5 Effect of sliding speed 251
8.6 Effect of temperature and contact pressure 252
8.7 Reaction kinetics of ZDDP tribofilms 253
8.7.1 Activation energy 253
8.7.2 Reaction order 259
8.8 Reaction kinetics of DDP tribofilms 260
8.8.1 Activation energy 260
8.8.2 Reaction order 263
8.9 Flowability of P-based tribofilms 263
8.9.1 Viscosity quantification using creep 264
8.9.2 Viscosity quantification using squeeze-flow 267
8.10 Summary 270

9 Conclusions, recommendations and outlook 273

9.1 Conclusions 273
9.1.1 Developed techniques 273
9.1.2 Additive decomposition and tribofilm composition 274
9.1.3 Effect of water 275
9.1.4 Tribological properties of the formed tribofilms 276
9.1.5 Reaction kinetics 276
9.1.6 Tribofilm structure and properties 277
9.2 Limitations and recommendations 279
9.3 Closing statement 283

References **285**

Appendix A AFM experimental uncertainty analysis **315**

A.1 Uncertainty propagation 315

A.2 Sources of uncertainty in the in-situ AFM measurements 317

A.2.1 Source I: temperature 317

A.2.2 Source II: normal force 318

A.2.2.1 Source II-i: force setpoint 319

A.2.2.2 Source II-ii: deflection sensitivity 319

A.2.2.3 Source II-iii: spring constant 322

A.2.2.4 Uncertainty propagation of the normal force . . 326

A.2.3 Source III: contact area 326

A.2.3.1 Source III-i: AFM tip radius 328

A.2.3.2 Source III-ii: reduced elastic modulus 332

A.2.3.3 Source III-iii: contact force 334

A.2.3.4 Uncertainty propagation of the contact area . . . 334

A.2.4 Source VI: contact pressure 334

A.2.5 Source V: scanning speed 335

Appendix B Characterization of synthesized polyphosphate glasses **337**

B.1 Surface analysis of polyphosphate glasses 337

B.1.1 XPS degradation analysis 337

B.1.2 XPS quantification of zinc phosphate glass 339

B.1.3 XPS quantification of iron phosphate glass 341

B.1.4 XPS quantification of mixed phosphate glass 343

B.1.5 Comparison between different glasses 345

List of figures

1.1 Overview of the average energy consumption of a typical internal-combustion-engine passenger car. Reprinted from Schwarz [10]. . 3

2.1 Schematic of friction phase diagram of surfactant monolayers. Reprinted from Singer [64]. 10

2.2 Effect of sliding distance on the microscopic wear. Reprinted from Gotsmann et al. [71]. 12

2.3 Illustration of a creep compliance curve during creep-recovery experiment. Reprinted from Rao [76]. 16

2.4 Typical loading-unloading behaviour of linear elastic material, straight line, and nonlinear material, hysteresis. Reprinted from Butt et al. [83]. 18

2.5 Effect of indentation depth, as compared to the tip radius, on the measured Hertz modulus. Reprinted from Mahaffy et al. [98]. . . 20

3.1 The different structures of ZDDP: (I) neutral dimeric in equilibrium with (II) neutral monomeric; (III) basic ZDDP. Reprinted from Harrison and Kikabhai [133]. 30

3.2 The different structures of DDP: (I) neutral and (II) acidic DDP. Reprinted from Kim et al. [136]. 31

3.3 The Fe−O−S ternary system that can be formed on the steel surface under rubbing. (A) is its Phase diagram. Reprinted from Watkins [14]. And (B) is its potential diagram at 673 K. Reprinted from Watanabe et al. [203] 44

3.4 Schematic of the assembly of in-situ AFM liquid cell. Reprinted from Gosvami et al. [30]. 54

3.5 Schematic of the assembly of high temperature liquid cell for in-situ XAS experiments. Reprinted from Morina et al. [162] 54

3.6 Schematic of the assembly of a high temperature liquid cell used for in-situ XAS experiments. Reprinted from Ferrari et al. [237]. . 55

3.7 Arrangements of atoms in the amorphous tribofilm. Reprinted from Martin et al. [178]. 60

3.8 Schematic of the structural model of the ZDDP tribofilm elucidating its multilayer characteristic. Reprinted from Bell et al. [17]. . . . 61

3.9 TEM Cross section image of the ZDDP Tribofilm layers and EDX semi-quantitative analysis of the elements constituting the different layers. Reprinted from Ito et al. [200]. 62

3.10 Schematic of the multilayer structure of the ZDDP tribofilm (a) before and (b) after washing with solvent. Reprinted from Bec et al. [36]. 63

3.11 Schematic of the patchy structure of the ZDDP tribofilm. Reprinted from Spikes [7]. 63

3.12 Comparison between the measured and predicted damping coefficient of the basic and neutral ZDDP. Reprinted from Georges et al. [260]. 70

3.13 Effect of the ZDDP tribofilm on the Stribeck curve after different rubbing periods. Reprinted from Taylor and Spikes [262]. 73

3.14 Schematic of the ordered structure of the compressed hydrodynamic layer. Reprinted from Georges et al. [264]. 73

3.15 Effect of water on the life of bearing based on 100% life at 0.01% water in addition to the available techniques to detect water and their range are indicated. Reprinted from Sheehan [272]. 77

4.1 Structure of PAO. Reprinted from Stachowiak and Batchelor [3]. 92

4.2 Synthesis procedure of zinc-, iron- and mixed zinc-iron phosphate glasses 94

4.3 Schematic of the mini-traction machine (MTM) used to perform all the tribological tests. It consists of a ball and disc, which can be rotated independently to achieve different slide-to-roll ratios. . 96

4.4 Measurement of the tribofilm thickness using SLIM accessory of the mini-traction machine. Reprinted from Kaperick [304]. 97

4.5 Stribeck curves of PAO-ZDDP oil after different rubbing times (min). The dashed gray line indicates the speed of 35 mm/s at which all the tribological tests were performed. 98

4.6 The Dimension Icon AFM (Bruker, USA) and the in-house developed liquid cell used in performing the in-situ tribotests. 100

4.7 Schematic of the light lever used to detect the deflection of the AFM cantilever. The inset shows the difference in response between soft and hard samples. Adapted from Butt et al. [83]. 101

4.8 Schematic of a) the assembly and b) a cross-section of the tribological apparatus used in the in-situ XAS experiments. The synchrotron X-ray incident beam and the XRF and XAS detector are also shown in a). The detector is placed in the vertical geometry at a right angle relative to both the incident beam and the tribological surface. 104

4.9 Friction force calibration curve of the large load compression cell used in the tribotester. The calibration equation used to fit the experimental data and the minimum weight detectable by the load cell are indicated. 105

4.10 Friction force calibration curve of the small load compression cell used in the tribotester. The calibration equation used to fit the experimental data and the minimum weight detectable by the load cell are indicated. 105

4.11 XRF maps (1.75 x 0.40 mm^2) of the distributions of P (left) and S (right) elements found on the disc after 10 minutes of shearing time. The maps were captured by scanning the disc surface in the lateral direction along lines of 1.75 mm and in the vertical direction at different heights of 0.4 mm relative to the incident beam. The schematic of the right-angled triangle abc (not to scale) was used to identify the size of the areas considered inside and outside wear scar. 108

4.12 Force curves using PeakForce QNM mode and the procedure to calculate deformation, dissipation and elastic modulus. Reprinted from Pittenger et al. [310]. 110

4.13 Schematic of the squeeze flow between two parallel plates assuming constant volume just before applying the constant load (left) and after a certain squeeze time (right). In case of constant area, the starting geometry is similar to the image on the right. 111

4.14 Schematic illustration of the basics of Raman spectroscopy. 113

4.15 Schematic illustration of the basics of XPS. 114

4.16 Penetration depth as a function of the glancing angle for smooth and rough surfaces calculated at the *k*-edge of S and P. The vertical dotted line marks the average critical angle for total external reflection for both P and S. 117

4.17 Schematic of the light lever used to detect the deflection of the AFM cantilever. The inset shows the difference in response between soft and hard samples. 119

4.18 Schematic illustration of the basics of white light interferometry. . 120

4.19 Schematic of the interplay between the composition of the tribofilm and its tribological, mechanical and rheological properties. The different techniques used to probe these properties are indicated. . 121

5.1 Effect of water on the evolution of the friction coefficient of PAO-ZDDP oil over rubbing time. Error bars where calculated based on at least 3 repetitions. 124

5.2 Effect of water on the evolution of the friction coefficient of PAO-ZDDP oil over rubbing time. 125

5.3 Evolution of the thickness of ZDDP tribofilms as measured by the MTM-SLIM over rubbing time in the presence and absence of water in the oil. Error bars where calculated based on at least 3 repetitions. 126

5.4 Wear scar images and depth profiles of MTM discs as measured by white-light interferometry after 120 minutes of rubbing times in (a) the presence and (b) absence of water in the oil. The images show part of the tribofilm on the wear scar was removed by EDTA. (c-d) depth profiles as indicated on (a) and (b). 127

5.5 Peak fitting of the different components composing the signals of a.) O1s, b.) P2p and Zn3s, c.) Fe2p and d.) C1s after different rubbing times in the presence and absence of water in the oil. . . 128

5.6 TEM-EDX analysis, which includes (a) cross-section of the wear scar after 120 min of rubbing in the absence of water. EDX analysis is also shown for the atomic concentrations of the main tribofilm components, i.e. O, S, P and Zn. (b) EDX spectra of the three main regions, i.e. the steel surface and the bottom base and bulk layers of the tribofilm. (c)-(f) EDX maps across the tribofilm shown in (a) for O, S, P and Zn, respectively. 131

5.7 TEM-EDX analysis, which includes (a) cross-section of the wear scar after 120 min of rubbing in the presence of 2% water in the oil. EDX analysis is also shown for the atomic concentrations of the main tribofilm components, i.e. O, S, P and Zn. (b) EDX spectra of the three main regions, i.e. the steel surface and the bottom base and bulk layers of the tribofilm. (c)-(f) EDX maps across the tribofilm shown in (a) for O, S, P and Zn, respectively. 132

5.8 Evolution of the atomic concentrations of the elements inside the wear scar in the absence of added water to the oil. Solid symbols are based on XPS analysis and open symbols are based on TEM-EDX analysis. Solid lines are the fits of the model described in Eq.5.4. . 133

5.9 Evolution of the atomic concentrations of the elements inside the wear scar in the presence of 2% added water to the oil. Solid symbols are based on XPS analysis and open symbols are based on TEM-EDX analysis. Solid lines are the fits of the model described in Eq.5.4. 133

5.10 Evolution of BO/NBO, P/O and P/Zn ratio inside the wear scar in the absence of added water to the oil. Solid lines are the fits of the model described in Eq.5.4. 134

5.11 Evolution of BO/NBO, P/O and P/Zn ratio inside the wear scar in the presence of 2% added water to the oil. Solid lines are the fits of the model described in Eq.5.4. 135

5.12 XPS depth profile of the main elements found in the tribofilm after 120 minutes of rubbing formed in the case of no added water to the oil. 136

5.13 XPS depth profile of the main elements found in the tribofilm after 120 minutes of rubbing formed in the case of 2% added water to the oil. 137

5.14 Effect of water on the evolution of O of the ZDDP tribofilm over the rubbing time. 138

5.15 Effect of water on the evolution of S of the ZDDP tribofilm over the rubbing time. 138

5.16 Effect of water on the evolution of P of the ZDDP tribofilm over the rubbing time. 139

5.17 Effect of water on the evolution of Zn of the ZDDP tribofilm over the rubbing time. 139

6.1 Evolution of the friction force during the in-situ tests using plain steel and DLC coated countersurfaces. 147

6.2 Wear scar width and depth as measured by white-light interferometry after the in-situ tests using different operating conditions. . . 148

6.3 Evolution of the P *k*-edge spectra of different synthesised zinc- and mixed zinc-iron polyphosphate glasses. Each curve is vertically offset for clarity by adding a constant, as specified on each curve, relative to the first curve. 149

6.4 Evolution of the P *k*-edge spectra of different synthesised iron polyphosphate glasses. For iron orthophosphate (a) is amorphous, (b) is semi-crystalline and (c) is crystalline. Each curve is vertically offset for clarity by adding a constant, as specified on each curve, relative to the first curve. 149

6.5 Evolution of the normalised S *k*-edge spectra of different standard compounds containing sulphur. Each curve is vertically offset for clarity by adding a constant, as specified on each curve, relative to the first curve. 151

6.6 Evolution of the ZDDP normalised fluorescence yield spectra of P *k*-edge after different heating times at 80 °C. Each curve is vertically offset for clarity by adding a constant, as specified on each curve, relative to the first curve. 152

6.7 Example of the peak fitting used to determine the areas of peak (a): the adsorbed ZDDP and peak (b): phosphate observed at the P *k*-edge. This example is for a ZDDP thermal film generated after 5 hr of heating time at 80 °C. 153

6.8 Evolution of the normalised heights of peak (a): adsorbed ZDDP and peak (b): phosphate at the P k-edge of ZDDP thermal film after different heating times at 80 °C. 154

6.9 Evolution of the ZDDP normalised fluorescence yield spectra of S k-edge after different heating times at 80 °C. Each curve is vertically offset for clarity by adding a constant, as specified on each curve, relative to the first curve. 156

6.10 Example of the peak fitting used to determine the area of the sulphides and sulphates peaks at the S k-edge. This example is for a ZDDP thermal film generated after 5 hr of heating time at 80 °C. 157

6.11 Evolution of the normalised heights of peaks (a) and (b): sulphide and peak (c): sulphate at the S k-edge of ZDDP thermal film after different heating times at 80 °C. 158

6.12 Evolution of the ZDDP normalised fluorescence yield spectra of P k-edge after different shearing times at 1.0 GPa and 80 °C. Each curve is vertically offset for clarity by adding a constant, as specified on each curve, relative to the first curve. 159

6.13 Evolution of the normalised heights of peak (a): adsorbed ZDDP and peak (b): phosphate at the P k-edge of ZDDP tribofilms after different shearing times at 1.0 GPa and 80 °C. 160

6.14 Evolution of the ZDDP normalised fluorescence yield spectra of S k-edge after different shearing times at 1.0 GPa and 80 °C. Each curve is vertically offset for clarity by adding a constant, as specified on each curve, relative to the first curve. 162

6.15 Evolution of the normalised heights of peaks (a) and (b): sulphide and peak (c): sulphate at the S k-edge of ZDDP tribofilms after different shearing times at 1.0 GPa and 80 °C. 163

6.16 Evolution of the ZDDP normalised fluorescence yield spectra of P k-edge after different shearing times at 1.0 GPa and 25 °C. Each curve is vertically offset for clarity by adding a constant, as specified on each curve, relative to the first curve. 164

6.17 Evolution of the normalised heights of peak (a): adsorbed ZDDP and peak (b): phosphate at the P k-edge of ZDDP tribofilms after different shearing times at 1.0 GPa and 25 °C. 165

6.18 Evolution of the normalised heights of peaks (a) and (b): sulphide and peak (c): sulphate at the S k-edge after different shearing times at 1.0 GPa and 25 °C. Each curve is vertically offset for clarity by adding a constant, as specified on each curve, relative to the first curve. 167

6.19 Evolution of the normalised heights of peak (a), (b) and (c) of S k-edge of ZDDP tribofilms after different shearing times at 1.0 GPa and 25 °C. 168

6.20 Evolution of the ZDDP normalised fluorescence yield spectra of P k-edge after different shearing times using DLC coated counter-surfaces at 1.0 GPa and 80 °C. Each curve is vertically offset for clarity by adding a constant, as specified on each curve, relative to the first curve. 169

6.21 Evolution of the normalised heights of peak (a): adsorbed ZDDP and peak (b): phosphate at the P k-edge of ZDDP tribofilms after different rubbing times using DLC coated counter-surfaces at 1.0 GPa and 80 °C. 170

6.22 Evolution of the ZDDP normalised fluorescence yield spectra of S k-edge after different shearing times at 1.0 GPa and 80 °C using DLC coated counter-surfaces. Each curve is vertically offset for clarity by adding a constant, as specified on each curve, relative to the first curve. 172

6.23 Evolution of the normalised heights of peaks (a) and (b): sulphide and peak (c): sulphate at the S k-edge of ZDDP tribofilms after different shearing times at 1.0 GPa and 80 °C using DLC coated counter-surfaces 173

6.24 Evolution of the ZDDP normalised fluorescence yield spectra of P k-edge after different shearing times at 2.2 GPa and 80 °C. Each curve is vertically offset for clarity by adding a constant, as specified on each curve, relative to the first curve. 174

6.25 Evolution of the normalised heights of peak (a): adsorbed ZDDP and peak (b): phosphate at the P k-edge of ZDDP tribofilms after different rubbing times at 2.2 GPa and 80 °C. 175

6.26 Evolution of the ZDDP normalised fluorescence yield spectra of S k-edge after different shearing times at 2.2 GPa and 80 °C. Each curve is vertically offset for clarity by adding a constant, as specified on each curve, relative to the first curve. 176

6.27 Evolution of the normalised heights of peaks (a) and (b): sulphide and peak (c): sulphate at the S k-edge of ZDDP thermal film after different shearing times at 2.2 GPa and 80 °C. 177

6.28 Comparison between the normalised areas of the adsorbed additive and phosphate peaks at the P k-edge of the ZDDP tribo- and thermal films at the end of each test. 179

6.29 Comparison between the normalised areas of the sulphide and sulphate peaks at the S k-edge of the ZDDP tribo- and thermal films at the end of each test. 180

6.30 Evolution of the DDP-1 normalised fluorescence yield spectra of P k-edge after different shearing times at 1.0 GPa and 80 °C. Each curve is vertically offset for clarity by adding a constant, as specified on each curve, relative to the first curve. 182

6.31 Evolution of the normalised peak heights of unreacted DDP-1 and phosphate P k-edge of DDP-1 tribofilms after different rubbing times at 1.0 GPa and 80 °C 182

6.32 Evolution of the DDP-1 normalised fluorescence yield spectra of S k-edge after different shearing times at 1.0 GPa and 80 °C. Each curve is vertically offset for clarity by adding a constant, as specified on each curve, relative to the first curve. 184

6.33 Evolution of the normalised heights of peak (a), (b) and (c) of S k-edge of DDP-1 tribofilms after different shearing times at 1.0 GPa and 80 °C. 184

6.34 Evolution of the DDP-2 normalised fluorescence yield spectra of P k-edge after different shearing times at 1.0 GPa and 80 °C. Each curve is vertically offset for clarity by adding a constant, as specified on each curve, relative to the first curve. 187

6.35 Evolution of the normalised peak heights of unreacted DDP-2 and phosphate P k-edge of ZDDP tribofilms after different rubbing times at 1.0 GPa and 80 °C 187

6.36 Evolution of the DDP-2 normalised fluorescence yield spectra of S k-edge after different shearing times at 1.0 GPa and 80 ^{o}C. Each curve is vertically offset for clarity by adding a constant, as specified on each curve, relative to the first curve. 189

6.37 Evolution of the normalised heights of peak (a), (b) and (c) of S k-edge of DDP-2 tribofilms after different shearing times at 1.0 GPa and 80 ^{o}C. 189

7.1 Schematic of the different scan lines used to raster scanning a $5 \times 5\,\mu m^2$ area using the AFM tip during the in-situ tests to generate tribofilms. 194

7.2 In-situ ZDDP tribotest using the AFM liquid cell, where a) schematic of the 128 scan lines used to raster scanning a $5 \times 5\,\mu m^2$ area, and b) the generated tribofilm after different scanning cycles at 80 ^{o}C and 7.3 GPa. The scale bar is in nm. 195

7.3 In-situ ZDDP tribotest using the AFM liquid cell, where a) schematic of the 64 scan lines used to raster scanning a $5 \times 5\,\mu m^2$ area, and b) the generated tribofilm after different scanning cycles at 80 ^{o}C and 7.3 GPa. The scale bar is in nm. 196

7.4 In-situ ZDDP tribotest using the AFM liquid cell, where a) schematic of the 32 scan lines used to raster scanning a $5 \times 5\,\mu m^2$ area, and b) the generated tribofilm after different scanning cycles at 80 ^{o}C and 7.3 GPa. The scale bar is in nm. 197

7.5 In-situ ZDDP tribotest using the AFM liquid cell, where a) schematic of the 16 scan lines used to raster scanning a $5 \times 5\,\mu m^2$ area, and b) the generated tribofilm after different scanning cycles at 80 ^{o}C and 7.3 GPa. The scale bar is in nm. 198

7.6 In-situ ZDDP tribotest using the AFM liquid cell, where a) schematic of the 8 scan lines used to raster scanning a $5 \times 5\,\mu m^2$ area, b) the generated tribofilm after different scanning cycles at 80 ^{o}C and 7.3 GPa, and c) a repetition of the same test. The scale bar is in nm. 199

7.7 In-situ ZDDP tribotest using the AFM liquid cell, where a) schematic of the 4 scan lines used to raster scanning a $5 \times 5\,\mu m^2$ area, and b) the generated tribofilm after different scanning cycles at 80 ^{o}C and 7.3 GPa. The scale bar is in nm. 200

7.8 In-situ ZDDP tribotest using the AFM liquid cell, where a) schematic of the single scan line used to raster scanning a $5 \times 5\,\mu m^2$ area, and b) the generated tribofilm after different scanning cycles at 80 ^{o}C and 7.3 GPa. The scale bar is in nm. 201

7.9 Durability of mature ZDDP tribofilms measured by following the evolution of the tribofilm thickness after different sliding cycles at 25 ^{o}C under different contact pressures ranging from 2.1 to 4.5 GPa. 202

7.10 Evolution of the ZDDP tribofilm thickness over time after two repetitions formed at 80 ^{o}C and 2.7 GPa. 204

7.11 Evolution of the ZDDP tribofilm thickness over time after two repetitions formed at 80 ^{o}C and 4.5 GPa. 205

7.12 Evolution of the ZDDP tribofilm thickness over time after two repetitions formed at 80 ^{o}C and 5.7 GPa. 207

7.13 Evolution of the ZDDP tribofilm thickness over time after two repetitions formed at 80 ^{o}C and 5.7 GPa. 207

7.14 Evolution of the ZDDP tribofilm thickness over sliding cycles at 80 ^{o}C while ramping the contact pressure from 4.0 to 7.2 GPa. . . . 208

7.15 Effect of contact pressure on the sliding cycles at which the tribofilm growth changes from linear to exponential. 209

7.16 Evolution of the growth rate of the ZDDP tribofilm formed at 80 ^{o}C over different contact pressures. The results of Gosvami et al. [30] were plotted for comparison. 211

7.17 Evolution of the growth rate of the ZDDP tribofilm formed at 80 ^{o}C over different contact pressures. The results of Gosvami et al. [30] were plotted for comparison. 211

7.18 Evolution of the growth rate of the ZDDP tribofilm over contact pressure formed at different temperatures. 212

7.19 Evolution of the growth rate of the ZDDP tribofilm over temperature formed under different contact pressures. 213

7.20 Evolution of the growth rate of the ZDDP tribofilm formed under different contact pressures and temperatures. The 3D surface was generated using the chemo-mechanical Arrhenius-type model suggested by Gotsmann and Lantz [71]. 214

7.21 In-situ ZDDP tribotest using the AFM liquid cell on H-DLC substrate, where a) schematic of the 64 scan lines used to raster scanning a $5 \times 5\,\mu m^2$ area, b) the substrate topography after different scanning cycles at 80 ^{o}C and 7.3 GPa, and c) the substrate topography after scanning at 120 ^{o}C and 7.3 GPa. The scale bar is in nm. 215

7.22 In-situ DDP-1 tribotest using the AFM liquid cell, where a) schematic of the 64 scan lines used to raster scanning a $5 \times 5\,\mu m^2$ area, and b) the generated tribofilm after different scanning cycles at 80 ^{o}C and 4.8 GPa. The scale bar is in nm. 216

7.23 In-situ DDP-1 tribotest using the AFM liquid cell, where a) schematic of the 64 scan lines used to raster scanning a $5 \times 5\,\mu m^2$ area, and b) the generated tribofilm after different scanning cycles at 80 ^{o}C and 5.6 GPa. The scale bar is in nm. 217

7.24 In-situ DDP-1 tribotest using the AFM liquid cell, where a) schematic of the 16 scan lines used to raster scanning a $5 \times 5\,\mu m^2$ area, and b) the generated tribofilm after different scanning cycles at 80 ^{o}C and 4.8 GPa. The scale bar is in nm. 218

7.25 In-situ DDP-1 tribotest using the AFM liquid cell, where a) schematic of the 8 scan lines used to raster scanning a $5 \times 5\,\mu m^2$ area, and b) the generated tribofilm after different scanning cycles at 80 ^{o}C and 4.8 GPa. The scale bar is in nm. 219

7.26 In-situ DDP-1 tribotest using the AFM liquid cell, where a) schematic of the 8 scan lines used to raster scanning a $5 \times 5\,\mu m^2$ area, and b) the generated tribofilm after different scanning cycles at 80 ^{o}C and 5.6 GPa. The scale bar is in nm. 220

7.27 In-situ DDP-1 tribotest using the AFM liquid cell, where a) schematic of the 4 scan lines used to raster scanning a $5 \times 5\,\mu m^2$ area, and b) the generated tribofilm after different scanning cycles at 80 ^{o}C and 4.8 GPa. The scale bar is in nm. 221

7.28 In-situ DDP-1 tribotest using the AFM liquid cell, where a) schematic of the 4 scan lines used to raster scanning a $5 \times 5\,\mu m^2$ area, and b) the generated tribofilm after different scanning cycles at 80 ^{o}C and 5.6 GPa. The scale bar is in nm. 221

7.29 In-situ DDP-1 tribotest using the AFM liquid cell, where a) schematic of the single scan line used to raster scanning a $5 \times 5\,\mu m^2$ area, and b) the generated tribofilm after different scanning cycles at 80 ^{o}C and 4.8 GPa. The scale bar is in nm. 223

7.30 Durability of mature DDP tribofilms measured by following the evolution of the tribofilm thickness after different sliding cycles at 25 ^{o}C under different contact pressures ranging from 2.1 to 5.2 GPa. 224

7.31 Effect of substrate on the in-situ DDP-1 tribotest using the AFM liquid cell, where a) schematic of the 64 scan lines used to raster scanning a $2 \times 2\,\mu m^2$ area, b) the generated tribofilm on iron polyphosphate substrate, c) the generated tribofilm on zinc polyphosphate substrate, and d) the generated tribofilm on mixed zinc and iron polyphosphate substrate, after different scanning cycles. The scale bar is in nm. 226

7.32 Evolution of the tribofilm thickness over sliding cycles for DDP-1 tribofilms formed at 80 ^{o}C and different contact pressures. 227

7.33 Evolution of the growth rate of the DDP tribofilm over contact pressure formed at different temperatures. 228

7.34 Evolution of the growth rate of the ZDDP tribofilm over temperature formed under different contact pressures. 229

7.35 Evolution of the growth rate of the DDP-1 tribofilm formed under different contact pressures and temperatures. The 3D surface was generated using the chemo-mechanical Arrhenius-type model suggested by Gotsmann and Lantz [71]. 230

8.1 Schematic of the formation of FeS clusters on the metal surface and the diffusion of S into steel, which induces stress corrosion cracking. 237

8.2 Effect of water on the difference in binding energy between Zn3s and P2p of the top 5–7 nm of the tribofilm over rubbing time. . . 243

8.3 Schematic of the caging effect of water on the initially formed phosphate species and the subsequent formation of a single and multiple bridges of hydrogen bonds between water molecules and PO_2^- groups of the decomposed ZDDP. 244

8.4 Comparison between the measured and calculated polymerisation number n in the absence of water in the oil. 245

8.5 Comparison between the measured and calculated polymerisation number n in the presence of water in the oil. 246

8.6 Effect of water on the evolution of the BO/NBO ratio, binding energy difference Δ between Zn3s and P2p, and chain length n over rubbing time. 246

8.7 Schematic of the tribofilms formed on bare steel (left) and DLC coated surfaces (right). 250

8.8 Evolution of the growth rate of the ZDDP tribofilm formed at 80 ^{o}C and 7.2 GPa over different sliding speeds. 252

8.9 Evolution of the growth rate of (a) ZDDP and (b) DDP-1 tribofilms formed under different contact pressures and temperatures. The 3D surfaces were generated using the chemo-mechanical Arrhenius-type model suggested by Gotsmann and Lantz [71]. 253

8.10 Evolution of activation energy E_a of the growth of the ZDDP tribofilms over contact pressure. 256

8.11 Evolution of activation energy E_a of the growth of the DDP tribofilms over contact pressure. 262

8.12 Viscosity quantification of triboreactive ZDDP films using creep method. a, Sample of masked images used to calculate the area evolution of the formed films. b, Evolution of the creep compliance, $J(t)$, over time for different ZDDP films formed at 80 °C and 4.5 GPa using different scanning lines, i.e. 8, 4 and 1. Arrows indicate instances of film removal. 265

8.13 Evolution of the creep compliance, $J(t)$, over time for different ZDDP tribofilms formed at 80 ^{o}C and 4.8 GPa using different scanning lines, i.e. 8, 4 and 1. 266

8.14 Evolution of the creep compliance, $J(t)$, over time for different DDP tribofilms formed at 80 ^{o}C and 5.6 GPa using different scanning lines, i.e. 8, 4 and 1. 266

8.15 Viscosity quantification of triboreactive ZDDP films using squeeze-flow method. a, Schematic of the squeeze flow between two parallel plates assuming constant volume just before applying the constant load (left) and after a certain squeeze time (right). b, Evolution of the total film thickness (symbols) and film thickness without wear (symbols and dashed line) after different sliding cycles at 25 °C under different contact pressures ranging from 2.1 to 4.5 GPa. Green areas indicate increase in film thickness whereas blue areas indicate film removal. The AFM images are $8.5 \times 8.5\,\mu m^2$ with colour ranges from 0-180 nm. c, Analysis of the film volume and area. d, Fit of the thickness at 2.7 and 3.7 GPa. 268

8.16 Viscosity quantification of triboreactive DDP-1 films using squeeze-flow method. a, Evolution of the total film thickness (symbols) and film thickness without wear (symbols and dashed line) after different sliding cycles at 25 °C under different contact pressures ranging from 2.1 to 5.2 GPa. Green areas indicate increase in film thickness whereas blue areas indicate film removal. The AFM images are $8.5 \times 8.5\,\mu m^2$ with colour ranges from 0-180 nm. b, Analysis of the film volume and area. c, Fit of the thickness at 3.7 GPa. 269

8.17 In-situ generation of ultrathin ZDDP triboreactive films. a, Schematic illustration of AFM Si tip raster scanning steel substrate submersed in PAO oil containing ZDDP additive at high temperature and contact pressure. b, Formation of mixed oxide-sulphide base layer on the steel substrate. c, Formation of iron and zinc polyphosphate on the sulphur-oxide base layer. d, In-situ evolution of the structure of the ZDDP film formed at 80 °C and 7.3 GPa. 271

A.1 Ramp of the set versus actual temperature as read from the cartridge heaters' controller of the in-house developed AFM liquid cell. . . 318

A.2 Evolution of the deflection sensitivity of one RTespa AFM cantilever (Bruker, USA) over sliding cycles measured at 80 °C during one of the in-situ tribotests. 320

A.3 Prediction of the evolution of the normalized elastic modulus of one RTespa AFM cantilever (Bruker, USA) over temperature using both the Einstein oscillator and Debye-Grüneisen models. 323

A.4 Evolution of the deflection sensitivity of two RTespa AFM cantilevers (Bruker, USA) over temperature. The inset of the figure shows the evolution of the deflection sensitivity over sliding cycles measured at 80 °C during one of the in-situ tribotests. 323

A.5 Force-displacement curves (trace and retrace) obtained with one RTespa AFM cantilever (Bruker, USA) of nominal spring constant 40 N/m showing that the tip-sample interaction lacks any adhesion force. 327

A.6 Evolution of the AFM topography images over sliding distance of rough Ti substrate used for tip estimation under small adhesion force versus large contact force. 329

A.7 Schematic of the effect of scanning using sharp versus worn tips on the resulting AFM topography images [396]. 329

A.8 Evolution of the estimated R_a and R_q over sliding distance under small adhesion force versus large contact force. 330

A.9 Evolution of the estimated R_{max} over sliding distance under small adhesion force versus large contact force. 330

A.10 Schematic of the effect of scanning sharp, rounded and normal features using sharp and worn tips on the resulting tip estimate [396]. 332

A.11 Evolution of the estimated AFM tip radius over sliding distance under small adhesion force versus large contact force. 333

B.1 XPS degradation analysis after different acquisition time of the Fe 2p signal of iron poly (0.33) phosphate glass. 337

B.2 XPS degradation analysis after different acquisition time of the O 1s signal of iron poly (0.33) phosphate glass. 338

B.3 XPS degradation analysis after different acquisition time of the P 2p signal of iron poly (0.33) phosphate glass. 338

B.4 XPS survey spectra of various zinc phosphate glasses. 339

B.5 XPS high resolution spectra of various zinc phosphate glasses. . . 340

B.6 XPS survey spectra of various iron phosphate glasses. 341

B.7 XPS high resolution spectra of various iron phosphate glasses. . . 342

B.8 XPS survey spectra of various mixed zinc-iron phosphate glasses. 343

B.9 XPS high resolution spectra of various mixed zinc-iron phosphate glasses. 344

B.10 Comparison between the XPS composition of various zinc, iron and mixed zinc-iron phosphate glasses. 345

B.11 BO/NBO ratio vs M/P ratio of various zinc, iron and mixed zinc-iron phosphate glasses. 345

B.12 BO/NBO ratio vs the difference in binding energy between Zn 3s and P 2p of various zinc and mixed zinc-iron phosphate glasses. . 346

B.13 Binding energy of O 2s signal of various zinc and iron phosphate glasses. 346

List of tables

2.1 Summary of models of contact mechanics [83, 90]. 19

3.1 Comparison between the surface characterisation techniques. . . . 29

3.2 Classification of the hard and soft acids and bases relevant to ZDDP [154]. 34

3.3 Elastic modulus and hardness of the ZDDP thermal and tribo-film. 67

3.4 Summary of the proposed antiwear mechanisms of ZDDP. 75

4.1 Summary of the operational variables for the tribological tests using MTM. 93

4.2 List of the materials used in the synthesis of the different phosphate glasses. 94

4.3 List of the materials used in the synthesis of the different phosphate glasses. 95

4.4 Summary of the operating variables for the tribological tests using the MTM rig. 95

4.5 List of the experimental conditions during the in-situ XAS measurements. 107

4.6 The acquisition parameters used during the XPS high resolution scans. 114

4.7 The fitting parameters used in the analysis of the high resolution XPS spectra. 115

5.1 XPS component analysis of the tribofilms formed in the case of 0%, and 2% (shown in parenthesis) added water in the oil. 129

5.2 Fitting parameters based on Eq. (5.4) for the different components of the top 5–7 nm of the ZDDP tribofilm. 141

6.1 Peak positions of P k-edge (FY) spectra of different synthesised inorganic phosphate glasses. 150

6.2 Peak positions of P k-edge (FY) spectra of the tribo- and thermal films of P-based additives. 152

A.1 Fitting parameters for the Einstein oscillator and Debye-Grüneisen models for Si and Al [390]. 322

B.1 XPS vs batch composition for zinc phosphate glasses. 339

B.2 XPS vs batch composition for iron phosphate glasses. 341

B.3 XPS vs batch composition for mixed zinc-iron phosphate glasses. . 343

Nomenclature

Roman Symbols

$\hbar$	Reduced Planck constant	$[1.054 \times 10^{-34}$ J.s]
A_{cont}	Contact area	[m^2]
A_r	Real contact area	[m^2]
A_w	Worn contact area	[m^2]
b	Lattice parameter	[m]
D	Sliding distance	[m]
E	Young modulus	[Pa]
E_{a}	Activation energy	[J]
E_f	Elastic modulus of the film	[Pa]
E_r	Reduced elastic modulus	[Pa]
E_s	Elastic modulus of the substrate	[Pa]
F_0	Contribution of adhesion to friction force	[N]
F_{adh}	Adhesion force	[N]
f_{a}	Attempt frequency	[s^{-1}]
F_f	Friction force	[N]
F_n	Normal force	[N]
G''	Viscous or loss modulus	[Pa]
G'	Elastic or storage modulus	[Pa]
G^*	Complex modulus	[Pa]

G_0	Instantaneous elastic modulus	[Pa]
H	Hardness	[HV]
J_0	Instantaneous creep compliance	[Pa^{-1}]
J_m	Mean creep compliance	[Pa^{-1}]
J_N	Non-recoverable compliance	[Pa^{-1}]
J_R	Total recoverable compliance	[Pa^{-1}]
K	Wear coefficient	[-]
K_B	Boltzmann constant	[1.38×10^{-23} $J.K^{-1}$]
K_z	Stiffness	[$N.m^{-1}$]
N	Avogadro number	[6.022×10^{23} mol^{-1}]
n	Number of worn asperities	[-]
r_k	Kelvin radius	[m]
R_r	Reduced radius of curvature	[m^{-1}]
T	Absolute temperature	[K]
t_{cont}	Contact time	[s]
V	Molar volume	[m^3mol^{-1}]
v	Sliding velocity	[$m.s^{-1}$]
V_a	Activation volume	[m^3]
V_{wear}	Total wear volume	[m^3]
V_p	Volume of the plastically deformed surface	[m^3]
G	Shear modulus	[Pa]
t	Time	[s]

Greek Symbols

α	Fraction of the unlubricated dry area	[-]
δ	Phase angle	[°]

$\dot{\gamma}$	Shear rate	$[s^{-1}]$
η	Viscosity	[Pa.s]
η_0	Zero shear viscosity	[Pa.s]
Γ	Number of atoms lost per second	$[\mathrm{s}^{-1}]$
γ	Strain	[–]
γ_0	Strain at zero time	[–]
γ_{LV}	Surface tension	$[\mathrm{Pa.m}^{-1}]$
γ_r	Recoverable strain	[–]
μ	Coefficient of friction	[-]
ν	Poisson ratio	[-]
ν_0	Characteristic velocity	$[\mathrm{m}.s^{-1}]$
ω	Angular frequency	$[\mathrm{rad.s}^{-1}]$
ψ	Delayed elasticity function	[–]
ψ_p	Plasticity index	[-]
ρ_{bulk}	Number density of the bulk material	$[\mathrm{mol.m}^{-3}]$
ρ_{surf}	Number density of the surface material	$[\mathrm{mol.m}^{-3}]$
σ	Shear stress	[Pa]
σ_0	Oscillatory stress amplitude	[Pa]
τ_0	Shear stress at zero pressure	[Pa]
τ_d	Shear strength of the dry contact	[Pa]
τ_l	Shear strength of the lubricant film	[Pa]
τ_m	Mean retardation time	[s]
Θ	Effective Einstein temperature	[K]
Θ_D	Debye temperature	[K]
ξ	Pressure dependence of shear stress	[-]

ι Unit imaginary number $\sqrt{-1}$

π $\simeq 3.14\ldots$

Acronyms / Abbreviations

AES Auger Electron Spectroscopy

AFM Atomic Force Microscopy

AISI American Iron and Steel Institute

ATR Attenuated Total Reflectance

BO Bridging Oxygen

DDP Ashless DialkylDithioPhosphate

DLC Diamond-Like Carbon

DMT Derjaguin-Muller-Toporov

EC Electronically Commutated

EDX Energy-Dispersive X-ray spectroscopy

EHL Elasto-Hydrodynamic Lubrication

EP Extreme Pressure

EPMA Electron Probe Micro Analysis

EXAFS Extended X-ray Absorption Fine Structure

FAT Fixed Analyzer Transmission

FEG Field Emission Gun

FIB Focused Ion Beam

FIEL Force Integration to Equal Limits

FT-IR Fourier Transform InfraRed

FWHM Full Width at Half Maximum

FY Fluorescence Yield

GDA Generic Data Acquisition

GL Gaussian-Lorentzian

GNP Gross National Product

HSAB Hard and Soft Acids and Bases

IFM Interfacial Force Microscopy

JKR Johnson-Kendall-Roberts

LB Langmuir-Blodgett

LI Linkage Isomer

MILE Maxon Inductive Little Encoder

MoDTC Molybdenum DiThioCarbamate

MTM Mini-Traction Machine

NBO Non-Bridging Oxygen

NI Nano-Indentation

PAO Poly-α-Olefin

PECVD Plasma Enhanced Chemical Vapour Deposition

PID Proportional–Integral–Derivative

PSD Position Sensitive Detector

PSE Plasma Surface Engineering

QNM Quantitative Nanomechanical Mapping

RMS Root-Mean Square

SAOS Small Amplitude Oscillatory Shear

SEM Scanning Electron Microscopy

SFA Surface-Force Apparatus

SIMS Secondary Ion Mass Spectroscopy

SLIM Spacer Layer Imaging Method

SRR Slide-to-Roll Ratio

TCP Tri-Cresyl Phosphate

TEM Transmission Electron Microscopy

TEY Total Electron Yield

UHV Ultra-High Vacuum

UNCD Ultra-Nano-Crystalline diamond

X-PEEM X-ray PhotoElectron Emission Microscopy

XANES X-ray Absorption Near Edge Structure (XANES)

XAS X-ray Absorption Spectroscopy

XPS X-ray Photoelectron Spectroscopy

XRF X-Ray Fluorescence

ZDDP Zinc DialkylDithioPhosphate

Chapter 1

Introduction

1.1 Background

At the Fifth Lubrication and Wear Convention, which took place in Plymouth - UK in 1967, David Tabor, a research professor at Cambridge University, presented a paper entitled “The Contribution of a Physicist to Tribology”. In this paper, he mentioned one important event in 1939 at the beginning of World War II, when he and Prof. Philip Bowden were trying to find a suitable name for their laboratory. This laboratory was dealing with topics related to friction and wear. It was not until the end of the war in 1945 when Tabor suggested to Dr. Stewart Bastow to choose the name "Tribo-physics" [1]. This name was derived from the Greek word ‘tribos’ meaning rubbing or sliding. Tabor commented that the choice served the purpose of “mystifying our sponsors so that all sorts of research activities could be undertaken in the course of our more general frictional investigations” [1]. What Tabor and his colleges did not realise at the time was that they were not discussing only a laboratory name but also the birth of a new field of science, i.e. tribology. All these efforts and years of work culminated in the publication of a landmark report by Jost in 1966 [2] on the "Present Position and Industry’s Needs", which addressed the importance of tribology and urged for proactive measures by government, academia and industry to embrace its concepts. The name tribology was quickly adopted by a committee of the Organisation for Economic Cooperation and Development in 1967 [3]. Soon after the committee defined tribology, it was used everywhere to address any issue that dealt with friction, wear or lubrication and it was recognised as a formal discipline. However, it should be mentioned that significant tribological works were accomplished prior to this formal inception of tribology [4].

The widely accepted definition of tribology is the one defined in the Oxford Dictionary "The study of friction, wear, lubrication, and the design of bearings; the science of interacting surfaces in relative motion." [5]. Thus tribology is, in essence, the search for relations between the microscopic interfacial phenomena and the observed macroscopic friction and wear. Furthermore, it often involves finding relationships between force and deformation, called constitutive laws, which is part of the study of contact mechanics. Establishing these relations is one of the most fundamental concepts that gives insight into the behaviour of materials under different operating conditions. Nonetheless, the horizon of tribology extends way beyond that; a good understanding of the tribological properties of soft and hard interfaces provides an essential unified methodology to understand the interplay between the macroscopic observables of friction and wear; and their origin at the microscopic level.

Another very important event took place in 1925 when John H Mackle patented the idea of blending different types of oils to achieve certain tribological properties [6], which is very similar to the current practice of using oil additives. This idea has been realised to be of great importance since then. Blending is considered a cheap alternative for developing new materials with different improved properties without investing in new chemistry. This can be easily demonstrated with the invention of the first known zinc dialkyldithiophosphate (ZDDP) as antiwear additive in 1941 by various groups including Lubri-zol, American Cyanimid and the Union Oil Company [7]. When the contacting surfaces are rubbing against each other, the ZDDP additive decomposes with a certain mechanism or possibly multi-stage mechanism [8] to form a protective antiwear film, which is called a tribofilm, on the contacting surfaces that helps mitigate wear. This functionality is very difficult to be achieved with plain oils without additives.

1.2 Motivation

One of the biggest challenges for industry is friction and wear, which consume material, energy and ultimately money. For example, in the automotive industry about 28% of the fuel energy is wasted due to friction losses in engine and transmission [9]. Therefore, by reducing friction by 1%, the annual fuel consumption worldwide is projected to be reduced by 1 billion litres based on the total consumption in 2015 (Fig. 1.1) [10]. Furthermore, more than 1% saving in the Gross National Product (GNP) of many industrial counties, such as USA [11], UK [2] and China [12], can be achieved through a proactive practice of tribology that optimises friction, wear and lubrication.

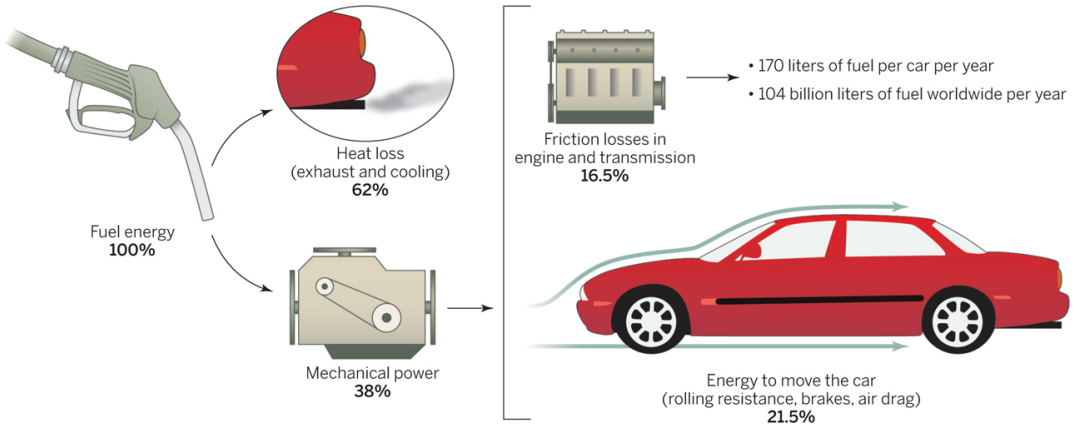

Fig. 1.1 Overview of the average energy consumption of a typical internal-combustion-engine passenger car. Reprinted from Schwarz [10].

One of the proactive measures taken by industry to reduce friction and wear is the use of oil additives such as molybdenum dithiocarbamate (MoDTC) and zinc dialkyldithiophosphate (ZDDP). MoDTC additive is used mainly as a friction modifier. It decomposes at high temperature and under shear to form MoS_2 sheets on the contacting surfaces, which reduce friction due to their interlayer sliding [13]. On the other hand, phosphorus containing additives such as ZDDP are widely used in the automotive industry as antiwear and antioxidant additives [7]. They can mitigate wear by i) forming a rigid sacrificial interface, called a tribofilm, at the contacting surfaces thus preventing adhesive wear [14–18], ii) digesting sharp particles worn from the contacting surfaces thus mitigating abrasive wear [19–21], iii) decomposing peroxy radicals thus limiting surface oxidation [22–24], or iv) a combination of the previous mechanisms. However, despite its ubiquitous use and many advantages, ZDDP contains zinc and phosphorus, which can degrade the catalyst performance of the catalytic converter in the vehicle's exhaust system and thus increases harmful emissions [25, 26]. Therefore, ever-growing strict environmental rules are currently imposed to reduce or zero the concentrations of Zn and P in the formulated oils [7].

In order to replace the ZDDP with more environmentally friendly additives, extensive experimental and modelling works have been carried out to understand its decomposition reactions, the formation and removal of its formed protective tribofilms and the possible interaction between other additives and substrates [7, 27]. However, the complete nature of the tribochemical reactions occurring on the rubbing surfaces under shear is still not fully understood. The rate of the decomposition reactions of oil additives and the associated rate of their tribofilms' formation under different operating conditions and on different surfaces are still yet unexplored areas though highly important for optimising the running-in period that can help reduce friction and wear. Furthermore, the role of the available

cations in the oil such as iron in the tribofilm formation is still controversial. Several studies [19, 20, 24, 28] suggested that iron is needed for the formation of tribofilms such as the ones of ZDDP. On the other hand, other studies [29–32] found that these tribofilms can form on surfaces other than steel.

The major obstacle in obtaining better understanding of the transient tribochemical nature at the tribological contacts is mainly due to the inability to directly probe the contact area, at which the tribochemical reactions occur. Most of the previous studies were carried out ex-situ after the tribological test is stopped and the contacting surfaces are cooled down and separated.

The alteration of the initial state of the sample brings about several limitations. Firstly, the surface analysis will be performed under different conditions from the test environment. This can change the composition of the newly formed surface film by exposing it to a new environment of different temperature and relative humidity [24, 33]. Furthermore, it can expose the surface to adventitious entities or contaminants such as carbon [34], which can attenuate the measured atomic concentrations depending on the electrons inelastic mean free path through the elements under study [35]. Secondly, rinsing the surface with a solvent to remove the excess oil, which is the typical practice before carrying out the ex-situ analysis especially under ultra-high vacuum (UHV) conditions, can remove part of the tribofilm layers and hence part of the information can be lost after washing [36]. Thirdly, the fact that the surface can only be probed after finishing the tribological test prevents capturing the early stage of the tribofilm formation. Therefore, it can severely limit our understanding of the dynamical tribochemical nature of oil additives and conceals the occurrence of any side reaction and the identification of any precursors or intermediates.

Another important but yet unexplored aspect, which can help replace the ZDDP additive with more environmentally friendly additives, is related to the exact origin of its superior antiwear protection. The majority of the previous works attributed this to the rigid sacrificial nature of the formed protective tribofilms on the rubbed metallic surfaces after the additive decomposes in the oil [14–18]. However, few studies speculated that the good antiwear properties of the formed tribofilm might have a rheological origin related to the ability of the film to flow. This can greatly influence friction, lubrication and adhesion properties of any tribological surface [37].

1.3 Research objectives

This study aims at obtaining a mechanistic understanding of the link between the rheological and mechanical properties, e.g. viscosity, tenacity and durability, of the antiwear tribofilms and their composition and ultimately their tribological performance in terms of friction and wear. In order to achieve this goal, we aim at fulfilling the following objectives:

1. To develop an in-situ miniature pin-on-disc tribotester and couple it with synchrotron XAS or Raman spectroscopy, which will help understand the reaction kinetics of antiwear additives and the composition evolution of the formed tribofilms in-situ and under realistic operating conditions.
2. To develop creep-based and squeeze flow-based methodologies using the AFM technique for measuring the rheological properties, i.e. creep and viscosity, of antiwear tribofilms.
3. To develop a heating liquid cell and couple it with the AFM in order to perform in-situ tribotests while probing the formed tribofilms over time. This will enable us to understand the evolution of the formation, structure, mechanical and rheological properties of antiwear tribofilms over time.

The results from the newly developed techniques will be combined with the results of various ex-situ techniques, including XPS, FIB-EDX and MTM-SLIM, in order to obtain corroborating evidence supporting the newly measured properties.

1.4 Thesis outline

The thesis is divided into nine chapters. Chapter one introduces the topic of the PhD and discusses the motivation and objectives of studying antiwear tribofilms. It also states the problem of the study, which is basically the lack of full understanding of the interplay between the composition of the tribofilm and its tribological, mechanical and rheological properties due to the limitations of the currently used experimental techniques. Chapter 2 discusses the basics of tribology, rheology and contact mechanics from the macro- to the nano-scale. It also reviews the possible characterisation techniques and the possible methods to quantify the bulk and interfacial rheological and mechanical properties of the formed tribofilms. Chapter 3 presents and discusses the state-of-the-art concerning P-based antiwear additives, such as ZDDP and DDP, and the different tribological, mechanical and rheological

properties of their formed tribofilms. It also describes the composition evolution until the mature tribofilm is formed. Chapter 4 describes the materials and methods that are used in this study. Chapter 5 presents the ex-situ results of the experimental work performed using XPS and FIB-EDX. On the other hand, the in-situ experimental results using XAS and AFM are presented in chapter 6 and 7, respectively. Chapter 8 provides an overall discussion of the results obtained in this study. Finally, chapter 9 summarises the important aspects discussed throughout the thesis and draws overall conclusions based on the obtained ex-situ and in-situ results. In addition, it highlights the limitations of the current work and suggests recommendations for future work.

Chapter 2

Basics of tribology, rheology and contact mechanics

This chapter reviews the basics of the main topics that will be needed to analyse the tribological and rheological experimental data. The chapter is divided into four main sections. The first section discusses the basics of tribology, i.e. friction and wear, from the macroscale to the nanoscale. Section two reviews the basics of rheology. In addition, it provides an overview of the models that can be used to fit the rheological data whether in bulk or using the AFM. Section three discusses various contact mechanics topics based on the elastic and plastic deformation theories. Finally, section four summarises the most important aspects discussed throughout the chapter.

2.1 Tribology: from macro- to nanoscale

Friction and wear are solely interfacial phenomena, which can be affected by the mechanical, rheological and chemical properties of the contacting surfaces and any adsorbed layers in between [38]. The properties of contacting surfaces include amongst others roughness, hardness, crystallinity, defects, viscosity and shear strength [39, 40]. These factors act on different length and time scales. The complexity of such a system can only be analysed and fully understood if the effects of each factor, which has the capacity to affect friction and wear, are studied independently and collectively by exploring the inter-synergy. Hence, one may study, for instance, the effect of surface roughness on friction and wear at the macroscopic scale using any of the conventional tribological rigs with different samples of different degrees of surface roughness. On the other hand, one could study the effect of surface roughness at the microscopic scale using AFM in

which the tip represents a single asperity contact. Ye et al. [40] measured the friction coefficient of the ZDDP tribofilm using conventional pin-on-disc rig and lateral force AFM. The reported values from the two techniques were in good agreement, which demonstrated the capability of the AFM to measure friction force successfully. More details on the advances of single asperity nano-tribology can be found in the review of Szlufarska et al. [41].

In the following subsections, the basics of friction and wear at the macro- and microscopic scales are reviewed in more detail.

2.1.1 Friction

Macroscopic friction is more established than the microscopic counterpart. The general observation of the macroscopic friction is that friction force, F_f, depends linearly on the applied normal load, F_n. The proportionality constant, μ, is the static coefficient of friction. This relation can be given as [42]:

$$F_f = \mu F_n \tag{2.1}$$

Several studies [43–47] showed that this relation holds true even for the microscopic friction, at least up to 250 nN, which corresponds to a very large contact pressure of a few GPa. Pidduck and Smith [48] showed that above 200 nN, a substantial increase of friction force occurred with increasing load. The authors related this behaviour to two possible reasons. One might be due to the removal of surface layers whereas the other could be related to non-linearity in the AFM cantilever or detector. Tsukruk et al. [49] observed a similar behaviour for monolayers of steric acid cadmium salts. The microscopic force observed by the AFM increased linearly with increasing the normal load until reaching 100 nN at which the friction force reached a plateau and then started to increase linearly with load. However, loads larger than 700 nN caused the friction force to increase substantially and deviate from the linear trend. The increase in the friction force was accompanied by a decrease in the monolayers thickness and vice versa. The plateau region was small that a linear fit for the data below a load of 700 nN was possible.

It should be noted that in the case of any adhesion force exists between the contacting surfaces, then an additional force is needed to separate the two surfaces. In this case, the friction force is given by [50]:

$$F_f = \mu(F_{\text{adh}} + F_n) = F_0 + \mu F_n \tag{2.2}$$

where $F_0 = \mu F_{\text{adh}}$ is a constant representing the contribution of adhesion to friction force. Meyer et al. [51] showed that below a certain threshold of normal force, i.e. 4 nN, the friction force measured on the bare silicon wafer or the one covered with Langmuir-Blodgett (LB) film was constant. According to this study, this behaviour might be related to changes in the adhesion and elasticity forces at the interface. These changes can influence the effective normal force directly. Mate et al. [52] also observed that before the linear increase of friction force over the normal load, a region of constant friction force appeared at small-applied loads between 1 and 2.5 nN. They attributed this region to stick-slip phenomenon occurring between the AFM tip and the graphite plane that had the same periodicity as the atomic structure of the probed surface. Mate et al. [52] suggested that the friction force observed at the microscopic scale had two contributions, i.e. a conservative direction-independent and dissipative direction-dependent contribution. The conservative part of the friction force can originate from the reversible elastic deformation of the tip, sample or substrate. On the other hand, the origin of the dissipative part can be related to plastic deformation or wear of the tip, sample and substrate; viscous dissipation or phonon generation.

Bowden and Tabor [53] showed that although the friction force at the macroscopic scale does not depend on the nominal contact area, it is directly proportional to the real contact area, which is recently confirmed by many studies [43, 44, 46, 54–61]. In the case of dry contacts, the friction force depends on the real contact area A_r as follows:

$$F_f = A_r \tau_d \tag{2.3}$$

whereas in the case of lubricated contacts:

$$F_f = A_r \left[\alpha \tau_d + (1 - \alpha)\, \tau_l\right] \tag{2.4}$$

where τ_d is the average shear strength of the dry contact, α is the fraction of the unlubricated dry area of the contact and τ_l is the average shear strength of the lubricant film, which is given by:

$$\tau_l = \frac{\eta \nu}{h} \tag{2.5}$$

where η is the viscosity of the lubricant film, h is the film thickness and ν is the relative sliding velocity. It should be noted that the exact value of α is not known. Hence, if a full coverage can be assumed, i.e. $\alpha = 0$, the relation becomes easier to implement with only two unknowns, A_r and τ_l. The real contact area A_r can

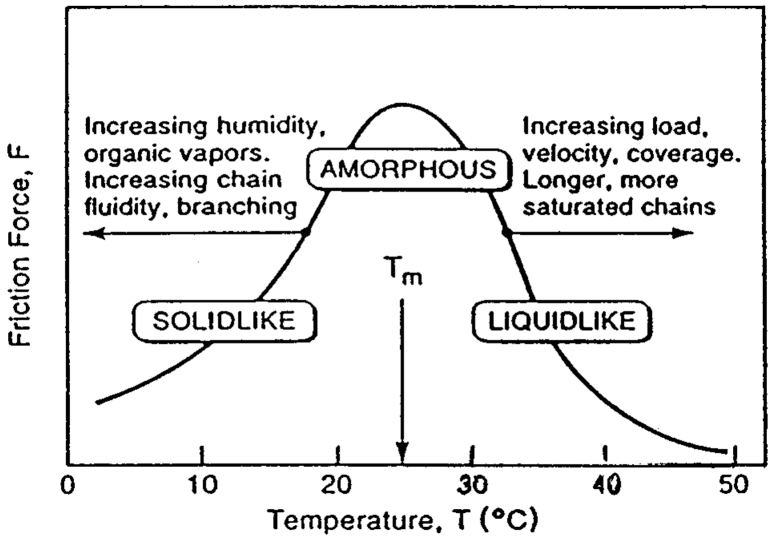

Fig. 2.1 Schematic of friction phase diagram of surfactant monolayers. Reprinted from Singer [64].

be calculated based on the contact radius given by any of the contact mechanics models discussed in section 2.3. For instance, in the case of Johnson-Kendall-Roberts (JKR) contact radius is used, the following relation can be obtained for the friction force:

$$F_f = \tau_l \pi \left[\frac{R}{E_r} \left(F + 3\pi R\gamma + \sqrt{6\pi R\gamma L + (3\pi R\gamma)^2} \right) \right]^{2/3} \tag{2.6}$$

It should be noted that this relation depends on the sliding speed through τ_l. The formula for τ_l can be used from Eq. (2.49) for low sliding speed or Eq. (2.50) for high sliding velocity, which were discussed in section 2.3. These formulae give a logarithmic dependence of friction force on the sliding velocity, which was confirmed by Gnecco et al. [62] for low velocities. However, Tsukruk et al. [49] indicated that a more complex relation between friction force and velocity exists. Liu et al. [63] showed that this complex relation can depend on the functional groups, phase transition, degree of saturation and chain length of the molecules forming the surface layer. Singer [64] and Yoshizawa et al. [50] showed that indeed a phase transition occurs with local temperature, which is affected by the sliding speed, as shown in Fig. 2.1. Similar behaviour could also be present in the case of the alkyl phosphate precipitates and polyphosphates layers forming the ZDDP antiwear film.

2.1.2 Wear

Wear is a stress controlled phenomenon, i.e. increases with increasing the normal load. In addition, recent studies suggested that wear might be a stress history dependant as well [65]. This can be explained by observing that the successive rubbing causes the surface atoms to be less stable and hence the surface becomes more prone to wear. There are mainly two views concerning the way the microscopic wear commences. The first one suggests that wear is consistent with plastic deformation and removal of nanoscale fragments. This was observed for silicon nitride AFM tips [66]. The other view conjectures that the microscopic scale wear occurs as a gradual atom-by-atom process with a stress-assisted thermally activated mechanism [65]. This was observed for smooth AFM tips coated with diamond-like carbon (DLC) [65, 66].

Following the first view, the total volume of sliding wear can be described by the Archard equation for macroscopic wear, which in its basic form is given by [67]:

$$V_w = K\frac{F_n D}{H} \tag{2.7}$$

where K is the dimensionless wear coefficient, F_n is the normal load, D is the sliding distance and H is the hardness of the softest contacting surfaces. The dimensionless wear coefficient can be used to relate the real contact area, A_r, consisting of N number of asperities to the worn contact area, A_w, consisting of n number of worn asperities, as follows:

$$K = \frac{V_w}{(F_n/H)\,D} = \frac{V_w}{V_p} = \frac{A_w}{A_r} = \frac{n}{N} \tag{2.8}$$

where $V_p = (F_n/H)D$ is the total volume of the plastically deformed surface. This means that K can also be used as a representation of the ratio of the volume removed by wear to one that is plastically deformed [68]. Regardless of its simplicity, Archard's equation seems to be successful in capturing the general trend of the macroscopic as well as the microscopic wear, as shown in Fig. 2.2. Nonetheless, Archard's equation has many limitations. For instance, the only considered material property is hardness. In addition, it does not take into account surface topography, time, speed, lubricant or lubrication regime [69]. However, it should be noted that other models than Archard's equation exist, which can also capture wear phenomena [70].

Following the other view of atom-by-atom wear, the wear rate of, for instance, an AFM tip can be represented by the change in the tip height h over time t, which can be given by [71]:

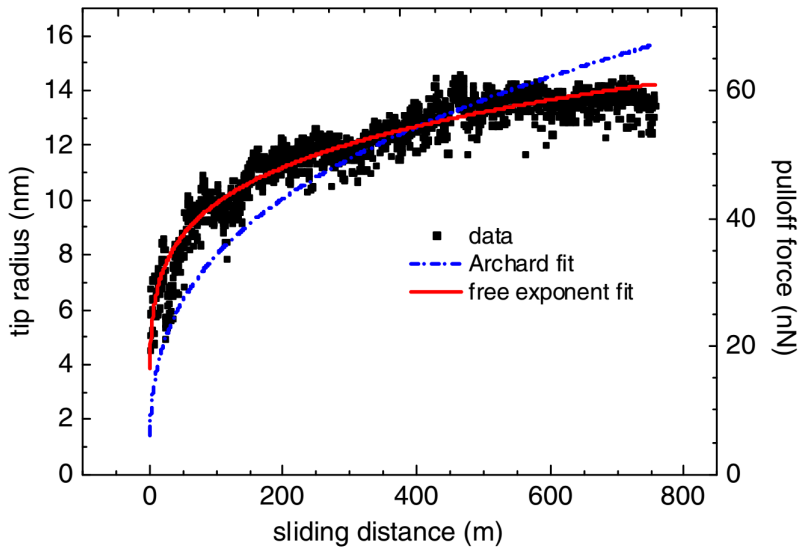

Fig. 2.2 Effect of sliding distance on the microscopic wear. Reprinted from Gotsmann et al. [71].

$$\frac{\partial h}{\partial t} = b f_{\mathrm{a}} \exp\left(-\frac{E_{\mathrm{a}} - V_{\mathrm{a}}\sigma}{k_{\mathrm{B}}T}\right) \tag{2.9}$$

where f_{a} is the attempt frequency that is of the same order as the atomic vibration, b is the lattice parameter, E_{a} is the activation energy, σ is the shear stress, k_{B} is the Boltzmann constant, T is the absolute temperature and V_{a} is the activation volume, which is an empirical material property rather than a physical one. This activation volume represents the amount of activation energy reduced through bond stretching by the effect of shear stress. Based on Eq. (2.9), Jacobs et al. [72] suggested that the number of atoms lost per second Γ can be given by:

$$\Gamma = \left[f_a \exp\left(-\frac{E_a}{k_{\mathrm{B}}T}\right)\right] \exp\left(\frac{\sigma V_a}{k_{\mathrm{B}}T}\right) \tag{2.10}$$

This is exactly the same as Eq. (2.9) suggested by Gotsmann and Lantz [71] but taking $b = 1$. The number of atoms lost per second Γ can be related to the total wear volume V_{wear}, as follows [65]:

$$\Gamma = \frac{V_{\mathrm{wear}} \times \rho_{\mathrm{bulk}}}{A_{\mathrm{cont}} \times \rho_{\mathrm{surf}} \times t_{\mathrm{cont}}} \tag{2.11}$$

where ρ_{bulk} and ρ_{surf} are the number density of the bulk and surface of the probed material, A_{cont} is the contact area and t_{cont} is the contact time. Based on these equations, the instantaneous wear rate of a conical tip of opening angle θ and radius a, moving under normal load F_{appl} and adhesion force F_{adh} with sliding

velocity $\nu = \partial d/\partial t$, where d is the sliding distance, can be given by [71] :

$$\frac{\partial a(d)}{\partial d} = \tan(\theta)\left(\frac{f_a b}{\nu_0}\right) \times \exp\left[-\frac{E_a}{k_B T} + \frac{V_a}{k_B T}\left(\tau_0 + \xi\frac{F_{\text{appl}} + F_{\text{adh}}}{\pi a^2}\right)\right] \tag{2.12}$$

where ξ, τ_0 and ν_0 are constants, which can be chosen as follows: ξ can be considered as the pressure dependence of shear stress, τ_0 is the shear stress at zero pressure, and ν_0 is a characteristic velocity. Gotsmann and Lantz [71] could fit this model successfully to the micro-wear data shown in Fig. 2.2, which seemed to give a better fit than Archard's equation. However, this proposed model concerns mainly activation energies occurring during sliding friction at small velocity. To account for large sliding velocities, Jacobs et al. [73] proposed a modification to Eq. (2.12). They assumed that the activation parameters for friction, which predominate at small velocity, are different from the ones for wear, which predominate at high velocity, as follows:

$$\frac{\partial a(d)}{\partial d} = \tan(\theta)\left(\frac{f_a b}{\nu_0}\right)\left(\frac{\nu}{\nu_0}\right)^{\left(1.5\frac{\Delta V_{\text{wear}}}{\Delta V_{\text{ftiction}}}-1\right)} \times \exp\left[-\frac{E_a}{k_B T} + \frac{\Delta V_{\text{wear}}}{k_B T}\left(\tau_0 + \xi\frac{F_{\text{appl}} + F_{\text{adh}}}{\pi a^2}\right)\right] \tag{2.13}$$

It should be noted that these different views of wear at the microscopic scale will help in finding good interpretations of the observed phenomena not only at the microscale but also at the macroscale. In addition, they give insight into the amount of force and number of taps or sliding distance that can be used without causing much wear of the AFM tip. This is crucial to avoid the misinterpretations brought by the changes of the contact area and hence contact pressure.

2.2 Rheology: basics and models

The rheological properties of materials are used mainly to probe not only the viscosity but also the microstructure. This can be performed using rheometry [74], which utilises standard methods such as steady shear, oscillatory shear, stress relaxation and creep in order to obtain shear viscosity, storage and loss moduli, relaxation modulus and creep compliance, respectively [75]. Oscillatory shear, creep and stress relaxation are discussed thoroughly in the subsequent sections due to their relevance to the in-situ AFM tribotests performed in this study.

2.2.1 Small Amplitude Oscillatory Shear (SAOS)

In the small amplitude oscillatory shear (SAOS) experiments, an oscillatory shear of small amplitude is applied. The small load is necessary such that the microstructure of the material being probed in undisturbed and thus the measured properties are only limited to the linear viscoelastic regime [74]. The SAOS experiments can be performed in stress- or strain-controlled mode. In the latter, a sinusoidal oscillating strain of a fixed amplitude γ_0 over a frequency sweep ω is applied, which can be expressed as [76]:

$$\gamma = \gamma_0 \sin(\omega t) \tag{2.14}$$

The resulting stress of amplitude σ along with the phase difference δ between the oscillating strain γ and stress σ are measured.

In the case of Newtonian fluids, the applied strain and resulting stress will be completely out of phase, i.e. $\delta = 90^{\circ}$. So, in this case the resulting stress can be given as:

$$\sigma = \eta\dot{\gamma} = \eta\dot{\gamma}_0 \cos(\omega t) \tag{2.15}$$

where η is the viscosity, and $\dot{\gamma}$ is the shear rate.

In the case of elastic solids, the applied strain and resulting stress will be completely in phase, i.e. $\delta = 0^{\circ}$. So, in this case the resulting stress can be given as:

$$\sigma = G\gamma = G\gamma_0 \sin(\omega t) \tag{2.16}$$

where G is the shear modulus.

In the case of viscoelastic materials, the applied strain and resulting stress will be partially out of phase, i.e. $\delta < 90^{\circ}$. So, in this case the resulting stress will have two components: an elastic one in phase with the strain and an out of phase viscous component:

$$\sigma = \sigma_0 \sin(\omega t + \delta) \tag{2.17}$$

which can be rewritten as:

$$\sigma = (\sigma_0 \cos\delta) \sin(\omega t) + (\sigma_0 \sin\delta) \cos(\omega t) \tag{2.18}$$

where $G' = (\sigma_0 \cos\delta)$ is the elastic or storage modulus and $G'' = (\sigma_0 \sin\delta)$ is the viscous or loss modulus. The ratio between the two moduli ($\tan\delta = G''/G'$) is called the loss tangent, which serves as an indication to how much the material

is more elastic or viscous. A $\tan\delta \ll 1$ indicates that the material behaviour is mainly elastic whereas a $\tan\delta \to 1$ indicates a prevalent viscous behaviour [77].

2.2.2 Creep–Recovery

In the creep experiments, a constant shear stress σ_0 is maintained and the time-dependent resulting strain $\gamma(t)$ is monitored. The applied stress should be kept small enough to preserve the material structure without distortion but large enough to get a good signal-to-noise ratio [78, 79]. When the shear stress is stopped at $t = t_1$, i.e. $\sigma(t_1) = 0$, the strain keeps evolving in what is called recovery experiment as illustrated in Fig. 2.3. The strain $\gamma(t)$ during the creep-recovery experiments can be given by [80]:

$$\gamma(t) = \gamma_0 + \gamma_r(t) + \left(\frac{\sigma_0}{\eta_0}\right) t \tag{2.19}$$

where γ_0 is the strain at $t = 0$, η_0 is the zero shear viscosity, and $\gamma_r(t)$ is the recoverable strain, which can be given as:

$$\gamma_r(t) = \gamma(t_1) - \gamma(t) \tag{2.20}$$

The creep compliance $J(t)$ can then be defined by dividing the resulting strain $\gamma(t)$ by the applied stress σ_0:

$$J(t) = J_0 + J_R\psi(t) + \frac{1}{\eta_0}t \tag{2.21}$$

where J_0 is the instantaneous creep compliance, J_R is the total recoverable compliance, and $\psi(t)$ is the delayed elasticity function. This function is typically zero at $t = 0$ and one for $t \longrightarrow \infty$. In the case of a Kelvin-Voigt model is used, which consists of a spring of constant G connected in parallel to a dashpot of viscosity η, $\psi(t)$ can be defined as follows:

$$\psi(t) = J_m\left[1 - \exp(-t/\tau_m)\right] \tag{2.22}$$

where J_m is the mean compliance and τ_m is the mean retardation time.

Based on Eq. (2.21), the creep-recovery response as schematically represented in Fig. 2.3, shows three main regions [76]:

- Region (A) of elastic deformation represented by the instantaneous compliance $J_0 = 1/G_0$, which is the inverse of the elastic modulus G_0. This part of deformation can be recovered instantaneously if the stress is removed.

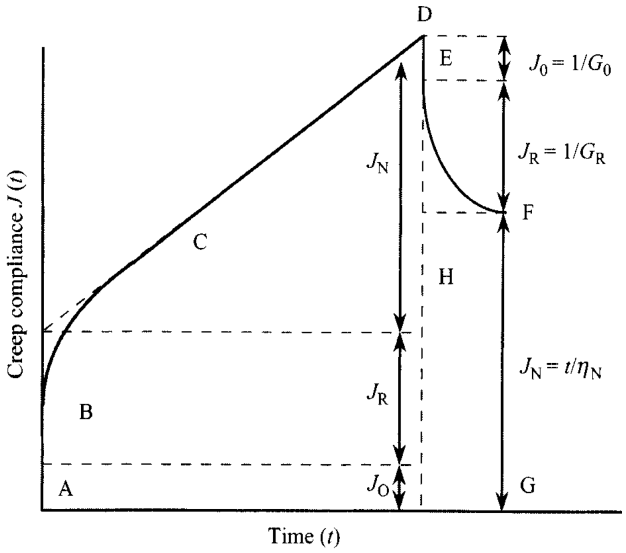

Fig. 2.3 Illustration of a creep compliance curve during creep-recovery experiment. Reprinted from Rao [76].

- Region (B) of retarded elastic deformation that evolves over time. The compliance J_R in this region depends on the delayed elasticity function $\psi(t)$. This part of deformation can be completely recovered if the stress is removed but will take long time depending on $\psi(t)$.
- Region (C) of viscous flow represented by non-recoverable compliance $J_N = t/\eta_0$. This part of deformation cannot be recovered if the stress is removed because part of the material structure is permanently deformed or distorted.

The recovery experiment starts with an instantaneous recovery of J_0 in region (E). This is followed by a slow retarded recovery of J_R in region (F).

2.2.3 Stress relaxation

The stress relaxation experiments are performed by maintaining a constant deformation, i.e. strain, on the sample while measuring the stress evolution over time [81]. For viscoelastic materials of instantaneous and delayed deformation, the response can be represented by a Maxwell model [77], which consists of a spring of constant G connected in series to a dashpot of viscosity η. If this mechanical system is deformed by a constant strain, the dashpot will have slow relaxation of time $\tau = \eta/G$ accompanied by the retraction of the spring. The shear modulus of the system can be defined as [77, 81, 82]:

$$G(t) = \frac{\sigma(t)}{\gamma} = G\exp(-t/\tau) \tag{2.23}$$

As real viscoelastic materials would have infinite number of relaxation times depending on the microstructure, the above equation becomes [82]:

$$G(t) = \int_1^\infty G_i \exp(-t/\tau_i) \tag{2.24}$$

For simplicity, the summation form of this equation for a limited number of relaxation times can also be used instead of the integral form.

2.3 Contact mechanics

The subject of contact mechanics studies the deformation behaviour of materials through, for example, examining the loading-unloading response when subjected to a specified level of force or deformation. In the case of ideally elastic materials, the material undergoes certain deformation during loading whereas after unloading the material restores its original shape completely as depicted schematically in Fig. 2.4. However, for ideally plastic materials, the material does not restore its shape but retains its deformed shape instead. The real material typically has a mixed behaviour between the ideally elastic and plastic responses, i.e. restores part of the deformed shape and retains part of the deformation. This behaviour is predominated by not only the mechanical properties of the sample but also the geometrical and mechanical properties of the probe itself [83, 84]. Even after taking into account the influence of the tip properties, the loading-unloading curves can still not necessarily be unique. For instance, a material with heterogeneity could have the same non-linear response as viscoelastic materials [85]. In the next subsections, the contact mechanics of elastic and plastic materials will be reviewed in more detail.

2.3.1 Elastic deformation theories

The most used elastic deformation models are Hertz [86], Johnson-Kendall-Roberts (JKR) [87], and Derjaguin-Muller-Toporov (DMT) [88]. In the case of a spherical probe of radius R exerting force F on a flat surface, one can use these models to calculate the contact radius a, the sample indentation δ, the contact pressure P and the adhesion force F_{adh} as listed in Table 2.1.

In this table, $x = y/a$ is the distance from the centre of the contact circle where $x = 1$ is the edge of the contact area, R_r is the reduced radius of curvature of the two contacting surfaces (in the next equations the subscript will be dropped

for simplification) and E_r is the reduced elastic modulus, which is defined as:

$$\frac{1}{E_r} = \frac{3}{4}\left(\frac{1-\nu_1^2}{E_1} + \frac{1-\nu_2^2}{E_2}\right) \tag{2.25}$$

where E is the Young modulus and ν is the Poisson ratio. The subscript 1 refers to the sample and 2 refers to the indenter. The above equation can be rearranged to get the reduced indentation modulus of the sample:

$$E_{r-1} = \frac{E_1}{(1-\nu_1^2)} = \left[\frac{4}{3}\frac{1}{E_r} - \frac{(1-\nu_2^2)}{E_2}\right]^{-1} \tag{2.26}$$

The elastic modulus of the sample is a combination of the elastic modulus of the film and the one of the substrate. This can be deduced from the indentation modulus using Song and Pharr model [89]:

$$\frac{1}{E_{r-1}} = (1-I_0)\frac{1}{E_s} + I_0\frac{1}{E_f} \tag{2.27}$$

where I_0 is given by:

$$I_0 = \frac{2}{\pi}\arctan\left(\frac{t}{a}\right) + \frac{1}{2\pi(1-\nu_f)} \times \left[(1-2\nu_f)\frac{t}{a}\ln\frac{1+(t/a)^2}{(t/a)^2} - \frac{(t/a)}{1+(t/a)^2}\right] \tag{2.28}$$

where the subscripts f and s refer to the film and substrate, respectively, and t is the film thickness. After determining E_f and E_s, the global stiffness K_z can be

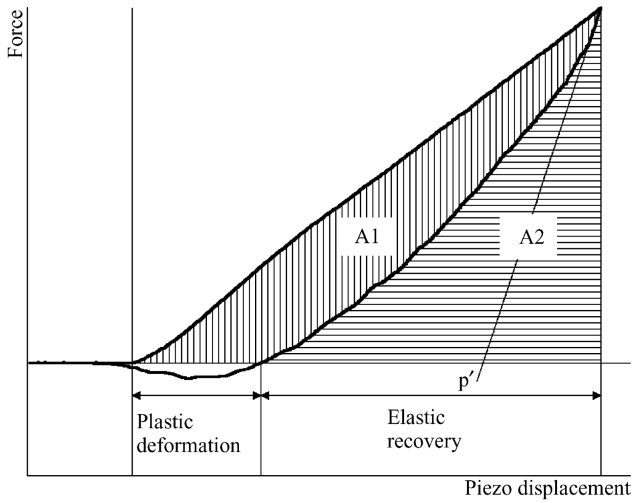

Fig. 2.4 Typical loading-unloading behaviour of linear elastic material, straight line, and nonlinear material, hysteresis. Reprinted from Butt et al. [83].

Table 2.1 Summary of models of contact mechanics [83, 90].

	Hertz	JKR	DMT
a	$\left(\frac{R_r F}{E_r}\right)^{1/3}$	$\left[\frac{R_r}{E_r}\left(F+2\pi R_r\gamma\right)\right]^{1/3}$	$\left[\frac{R}{E_r}\left(F+3\pi R\gamma+\sqrt{6\pi R\gamma L+\left(3\pi R\gamma\right)^2}\right)\right]^{2/3}$
δ	$\frac{a^2}{R_r}=\left(\frac{F^2}{RE_r^2}\right)^{1/3}$	$\frac{a^2}{R_r}=\frac{\left(F+2\pi R_r\gamma\right)^{2/3}}{\sqrt[3]{RE_r^2}}$	$\frac{a^2}{R_r}=\left(\frac{6\pi a\gamma}{E_r}\right)^{2/3}$
P(x)	$\frac{3E_r a}{2\pi R_r}\sqrt{1-x^2}$	$\frac{3E_r a}{2\pi R_r}\sqrt{1-x^2}$	$\frac{3E_r a\sqrt{1-x^2}}{2\pi R_r}-\sqrt{\frac{3E_r\gamma}{2\pi a}}\frac{1}{\sqrt{1-x^2}}$
F_{adh}	0	$2\pi R_r\gamma$	$\frac{3}{2}\pi R_r\gamma$

defined as [36]:

$$\frac{1}{K_z}=\frac{1}{1+2t/\pi a}\left(\frac{t}{\pi a^2 E_f}+\frac{1}{2aE_s}\right) \tag{2.29}$$

In case of the applied pressure value exceed a certain threshold value H_0, some molecular arrangements might occur in the film that can change the mechanical properties of the film such as its elastic modulus. To overcome this, Bec et al. [36] proposed that the film modulus E_f could be given by:

$$E_f=E_{f_0}\left(\frac{P}{P_0}\right) \tag{2.30}$$

where E_{f_0} is the elastic modulus of the film when the applied pressure P is lower than some threshold value of P_0.

It should be noted that there will be always uncertainties in measuring the film thickness and its elastic modulus. Bec et al. [91] presented a guide to determine the elastic properties of a thin film on substrate from nanoindentation experiments. They compared the previous model proposed by Bec et al. [36] with the models proposed by Perriot and Barthel [92], Gao et al. [93] and Rar et al. [94]. The authors concluded that the uncertainties in the film thickness and elastic modulus lead to similar results regardless of the choice of the model.

From Table 2.1, the work of adhesion per unit area, γ, can be related to the surface tension of the tip-medium γ_{tm}, sample-medium γ_{sm} and sample-tip γ_{st} according to Duprè equation [83]:

$$\gamma=\gamma_{tm}+\gamma_{sm}-\gamma_{st} \tag{2.31}$$

The work of adhesion depends on many factors including surface roughness, surface contamination and alignment of atoms of the tip and substrate [95, 96]. Typically, the surface tension of material-air is the easiest to measure using pendant drop measurements. Apart from this method, the surface tension between two materials can also be calculated using the Good-Girifalco-Fowkes rule [97]:

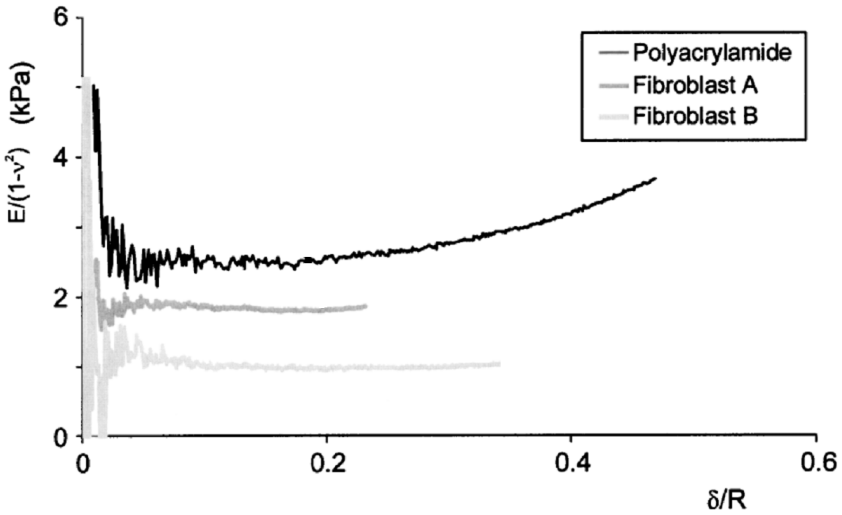

Fig. 2.5 Effect of indentation depth, as compared to the tip radius, on the measured Hertz modulus. Reprinted from Mahaffy et al. [98].

$$\gamma_{12} = \gamma_1 + \gamma_2 - 2\Phi\sqrt{\gamma_1\gamma_2} \tag{2.32}$$

where Φ is equal to unity in the first order approximation. However, in case of the molar volumes, V, of the two materials are different, then Φ can be calculated using the formula [97]:

$$\Phi = \frac{4\left(V_1 V_2\right)}{\left(\sqrt{V_1} + \sqrt{V_1}\right)^2} \tag{2.33}$$

Hertz model does not take into account the adhesion force between the indenter and sample. Thus, it can be applied when the adhesion force is negligible as compared to the applied load. In addition, the model suffers from other limitations. These limitations become obvious by plotting the model's prediction, $\frac{3}{4}F/\sqrt{R\delta^3} = E/\left(1-\nu^2\right)$ against the function δ/R. The expected result should be a straight horizontal line representing a constant force or modulus with the different indentation depths. However, the results of Mahaffy et al. [98] on a polyacrylamide film and two fibroblasts showed that this model holds true only at intermediate indentation depths, as shown in Fig. 2.5. If the depth is small, the uncertainties of the position of contact creates large variance on the measured force or modulus. However, if the indentation depth approaches the radius of the spherical probe, the results deviate from Hertz model as this model is based on the assumption of spherical contact area. One way to circumvent the difficulty in determining the contact radius accurately is by using the force integration to equal limits (FIEL) approach developed by A-Hassan et al. [99]. This approach overcomes the problems of identifying the exact contact area between the tip and sample and the exact cantilever spring constant. The FIEL is based mainly on

the Hertz model that relates the force of the AFM cantilever to the indentation depth using the relation:

$$F = E_r \sqrt{R} \delta^{3/2} \tag{2.34}$$

Thus, probing two locations at the surface while imposing the condition $F_1 = F_2$, leads to:

$$E_{r1} \sqrt{R} \delta_1^{3/2} = E_{r2} \sqrt{R} \delta_2^{3/2} \tag{2.35}$$

Taking the integral of the force gives the work done by the probe at every position:

$$w_1 = \int_0^{\delta_1} E_{r1} \sqrt{R} \delta_1^{3/2} \mathrm{d}\delta = \frac{2}{5} E_{r1} \sqrt{R} \delta_1^{5/2} \tag{2.36}$$

Similarly,

$$w_2 = \frac{2}{5} E_{r2} \sqrt{R} \delta_2^{5/2} \tag{2.37}$$

Thus, the relative work at the two probed locations can be given by:

$$\frac{w_1}{w_2} = \left(\frac{E_{r1}}{E_{r2}} \right)^{2/3} \tag{2.38}$$

This ratio relates the work directly to the local reduced elastic modulus E_r. This avoids any error due to uncertainties of measuring the contact area or the Poisson ratio. Nevertheless, the FIEL approach suffers from different limitations. One of the limitations is the assumption of sample isotropy. In addition, the approach is based on the Hertz model and therefore it suffers, in principle, from the same limitations of this model including the assumption of no adhesion force.

It was found experimentally that load dependence on contact area is in good agreement with the DMT model [44, 58] or JKR model [60]. In the case of large tips and soft samples with large adhesion force, the JKR model can be applied whereas the DMT model can be used in the case of small tips and stiff samples with small adhesion force. A better criteria to choose which of the models should be applied is to use the parameter λ that was proposed by Maugis [100], which is given by:

$$\lambda = \frac{2.06}{D_0} \left(\frac{R \gamma^2}{\pi E_r^2} \right)^{1/3} \tag{2.39}$$

where D_0 is a typical atomic dimension, which can be taken as the separation distance between the tip and substrate in repulsive contact. To calculate this parameter, the work of adhesion and the reduced elastic modulus must be known. At the asymptotic limit of $\lambda \to 0$, the DMT model should be used, whereas when $\lambda \to \infty$, the JKR model should be used. Between those limits, the extended Maugis model, described elsewhere [100], should be used.

Apart from the parameter λ, the Tabor coefficient can also be used to decide which model is more appropriate. This coefficient represents the ratio between the adhesion interaction and elastic deformation as follows [101]:

$$\mu = \left(\frac{16R\gamma^2}{9D_0^3 E_r^2} \right)^{1/3} \tag{2.40}$$

Typically, for $\mu \gg 1$, soft material is encountered and hence the JKR model is more appropriate. The analytical and experimental results of Greenwood [102] confirmed the validity of this coefficient.

Fogden and White [103] generalised the Hertz and JKR models by considering the force arises due the presence of condensible vapour atmosphere. The extent to which capillary forces might distort the contact is governed by the parameter k, which is defined as:

$$k = \frac{3\pi^{1/2} E_r \left(r_k - \frac{1}{2} D_0 \right)^{3/2}}{2^{3/2} \left(2\gamma_{\mathrm{LV}} R^{1/2} \right)} \left(1 - \frac{D_0}{2r_k} \right)^{-1} \tag{2.41}$$

where r_k is the Kelvin radius of the formed meniscus and γ_{LV} is the surface tension of the meniscus fluid with air. The parameter k is typically large, i.e. less distorting effect, for systems consisting of small and hard spheres. In this case the generalised Hertz model can be given by:

$$F = \frac{E_r}{R} \left[a^3 - 4\pi\gamma_{LV} \left(1 - \frac{D_0}{2r_k} \right) R^2 \right] \tag{2.42}$$

On the other hand, when the parameter k is small, i.e. large distorting effect in the case of large and soft spheres, the generalised Hertz model can be given by:

$$F = \frac{E_r}{R} \left[a^3 - (a_0 a)^{3/2} \right] \tag{2.43}$$

where a_0 is the contact radius at zero load. This generalised Hertz model shows that due to capillary condensation forces, the load F changes by a certain value equals to the capillary force. This indicates that the capillary force can produce

similar behaviour to adhesion, which is taken into account in the DMT and JKR models by a shift in the applied load [54].

The different previously discussed models are valid for spherical probes. For other shapes, the force-indentation follows a power law related to the probe geometry, which is given by [104]:

$$F = \alpha\delta^n \tag{2.44}$$

where α and n are constants related to the geometry of the probe, e.g. $n = 2$ for cones and $n = 1.5$ for spheres and paraboloids [83]. Apart from the probe geometry, temperature can affect the mechanical properties predicted by the previously discussed models. For example, Wachtman et al. [105] proposed that the Young's modulus depends on temperature according to the relation:

$$E(T) = E(0) - BT\exp\left(\frac{-T_0}{T}\right) \tag{2.45}$$

where $E(0)$ is the Young's modulus at temperature of 0 K and B is a constant related to Grüneisen parameter γ and Debye temperature Θ_D, which is given by:

$$\Theta_D = \frac{\hbar\nu_D}{k}\left(\frac{6\pi^2 N}{V_0}\right)^{\frac{1}{3}} \tag{2.46}$$

where ν_D is Debye velocity, k is the Boltzmann constant, N is the Avogadro number, $\hbar$ is the reduced Planck constant ($\hbar = h/2\pi$) and V_0 is the atomic volume at 0 K. Taking the value of the B constant into account, Grüneisen and Debye proposed the following expression [106, 107]:

$$E(T) = E(0) - \frac{9\left(1-2\nu_D\right)\pi^4 R\Theta_D\gamma\left(3\gamma-1\right)}{5V_0}\left(\frac{T}{\Theta_D}\right)^4 \tag{2.47}$$

Another expression can also be found using the Einstein oscillator [107]:

$$E(T) = E(0) - \frac{3\left(1-2\nu_D\right)s}{\left(exp\left(\frac{\Theta}{T}\right)-1\right)} \tag{2.48}$$

where Θ is the effective Einstein temperature and s is a parameter related to the contribution of zero point vibration energy to elastic stiffness. Adiga et al. [107] found that for ultrananocrystalline diamond (UNCD) in the range of temperature between 63 K and 450 K, Einstein oscillator expression was a better fit to the experimental data than Grüneisen and Debye expression.

Temperature accompanied by sliding can also alter the shear stress at the interface. Briscoe and Evans [108] related the shear stress τ to temperature, normal pressure $P = (F_{\text{app}} + F_{\text{adh}})/(\pi a^2)$ and velocity ν using the equation:

$$\tau = \tau_0 + \xi P \left(\frac{k_{\text{B}}T}{V_{\text{a}}}\right) \ln\left(\frac{\nu}{\nu_0}\right) \tag{2.49}$$

where τ_0, ξ and ν_0 are constants. This relation is valid for low sliding speeds. For higher speeds, the relation can be given by [109]:

$$\tau = \tau_0 - \Delta F \ln\left(\frac{\nu}{\nu_0}\right)^{2/3} \tag{2.50}$$

where τ_0 and ΔF are constants.

Several remarks should be mentioned on the elastic deformation theories, especially Hertz, DMT and JKR models. One is that they are based on the assumption that a perfectly smooth probe of well-defined shape is contacting a perfectly flat and smooth plane. Obviously, this assumption is not always fulfilled as the probe might be worn even over the first few indentations in addition to the fact that real surfaces are not necessary smooth or isotopic. This can lead to errors in calculating the contact area and deformation; and ultimately the elastic modulus and hardness [110]. The other remark is that in the case that these models are used to quantify AFM indentation data, some errors might arise from the buckling of the AFM cantilever. That is to say, the AFM cantilever does not apply only a normal force but also a friction force due to its slight sliding in the lateral direction. The generated friction force, although small in magnitude, can interfere with the mechanical properties that are being probed [111–113].

2.3.2 Plastic deformation theories

During indentation tests, some plastic deformation might occur as illustrated in Fig. 2.4. Several studies proposed different treatments to account for this response. For instance, Oyen and Cook [114] presented a practical guide for the analysis of the deformation data. In addition, Nix [115] established an in-depth analysis of the mechanical properties in the case of thin films and described in detail the stresses occurring in these films. Oliver and Pharr [84] established a method to determine the modulus and hardness of materials when subjected to a specified level of force or deformation. This method is the most cited and most used of all other methods. The novel method takes into account the nonlinear curvature of the unloading curve by letting the contact area change continuously during

unloading. The analytical solution and the dynamic model they proposed to solve this problem can be found in the original paper. More recently, Oliver and Pharr [116] reviewed the mechanics governing the elastic-plastic indentation and updated their original method for calculating the elastic modulus and hardness. From the force displacement data, similar to the one depicted in Fig. 2.4, the plasticity index ψ_p can be defined as the ratio between the energy used for plastic deformation A_1 and the total energy dissipated, i.e. for elastic and plastic deformations, $A_1 + A_2$, as follows [83]:

$$\psi_p = \frac{A_1}{A_1 + A_2} \tag{2.51}$$

The reduced elastic modulus E_r and hardness H of the sample can be calculated using the following formulae [83, 116]:

$$\frac{dF}{d\delta}|_{\delta_{max}} = \frac{2\beta_1}{\sqrt{\pi}} E_r \sqrt{A_{max}} \tag{2.52}$$

$$H = \frac{F_{max}}{A_{max}} = \frac{F_{max}}{\beta_2 P'^2} \tag{2.53}$$

where β_1 and β_2 are geometrical parameters that depend on the indenter, A_{max} is the maximum contact area at the maximum indentation δ_{max} and P' is the intercept of the slope of the last linear part of the unloading curve with the abscissa.

The accurate determination of hardness and Young's modulus of ultra-thin tribofilms on hard substrates requires several considerations. First, the indentation depth should be typically less than 20% of the film thickness in order to avoid any substrate effect. Second, the exact contact area of the indenter into the sample A_{max} should be carefully determined, which in turn requires a careful determination of the exact indenter shape and indentation depth. Different factors could affect the measurement of contact area [116]. These include tip defects, pile-up or sink-in phenomena around the indent and surface roughness [117]. One way to circumvent these issues is to image the contact area by AFM or other imaging techniques to find A_{max} [83]. However, there are different difficulties of using AFM as imaging technique. One of the main difficulties is the applied force that should be as low as possible to avoid scratching or wearing the surface especially if extremely soft or easily deformed. Bec et al. [117] found that the contact area A and radius of contact a can be related to the theoretical plastic penetration depth δ as follows:

$$A = \frac{\delta^2}{\alpha} \tag{2.54}$$

$$2a = \frac{\delta}{\beta} \tag{2.55}$$

$$\delta = h_R h_0 \tag{2.56}$$

where α and β are constants depending on the geometry of the indenter, h_R is the tip defect height and h_0 is the measured plastic depth. These values can be compared to the values obtained by the imaging techniques to check their validity for the system under study.

2.4 Summary and concluding remarks

The chapter reviewed some basic topics related to the tribological, mechanical and rheological characterisation of ultra-thin tribofilms. The chapter reviewed the basics of tribology, i.e. friction and wear, from the macroscale to the nanoscale. It also discussed in detail the basics of rheology and contact mechanics including relevant models that can be used to quantify the mechanical and rheological properties of ultra-thin films such as ZDDP and DDP tribofilms. The reviewed models and literature will help better analyse the various obtained experimental data.

In the following chapter, a state-of-the-art review is presented about the tribological, mechanical and rheological properties of the ultra-thin ZDDP and DDP tribofilms. In addition, the link between these properties and the composition of the formed tribofilms as well as the effect of the operating conditions are discussed thoroughly.

Chapter 3

Literature review

This chapter reviews the state-of-the-art knowledge about the composition of ZDDP and DDP antiwear films as well as their tribological, mechanical and rheological properties. In addition, it discusses the effect of operating conditions on these properties and the different techniques used to characterise them. The chapter is divided into nine main sections. The first one introduces the different antiwear additives. Section two discusses their physical and chemical nature. Section three presents the reactions of the P-based additives in base oils and their decomposition mechanisms, i.e. thermal, hydrolytic and oxidative. Section four provides a detailed discussion on the composition of the ZDDP and DDP antiwear films. The recent findings, tools and methods to examine the mechanical, rheological and tribological properties of these films are discussed in sections five, six and seven, respectively. Section eight reviews the effect of water on these properties at the macro- and microscopic scales. Finally, section nine summarises and draws conclusions on the most important aspects and knowledge gaps discussed throughout the chapter.

3.1 Introduction

Zinc dialkyldithiophosphate (ZDDP) is one of the most widely used additives, whether in oils or greases. ZDDP is multifunctional as it can work as antiwear, antioxidant and anticorrosion additive [118]. It exhibits these beneficial functionalities by its ability to decompose under rubbing, heating or possibly high pressure to form a protective film. In the case of this film is formed during heating without rubbing it is called a thermal antiwear film whereas in the case of rubbing, the film is called a tribofilm [119]. The antiwear mechanism of this tribofilm originates from its capability to separate the contacting surface [14–18], to digest

the abrasive wear debris [19–21] and to decompose peroxides and peroxy-radicals [22–24].

Despite the numerous benefits of using the antiwear ZDDP additive, it has disadvantages as well. Firstly, ZDDP increases micropitting of the steel surface and thus decreases its bearing life [120–123]. Secondly, it can poison the catalyst in the cars equipped with a catalytic converter and therefore degrades the converter's capability to reduce harmful emissions in the exhaust gas [25, 26]. This led to an ever expanding strict rules on the allowed concentrations of ZDDP, phosphorus and zinc in the oil [7, 89]. The trend of these rules suggests that the ZDDP should be replaced. One of the available options is to use neutral or acidic ashless dialkyldithiophosphate (DDP). The ashless additives can provide better [124, 125], comparable [126] or worse [127, 128] antiwear properties than the ZDDP, which seem to depend greatly on the operating conditions, properties of contacting surfaces and chemistries of base oil and additives.

Replacing the ZDDP completely is not an easy task due to the lack of complete understanding of the complex pathways involved in its decomposition reactions and the possible interactions with the other additives in the oil. This statement is also true for the case of the DDP, which shares in general the same complexity. Nonetheless, despite these difficulties, a myriad of experimental works were carried out over the last 70 years in order to understand the ZDDP decomposition reactions. These works have been discussed in different reviews [7, 129, 130]. The review of Barnes et al. [129] discussed the role of the ZDDP in the oil and its functions as an antioxidant and antiwear additive. In addition, the review covered the interactions between the ZDDP and various other components that can be present in the oil. The ZDDP review of Spikes [7] presented a historical overview of the additive starting from its inception until its current use. The review focused on the reaction mechanisms of the ZDDP in the oil and the composition of the formed protective tribofilm and its formation and removal kinetics. It also examined the contribution of different experimental techniques to our current understanding of the ZDDP tribochemistry. Finally, the review of Nicholls et al. [130] focused on the decomposition reactions of the ZDDP in the absence and presence of other components in the oil, the composition of the formed tribofilms and their mechanical properties. This review is the last one focusing on the ZDDP and was presented more than a decade ago.

It should be noted that the early works in the field of tribology focused on using a single surface characterisation technique such as XPS, FTIR and EDX to study the complex tribochemistry of the ZDDP and DDP tribofilms. However, every technique, despite its numerous advantages, has certain limitations as summarised

Table 3.1 Comparison between the surface characterisation techniques.

Method	Atmosphere[a]	Sensitivity	Chemical information	Structure	Lateral resolution	Detected depth
XPS	UHV	1 %	Yes	No	10 μm	3-8 nm
AES	UHV	1 %	Yes	No	20 nm	3-8 nm
XAS	UHV-A	50 ppm	Yes	Yes	50 nm-mm	1 nm - bulk
EDX	HV	0.1 %	No	No	1 μm	1 μm
Raman	A	0.1 at.%	Yes	Yes	1 μm	0.2-10 μm
FTIR	A	1 ppm	Yes	Yes	10-100 μm	20 Å-1 μm
SIMS	HV	$<$ 1 ppm	No	No	60 μm	0-10 μm
XRD	A	1 %	No	Yes	30 μm	0.1-10 μm
XRF	A	1 ppb	No	No	1 cm	Bulk
AFM	A	NA	No	Yes	$<$ 0.1 Å	0.1 Å

[a] Experimental atmosphere whether ambient (A), high vacuum (HV) or ultra-high vacuum (UHV).

in Table 3.1, which are mainly related to the experimental atmosphere; whether ambient (A), high vacuum (HV) or ultra-high vacuum (UHV); detection sensitivity, chemical and structural information capability, lateral resolution and sampling depth. Therefore, as more and more of these techniques become available added to the insufficient information gathered from a single technique only, the recent tribological studies have started employing what is commonly known as the multi-technique approach. In this approach, observations and evidence are collected from various experimental techniques to help understand not only the composition but also the tribological and mechanical properties of ZDDP and DDP tribofilms.

Despite the extensive research in the tribological and mechanical properties of the ZDDP and DDP tribofilms and their compositions, the link between these properties is still not clear. This review aims at discussing these properties and highlighting the different links between them in order to provide a clearer picture on their tribochemistry in the base oil and the properties of the formed antiwear films. As the main body of the literature is related to the ZDDP and due to the large similarities between the ZDDP and DDP additives, the focus of this review will be mainly on the ZDDP while making a direct comparison to the DDP whenever appropriate.

3.2 Chemical nature of ZDDP and DDP

Most of the added ZDDP to the base oil is either neutral, basic or hybrid of both [7, 129, 131, 132], which are depicted in Fig. 3.1. Similarly, the DDP can be either neutral, acidic or a mixture of both, as depicted in Fig. 3.2. The

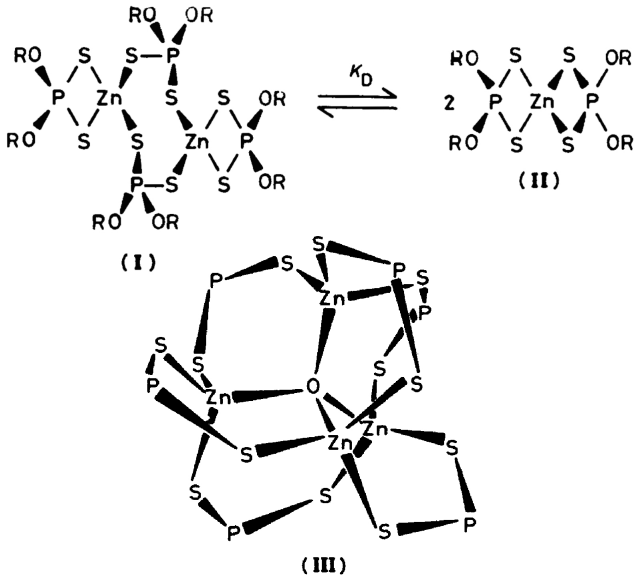

Fig. 3.1 The different structures of ZDDP: (I) neutral dimeric in equilibrium with (II) neutral monomeric; (III) basic ZDDP. Reprinted from Harrison and Kikabhai [133].

neutral ZDDP usually exists in equilibrium state between the monomeric structure ($Zn[PS_2(RO)_2]_2$) shown in Fig. 3.1(i) and the dimeric one ($Zn_2[PS_2(RO)_2]_4$) shown in Fig. 3.1(ii) [133]. On the other hand, the basic ZDDP is stable and has a structure with the chemical formula ($Zn_4[PS_2(RO)_2]_6O$) [131, 132, 134, 135], which is depicted in Fig. 3.1(iii).

Within these types of ZDDP and DDP additives, new categories can be defined as primary, secondary, tertiary, etc, depending on the number of carbon atoms, i.e. one, two or three respectively, that are attached to the carbon atom of the alkyl (R) group [134]. These functional groups predetermine the thermal stability of the additive, which can be arranged as follows [132]:

$$\text{aryl} > \text{primary alkyl} > \text{secondary alkyl}$$

It is interesting to note that the least thermally stable additive provides the best wear protection. Therefore, according to the alkyl functional group (R), the wear protection performance can be arranged as follows [7]:

$$\text{secondary alkyl} > \text{primary alkyl} > \text{aryl}$$

This can be attributed to the fact that primarily the decomposition process of the additive is thermally activated, which will be discussed in more detail in the subsequent sections.

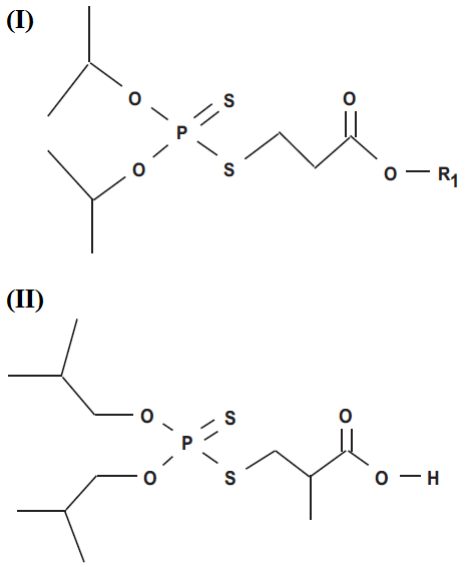

Fig. 3.2 The different structures of DDP: (I) neutral and (II) acidic DDP. Reprinted from Kim et al. [136].

3.3 Reactions of ZDDP and DDP

Different theories were proposed to explain the reactions of P-based additives, such as ZDDP and DDP, in lubricating oils, which can be grouped into three main categories [7]: i) ligand exchange, ii) peroxides and peroxy-radicals decomposition and iii) thermal, oxidative or hydrolytic degradation. These reactions can have very complex pathways due to the fact that the commercial oils containing ZDDP or DDP may as well contain some impurities, other additives, detergents or dispersant that might alter these paths and ultimately alter the precursors and the final reaction products forming the tribo- or thermal films [137].

To avoid such complexities, the three reactions mentioned earlier will be discussed in detail in the following sections assuming that only the P-based additive is present in the oil.

3.3.1 Ligand exchange

During the ligand exchange reaction, the zinc cations (Zn^{2+}) in the ZDDP or any of its decomposition products can be exchanged by another cation. For example, the Zn^{2+} in the monomeric form of the neutral ZDDP can undergo a ligand exchange reaction with another metal ion (M^{2+}), as follows [7]:

$$Zn[PS_2(RO)_2]_2 + M^{2+} \longrightarrow M[PS_2(RO)_2]_2 + Zn^{2+} \tag{3.1}$$

The relative order of the ability of one cation to replace another one is as follows [138]:

$$Pd^{2+}>Au^{3+}>Cu^{+}>Cu^{2+}>Fe^{3+}>Pb^{2+}>Zn^{2+} \tag{3.2}$$

This means that Zn^{2+} can be replaced easily by Fe^{3+}, which can be released from the metal surface as a result of wear of parts of the contacting surfaces. This reaction is very important as the nature of the metal cations in the substrate or the metal dialkyl dithiophosphate molecules can alter the thermal decomposition process by changing the decomposition temperature and kinetics and possibly the final composition of the formed tribofilm [139].

3.3.2 Decomposition of peroxides and peroxy-radicals

Peroxides and peroxy-radicals can oxidise the steel surface as follows [22]:

$$ROO\dot{} + Fe \longrightarrow R\dot{O} + FeO \tag{3.3}$$

$$2\,ROOH + Fe \longrightarrow 2\,R\dot{O} + 2\,OH^{-} + Fe^{2+} \tag{3.4}$$

$$ROOH + Fe^{2+} \longrightarrow R\dot{O} + OH^{-} + Fe^{3+} \tag{3.5}$$

Several studies [22, 23] found that in the presence of hydrogen peroxide, the oil that has antiwear additives, such as ZDDP, results in less wear than the oil without the additive. This suggested that one of the different antiwear mechanisms to protect the contacting surfaces is by decomposing the peroxides and hence terminating the oxidation chain reaction. However, other authors noted that when the antiwear additive acts as an antioxidant additive it cannot completely protect the surface from wear [140]. This indicates that the additive is used in decomposing the peroxides instead of forming a protective film. Therefore, there is a need to tailor the proactive tribological considerations based on not only the general application but also the operating conditions while inspecting the compatibility between the additive and contacting surfaces [141].

3.3.3 Formation of tribo- and thermal films

The currently accepted view on the formation of tribo- and thermal films regards the decomposition of P-based antiwear additives as a thermally-activated and stress-assisted reaction [30, 142, 143], which can be catalysed by either heat or

mechanical action in the form of rubbing or shear at the interface of the contacting bodies. Nevertheless, the classical view of this decomposition reaction considers it as a chemical reaction that can be either thermal, oxidative, hydrolytic or hybrid. These mechanisms will be discussed in detail in the following sections while highlighting the effect of rubbing on the reaction kinetics and the final decomposition products.

3.3.3.1 Thermal decomposition

Numerous studies suggested that the decomposition of the ZDDP or DDP additive occurs thermally [136, 137, 144–146], which means that the extent and rate of the decomposition process are temperature dependent. The high temperature is especially needed at the early stage of the decomposition process as reported by Jones and Coy [8]. This was based on the observation that after the initial decomposition of the ZDDP at high temperature, the decomposition continued at a high rate even at low temperature as indicated by the continuous formation of white deposition in the oil. This suggested that the reaction can be multistage where intermediates must be formed before the final products. The initial stage of this multistage reaction can occur at elevated temperature in solution [30, 137, 147–149] or on the steel surface, which was argued to be essential for this process [15, 38, 150, 151].

In the case that the steel surface is not required, it was suggested that the formation of the protective film at high temperature can occur due to an in-situ deposition process on the steel surface by one or more of the following mechanisms [149]:

1. Polymerisation of small molecules to form a complex large molecule on the steel surface.
2. Isomerisation of one or more of the additive molecules to other molecules deposited on the steel surface as a protective layer.
3. Decomposition of the additive molecules and the deposition of the resulting products on the steel surface.
4. Chemical reaction between two or more intermediate molecules to form the surface layer.

On the other hand, Coy and Jones [150] suggested that the availability of the steel surface can play a vital role in the thermal decomposition process. A reaction

Table 3.2 Classification of the hard and soft acids and bases relevant to ZDDP [154].

Type	Hard	Soft	Borderline
Acid	tetravalent phosphorus –P–	Tetravalent carbon (CH_4)	ferrous Fe^{2+}, Zn^{2+}
Base	H_2O, OH^-, O^{2-} Phosphoryl (P=O), PO_4^{-3} , ROH, RO-, SO_4^{-2}	Thiophosphoryl (P=S) Thiolate (RS^-) Phosphine (PR_3)	sulphite (SO_3^{-2})

with the steel surface can transform the organic phosphates into inorganic ones, which can subsequently polymerise to a range of polyphosphates [8].

Jones and Coy [8] explained these reactions based on Pearson's hard and soft acids and bases (HSAB) principle [152–156]. The principle suggests stable pathways for any chemical reaction according to the general observation that hard acids prefer to form bonds with hard bases whereas soft acids favour forming stable compounds with soft bases. Following the hardness classification of the acids and bases of the most relevant compounds to ZDDP and DDP additives, which are summarised in Table 3.2, Jones and Coy [8] proposed that the following chain of reactions can take place during the thermal decomposition of the ZDDP:

1. Migration of the soft acid alkyl from the hard base oxygen atoms to the soft base sulphur atoms of thiophosphoryl (P=S)

2. Formation of phosphorus acid as a result of the elimination of the thioalkyl (−SR) functions.

3. Formation of phosphates P−O−P as a result of the nucleophilic reaction of one hard acid tetravalent phosphorus O−P in one short phosphate segment with a hard base oxygen bonded to another phosphate segment O−P.

4. Formation of zinc mercaptide $Zn(SR)_2$ as intermediate, which upon reaction with an alkylating agent forms dialkyl sulphide whereas upon reacting with mercaptide forms dithiophosphate, trithiophosphate and finally tetrathiophosphate.

5. Formation of a mixture of zinc thiophosphate, zinc pyro-thiophosphate and zinc polypyro-thiophosphate as a final deposition.

Although the predictions of Jones and Coy [8] do not entirely match the current consensus that the final decomposition product is a mixture of zinc pyro-, poly- and meta-phosphate glass, the way they utilised the HSAB principle to explain

the thermal decomposition reaction was revolutionary at the time. They were one of the first to explore the thermal decomposition mechanism not as a black box but as a tractable chain of chemical reactions in which several intermediates can be identified. It took nearly two decades until Martin and co-workers [19] explored the HSAB in more detail to explain various important parts of the ZDDP reactions using the chemical hardness approach while matching the predictions with the experimental findings. This will be discussed in the following section.

3.3.3.2 Thermo-oxidative decomposition

A number of studies proposed that the decomposition reaction of the P-based additives is a thermo-oxidative in nature. Willermet et al. [157] suggested that the antiwear additive decomposition takes an oxidative pathway in the case of an equimolar quantity of free radicals is present in the oil, otherwise a thermally controlled decomposition occurred. However, the authors pointed out that in some localised areas of a thermally controlled decomposition, products of a thermo-oxidative controlled decomposition coexisted as well. Based on this observation, they concluded that apart from the availability of free radicals, stress plays a controlling role in determining the predominant decomposition pathway. To test the hypothesis of the thermo-oxidative controlled decomposition, which is controlled by the availability of O_2, Willermet et al. [157] conducted their tribological experiments in air and argon atmospheres. In the two cases, they did not observe any differences in the tribofilm composition. This should have necessary ruled out the oxidative decomposition mechanism. However, the authors argued that the experimental conditions somehow did not allow the oxidative decomposition to compete well with the thermal one. This apparent discrepancy can be related to the role of the ZDDP as an antiwear additive and oxidation inhibitor [7, 129], i.e. helps decompose the peroxy-radicals [158, 159].

Yin et al. [118] proposed a thermo-oxidative mechanism for the ZDDP tribofilm growth starting with the strong chemisorption of the ZDDP to the oxide layer on the steel surface followed by the fast formation of long polyphosphate chains and the slow formation of short polyphosphate chains, which can be summarised as follows:

- Step 1: Physisorption or chemisorption

$$Zn[(RO)_2PS_2]_2\,(\text{solution}) \longrightarrow Zn[(RO_2)PS_2]_2\,(\text{adsorbed}) \tag{3.6}$$

- Step 2: Formation of long polyphosphate chains

$$Zn[(RO)_2PS_2]_2 + O_2(\text{or ROOH}) \longrightarrow Zn(PO_3)_2 + \text{sulphur species} \quad (3.7)$$

- Step 3: Formation of short polyphosphate chains

$$Zn(PO_3)_2 + FeO \longrightarrow FeZnP_2O_7 \quad (3.8a)$$

or

$$Zn(PO_3)_2 + 2\,FeO \longrightarrow Fe_2Zn(PO_4)_2 \quad (3.8b)$$

Following Yin et al. [118], Najman et al. [127] proposed similar steps for the decomposition of the DDP additive, as follows:

- Step 1: Physisorption or chemisorption

$$(RO)_3PS_2\,(\text{solution}) \longrightarrow (RO)_3PS_2\,(\text{adsorbed}) \quad (3.9)$$

- Step 2: Formation of long polyphosphate chains

$$(RO)_3PS_2 + O_2 + FeO \longrightarrow Fe(PO_3)_2 + \text{sulphur species} \quad (3.10)$$

- Step 3: Formation of short polyphosphate chains

$$Fe(PO_3)_2 + FeO \longrightarrow Fe_2P_2O_7 \quad (3.11)$$

- Step 4: Formation of sulphate species

$$S + \tfrac{3}{2}\,O_2 + FeO \longrightarrow FeSO_4 \quad (3.12)$$

Similar to the above reactions, Martin and co-workers [19, 20, 160] suggested that the depolymerisation of the initially formed long phosphate chains of the ZDDP tribofilm into shorter ones is a result of their reaction with iron oxides on the steel surface, as follows:

$$5\,Zn(PO_2)_2 + Fe_2O_3 \xrightarrow{\theta,\tau,P} Fe_2Zn_3P_{10}O_{31} + 2\,ZnO \quad (3.13)$$

which can be accompanied by other intermediate reactions, such as:

$$4\,Zn_6(P_{10}O_{29}S_2) + 10\,Fe_2O_3 \longrightarrow 10\,Fe_2Zn(P_2O_7)_2 + 8\,ZnS + 6\,ZnO \tag{3.14}$$

These proposed reactions were justified based on Pearson's principle of hard and soft acids and bases (HSAB) [152]. According to this principle, the harder acid Fe^{3+} than Zn^{2+} will react preferentially with the hard base tetravalent phosphorus. Thus, under high temperature, shear and pressure, iron can be easily digested by the zinc phosphate glass to form mixed iron and zinc phosphates. However, under severe conditions of shear, the authors suggested that the digestion of iron can convert the long zinc phosphate chains completely into short iron phosphate chains according to the following reaction:

$$Zn(PO_3)_2 + Fe_2O_3 \xrightarrow{\theta,\tau,P} 2\,FePO_4 + ZnO \tag{3.15}$$

As these reactions need iron oxide and thus wear to commence near the metal surface, the tribofilm is expected to have a uniform structure of zinc phosphate free of iron in the case of mild wear conditions whereas it should have a layered structure in the case of severe wear. In this structure, the short chains of zinc and iron phosphate or iron phosphate are formed on the metal surface whereas the long chains of zinc phosphate are continuously formed away from the metal surface.

Fuller et al. [28] suggested a thermo-oxidative decomposition mechanism similar to one proposed by Yin et al. [118] but with two main modifications. The first one concerns the additive adsorption (step 1 in Eq. (3.6)). It was suggested that when the antiwear additive such as the ZDDP adsorbs to the steel surface, it undergoes a transformation into a rearranged linkage isomer in which the alkyl groups have migrated from O to S atoms. This alkylation reaction is based on the mechanism proposed by Jones and Coy [8], which was discussed in the previous section. However, Fuller et al. [28] further suggested that in this linkage isomer all the sulphurs are partially or totally replaced by oxygen. The other modification concerns the formation of the short phosphate chains (step 3 in Eqs. (3.8a) and (3.8b)). Instead of being a product of the reaction of the long phosphate chains with iron oxide, the short phosphate chains can also be formed as a product of the reaction between the long phosphate chains and water, which increases with increasing temperature. These steps can be summarised for the case of the ZDDP additive as follows:

- Step 1: Physisorption or chemisorption of ZDDP to the metal surface

$$\mathrm{Zn[(RO)_2PS_2]_2\,(solution)} \longrightarrow \mathrm{Zn[(RO)_2PS_2]_2\,(ZDDP\,adsorbed)} \quad (3.16)$$

- Step 2: Decomposition of ZDDP to LI-ZDDP

$$\mathrm{Zn[(RO)_2PS_2]_2\,(solution)} \longrightarrow \mathrm{Zn[O_2P(SR)_2]_2\,(LI{-}ZDDP\,in\,solution)} \quad (3.17)$$

- Step 3: Physisorption or chemisorption of any LI-ZDDP in oil to the metal surface

$$\mathrm{Zn[O_2P(SR)_2]_2\,(solution)} \longrightarrow \mathrm{Zn[O_2P(SR)_2]_2\,(LI{-}ZDDP\,adsorbed)} \quad (3.18)$$

- Step 4: Thermal-oxidation of ZDDP and LI-ZDDP to form long polyphosphate chains

$$\mathrm{Zn[O_2P(SR)_2]_2 + O_2\,(or\ ROOH)} \longrightarrow \mathrm{Zn(PO_3)_2 + sulphur\ species} \quad (3.19)$$

- Step 5: Hydrolysis of the long polyphosphate chains to form short polyphosphate chains

$$\mathrm{7\,Zn(PO_3)_2 + 6\,H_2O} \longrightarrow \mathrm{Zn_7(P_5O_{16})_2 + 4\,H_3PO_4} \quad (3.20)$$

$$\mathrm{2\,Zn(PO_3)_2 + 3\,H_2O} \longrightarrow \mathrm{Zn_2P_2O_7 + 2\,H_3PO_4} \quad (3.21)$$

Bell et al. [17] suggested that the adsorption step described earlier occurs only on localised areas of the wear scar where asperities are rubbing against each other. This heterogeneity in the adsorption was suggested to be responsible for the noticed heterogeneity of the tribofilm thickness and composition. In addition, the authors suggested that after the adsorption of the rearranged linkage isomer (step 3) and before the formation of the long polyphosphate chains (step 4), sulphide products can react with the steel surface to form iron sulphide (FeS).

3.3.3.3 Hydrolytic decomposition

Few studies suggested that the decomposition of P-based additives such as the ZDDP is hydrolytic in nature, i.e. catalysed by water. In order to provide evidence for this mechanism, Spedding and Watkins [137] showed that in the absence of water, e.g. by heating the sample up to 100-170 ^{o}C in order to evaporate all water

as well as by flooding the sample with dry nitrogen, the decomposition reaction was suppressed. In contrast, when the sample was flooded by water-saturated nitrogen, a rapid decomposition rate was observed. Therefore, they proposed that the following hydrolysis reaction chain can take place:

1. alcohol formation

$$\mathrm{RO{-}P{-} + H_2O \longrightarrow ROH + HO{-}P{-}} \tag{3.22}$$

2. alcohol dehydration to olefin

$$\mathrm{ROH \xrightarrow{H^+} R'{=}CH_2 + H_2O} \tag{3.23}$$

   The sum of the above two reactions demonstrates the catalytic action of water in the overall reaction, as follows:

$$\mathrm{RO{-}P{-} \xrightarrow{H_2O} R'{=}CH_2 + HO{-}P{-}} \tag{3.24}$$

3. polyphosphate formation

$$\mathrm{{-}P{-}OH + HO{-}P{-} \longrightarrow {-}P{-}O{-}P{-} + H_2O} \tag{3.25}$$

4. hydrogen sulphide formation due to the consumption of water by the sulphur species

$$\mathrm{{-}P{=}S + H_2O \longrightarrow {-}P{=}O + H_2S} \tag{3.26}$$

It should be noted that when Spedding and Watkins [137] conducted tests at 200 ^{o}C, at which most of the water should evaporate, the decomposition proceeded without any significant reduction in the reaction rate. Willermet et al. [24] argued that even lower temperatures than 200 ^{o}C could not slow down the reaction rate. This either disproves the hydrolytic decomposition mechanism or simply suggests that more complex reaction pathways or multiple mechanisms, e.g. thermo-hydrolytic or thermo-oxidative-hydrolytic, can take place at the same time.

3.4 Composition of antiwear films

The tribo- and thermal films of P-based additives such as the ZDDP and DDP have a dynamic tribochemical nature as their compositions change continuously during

the decomposition process [118, 161–164]. Nevertheless, the typical decomposition products of such additives are some volatile products, e.g. olefins and mercaptans, and some non-volatile products [146]. The non-volatile products can be oil soluble, e.g. organic sulphur-phosphorus compounds, or can be oil insoluble, e.g. phosphate polymers, zinc or iron thio- and poly-phosphate [8, 144, 146]. This indicates that the formed antiwear films, in general, consist mainly of Zn or Fe, P, S, O and C. This was confirmed using electron probe micro analysis (EPMA) [17, 165], scanning electron microscopy (SEM) [16, 17, 34, 144, 165–167], Auger electron spectroscopy (AES) [16, 34, 157, 165, 166, 168], X-ray fluorescence (XRF) spectroscopy [14, 15, 145, 169, 170], X-ray photoelectron spectroscopy (XPS) [14, 17, 34, 38, 151, 157, 168, 171–174], X-ray absorption near edge spectroscopy (XANES) [28, 118, 161, 163, 172, 175–177] and secondary ion beam spectroscopy (SIMS) [14, 17, 137]. Willermet et al. [34] found that the carbon can only be detected in the thinnest parts of the tribofilm. This suggested that this carbon was originated from the environment or steel substrate but not a real part of the tribofilm. Ancillary experiments conducted by Lindsay et al. [168] supported the same conclusion that carbon existed as a result of adventitious sources, i.e. contaminants. Furthermore, the results of Martin et al. [178] showed that no carbon existed in the samples under study, which confirms its adventitious nature.

It should be noted that although the composition of the tribo- and thermal films are similar they are not completely identical. Kasrai et al. [172] found differences in the ratio of the elements forming the thermal film and tribofilm. Hence, other factors than the high temperature, e.g. reaction with the steel surface, rubbing and high contact pressure, can also play a role in determining the final decomposition products [150, 172].

In the subsequent sections, the decomposition species of the ZDDP and DDP additives will be discussed in detail. Phosphorus, zinc and iron species will be examined first followed by sulphur species. The role of the operating conditions on the formation of these species will be discussed as well.

3.4.1 Phosphorus, zinc and iron species

The solid precipitates of the decomposition reaction of the ZDDP or DDP additive is a complex mixture of zinc or iron polyphosphates depending on the available cations. DDP forms, in general, tribofilms of short chains of iron polyphosphate [127, 136, 164, 179, 180] with a minor concentration of sulphur species consisting mainly of iron sulphate under high contact pressure [181, 182] and iron sulphides, e.g. FeS or FeS_2, under low pressure [164, 181]. On the other hand, the ZDDP

forms tribo- and thermal films of zinc phosphate of different chain lengths and a small content of sulphur in the reduced form of sulphides [8]. The chain length is typically a complex function of the operating conditions, e.g. load and temperature, as well as the type of additives, dispersant and contaminants such as water that can be present in the oil. For instance, in the case of thermal films, increasing the temperature can lead to the formation of longer chains of polyphosphates [137]. However, in the case of tribofilms formed under rubbing, increasing the temperature can lead to the formation of short chain pyrophosphate [146]. This apparent controversy can be attributed to the observation that regardless of the oil temperature short phosphate chains are likely to be formed near the steel surface as a result of the depolymerisation reaction occurring to the long phosphate chains [19, 20, 183–186]. The depolymerisation can occur due to the high shear stress at the asperity-asperity contacts, which can possibly cleave the long phosphate chains into shorter ones, and to wear that can remove the weakly adhered long phosphate chains from the surface [186]. In addition, other studies [19, 20, 183] suggested that in the presence of iron oxide the long phosphate chains are depolymerised into short ones of mixed Fe-Zn or Fe phosphates, as discussed in section 3.3.3.2. The depolymerisation effect is significant especially in the case of ZDDP tribofilms consisting initially of long to medium phosphate chains, whereas it might not affect the short chains of iron phosphate predominantly formed in the case of the DDP additive [181].

The ratios between metal cations (M^+) and phosphorus (P) [187] on the one hand, and between oxygen (O) and phosphorus (P) [157] on the other hand, are useful indicators for the length of the phosphate chains. For instance, in the case of the ZDDP, assuming that the zinc phosphates have a general formula of $x(\mathrm{ZnO}).(1-x)\mathrm{P_2O_5}$, then the chain length n can be related to the ratio of the mole fraction of ZnO, x, to the one of $\mathrm{P_2O_5}$, $1-x$, as follows [188]:

$$\frac{x}{1-x} = \frac{n+2}{n} \tag{3.27}$$

Alternatively, if the zinc phosphate is assumed to have the general formula $\mathrm{Zn_{n+2}[P_nO_{3n+1}]_2}$, for odd n and $\mathrm{Zn_{(n+2)/2}P_nO_{3n+1}}$ for even n, then the chain length can be related to ratio of the atomic concentration of phosphorus to the one of oxygen, as follows [20]:

$$\mathrm{P/O} = \frac{n}{3n+1} \tag{3.28}$$

These two ratios above appeared to give comparable results for the chain length of phosphates [189]. Alternatively, another option to quantify the length of the

phosphate chains would be the intensity ratio of the bridging oxygen (BO) to non-bridging oxygen (NBO) [183, 189–194], as follows:

$$\mathrm{BO/NBO} = \frac{1}{2}\frac{n-1}{n+1} \tag{3.29}$$

Based on Eq. (3.27), the phosphate chains seem to change from metaphosphate ($n \to \infty$) at $x = 0.5$, to orthophosphate ($n \to 1$) at $x = 0.75$. As the chain length changes drastically over a small concentration range of ZnO, or FeO and Fe_2O_3 in the case of DDP, one should examine the presence of zinc and iron more closely. Increasing the metal oxides content of these cations in the phosphate can increase the fragmentation of the long chains and thus depolymerises them into shorter chains [194–197].

3.4.2 Sulphur species

There is no clear consensus on the evolution of the sulphur species present in the tribo- and thermal films. For instance, Bird and Galvin [151] suggested that the thermal film contains sulphur in the form of sulphate and free sulphur whereas the tribofilm contains large patchy areas of sulphide and a small amount of sulphate. Zhang et al. [128] showed that for the ZDDP tribofilms, the evolution of P/S ratio was nearly constant over time, whereas it showed a gradual increase in the case of DDP tribofilms. Kim et al. [136] observed that for the ZDDP the sulphate concentration increases with heating while sulphide decreases possibly due to its oxidation to sulphate. For one of the tested DDPs, both sulphides and sulphates were detected whereas for the other no sulphides were observed but only sulphates with a similar behaviour to the ZDDP. Similarly, Najman et al. [182] showed that the DDP reacts rapidly with the substrate covered with oxides, which leads to the oxidation of the sulphur species into iron sulphate. This was confirmed for both neutral and acidic DDPs [198]. Other studies [127, 181] showed that under high contact pressure, DDP tribo- or thermal films contain Fe sulphate near the steel surface whereas under less harsh conditions initially mixed iron sulphide, as FeS and FeS_2, and sulphate, as $FeSO_4$, are formed where the sulphides can oxidise over rubbing time yielding primarily sulphates at the end.

The role of the operating conditions can explain some of the conflicting results. For instance, Zhang et al. [164] reported that the DDP additive forms mainly FeS whereas the ZDDP forms FeS in the early stage near the metal surface and ZnS in the later stages. The observed sulphides in the case of DDP, which is in

contrast to the previously discussed studies suggesting sulphates, can be related to the different operating conditions used while generating the various tribofilms.

The complex decomposition reaction of the antiwear additives might have several intermediates. One of these intermediates, which might be formed initially in the solution even at low temperature and be deposited on the metal surface, can be a sulphur-rich thiophosphate [144]. Subsequently, when the temperature of the oil is raised or the local temperature at the asperity-asperity contacts of the rubbing surfaces increases due to frictional heating, the reaction between the thiophosphate deposit and rubbing surfaces becomes possible to occur.

The amount of the deposits of the sulphur-rich thiophosphate and its rate depend closely on the thermal stability of the additive. In the case of the ZDDP, Spedding and Watkins [137] found that by increasing the temperature, more of the sulphur is consumed. In contrast, Kim et al. [136] found that for the ZDDP the progression of heating makes the thermal films richer in sulphur whereas for the DDP it makes the films richer in phosphorus. Despite the trend, this indicates that the local temperature during the tribofilm formation can be inferred from the local composition. This is possible by examining the local ratio of zinc to sulphur or phosphorus to sulphur, which indicates the minimum temperature attained during the formation of that part of the tribofilm [144].

Several other studies [14, 16, 17, 127, 128, 164, 179, 182, 199] suggested that the decomposition products can be a result of a direct reaction between the additive and contacting surfaces instead of being formed in the oil and deposited on the surface. This starts with the adsorption of the additive to the steel surface with the maximum coverage occurs when the additive molecules are flat on the surface, which means that the sulphur atoms lay near the surface [199]. Several authors [151, 200–202] have already found that the amount of sulphur chemisorption products are higher on the steel surface. Bell et al. [17] suggested that immediately after the adsorption of the ZDDP to the steel surface, sulphide products from the decomposition of the ZDDP react with the steel surface to form iron sulphides. In agreement with these results, Loeser et al. [173] also found that the amount of sulphur is localised in the areas of high pressure, i.e. asperity-asperity contacts. These various reports indeed corroborate the observation of Dacre and Bovington [199] that initially the four sulphur atoms should be near the steel surface.

Watkins [14] suggested that FeS reacts with the oxide layer to form a eutectic system, which its phase and potential diagrams are depicted in Fig. 3.3. This system has a melting temperature of 900 ^{o}C and was postulated to form a viscous film at the contacting surfaces under extreme conditions. The results of Glaeser

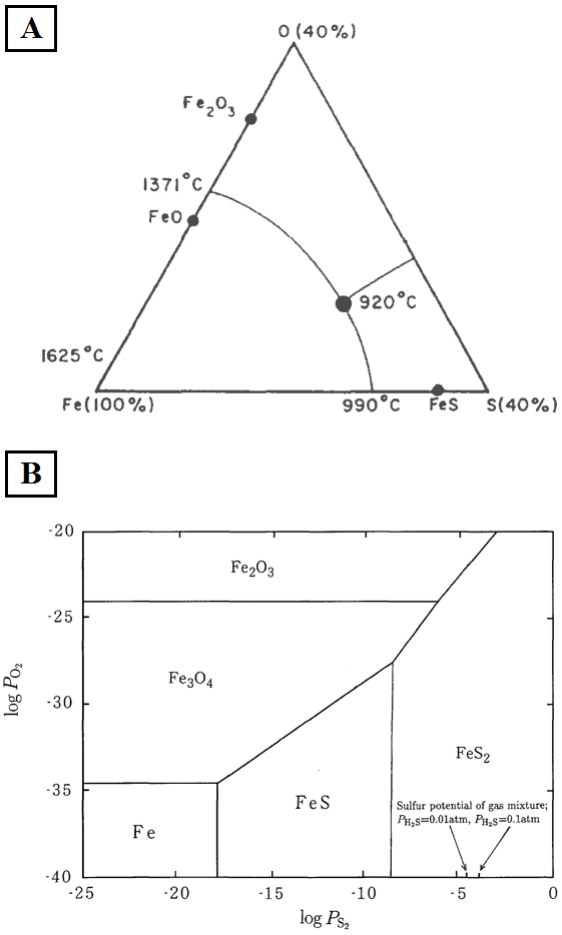

Fig. 3.3 The Fe−O−S ternary system that can be formed on the steel surface under rubbing. (A) is its Phase diagram. Reprinted from Watkins [14]. And (B) is its potential diagram at 673 K. Reprinted from Watanabe et al. [203]

et al. [16] supported the idea of the formation of iron-oxide-sulphide complex. On the other hand, Barcroft et al. [144] could not detect any complex mixture of zinc oxide, phosphate, and sulphide as the one proposed by Watkins [14]. Nevertheless, they suggested that this system can still be formed at the asperity-asperity contacts where temperature can be high. Bell et al. [17] suggested that the iron sulphide and iron oxide can enter the phosphate layer as cations or fragments from the worn surface. They also suggested that the replenishment of sulphur and oxide to the layer on the steel surface occurs continuously either by entrainment, mixing, or diffusion. Similar to these findings, Glaeser et al. [16] suggested that the iron sulphide forms a chemisorbed layer of iron-sulphide-iron oxide that prevents direct contact between asperities.

Nevertheless, it should be noted that other studies [151, 157, 166, 168] showed that iron is absent in the formed tribofilm, i.e. iron detected was mainly iron oxide rather than iron sulphide. These results led to the conclusion that the tribofilm is deposited over the substrate rather than being a result of a chemical reaction

with the rubbing surface. This also suggests that the formation of the tribofilm occurs through a thermal route rather than an oxidative one.

3.4.3 Factors affecting the tribofilms' composition and formation

3.4.3.1 Material of counterbodies

As the additive molecules adsorb to the substrate before decomposing to form a tenacious tribofilm, it is expected that the type of substrate, e.g. steel, DLC-coated, ceramic and etc, should have an important effect on the tribofilm formation and its tenacity. There are two views related to the effect of substrate. The first considers the substrate effect to be mainly related to its mechanical properties such as hardness. On the other hand, the second view considers that the substrate effect is related to a more complex chemo-mechanical rather than mechanical properties of the rubbing interfaces, such as the chemical, electronic and structural properties of the substrate. These two views are discussed in the following sections with much of the emphasis is put on the second.

Mechanical properties: Several studies investigated the effect of the mechanical properties of the substrate, especially hardness and elastic modulus, on the tribofilm formation. The overall conclusion is that the tribofilm formation, friction and wear are affected by not only the mechanical properties of the substrate but also the compatibility between the substrate and additive [141]. For instance, Li et al. [204] used XANES to investigate the effect of steel hardness on the composition of the formed ZDDP antiwear films. The results indicated that longer phosphate chains are formed on the hard substrates. The results also indicated that the softer the substrate the larger the surface roughness, tribofilm thickness, wear scar width and friction. Furthermore, more uniform but thinner tribofilms were formed on the hard substrate but less uniform but thick tribofilms were formed on the soft ones. FIB/SEM was used to examine the elements present in the formed tribofilms and to assess the substrate damage based on the dimensions of the wear scar. It was found that mainly sulphides and few sulphates were formed on the hard substrates whereas the soft ones contained more sulphates and fewer sulphides.

Sheasby et al. [205] also studied the effect of steel hardness on the formation of protective tribofilm and wear performance. The study found that the wear performance was enhanced with increasing the substrate hardness, although wear

was in general small, even for the soft substrates. The results showed that in several occasions, medium softened substrates resulted in less wear than harder substrates. They argued that mechanical mixing can occur between the formed tribofilm and the soft substrate, which can result in improving the overall mechanical properties of the interface and thus better resisting wear. However, the results of Vengudusamy et al. [32], using six different types of DLCs of hardness ranged from about 760 to 6800 HV, suggested that there is no direct correlation between wear resistance of the contacting surfaces and the surface hardness. This further highlights the significance of tailoring the tribological and mechanical properties of the interface by taking into account the compatibility between the substrate and used additives [141].

Chemo-mechanical properties: Apart from hardness, the substrate chemical properties are expected to affect the decomposition of the antiwear additives and the formation of their protective tribofilms. This effect is manifested in the fundamental question of whether there is a substantive requirement for the presence of metal cations, e.g. Fe, W and Ti, for the tribofilm to be formed or such metallic cations are dispensable. There is a definite consensus that the ZDDP molecules can adsorb to steel surfaces and decompose to form protective tribofilms of excellent tenacity [7, 129, 130]. Furthermore, other studies showed that ZDDP tribofilms can also be formed on surfaces other than steel. For instance, Zhang and Spikes [142] were able to generate ZDDP tribofilms on a WC substrate. The results showed that the rate of formation ranges from 0.2 to 0.7 nm/min depending on the interfacial shear stresses. Similarly, Gosvami et al. [30] using elaborate in-situ AFM tribotests showed that the ZDDP can adsorb and decompose to form tribofilms on both Fe-coated and uncoated Si substrates with a similar rate depending on the temperature and contact pressure. It is not clear whether the ability to form tribofilms in these cases was due to the presence of W and Si in particular or due to the operating conditions. This can be better understood by studying some cases of coated surfaces, e.g. DLC, both non-doped and doped with various metallic cations. For such surfaces, the exact chemo-mechanical nature of the coating is expected to play a vital role in the adsorption and decomposition of the P-based additives.

The wear and friction performance of DLC coatings and the properties of any formed tribofilms on them were reviewed extensively in the literature [141, 206–210]. Several previous studies reported that the P-based additives such as ZDDP can react and form protective tribofilms on DLC coatings even without containing any doped metallic cations [31, 32, 211–215]. In contrast, other studies found

that no tribofilms can be formed on non-doped DLC without metallic cations [216–221]. We will review some of these reports and try to identify the reasons behind this apparent discrepancy. The available literature will be divided into three main themes: i) formation of tribofilms on DLC, ii) structure of the formed tribofilms on DLC and iii) effect of the formed tribofilms on friction and wear.

i. **Formation of tribofilms on DLC coatings**

Regarding the formation of tribofilms on DLC coatings, it is interesting to note that the literature is somehow divided between two contrasting views. The first suggests that no tribofilm formation is possible on non-doped DLC whereas the other suggests that the formation is possible on any type of DLC coatings.

In support of the first view, Haque et al. [216] found, using XPS, that no ZDDP-derived tribofilm was formed on a-C:H DLC even in the case of one of the counterbodies is made of cast iron. The role of iron cations was suggested to be deactivated by the presence of a carbon transfer layer, which might be graphitic, on the cast iron counterbody. This is also in line with the results of Bouchet et al. [220] regarding the interaction of the ZDDP and MoDTC additives with hydrogen-free DLC (a-C), hydrogenated (a-C:H) and Ti-doped (Ti-C:H) DLC coatings. The XPS and TEM/EELS analysis revealed that no P-derived tribofilm was formed and no iron was present, which indicated that the pin surface was protected by a transfer layer from the DLC. Similarly, Podgornik et al. [217] investigated the effect of coating one contacting surface or both with WC doped hydrogenated DLC coatings (Me-C:H) in the presence of ZDDP antiwear additive. Based on the SEM/EDX analysis, the study found that no P-based antiwear tribofilm was formed on the DLC coating. Furthermore, Podgornik and co-workers [219, 222] using SEM/EDX confirmed that for (a-C:H) DLC no tribofilm was formed for both S-based and P-based additives. The results also suggested that probably W from the coating can combine with S to form a protective layer. Furthermore, Ban et al. [221] tested the reaction of Si-doped (a-Si:H) and non-doped (a-C:H) DLC coatings with ZDDP. Using XPS, no tribofilm was detected on the (a-C:H) DLC coating whereas a P-based tribofilm was formed on the Si-doped DLC. Kalin et al. [223] also found that for the self-mated (DLC/DLC) non-doped and doped Ti-, W-, and Si-DLC coatings, the EDX and FTIR results did not provide evidence to support a reaction between the DLC coatings and the extreme pressure (EP) additives. In another study, Kalin et al. [213] found that the tribo- and thermal films can be formed on the Ti-doped DLC, which was found to have 10 times higher activity than the W-doped (P/S $>$ 25

folds). They also found some reactivity with a-C:H DLC but much slower. They concluded that the metal doped DLCs behave more like metal steel that catalyses the decomposition of the additive and the formation of tribo- or thermal films.

In contrast to the previous view, Akbari et al. [215], using ATR-FTIR and XPS, found that the thermal films can be formed equally on bare steel surfaces and Si-doped (a-Si:H) and non-doped (a-C:H) DLC coatings. The thickness of the thermal films as estimated from XPS sputtering was thicker in the case of bare steel as compared to the coated ones, which suggested that steel can still catalyses the thermal decomposition of the ZDDP even without rubbing. Apart from this, the decomposition products of the ZDDP does not seem to be affected by the substrate as the short chain pyrophosphate and zinc oxide was detected on all the tested surfaces. Nonetheless, ATR-FTIR showed that organic sulphides (R-S) were present on all the surfaces but sulfhydryl (R–SH) groups were detected on the steel surface only. These species were confirmed by their XPS analysis except for the H-S, which could not be resolved. Nevertheless, it should be noted that these results apply only to thermal films, which could indicate that in the case of tribofilms any formed species on the DLC coatings, especially if non-doped, are of low tenacity and thus under rubbing can be easily removed. This can partly explain the discrepancy in the literature regarding whether a tribofilm can be formed on non-doped DLC coatings or not. However, other studies, e.g. see [31, 32, 211], suggested that tribofilms can indeed be formed on the non-doped DLCs. However, despite the assertion, the data provided do not seem to be conclusive for the a-C:H non-doped DLC, as will be discussed in the next paragraph describing the structure of what was perceived to be a tribofilm on DLC coatings.

ii. **Structure of the tribofilms formed on DLC coatings**

The studies that showed a formation of P-based tribofilms on DLC coatings indicated unique tribofilms' structures with some similarities to the ones formed on bare steel surfaces. For instance, Vengudusamy et al. [32] analysed the ZDDP tribofilms possibly formed on six different types of DLCs using various experimental techniques including AFM, SLIM, ToF-SEM and EDX. The DLCs had a hardness ranging from about 760 to 6800 HV. The structure of the tribofilm was analysed using the AFM. The study found that a tribofilm with a pad-like structure similar to one formed on steel surfaces can only be observed in the case of a DLC containing metallic elements, e.g. W-doped DLC. For the other types of DLC, tribofilms of minuscule amount with

scattered patches were formed instead. The thickness of the pads formed on the W-DLC was < 30 nm, which was much larger than the one formed on the other types of DLC. This may suggest that the metallic cations can catalyse the decomposition of the additive and the formation of a protective tribofilm. SLIM interferometry images after different rubbing times showed an interesting behaviour that the tribofilms formed on DLC-DLC contacting surfaces are less tenacious than the ones formed on metal surfaces, which was also reported by other studies as well [31, 211]. The low tenacity was evidenced based on the decrease in the concentrations of the decomposition products over rubbing cycles. The ToF-SIMS analysis of Equey et al. [211] and the XPS and TEM/EELS analysis of Haque et al. [216] showed that no iron is present in the formed tribofilms on DLC surfaces, which suggests that the low tenacity to the surface can be related to the absence of mixed oxide/sulphide base layer.

In agreement with the previous discussion, Equey et al. [211] using AFM found that the tribofilm seemed to lack the pad-like structure observed in the tribofilms formed on steel surfaces but instead it appeared to have a similar structure like the one of DLC coating, i.e. rounded nodular structure. The AFM images indicated that the tribofilm does not cover the metal surface completely but forms more like scattered islands of thickness up to 100 nm. In a different study, Equey et al. [31] tested the decomposition of ZDDP, butylated triphenyl phosphorothionate (b-TPPT) and amine phosphate (AP) additives on (a-C:H) DLC coating. Using ToF-SIMS and AFM, it was found that the ZDDP and b-tPPT can form thin tribofilms, although AFM was unable to quantify their thicknesses as they seemed to be within the roughness of the DLC coating. This is in line with the conclusions of Topolovec et al. [212] regarding (a-C:H) DLC and Cr-doped non-hydrogenated and graphitic DLC coatings.

The above discussion indicates that the main factor behind the wide disparity between the observations of the tribofilm formation on DLC coatings is the tribofilm tenacity. Any formed tribofilm does not seem to strongly adsorb to the DLC surface, especially if non-doped, leading to its effortless removal under rubbing once formed. Another explanation was provided by Kalin and Vižintin [224] who suggested the presence of a different thermal activation barrier for the additive reaction with doped as opposed to non-doped DLC, which is also different from the one of steel. The difference was attributed to the low thermal conductivity of the non-doped DLC in comparison to steel or

metal doped-DLC. This can lead to higher contact temperature that helps in decomposing the additive and forming a tribofilm.

iii. **Effect of the formed tribofilms on friction and wear**
Apart from the additive decomposition to form a tribofilm on the DLC surface, its role in friction and wear is contentious. For instance, Haque et al. [225] suggested that the decomposition of the ZDDP additive seems to be essential in protecting the surface from polishing wear. This was based on the observation that outside the boundary lubrication regime where the conditions might not be suitable for the decomposition of the additive, the coating surface undergoes sp^3 to sp^2 conversion (possibly graphitisation), which reduced friction and the DLC hardness leading to more wear. Yang et al. [226] showed that the extent of this is additive dependent but could not establish a direct relation between the friction reduction and sp^2/sp^3 ratio in the coating or between the hardness reduction and wear volume. Contrary to these results, Vengudusamy et al. [32] suggested that no graphitisation takes place because of rubbing and that for most of the tested DLCs including a similar a-C:H DLC coating used by Haque et al. [225], wear was less in the absence of ZDDP than in its presence. In contrast, the results of Bouchet et al. [220] suggested that ZDDP additives can improve wear properties of the hydrogen-free DLC (a-C), hydrogenated (a-C:H) and Ti-doped (Ti-C:H) DLC coatings. Similarly, Equey et al. [211] tested (a-C:H) DLC coating and found that although wear was insignificant in the presence or absence of the ZDDP, its absence caused some abrasive wear scars to appear on the surface of the coating.

Kalin and Vižintin [224] investigated the interactions occurring between the contacting surfaces when only one of them is coated, i.e. DLC vs steel. They studied a-C:H, Ti-C:H, a-C:H/a-C:H-W multilayer and a-C:H/a-Si:O single layer when interacting with antiwear additive (mixture of amine phosphates) and EP additive (dialkyl dithiophosphate). Wear was found to be dependent on the coating and additive types. Metal doped DLCs and steel were found to have similar tribological behaviour except for steel/W-DLC, which shows large friction and wear. The EDX surface analysis shows no P-derived tribofilm was formed on the DLC coatings. In the case of non-doped DLC, the additive presence seems to increase wear whereas the opposite was found in the case of doped DLCs. They related this to the formation of a soft tribofilm on the metal surface or metal doped DLC coating instead of a transfer layer from the coating. The soft tribofilm can decrease wear of the substrate more than in the case where the additive is not present.

In line with these results, Podgornik et al. [217] tested the effect of coating one contacting surface or both with WC doped hydrogenated DLC coatings (Me-C:H) in the presence of ZDDP antiwear additive and found that although no P-based antiwear tribofilm was formed on the DLC coating, the additive type seems to have a great effect on the running-in period. Interestingly, the results showed that the DLC/iron combination gives the best tribological performance in terms of low friction and wear, which is in line with other studies [218]. The EDX analysis revealed that in this case a mixed material from the DLC coating and decomposition material from the additive can form a protective tribofilm on the uncoated or exposed steel surfaces, which seems to exhibit a superior protective properties than the individual components. Donnet and Grill [227] indicated that the low shear stress of the carbon-rich transfer layer formed on the DLC is responsible for the improved tribological properties in comparison to steel surfaces. Ban et al. [221] tested the reaction of Si-doped (a-Si:H) and non-doped (a-C:H) DLC coatings with ZDDP. Using XPS, a P-based tribofilm was formed on the Si-doped DLC, which seemed to have low shear stress that helped lower friction force. In contrast, Kalin et al. [223] found that for the self-mated (DLC/DLC) non-doped and doped Ti-, W-, and Si-DLC coatings, the use of EP additives mitigated wear but friction relatively increased. The increases in friction suggested a formation of a high shear strength interface, despite the observed reduction in surface roughness. However, the EDX and FTIR results did not provide evidence to support a reaction between the DLC coatings and additives.

Based on the above discussion, any tribofilm formed on the DLC coating can generally serve two purposes [214]. First, it can form a lubricating layer that helps separating the contacting surfaces. Second, the formed layer is soft and thus can reduce the peak shear stresses and strains at the surface of the coating [228, 229]. This can result in possibly graphitisation suppression and wear reduction [214] though the effect on friction can be higher or lower depending on the type of the formed interface, i.e. friction increases in the case of ZDDP tribofilms but decreases in the case of carbon-rich layers.

3.4.3.2 Type of base oil

P-based additives, such as ZDDP and DDP, can be represented typically as a polar moiety, attached to P or S atom, and a non-polar tail, which is typically an alkyl moiety [230]. The affinity of such a molecule to the steel surface originates from the molecules' polarity due to the electron charge difference, i.e. asymmetric charge

distribution, between the different parts of the molecule due to the difference in electronegativity between the bonded atoms [230]. Tomala et al. [231] used the AFM to study the effect of base oil polarity on the decomposition of the ZDDP. The study found that in the case of non-polar oils, the tribofilms were formed faster, thicker and caused less surface roughening than the ones formed in the case of polar oils. The explanation behind this is that polar base oils, as expected, have a large affinity to the steel surface and thus compete with the additive and hinder its accessibility to the metal surface. On the other hand, non-polar oils was found to improve the additive accessibility to the steel surface, which results in accelerated formation of thicker tribofilms than in the case of polar oils [230, 232]. The composition of the tribofilms formed in polar and non-polar oils were similar consisting mainly of phosphate but a difference was observed in the formed sulphur species. For the ZDDP in polar oils, sulphide species were formed as opposed to the mixture of sulphide and sulphate species in the case of non-polar oils [230].

Kar et al. [233] used TEM, SEM, XPS, AFM and microhardness tests to investigate the effect of base oil polarity on the decomposition of additives. The results showed that polar oils provided smoother tribofilms than the ones formed in non-polar oils. The results indicated that the coverage of polar oils on the metal surface enhanced the effective lubrication and protected the metal surface. In contrast, other studies [234, 235] found that the P-containing additives reduce wear more efficiently when used in non-polar oils due to the ease of access of the additive to the steel surface and thus the better formation of the protective antiwear tribofilm. Suarez et al. [232] used SLIM, SEM-EDX XPS, AFM and nanoindentation to study the effect of oil polarity on the interplay between the tribological properties and composition of the formed ZDDP antiwear tribofilms. The study showed that the tribofilm thickness is not the only parameter determining the wear and friction performance but the composition can play a vital role as well. The results showed that although the polar base oil suppresses the formation of thick tribofilms and decreases their formation rate, it reduces friction more efficiently than the thicker tribofilms formed in the non-polar oils. The tribofilm structure in the polar oil seemed smoother and more homogeneous and continuous than the one formed in non-polar oils. This smoother tribofilm provided better wear properties, which was proposed to be related to the harder tribofilm formed in the case of polar oils as opposed to the softer tribofilm in the case of non-polar oil. The study suggested that this softer tribofilm leads to a larger contact area and thus larger wear. However, larger contact area should necessarily mean lower contact pressure and thus wear is expected to be less. This discrepancy cannot be explained based on hardness point of view only. In addition, measuring the hardness of a tribofilm of thickness less than 40 nm with the NI technique using

an indentation depth of 20 nm, will inevitably include a significant effect from the hard substrate underneath.

3.4.3.3 Duration of rubbing and heating

The duration of rubbing and heating can greatly affect the composition of the formed tribofilms and therefore their antiwear properties. Yin et al [118] used XANES to study the decomposition species of the ZDDP after different rubbing times, i.e. 5 min, 30 min, 6 hr and 12 hr. They also investigated the effect of rubbing a mature film formed after 30 min in base oil for another 5.5 hr to examine the durability of the tribofilm and the effect of rubbing without additives. The results indicated that the tribofilms formed after short rubbing times exhibit different fingerprints than the ones formed after longer rubbing times, which suggested that different species are formed initially before the phosphate chains. They also found that initially a large concentration of unreacted ZDDP adsorbs to the metal surface, which can coexist with the reacted ZDDP. Rubbing the ZDDP tribofilm in base oil led to the depolymerisation of the long chains into shorter ones.

Similarly, Gosvami et al. [30] used the in-situ AFM liquid cell shown in Fig. 3.4 to study the evolution of ZDDP tribofilms over time. The study showed that initially the tribofilm volume increased linearly over rubbing time. However, after a certain threshold the volume started to have exponential growth. The EDX and Auger electron spectroscopy (AES) analysis of the tribofilm revealed that it consisted mainly of Zn, P and S. Furthermore, the distribution of Fe was uniform inside and outside the wear scar indicating that the tribofilm does not have any significant amount of Fe, if any.

Different other studies also used in-situ XANES to follow the change in composition of ZDDP thermal films over heating time. For instance, Morina et al. [162] studied the formation of thermal films using the in-situ XANES heating cell shown in Fig. 3.5. In order to have a surface sensitive signal, the in-situ experiments were performed in the total external reflectance mode by tilting the samples to an angle less than the glancing angle. The XANES results showed that in the beginning of the thermal decomposition reaction, sulphide and sulphate species are formed. The sulphate formation was related to the effect of relative humidity [33, 162, 236], i.e. water contamination in the oil. The presence of sulphate species was also detected by Ferrari and co-workers [237, 238] who used the heating cell shown in Fig. 3.6 to follow the ZDDP thermal films over heating time.

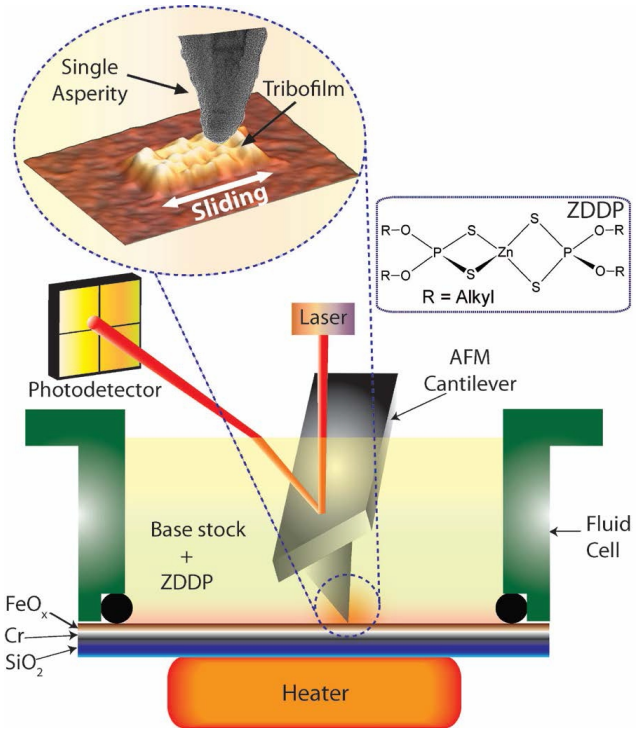

Fig. 3.4 Schematic of the assembly of in-situ AFM liquid cell. Reprinted from Gosvami et al. [30].

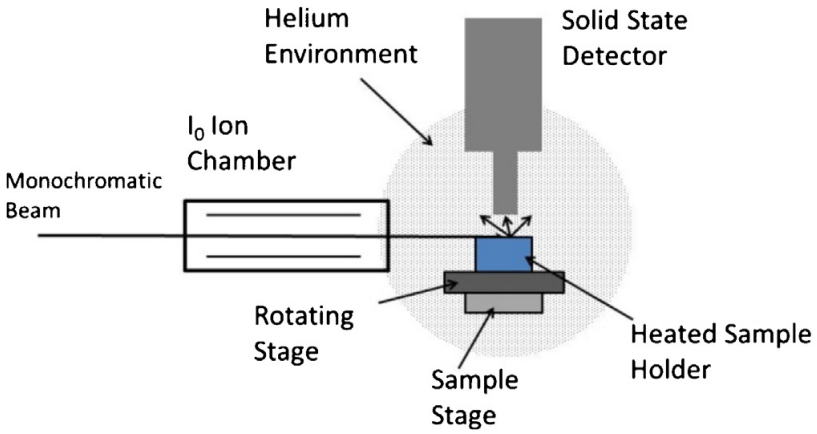

Fig. 3.5 Schematic of the assembly of high temperature liquid cell for in-situ XAS experiments. Reprinted from Morina et al. [162]

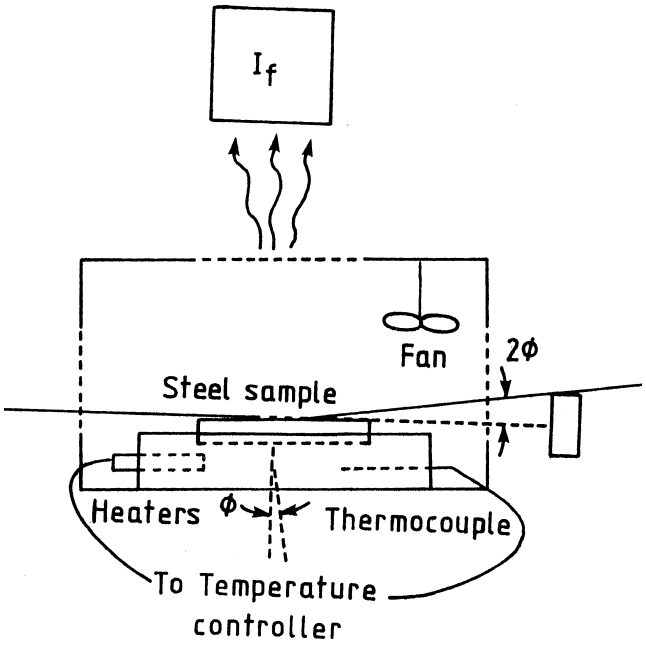

Fig. 3.6 Schematic of the assembly of a high temperature liquid cell used for in-situ XAS experiments. Reprinted from Ferrari et al. [237].

For the DDP antiwear additives, Kim et al. [136] tested two types of DDPs and compared them with ZDDP. They performed these experiments at 170 ^{o}C at which the additive decomposes in the oil and produces solid precipitates, which are subsequently deposited on steel coupons underneath. The results indicated that the progression of heating makes the ZDDP thermal films richer in sulphur whereas the DDP films richer in phosphorus. Zhang et al. [128] found that the evolution of P/S ratio was nearly constant over time for the ZDDP tribofilms, whereas it showed a gradual increase for the case of DDP tribofilms. This is despite the general increase in the tribofilm thickness over rubbing time, which indicates that the composition evolves mainly during the initial stage of rubbing [127]. Najman et al. [127] suggested that initially the DDP additive reacts rapidly with the substrate covered with oxides, which leads to the oxidation of the sulphur species into iron sulphate. These species do not help in protecting the contacting surfaces but only does the subsequently formed phosphate [182].

The DDP additive forms Fe phosphate of short chains whereas the ZDDP forms initially zinc phosphate of short chains that grow into longer ones away from the metal surfaces whereas the layers near the substrate remain of shorter chains due to the presence of Fe cations near the steel substrate [127, 164].

3.4.3.4 Concentration of additive

The concentration of the ZDDP affects its adsorption and coverage on the metal surface [202, 239], i.e. the larger the concentration of the ZDDP, the larger its adsorption and coverage. Yin et al [118] used XANES to study the effect of the ZDDP concentration, i.e. 0.25%, 0.5%, 1.0% and 2.0 wt.%, on the decomposition species. The results showed that a low concentration of ZDDP can lead to the formation of short phosphate chains whereas a high concentration leads to the formation of long chains in addition to the short ones and unreacted ZDDP. Furthermore, Tomala et al. [231] found that the larger the additive concentration (i.e. 2 % and 5 %) the thicker the tribofilm and the larger its roughness. Similarly, Ghanbarzadeh et al. [240] indicated that increasing the additive concentration increases the formation rate and terminal film thickness and decreases the average wear depth. Thus, the additive concentration evidently has a strong effect on the decomposition kinetics. This is further supported by the study of Akbari et al. [215] of the effect of ZDDP concentration, i.e. 1%, 2.0% and 20 wt.%, on the composition of thermal films formed on bare steel, Si-doped (a-Si:H) and non-doped (a-C:H) DLC coatings. The results showed that the thickness of the thermal film increases linearly with the concentration with a rate about 2.75 nm/min on bare steel and 1.5 nm/min on a-C:H DLC coating.

3.4.3.5 Temperature and load

Temperature and load are expected to affect not only the composition of the formed tribofilm but also its structure as well as its tribological and mechanical properties. Zhang and Spikes [142] showed using the AFM that at low temperature of 60 ^{o}C the tribofilm morphology was spiky of roughness similar to the large initial roughness of the substrate. As temperature increased to 100 and 120 ^{o}C, the tribofilm thickness increased and a more pad-like structure was formed with wide pads elongated in the direction of rubbing. Similarly, Yin et al [118] showed that the high temperature accelerates the decomposition of the unreacted ZDDP and helps increase the length of the formed polyphosphate chains. However, the study found that after a certain threshold, the high temperature can be detrimental to the chains length. Short chains were formed at 200 ^{o}C as opposed to the long chains formed at 100 and 150 ^{o}C. The study also found that high temperatures promote sulphate species formation. At 100 ^{o}C, sulphide species were detected whereas sulphate species were found at 200 ^{o}C. Other studies observed a similar effect for the load [181]. For instance, under high contact pressure, the DDP additive forms mainly sulphate, e.g. $FeSO_4$, whereas under low pressure mainly

disulphide (FeS_2). Contact pressure did not seem to affect the already short chains composing the DDP tribofilms but reduced the chain length of the ZDDP tribofilms from long to medium.

Similar to load, temperature can notably increase the formation rate and terminal film thickness of the formed tribofilms but decrease the average wear depth [240]. The tribofilm thickness during the early stages of rubbing, e.g. running-in period, and not only the steady state thickness, seems to be responsible for the antiwear protection [240]. Similarly, Parsaeian et al. [241, 242] found that by reducing the temperature from 100 to 80 ^{o}C, the tribofilm thickness decreases accompanied by a conspicuous increase in wear.

The effect of temperature on the mechanical properties of postmortem tribofilms was studied by Pereira et al. [243] using nanoindentation. The tribofilms consisted mainly of polyphosphate of medium chain length and sulphides as indicated by the XANES analysis. The tribofilm thickness measurement based on FIB-SEM cross-section suggested a thickness of 180±60 nm, which is consistent with the XANES P k-edge estimation of 105 nm. The evolution of the indentation modulus over temperature, i.e. from 25 to 200 ^{o}C, showed that up to 200 ^{o}C the modulus was nearly constant at around 100 GPa but dropped to about 70 GPa at 200 ^{o}C. The decrease in the modulus might be responsible for the good antiwear properties of the ZDDP tribofilm, i.e. the low modulus means a compliant sacrificial tribofilm that can be easily worn instead of the substrate.

The combined effect of load and temperature on the evolution of ZDDP tribofilms was investigated by Gosvami et al. [30] using in-situ AFM tribotests. The study showed that temperature exponentially increases the growth rate of the tribofilm. Similar to temperature, load ranging from 2 to 7 GPa, appears to increase the growth rate of the tribofilm exponentially until reaching steady state. Therefore, the study concluded that load and temperature have the same catalytic effect on the tribofilm formation. This is in agreement with the results of Yin et al [118], which found that load has the same effect as temperature, i.e. accelerating the decomposition of the unreacted ZDDP and the formation of long phosphate chains. The study also found that load does not affect the sulphur species type or concentration, i.e. sulphides were the only sulphur species to be formed and their intensity did not change much with load. Zhang and Spikes [142] showed using SLIM that in the EHL regime the larger the load (50-75 N) the faster the tribofilm formation and thicker the terminal thickness of the formed tribofilms on WC. The formation rate ranges from 0.2 to 0.7 nm/min depending on the maximum shear stress (220-250 MPa) at the edge of the tribofilm. Similarly, Tomala et al.

[231] found that the larger the load, ranging from 1.3 to 2.4 GPa, the thicker the tribofilm and the larger its roughness.

The effect of load on the ZDDP decomposition was also studied by Ji et al. [244] using XANES and AFM. The results indicated that the formed tribofilms consisted of polyphosphate of thickness between 10-100 nm. The results also showed that the larger the load the thicker the tribofilm. Additionally, based on the correlation between the friction force behaviour and electrical contact resistance measurements, they concluded that the ZDDP decomposition and tribofilm formation undergo three different stages:

1. Induction period, which increases with load and generally decreases with sliding speed. During this period, ZDDP molecules adsorb to the substrate and friction increases.

2. Tribofilm growth period during which tribofilm thickness increases and friction stays constant.

3. Tribofilm growth and removal period during which tribofilm thickness and friction stay constant.

The effect of load and temperature on DDP additives seems to be similar to the one of ZDDP. It was reported that the higher the temperature the thicker the thermal film [179]. Furthermore, the tribofilm thickness was found to be at least twice the thickness of the thermal film [179] and in general increases gradually over rubbing time [127], which suggests that load and temperature can both help accelerate the decomposition reaction.

In summary, the above discussion suggests a similar effect of temperature and contact pressure on the growth rate of ZDDP and DDP tribofilms, which indicates they have a catalytic effect on the additive decomposition process. Thus, it can be stated that the decomposition of P-based additives is a thermally and mechanically assisted reaction, which can be activated by the availability of either shear or heat.

3.4.3.6 Sliding and rolling speeds

It is understood that the ratio of sliding to rolling speeds can affect the contact severity and thus the lubrication regime. To further understand this effect on the decomposition of the ZDDP, Suarez et al. [230] followed the ZDDP tribofilm formation under different levels of slide-to-roll ratio (SRR), i.e. 0, 2, 5 and 10 %. The study found that the larger the SRR, the faster the tribofilm formation.

However, the study showed that the exact sliding percentage, as long as > 0, does not have a significant effect on the limiting tribofilm thickness. On the other hand, the SRR appeared to have a different effect on the topography of the tribofilm depending on the base oil. In the case of polar oil, the tribofilm appeared homogeneous throughout the different levels of the SRR. When non-polar oil was used, low SRR generated smooth tribofilms whereas large SRR ($\geq 5\%$) generated a rougher pad-like structure. That is the larger the SRR is, the rougher the tribofilm topography becomes and the more the structure appears patchy.

The effect of sliding speed on the ZDDP decomposition was also investigated by Ji et al. [244] using XANES and AFM. The results showed that lower velocities and higher load increase the tribofilm thickness whereas higher speeds and lower loads decrease the tribofilm thickness. In terms of friction relation to velocity, there was no simple relation. Under all the tested loads there seems to be a certain threshold of sliding speed below which the friction appears to decrease with increasing the sliding speeds whereas the opposite trend was observed above this threshold.

The effect of high SRR, i.e. 50% to 230%, on the ZDDP tribofilm formation was examined by Shimizu and Spikes [245] using SLIM, EDX and AFM. The study found that in the mixed sliding and rolling condition, the formation rate of the tribofilm is less sensitive to the exact SRR, which indicates that the rubbing time is far more important than the sliding distance.

3.5 Mechanical properties of antiwear films

3.5.1 Structure

The first report on the structure of the P-based antiwear films goes back to the study of Bird and Galvin [151] who suggested that the ZDDP tribofilm is polymeric and has a patchy structure. The authors conjectured that the first layer of this structure is a discontinuous sulphide, possibly zinc sulphide, or sulphate layer covering the metal surface. This layer in turn is covered with islands of unknown compounds containing Zn, P, and S. They also found that the ratio of Zn:P:S changes considerably along and across the wear scar. This heterogeneity can be related to the different local conditions, e.g. temperature, pressure and load. For instance, Sheasby et al. [165] and Palacios [18] observed that at low temperatures, e.g. 35 ^{o}C, a thin but uniform film was formed as compared to a thick but less uniform film at higher temperatures, e.g. 150 ^{o}C. The tribofilm

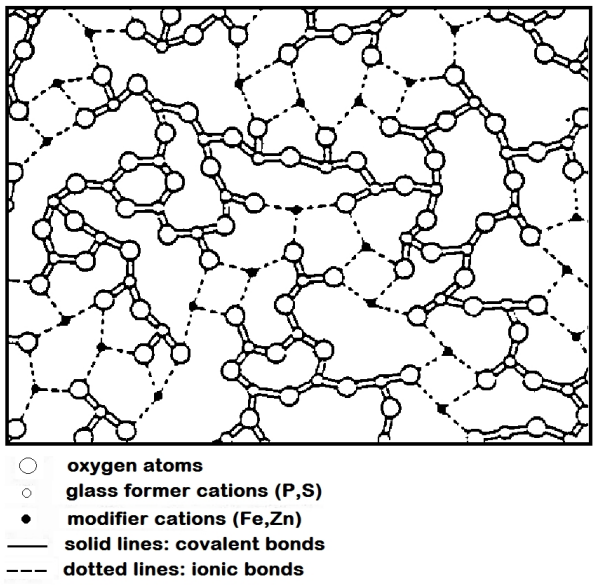

Fig. 3.7 Arrangements of atoms in the amorphous tribofilm. Reprinted from Martin et al. [178].

formed at high temperature was patchy in nature suggesting that it was only formed at the asperity-asperity contacts where temperature was high. In addition, the thickness was not found uniform amongst the different patches. Martin et al. [178] used X-ray absorption fine structure (XAFS) spectroscopy to show that the ZDDP wear particles have a continuously random amorphous structure, as depicted in Fig. 3.7. This structure was hypothesised to be formed due to friction- and shear-induced atomic-scale mixing processes at the interface [178] in addition to the digestion of the iron oxide by the phosphate layers near the metal surface [19]. Furthermore, it could be formed due to thermal effects by the interface quenching [178].

Later on, the tribofilm was identified of having a multilayer structure [17, 20, 36, 118, 246, 247]. The layers close the substrate appear to be solid and adhere strongly to the rubbed surface. However, the outer layers are viscous or semi-solid of hydrocarbons and organic radicals, which adhere weakly to the lower layers and hence they can be removed easily by rinsing with a solvent [17, 36, 246]. The concentrations of these products decrease along the depth whereas the concentrations of iron, iron oxide and iron sulphide increase. Above the iron sulphide/oxide layer, a layer of amorphous polyphosphate glass was identified, which can contain zinc oxide and zinc sulphide, as depicted in Fig. 3.8. The mechanical and physical properties of this amorphous 3D network are predetermined by the Zn^{2+} cations and organic radicals. However, the layers near the metal surface are mainly affected by Fe^{2+} and Fe^{3+} cations. Bell et al. [17] reported that the detected phosphate was similar to P_2O_5 glass. Therefore, they proposed that the ZDDP

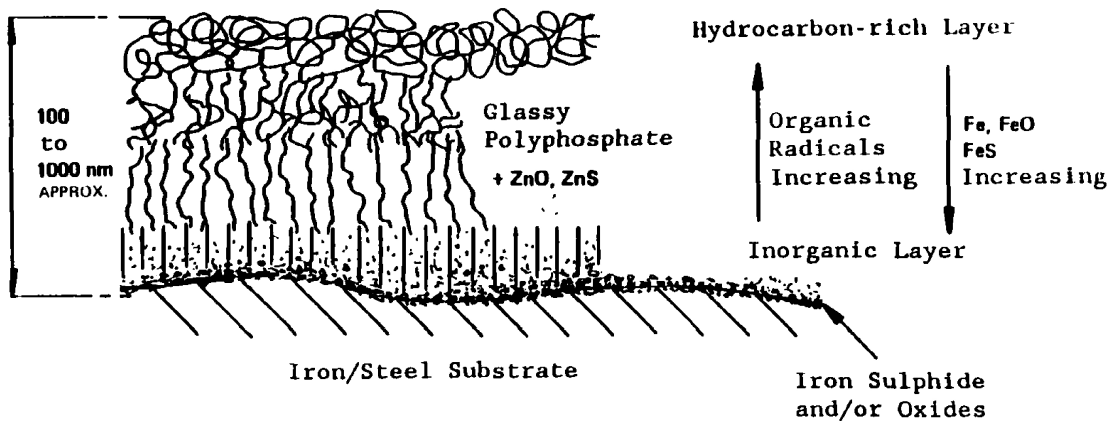

Fig. 3.8 Schematic of the structural model of the ZDDP tribofilm elucidating its multilayer characteristic. Reprinted from Bell et al. [17].

tribofilm consists mainly of glassy polyphosphate that has different physical and mechanical properties along the depth of the tribofilm. In addition, they noticed that the molar ratio of M_2O/P_2O_5 increased from 1.2 at the outer surface to about 2 in the bulk of the tribofilm. This suggested that the outer layers have longer chain length than those in the bulk. This also indicated that the outer layers have less concentration of zinc. Furthermore, recent experiments conducted by Ito et al. [200, 201] showed that the concentration of zinc is much higher near the metal surface, as shown in Fig. 3.9. This indicates that the cation exchange reaction between zinc and iron at high temperature should have occurred during the initial stage of the ZDDP decomposition. This also suggests that the presence of zinc near the metal surface plays a significant role in the observed short phosphate chains near the substrate.

Yin et al. [118] noticed that the XANES results of the Total Electron Yield (TEY), which is surface sensitive, and Fluorescence Yield (FY), which is bulk sensitive, were different. This suggested that the tribofilm has a layered structure consisting of a layer of short phosphate chains laid with a layer of long phosphate chains. Bec et al. [36] used the Surface-Force Apparatus (SFA) to determine the structure of the ZDDP tribofilm. The authors reported a full schematic of the ZDDP tribofilm before and after washing with solvents as shown in Fig. 3.10. The tribofilm appeared to be patchy and every patch has several layers. Using the AFM, Warren et al. [248] and Graham et al. [249] further confirmed that the tribofilm has a patchy-like structure. In addition, they observed stripes of discontinuous ridges along the wear scar. Pidduck and Smith [48] also observed that these patches were elongated in the direction of sliding. The estimated film thickness was in the range of 100-140 nm, which is in agreement with the recent measurements using the Spacer Layer Imaging Method (SLIM) of the

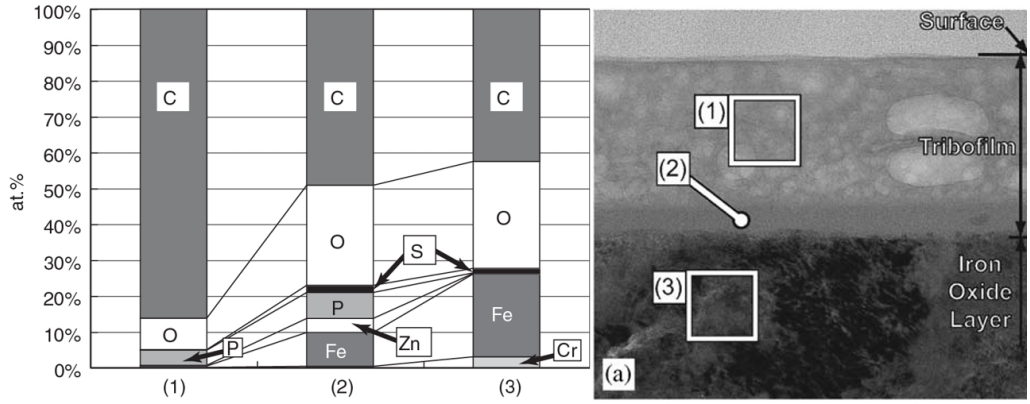

Fig. 3.9 TEM Cross section image of the ZDDP Tribofilm layers and EDX semi-quantitative analysis of the elements constituting the different layers. Reprinted from Ito et al. [200].

Mini-Traction Machine (MTM) [250]. In addition, the results of Bec et al. [36] indicated that the tribofilm thickness and friction coefficient change substantially from one position to another. This suggests that these parameters should be considered as local properties rather than as averaged values.

Aktary et al. [251] followed the topography evolution of ZDDP thermal films using Atomic Force Microscopy (AFM). During the first two hours, the structure appeared as isolated islands of phosphate precipitates, as confirmed by the Fourier Transform Infrared spectroscopy (FTIR). However, after 3-6 hr, these islands coalesced and the thermal film became smooth and continuous. The thickness of the film increased linearly with immersion time and continued to increase even after 6 hr during which it reached an average thickness of 420 nm. The results indicated that there is some correlation between the structure, thickness and morphology of the thermal film. The FTIR results showed that the early formed thin film of isolated islands consists of shorter phosphate chains than the mature thick and continuous film. The recent study of Aktary et al. [167] showed that the ZDDP tribofilm evolves in the same way as the thermal film. The only difference found was that after long rubbing time, the continuous film disintegrates to form very small pads. The results of Canning et al. [252] confirmed that the tribofilm is largely heterogeneous in the lateral direction. The tribofilm was found to have ridges of mainly long phosphate chains and troughs of mainly short phosphate chains. Same conclusions were also reached by Nicholls and co-workers [29, 89, 130, 177] using X-ray Photoemission Electron Microscopy (X-PEEM) and AFM. The results of these studies showed that the ZDDP tribofilm is also heterogeneous along the depth. The large pads of the tribofilm were found to have a multilayer system where long polyphosphate chains lay on the top of short polyphosphate chains. Based on these results amongst others, Spikes [7]

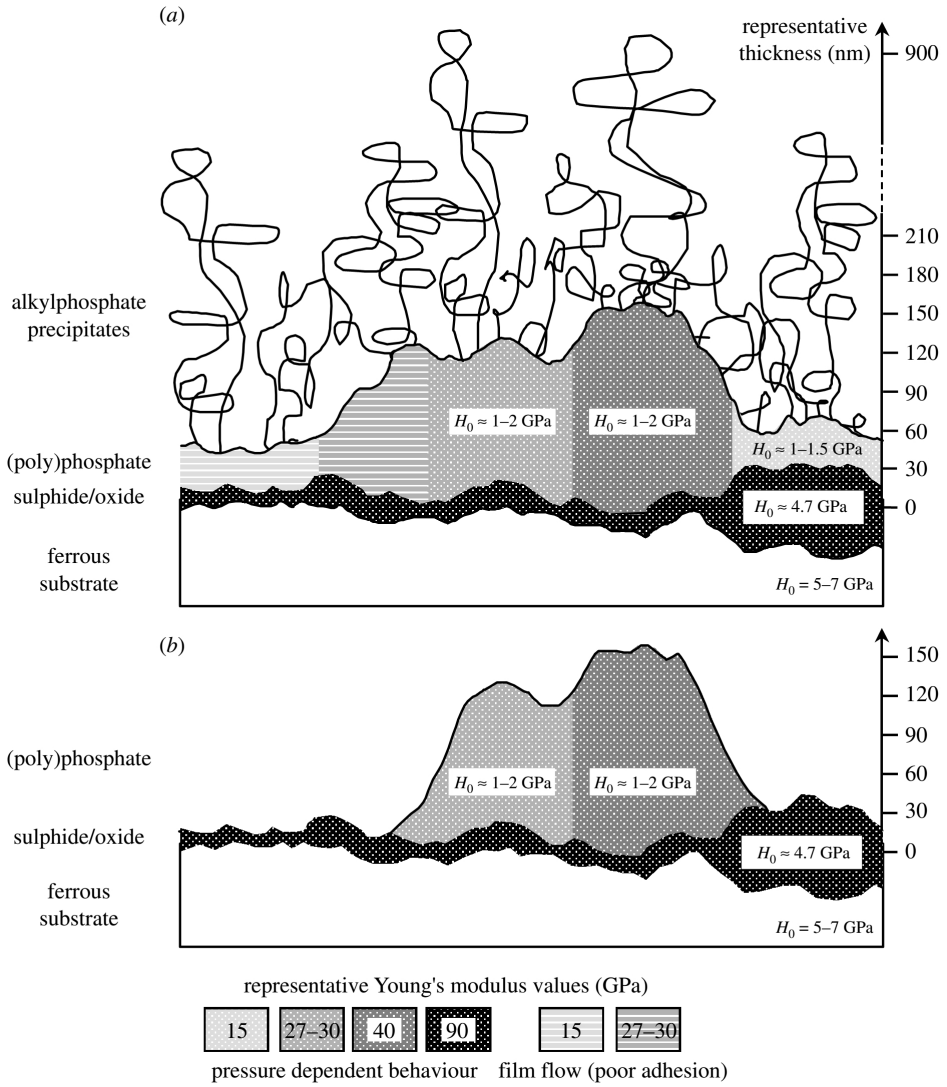

Fig. 3.10 Schematic of the multilayer structure of the ZDDP tribofilm (a) before and (b) after washing with solvent. Reprinted from Bec et al. [36].

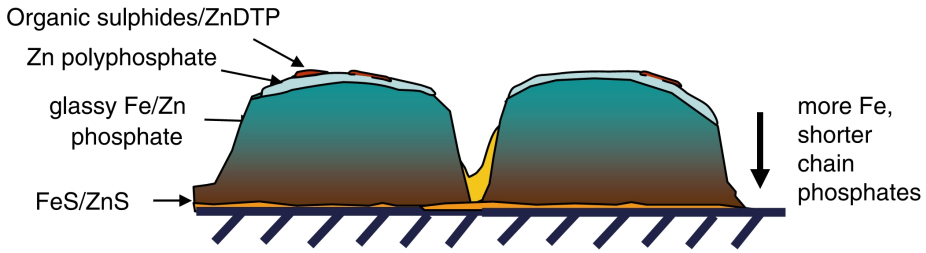

Fig. 3.11 Schematic of the patchy structure of the ZDDP tribofilm. Reprinted from Spikes [7].

proposed that the ZDDP tribofilm has a structure similar to one depicted in Fig. 3.11. This structure is in line with the findings of the previous studies that the tribofilm consists of multilayer structure, which is largely heterogeneous in the lateral direction and along its depth. This is also similar to the structure of DDP tribofilms, which initially appears less patchy than the ones of ZDDP but eventually the two provide a similar uniform pad-like structure [127, 128]. Distinctively though, the DDP additive forms Fe phosphate of predominantly short chains as opposed to the initially zinc phosphate of short chains that grow into longer ones away from the metal surface in the case of ZDDP [127, 164]. Furthermore, the formation of iron sulphides or sulphates in the DDP tribofilms near the metal surface depends greatly on the operating conditions [181], as discussed in detail in the previous sections.

The structures proposed by Bec et al. [36], Martin et al. [20] and Spikes [7] seem to be the most accepted picture of the structure of P-based antiwear tribofilms up to date.

3.5.2 Hardness and elastic modulus

Due to the largely heterogeneous nature of the ZDDP or DDP antiwear films, whether tribofilms or thermal films, probing their mechanical properties is a complex and intricate task. The main difficulties are attributed to the error brought by averaging over a large area and propagated by the different uncertainties associated with every experimental technique. This necessitates the need to analyse a large area of the sample at a high lateral resolution and at different length scales. Measuring the mechanical properties at a small length scale became feasible with the advent of the AFM, interfacial force microscope (IFM) and nanoindentation.

Many studies have already used the AFM to study the mechanical properties of the ZDDP tribofilms [40, 48, 167, 174, 248, 249, 251, 253–255] as well as tribofilms of other additives [256, 257]. This enormous work concluded that the layers close to the metal surface are most likely elastic solid whereas the outer layers are probably viscous. This indicates that the layers in between can have a combination of the two. Furthermore, Warren et al. [248] observed stripes of discontinuous ridges along the wear scar. These stripes were speculated to originate from repetitive sliding, which suggested that the ridges were the only part of the tribofilm that carry the load. In agreement with these results, the experiments of Graham et al. [249] showed that these ridges were elongated in the sliding direction. Aktary et al. [167] attributed this heterogeneity in the tribofilm growth to the local variations in the contact pressure between the contacting surfaces. However, as

the tribofilm is not heterogeneous only in the lateral direction but also along its depth, this indicates that the heterogeneity of the tribofilm is not only due to the local variations in the contact pressure [174]. Warren et al. [248] proposed three possibilities for the patchy structure of the P-based tribofilms, which are as follows:

1. Ridges are formed due to the high contact pressure between the asperities whereas the troughs are formed due to the three body interaction between the wear debris and the contacting surfaces.

2. Ridges are formed due to the repeated rubbing between the asperity contacts at the same average locations whereas the troughs are formed due to occasional contact between the asperities at the troughs regions.

3. Ridges are formed due to the repeated rubbing between the asperity contacts whereas the troughs are originated from the flow of some material from the ridges to troughs' regions.

The authors suggested that the way the ridges and troughs appeared indicated that the third mechanism is likely to be the case. Other possibilities to account for the heterogeneity in the tribofilm growth have also been proposed recently by Gosvami et al. [30] to be due to the following:

1. Heterogeneous random nucleation sites due to the surface roughness or any surface defects.

2. Instabilities in the decomposition and growth mechanisms due to any variations in the operational conditions.

These possibilities are plausible and can be combined with the ones proposed by Warren et al. [248] to give a wider understanding.

To quantify the mechanical properties of the ZDDP or DDP tribofilms, several studies attempting at measuring the elastic modulus using nanoindentation, AFM and SFA. Table 3.3 summarises the indentation modulus that was reported for the ZDDP and the measurement conditions. Aktary et al. [167] measured the elastic modulus of the ZDDP tribofilm after different rubbing times and found that the modulus and hardness of the tribofilm are independent of the rubbing time. They explained this result by pointing out that the majority of the bulk material of the tribofilm at any time consists mainly of short polyphosphate chains. Therefore, the nanomechanical properties are predetermined by the properties of this bulk material. However, Nicolls et al. [29] reported that the large pads of the tribofilm

consist mainly of long polyphosphate chains whereas the small pads and troughs consist of short chains. Graham et al. [249] showed that the pads have a great elastic response. The measured indentation modulus was about 180-250 GPa at the centre of the pad compared with 50-110 GPa at the edge. Nicolls et al. [177] found that the indentation modulus was 120 GPa at the centre of the pad compared with 90 GPa at the edge. In a later study, Nicolls et al. [29] reported an indentation modulus of 80 GPa for the large pads but could not measure the modulus of the small pads due to the effect of the substrate on the indentation measurements of these thin regions.

This wide range of values of the reported indentation modulus could be related to the extent of the additive decomposition to form polyphosphates [89] in addition to the intrinsic uncertainties associated with probing such thin heterogeneous films using any indentation technique.

In contrast to the aforementioned studies, which suggested that the tribofilm is highly elastic, Aktary et al. [167] found that the ZDDP tribofilm exhibits high plasticity. They suggested that this is in line with the sacrificial nature of the tribofilm, which is continuously formed and removed at the interface. Conversely, Warren et al. [248] showed that the ridges of the tribofilm exhibit a great capacity of elastic deformation, which was also confirmed by the results of Graham et al. [249] and Ye et al. [253] showing that the ridges of the ZDDP tribofilm resist plastic deformation to a great extent.

Ye and co-workers [174, 253, 254] studied various tribofilms formed in oils containing ZDDP and ZDDP/MoDTC additives. In the two cases, the results showed a gradual increase of hardness and modulus over depth until they reach the ones of the substrate. This was considered as evidence that the tribofilm consists of a multilayer system of a hard layer covered by a softer one. Similarly, Bec et al. [36] showed that the ZDDP tribofilm resists indentation by increasing hardness and elastic modulus with the indentation depth. Therefore, they suggested that the heterogeneity of the mechanical properties of the tribofilm along its depth is due to work hardening but not a real intrinsic property. However, in contrast to these results, the loading-unloading experiments of Warren et al. [248] using AFM indicated that the tribofilm ridges have two layers of which the one that is more compliant lay beneath the stiffer surface layer. The base layer seemed to exhibit a significant tenacity, which was manifested in the apparent adhesion during the retraction of the AFM tip from the sample. These features were neither observed in the troughs of the tribofilm nor in the thermal film. The mechanical properties of the trough region of the tribofilm seemed identical to the ones of the thermal film. Based on these results, Warren et al. [248] suggested that the thermal

Table 3.3 Elastic modulus and hardness of the ZDDP thermal and tribo-film.

Material	Elastic modulus (GPa)	Method	Lubricant	Test conditions	Ref.
5 min Tribofilm 10 min Tribofilm 40 min Tribofilm 1 hr Tribofilm 2 hr Tribofilm 3 hr thermal film	88.5±23.7 92.8±18.6 88.6 ± 29.9 88.9 ± 12.1 96.1 ± 25.7 34.8 ± 9.7	nanoindentation	1.49 wt% ZDDP in MCT-10.	Plint 100 C 225 N 25 Hz	[167]
1 hr tribofilm edge of pad 1 hr tribofilm centre of pad	87.8 ± 3.9 119.5 ± 5.8	nanoindentation	1.2 wt.% ZDDP in MCT-10.	Plint 100 C 220 N 25 Hz	[177]
Sulphide oxide $t \leq 80$ nm Polyphosphate $20 < t < 30$ nm Polyphosphate $70 < t < 100$ nm Polyphosphate $t > 140$ nm	90 15 27 − 30 40	SFA		Amsler 100 C 400 N 5 hr	[36]
6 hr tribofilm trough 6 hr tribofilm ridge 1 hr thermal film	25 81 36 ± 9	IFM	1.2 wt.% ZDDP in paraffinic base oil	Plint 100 C 220 N 25 Hz 200 C	[248]
Large pads ridges Large pads troughs Small pads Off pads	209 ± 38 87 ± 23 74 ± 20 37 ± 7.3	IFM	5 mM/kg ZDDP in paraffinic base oil	Plint 100 C 225 N 25 Hz	[249]
1 hr tribofilm	85.1 ± 11.1	Nanoindentation and IFM	1.2 wt.% ZDDP in MCT-10.	Plint 100 C 220 N 25 Hz	[258]
1 hr tribofilm ridges 1 hr tribofilm troughs	80.5 ± 4.5 30	Nanoindentation	1.2 wt.% ZDDP in MCT-10.	Plint 100 C 220 N 25 Hz	[177]
10 min tribofilm 1 hr tribofilm	78 − 110 ± 8 97 − 110 ± 8	Nanoindentation and IFM	1.2 wt.% ZDDP in MCT-10.	Plint 60 C 60 N 25 Hz	[29]
1 hr tribofilm	80 − 215 depends on contact depth	nanoindentation	ZDDP in 5W-30 SG engine oil	Pin-on- disc 490 N 0.03 m/s	[253]

film is formed first as a precursor to the tribofilm. In line with these results, Kim et al. [124] showed that the surface layer of the ZDDP tribofilms, away from the substrate, is harder than the bulk layers. In contrast, DDP tribofilms showed a more compliant tribofilm without the presence of a hard surface layer. They suggested that the hard crust protects against wear while the compliant bulk helps dissipate energy. This is despite the fact that they observed that the more compliant but thicker DDP tribofilm showed a much better tribological performance than the one of ZDDP. To resolve this discrepancy, they suggested that the effective coverage of the DDP tribofilm is higher than the ZDDP one leading to better protection against wear.

Based on the discussion above, it can be concluded that the ZDDP and DDP antiwear films have rich mechanical properties. These properties can be affected by the decomposition mechanism, load and temperature. In addition, the mechanical properties might also be affected by the rheological properties of the tribofilm. For instance, in case of the tribofilm is viscoelastic then its mechanical response can look similar to the plastic behaviour of a compliant material [85]. Moreover, a viscoelastic tribofilm may suggest that its mechanical properties are rate dependent. Hence, the history and rate of measurement can play a major role in the measured properties. Therefore, studying the rheological properties of the antiwear tribofilm is necessary to give insight into its mechanical as well as tribological properties. These rheological properties will be discussed in detail in the subsequent section after the tenacity and durability of the tribofilm is reviewed.

3.5.3 Tenacity and durability

In order to study the tenacity and durability of ZDDP tribofilms, Bancroft et al. [119] examined the effect of the ZDDP concentration in oil on the tribofilm that has already been formed. After the formation of the tribofilm, the base oil containing ZDDP was replaced with oil without ZDDP and then the rubbing continued for extended periods of 6 to 24 hr. The tribofilm showed a great thermal and mechanical stability even after rubbing for periods as long as 24 hr. In addition, the results showed that rubbing the tribofilm in base oil has two main effects. The first one is that the tribofilm maintains a certain thickness above 30 nm without being completely removed by rubbing. The second effect is that the polyphosphate chains become shorter in the form of orthophosphate and pyrophosphate. Ancillary experiments of Suominen Fuller et al. [176] showed that when the oil of mature ZDDP tribofilm was replaced by base oil without

ZDDP, no change occurred in the tribofilm thickness with further rubbing in the base oil. However, Parsaeian et al. [259] found that rubbing premature tribofilm (after 25 min rubbing: before reaching steady state thickness) in base oil without ZDDP causes an initial sharp decrease in the tribofilm thickness after the first few minutes of rubbing. The reduction was about 20-70 nm depending on load and temperature, i.e. the higher the load or temperature the higher the removal. The sharp decrease in the tribofilm thickness was followed by a steady state period during which the tribofilms maintained its thickness without any further removal. Adding fresh oil containing ZDDP again after 60 min of total rubbing time (35 min of rubbing in base oil) results in a fast growth of the tribofilm thickness similar to the initial growth rate before replacing the oil with base oil. On the other hand, rubbing mature tribofilm in base oil (after 180 min rubbing: after reaching steady state thickness) results in just a small decrease in the tribofilm thickness. As indicated before, increasing temperature or load after replacing oil with base oil resulted in more immediate removal of the tribofilm. However, temperature and load did not show any monotonic trend on the steady state thickness. The drop in the tribofilm thickness was investigated using XPS, which showed that before replacing the oil with base oil the top layer of the tribofilm contains longer phosphate chains. This layer seems to be the one removed after replacing the oil, which suggests that it is softer and less tenacious than the layers underneath it. It was also found using XPS analysis that if rubbing is continued again by adding fresh oil containing ZDDP, the removed long phosphate chains can be formed again.

3.6 Rheological properties of antiwear films

The friction, lubrication and adhesion properties of any tribological surface are greatly affected by the rheological properties of the interface [37]. These properties can undergo changes when using additives such as ZDDP or DDP, which can form a protective tribofilm of transient thickness covering the interface. In order to quantify these changes, the rheological properties of the thin antiwear film should be measured. This can be mainly achieved using two methods. The first one is by generating a thick tribo- or thermal film that can be scratched and removed for ex-situ analysis using the bulk or interfacial rheometry. The second possible method is by measuring these properties in-situ. The in-situ rheological measurements of the antiwear tribo- or thermal films or generally speaking any thin film on a substrate are performed, in essence, in the same way as the bulk rheological measurements, e.g. creep and shear, but using different experimental

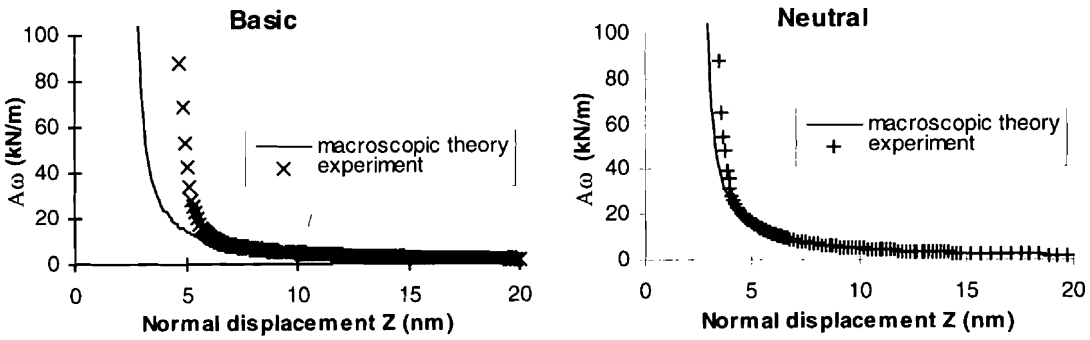

Fig. 3.12 Comparison between the measured and predicted damping coefficient of the basic and neutral ZDDP. Reprinted from Georges et al. [260].

techniques such as SFA and AFM. For instance, Georges et al. [260] used SFA to measure the rheological and mechanical properties of the ZDDP physisorbed films by imposing an oscillatory motion in three different directions, i.e. x, y and z axes. This enabled them to measure the damping coefficient, normal stiffness and lateral stiffness at different separation distances between the ball and disc. They could then relate the measured damping coefficient (A_ω) at a certain oscillatory frequency (ω) and a separation distance (D) to viscosity (η) using the following relation:

$$A_\omega = \frac{6\pi\eta R^2\omega}{D - 2L_h} \tag{3.30}$$

where R is the ball radius and L_h is the total thickness of any adsorbed layers on each surface. Good agreement between the experimental data and the damping coefficient given by the previous equation was found as shown in Fig. 3.12. One interesting result is the approximately exponential increase in the viscosity at small separation distances, which has the effect of increasing the viscous resistance to sliding. Another important finding is that the elastic compressive and shear moduli appeared to increase with reducing the separation distance. The authors related this observation to a possible compaction of the heterogeneous physisorbed layers. In agreement with these results, Bec et al. [36] suggested that the contact pressure could compact the loose layers of the ZDDP tribofilm and transfer them into a solid polyphosphate.

Bec et al. [36] used SFA to measure the mechanical and rheological properties of the ZDDP tribofilm. The results showed that the sulphide and phosphate layers exhibit elastoplastic properties. This suggests that the ZDDP tribofilm can be polymeric in nature [151] and its rheological properties, similar to the mechanical properties, vary along the depth of the tribofilm [17]. This was confirmed by Pidduck and Smith [48] and Bec et al. [36] who reported that the base layer of sulphide resists flow significantly whereas the top layer of alkyl phosphate precipitates behaves as a viscous polymer, which does not resist flow

and could be easily removed. Similarly, the bulk layers of polyphosphates forming the ridges of the tribofilm can also be removed easily leaving trough regions of bare sulphide/oxide layers. This suggested that the polyphosphate layers in the trough originated from the ridges material, i.e. alkyl phosphate precipitates and polyphosphates, that flowed into trough regions by shear flow. Bec et al. [36] reported a viscosity of 5×10^4 - 3×10^5 Pa.s for the alkyl phosphate layer and 10^8 Pa.s for the polyphosphate layer.

Based on the aforementioned discussion, it can be concluded that the P-based antiwear films have rich rheological properties. However, no elaborate study was conducted so far to unravel all these properties and to provide conclusive insights into the relation between the rheological, mechanical and tribological properties of the ZDDP or DDP tribo- and thermal films.

3.7 Tribological properties of antiwear films

3.7.1 Friction mechanism

Many studies aimed at understanding the genesis of friction of the P-based tribofilms using different techniques. For example, Ye et al. [254] used the nanoscratch method combined with AFM imaging and observed that the tribofilm exhibits different friction coefficients depending on the contact depth, which indicated that different levels of shear strength exist within the tribofilm. The lowest friction coefficient found was at few nanometres beneath the surface, which was attributed to the presence of an ultra-low friction inner skin layer that can act as a type of solid lubricant to reduce friction. In another study, Ye et al. [255] showed that the inner skin layer exhibits a low shear modulus and can yield easily, which can explain the capability of this layer to reduce friction. The heterogeneous friction behaviour along the depth is also accompanied by a heterogeneity along the surface as reported by Neitzel et al. [261] who observed that friction is different at different length scales. For instance, within a material exhibiting a high friction coefficient, areas of low friction at the nano- or microscopic scale might exist. These small domains of low friction force can affect the macroscopic friction or induce slip.

Taylor et al. [250] reported that ZDDP forms a thick solid-like film on the wear scar that produces an effective surface roughening. This increased roughness can inhibit the entrainment of the fluid film between the contacting surfaces and thus results in a higher friction than in the case of surfaces not covered with

the ZDDP tribofilm, as shown in Fig. 3.13. However, the results of Taylor and Spikes [262] showed that even smooth ZDDP tribofilms can increase friction. This suggested that whether the ZDDP tribofilm is rough or smooth, it can inhibit the entrainment of the lubricating film between the rubbing contacts and hence increases friction. This apparent increase in friction was also suggested to represent a shift in the Stribeck curve to a higher speed, which means that the tribofilm is capable of maintaining the boundary lubrication condition up to a higher speed than in the case of bare contacts without a tribofilm.

A different explanation for the increase in friction force when the ZDDP tribofilm is present on the steel surface was provided by Suarez et al. [232]. Assuming that the friction force can be given by the following equation:

$$F_f = \tau_{\text{ZDDP}} A_{\text{ZDDP}} + \tau_{\text{steel}} A_{\text{steel}} \tag{3.31}$$

where τ_{ZDDP} and τ_{steel} are the mean shear strength of the ZDDP tribofilm and steel surface, respectively, and A_{ZDDP} and A_{steel} are the real contact area of the ZDDP tribofilm and steel surface, respectively. Therefore, increasing the tribofilm thickness increases the contact area (A_{ZDDP}) and thus increases the friction force.

The increased friction of the antiwear tribofilms over time can also be explained based on the observations of Mazuyer et al. [263] that after a certain threshold of contact time the layers covering the rubbing surfaces can interact and hence the mechanical properties, e.g. shear elastic modulus and interfacial shear strength, become a function of the contact time. In the case of the ZDDP tribofilm, this means that the longer the rubbing time, the thicker the tribofilm will be and thus the stronger the interactions can occur between the tribofilms covering the contacting surfaces, which leads to higher friction.

Georges et al. [264] highlighted the steric action of the adsorbed layers on friction. When the separation distance is small, the pressure is high. In this case, the fluid starts to have an ordered structure in the direction of shear, as shown in Fig. 3.14. This was inferred from the observation that the stabilised friction coefficient was found to be inversely proportional to the sliding speed. In addition, Li et al. [265] showed that the strength of adhesion of the interfacial layers adsorbed on a substrate has great influence on friction. In the case of a single layer that adhered loosely, friction was maximum due to the puckering effect of the layer when probed by the AFM tip. On the other hand, in the case of a bulk material with strongly adhered layers, this puckering effect is suppressed and the thickness does not have any effect on friction after a certain threshold value.

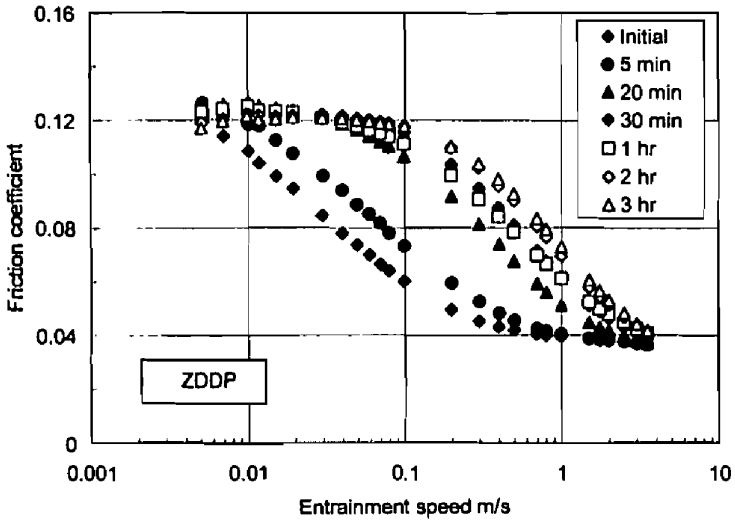

Fig. 3.13 Effect of the ZDDP tribofilm on the Stribeck curve after different rubbing periods. Reprinted from Taylor and Spikes [262].

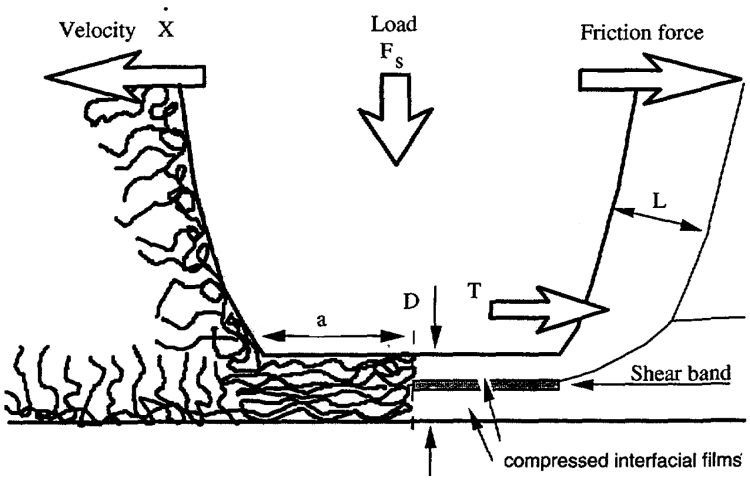

Fig. 3.14 Schematic of the ordered structure of the compressed hydrodynamic layer. Reprinted from Georges et al. [264].

Ancillary results of Lee and co-workers [266, 267] suggested the same trend for different materials including MoS_2.

The fact that sulphur might be the first to reach the metal surface is very crucial in order to relate the mechanism of additive decomposition and tribofilm formation to friction and wear. In the case of sulphur containing deposits are formed initially at the metal surface, then we can infer two main points. Firstly, during the running-in period, the sulphur rich layer is the one that predetermines the observed friction and wear. Therefore, if the porous FeS_2 is the main component of this layer, which is suggested in the case of surfaces covered with Fe_2O_3 or Fe_3O_4 as shown in the potential diagram in Fig. 3.3, friction will be small. However, a larger friction is expected in the case of a base layer consisting of a dense and uniform FeS, which is likely to be formed on bare iron [203]. Furthermore, the

existence of a sulphur rich layer as a base layer on the metal surface indicates that the subsequently formed layers should be deposited on this layer, whether fully or partially, rather than completely on the metal surface itself.

3.7.2 Antiwear mechanism

The ZDDP additive when decomposed under high contact pressure or heat can form a superior antiwear tribofilm on contacting surfaces. The DDP additive can provide better [124, 125], comparable [126] or worse [127, 128] antiwear properties to the ones of ZDDP, which seem to depend greatly on the operating conditions, properties of contacting surfaces and chemistries of base oil and additives.

Since the first inception of the ZDDP in the late 1930s, extensive studies on the genesis of its antiwear mechanism have been carried out [7]. Table 3.4 summarises the several theories and mechanisms that were proposed to explain the capability of the formed antiwear tribofilms in protecting the contacting surfaces from severe wear. These different mechanisms can be categorised depending on whether the cause of protection is rheological, mechanical or chemical.

Initially, it was suggested that the antiwear mechanism of antiwear additives is based on forming a thicker hydrodynamic film. This thick film can reduce the stress at the contacting asperities and hence reduces wear [18]. The sulphides, phosphorus compounds and oxides were also found to have good lubricating properties that help mitigate wear [268]. Molina [146] suggested that the ratio between the crystalline and amorphous regions of the antiwear film might be important in evaluating the antiwear action of the tribofilm. Molina's results indicated that the amorphous pyrophosphate has better lubricating properties that the crystalline phosphate. In line with these results, it was suggested that the polyphosphate, which has a low melting temperature of 200-300 ^{o}C, melts and forms a viscous glass on the contacting surfaces that helps reduce wear [14]. In addition, the interfacial iron-oxide-sulphide eutectic system was also proposed to form a viscous film at the contacting surfaces under extreme conditions and hence separates the contacting surfaces and reduces wear [14, 16]. Same mechanism was also proposed for the FeS layer covering the asperity-asperity contacts [17]. Interestingly, the amount of sulphur in the tribofilm was found to increase with increasing load [18], which highlights the smart action of ZDDP to reduce wear. This smart action was explored by So and Lin [247] who indicated that the plastic deformation is responsible for increasing the temperature at the asperities and hence the decomposition of the additive. Additionally, this plastic deformation creates subsurface defects that enhances the mixing and reaction

Table 3.4 Summary of the proposed antiwear mechanisms of ZDDP.

Authors	Mechanism	Details
Watkins [14]	Rheological & mechanical	Formation of a viscous glass on the contacting surfaces that flows and acts as a barrier
Gansheimer [268]	Rheological & mechanical	Good lubricating properties of sulphides, phosphorus compounds and oxides
Rounds [15]	Rheological & mechanical	Formation of oriented sacrificial layer that reduces shear stresses and acts as a barrier
Bec et al. [36]	Rheological & mechanical	Formation of a grease- or gel-like hydrocarbon-rich layer that has low shear strength
Watkins [14], Glaeser et al. [16]	Mechanical	Formation of an interfacial iron-oxide-sulphide eutectic system as a barrier
Bell et al. [17]	Mechanical	Formation of FeS on the surface as a barrier
Bell et al. [17]	Mechanical	Formation of a low shear stress layers that reduce fatigue wear and delamination processes.
So et al. [145]	Mechanical	Balance between the tribofilm formation and its removal
So and Lin [247]	Mechanical	Formation of a compliant protective tribofilm
Palacios [18]	Mechanical	Formation of a thick hydrodynamic film as a barrier
Habeeb and Stover [22]	Chemical	Decomposition of peroxides
Belin et al. [21], Martin et al. [19, 20]	Chemical	Digestion of sharp wear particles of iron oxide
Molina [146]	Chemical	Formation of an amorphous glass rather than a crystalline one.

of the decomposition products, i.e. P, S, Zn and O, with the rubbing surface. Accordingly, So et al. [145] suggested that the antiwear mechanism depends closely on the ratio between the tribofilm formation and its removal. In addition, Habeeb and Stover [22] reported that the ZDDP tribofilm can also reduce wear by decomposing the peroxides. On the other hand, other studies [19–21] suggested that the antiwear action and the absence of severe abrasive wear is due to the digestion of the iron oxide generated during wear into the amorphous phosphate structure of the formed interfacial tribofilm.

Bell et al. [17] suggested that a layer exists in the tribofilm with a low shear stress that helps reduce fatigue wear and delamination processes. In addition, they proposed that the adhesion between the different layers is expected to be crucial for the load carrying capability of the tribofilm and other wear and friction performance. On the other hand, Rounds [15] proposed that the P-based additives such as ZDDP can act by a mechanism similar to the one of the fatty acid by forming an oriented sacrificial layer covering the surface. This antiwear capability depends on the formed hydrocarbon chain length and chain branching. Accordingly, the hydrocarbon-rich layer at the outermost of the tribofilm seems to play a role in reducing wear [36]. This layer seemed to have a grease- or gel-like nature that has a low shear strength, which helps in redistributing the concentrated loads at the asperities and therefore reduces the high shear stresses at the asperity-asperity contacts and thus mitigates wear.

In summary, the unique antiwear properties of the ZDDP or DDP tribofilms seem to be related not only to its adhesion, hardness and elasticity but also to the capability of the formed tribofilm to maintain local order on the molecular scale through the flow, rearrangement and change in composition of the interfacial layers.

3.8 Antiwear films in humid environments

Corrosion phenomena typically involves water and oxygen [269], which are abundant at any interface. This makes water one the main elements in the corrosive environment. Water can affect the bearing performance in different ways [270]. On the one hand, it can shorten the bearing life, as shown in Fig. 3.15, due to rust, hydrogen embrittlement and oxidation. On the other hand, water can accelerate wear due to the oxidation of the lubricating film and the destabilisation of the protective tribofilm. Therefore, the relative degree of saturation of water in the oil is one of the important factors to consider. Water can enter the oil from the humid

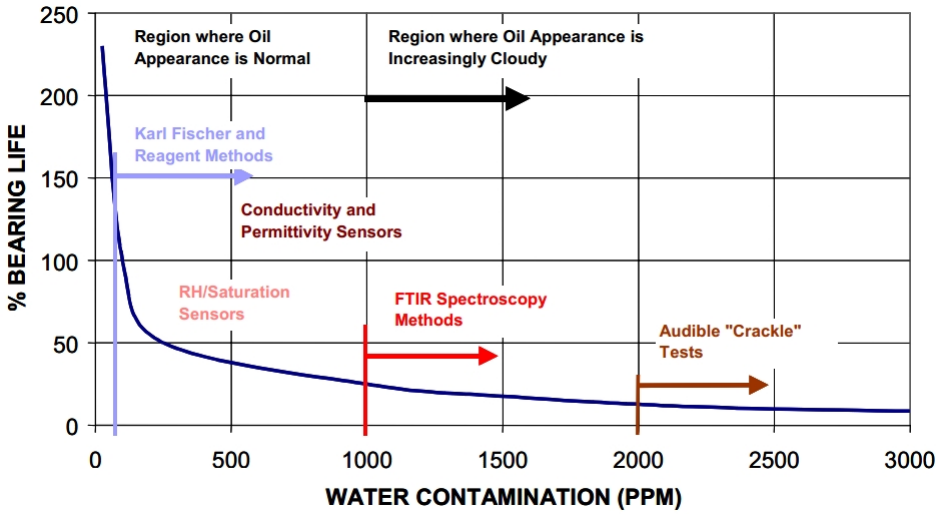

Fig. 3.15 Effect of water on the life of bearing based on 100% life at 0.01% water in addition to the available techniques to detect water and their range are indicated. Reprinted from Sheehan [272].

air or directly as a free water. The temperature of the oil determines whether this water will mix with the oil as a dissolved water, i.e. below the saturation temperature, or as a free water, i.e. above the saturation temperature [271].

In the following subsections, a review is provided on the effect of water on the composition and tribological properties of the P-based antiwear film.

3.8.1 Effect of water on the composition of tribofilms

Rounds [169] showed that water accelerates the ZDDP decomposition and reduces S, P and Zn contents in the antiwear film. These changes are additive dependent and can be related to the formation of acidic hydrolysis products. In contrast, the results of Nedelcu et al. [236] showed that water inhibits the growth of the ZDDP tribofilm. This effect was manifested in the formation of shorter chains of polyphosphates. The authors attributed these effects to the depolymerisation reactions of the long polyphosphate chains and to the increased surface distress in the presence of water. Ancillary experiments carried out by Cen et al. [33] showed that water indeed inhibits the formation of the protective tribofilm. In addition, they noticed that shorter phosphate chains are formed with increasing the amount of water in the oil.

In line with these results, Parsaeian et al. [273] found that the smaller the relative humidity the thicker the tribofilm and the longer the formed phosphate chains. The trend holds true for the two tested temperatures, i.e. 80 and 98 ^{o}C. This was explained by the difficulty of ZDDP molecules to reach and react with

the steel surface in an oil containing higher amount of free or dissolved water. In another study, Parsaeian et al. [241] studied the effect of water contamination in oil, i.e. 0, 0.5, 1.5 and 3 wt.%, on wear and tribofilm thickness. The results showed that the larger the water content is present in oil the thinner the tribofilm thickness. Similar findings were also reported by Faut and Wheeler [274] for tricresyl phosphate (TCP) additive.

All these results highlight the fact that the presence of water affects not only the rate of the additive decomposition but also the final composition of the protective film. Owing to the high affinity of phosphates to water [17], when water contamination occurs, some water molecules will react with the phosphate and replace ZnO, whereas some amount of water will stay unreacted. This will affect the ratio of ZnO/P_2O_5 and thus the phosphate chain length. Furthermore, the presence of unreacted water is expected to affect this ratio up or down depending on the localisation of water, i.e. at the metal surface or in the bulk. Therefore, to better understand the effect of water on the composition of ZDDP or DDP antiwear film, the focus should be given to trace the composition without water and study how water can change this morphology.

3.8.2 Effect of water on the tribological properties of tribofilms

There are only few studies [33, 236, 241, 242, 273] on the effect of water on the friction and wear performance of the P-based antiwear film, i.e. mainly of ZDDP. These studies mainly showed that water inhibits the formation of the protective tribofilm and increases wear. The authors attributed these effects to the depolymerisation reactions of the long polyphosphate chains and to the increased surface distress in the presence of water. Other reasons for the increased wear in the presence of water in the oil can also be related to corrosion, hydrogen embrittlement and accelerated fatigue due to the possible condensation of small amount of water in the microcracks.

Cen et al. [33] found that the effect of water on friction is less prominent than the case of wear. However, although their results showed that up to a moderate amount of water, friction is not affected, the experiments conducted in a humid atmosphere of a relative humidity 90%, showed that the friction coefficient drops by about 40%. It should be noted that this behaviour of friction can be related to the one of wear. Due to the larger wear in the case of large water contamination, surface smoothing can occur during the induction period that can lead to a reduction in friction coefficient. In addition, this reduction can also be

related to the formation of thinner tribofilm of short polyphosphate chains when high water concentration is present in the oil.

These scarce results highlight the importance to study the effect of water on the decomposition of antiwear additive and the final composition. Understanding the effect of water on these processes helps control the wear and friction performance by just controlling the amount of water in the oil and its evaporation rate. In addition, understanding the effect of water provides insight into the reaction kinetics of the ZDDP or DDP tribofilm formation and its behaviour in different environments.

3.9 Summary

3.9.1 Knowledge gaps

Throughout this chapter, an overview of the state-of-the-art of the different aspects concerning the P-based antiwear additives such as ZDDP and DDP were presented and discussed. The main knowledge gaps were found centring on the possible decomposition reactions of the additives and the chemical and physical nature of the formed antiwear films and their possible rheological properties that can enable them to reduce wear. Furthermore, the most significant knowledge gap was found to be related to the inability of the current experimental techniques to capture the chemical reactions between rubbing contacts in-situ without altering the contact condition. These gaps are summarised in more detail in the subsequent sections.

3.9.1.1 Decomposition mechanisms of antiwear additives

Over the last 70 years, different theories were proposed to explain the decomposition reactions of P-based antiwear additives to form protective tribofilms covering the contacting surfaces. These works were discussed in different reviews [7, 24, 129, 130]. However, despite being studied extensively, the exact reaction pathways of the decomposition process of these antiwear additives are still not fully elucidated. Yin et al. [118] proposed a mechanism for the growth of ZDDP tribofilms starting with the strong chemisorption of the ZDDP additive to the oxide layer on the steel surface. The step is followed by the fast formation of long polyphosphate chains and the slow formation of short phosphate chains. On the other hand, Jones and Coy [8] proposed that the decomposition of the ZDDP starts with the migration of the alkyl groups from oxygen to sulphur atoms, i.e. by self-alkylation or transalkylation, followed by the formation of phosphoric acid

as a result of thioalkyl (−SR) elimination. Finally, the phosphate chains P−O−P are formed as a result of nucleophilic substitution of one phosphorus species with another. Fuller et al. [28] combined the mechanisms of Yin et al. [118] and Jones and Coy [8] and suggested that when the ZDDP adsorbs to the metal surface it is transformed into a rearranged ZDDP or linkage isomer (LI-ZDDP) in which the alkyl groups have migrated from O to S atoms. In this LI-ZDDP all the sulphur atoms originally bound to Zn, are partially or totally replaced by oxygen. Finally, thermal-oxidation of LI-ZDDP occurs to form long polyphosphate chains.

To validate the occurrence of these reactions, previous works presented indirect evidence based on different surface analysis techniques, e.g. XPS and XANES, to support the identification of certain decomposition reactions. The majority of these studies, however, were performed mainly on mature tribofilms, i.e. after rubbing for a long time. There are only a few studies [118, 161–164] that have attempted to examine the decomposition process and the change in the tribofilm composition primarily during the running-in period at short rubbing times. The lack of such studies makes it difficult to gain insight into many of the theories proposed in the literature regarding the reaction pathways of the decomposition process of P-based additives. This study aims at utilising a combination of techniques, i.e. XPS, XANES, TEM-EDX and AFM, to examine the decomposition process of P-based additives over different rubbing times especially during the early stages of the reaction. This should give more insight into the morphology and composition evolution of the formed tribofilm and the possible decomposition mechanisms.

3.9.1.2 Composition of antiwear tribofilms

There is a solid consensus that under rubbing and heating, ZDDP decomposes to form a protective tribofilm that consists mainly of Zn, P, S and O. This was confirmed using SEM [16, 17, 34, 144, 165–167], AES [16, 34, 157, 165, 166, 168], XRF [14, 15, 145, 169, 170], XPS [14, 17, 34, 38, 151, 157, 168, 171–174], XANES [28, 118, 161, 163, 172, 175–177] and SIMS [14, 17, 137]. However, the exact composition and its association with the operating conditions is still not fully understood. For instance, it is still unclear why the short chain phosphates are present in the bulk of the tribofilm near the metal surface as opposed to the long ones near the tribofilm surface. Fuller et al. [28] related this to the reaction between the long chain phosphate and water, which can depolymerise the long chains into shorter ones. Others [275] related it to the ability of phosphate glass to dissolve sulphides. Furthermore, several other studies [19, 20, 118, 276] suggested that the cation exchange reaction between Fe and Zn necessitates the depolymerisation of the long chains, which ends up forming a composite

Fe-Zn polyphosphate matrix of short chains. However, this reaction requires a temperature as high as 1300 K [183], which is not attainable during any normal tribological conditions. Nonetheless, it was suggested that the local temperature, i.e. the flash temperature, at the asperity-asperity contacts can be much higher than the oil temperature and hence the reaction can occur. The evidence for the formation of the Fe-Zn polyphosphate was drawn based on the observation that iron is present in the tribofilm and its concentration increases towards the steel surface [7, 17, 118, 277]. Most of these studies that suggested the presence of iron in the tribofilm were based on sputtering the tribofilm with an ion gun to acquire spectra at different depths, i.e. depth profiling. However, depth profiling using high energy ions can induce preferential sputtering, i.e. better yield, of certain components of the tribofilm more than the others, which can be misleading [278]. Therefore, the results from sputtering experiments should be complemented with other methods such as Focused Ion Beam (FIB) for cross sectional analysis of the samples using SEM-TEM that can provide excellent resolution and surface sensitivity.

In contrast to the studies based on sputtering, several other studies [151, 157, 163, 164, 166, 168] showed that iron is absent from the formed tribofilm. In particular, Nicholls et al. [163] showed that even after 10 s of rubbing the phosphate has most likely Zn^{2+} cations rather than Fe^{2+}.

Part of this work will aim at providing insight into the composition evolution of ZDDP and DDP tribofilms and the polymerisation and possibly depolymerisation reactions of the phosphate chains composing them over different rubbing times.

3.9.1.3 Reaction kinetics of the tribofilms formation

Little is known about the exact kinetics of the decomposition reactions of P-based antiwear additives, such as ZDDP, and the formation of their protective tribofilms. The main obstacles originate from the nature of these tribo-induced reactions that can follow different complex pathways. In addition, the commercial oils containing the antiwear additive may also contain some impurities, other additives, detergents or dispersant that might alter the decomposition pathways and ultimately alter the precursors and the final reaction products, i.e. the tribofilm composition [137]. In addition, the decomposition kinetics are often dictated by the true local conditions of temperature, pressure and load at the asperity contacts rather than the calculated and imposed ones [151]. This complicates and obscures the correlations between the operational conditions and the decomposition kinetics.

Based on the available literature, temperature and contact pressure seem to have the same catalytic effect on the decomposition reaction of antiwear additives [30, 118]. However, it is still not clear whether temperature and contact pressure have a combined additive effect, or one has a bigger effect than the other. Furthermore, the rate of the decomposition reaction has been suggested by Gosvami et al. [30] to initially follow a zeroth order, which after long sliding cycles starts to follow a more complex fractional rate of about 0.3. However, previous results suggested a first order reaction kinetics for the decomposition of materials of similar functional groups found in ZDDP, e.g. dimethyl and diethyl disulphide [279] and other groups under shear [280, 281]. Hence, we need to explore the reaction kinetics of the P-based additives in more detail taking into account the effect of various levels of temperature (25–120 °C) and contact pressure (2–7 GPa).

3.9.1.4 Effect of water on antiwear tribofilms

The wide breadth of literature concerning the P-based antiwear additive has thus far focused on understanding the composition, tribological and mechanical properties of their antiwear films under different levels of temperature, load and rubbing time [7, 129, 130]. However, there are only a few studies [24, 33, 137, 169, 236], which focused on understanding the effect of impurities or contaminants such as water in the oil. Water, in particular, is expected to alter the pathways of the reactions associated with the decomposition of the antiwear additive and the formation of the protective tribofilm. The different possible reaction pathways in the presence of water in the oil led to some conflicting findings in the literature. For instance, Rounds [169] studied the effect of free water on the decomposition of ZDDP and showed that water accelerates the rate of ZDDP decomposition and the formation of the tribofilm. In agreement with these findings, several studies suggested that the ZDDP decomposition is hydrolytic in nature, i.e. catalysed by water. For example, Spedding and Watkins [137] showed that in the absence of water, e.g. by heating the sample up to 100-170 °C in order to evaporate all water in addition to flooding the sample with dry nitrogen, the decomposition reaction was suppressed. In contrast, when the sample was flooded with water-saturated nitrogen, a rapid decomposition rate was observed. Nevertheless, when the tests were conducted at 200 °C, at which most of the water should evaporate, the decomposition proceeded without any significant reduction in the reaction rate. Willermet et al. [24] argued that even a lower temperatures than 200 °C could not slow down the reaction rate, which challenges the premise of the hydrolytic decomposition mechanism. Furthermore, this mechanism contradicts several recent studies that showed an opposite trend in the presence of water. For

instance, the results of Nedelcu et al. [236] showed that water inhibits the growth of the ZDDP tribofilm. This effect manifested itself in the formation of shorter chains of polyphosphates. Other ancillary experiments [33, 241, 242, 273] also showed that water indeed inhibits the formation of the protective tribofilm. The reported results suggested that the larger the amount of water present in the oil, the shorter the formed phosphate chains. In addition, Faut and Wheeler [274] also reported similar findings for tricresyl phosphate (TCP) additive.

Although there seems to be a wider support for the finding that the decomposition of the ZDDP is hindered in the presence of water, which was basically inferred from the formation of shorter phosphate chains [33, 236, 273] or thinner tribofilms [241, 242, 273], the reason behind this suppression is not completely known. Furthermore, the mechanism of short chains formation and its rate remain unresolved. Fuller et al. [28] suggested that the short phosphate chains can be formed as a product of the reaction between the initially-formed long chains and water, which intensifies with increasing temperature. Similar conclusions were drawn by other studies [33, 236, 273], which suggested that water can induce a depolymerisation reaction that shortens the long polyphosphate chains. Furthermore, Nedelcu et al. [236] showed that an increase in surface distress in the presence of water, which was inferred from the high density of surface micropits, can be responsible for the formation of the short phosphate chains.

It should be noted though that these conclusions still do not give clear answer about the rate at which the long phosphate chains depolymerise into shorter ones. In addition, the mechanism by which water possibly reacts with the ZDDP to suppress or delay the decomposition reaction is not fully elucidated. Therefore, part of this work will aim at providing insight into the reaction kinetics of the ZDDP decomposition in the presence of water and the rate of polymerisation and possibly depolymerisation reactions of the formed phosphate chains. This will be achieved by following the formation of the ZDDP tribofilm over different rubbing times, which should enable us to examine the different changes in the tribofilm composition over time that can occur not only to the zinc polyphosphate chains but also to the other species in the tribofilm such as sulphur.

3.9.1.5 Role of cations in tribofilms formation

The available literature still lacks the conclusive answer to the question of whether there is a substantive requirement for the presence of metal cations, e.g. Fe, W and Ti, for the tribofilm to be formed or such metallic cations are dispensable. There is a definite consensus that the ZDDP molecules can adsorb to steel surfaces

and decompose to form protective tribofilms of excellent tenacity [7, 129, 130]. Moreover, other studies showed that ZDDP tribofilms can also be formed on surfaces other than steel. For instance, Zhang and Spikes [142] were able to generate ZDDP tribofilms on WC substrate. The results showed that the rate of formation ranges from 0.2 to 0.7 nm/min depending on the interfacial shear stresses. Similarly, Gosvami et al. [30] using elaborate in-situ AFM tribotests showed that the ZDDP additive can adsorb and decompose to form tribofilms on both Fe-coated and uncoated Si substrates with a similar rate depending on the temperature and contact pressure. It is not clear whether the ability to form tribofilms in these cases was due to the presence of W and Si in particular or due to the operating conditions. Furthermore, for other surfaces such as the ones coated with DLC, the exact chemo-mechanical nature of the coating is expected to play a vital role in the decomposition of ZDDP.

The wear and friction performance of DLC coatings and the properties of any formed tribofilms on them were reviewed extensively in the literature [141, 206–210]. Several previous studies reported that the P-based additives such as ZDDP can react and form protective tribofilms on DLC coatings even without containing any doped cations [31, 32, 211–215]. In contrast, other studies found that no tribofilms can be formed on non-doped DLC coatings without metallic cations [216–221].

The main factor behind the wide disparity between the formation and absence of tribofilms on DLC coatings should be examined closely. In addition, part of this study aims at investigating the role of cations in the decomposition reactions of P-based additives using in-situ AFM tribotests. It will also shed more light on the formation kinetics on different surfaces including DLC coatings while examining the tenacity and durability of any formed tribofilms. Testing various types of P-based additives, whether contain zinc or not, on different surfaces, whether contain iron or not, is crucial in developing a mechanistic understanding of the role of cations in the decomposition of antiwear additives and the formation of their protective tribofilms.

3.9.1.6 Rheological properties of antiwear tribofilms

The use of the P-based additives is ubiquitous in many industries due to their superior antiwear capability. The general consensus regarding the origin of the antiwear mechanism is that it can be due to the i) formation of a rigid sacrificial interface at the contacting surfaces thus preventing adhesive wear [14–18], ii) digestion of sharp particles worn from the contacting surfaces thus mitigating

abrasive wear [19–21], iii) decomposition of peroxy radicals thus limiting surface oxidation [22–24], or iv) combination of the previous mechanisms. The various proposed mechanisms are either mechanical or chemical in nature. However, few studies suggested that the good antiwear properties of the ultra-thin tribofilms formed on the contacting surfaces might have a rheological origin, which can greatly influence friction, lubrication and adhesion properties of any tribological surface [37]. For instance, it was suggested [17, 36, 48] that the layers close to the metal surface, e.g. sulphides and phosphates, are most likely elastic or elastoplastic solids that can be polymeric in nature [151] whereas the outer layers are probably viscous. This indicates that there can be layers in between that have a combination of the two and thus contribute differentially to the overall behaviour of the tribofilm [17]. The top viscous layer can explain the patchy pad-like structure of the tribofilm as a final solidified image of the once hot flowing glass. The ridges of this glass are formed due to asperity-asperity contacts whereas the troughs originate from possibly the flow of some material from the regions of ridges to troughs [36, 248]. Other theories suggested that the pad-like structure is formed due to local variations in contact pressure [167] or surface heterogeneity [30]. However, previous results, e.g. see [7, 20, 36], showed that the tribofilm is also heterogeneous vertically over its depth, which indicates that the heterogeneity of the tribofilm is not solely due to local lateral variations in contact pressure [174].

Based on the discussion above, it can be concluded that the P-based antiwear films have rich mechanical and rheological properties. These properties can be affected by the decomposition degree of the additive and previous thermal and shear history, e.g. sliding and rolling cycles, temperature and load. In addition, the mechanical properties might also be affected by the rheological properties of the tribofilm. For instance, in case of the tribofilm is viscoelastic then its mechanical response can look similar to the plastic behaviour of a compliant material [85]. In addition, its mechanical properties can be rate dependent. Hence, the way the material is measured and how fast it is measured can play a major role in the observed properties. Therefore, this study aims at examining the rheological properties of P-based tribofilms in order to provide better insight into any possible correlations between the rheological, mechanical and tribological properties of the tribofilms and how they are linked to the composition.

3.9.1.7 In-situ evaluation of tribofilms evolution

Extensive experimental and modelling works have been carried out in order to understand the decomposition reactions of oil additives, the formation and

removal of their formed tribofilms and the possible synergy between them [7, 27]. Nonetheless, the complete nature of the tribochemical reactions occurring on the surfaces under shear is still not fully understood. The rate of the decomposition reactions of oil additives and the associated rate of their tribofilms formation under different operating conditions and on different surfaces are still yet unexplored areas though highly important for optimising the running-in period. Furthermore, the role of the available cations in the oil such as iron in the tribofilm formation is still controversial. Several studies [19, 20, 24, 28] suggested that iron is needed for the formation of tribofilms such as the ones of ZDDPs. On the other hand, other studies [29–32] found that these tribofilms can form on surfaces other than iron.

The major obstacle in obtaining better understanding of the transient tribochemical nature at the tribological contacts is mainly due to the inability to probe the contact area directly. Most of the previous studies were carried out ex-situ after the tribological test is stopped and the contacting surfaces are cooled down and separated. This alteration of the initial state of the sample brings about several limitations. Firstly, the surface analysis will be performed under different conditions from the test environment. This can change the composition of the newly formed surface film by exposing it to a new environment of different temperature and relative humidity [24, 33]. Furthermore, it can expose the surface to adventitious entities or contaminants such as carbon [34], which can attenuate the measured atomic concentrations depending on the electrons inelastic mean free path through the elements under study [35]. Secondly, rinsing the surface with a solvent to remove the excess oil, which is the typical practice before carrying out the ex-situ analysis especially under ultra-high vacuum (UHV) conditions, can remove part of the tribofilm layers and hence part of the information can be lost after washing [36]. Thirdly, the fact that the surface can only be probed after finishing the tribological test prevents capturing the early stage of the tribofilm formation. Therefore, it can severely limit our understanding of the dynamical tribochemical nature of oil additives and conceals the occurrence of any side reaction and the identification of any precursors or intermediates. Nonetheless, regardless of these limitations, several ex-situ and in-situ studies examined the tribological contacts after different shearing times and operating conditions, which provided significant insights into the complex tribochemistry of the additives decomposition and the formation of functional tribofilms.

The ex-situ studies were carried out mainly using X-ray photoelectron spectroscopy (XPS) [34, 174], Raman spectroscopy [282, 283], Fourier transform infrared spectroscopy (FT-IR) [251] and X-ray absorption spectroscopy (XAS) [163, 177]. The XAS studies investigated the reactions of different oil additives

including ZDDP [29, 128, 284], DDP [128, 180], potassium triborate [285], phosphate ester additives [179], and other different organosulphur additives [286]. These studies examined the composition of the formed tribofilms, whether on iron [258], Al-Si alloys [29, 287] or other coated surfaces [258]. In addition, several other studies [177, 288] examined the effect of detergents and dispersants on the decomposition reactions and the synergy between the different oil additives. Some of these XAS measurements were combined with X-ray photoelectron emission microscopy (X-PEEM) [89, 163, 285] and Photoelectron Emission Microscope by Synchrotron Undulator Illumination (PEMSUI) technique [289]. A review of the different contributions of these various XAS techniques to tribology was provided by Nicholls et al. [163], which highlighted the importance of XAS especially in studying the reactions of oil additives and the composition of the formed tribofilms.

Although the majority of the previous studies focused on using mainly ex-situ techniques, there is also a number of studies that attempted to probe the chemistry and composition of various materials using in-situ techniques such as vacuum XPS [290, 291], Raman spectroscopy [282, 292] and Attenuated Total Reflectance (ATR)-FTIR [293, 294]. However, these techniques have some drawbacks in addition to their advantages. For instance, despite the surface sensitivity of the UHV-XPS technique, the need for a high vacuum environment necessitates that the tribological experiments to be performed in dry condition without the use of lubricants and additives. The use of Raman spectroscopy can overcome this problem as the surface analysis can be performed under ambient atmosphere. However, not all the vibrational modes of the tribofilms constituents are expected to be Raman active, which depends on the spectroscopic selection rules that requires a change in the polarizability of the molecule [295]. Furthermore, this technique has a large sampling depth, which makes it surface insensitive [296]. In addition, the need to use a transparent sapphire window as one of the counterparts adds a fingerprint of this material to the acquired data. The sapphire window also limits the usage of this technique to an inert surface slides past another surface. The ATR-FTIR technique solves this problem by utilising the total internal reflection through a germanium crystal that can be coated with a thin iron layer of few nanometres. Nevertheless, there are certain difficulties associated with this technique. Due to the ultra-thin coated layer on the crystal, the tribological tests cannot be performed under severe conditions involving wear, which limits the technique to mild operating conditions. Another issue with this technique is related to the possible change in the acquired signal depending on [297]: i) the refraction index of the germanium crystal, which can change with temperature, ii) any local variations in the thickness of the Fe coating on the germanium crystal and iii) the heterogeneity of the tribofilm thickness and composition, which can

lead to variations in the penetration depth of the evanescent wave and effectively the sampling depth. These variations can affect both the intensity and chemical shift of the acquired signal.

In addition to these in-situ techniques, there were numerous studies that utilised in-situ XAS to study the evolution over time of different materials such as catalysts [298, 299], electrodes (cathode materials) of metal oxides [300, 301] and tribofilms of oil additives [162, 238]. Morina et al. [162] and Ferrari et al. [238] studied the evolution of ZDDP thermal films in-situ after different heating times using a heating cell combined with XAS. In order to have a surface sensitive signal, they performed the in-situ experiments in the total external reflectance mode by tilting the samples to an angle less than the glancing angle.

So far, to our best knowledge, there are no reports on the in-situ evolution of the tribofilms of oil additives under realistic conditions involving shear between contacting surfaces using XAS technique. This study aims at developing a technique that allows examining the composition of these tribofilms in-situ under the same testing conditions after different shearing times. This should provide a better understanding of the additives decomposition reactions and their kinetics without altering the sample condition. As a case study, this newly developed technique will be used to follow the composition of ZDDP and DDP additives after different shearing times while keeping the sample at the same testing conditions, i.e. same temperature and without rinsing the surface or altering its state.

3.9.2 Concluding remarks

Throughout this chapter an overview of the state-of-the-art knowledge of the different aspects concerning the P-based antiwear films of ZDDP and DDP additives were presented and discussed. At first, a review was provided on the chemical and physical nature of the antiwear film and the possible reactions during its formation. It was shown that the P-based additives can decompose in different mechanisms, i.e. thermally, hydrolytic or oxidative, to form a complex antiwear film consisting mainly of Zn/Fe, P, S and O. The formation kinetics of these elements are still not fully elucidated. All the recent studies confirmed that the formed P-based antiwear films have a patchy layered structure of large and small pads. The large pads exhibit a great elastic response. The elastic modulus, hardness and thickness of these pads are not uniform but vary along the surface and depth. As these properties change substantially from one position to another, this suggests that they should be considered as local properties rather than averaged values.

The P-based antiwear tribofilms help protect the contacting surfaces by different mechanisms including the digestion of sharp particles and formation of sacrificial rigid layers of good mechanical properties, e.g. elasticity and hardness. There is a lack of studies, however, focusing on the role of the rheological properties of the P-based tribofilms on their durability and antiwear capability.

A systematic study taking into account the aforementioned factors seems to be crucial, which should provide better insight into the origin of the superior antiwear properties of ZDDP and DDP tribofilms in order to be able to optimise their properties and eventually replace them with more environmentally friendly additives.

Chapter 4

Materials and methods

This chapter discusses the materials and experimental methods used to study the tribological, mechanical and rheological properties as well as the composition of ZDDP and DDP tribofilms under different operating conditions of temperature, load and rubbing time. The chapter is divided into three main sections. Section one provides information regarding the materials used in this study and the reasons behind choosing them. It also describes the synthesis procedure of some standard P-based glasses that were used in the identification of the different species within the formed P-based tribofilms. Section two discusses the tribological, mechanical and rheological measurements utilised to probe the properties of ZDDP and DDP antiwear tribofilms. In addition, it presents the surface analysis techniques that were used to examine the composition of the tribofilms. Finally, section three summarises the most important points discussed throughout the chapter.

4.1 Materials

4.1.1 Oils and additives

Mineral oils used to be the most widely used lubricants for various industrial applications [3, 302]. However, mineral oils have many disadvantages including high volatility under high vacuum and low thermal stability, e.g. could oxidise and loose viscosity above 100 ^{o}C and become highly viscous below 0 ^{o}C [302]. The need to improve these limitations to enhance the lubrication reliability pushed towards synthesising artificial substitutes for mineral oils, which are called synthetic oils. Amongst these synthetic alternatives, poly-α-olefins (PAOs) are the most widely used oils [3]. PAOs are formed as a result of the polymerisation of olefins [3], which are unsaturated hydrocarbons with a formula as depicted in Fig. 4.1.

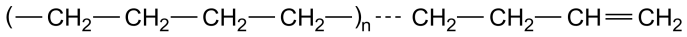

Fig. 4.1 Structure of PAO. Reprinted from Stachowiak and Batchelor [3].

The PAO oil used in this study has a density of 830 kg.cm^{-3} and a viscosity of 18.7 and 4.2 cSt at 40 and 100 ^{o}C, respectively, which corresponds to a viscosity index of 131. Based on this oil, two different formulations were used; one contains secondary ZDDP whereas the other contains DDP additive. The amount of additive was added such that the concentration of P in the oil was fixed at 0.8 wt.%.

The model system of PAO with ZDDP antiwear additive has already been studied extensively in the literature, which makes it ideal choice with good a priori information related to different aspects of the tribological and mechanical properties of the formed tribofilms. In addition, the chosen additives are expected to generate thick tribofilms that possess high viscosity and various degrees of elasticity. The large thickness of the tribofilm is very crucial to this study as it enables us to probe the composition of the tribofilm as well as its mechanical and rheological properties with negligible interference from the substrate.

In order to investigate the kinetics of the decomposition reaction of the P-based antiwear additives and the early stage formation of P and S species, we needed to slow down the decomposition reaction. This was accomplished using two different approaches. The first one was based on using mild operating conditions of temperature, load and speed, which can delay the thermally and mechanical assisted decomposition process. On the other hand, the second approach was based on adding water to the oil, which can hinder the decomposition reaction by either forming complexes with the additive's molecules in the oil [33] or competing with them on the available metal surface [236]. The second approach also enabled us to investigate the effect of water on the composition of P-based antiwear films. For this purpose, the fresh PAO-ZDDP oil was tested and compared with oils having mixed water of 2 wt.%. To assure the homogeneous distribution of water in the oil, the prepared samples were shaken by hand for one minute then placed in ultra-sonication bath for 10 minutes. After mixing, a sample of 100 ml to be used for the tribological tests was placed under vacuum at room temperature until all the entrapped air bubbles were removed.

The concentration of water in the oil and its evaporation rate were measured using Mettler KF V30 Karl Fisher titrator by measuring samples of about 3 ml taken using a syringe from the oil bath of the test after different heating times.

4.1.2 Standard phosphate glasses

In order to quantify the decomposition species and thus the composition of the formed P-based tribofilms, several phosphate glasses were synthesised. The glasses consist mainly of zinc-, iron- and mixed zinc and iron phosphates of a wide range of chain lengths. The general reaction used to synthesise the different glasses was based on mixing ammonium dihydrogen phosphate ($NH_4H_2PO_4$), zinc oxide (ZnO) and iron(III) oxide (Fe_2O_3) with certain proportions, as follows:

$$x_1(NH_4H_2PO_4) + x_2(ZnO) + x_3(Fe_2O_3) \longrightarrow 1.5x_1(H_2O) + x_1(NH_3) + 0.5x_1(P_2O_5)x_2(ZnO)x_3(Fe_2O_3) \quad (4.1)$$

where x_i is the number of the moles of each reactant i, which values are summarised in Table 4.1 for the different glasses.

The materials used in the synthesis of the phosphate glasses are listed in Table 4.2 and the synthesis protocol is shown in Fig. 4.2. At first, the reactants were mixed in alumina crucibles and then placed in high temperature furnace. The furnace temperature was ramped to 1473 K at a rate of 1.8 K/min. After a dwelling time of 2 hrs, the glasses were quenched in room temperature. To avoid crack formation within the glass due to internal stresses, the glass was annealed

Table 4.1 Summary of the operational variables for the tribological tests using MTM.

Glass	x_1	x_2	x_3	O/P[a]	M/P[b]
Zn metaphosphate	1.0	0.50	0	3.0	0.50
Zn polyphosphate	0.86	0.57	0	3.16	0.66
Zn pyrophosphate	0.66	0.67	0	3.52	1.02
Zn orthophosphate	0.50	0.75	0	4.0	1.5
Fe $poly_{33}$-phosphate	1.50	0	0.25	3.0	0.33
Fe $poly_{50}$-phosphate	1.43	0	0.33	3.24	0.49
Fe $poly_{67}$-phosphate	1.20	0	0.40	3.50	0.67
Fe $poly_{100}$-phosphate	1.0	0	0.50	4.0	1.0
$Zn_{25}Fe_{75}$-phosphate	1.06	0.40	0.07	3.08	0.51
$Zn_{50}Fe_{50}$-phosphate	1.14	0.20	0.14	3.04	0.42
$Zn_{75}Fe_{25}$-phosphate	1.24	0.15	0.23	3.18	0.49

[a] Thermal film with no applied contact pressure.
[b] Rubbing time of tribofilms. For thermal films outside the wear scar, the acquisition time should be added.

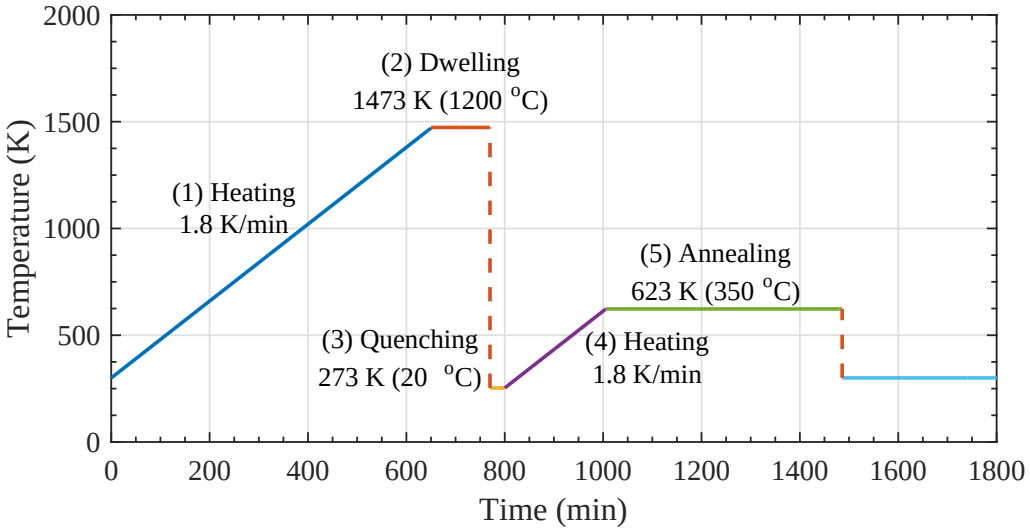

Fig. 4.2 Synthesis procedure of zinc-, iron- and mixed zinc-iron phosphate glasses

Table 4.2 List of the materials used in the synthesis of the different phosphate glasses.

Material	Supplier	Comments
Ammonium dihydrogen phosphate ($NH_4H_2PO_4$)	Fisher Scientific	purity > 99.9%
Zinc oxide (ZnO)	Sigma-Aldrich	purity > 99.9%
Iron(III) oxide (Fe_2O_3)	Sigma-Aldrich	purity > 99.0%
High-alumina crucibles	Sigma-Aldrich	capacity 20 mL
Zn phosphate ($Zn_3(PO_4)_2$)[a]	Sigma-Aldrich	purity > 99.99%

[a] Used for comparison with the synthesised glasses.

to 623 K at a rate of 1.8 K/min for a dwell time of 8 hours. The glass was then taken out of the oven to cool down at room temperature.

4.1.3 Standard sulphur samples

In order to identify the species formed in the ZDDP or DDP tribofilms, which apart from phosphorus contain also sulphur species, several sulphur standard samples were studies using XPS and XANES. This will enable us to have a parallel comparison with the ex-situ and in-situ data as well as with the available data in the literature.

The sulphur samples, which are listed in Table 4.3, were obtained in powder form of high purity typically > 99.9 % except for the naturally occurring minerals of pyrite and sphalerite. Prior to the surface analysis, the powder samples were ground and pressed into plates of diameter 5 mm and variable height above 3 mm.

Table 4.3 List of the materials used in the synthesis of the different phosphate glasses.

Material	Supplier	Comments
Zinc sulphide (ZnS)	Sigma-Aldrich	purity > 99.9%
Iron(II) sulphide (FeS)	Alfa Aesar	purity > 99.9%
Iron disulphide (FeS_2)	Sigma-Aldrich	purity > 99.8%
Pyrite (FeS_2)	Alfa Aesar	Natural mineral[a]
Sphalerite ((Zn,Fe)S)	Alfa Aesar	Natural mineral[a]
Zinc sulphate monohydrate $ZnSO_4 \cdot H_2O$	Sigma-Aldrich	purity > 99.9%
Iron (II) sulphate hydrate ($FeSO_4 \cdot xH_2O$)	Sigma-Aldrich	purity > 99.9%
Iron(III) sulphate hydrate ($Fe_2(SO_4)_3 \cdot xH_2O$)	Sigma-Aldrich	purity > 99.9%

[a] Purity could not be verified.

Table 4.4 Summary of the operating variables for the tribological tests using the MTM rig.

Operational variable	Value
Material	PAO+ZDDP
Temperature (^{o}C)	80
Load (N)	60
Entrainment Speed (mm/s)	35
Water (wt.%)	0, 2
Time (minutes)	2.5, 5, 10, 20, 30, 60, 120

4.2 Experimental methods

4.2.1 Tribological characterisation techniques

The tribological tests were performed in two sets; the first set was carried out ex-situ using the mini-traction machine (MTM) rig, whereas the second one was performed in-situ using a newly developed liquid cell coupled with the AFM and a miniature pin-on-disc tribological rig coupled with XAS. The details of these techniques will be discussed in the subsequent sections.

4.2.1.1 Mini-Traction Machine (MTM)

To investigate the evolution of the reaction kinetics of the ZDDP and DDP antiwear additives and the evolution of the composition and structure of the formed tribofilms, different tests were performed at different rubbing times using the experimental parameters listed in Table 4.4.

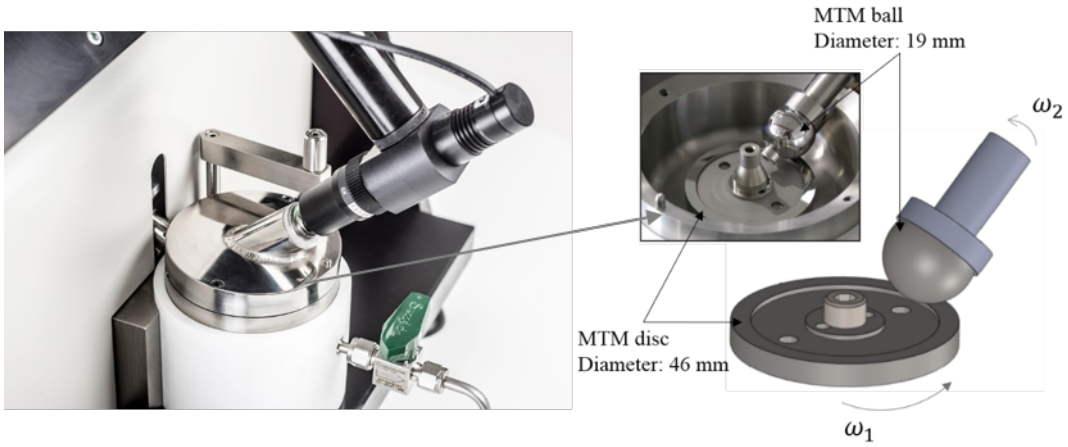

Fig. 4.3 Schematic of the mini-traction machine (MTM) used to perform all the tribological tests. It consists of a ball and disc, which can be rotated independently to achieve different slide-to-roll ratios.

All the tribological tests were performed at a constant realistic temperature of 80^{o}C. The low temperature was chosen in order to slow the decomposition reaction and to be able to detect the formation of any intermediate species. As rolling is as important as sliding to engineering applications such as bearing elements, the Mini-Traction Machine (MTM) rig shown in Fig. 4.3, was used to perform the tribological tests under rolling and sliding conditions due to its capability to rotate the ball and disc independently. The spacer-layer imaging method (SLIM) in MTM rig, which was developed by Cann et al. [303] and is shown schematically in Fig. 4.4, was used to measure the average tribofilm thickness after the different rubbing times. The level of slide-to-roll ratio (SRR) for all the tribological experiments was fixed at 5%, which corresponds to mainly rolling conditions with a minuscule amount of sliding. Similar to the low temperature, the low SRR was chosen in order to slow the decomposition reaction to be able to detect the formation of any intermediate species. The SRR ratio reported in this work is defined as the ratio of the speed difference (ΔU) between the two contacting surfaces to their average speed, i.e. the entrainment speed, (U_e), as follows:

$$\begin{aligned} \text{SRR } \% &= \frac{\Delta U}{U_e} \times 100\% \\ &= \frac{U_1 - U_2}{(U_1 + U_2)/2} \times 100\% \end{aligned} \tag{4.2}$$

where the subscripts 1 and 2 refers to the disc and ball, respectively.

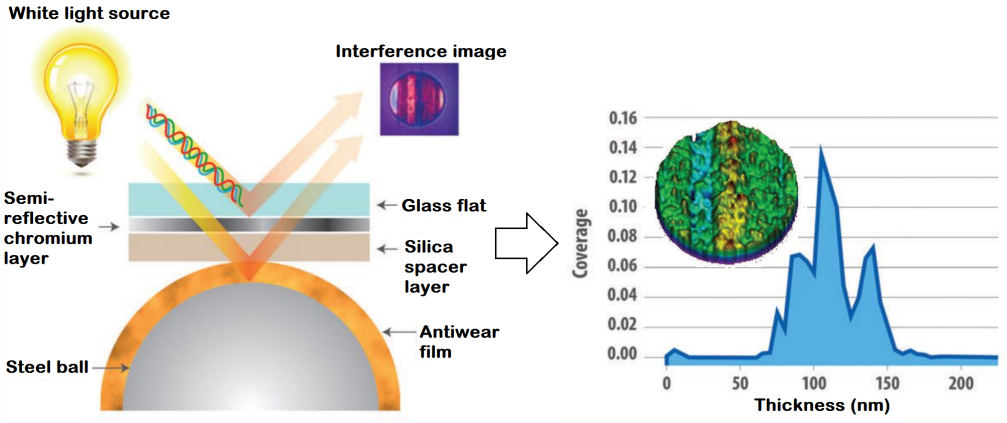

Fig. 4.4 Measurement of the tribofilm thickness using SLIM accessory of the mini-traction machine. Reprinted from Kaperick [304].

The ball and disc were made of AISI 52100 bearing steel. The ball, $D = 19$ mm, and disc, $D = 46$ mm, are polished and both have a nominal roughness of about 13 nm. These values are based on the root mean square (RMS) roughness, which is defined as the RMS deviation of the profile from its mean, which is given by [305]:

$$R_{\mathrm{q}} = \left[\frac{1}{n}\int_0^n y^2(x)dx\right]^{1/2} \tag{4.3}$$

The tribological tests using the MTM were carried out at an entrainment speed of 35 mm/s and a normal load of 60 N, which corresponds to a contact pressure of 1.2 GPa. One way to estimate the lubrication regime under these conditions is by calculating the λ ratio. This ratio represents the local film variation as a function of the local surface roughness. In other words, it is the ratio of the minimum film thickness to the composite RMS surface roughness of the two contacting surfaces, as follows [306]:

$$\lambda = \frac{h_0}{\left(R_{\mathrm{q1}}^2 + R_{\mathrm{q2}}^2\right)^{1/2}} \tag{4.4}$$

where h_0 is the minimum film thickness [m] given by [307]:

$$h_0 = 3.63\left(\frac{U_e\eta_0}{E_r R'}\right)^{0.68}(\alpha E')^{0.49}\left(\frac{W}{E_r R'^2}\right)^{-0.073}\left(1 - e^{-0.68k}\right)R' \tag{4.5}$$

where η_0 is the viscosity of the lubricant at atmospheric pressure [Pa.s], R' is the reduced radius of curvature in the direction of rolling [m], W is the contact load [N] and k is the ellipticity parameter, which is the ratio between the semi-axis of the contact ellipse in the transverse direction [m] and the semi axis in the direction of motion [m], and α is the pressure-viscosity coefficient [m^2/N], which

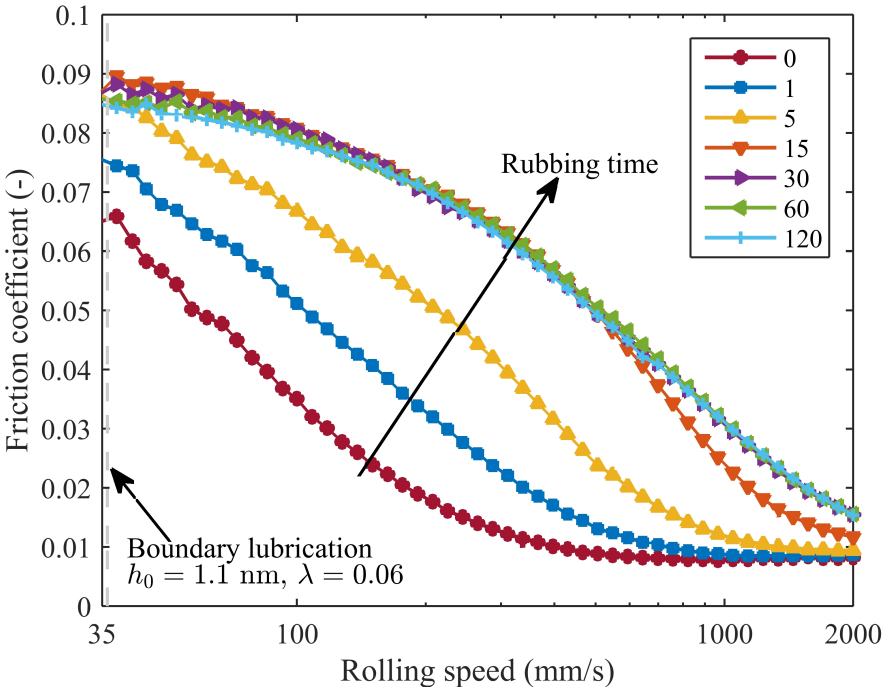

Fig. 4.5 Stribeck curves of PAO-ZDDP oil after different rubbing times (min). The dashed gray line indicates the speed of 35 mm/s at which all the tribological tests were performed.

can be estimated using the following empirical relation [3]:

$$\alpha = [0.6 + 0.965 \log_{10}(\eta_0/1000)] \times 10^{-8} \tag{4.6}$$

E_r in Eq. (4.5) is the reduced Young's modulus [Pa], which is defined as:

$$\frac{1}{E_r} = \frac{3}{4}\left(\frac{1-\nu_1^2}{E_1} + \frac{1-\nu_2^2}{E_2}\right) \tag{4.7}$$

where E is the Young's modulus and ν is the Poisson ratio. The subscripts 1 and 2 refer to the ball and disc, respectively.

Based on the above relations, h_0 and λ were estimated to be 1.1 nm and 0.06, respectively. As $\lambda \ll 1$, it is expected that the lubrication regime is boundary. However, this is only valid in the beginning of the tribological test because surface smearing and wear can occur during the running-in period due to the asperity interactions, which can change the surface roughness and hence the lubrication regime. Nevertheless, it was estimated that even if the surface roughness of the disc and ball drops from 13 nm to 3 nm, λ is still much below 1, i.e. 0.27, and hence the lubrication regime is still boundary. To validate this estimation, different Stribeck curves, which are shown in Fig. 4.5, were obtained after different rubbing times. It is evident that for the chosen speed of 35 mm/s the lubrication regime

remains boundary during the whole period of the tribological test, i.e. 120 minutes. Based on these curves, it is clear that the lubrication regime remains boundary over the different rubbing times as long as the entrainment speed is less than 40 mm/s.

4.2.1.2 Development of a new AFM liquid cell

To investigate the structural and textural evolution of the P-based tribofilms at the microscopic scale, a new setup was developed, which is shown in Fig. 4.6 for evaluating these properties over time while performing in-situ tribotests. The setup consists of a Dimension Icon Bruker AFM equipped with an in-house developed liquid cell. The cell consists of an aluminium body where the sample under study, i.e. a disc of average Rq roughness of 12 nm, can be fixed using M4 bolt in the centre. This was enough to fix the sample and avoid any drift due to the high contact pressures used during the in-situ tests. The liquid cell itself was mounted on the AFM stage using four magnets. Two cartridge heaters (Watlow, UK) were used to heat the cell, which were inserted inside at a distance 3 cm apart. The two heaters were needed in order to avoid any microflow due to thermal variations within the oil. This effect was also minimised by limiting the oil volume to less than 3 ml through reducing the size of the liquid cell. The temperature of the cartridge heaters were controlled using a PID controller (Watlow, UK) through a closed loop algorithm with two thermocouples integrated in the heaters. Furthermore, one external thermometer was used frequently to double check the temperature of the oil.

The AFM cantilevers used in the in-situ tests are all of RTespa 300 type (Bruker, USA). The cantilever is made of antimony (n) doped Si and is rectangular in shape with length, width and thickness dimensions of $125 \times 40 \times 3.4$ μm^3. An additional layer of 40 nm of reflective aluminium is coated on the backside of the cantilever in order to enhance the laser signal. The cantilever has a nominal spring constant of 40 N/m and a resonant frequency of 300 kHz. The high spring constant was needed in order to be able to apply large contact forces that are sufficient to form adequate volume of the tribofilm within a reasonable period of time. However, the large stiffness can compromise the sensitivity of the cantilever, which is needed in order to have a large deflection at small forces [83]. The cantilever sensitivity was measured using force curves obtained on a hard substrate, i.e. a sapphire sample, before, during and after the in-situ tests following standard procedures described elsewhere [83, 113]. Nonetheless, a brief description is provided here for completeness. Fig. 4.7 shows a schematic of a laser beam deflected from the AFM cantilever and detected by a position sensitive detector (PSD). The deflection

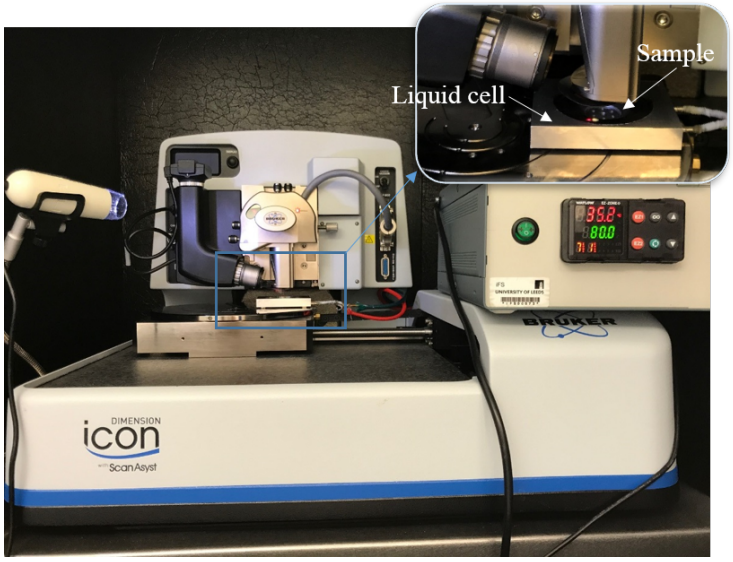

Fig. 4.6 The Dimension Icon AFM (Bruker, USA) and the in-house developed liquid cell used in performing the in-situ tribotests.

of the cantilever Z_c can be related to the difference between the initial and final voltages or currents of the PSD before and after the deflection occurs Δ_{PSD} using the following relation:

$$Z_c = \frac{L_c}{3d}\Delta_{\text{PSD}} = \frac{FL_c^3}{3Ew_c t_c} \tag{4.8}$$

where F is the force applied to the probe, E, L_c, w_c, t_c are the Young's modulus, length, width and thickness of the cantilever, respectively, and d is the distance between the end of the cantilever and the PSD.

The ratio $L_c/3d$ dictates the cantilever sensitivity. However, this cannot be determined accurately as there is large uncertainty related to the exact values of L_c and d. One way to determine the cantilever sensitivity is to perform a force curve on an infinitely hard substrate. On this hard surface, Z_c should have a linear relation with Δ_{PSD}. This is not the case if a soft substrate is used, which is demonstrated in the inset of Fig. 4.7.

From Eq. (4.8), the possible ways to increase the cantilever sensitivity are through having: i) long and thin cantilever, ii) soft cantilever of small Young's modulus, iii) short distance between the end of the cantilever and the PSD, or iv) large forces applied to the probe. Another way to increase the sensitivity is to coat the backside of the cantilever, i.e. opposite to the tip, with a reflective coating. As mentioned before, the cantilevers used in this study has aluminium reflective coating that helps increase the laser signal by up to 2.5 times.

The cantilever tip, which is made of the same material as the cantilever, is a three-sided pyramid in shape with a nominal height of 12 μm and nominal radius

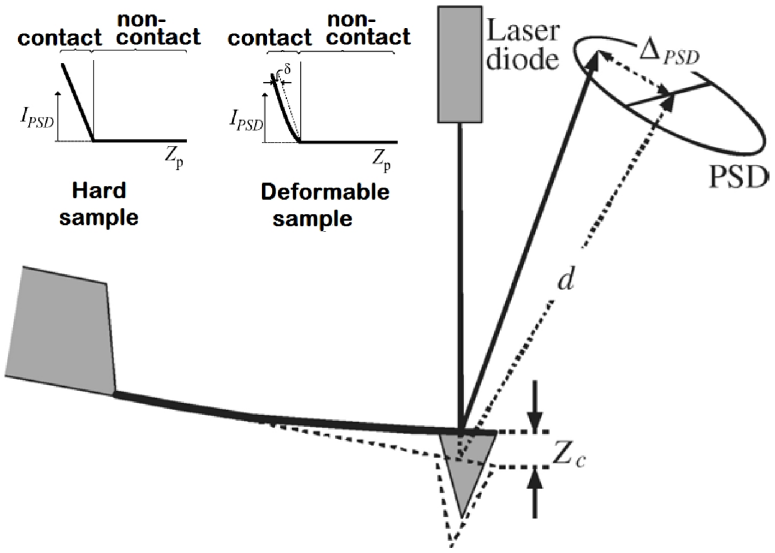

Fig. 4.7 Schematic of the light lever used to detect the deflection of the AFM cantilever. The inset shows the difference in response between soft and hard samples. Adapted from Butt et al. [83].

of 8 nm. It should be noted that all the numeric values noted here are based on the manufacturer's specification and thus certain deviation is expected in these values.

The in-situ tests were performed using a multi-pass two-directional raster scanning. The number of sliding cycles varies from one test to another but the exact values are reported when the data are discussed. The rubbing speed of the AFM during the in-situ tests was fixed at a rate of 200 μm/s scanning an area of 5×5 μm^2. After a specific number of cycles, the tribotests were interrupted to capture high quality AFM images of an area of 10×10 μm^2, which is centred around the rubbed area. These were captured at a low contact force < 100 nN, and a speed of 40 μm/s. The scanning angle throughout the tribotests and imaging was fixed at 90^o, i.e. perpendicular to the axis of the cantilever, in order to collect friction maps of the surface.

Smith et al. [308] suggested that probing the sample properties using large beads, e.g. 5 μm, is better than using sharp AFM tips. The large bead makes larger contact area than the traditional AFM tip, which reduces the contact pressure and thus preserves the sample from wear. In addition, using a spherical bead gives a well-defined contact area, which in the case of the AFM tip is hard to determine. The main limitations of using beads are related to the lengthy waiting period before any tribofilm is detected in addition to the reduction in the lateral resolution. As we aim at studying the morphology evolution of the tribofilms, a high lateral resolution is required, which deems the option of using colloidal cantilevers with beads inadequate for the purpose.

To examine the role of the chemo-mechanical nature of the substrate in the adsorption and decomposition of the P-based antiwear additives, the same procedure discussed above was repeated for different surfaces including AISI 52100 bearing steel, non-doped (a-C:H) DLC coating and different glasses of zinc-, iron- and mixed zinc-iron phosphates. This along with the different additives used, i.e. ZDDP and DDP, will also enable us to study the role of cations in the decomposition of the antiwear additives and the formation of their tribofilms.

The Cr:WC:a-C:H DLC coating consisted of a Cr base layer and an a-C:H top layer. In between these two layers, a graded interlayer of WC was deposited in order to improve adhesion and grading of the mechanical properties between the two materials. The coating was prepared using a hybrid magnetron sputtering and plasma enhanced chemical vapour deposition (PECVD). The deposition temperature during the entire process was lower than 200 ^{o}C. At first, prior to any layer coating, a Plasma Surface Engineering (PSE) step was used to etch and clean the substrate using a bias etching voltage of -200 V through a W filament plasma source for 45 min. Afterwards, the Cr coating layer was deposited using reactive magnetron sputtering for 25 min without surface bias. Immediately after the previous step stopped, acetylene gas was introduced to begin the a-C:H layer deposition using PECVD for 150 min using a surface bias of -780 V. This procedure resulted in an overall coating thickness of $2 \pm 0.3\,\mu$m with a hardness of about 70 on Rockwell scale.

4.2.1.3 Development of a new in-situ XAS tribometer

The complex tribochemical nature of lubricated tribological contacts is inaccessible in real time without altering the initial state of the contacting surfaces. To overcome this limitation, a new design of a pin-on-disc tribological apparatus was developed and combined with synchrotron X-ray absorption spectroscopy (XAS). Using the newly developed rig, it is possible to study in-situ the transient decomposition reactions of various oil additives on different surfaces under a wide range of realistic operating conditions of contact pressure (0.5 - 3.0 GPa), temperature (25 - 120 ^{o}C) and sliding speed (30 - 3000 rpm or 0.15 - 15 m/s).

The design of the tribotester is shown in Fig. 4.8. In this pin-on-disc apparatus the disc is rotating and the pin is stationary. The rotation of the disc is achieved using an Electronically Commutated (EC) flat brushless motor (Maxon Motor, Switzerland) of 12 pole pairs. The motor has a nominal torque of 0.444 Nm, which is larger than the calculated needed torque of 0.25 Nm at 50 N maximum load and thus there was no need to use a gearbox. The motor has a diameter of 90 mm

and a velocity range of 30 – 3000 rpm, or 0.15 – 15 m/s calculated at the central diameter of a wear scar of 97.5 mm. The control of the position and speed of the rotor was performed in a closed loop mode using a MILE digital incremental encoder (Maxon Motor, Switzerland), which has a resolution of 6400 counts/turn. The speed resolution at zero load condition was better than ±0.1 rpm (0.5 mm/s) whereas at 50 N it was better than ±0.5 rpm (2.5 mm/s), which was verified by monitoring the real speed of the motor read by the encoder at 30, 50, and 100 rpm.

The disc has a standard dimension of 1 mm thickness, 110 mm outer diameter and 85 mm inner diameter. The large size was chosen in order to increase the curvature of the wear scar and thus make it easier to be identified. In addition, the large size allows a larger area of the wear scar to be scanned during the XAS experiments and thus obtaining a more accurate averaged signal. The disc was fitted on a lower extruded surface of 1.9 mm depth and 85 mm diameter on the disc holder. To secure the disc, a fixture of a washer shape with a 1 mm protrusion at its outer diameter was screwed to the disc holder and tightened on the disc. The disc holder itself was closely fitted to the motor shaft in order to maximise the power transfer efficiency and reduce the backlash.

The pin of the apparatus consists of a ball fixed at one face without any allowed rotation using an M5 socket head cap screw. The standard size of the ball that was used during the XAS experiments was 5.5 mm, although smaller and larger sizes, i.e. 5, 6 and 6.5 mm, can be permitted as well.

The oil reservoir containing the disc and its holder was heated using two 300 W FIREROD cartridge heaters (Watlow Electric Manufacturing Co., USA) of $1/4''$ diameter and $4''$ length. These heaters were controlled in a closed-loop mode using an EZ-ZONE controller of two integrated PID channels (Watlow Electric Manufacturing Co., USA). The temperature of the oil was measured using two K-type thermocouples embedded in the middle location of the cartridge heaters. Using two thermocouples instead of one insures the homogeneity of temperature throughout the oil reservoir by controlling the temperature at two different locations.

The load was applied using calibrated slotted test weights on a hanger attached to the end of a loading arm. The alignment of this arm and the apparatus was checked using an electronic spirit level (Magnetic DXL360S Digital Protractor angle finder, 360° inclinometer), which has a resolution of 0.01^o, accuracy of 0.05^o and measuring range of 360^o for a single axis and $\pm 40^o$ for dual axis.

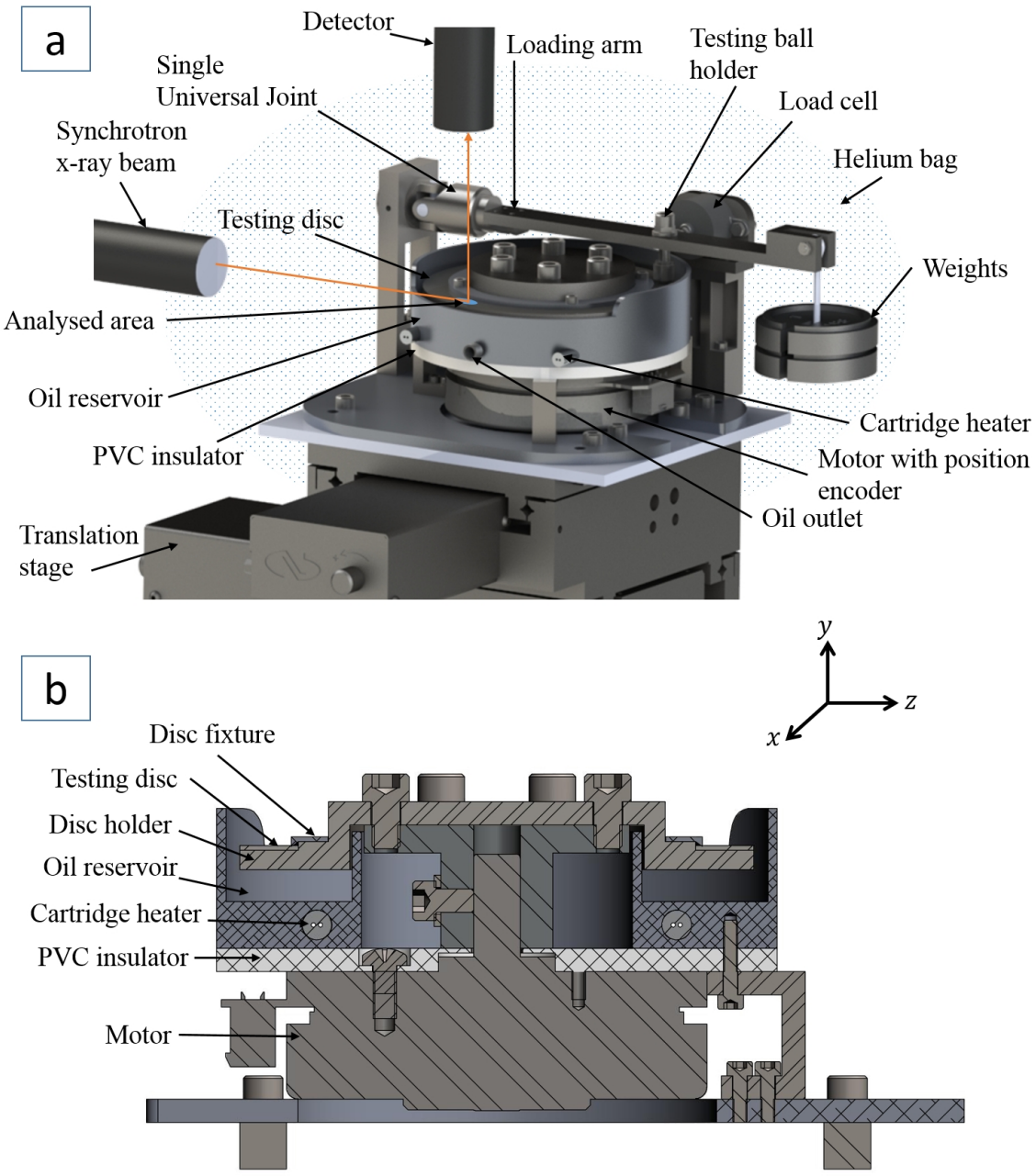

Fig. 4.8 Schematic of a) the assembly and b) a cross-section of the tribological apparatus used in the in-situ XAS experiments. The synchrotron X-ray incident beam and the XRF and XAS detector are also shown in a). The detector is placed in the vertical geometry at a right angle relative to both the incident beam and the tribological surface.

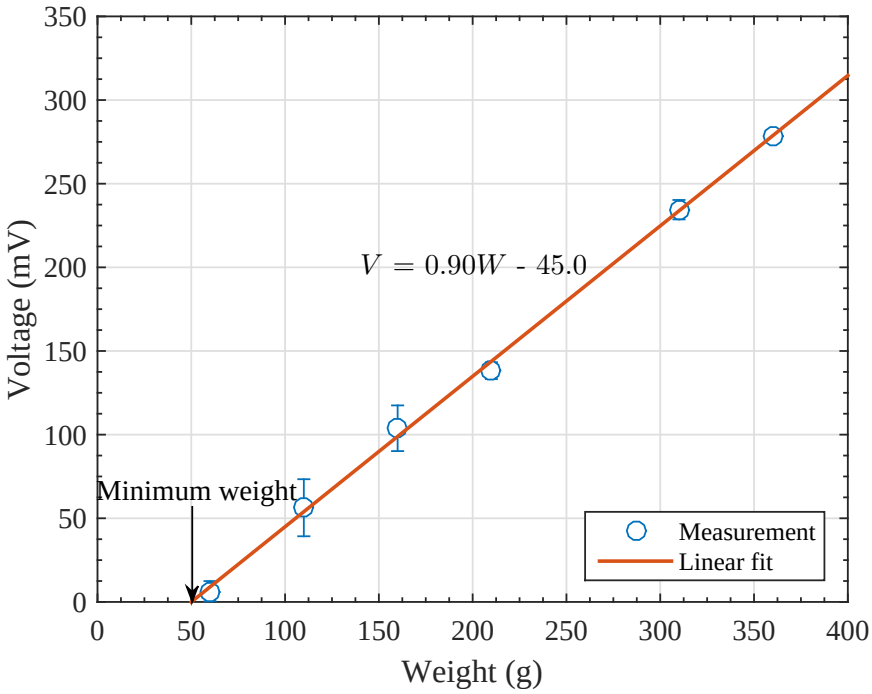

Fig. 4.9 Friction force calibration curve of the large load compression cell used in the tribotester. The calibration equation used to fit the experimental data and the minimum weight detectable by the load cell are indicated.

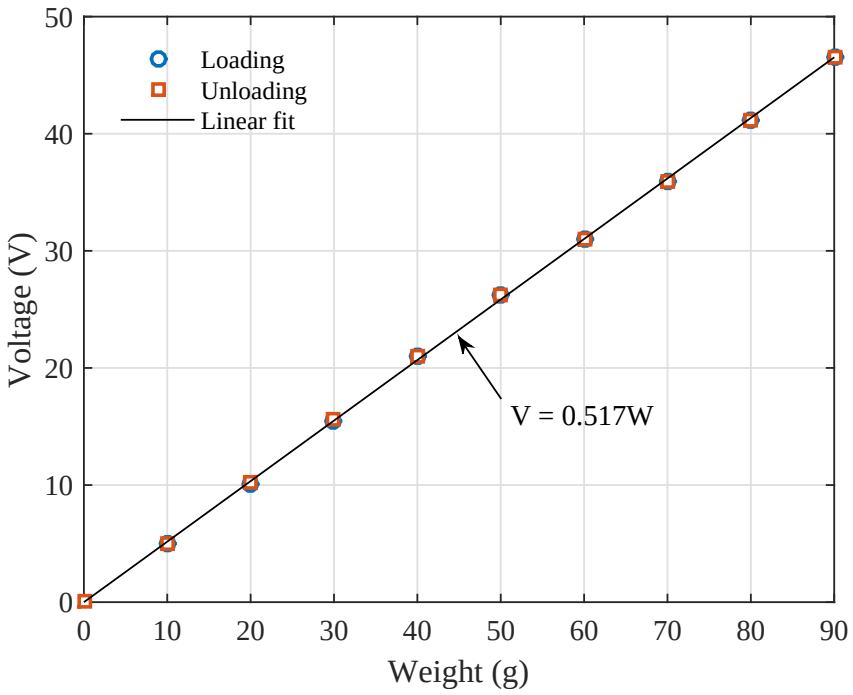

Fig. 4.10 Friction force calibration curve of the small load compression cell used in the tribotester. The calibration equation used to fit the experimental data and the minimum weight detectable by the load cell are indicated.

The friction force was measured using two different load cells depending on the estimated friction force, i.e. high load cell for forces > 1.0 N and low load cell for forces ≤ 1.0 N. The high load cell was a compression load cell (Phidgets Inc., Canada) of a load capacity ranging from 0 to 4.5 kg. Fig. 4.9 shows the friction force calibration curve of the cell. In the range of the measured loads, the output voltage appears to increase linearly with the added weights with a slope of 0.9 V/Kg, which is slightly different from the one of 1.0 V/Kg suggested by the manufacturer. The creep of the cell was found to be $\pm$ 0.5 mV/hr, which is within the suggested long term deviation creep of 5 mV, i.e. about 50 g, suggested by the manufacturer. For small friction forces ≤ 1.0 N, a shear load cell (Phidgets Inc., Canada) was used, which has a load capacity ranging from 0 to 100 g. Fig. 4.9 shows the friction force calibration curve of this cell. In the range of the measured loads, the output voltage was directly proportional to the added weights with a slope of 0.517 V/g. The output voltage signal was amplified and conditioned using a Wheatstone bridge amplifier (Phidgets Inc., Canada). The maximum uncertainty in the measured load due to the non-linearity, hysteresis and creep of the load cell was better than $\pm$50 mg, as suggested by the manufacturer and verified experimentally.

The counterbodies consisted of a ball, which is stationary and free of rolling, and a disc, which rotates with the motor. The disc has a diameter of 110 mm and was made of spring steel (AISI 1074 / SAE 5165) of average hardness of 47 on Rockwell scale. The ball has a diameter of 5.5 mm and was made of grade 100 hardened steel (AISI 52100) of average hardness of 64 on Rockwell scale.

The Cr:WC:a-C:H DLC coating consisted of a Cr base layer and an a-C:H top layer, which was the same recipe discussed in section 4.2.1.2 used for the in-situ AFM tribotests.

The experimental conditions during the in-situ XAS experiments are summarised in Table 4.5. The sliding speed for all the listed tests was fixed at 50 rpm. The large contact pressure, low sliding speed and low hardness of the disc compared to the ball suggest that a clear wear scar should appear on the disc, as the experiments were performed in the boundary lubrication regime in which asperity-asperity contact occurs. This was verified by the visual inspection of the disc even after a few seconds of shearing.

The experiments were performed under helium environment. The choice of helium is advantageous in many ways. The low atomic number helium reduces absorption of low-energy phosphorus and sulphur fluorescence signals. In addition, owing to its unique characteristics of being colorless, odorless, non-toxic and non-flammable gas it can be used at ambient and high temperatures without

Table 4.5 List of the experimental conditions during the in-situ XAS measurements.

#	Counter surfaces	Additive	T (^{o}C)	P (GPa)	Duration
1	Steel ball/Steel disc	ZDDP	80	-[a]	2.5, 5, 10, 20, 30,
2	Steel ball/Steel disc	ZDDP	80	2.2	60 min[b]
3	Steel ball/Steel disc	ZDDP	80	1.0	
4	Steel ball/Steel disc	DDP1	80	1.0	6s, 30s, 1 min,
5	Steel ball/Steel disc	DDP2	80	1.0	2.5 min, 5 min,
6	Steel ball/Steel disc	ZDDP	25	1.0	10 min, 20 min
7	DLC ball/Steel disc	ZDDP	80	1.0	

[a] Thermal film with no applied contact pressure.
[b] Rubbing time of tribofilms. For thermal films outside the wear scar, the acquisition time should be added.

health risks. Furthermore, helium is an inert gas and thus it is not expected to interact or react with the metal surface or the oil and its additives. The helium environment also helps exclude water contamination, which originates from the humidity carried by the ambient air, from affecting the chemical reactions under study. Although this is different from the real testing conditions that are affected by the presence of oxygen and water, it helps understanding the fundamental reactions with less complexity by excluding these factors. The initial theory regarding the decomposition mechanisms of ZDDP suggests that they can be thermal [137, 144], thermo-oxidative [28, 118], hydrolytic [137] or hybrid. Focusing our attention on one mechanism only, i.e. thermal, helps understanding the extent of contribution of the other mechanisms by comparing our results with the ones reported in the literature under more realistic conditions.

During the acquisition of the XANES spectra, shearing was stopped but the temperature control was maintained. Although for real in-situ experiments the test conditions should not be altered, stopping shearing during the spectra acquisition was performed in order to obtain time-resolved information both inside and outside the wear scar. This is a first step towards a complete in-situ technique by acquiring the signal while the disc is rotating, which is planned for the next beam time.

The location of the wear scar on the disc was identified by elemental mapping of P and S using scanning micro-X-ray fluorescence (XRF) mapping, as shown in Fig. 4.11 plotted using PyMca Application (version 5.1.1). The maps were acquired from an area of 1.75 mm x 0.40 mm by moving the tribotester in the lateral direction (x), in the horizontal plane perpendicular to the incident beam, from -0.40 mm to 1.35 mm with a step size of 0.01 mm and changing its height along the y-axis, in the vertical plane, from -0.80 mm to -1.20 mm with a step size of 0.02 mm. The mapping was performed using an excitation energy of 2600

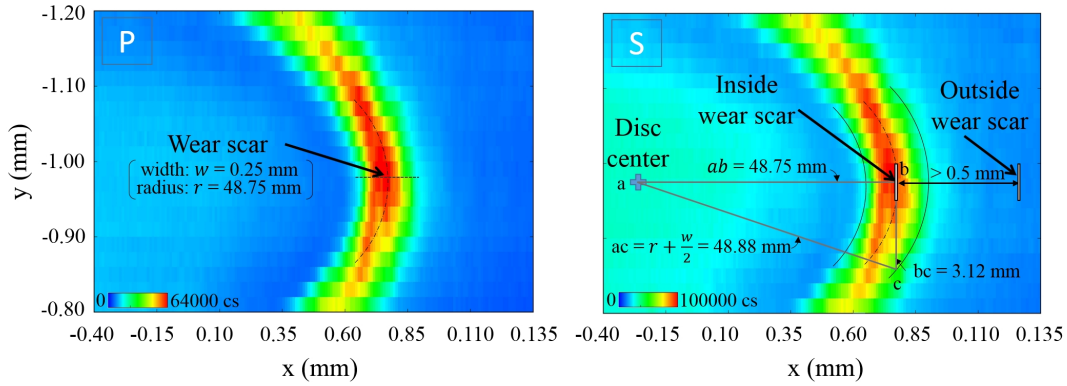

Fig. 4.11 XRF maps (1.75 x 0.40 mm^2) of the distributions of P (left) and S (right) elements found on the disc after 10 minutes of shearing time. The maps were captured by scanning the disc surface in the lateral direction along lines of 1.75 mm and in the vertical direction at different heights of 0.4 mm relative to the incident beam. The schematic of the right-angled triangle abc (not to scale) was used to identify the size of the areas considered inside and outside wear scar.

eV, which is sufficient to observe the K shell peaks for both P and S elements of interest as it is about 300 eV higher than the maximum $k\alpha$ emission energy of P (2010 eV) and S (2309 eV). The energy window for the $k\alpha$ P peak was defined between 1880 eV and 2100 eV whereas for the $k\alpha$ S peaks was defined between 2200 eV and 2400 eV. During acquisition, the data were analysed online through the GDA (Generic Data Acquisition) software (version 8.34) associated with beam I18 by fitting the spectra with Gaussian peaks at the regions of interest and subtracting the background using a linear fit.

The regions considered inside and outside the wear scar as specified in Fig. 4.11 were determined based on the diameter of the wear scar and footprint of the beam. As the rig is designed such that the ball shears the disc in the middle region between its internal and external diameters, this results in a wear scar diameter of 97.5 mm measured from the centre of the disc. Taking into account that the rig was at a glancing angle of 2^o, and the width and length of the incident beam were 50 μm and 200 μm, respectively, this produced a beam footprint of 50 μm x 2800 μm on the disc. Due to the large diameter of the wear scar, the region inside the wear scar can accommodate a beam footprint up to 6.2 mm. To insure that the signal is within the wear scar without overlapping with regions from outside, the beam was centred on the middle point of the wear scar at the brightest and furthest spot to the left of the disc, as shown in Fig. 4.11. The region outside the wear scar was selected to be at the same y-coordinate of the region inside the wear scar, i.e. same sample height, but with an x-coordinate greater than 0.5 mm.

After the XFR maps acquisition and sample positioning, the XAS spectra of P and S k-edges were acquired in two locations, i.e. one inside and one outside

the wear scar, which took typically about 15 minutes per scan. The scans were repeated 3 times to obtain a better signal to noise ratio, although a good ratio was also obtained using a single scan only. The scanning parameters of the pre-edge, edge and post-edge regions of S and P k-edges were as follows. The pre-edge energy step was fixed to 3 eV with a time step of 0.5 s. The edge energy step was fixed at 1 eV with a time step of 0.5 s. Finally, the EXAFS step was set to a high resolution of 0.1 eV with a long time step of 3 s in order to obtain a better signal for data fitting and analysis. Finally, Athena software (version 0.9.24) was used to correct the background and normalise the acquired data following standard procedures suggested by Ravel and Newville [309].

4.2.2 Mechanical characterisation

The mechanical properties of the tribofilm, which are related to its durability and tenacity, were quantified by following the evolution of the structure of the tribofilm over different levels of contact pressure. However, in order to avoid any contribution from the tribofilm growth under the applied high contact pressure, these experiments were performed by shearing mature tribofilms at ambient temperature of 25 ^{o}C using fresh base oil that does not contain any antiwear additive. The applied contact pressures ranged from 2.0 to 7.0 GPa following the same procedure described earlier for generating the tribofilms.

Another set of experiments was also used to quantify the adhesion, dissipation, deformation and elasticity of the tribofilm using the AFM force-distance curves, as shown schematically in Fig. 4.12. These data were collected in-situ during different stages of the tribofilm formation. The procedure itself is considered the least destructive to the AFM probe and tribofilms of all the AFM modes [310]. This can be easily demonstrated by examining the way this mode works. Following Fig. 4.12, at point A the AFM tip is still away and not touching the surface. When the tip approaches the surface, the attractive forces, e.g. van der Waals, electrostatics and capillary forces, grow until they overcome the stiffness of the cantilever and pull the tip down towards the surface at point B, which is called the snap-in point. At this point, the tip stays on the surface accompanied by a rise in the normal force and deformation until the Z-position of the modulation, represented by a dashed line in Fig. 4.12, reaches its lowest position at point C. This is the position at which the peak force occurs. After reaching the peak force, the cantilever starts to retract while the tip is still attracted to the surface due to adhesion and other short range forces. At point D, which is called the pull-off point, the cantilever's pulling force overcomes the short range forces and the tip

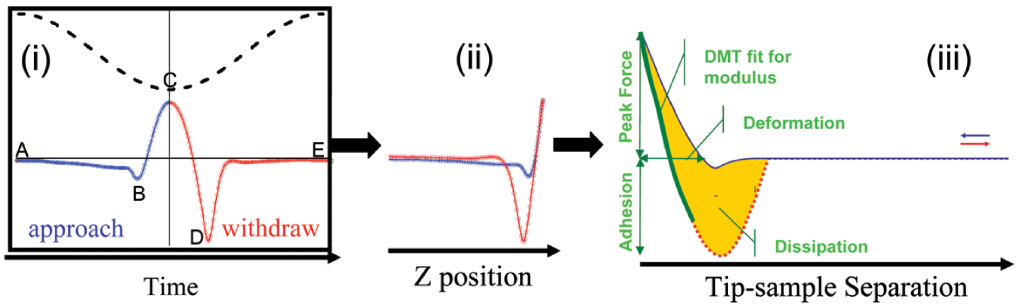

Fig. 4.12 Force curves using PeakForce QNM mode and the procedure to calculate deformation, dissipation and elastic modulus. Reprinted from Pittenger et al. [310].

is released from the surface. Fig. 4.12(iii) illustrates how the different mechanical properties, i.e. adhesion, dissipation, deformation and elasticity of the sample, are extracted from force-separation curves analysed in real time. Young et al. [110] compared the capability of this method to measure the Young's modulus of different materials as compared to nanoindentation. The study showed that the two methods give in essence similar results for most of the tested samples.

4.2.3 Rheological characterisation

The rheological properties of the P-based antiwear tribofilms were mainly quantified using the AFM. In order to obtain these properties, several considerations were taken into account. First, the geometry of the tip-substrate counterbodies was simplified to a plate-plate geometry without a direct contact between them but separated by the tribofilm, as depicted in Fig. 4.13. This is especially true for worn tips and for tribofilms of thickness larger than the substrate roughness, i.e. $>$ 10 nm. It follows from the previous point that the gap between the upper and lower plates can be taken as the tribofilm thickness. At the limiting case of small gaps, viscosity is not affected by the shear rate but by the shear stress despite the apparent increase in the measured viscosity with the gap [311]. The interfacial shear stress was estimated to be only dependent on the friction coefficient and contact pressure, i.e. $\sigma = \mu P$.

Taking into account the above considerations, the rheological properties of the ultra-thin P-based tribofilms were quantified using creep experiments in which a fixed stress is applied and the resulting deformation is observed. This was discussed in detail in section 2.2.2. In the creep experiments performed in this study, the AFM tip applies a constant stress via contact pressure on a certain initial area of the formed tribofilm, which undergoes deformation and flowability in the lateral direction. Therefore, following the area evolution of the tribofilm as compared to its initial area under the AFM tip would result in obtaining the

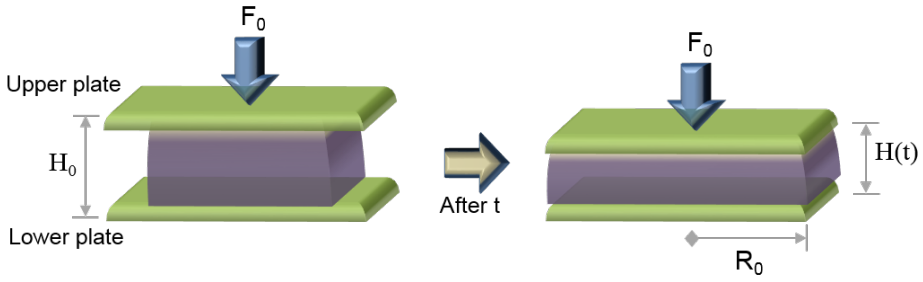

Fig. 4.13 Schematic of the squeeze flow between two parallel plates assuming constant volume just before applying the constant load (left) and after a certain squeeze time (right). In case of constant area, the starting geometry is similar to the image on the right.

strain evolution. The creep compliance can then be found by dividing the strain by the applied stress given by the contact pressure multiplied by the friction coefficient, assuming the two are constant. In the limit of linear viscoelasticity, the creep compliance $J(t)$, can be defined as:

$$J(t) = J_0 + J_R\psi(t) + \frac{1}{\eta_0}t \tag{4.9}$$

where J_0 is the instantaneous creep compliance, J_R is the total recoverable compliance and $\psi(t)$ is the delayed elasticity function, which is zero at time zero and one for $t \longrightarrow \infty$.

Another independent method based on squeeze flow analysis was also used to estimate the viscosity of the P-based tribofilms. This analysis is based on squeezing the formed tribofilm between two parallel plates, e.g. AFM tip and substrate, using a fixed volume or area assumption, as depicted in Fig. 4.13. The fixed area formulation estimates the Newtonian viscosity μ by following the gap evolution $H(t)$, i.e. the tribofilm thickness, between the two plates as follows [312]:

$$H(t) = H_0\left(1 + \frac{4H_0^2F_0t}{3\pi\mu R^4}\right)^{-1/2} \tag{4.10}$$

whereas the fixed volume assumption predicts the change in the film thickness to evolve over time as follows:

$$H(t) = H_0\left(1 + \frac{8H_0^2F_0t}{3\pi\mu R_0^4}\right)^{-1/4} \tag{4.11}$$

where H_0 is the initial tribofilm thickness just before applying load F_0, $H(t)$ is the tribofilm thickness over time, R_0 is the initial radius of the squeezed film, which for the fixed area method can be taken as the tip radius, and $R(t) = R_0(H_0/H(t))^{1/2}$. In the case the area between the AFM tip and substrate can be assumed to be always covered with the tribofilm, the constant area method can be applied otherwise the fixed volume method can be more appropriate.

4.2.4 Surface analysis techniques

Each surface analysis technique can provide complementary information regarding the composition and structure of the different products in the formed tribofilms [157]. Thus, in order to probe the different properties of the antiwear films completely, there is a need to combine the results of multiple surface analysis techniques, e.g. Raman, XAS and XPS [157, 166]. Therefore, the surface analysis performed in this study used a combinatorial approach utilising a wide range of experimental techniques, which are discussed in detail in the subsequent sections.

4.2.4.1 Raman spectroscopy

Raman spectra were performed using a Renishaw InVia Raman microscope, as illustrated in Fig. 4.14. The excitation laser used has a wavelength of 485 nm. The laser spot has high spatial resolution < 1 µm. The acquisition range was in the 200–2000 cm^{-1} region where all the tested antiwear films showed relevant features in their Raman spectra. The acquisition time was fixed at 400 s using 5 and 10% laser power. The low laser power was chosen to avoid sample degradation. The temperature of the measurements was controlled at 25 ^oC and the relative humidity was about 35% in uncontrolled humid atmosphere. Before performing the experiments a quick calibration using a Si(100) target was performed to check the Si peak is at 520 cm^{-1}. Different types of spectra were acquired. This included single scans of points of interest. In addition, map scanning was also performed on regions of interest. One of these regions was across the wear scar to check the heterogeneity of the tribofilm composition.

After acquiring Raman spectra, several pre-processing techniques were implemented on the acquired spectra. The first one was baseline subtraction using smooth spline that kept all the data points above zero. Certain degree of smoothing was required, which was performed using Savitzky–Golay smoothing filter based on the least-squares fitting of polynomials to segments of the data. After smoothing the data, the spectrum was fitted with different Gaussian peaks using

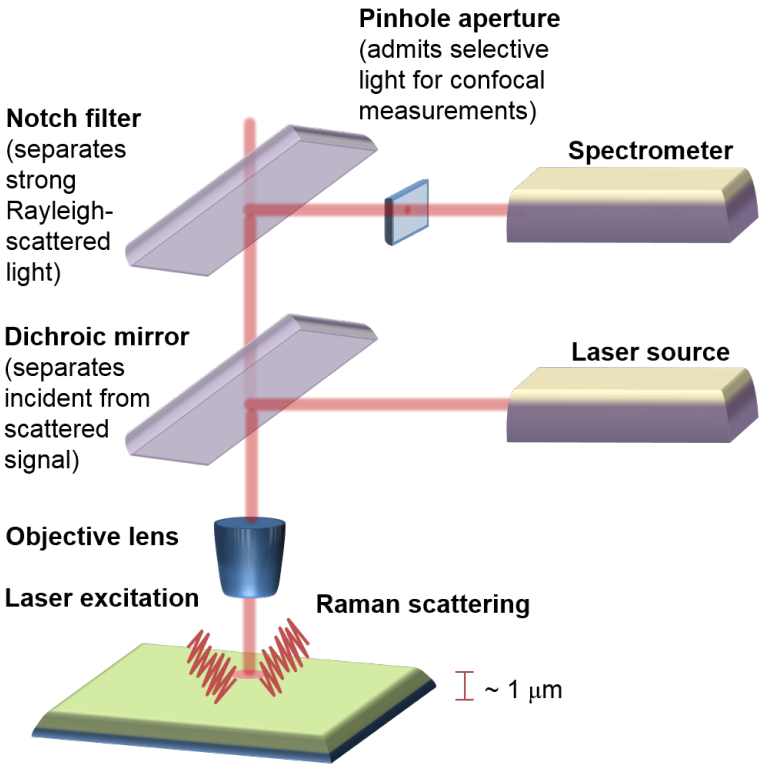

Fig. 4.14 Schematic illustration of the basics of Raman spectroscopy.

WiRE 3.4 software from Renishaw. Assignments to these peaks were done based on the available literature. For P-based additives such as ZDDP, a recent study summarised these assignments [283]. We also used the synthesised samples of zinc, iron and mixed zinc and iron phosphate glasses to determine the peaks assignments.

After these steps, the data can be presented in different ways, e.g. maps of intensity, full width at half maximum (FWHM) or Raman shift of a certain peak. Another way of getting meaningful information is to plot the Raman shift of a certain peak of interest versus its FWHM [313].

4.2.4.2 X-ray Photoelectron Spectroscopy (XPS)

The XPS surface analysis was performed using a PHI (Model 5000) Versa Probe spectrometer (ULVAC-PHI, Chanhassen, MN, USA), as illustrated in Fig. 4.15. The X-ray source used to collect all the spectra is a monochromatic Al Kα (23.7 W, 1486.6 eV), which has a beam diameter of 100 μm. The source analyser angle at which the photoelectrons were collected was fixed at 45^o. A survey scan and high resolution scans of six regions of interest, i.e. C1s, O1s, Fe2p, P2p, Zn2p and S2p, were acquired simultaneously for all the samples at four locations, i.e. three inside and one outside the wear scar. Zn 3s signal was acquired within the

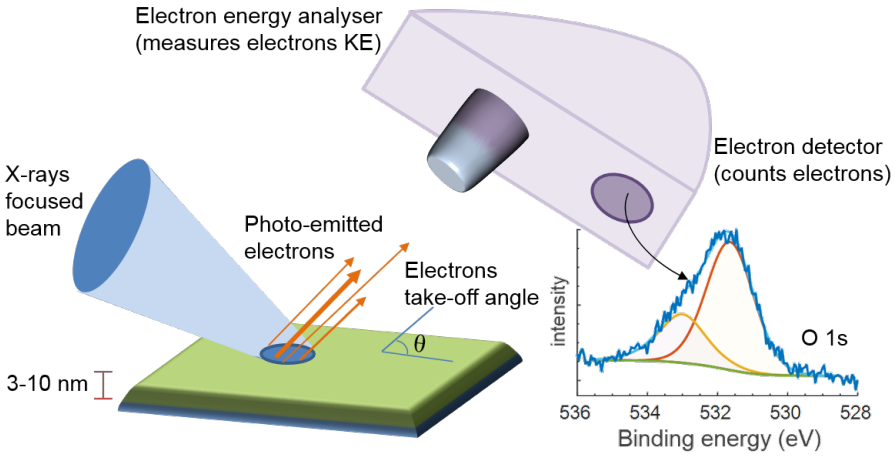

Fig. 4.15 Schematic illustration of the basics of XPS.

Table 4.6 The acquisition parameters used during the XPS high resolution scans.

Element	Lower end (eV)	Width (eV)	No. sweeps	Step size (eV)[a]
C_{1s}	277	20	30	0.05
Fe_{2p}	702	20	20	0.05
Fe_{3s}[b]	82	29	30	0.05
O_{1s}	525	16	10	0.05
P_{2p}[c]	126	20	30	0.05
Zn_{2p}	1015	16	10	0.05
Zn_{LMM}	480	35	15	0.05
Valence[b]	-5	40	30	0.05

[a] For the standard Fe- and mixed Zn-Fe phosphate glasses, the step size was increased to 0.1 eV to avoid degradation.
[b] Acquired only in the case of standard phosphate glasses.
[c] The same scan includes Zn_{3s}.

same region of P 2p. For the standard phosphate glasses, Fe 3s and the valence band regions were also scanned. A summary of the acquisition parameters used during the XPS high resolution scans is presented in Table 4.6. The survey scans were carried out in a fixed analyser transmission (FAT) mode using a pass energy of 187.85 eV and an energy step size of 0.5 eV. The high resolution spectra were also acquired in FAT mode but using a pass energy of 46.95 eV and an energy step size of 0.05 eV. The energy step size was increased to 0.1 eV in the case of Fe- and mixed Fe-Zn-phosphate glasses in order to avoid degradation. During the different signal acquisitions, the pressure of the main ultra-high vacuum chamber was below 1.0×10^{-7} Pa.

Depth profiles were obtained by sputtering the samples using Ar source. The sputter energy was fixed at 2.0 keV. During the sputtering procedure, an electron

Table 4.7 The fitting parameters used in the analysis of the high resolution XPS spectra.

Element	Assignment	B.E. (eV)	FWHM (eV)	Line shape
C_{1s}	Aliphatic	285	1.2–1.4	GL(60)
	C−O	286–287	1.2–1.4	GL(60)
	C=O	288–289	1.2–1.4	GL(60)
Fe_{2p}	Fe metal	706–707	0.9–1.1	GL(60)T(0.8)
	FeO	709–710	2.4–2.8	GL(60)T(0.8)
	Fe_2O_3	712–713	2.4–2.8	GL(60)T(0.8)
O_{1s}	FeO	529–530	1.4–1.6	GL(30)
	NBO	531–532	1.4–1.6	GL(30)
	BO	532–533	1.4–1.6	GL(30)
P_{2p}	Phosphate	133–134	1.6–1.8	GL(30)
	Phosphate	134–135	1.6–1.8	GL(30)
Zn_{2p}	Phosphate	1022-1023	1.6–1.8	GL(65)
Zn_{3s}	Phosphate	140–141	2.2–2.6	GL(60)
Zn_{LMM}	^1G	498–500	2.5–3.0	GL(30)
	^3F	495–496	2.5–3.0	GL(30)

neutraliser was active in order to compensate for any charge accumulation on the surface of the sample.

The analysis of the spectra was performed using CasaXPS software (v2.3.17). The background baseline of all the signals was subtracted using a standard Shirley background line type. As Fe2p, P2p, S2p and Zn2p have a spin-orbit splitting, which means that the total signal is formed of a doublet of 2p 3/2 and 2p 1/2, only the prominent signal of 2p 3/2 was reported in this study.

The deconvolution of the different components within all the signals was performed by fitting them with peaks having Gaussian/Lorentzian product formula line shape. The different parameters and constraints used for fitting the spectra and the assignments to these peaks are listed in Table 4.7, which were obtained based on the available literature [183, 190, 192, 194, 314, 315] and our synthesised standard phosphate glass samples of similar composition to the P-based tribofilms as listed in appendix B. As a quick calibration procedure to compensate any charging during data acquisition, the difference between the measured binding energy of the aliphatic component (C–C, C–H) of C1s signal and its expected value at 285.0 eV was used to shift the binding energy of the other signals. Furthermore, an additional calibration was performed, using the method proposed by Smith [35], to account for the effect of the adventitious hydrocarbon contamination layer on the surface of the samples on the intensity of the signals of interest.

It should be noted that Raman and XPS were used after cleaning the sample with heptane. Several studies [36, 199] investigated the effect of rinsing on the physisorbed and chemisorbed layers of antiwear films. For instance, Dacre and Bovington [199] found that certain types of solvents, e.g. hexadecane, did not affect these layers whereas other solvents, e.g. methanol, removed only the physisorbed layers but not the chemisorbed ones. This suggests that in the worst-case scenario only the physisorbed layers will be removed but the rest of the tribofilm will stay intact, which was also concluded by Bec et al. [36]. Therefore, it can be stated that rinsing is expected to have some effect on Raman or XPS spectra especially in the case of studying the coverage of the tribofilm. However, this effect is not expected to be significant.

4.2.4.3 X-ray Absorption Spectroscopy (XAS)

The XAS experiments were performed using the I18 microfocus spectroscopy beamline at the Diamond Light Source – Oxford (UK). The technical details of this beamline were discussed in detail by Mosselman et al. [316]. The I18 has an X-ray beam of a high spatial resolution of 2 μm x 2 μm and energy range between 2.05 keV and 20.5 keV. The high spatial resolution of this beamline allows the analysis of heterogeneous samples such as ZDDP tribofilms by providing insight into the local variations in composition. The P and S k-edges were acquired using the fluorescence yield (FY) mode. The fluorescence detector (Hitachi, USA), which was positioned vertically at a distance 20 cm above the sample, was a four-element Vortex-ME4 silicon drift detector with Xspress3 electronics processing (Quantum Detectors, UK). It should be noted that the vertical geometry of the detector relative to the surface can have a detrimental effect on the acquired signal especially for thick and concentrated samples. It can increase the elastic and Compton scattering by at least one order of magnitude, which can result in an overall decrease in the signal-to-noise ratio and deterioration of the peaks heights [317]. However, although the vertical geometry worsens the inevitable attenuation of the signal amplitude, it has a negligible effect on the energy shifts. Thus, for comparing the positions of different peaks under the same conditions, the vertical measurement geometry is sufficient.

As in the FY mode, X-ray beam can easily penetrate the formed tribofilm, which has a few tens of nanometres thickness, the technique is mostly considered surface insensitive. However, the surface sensitivity can be largely increased by aligning the sample below the critical glancing angle relative to the incident beam. This results in a total external reflection with an evanescent wave interacting with only a few nanometres, i.e. less than 10 nm, of the surface layers and decaying

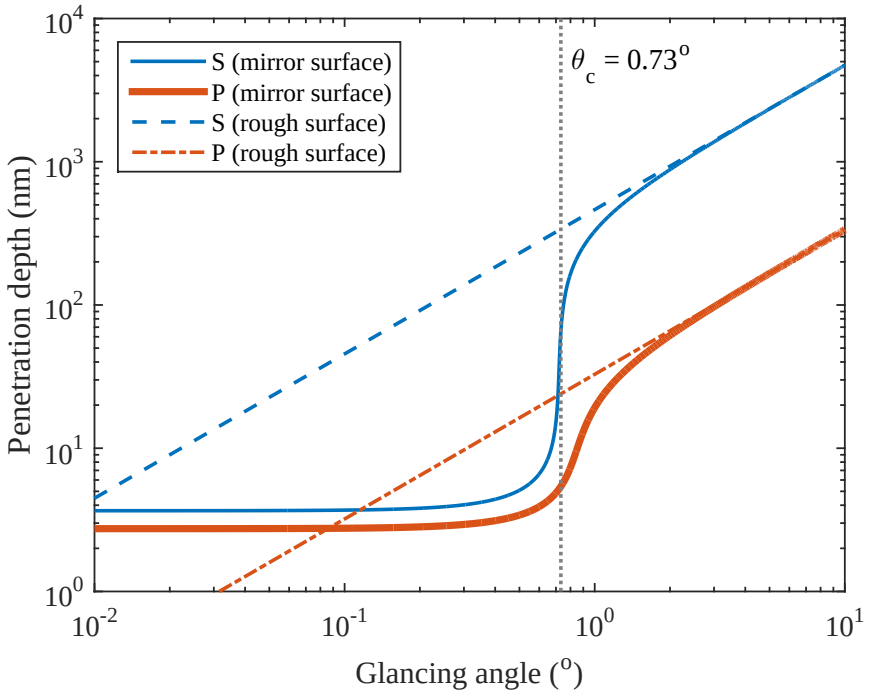

Fig. 4.16 Penetration depth as a function of the glancing angle for smooth and rough surfaces calculated at the k-edge of S and P. The vertical dotted line marks the average critical angle for total external reflection for both P and S.

exponentially with the penetration depth. The critical angle θ_c can be given by [318]:

$$\theta_c = \sqrt{\frac{N_A \rho r_e \lambda^2 f_1^0(\lambda)}{A\pi}} \tag{4.12}$$

where N_A is Avrogado's number (6.022×10^{23} atoms/mol), ρ is the density (g/cm^3), A is the atomic mass (g/mol) of the probed element, r_e is the classical electron radius (2.818×10^{-13} cm), λ is the wavelength (cm) of the incident beam and $f_1^0(\lambda)$ is the real part of the complex atomic scattering factor, which for primary X-rays can be approximated to the first order by the atomic number Z of the target. Using a simplistic assumption that the tribofilm consists mainly of sulphur ($\rho = 2.1$ g/cm^3) or phosphorus ($\rho = 1.8$ g/cm^3), equation (Eq. (4.12)) suggests that the average critical glancing angle is less than 0.73^o, as shown in Fig. 4.16, for both P and S at their average k-edge of 2150 eV and 2473 eV, respectively. A more realistic assumption that the ZDDP tribofilm consists mainly of zinc polyphosphate [7] ($\rho = 3.3$ g/cm^3 [319]) suggests a critical glancing angle of 0.80^o.

Another parameter that is as important as the glancing angle is the penetration depth of the incident beam into the probed sample. The probed penetration depth z at any angle α_1 around the critical glancing angle is given by [318]:

$$z = \frac{\lambda}{4\sqrt{2}\pi} \frac{1}{\left[\sqrt{\left(\alpha_1^2 - \theta_c^2\right)^2 + 4\beta^2} - \left[\alpha_1^2 - \theta_c^2\right]\right]^{1/2}} \tag{4.13}$$

where β is the imaginary part of the refractive index, which is related to the mass attenuation coefficient, μ/ρ (g/cm^4) reported for different materials [320], as follows:

$$\beta = \frac{\lambda}{4\pi}\left(\frac{\mu}{\rho}\right)\rho \tag{4.14}$$

where μ is the linear attenuation coefficient (cm^{-1}) and ρ is the density of the probed element (g/cm^3). A simpler formula for the penetration depth z at an angle much less than this critical angle, e.g. 0.1^o, can be given by:

$$z = \frac{\lambda}{4\pi\theta_c} \tag{4.15}$$

Figure Fig. 4.16 shows the change in the penetration depth with the glancing angle calculated for P and S at their k-edge photon energy. For an angle much below the critical angle, it is possible to achieve a surface sensitivity of approximately 3 nm for both S and P. However, this is only true in the case of a mirror smooth surface at which the specular reflection can result in a total external reflection. On the other hand, for rough surfaces, diffuse reflection causes the loss of the total external reflection and therefore the penetration depth becomes a linear function of the glancing angle.

As the disc surface has a 0.1 μm root-mean square (RMS) roughness and similarly the patchy tribofilm formed on the surface, this condition does not favour the total external reflection. Therefore, the disc was held at an incident angle of 2^o relative to the incident beam, which should give penetration depths greater than 100 nm and 1 μm for P and S, respectively. This should allow us to probe the whole thickness of the tribofilm and track its overall compositional changes as a function of time instead of the top surface layers only.

4.2.4.4 Focused Ion Beam (FIB)

In order to study the layers of the formed tribofilm on the metal surface, thin sections across the wear scar were prepared using a precise high resolution Focused Ion Beam (FIB) microscope (FEI Nova 200 NanoLab) equipped with a Field Emission Gun - Scanning Electron Microscope (FEG-SEM). The tilt of the sample was precisely controlled using an automated positioning stage fitted inside the FIB microscope. Fig. 4.17 shows a cross-section across the wear scar prepared using FIB. In order to minimise the tribofilm damage, initially a Pt-based protection

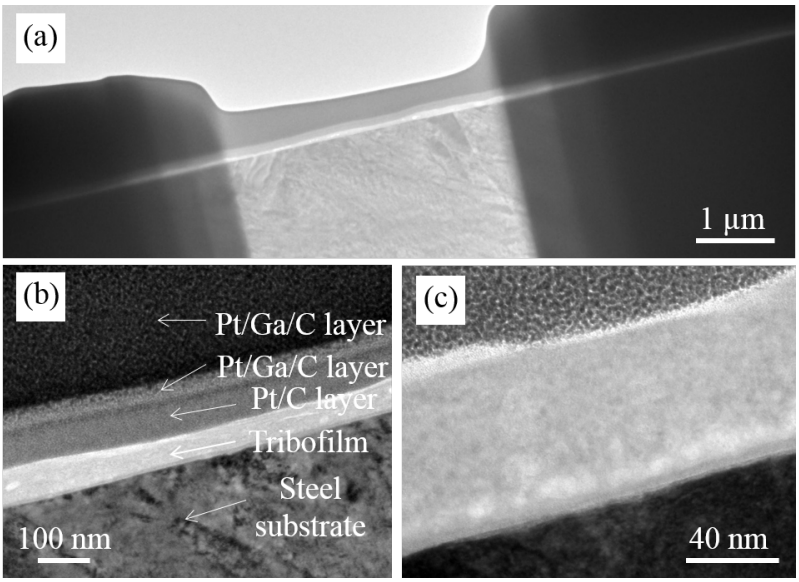

Fig. 4.17 Schematic of the light lever used to detect the deflection of the AFM cantilever. The inset shows the difference in response between soft and hard samples.

layer of a thickness about 70 nm was sputtered and deposited on the tribofilm using electron-beam induced deposition (EBID) using metal carbonyls of Me(CO)x as a precursor. The low energy electron impact typically does not result in any significant damage to the substrate, as indicated in the clean interface between the tribofilm and the EBID layer. However, it causes carbon contamination from the carbon-based precursor throughout the deposited layers.

A second thick Pt layer of about 500 nm, which is sputtered using ion beam-induced deposition (IBID) through a 30 keV Ga^+ focused ion beam, was deposited on the initial layer. The high energy Ga^+ ions cause damage to the initially deposited sacrificial protection layer of Pt/C, which is manifested in the appearance of a third layer between the first base layer of Pt/C and the second top layer of Pt/Ga/C.

4.2.4.5 Transmission Electron Microscope (TEM)/Energy-Dispersive X-ray spectroscopy (EDX)

The prepared FIB thin sections were imaged using a 200 kV Transmission Electron Microscope (TEM) (FEI Tecnai TF20), which is fitted with a high angle annular dark field (HAADF) detector. The composition across the prepared section was examined by acquiring Energy-dispersive X-ray (EDX) spectra at different points across the sample using Oxford Instruments INCA 350 EDX system with X-Max SDD detector, which is fitted to the TEM.

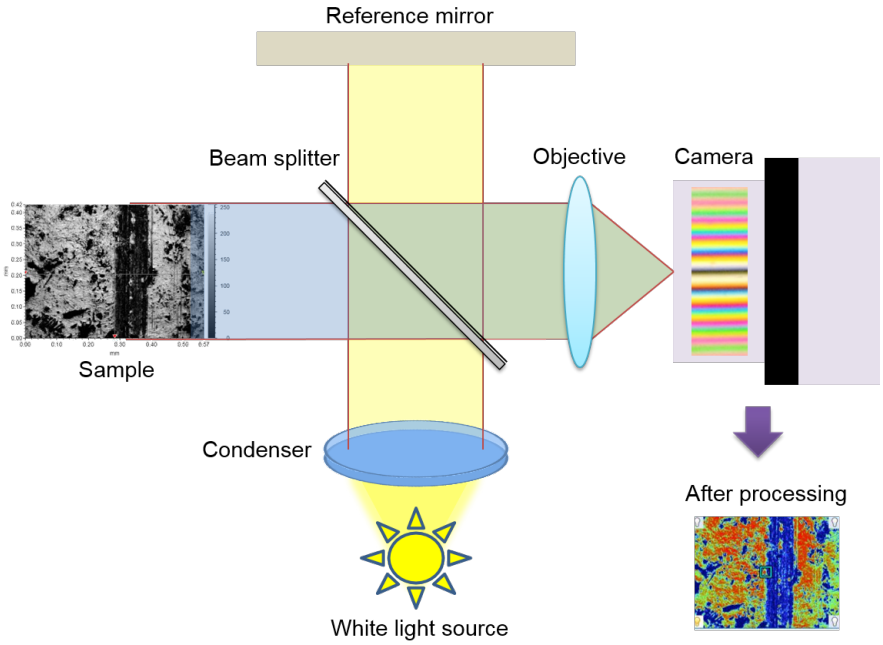

Fig. 4.18 Schematic illustration of the basics of white light interferometry.

4.2.4.6 White light interferometry

NPLEX white light interferometer (Bruker, USA) was used to obtain 3D images of the worn samples in order to quantify the wear volume. Fig. 4.18 illustrates the basics of using interferometry to map worn surfaces. Initially, a white light source shines through a beam splitter that directs light to the sample and an internal reference mirror (flat surface). The phase difference between the images of the worn sample and reference flat surface results in a constructive and destructive interference. The interference pattern, which is collected by a camera, is analysed in this work using Vision64 software (Bruker, USA). The wear volume is then calculated by measuring the width and depth of the wear scar at different locations. All the reported wear measurement in this work are based on the disc countersurface after rinsing in heptane and then removing part of the tribofilm using a droplet of 0.05 M EthyleneDiamineTetraAcetic acid (EDTA) solution in distilled water placed on the wear scar for 60 s [321, 322].

4.3 Summary

This chapter discusses the materials and experimental methods used to study the composition of ZDDP and DDP antiwear films as well as their tribological, mechanical and rheological properties. The summary of these methods is described schematically in Fig. 4.19.

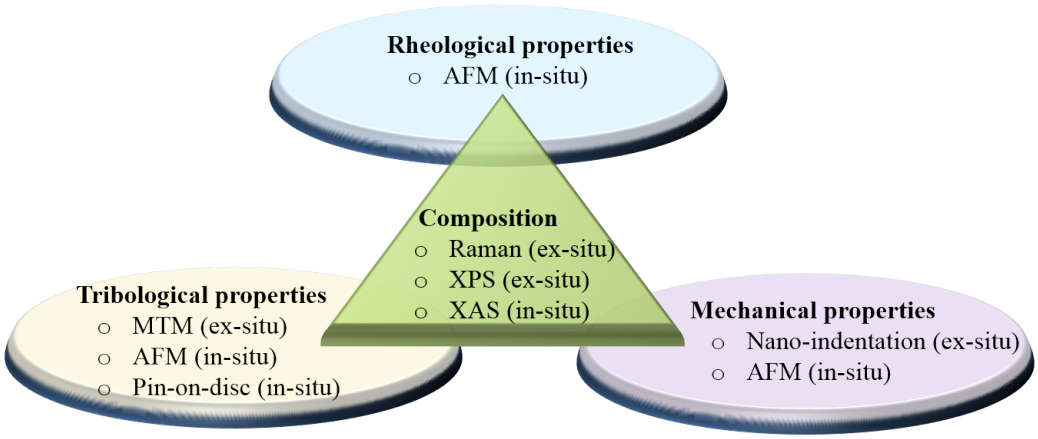

Fig. 4.19 Schematic of the interplay between the composition of the tribofilm and its tribological, mechanical and rheological properties. The different techniques used to probe these properties are indicated.

The MTM-SLIM and newly developed pin-on-disc rig were used to study ex-situ the tribological properties of P-based tribofilms. AFM will be used to perform in-situ tribological measurements at the microscopic scale using a newly developed high temperature liquid cell. Comparisons with the macroscopic ex-situ measurements can provide insights into the mechanisms of which the P-based tribofilms used to enhance antiwear performance. AFM will also be used to probe the mechanical and rheological properties of the formed tribofilms in-situ. The mechanical properties will be probed by studying the durability and tenacity of the tribofilm at different temperature and contact pressure. On the other hand, the rheological properties will be probed using a newly developed methodology utilising creep and squeeze flow analysis. Finally, surface analysis techniques, i.e. Raman, XAS and XPS, will be used to probe the composition of the tribofilm in-situ and ex-situ. The ultimate goal of using these different techniques is to obtain compositional and structural information of the decomposition products of ZDDP and DDP tribo- and thermal films.

In the next chapters, the ex-situ results will be discussed first followed by the discussion of the in-situ results.

Chapter 5

Reaction kinetics of ZDDP tribofilms using ex-situ techniques

This chapter investigates the evolution over time of the decomposition reaction of the zinc dialkyldithiophosphate (ZDDP) additive in poly-α-olefin (PAO) synthetic oil in the presence and absence of water contamination in the oil. The study also follows the evolution of the composition of the formed ZDDP protective antiwear tribofilms and the changes in reaction kinetics after different rubbing times. The chapter is divided into four sections. Section one discusses the tribological results of friction, wear and tribofilm thickness. Section two discusses the surface analysis results using a combinatorial experimental techniques including XPS and TEM/EDX. Section three presents the evolution of the reaction kinetics of the ZDDP additive and the composition of the formed tribofilm over time. Finally, section four summarises the main points discussed throughout the chapter.

5.1 Tribological tests

The progression of the friction coefficient over 120 minutes of rubbing time and the effect of water on this evolution are shown in Fig. 5.1. The presence of water in the oil appears to have a potent effect on friction, which is more prominent during the early stage of the tribotest than in the later stages in which the friction coefficient reaches steady state. This small effect of water on the steady state friction is in agreement with the findings of previous studies [33, 323], which related it to the evaporation of water from the oil. As more water is present in

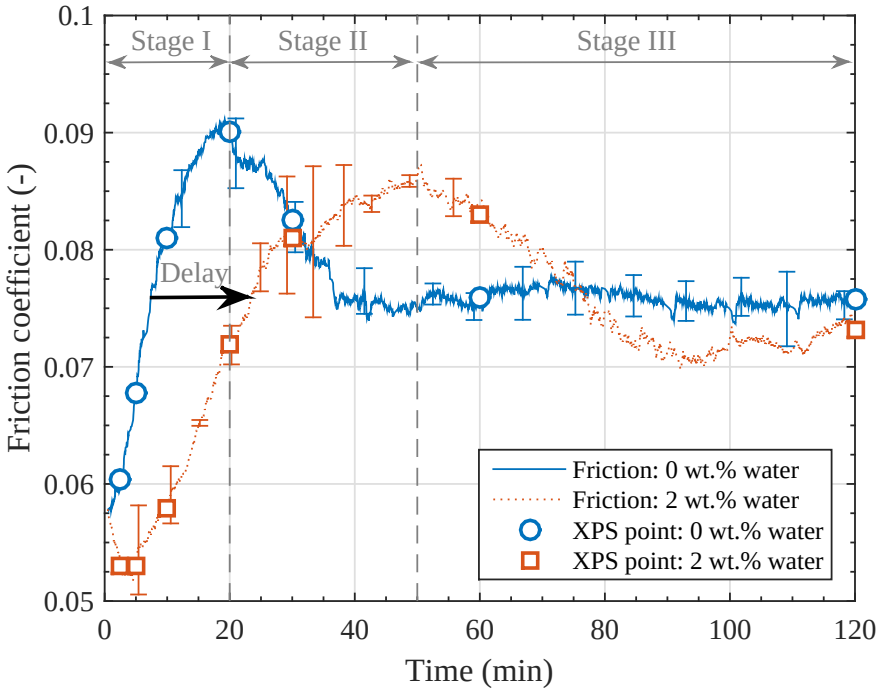

Fig. 5.1 Effect of water on the evolution of the friction coefficient of PAO-ZDDP oil over rubbing time. Error bars where calculated based on at least 3 repetitions.

the oil during the running-in period than in the later stages, as shown in Fig. 5.2, friction is expected to be more affected.

The friction coefficient seems to follow three different stages, whether water is present in or absent from the oil. The first stage occurs during the running-in period, i.e. $t < 20$ minutes, in which the friction coefficient in the absence of water from the oil increases from 0.05 to 0.092. Similarly, the presence of water appears to increase the friction coefficient but to a slightly lower value of 0.085, which is reached after a longer running-in period extending to 50 minutes instead of 20 minutes. Following this increase, the friction coefficient decreases until reaching a steady state value of 0.077 in the absence of water and 0.072 in the presence of water in the oil.

The transient behaviour of friction can be related to the tribofilm thickness as suggested by Taylor and Spikes [262], i.e. the thicker the tribofilm the higher the friction. This relation can be examined by following the evolution of the tribofilm thickness over rubbing time, which is shown in Fig. 5.3. The thickness evolution seems to resemble the one of the coefficient of friction, which is clear from the general trend of the initial increase in thickness then decrease followed by steady state. The effect of water on this evolution, which is shown in the same Fig. 5.3, does not appear to be uniform throughout the test but follows three different phases instead. The first one occurs during the running-in period, i.e. at $t < 20$ min, in which water does not seem to affect the thickness. This is

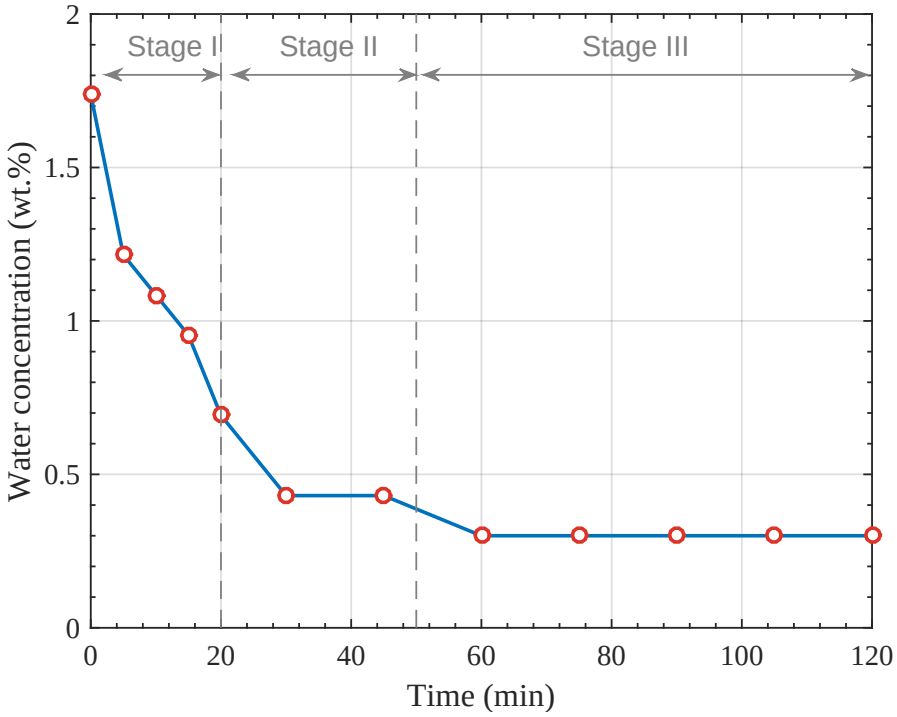

Fig. 5.2 Effect of water on the evolution of the friction coefficient of PAO-ZDDP oil over rubbing time.

followed by a second phase, which extends up to $t < 50$ min, in which water has an adverse effect, i.e. reduces the thickness of the tribofilm. Lastly, at $t > 50$ min water appears to have a beneficial effect that leads to the formation of a thicker tribofilm than in the case of no added water. However, it should be noted that the last phase ends with a tribofilm thickness that is similar whether water is absent from or present in of the oil. In addition, although these three phases resemble the coefficient of friction evolution, the timing is not exactly matched. This indicates that the transient changes in the friction coefficient are not only a function of the tribofilm thickness but also the composition as well.

The initial continuous increase in the friction coefficient during the running-in period can be related to the smearing and wear of the asperities and to the continuous increase in the length of the phosphate chains composing the tribofilm. These chains covering the contacting surfaces can interact with each other and thus increase friction. On the other hand, when water is present in the oil, shorter phosphate chains are formed [236], which have shorter relaxation time than the one required for any significant interactions to occur between the extended chains across the contact. This can explain the slower growth in the friction coefficient and the reduced maxima reached after 60 minutes of rubbing as compared to the case after 20 minutes when water is absent from the oil. The results thus seem to suggest that the increased friction in the beginning of the test is related to

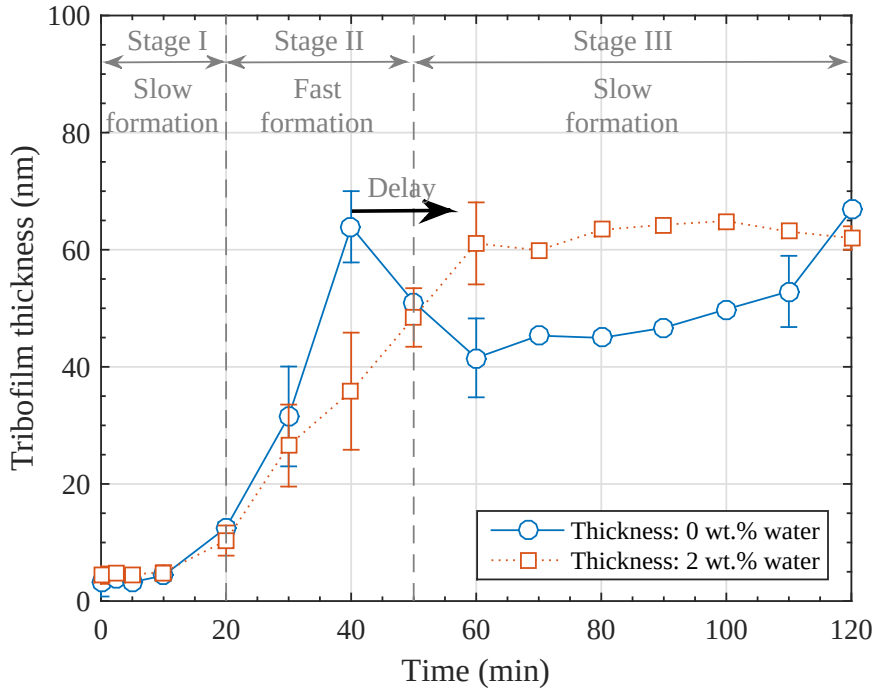

Fig. 5.3 Evolution of the thickness of ZDDP tribofilms as measured by the MTM-SLIM over rubbing time in the presence and absence of water in the oil. Error bars where calculated based on at least 3 repetitions.

the interactions between the phosphate chains covering the contacting surfaces rather than the tribofilm thickness. The longer the phosphate chains, the larger the interactions and thus the larger the friction.

The decline in the friction coefficient after reaching a maxima can be related to two different mechanisms. Firstly, the long phosphate chains can align in the direction of shear and thus reduce the interfacial shear stress and friction [324]. Secondly, the long phosphate chains, which have lower packing density than the shorter ones [325], can form less compact layers and thus less puckering occurs at the asperity contacts. This is in line with several previous studies [265–267], which showed that in the case of a single layer adhering loosely to the substrate, friction was maximum as compared to the case of a bulk material with strongly adhered layers. Therefore, the drop occurring between 20 and 60 minutes of rubbing can be related to the enhanced packing density of the arranged chains in the direction of shear.

Wear is not reported in this work as it was insignificant in all the tribological tests. This is evident from the different profiles across the wear scar shown in Fig. 5.4 after 120 minutes of rubbing in the presence and absence of water in the oil. The negligible wear is a result of the mild operating conditions of nearly rolling (SRR = 5%). In addition, it can indicate that even after 120 minutes of

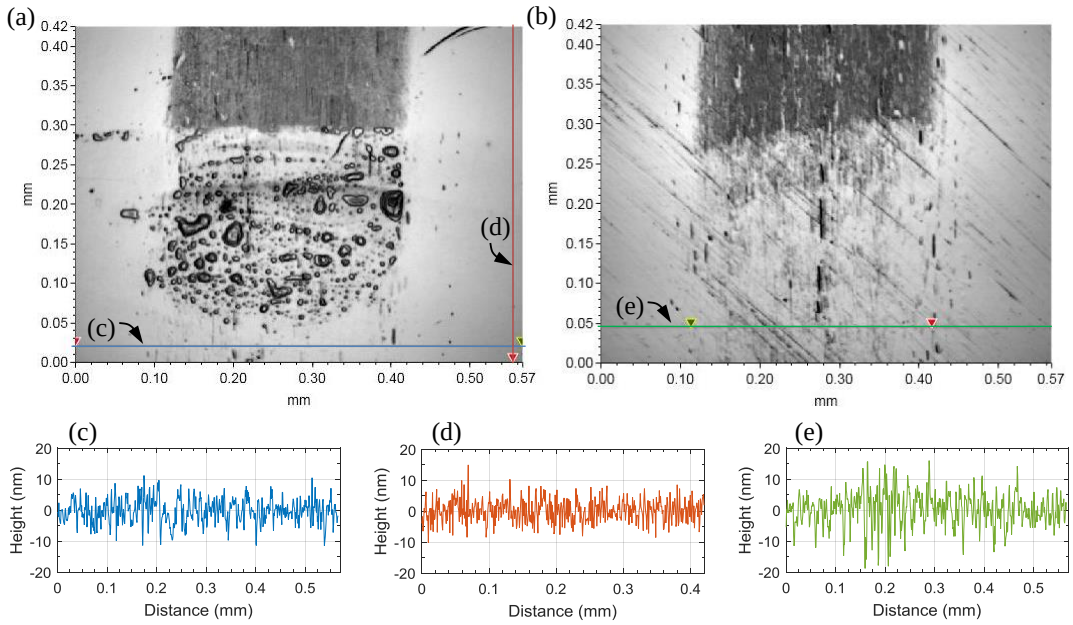

Fig. 5.4 Wear scar images and depth profiles of MTM discs as measured by white-light interferometry after 120 minutes of rubbing times in (a) the presence and (b) absence of water in the oil. The images show part of the tribofilm on the wear scar was removed by EDTA. (c-d) depth profiles as indicated on (a) and (b).

rubbing, the tribofilm was largely durable to the extent that it provided a full protection to the steel surface underneath.

5.2 Surface analysis

The identification of the different components composing the signals of O1s, P2p, Zn2p, S2p, C1s, and Fe2p was carried out by fitting each signal with a specific number of peaks, as shown in Fig. 5.5. The full analysis is summarised in Table 5.1, which lists the binding energies of these components over rubbing time in the absence and presence of water in the oil.

O1s signal was fitted with three main peaks as shown in 5.5a. The first one was attributed to the bridging oxygen (BO), which represents the oxygen bridging the phosphorus atoms in the phosphate chains (P−O−P). The second peak was attributed to the non-bridging oxygen (NBO), which represents mainly the oxygen within a terminating phosphate group ($-PO_x$) such as −P=O, P−O−Zn and P−O−Fe(III) [189]. Finally, the third peak was attributed to the metal oxide, e.g. Fe_2O_3 and FeO. In all the tribotests, the BO, NBO and MO were identified at 533.06 ± 0.2 eV [20, 183, 186, 190, 192–194, 314, 326–331], 531.76 ± 0.2 eV [20, 183, 186, 190, 192–194, 294, 314, 326–331], and 530.36 ± 0.3 eV [20, 186, 190, 192, 193, 294, 314, 328, 332, 333], respectively. The presence of

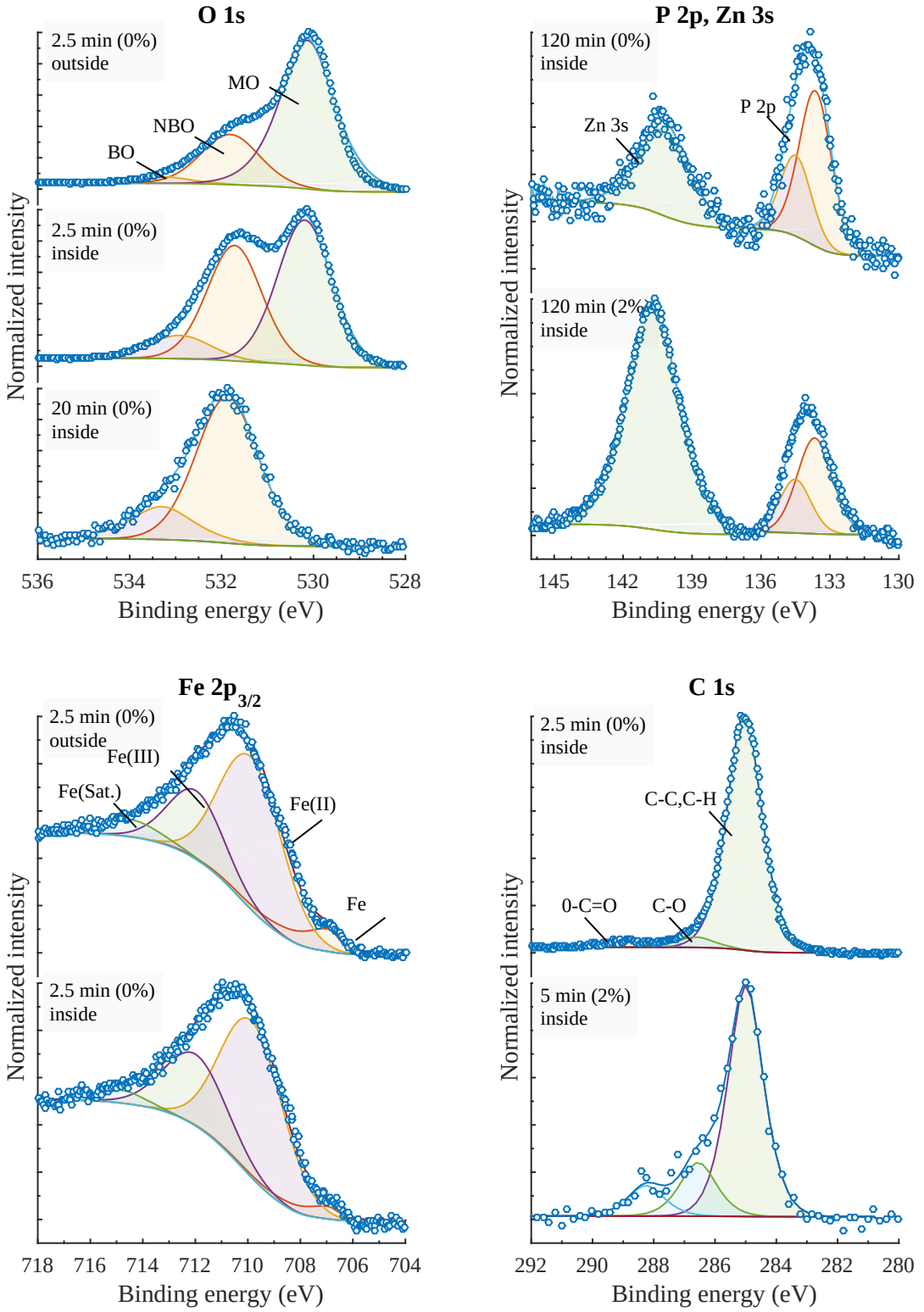

Fig. 5.5 Peak fitting of the different components composing the signals of a.) O1s, b.) P2p and Zn3s, c.) Fe2p and d.) C1s after different rubbing times in the presence and absence of water in the oil.

Table 5.1 XPS component analysis of the tribofilms formed in the case of 0%, and 2% (shown in parenthesis) added water in the oil.

Time (min)	2.5	5	10	20	30	60	120
Component	Binding energy (±0.05 eV)						
O1s: BO	533.05	532.25	533.09	532.76	533.06	533.13	533.15
	-	(533.37)	(533.08)	(533.82)	(532.73)	(533.08)	(533.14)
O1s: NBO	532.79	531.92	531.82	531.21	531.73	531.70	531.72
	-	(531.65)	(531.68)	(531.68)	(531.57)	(531.65)	(531.77)
O1s: MO	530.25	530.60	530.65	530.73	-	-	-
	-	(530.00)	(530.21)	(530.58)	-	-	-
Zn3s	-	140.36	140.47	140.42	140.42	140.40	140.31
	-	(140.43)	(140.37)	(140.32)	(140.28)	(140.41)	(140.46)
P2p 3/2	133.55	133.57	133.64	133.64	133.53	133.64	133.66
	-	(133.55)	(133.49)	(133.41)	(133.44)	(133.55)	(133.44)
S2p 3/2	162.13	162.22	162.33	162.27	162.23	162.37	162.31
	-	(162.29)	(162.23)	(162.11)	(162.09)	(162.18)	(162.24)
(Zn3s-P2p)	-	6.79	6.82	6.78	6.89	6.76	6.65
	-	(6.88)	(6.88)	(6.91)	(6.84)	(6.86)	(7.01)
				Ratio			
BO/NBO	0.24	0.31	0.31	0.25	0.37	0.32	0.38
	-	(0.26)	(0.23)	(0.25)	(0.26)	(0.26)	(0.15)
P/Zn	0.1	0.99	0.92	1.25	1.02	1.23	1.30
	-	(0.53)	(0.54)	(0.52)	(0.61)	(0.65)	(0.41)

water does not appear to have a clear trend on these binding energies as the effect is small whether during the running-in period in which water concentration is highest or during the later stages where water evaporates.

Zn3s signal appeared at 140.5 ± 0.05 eV as shown in 5.5b, which can be attributed to zinc phosphate [183, 191, 192].

Zn2p signal appeared at 1022.5 ± 0.1 eV, which can be equally assigned to ZnS, $Zn(SO_4)$ and ZnO [314, 333] or zinc phosphate [183, 191, 192, 328, 329].

P2p appeared at 133.55 ± 0.1 as shown in 5.5b, which can be ascribed to zinc phosphate [186, 190, 192, 194] or possibly $Fe(PO_4)$ [190, 277, 314]. The shift to higher binding energy indicates that the short phosphate chains are polymerised into longer ones [183, 186, 190–192, 194]. The presence of water seems to reduce this the binding energy with the continued rubbing, which implies that shorter chains were formed.

S2p signal appeared at 162.23 ± 0.1 eV, which can be assigned to sulphide [186, 314, 334, 335] or equally to thiophosphate or organosulphur [314]. Sulphate signal at 168.5 ± 0.1 eV was detected at the beginning of the test, i.e. after 2.5

minutes, which can be assigned to $FeSO_4$ [336] or $Fe_2(SO_4)_3$ [334]. In the case of water is present in the oil, no measurements at the early stages of the test, i.e. 2.5 minutes, were possible, therefore, the presence of sulphate cannot be confirmed in this case. Nevertheless, similar to P2p, in general water reduced the binding energy of the sulphide signal with rubbing.

Fe2p signal, which was detected only during the running-in period, was not affected by the presence of water. This signal was broad as shown in 5.5c, which suggests that a mixture of FeO and Fe_2O_3 is present on the surface [337]. Three main peaks were identified at 710.1 ± 0.2 eV, 711.2 ± 0.2 eV, and 713.0 ± 0.2 eV. The peak at 710.1 ± 0.5 eV can be assigned to Fe(II) oxide [186, 190, 333, 335, 338, 339] whereas the one at 711.2 ± 0.5 eV to Fe(III) oxides [186, 190, 333, 334, 338–340], or $FeSO_4$ [186, 333, 339]. The third peak, which appeared at 713.0 ± 0.5 eV, can be ascribed to $Fe_2(SO_4)_3$ [333, 334, 339] or possibly iron phosphate [186, 190, 314]. During the first 2.5 minutes of rubbing an additional peak was identified at 707.1 ± 0.2 eV, which can be assigned to metallic iron [314, 328, 334, 338, 339], or FeS_2 [334].

C1s was mainly fitted to a single peak at 285.0 eV as shown in 5.5d, which was ascribed to aliphatic carbon (C-C, C-H). However, near the steel surface, i.e. at rubbing times < 10 minutes, three more peaks were identified at 283.0 ± 0.1, 286.5 ± 0.1 and 288.6 ± 0.1 eV. These peaks were ascribed to iron carbide, hydroxyl (COH) and carboxyl (COOH) groups, respectively [341, 342]. The presence of water appeared to enhance the intensity of these groups.

5.2.1 TEM/EDX cross-section analysis

To confirm the change in the composition of the ZDDP tribofilm over time, a post-mortem cross section was prepared using FIB and analysed using TEM/EDX technique, which has high spatial resolution comparable to the beam diameter of about 2-5 nm [343]. Figs. 5.6 and 5.7(a) show a section across the tribofilms formed in the last stage of the tribotest after 120 minutes of rubbing in the presence and absence of water in the oil, respectively. The tribofilms were found to have average thicknesses of 75 ± 5 and 60 ± 5 nm, in the presence and absence of water in oil, respectively, which match the ones measured by MTM-SLIM as reported in Fig. 5.3. Furthermore, the tribofilms show two distinctive features. The first one consists of dark hollow regions across the tribofilm that are mainly rich in carbon. The second feature composes the majority of the tribofilm, which extends between the steel surface and the tribofilm's top layer. A comparison between the EDX spectra of the steel substrate and tribofilm's base and bulk

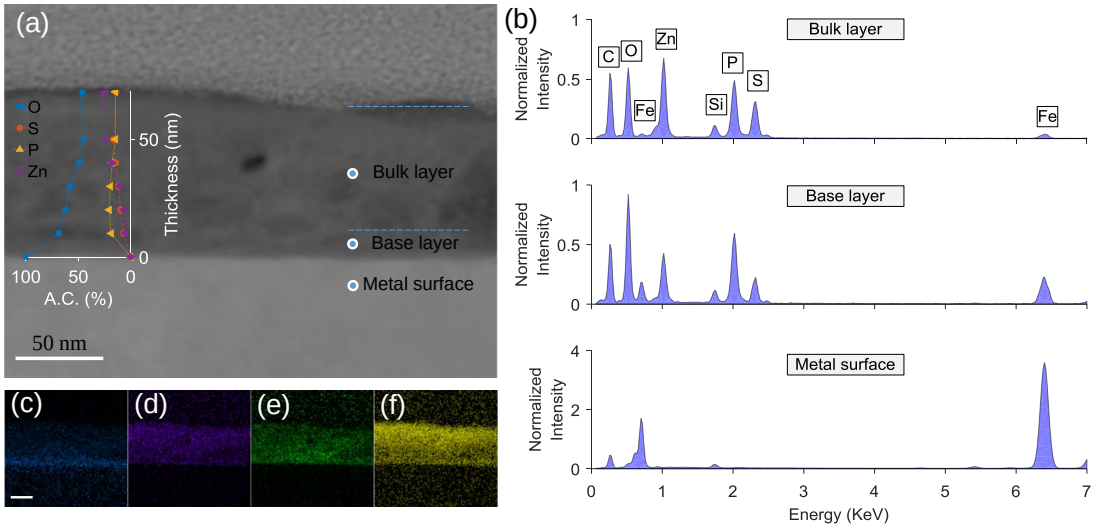

Fig. 5.6 TEM-EDX analysis, which includes (a) cross-section of the wear scar after 120 min of rubbing in the absence of water. EDX analysis is also shown for the atomic concentrations of the main tribofilm components, i.e. O, S, P and Zn. (b) EDX spectra of the three main regions, i.e. the steel surface and the bottom base and bulk layers of the tribofilm. (c)-(f) EDX maps across the tribofilm shown in (a) for O, S, P and Zn, respectively.

layers is shown in Figs. 5.6 and 5.7(b) in the presence and absence of water in the oil, respectively. The results show that the base layer and bulk layers consist mainly of P, O, S, Zn and Fe. The concentration of Fe seems to decrease sharply from the base layer to the bulk ones. This can possibly be due to two reasons. First, wear and mechanical mixing occurring near the steel surface can cause iron particles and cations to be digested in the tribofilm's layers. Second, as the thickness of the base layer is small, i.e. < 10 nm, a small misalignment of the cross-section can cause the EDX to pick a signal from the steel surface.

The changes in the atomic concentrations of the main elements forming the tribofilm calculated from several EDX spectra across the tribofilm are overlaid on Figs. 5.6 and 5.7(a) and replotted in Figs. 5.8 and 5.9. The results show that in the absence or presence of water in oil, the atomic concentrations of P, S and Zn monotonically increase along the tribofilm thickness until reaching steady state value towards the tribofilm surface. In contrast, the concentration of oxygen monotonically decreases until reaching steady-state.

Another distinctive feature in the EDX results is the one related to the evolution of P and Zn. In the absence of water, the layers near the steel substrate seem to have larger concentration of P in comparison to Zn. Away from the base layer, the trend reverses with the progressive increase in the concentration of Zn and nearly constant concentration of P. On the other hand, the presence of water seems to result in larger concentration of Zn near the steel surface, which

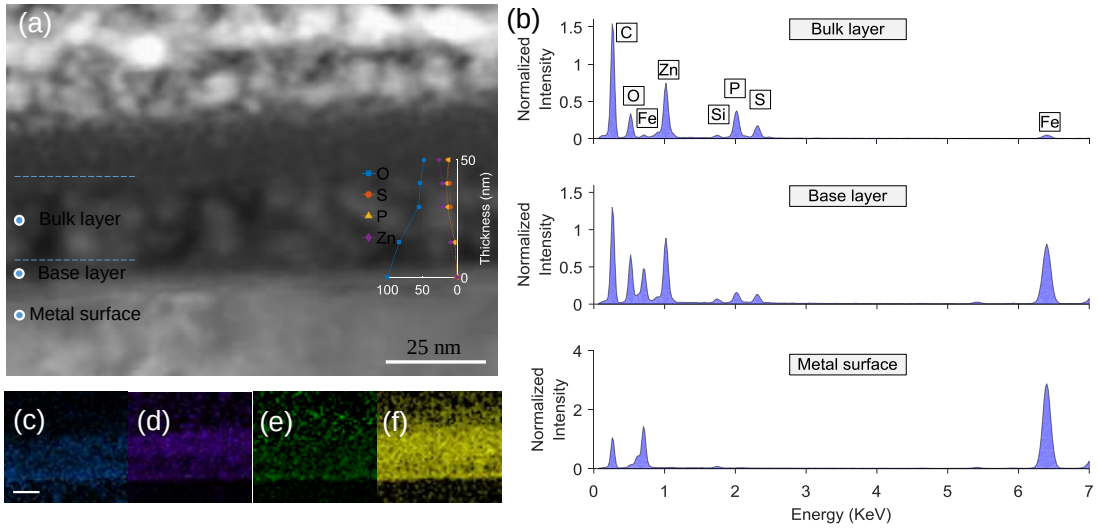

Fig. 5.7 TEM-EDX analysis, which includes (a) cross-section of the wear scar after 120 min of rubbing in the presence of 2% water in the oil. EDX analysis is also shown for the atomic concentrations of the main tribofilm components, i.e. O, S, P and Zn. (b) EDX spectra of the three main regions, i.e. the steel surface and the bottom base and bulk layers of the tribofilm. (c)-(f) EDX maps across the tribofilm shown in (a) for O, S, P and Zn, respectively.

progressively increases along the tribofilm thickness and overall stays higher than the P concentration.

5.2.2 XPS concentration evolution

To obtain a better insight into the composition evolution over time, the atomic concentrations of the different elements found after various rubbing times in the top 5–7 nm of the tribofilm were plotted in Figs. 5.8 and 5.9 in the absence and presence of water in oil, respectively. The concentrations obtained by the TEM-EDX analysis were also plotted for comparison. The rubbing times for these EDX points were obtained by a direct conversion between thickness and rubbing time. This was performed by matching the thickness at which the EDX point was measured with the one measured by MTM-SLIM after a certain rubbing time (Fig. 5.3). A good agreement between the concentrations measured by EDX and XPS was found for O, P and S. However, the EDX analysis largely underestimated the concentration of Zn by more than 50%. Nonetheless, similar to the EDX results, the XPS analysis indicates that during the running-in period, i.e. < 20 minutes, the concentrations of Zn, P and S increased substantially whereas the concentration of O decreased abruptly. However, after the running-in period, these concentrations seem to approach an equilibrium state with no significant change. The good agreement between the EDX and XPS results is evident especially in

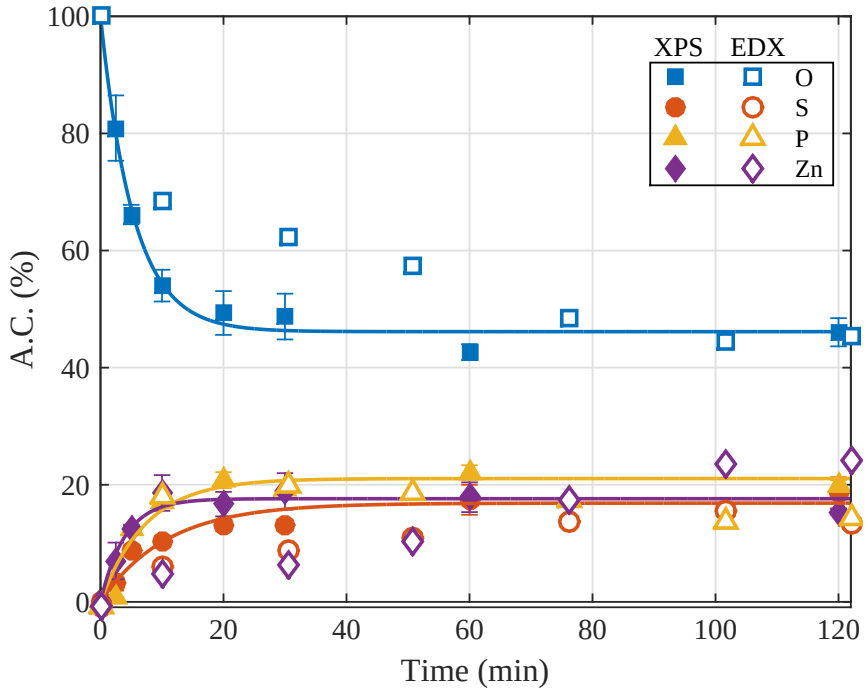

Fig. 5.8 Evolution of the atomic concentrations of the elements inside the wear scar in the absence of added water to the oil. Solid symbols are based on XPS analysis and open symbols are based on TEM-EDX analysis. Solid lines are the fits of the model described in Eq.5.4.

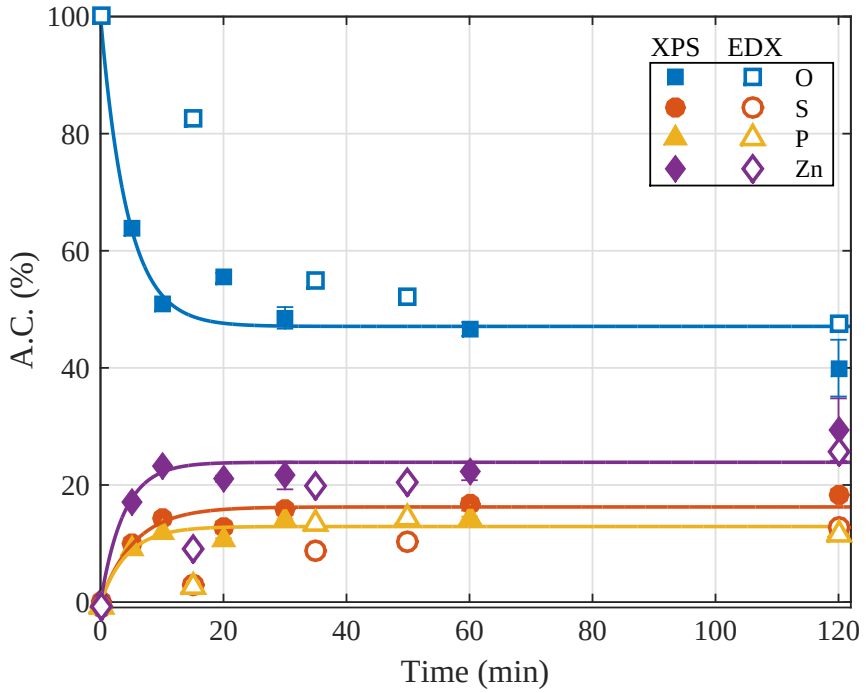

Fig. 5.9 Evolution of the atomic concentrations of the elements inside the wear scar in the presence of 2% added water to the oil. Solid symbols are based on XPS analysis and open symbols are based on TEM-EDX analysis. Solid lines are the fits of the model described in Eq.5.4.

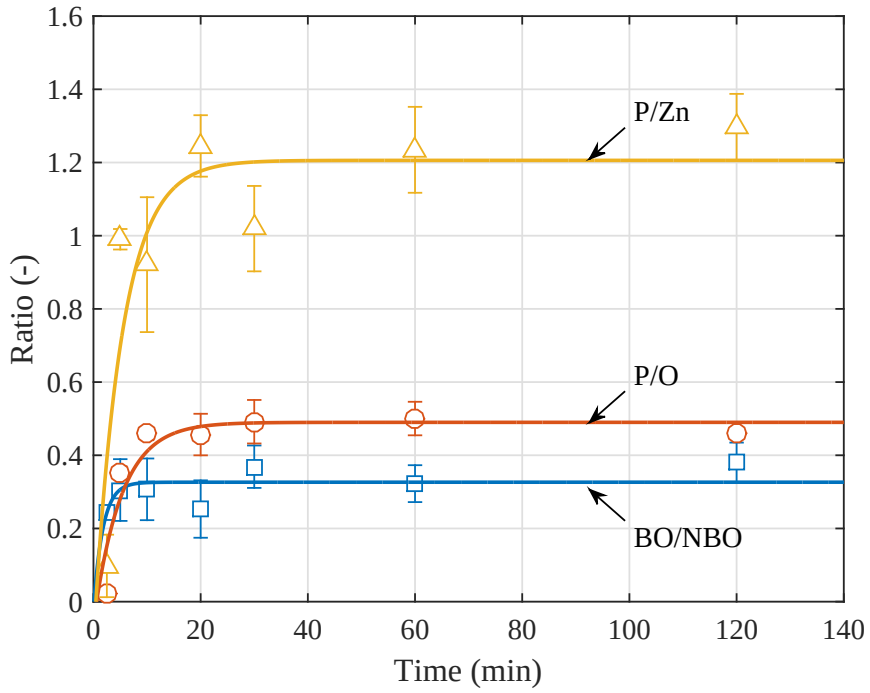

Fig. 5.10 Evolution of BO/NBO, P/O and P/Zn ratio inside the wear scar in the absence of added water to the oil. Solid lines are the fits of the model described in Eq.5.4.

this steady state region. In the bulk thick layers of the tribofilm, it was possible to acquire EDX spectra at five points. In contrast, it was not possible to capture more than one point in the base layer, i.e. less than 20 minutes of rubbing, as the tribofilm thickness was less than 10 nm. Nevertheless, in general, EDX captured a similar trend to the one of XPS at least in the steady state region in which the concentrations of O, P, S and Zn generally do not change over rubbing time.

The evolution of BO/NBO, P/O and P/Zn ratios obtained from the XPS analysis is shown in Figs. 5.10 and 5.11 in the absence and presence of water in oil, respectively. The results indicate that in the absence of water the ratios of P/O and P/Zn of the immature tribofilms formed at the beginning of the tribotest, i.e. $\leq$ 5 minutes of rubbing, appear to arise from virtually nothing after 2.5 minutes of rubbing to a value of 0.35 and 0.99, respectively, just after another further 2.5 minutes of rubbing. This suggests the formation of short chains $ZnPO_4$. In line with these results, BO/NBO and S/Zn ratios were 0.24 and 0.48, respectively, even in the first 2.5 minutes, suggesting that initially sulphide species such as ZnS might be formed as a precursor of the short chain phosphate.

In the more mature tribofilms formed between 5 and 120 minutes of rubbing, the XPS analysis revealed a general trend that the ratios of BO/NOB, P/O, P/Zn and S/Zn increase over rubbing time. The increase in the P/O and P/Zn ratios (31.4%, 31.3%, respectively) was half the increase in the S/Zn ratio (72.9%)

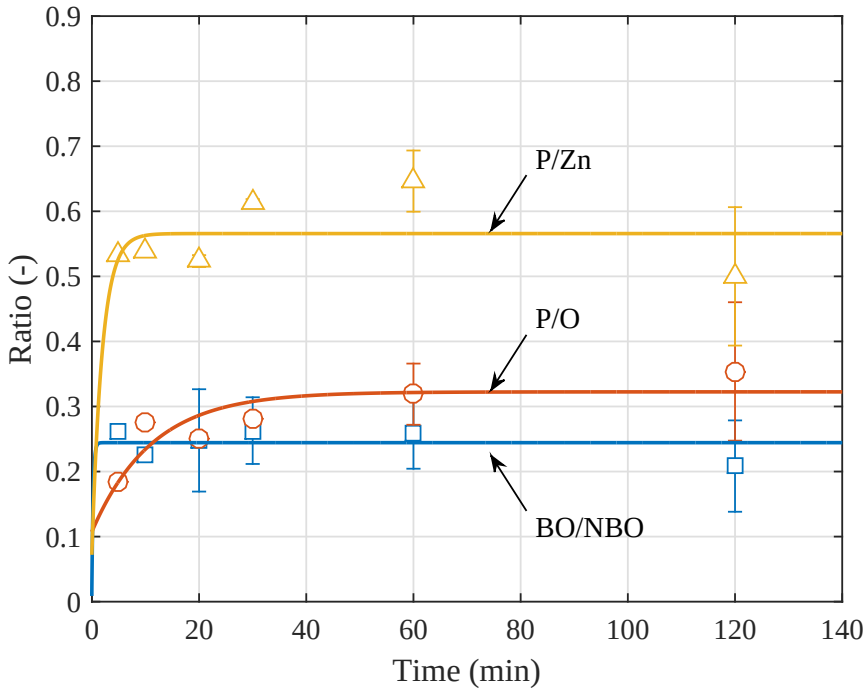

Fig. 5.11 Evolution of BO/NBO, P/O and P/Zn ratio inside the wear scar in the presence of 2% added water to the oil. Solid lines are the fits of the model described in Eq.5.4.

despite the large initial ratio of the latter. This highlights that the formation of the sulphur species in the beginning of the tribotest is faster than the one in the later stages.

The trend of these ratios generally matches the one in the presence of water (Fig. 5.11). However, in this case water seems to impede the growth of the ratios to levels much lower than the ones in the absence of water. For instance, BO/NBO ratio did not change at all over the rubbing time and stayed around 0.25 corresponding to short chains $ZnPO_4$.

5.2.3 XPS depth analysis

Figs. 5.12 and 5.13 show the depth profiles of the elements found in the ZDDP tribofilms formed after 120 minutes of rubbing in the absence and presence of water in the oil, respectively. The results indicate that water lowers the concentration of phosphorus whereas it generally enhances the formation of more zinc and sulphur species. Furthermore, near the steel surface, the concentration of oxygen was high, which indicates the presence of metal oxide layer. On the top of this layer, sulphur appears at high concentration especially in the presence of water. This is in agreement with several previous studies [151, 200–202], which suggest that the amount of sulphur chemisorption products are higher on the steel surface. In

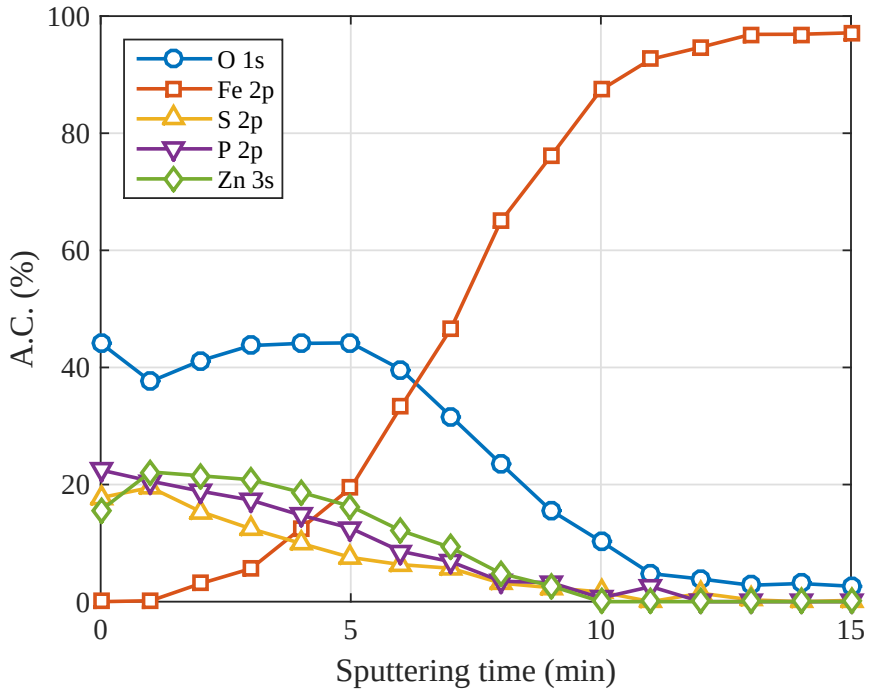

Fig. 5.12 XPS depth profile of the main elements found in the tribofilm after 120 minutes of rubbing formed in the case of no added water to the oil.

addition, several other studies [17, 164, 190, 277] proposed that Fe/Zn sulphides and oxides as well as Fe/Zn sulphate [277] can be present at the metal surface. On the other hand, other studies, [20, 189] showed using XPS that no oxide or sulphide is present at the interface.

It should be noted that as the previous studies and the results reported here are based on sputtering the tribofilm with ion gun, this process can significantly affect the interpretation of the results. Many studies found that apart from changing the electronic configurations of light elements such as N and O [344], the high energy ions can lead to preferential sputtering and chemical reduction of elements like S [345–348]. This preferential sputtering can be misleading as the detected signal will be proportional to the sputtering yield rather than the concentration of the atoms in the bulk [278].

5.3 Kinetics of ZDDP decomposition reaction

The tribofilm's main components, i.e. P, Zn, S and O, appear to undergo two distinctive reaction phases over rubbing time, as indicated in the evolution of their atomic concentrations shown in Figs. 5.14 to 5.17. The first phase, which occurs during the running-in period, is characterised by a fast transient burst stage in which the atomic concentrations of the elements forming the tribofilm

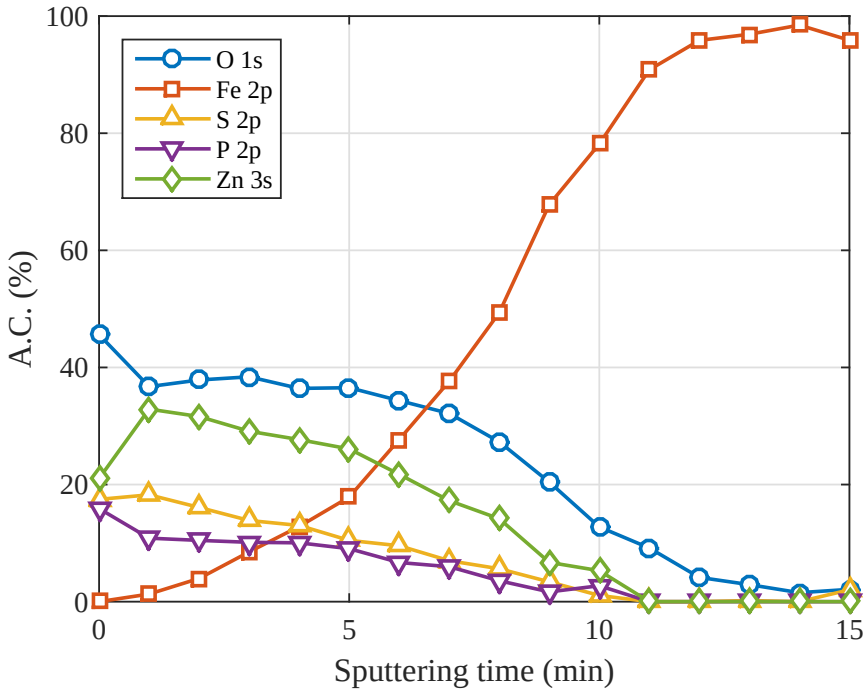

Fig. 5.13 XPS depth profile of the main elements found in the tribofilm after 120 minutes of rubbing formed in the case of 2% added water to the oil.

grow exponentially despite the small increase in the tribofilm thickness. On the other hand, the second phase, which occurs at rubbing times > 20 minutes, is characterised by an intangible growth in the atomic concentrations that appear as asymptotically approaching steady state despite the fast growth in the tribofilm thickness over the same period. These two different phases indicate that the formation rate of the different species composing the tribofilm is not uniform throughout the tribological test. This observation is in agreement with the tribofilm thickness results discussed in Fig. 5.3 and the results of Gosvami et al. [30], which suggested that during the early stage of rubbing, the tribofilm growth of ZDDP is slow and follows a linear trend but as rubbing continues the growth starts to exhibit a much faster logarithmic trend. Similar trend can also be seen in the results of Zhang et al. [142] for the ZDDP thermal film.

Gosvami et al. [30] suggested that the ZDDP additive decomposes initially with a zero reaction rate n=0.12±0.11, which as rubbing continues increases to about 0.22±0.02. However, based on the observed growth trend of the ZDDP decomposition components, the polymerisation reaction of the phosphate chains seems to follow a first-order reaction kinetics. Assuming that the polymerisation of every chain starts with an initial concentration C_o of short chain phosphate and over time is polymerised into long polyphosphate chain with a concentration

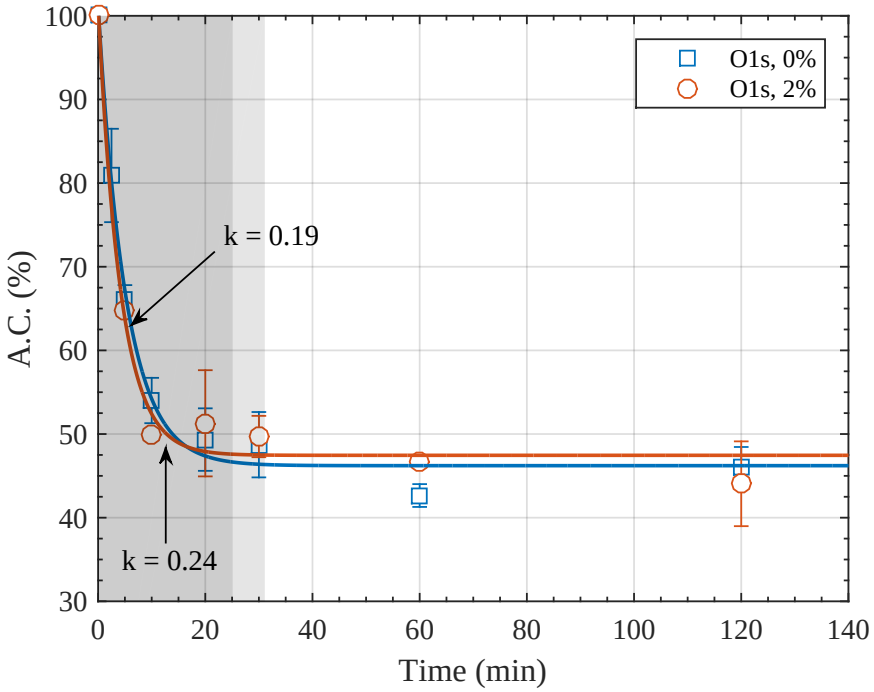

Fig. 5.14 Effect of water on the evolution of O of the ZDDP tribofilm over the rubbing time.

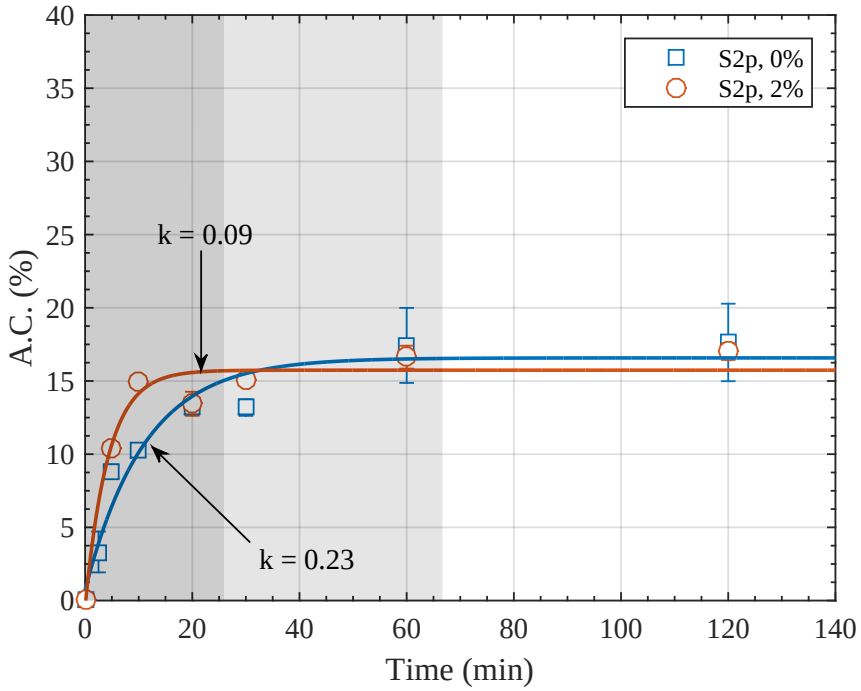

Fig. 5.15 Effect of water on the evolution of S of the ZDDP tribofilm over the rubbing time.

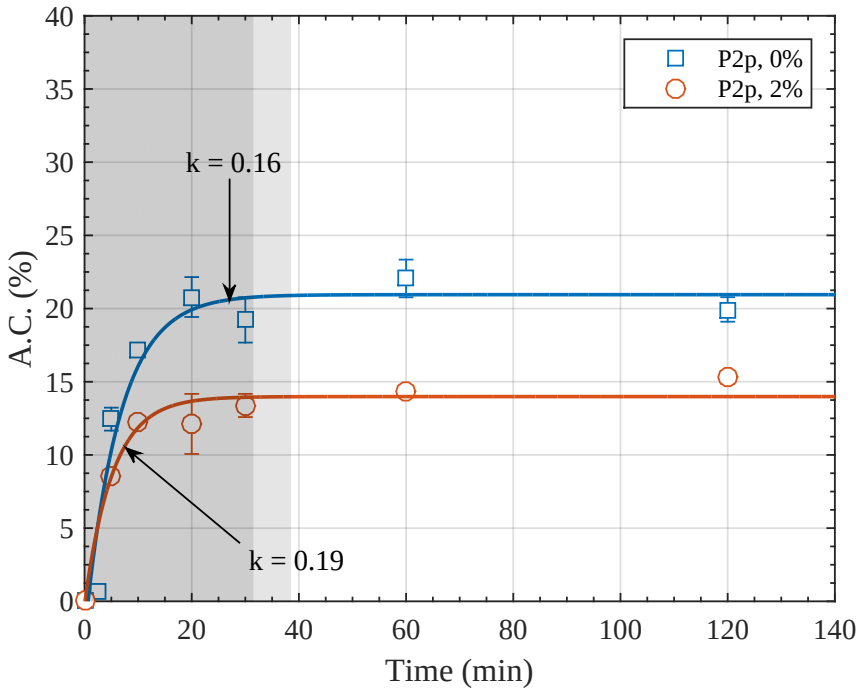

Fig. 5.16 Effect of water on the evolution of P of the ZDDP tribofilm over the rubbing time.

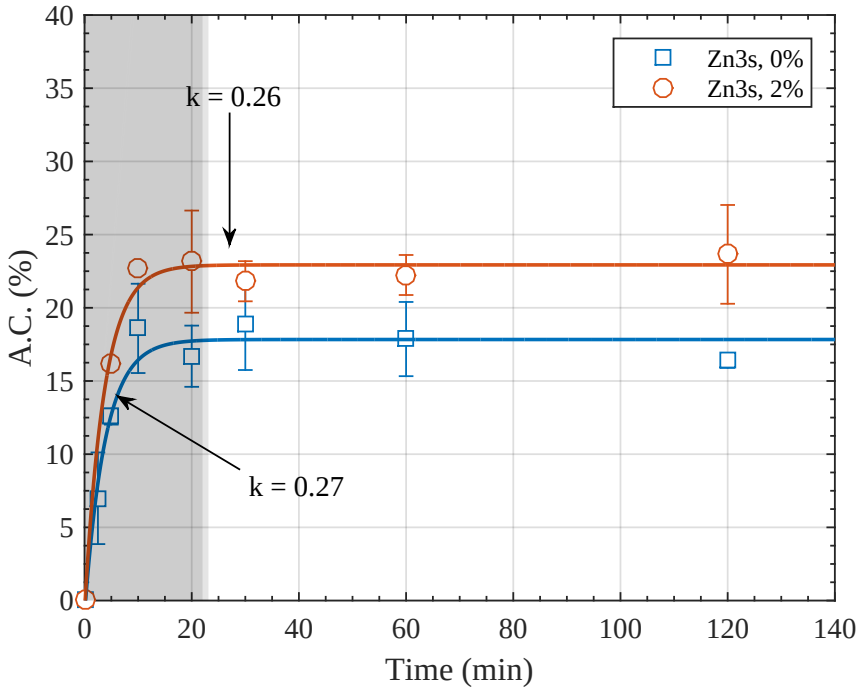

Fig. 5.17 Effect of water on the evolution of Zn of the ZDDP tribofilm over the rubbing time.

C_p, the following overall simplified reaction can be proposed:

$$C_o \xrightarrow{T,P,\dot{\gamma}} C_p \tag{5.1}$$

As this is assumed to be a non-reversible reaction, the increase in the concentration of the formed chains over time can be expressed as:

$$\frac{d}{dt}\left(C_p\right) = k\left(C_o\right) \tag{5.2}$$

where k is the reaction rate coefficient. To simplify the integration of this equation, C_o can be expressed in terms of the equilibrium concentration C_e at $t \to \infty$, as follows:

$$\frac{d}{dt}\left(C_p\right) = k\left(C_e - C_p\right) \tag{5.3}$$

Upon integration and few arrangements, the solution to the above equation forms the first order rate law, which gives the concentration at any time t as:

$$C_p(t) = C_e\left[1 + \left(\frac{C_0 - C_e}{C_e}\right)\exp\left(-kt\right)\right] \tag{5.4}$$

The growth rate of the ZDDP composition products can also be viewed using the concept of the boundary layer solution, which encompasses two solutions. The first one can be used to describe the fast exponential reaction kinetics near the surface, which occurs at short rubbing times and can be expressed as follows:

$$C_p(t) = C_0\exp\left(kt\right) = C_0\left(1 + \frac{r}{100}\right)^{t/p} \tag{5.5}$$

where k is growth constant representing the frequency at which the concentration change by a factor $e \approx 2.7$, r is the percent increase of the concentration over a time period p.

The second solution for the boundary layer reaction, which can be used to describe the slow kinetics away from the surface occurring at long rubbing times, can be modelled by a constant concentration C_0, as follows:

$$C_p(t) = C_0 \tag{5.6}$$

Therefore the final solution can be formed by adding the two solutions, as follows:

$$C_p(t) = C_0\left(1 \pm \exp\left(kt\right)\right) = C_0\left[1 \pm \left(1 + \frac{r}{100}\right)^{t/p}\right] \tag{5.7}$$

Table 5.2 Fitting parameters based on Eq. (5.4) for the different components of the top 5–7 nm of the ZDDP tribofilm.

Element	O		P		Zn		S	
	0%	2%	0%	2%	0%	2%	0%	2%
C_e	46.2	46.4	21.0	13.2	17.6	24.4	17.2	16.0
C_0	100	100	0	0	0	0	0	0
k	0.19	0.23	0.16	0.23	0.27	0.23	0.08	0.22

The plus or minus sign corresponds to exponential growth or decay, respectively. The reaction rate described by this equation, which is based on the boundary layer solution, and the one described in Eq. (5.4) are identical in the case of the initial concentration (C_0) of element of interest is zero.

The model described in Eq. (5.4) is suitable in the case of a single growth or a single degradation of a component. However, in the case of phosphate chains in a tribofilm, they are expected to have a multimode mechanism of growth and cessation. To account for this more complicated system, a model with two reaction rates can be used by adding the outcome of two models similar to the one described earlier in Eq. (5.4). The first model accounts for the growth whereas the second one accounts for the cessation of the phosphate chains. In this case, the two are assumed to occur simultaneously and are mutually exclusive and hence the addition can been used. However, in the more complex tribological contact a strong synergy is more plausible as the longer the phosphate chains are formed the more the cessation is expected. Nevertheless, for simplicity, the chains growth and cessation will be assumed to occur independently and non-contemporarily, and thus the single mode model described in Eq. (5.4) will be used to fit the data.

Using the fitting parameters listed in Table 5.2, Figs. 5.14 to 5.17 show the results of fitting the proposed growth model to the XPS data of O, P, S and Zn whereas the previous Figs. 5.10 and 5.11 show the fitting results for BO/NBO, P/O and P/Zn in the presence and absence of water in the oil. The model appears to fit the data extremely well using two fitting parameters only, i.e. C_e and k. The use of only two fitting parameters was justified by considering that initially no P, Zn or S exists on the surface, i.e. their initial concentration $C_0 = 0$, but only O exits initially with $C_0 = 100$.

The fitting shows that in the absence of water in the oil the reaction rate coefficients k for the main components forming the phosphate chains, i.e. O and P, fall in a similar range, i.e. $k \approx 0.16 - 0.19$, which is similar to one of P/O and P/Zn ratios. The reaction rate of Zn appears to be much higher, i.e. $k \approx 0.27$,

which suggests that zinc undergoes multiple transformations during the early stage of the reaction. This is supported by another evidence that Zn initially forms sulphide and sulphate species on the metal surface, which is followed by forming short and ultimately long zinc phosphate chains. The growth of the phosphate chains is clear from the high reaction constant, $k = 0.57$ of BO/NBO, which suggests a very fast growth.

The growth rates of the atomic concentrations of Zn, P and O appear to be at least as twice as the rate of S, which has a rate coefficient $k = 0.08$. These different kinetics suggest that the sulphide species keeps forming even away from the metal surface at later stages of rubbing. This is evident from the high concentration of sulphur found in all the layers forming the tribofilm.

In the presence of water in the oil, the fitting results show that the equilibrium concentrations of O and S are nearly unchanged. However, water decreases the equilibrium concentration of P and increases the one of Zn by about 38%. Furthermore, for all the components of the tribofilm, water appears to increase the reaction rate k substantially between 15–175%, which suggests that the decomposition reaction is faster.

5.4 Summary and concluding remarks

Throughout this chapter, the evolution of the decomposition reaction of the ZDDP additive and the composition of the formed ZDDP protective antiwear tribofilms were followed over time in the presence and absence of water contamination in the oil. In addition, the changes in the reaction kinetics after different rubbing times were examined. The main results are summarised below:

1. The different kinetics that govern the evolution of friction and tribofilm growth indicate that the changes in the friction force are not only a function of the tribofilm thickness but also the composition.

2. Before the formation of the zinc phosphates, the decomposition of ZDDP has an important precursor, namely, the formation of a sulphur-rich layer. This seems to suggest the necessity to form a mixed oxide-sulphide base layer on the metal surface to promote the tribofilm growth.

3. The precursors' reaction kinetics seem to evolve nearly instantly, however the formation of zinc phosphate has a transient burst phase near the metal surface followed by a slow phase until asymptotically approaching steady state. Based on the observed growth trend of the ZDDP decomposition components,

the polymerisation reaction of the phosphate chains was suggested to follow a first-order reaction kinetics.

4. The formation of the zinc phosphate starts initially with short phosphate chains, which are apparently formed due to the excess concentration of metal oxides on the surface. As the oxides concentration decreases away from the surface, this leads to the polymerisation of the short chains into long ones.

5. Water accelerates the decomposition of ZDDP, which follows first-order reaction kinetics as in the absence of water in the oil, and results in early growth termination.

6. The effect of water on the concentrations of the decomposition products can vary between a small short-term effect limited to the running-in period, such as in the case of O and S, and a large long-term effect such as in the case of P and Zn.

7. Water can hinder the polymerisation reaction in the early stages of rubbing and hence short phosphate chains are formed.

8. The initial alteration of the tribofilm occurring due to the presence of water during the running-in period cannot be reversed even if water is removed from the oil in the subsequent stages by evaporation.

In the following chapter, the decomposition reaction of ZDDP and the composition of the formed tribofilms will be followed in-situ using the newly developed synchrotron XAS methodology described in chapter 4. In order to investigate the role of cations, ashless DDP additives without zinc and H-DLC coated substrates without metallic cations will be studied as well.

Chapter 6

Morphology of ZDDP and DDP tribofilms using in-situ XAS

The complex tribochemical nature of lubricated tribological contacts is inaccessible in real time without altering their initial state. To overcome this issue, a pin-on-disc tribological apparatus was developed and combined with synchrotron X-ray absorption spectroscopy (XAS). Using the designed apparatus it is possible to study in-situ the transient decomposition reactions of various oil additives on different surfaces under a wide range of realistic operating conditions of contact pressure (1.0 - 3.0 GPa), temperature (25 - 120 ^{o}C) and sliding speed (30 - 3000 rpm or 0.15 - 15 m/s). To follow the composition evolution of the tribo- and thermal films antiwear additives and the changes in their reaction kinetics over time, several tribological tests were performed at different contact pressures (1 and 2.2 GPa) and temperatures (25 and 80 ^{o}C). Furthermore, to examine the effect of metallic cations on the tribofilms formation, ZDDP and ashless DDP additives were considered in addition to different countersurfaces, i.e. plain steel and non-doped hydrogenated DLC.

The first section of this chapter presents the tribological results, i.e. friction and wear, over the wide range of tested conditions. Sections two, three and four discuss the in-situ XAS spectra of S and P k-edges over heating and shearing times using ZDDP, DDP-1 and DDP-2 antiwear additives, respectively. Finally, section five summarises the main results discussed throughout the chapter.

6.1 Friction and wear performance

The evolution of the friction coefficient over time using plain and DLC coated countersurfaces rubbed at 25 and 80 °C are shown in Fig. 6.1. In the case of plain hardened spring steel surfaces rubbed at high temperature, the friction coefficient after the running-in period was maximum around 0.12. On the other hand, in the case of the surfaces rubbed at low temperature or surfaces were coated with H-DLC, the friction coefficient was lower at 0.09. Another interesting feature is the difference in the running-in period between the tests. The plain steel countersurfaces showed a relatively large change in the friction coefficient from initially 0.10 to 0.12, whereas for the other cases, the friction coefficient changed only slightly.

The evolution of the friction coefficient can be related to the presence or absence of the ZDDP tribofilm on the contacting surfaces. Previous studies [250, 262, 349] showed that the formation of ZDDP tribofilms causes an increase in the friction coefficient. This was related to either the ability of the tribofilm to hinder the oil entrainment between contacting surfaces or the increased roughness of the formed tribofilm. The inability to form a tribofilm at low temperature is expected as the formation rate under such conditions can be extremely slow [350]. This is because of the thermal decomposition nature of the ZDDP additive, which requires high temperature to activate the reaction of the additive in the oil and consequently the formation of a protective tribofilm on the contacting surfaces.

The friction results of the surfaces coated with non-doped H-DLC seem to suggest that no tribofilm was formed on the surface, which is supported by the similar friction behaviour to the case of plain countersurfaces rubbed at low temperature. The absence of any formed tribofilm on non-doped H-DLC was reported extensively in the literature [216–221], whereas other studies found that some thin tribofilms can be formed [31, 32, 211–215]. The formation and composition of such films will be investigated further using the in-situ surface analysis of XAS P and S k-edges, which is discussed in detail in the subsequent sections.

The friction behaviour of DDP-1 seems to be similar to the one of ZDDP on DLC substrate, i.e. has a low stable friction coefficient lower than 0.1. The minor changes occurring from the beginning to the end of the test could indicate that the additive might have not decomposed completely to form a protective tribofilm. On the other hand, the friction coefficient of the DDP-2 additive was slightly larger around 0.11 and shows fluctuations over rubbing time. The origin of this instability can be related to two possible causes. First, extensive wear and surface

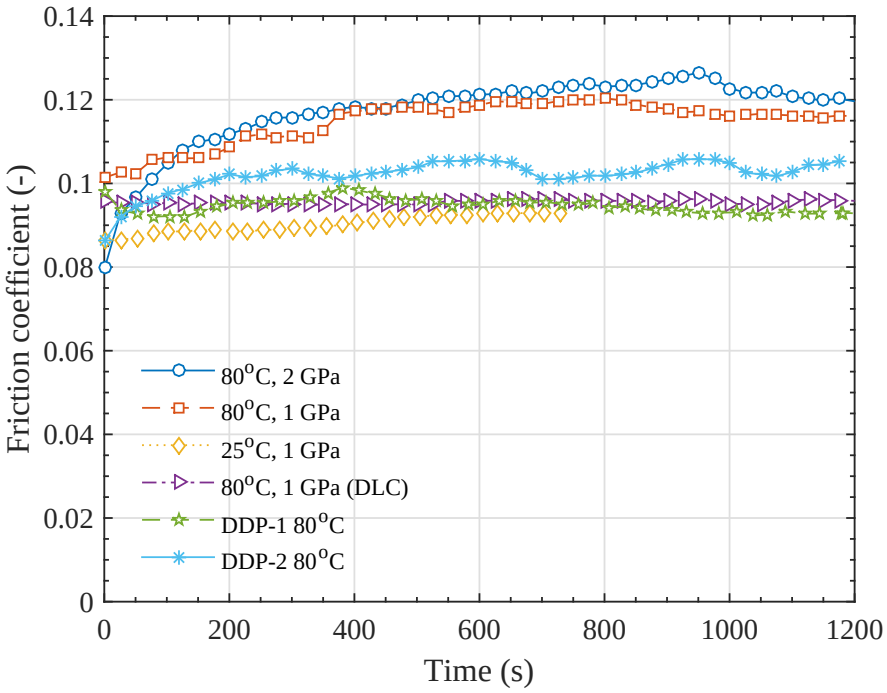

Fig. 6.1 Evolution of the friction force during the in-situ tests using plain steel and DLC coated countersurfaces.

damage might have occurred to the steel substrate without the formation of a protective antiwear tribofilm. Second, a protective tribofilm is formed but has low tenacity and possibly undergoes several formation and removal cycles.

The wear results obtained using white light interferometry are shown in Fig. 6.2. In the case of the ZDDP additive, the width and depth of the wear scar seem to decrease with decreasing the load and rubbing time or increasing the temperature. This is expected as the less harsh the operating conditions become the less the wear would result. The beneficial effect of temperature on wear is related to the formation of a protective tribofilm on the contacting asperities at high temperature that helps protect the rubbing surfaces. However, at low temperature this tribofilm cannot be formed, which results in higher wear.

In the case of DLC coated countersurfaces, no wear was detected. In addition, no visible wear track or tribofilm was discernible.

The ashless DDPs seem to provide a similar wear protection to the one of ZDDP under the same operating conditions. This may indicate that, similar to the ZDDP, the ashless DDPs were decomposed to form protective tribofilms on the rubbing surfaces. The in-situ evolution of the chemical composition of these tribofilms and the others formed under different operating conditions will be discussed in detail in the subsequent sections.

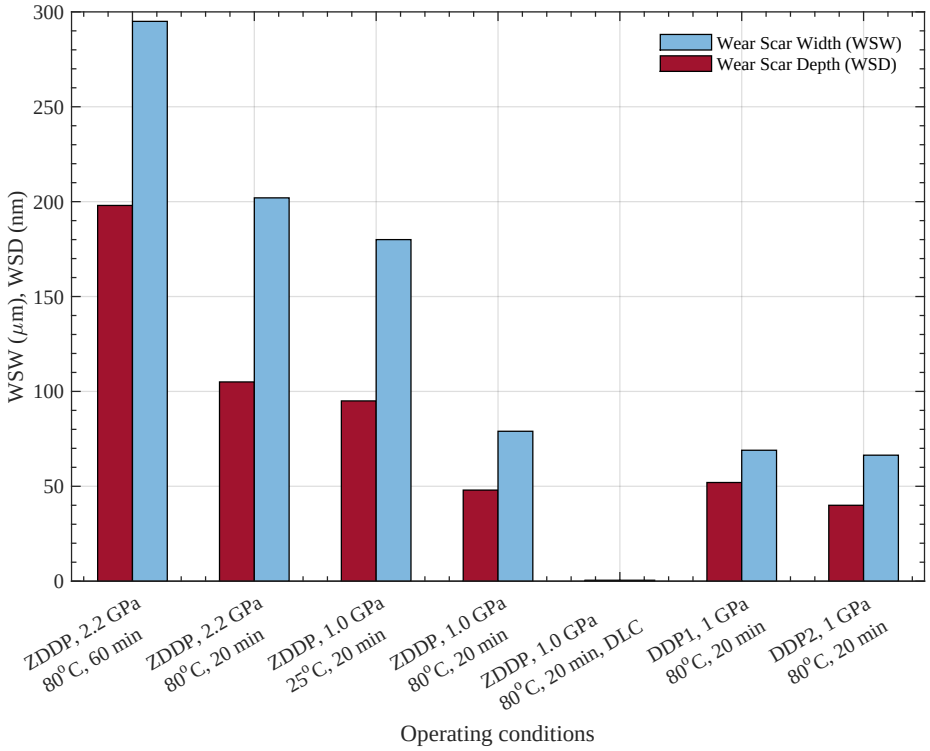

Fig. 6.2 Wear scar width and depth as measured by white-light interferometry after the in-situ tests using different operating conditions.

6.2 XAS analysis of standard samples

In the following sections, the P *k*-edge spectra will be characterised first followed by the characterisation of the S *k*-edge spectra.

6.2.1 P *k*-edge spectra of synthesised phosphate glasses

The P *k*-edge spectra of different synthesised zinc-, iron- and mixed zinc-iron polyphosphate glasses are shown in Figs. 6.3 and 6.4. The initial inspection of the data indicates that the spectra of the various glasses appear to have four main peaks, as listed in Table 6.1. The first peak, (a), was observed at the low energy range at 2153.0±0.5 eV. As this is the main k-edge peak in the different glasses, it can be assigned to phosphate whether of short or long phosphate chains [162, 258, 288]. A pre-edge peak (a') was mainly observed at 2148.0 eV in the glasses containing iron. Thus, this peak can be assigned to iron- or mixed iron-zinc phosphate of short or long chains.

The second peak (b) appeared at 2156.2 eV as a shoulder to peak (a) only in the case of iron ortho-phosphate. Additional two peaks, (c) and (d), appeared around 2161.5±1.0 eV and 2170.0±1.0 eV, respectively, in the high energy post-edge region. The presence or absence of these two peaks can be related to the

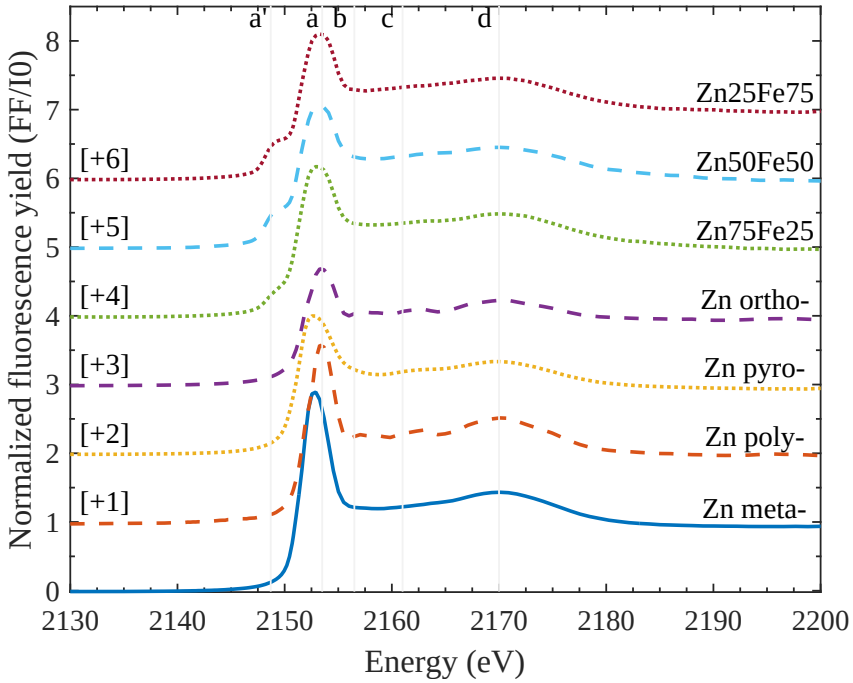

Fig. 6.3 Evolution of the P *k*-edge spectra of different synthesised zinc- and mixed zinc-iron polyphosphate glasses. Each curve is vertically offset for clarity by adding a constant, as specified on each curve, relative to the first curve.

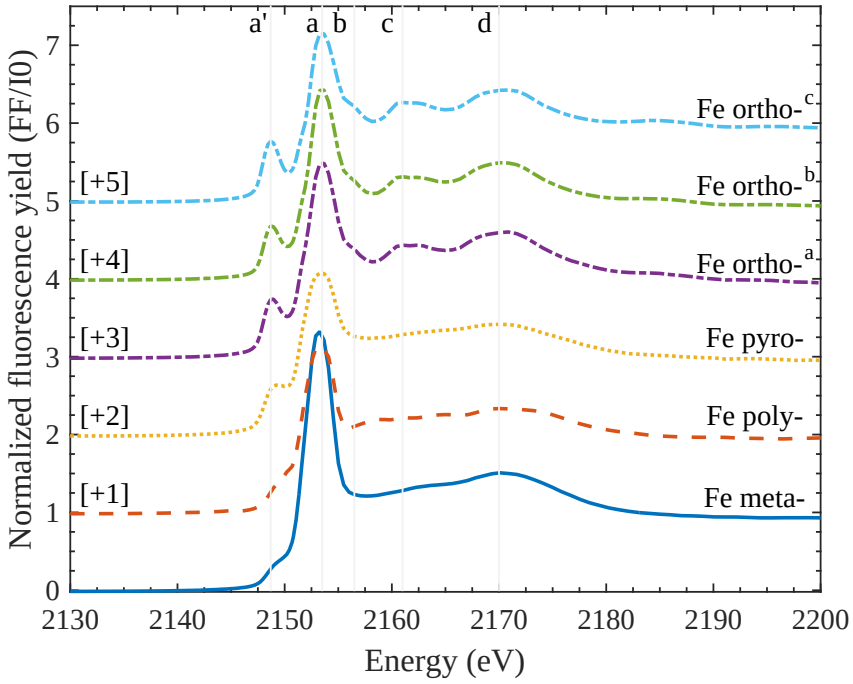

Fig. 6.4 Evolution of the P *k*-edge spectra of different synthesised iron polyphosphate glasses. For iron orthophosphate (a) is amorphous, (b) is semi-crystalline and (c) is crystalline. Each curve is vertically offset for clarity by adding a constant, as specified on each curve, relative to the first curve.

Table 6.1 Peak positions of P *k*-edge (FY) spectra of different synthesised inorganic phosphate glasses.

Compound	P *k*-edge peak positions (±0.1 eV)			
	a	b	c	d
Zn metaphosphate	2152.8	–	2161.4	2169.9
Zn polyphosphate	2153.1	–	2161.3	2170.3
Zn pyrophosphate	2153.4	–	2161.7	2170.2
Zn orthophosphate	2153.5	–	2161.7	2170.1
Fe $poly_{33}$-phosphate	2153.3	–	2162.6	2170.7
Fe $poly_{50}$-phosphate	2153.2	–	2162.1	2169.7
Fe $poly_{67}$-phosphate	2153.1	–	2161.4	2170.3
Fe $poly_{100}$-phosphate	2153.1	2156.2	2161.7	2170.4
$Zn_{25}Fe_{75}$-phosphate	2152.9	–	2160.7	2169.7
$Zn_{50}Fe_{50}$-phosphate	2153.0	–	2160.8	2169.6
$Zn_{75}Fe_{25}$-phosphate	2153.1	–	2160.4	2169.3

oxidation state and arrangements of the different elements within the phosphate structure composing the glass [351]. For instance, peak (c) was only observed as a clear distinctive peak in the case of short chain phosphates such as zinc- and iron orthophosphates. For the phosphates of longer chain length, peak (c) tended to vanish while peak (d) became more visible and of wider FWHM.

6.2.2 S *k*-edge spectra of sulphur samples

The normalised S *k*-edge spectra of different standard compounds containing sulphur is shown in Fig. 6.5. The main k-edge peaks of these samples seem to appear at different positions. For instance, the main peak appears in the case of elemental sulphur at 2472.1 eV, FeS at 2470.0 eV [127], FeS_2 at 2472.0 eV [182], ZnS at 2473.0 eV [285], $FeSO_4$ and $ZnSO_4$ at 2482.0 eV [286, 288].

Several other secondary peaks appeared in the S *k*-edge spectra especially at the high energy range, e.g. at 2491.0 and 2499.0 eV, which can be mainly related to the presence of sulphate species despite appearing in some sulphide compounds as very weak peaks.

The fingerprints of the different species will be used to identify the elements forming the ZDDP tribo- and thermal films after different heating and rubbing times, as discussed in the subsequent sections.

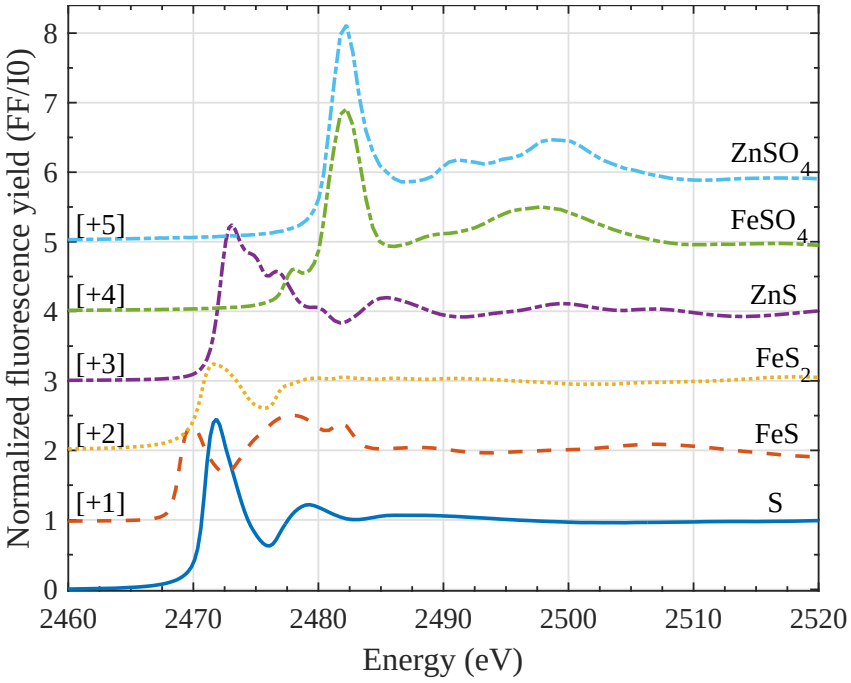

Fig. 6.5 Evolution of the normalised S k-edge spectra of different standard compounds containing sulphur. Each curve is vertically offset for clarity by adding a constant, as specified on each curve, relative to the first curve.

6.3 XAS analysis of ZDDP thermal and tribofilms

6.3.1 ZDDP thermal films formed at 80°C

In the following sections, the P k-edge spectra will be characterised first followed by the characterisation of the S k-edge spectra.

6.3.1.1 Characterisation of P k-edge spectra

The evolution of the normalised P k-edge spectra after different heating times is shown in Fig. 6.6. The P k-edge spectra show four main peaks, as listed in Table 6.2. The first one, peak (a), appears in the low energy range at 2150.0 eV, which corresponds to unreacted ZDDP adsorbed to the steel surface. The second peak (b) appears at 2152.5 eV, which can be assigned to zinc phosphate whether of short or long phosphate chains [162, 258, 288]. The absence of a distinctive pre-edge peak, (a′), at 2148.0 eV indicates that iron (III) phosphate ($FePO_4$) of short chains is absent or of low concentration, but it does not provide any information regarding the presence of any iron phosphates of longer chains [179] (see also Figs. 6.3 and 6.4).

Additional two peaks, (c) and (d), appear at 2159.0 eV and 2169.5 eV, respectively, in the high energy post-edge region. The presence or absence of these two

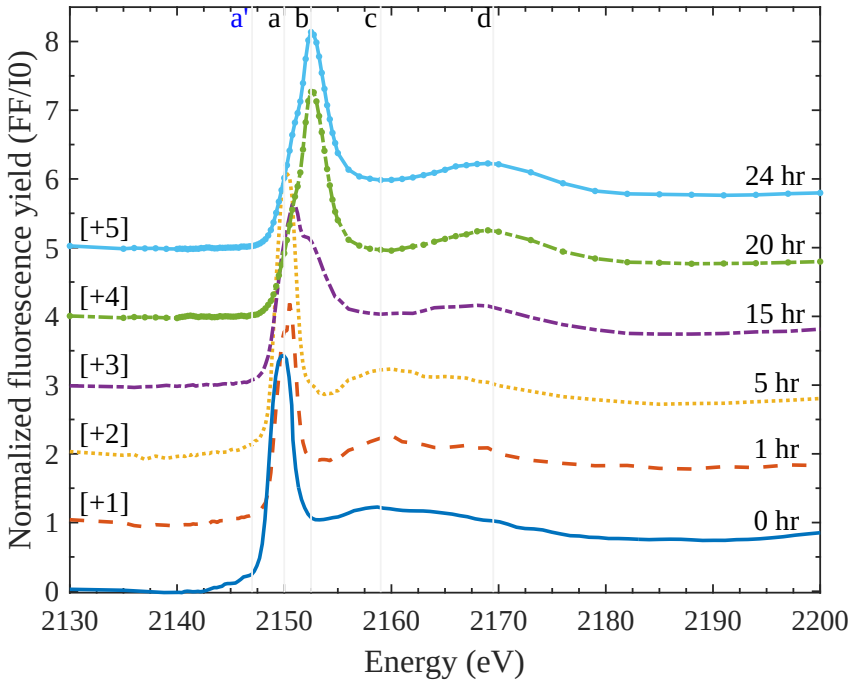

Fig. 6.6 Evolution of the ZDDP normalised fluorescence yield spectra of P *k*-edge after different heating times at 80 °C. Each curve is vertically offset for clarity by adding a constant, as specified on each curve, relative to the first curve.

Table 6.2 Peak positions of P *k*-edge (FY) spectra of the tribo- and thermal films of P-based additives.

P-based films	P *k*-edge peak positions (±0.1 eV)			
	a	b	c	d
ZDDP thermal films	2150.0	2152.5	2159.0	2169.5
ZDDP tribofilms	2150.4	2152.7	2160.0	2169.0

peaks can be related to the structure and composition of the formed phosphate species. The post-edge peaks can provide information regarding the oxidation state and arrangements of the different elements within the phosphate glass structure composing the tribofilm [351].

The P *k*-edge spectra show different subtle changes during heating, which can provide insight into the transient composition of the formed thermal films. The main changes are related to the evolution of peak (a) relative to peak (b) and the presence of the post-edge peaks (c) and (d) over heating time.

During the initial stage of heating, i.e. < 5 hours, the low energy peak (a) corresponding to unreacted ZDDP dominates the higher energy peak (b) corresponding to zinc phosphate. As heating continued, ZDDP was consumed

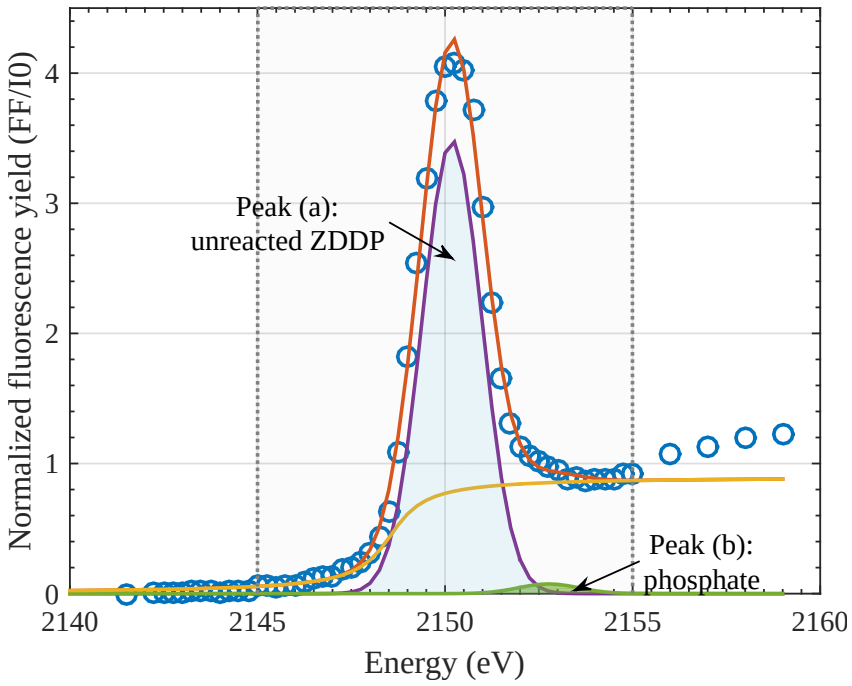

Fig. 6.7 Example of the peak fitting used to determine the areas of peak (a): the adsorbed ZDDP and peak (b): phosphate observed at the P *k*-edge. This example is for a ZDDP thermal film generated after 5 hr of heating time at 80 °C.

to form phosphate glass, which is obvious from the substantial decrease in the height of peak (a) of the unreacted ZDDP along with the simultaneous increase in the height of peak (b) of zinc phosphate. After 20 hours, the individual peak (a) becomes convoluted in peak (b) and appears as a shoulder. Similar conclusions can also be drawn from the height and photon energy of the post-edge peaks (c) and (d). After short heating times, these peaks were present as distinctive peaks. As heating continued, the height of peak (c) decreased until it disappeared after 20 hours whereas the height of peak (d) showed opposite trend. This progressive change over heating time suggests a gradual evolution in the composition of the thermal film matrix and the length of the formed phosphate chains.

The qualitative changes in the XAS P *k*-edge spectra can be quantified by fitting the peaks of the unreacted ZDDP, peak (a), and phosphate, peak (b). An example of the peak fitting used to determine the area of the unreacted ZDDP and phosphate peaks at the P *k*-edge is shown in Fig. 6.7 for a ZDDP thermal film generated after 5 hours of heating. Based on the shown fitting model, Fig. 6.8 presents the evolution of the areas of these peaks after different heating times. It can be clearly observed that during the initial stage of heating, i.e. stage I: during the first 5 hours, the area of the unreacted ZDDP peak appeared to increase over time. In contrast, the area of the phosphate peak was negligible indicating that

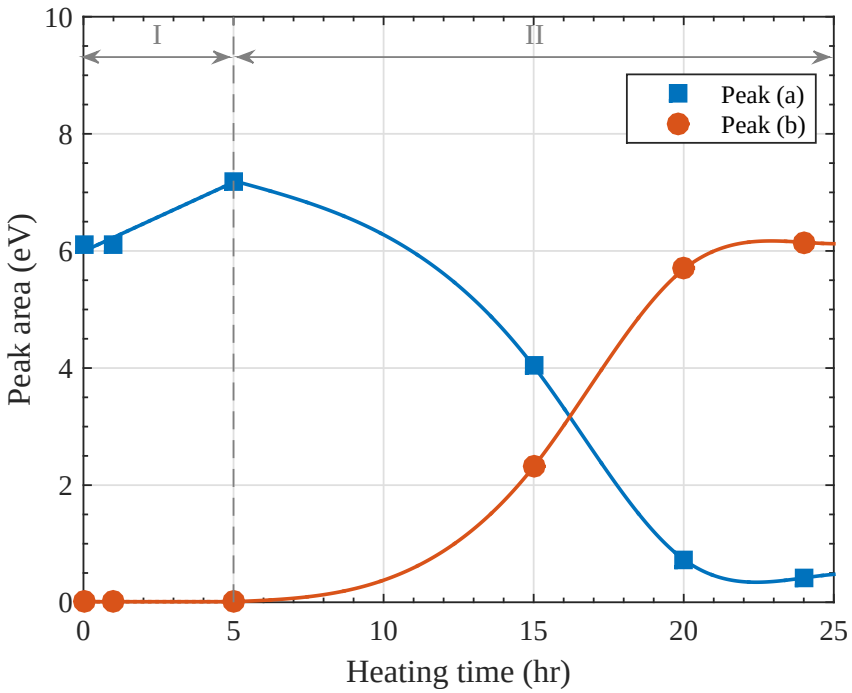

Fig. 6.8 Evolution of the normalised heights of peak (a): adsorbed ZDDP and peak (b): phosphate at the P *k*-edge of ZDDP thermal film after different heating times at 80 °C.

no phosphate species were formed. After this initial phase, i.e. after the first 5 hours of heating, stage II starts in which the peak area of the unreacted ZDDP decreased initially exponentially over heating time with a mean rate of 0.15 eV/hr before reaching steady state. In contrast, the phosphate peak showed an opposite trend of increasing in area exponentially, but with a similar rate, before reaching steady state. This possibly indicates a continuous consumption of the unreacted ZDDP to form more phosphate species. The progressive change in composition throughout the decomposition process confirms that the ZDDP thermal films have a dynamic chemical nature similar to the tribofilms [118, 161–164]. The ZDDP can decompose thermally to form films of a large content of phosphate bonds, e.g. P−O−, P=O and P−O−P [8]. The chain length of the formed polyphosphates is typically a complex function of the operating conditions, e.g. load and temperature, as well as the oil additives, dispersant and contaminants such as water [146]. In general, by increasing the heating time, longer chains of polyphosphates are formed until they reach a uniform chain length. That is because in the beginning of the thermal test short phosphate chains are likely to be formed near the steel surface as a result of the depolymerisation reaction occurring to the long phosphate chains [19, 20, 183–186]. The depolymerisation can occur due to the reaction of the initially formed long phosphate chains with metal oxides, e.g. ZnO, FeO or Fe_2O_3, near the substrate, which can cleave the long chains into shorter ones of mixed Fe-Zn or Fe phosphates [19, 20, 183]. As the

concentration of the metal oxides decreases drastically as the tribofilm thickness increases [7, 20, 36, 200, 201], the fragmentation of the long chains diminishes leading to the formation of longer chains over heating time.

The initial changes in the adsorbed ZDDP as revealed by the XAS surface analysis, which show a delay between the adsorption of ZDDP and the formation of phosphate species, indicate the presence of an initial induction period. This confirms the suggestion of few previous reports about the possible presence of this period preceding the tribofilm formation [244]. This is also in line with the results of Yin et al [118] regarding the decomposition species of ZDDP after different rubbing times, i.e. 5 min, 30 min, 6 hr and 12 hr. The results indicated that the tribofilms formed after short rubbing times exhibit different fingerprints than the ones formed after longer rubbing times, which suggested that different species are formed initially before the phosphate chains. They also found that initially a large concentration of the unreacted ZDDP adsorbs to the steel surface, which can coexist with the subsequently reacted ZDDP.

The duration of the induction period can last for hours in the case of thermal films whereas it is shortened to only a couple of minutes in the case of tribofilms, as discussed in the following sections. This confirms that the ZDDP decomposition and tribofilm formation are thermally and mechanically assisted processes in which rubbing can largely accelerate the reaction [30]. Therefore, the composition of the thermal films can take much longer time to evolve but eventually can approach the one of the tribofilm [172, 352].

6.3.1.2 Characterisation of S *k*-edge spectra

The evolution of the normalised S *k*-edge spectra after different heating times is shown in Fig. 6.9. The clear change observed in the S *k*-edge spectra confirms the advantage of using this in-situ technique for following the chemical changes without interfering with the sample or the testing conditions.

The S *k*-edge spectra appeared to have three main and two secondary peaks, as listed in Section 6.3.2.1. The first main peak, (a), appears at 2472.9 eV, which can be assigned to ZnS or alkyl sulphide [285]. The second main peak, (b), appears at 2476.2 eV, which can be related to alkyl disulphide from the adsorbed ZDDP [288]. The third main peak, (c), appears at 2481.9 eV, which can be attributed to $ZnSO_4$ [288] or $FeSO_4$ [286, 288].

Two other secondary peaks appear after different heating times. The first peak, (a'), appears in the pre-edge region at 2469.5 eV, which can be related to the presence of FeS [288]. On the other hand, the second secondary peak, (d),

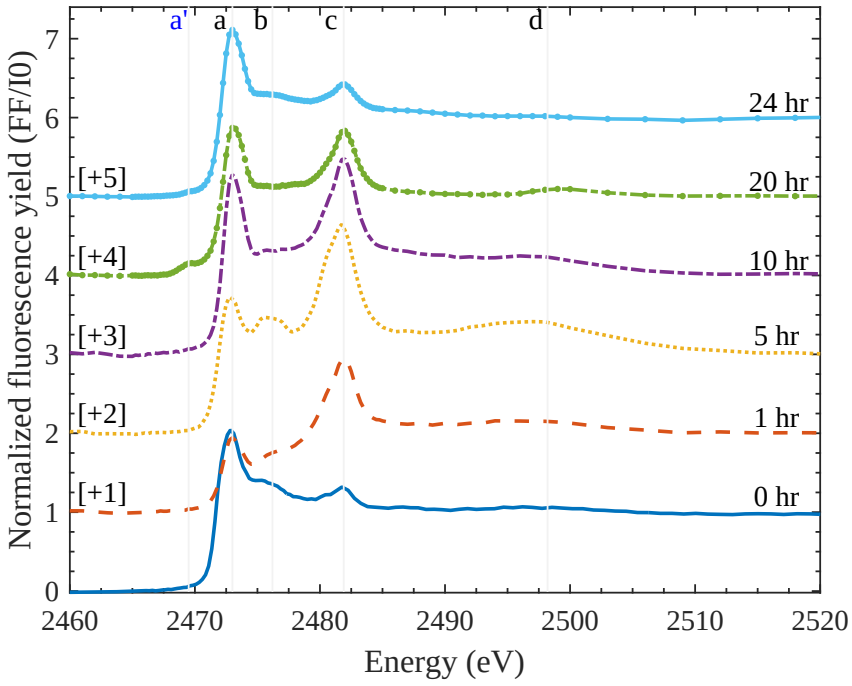

Fig. 6.9 Evolution of the ZDDP normalised fluorescence yield spectra of S *k*-edge after different heating times at 80 °C. Each curve is vertically offset for clarity by adding a constant, as specified on each curve, relative to the first curve.

which appears at 2498.2 eV, can be mainly related to the presence of sulphate species. For instance, peak (d) does not appear in the unreacted ZDDP spectrum and after short heating time during which the unreacted ZDDP dominates the XANES spectrum. As more sulphate is formed with the progressive heating, peak (d) starts to appear and becomes visible after long heating time, i.e. $>$ 1 hour.

The S *k*-edge spectra show different subtle changes during heating, which can provide insight into the transient composition of the formed thermal films. The main changes are related to the evolution of peak (a) relative to peak (b) and (c) and the presence of the pre- and post-edge peaks (a') and (d), respectively, over heating time.

During the initial stage of heating, i.e. $<$ 5 hour, the low energy peaks (a) and (b) corresponding to organic sulphides from the unreacted ZDDP dominate the higher energy peak (c) corresponding to sulphate species. As heating continued, ZDDP was decomposed to form initially sulphate species, which is obvious from the substantial decrease in the heights of peaks (a) and (b) of the organic sulphide in the unreacted ZDDP along with the simultaneous increase in the height of peak (c) of sulphate. In agreement with these results, Kim et al. [136] observed that for ZDDP the sulphate concentration increases with heating while sulphide decreases possibly due to its reaction with the substrate covered with oxides leading to the oxidation of the sulphur species into iron sulphate [182].

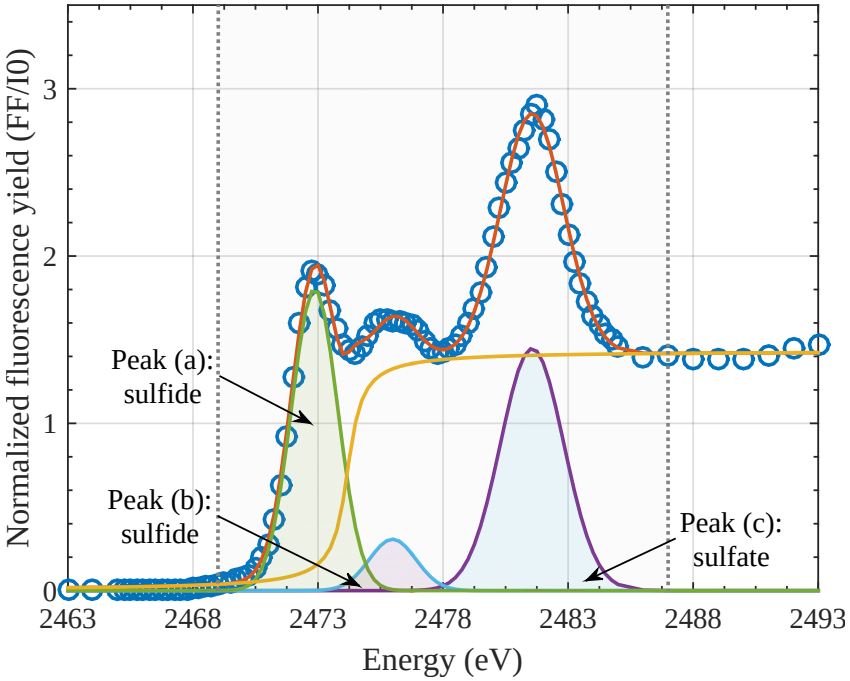

Fig. 6.10 Example of the peak fitting used to determine the area of the sulphides and sulphates peaks at the S *k*-edge. This example is for a ZDDP thermal film generated after 5 hr of heating time at 80 °C.

After 5 hours, peak (a) started increasing while peak (c) decreased, which suggests that the formed sulphate species are reduced to sulphide species. A similar trend can also be found by following the height and photon energy of the post-edge peak (d). After short heating times, this peak does not appear as a distinctive peak. However, as heating continued, its height started to increase with the height of sulphate peak (c) until it disappeared after 20 hours. This progressive change over heating time suggests a gradual evolution in the composition of the thermal film matrix favouring the initial formation of sulphate species, which eventually can be reduced to more stable sulphide species. This is in line with the results of several previous studies [19, 20, 28, 118, 160, 162, 164, 243] suggesting that the ZDDP additive forms mainly sulphide species in the final stages of the decomposition reaction.

The qualitative changes in the XAS S *k*-edge spectra can be quantified by fitting the peaks (a) and (b) of the sulphides and peak (c) of sulphate. An example of the peak fitting used to determine these areas at the S *k*-edge is shown in Fig. 6.10 for a ZDDP thermal film generated after 5 hours of heating. Based on this fitting model, Fig. 6.11 shows the evolution of the areas of these peaks after different heating times. It can be clearly observed that during the initial stage of heating, i.e. stage (I) during the first five hours, the area of sulphate, peak (c),

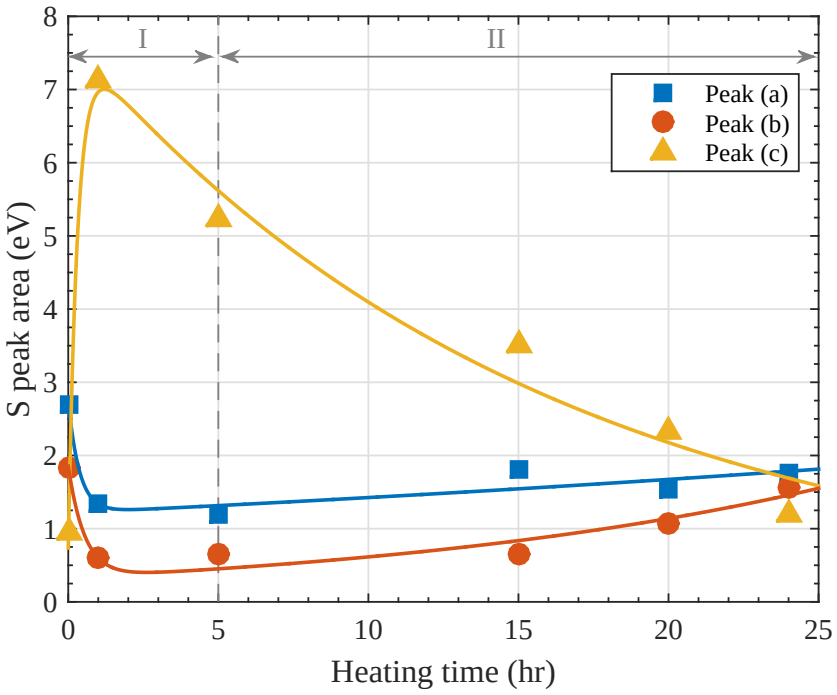

Fig. 6.11 Evolution of the normalised heights of peaks (a) and (b): sulphide and peak (c): sulphate at the S *k*-edge of ZDDP thermal film after different heating times at 80 °C.

appeared to increase drastically over time with a rate of 6 eV/hr. In contrast, the areas of sulphide, peak (a), and organic sulphide, peak (b), decreased over the same period with an average rate of 1.4 eV/hr.

With the progression of heating, the decomposition of ZDDP enters a second phase, i.e. stage (II) after the first five hours of heating, in which the peak area of sulphate decreased gradually over heating time with a mean rate of 0.25 eV/hr. In contrast, the sulphide peaks showed an opposite trend of increasing in area, but with a much slower rate of 0.04 eV/hr. This possibly indicates a continuous consumption of the sulphate to form more stable sulphide species.

The unmatched rate of sulphate consumption with sulphide formation is essentially an inherent limitation of the XANES technique, which does not provide a direct measure of the amount of sulphur if the formed sulphur species differ over time. Basically, XANES signal depends not only on the oxidation state but also the molar mass of the various sulphur species within the probed sample. This means that XANES would show that $Zn_2(SO_4)_3$ has three times the amount of sulphur found in $Zn(SO_4)$, despite the similarity in the oxidation state.

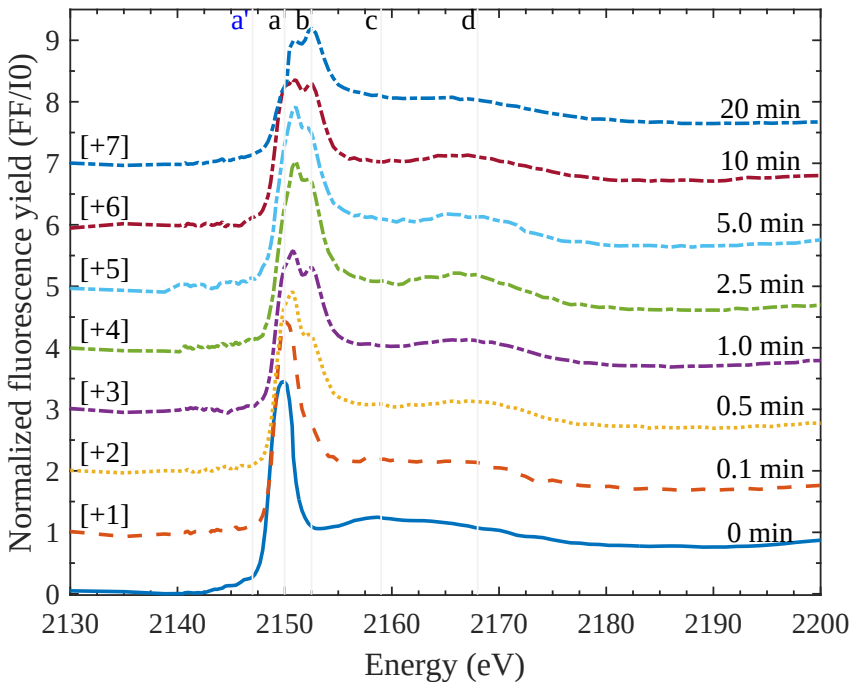

Fig. 6.12 Evolution of the ZDDP normalised fluorescence yield spectra of P *k*-edge after different shearing times at 1.0 GPa and 80 °C. Each curve is vertically offset for clarity by adding a constant, as specified on each curve, relative to the first curve.

6.3.2 ZDDP tribofilms formed at 80°C and 1.0 GPa

6.3.2.1 Characterisation of P *k*-edge spectra

The evolution of the P *k*-edge spectra of the ZDDP tribofilm inside the wear scar is shown in Fig. 6.12. The initial inspection of the data indicates that the changes in the tribofilm spectra over rubbing time are comparable to the ones of the thermal films discussed in the previous section, but the spectra seem to evolve at a faster rate.

Similar to the thermal film, the P *k*-edge spectra of the tribofilm appeared to have four main peaks, as listed in Table 6.2. The first one, peak (a), was observed at the low energy range at 2150.4 eV. As this peak distinctively appeared before shearing has started, it can be assigned to unreacted ZDDP adsorbed to the steel surface. The second peak (b) appeared at 2152.5 eV, which can correspond to zinc phosphate whether of short or long phosphate chains [162, 258, 288]. A pre-edge peak (a') was not observed at 2148.0 eV, which indicates that iron (III) phosphate ($FePO_4$) of short chains or any other iron phosphates of longer chains may either be absent, has low concentration or form localised isolated patches within the tribofilm.

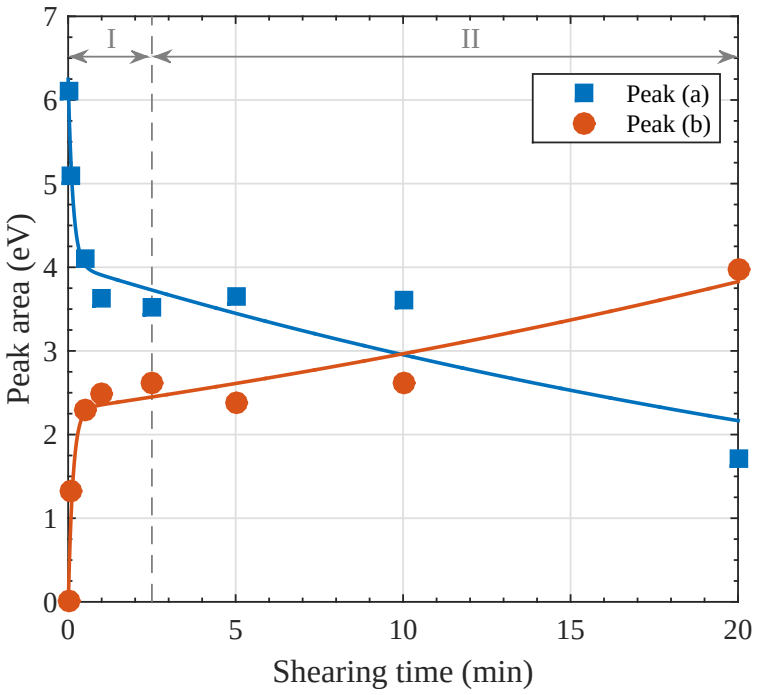

Fig. 6.13 Evolution of the normalised heights of peak (a): adsorbed ZDDP and peak (b): phosphate at the P *k*-edge of ZDDP tribofilms after different shearing times at 1.0 GPa and 80 °C.

Additional two peaks, (c) and (d), appeared at 2160.0 eV and 2169.0 eV, respectively, in the high energy post-edge region. As indicated before, The presence or absence of these two peaks can be related to the oxidation state and arrangements of the different elements within the phosphate glass structure composing the tribofilm [351]. For instance, peak (c) was only observed before shearing has begun, i.e. in the unreacted ZDDP spectrum, and after short rubbing time during which the unreacted ZDDP dominated the XANES spectrum. As rubbing continued, more of the unreacted ZDDP was decomposed to form phosphate species. This caused peak (c) to vanish and peak (d) to become more visible after long rubbing time.

Based on the fitting model described in Fig. 6.7, the quantitative changes in the area of the peaks of the unreacted ZDDP and phosphate at the P *k*-edge are shown in Fig. 6.13 after different shearing times. Contrary to the slowly evolving thermal film discussed in the previous section, the tribofilm does not appear to have an initial induction period in which the unreacted ZDDP molecules just adsorb to the surface without any phosphate formation. Shearing the interface between the contacting surfaces seems to vastly shorten the induction period, which confirms the findings of the previous reports [30] that the ZDDP decomposition and tribofilm formation are thermally and mechanically assisted processes in which shear can greatly accelerate their kinetics. Hence, the first apparent phase, i.e.

Peak positions of S *k*-edge (FY) spectra of the tribo- and thermal films of P-based additives.

P-based films	S *k*-edge peak positions (±0.1 eV)			
	a	b	c	d
ZDDP thermal film	2472.9	2476.2	2481.9	2498.2
ZDDP tribofilm	2472.9	2476.1	2481.9	2498.2

stage (I) during the first few minutes of shearing, starts directly without delay with the swift consumption of the unreacted ZDDP to form phosphate species. The consumption of the ZDDP and the simultaneous formation of phosphates occur at a fast average rate of 2.2 eV/min.

With the progression of rubbing, the decomposition of the unreacted ZDDP entered a second phase, i.e. stage (II) after the first two minutes of shearing. The main characteristics of this phase is the slow decrease in the area of the unreacted ZDDP peak at a rate of 0.09 eV/min accompanied by the slow increase in the area of the phosphate peak at a similar rate. The comparable rates suggest that the unreacted ZDDP is continuously consumed to form the phosphate species without much of replenishment. This can indicate that the ZDDP molecules adsorb preferentially to the polar steel surface whereas it lacks this ability when the steel is covered by the mixed organic and non-organic tribofilm.

6.3.2.2 Characterisation of S *k*-edge spectra

The evolution of the normalised S *k*-edge spectra after different shearing times is shown in Fig. 6.14. Similar to the ZDDP thermal film, the S *k*-edge spectra of the tribofilm appeared to have three main and two secondary peaks, as listed in Section 6.3.2.1. The first main peak, (a), appeared at 2472.9 eV, which can be assigned to ZnS or alkyl sulphide [285]. The second main peak, (b), was observed at 2476.2 eV, which can be related to alkyl disulphide from the adsorbed ZDDP [288]. The third main peak, (c), appeared at 2481.9 eV, which can be attributed to $ZnSO_4$ [288] or $FeSO_4$ [286, 288].

Two other secondary peaks appeared in the S *k*-edge spectra after different shearing times. The first peak (a') was expected in the pre-edge region at 2469.5 eV. The absence of this peak indicates that FeS or any other iron-based sulphide or sulphate species are either patchy, of low concentration or completely not present in the tribofilm. The other secondary peak, (d), which appeared at 2498.2 eV, can be mainly related to the presence of sulphate species. Peak (d) did not appear before shearing has started, i.e. in the unreacted ZDDP spectrum, neither did it

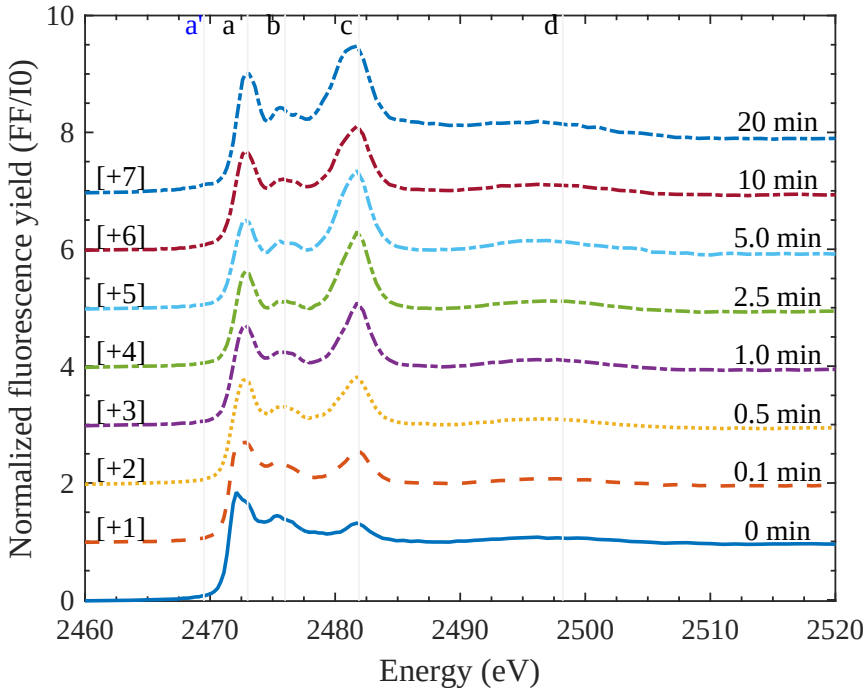

Fig. 6.14 Evolution of the ZDDP normalised fluorescence yield spectra of S *k*-edge after different shearing times at 1.0 GPa and 80 °C. Each curve is vertically offset for clarity by adding a constant, as specified on each curve, relative to the first curve.

appear after short shearing time during which the unreacted ZDDP dominated the XANES spectrum. However, as more sulphate was formed with the progression of shearing, peak (d) emerged and became more visible as shearing continued.

The evolution of the S *k*-edge spectra of the tribofilm inside the wear scar showed a similar trend to the one observed in the spectra of the thermal films. As observed in the previous cases, before shearing started the sulphur composing the tribofilm was observed mainly in the reduced form, i.e. mainly organic disulphides. However, after shearing for a short period of time the sulphur composing the tribofilm started to appear in the oxidised form of sulphate, which increased in concentration with the progressive shearing, as indicated in the change of the heights of peak (a) and (c). These observations are in agreement with the previously reported ex-situ XAS study of Yin et al. [118], which found that sulphate can be formed in the tribofilm during the early stage of the test. This was related to the high temperature at the contacting asperities during the running-in period due to surface smearing and wear, which favours the formation of sulphate. However, after smoothing the rough asperities, the local temperature at the asperity contacts drops below the critical temperature for sulphate formation and thus the more stable ZnS is formed instead.

The qualitative changes in the XAS S *k*-edge spectra can be quantified by fitting the peaks of the sulphides, peaks (a) and (b), and sulphate, peak (c), using

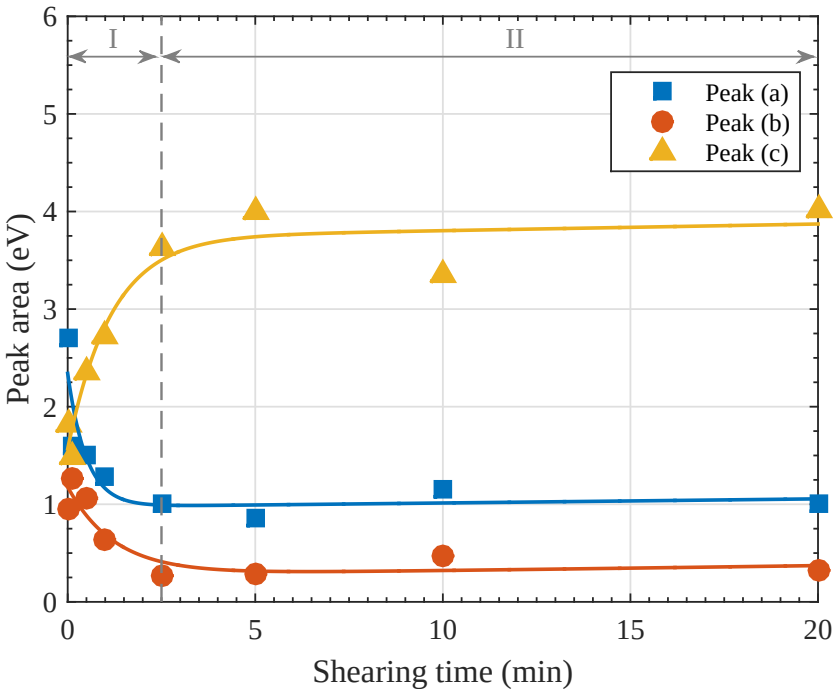

Fig. 6.15 Evolution of the normalised heights of peaks (a) and (b): sulphide and peak (c): sulphate at the S *k*-edge of ZDDP tribofilms after different shearing times at 1.0 GPa and 80 °C.

the fitting model described in Fig. 6.10. Fig. 6.15 shows the evolution of the areas of these peaks after different shearing times. During the initial stage of shearing, i.e. stage (I) during the first 2.5 minutes, the area of sulphate, peak (d), appeared to increase exponentially over time with an average rate of 2.6 eV/min. In contrast, the areas of sulphide, peak (a), and organic sulphide, peak (b), decreased over the same period with a rate of 0.27 eV/min and 1.2 eV/min, respectively.

With the progression of shearing, the decomposition of the unreacted ZDDP enters stage (II), i.e. after the first 2.5 minutes of shearing. Over this period, the change in the peak areas of sulphides and sulphate seems to be negligible. The constant concentrations may be a result of the relatively less harsh operating conditions as compared to the tribofilm formed at high contact pressure. In addition, the transformation of sulphate to sulphide seems to require longer time than the short period of the tribotest, i.e. 20 minutes.

6.3.3 ZDDP tribofilms formed at 25°C and 1.0 GPa

6.3.3.1 Characterisation of P *k*-edge spectra

The evolution of the P *k*-edge spectra inside the wear scar is shown in Fig. 6.16. Similar to the thermal films and tribofilms formed at high temperature, discussed

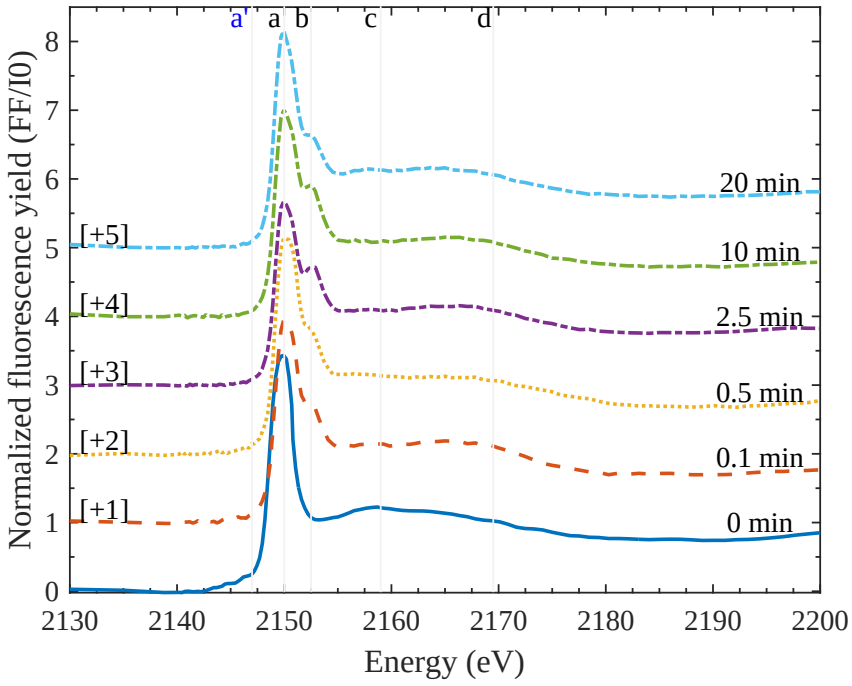

Fig. 6.16 Evolution of the ZDDP normalised fluorescence yield spectra of P *k*-edge after different shearing times at 1.0 GPa and 25 °C. Each curve is vertically offset for clarity by adding a constant, as specified on each curve, relative to the first curve.

before, the P *k*-edge spectra of the tribofilm at low temperature appeared to have four main peaks. The first one, peak (a), appeared at the low energy range at 2150.4 eV, which corresponds to unreacted ZDDP adsorbed to the steel surface. The second peak (b) started to appear at 2152.7 eV only after rubbing has begun. Thus, this peak can be assigned to zinc phosphate whether of short or long phosphate chains [162, 258, 288]. It is worth noting that as the pre-edge peak (a') at 2148.0 eV, which is a fingerprint of iron, was absent, iron phosphate species might not be present in the tribofilm or it can be present but in localised isolated patches or of low concentration.

Additional two peaks, (c) and (d), appeared at 2160.0 eV and 2169.0 eV, respectively, in the high energy post-edge region, which can be related to the oxidation state, molar mass and structure of the phosphate glass composing the main bulk of the tribofilm [351]. Contrary to the tribo- or thermal films formed at high temperature, peak (c) corresponding to adsorbed unreacted ZDDP did not seem to disappear after long shearing times. This may suggest that the decomposition of the unreacted ZDDP at low temperature to form phosphate glass occurs slowly and immaturely. Therefore, within the time of experiments, plenty of unreacted ZDDP molecules are still present on the surface.

The quantitative changes in the areas of the peaks of the unreacted ZDDP and phosphate at the P *k*-edge were found based on the fitting model presented in

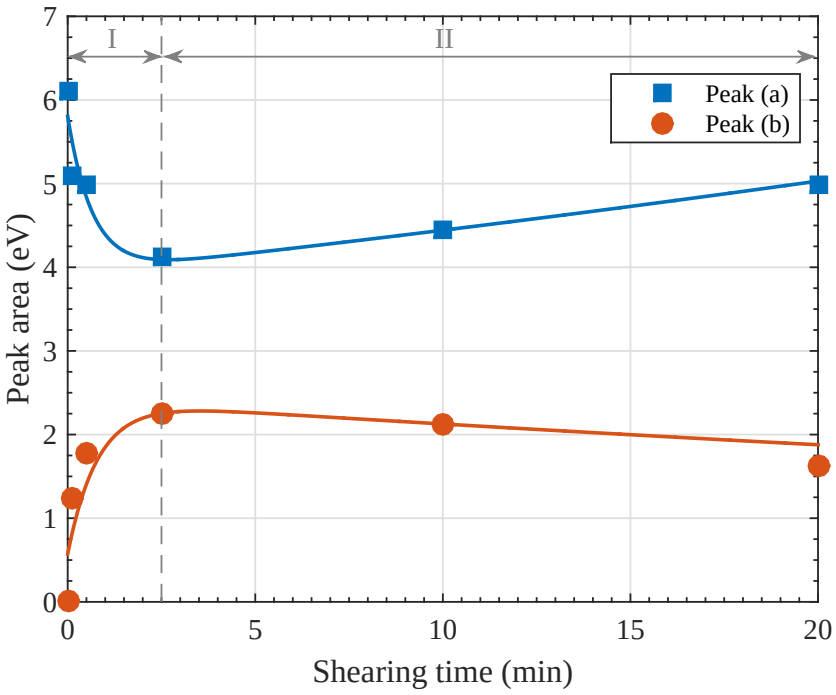

Fig. 6.17 Evolution of the normalised heights of peak (a): adsorbed ZDDP and peak (b): phosphate at the P *k*-edge of ZDDP tribofilms after different shearing times at 1.0 GPa and 25 °C.

Fig. 6.7, and are shown in Fig. 6.17 after different shearing times. Contrary to the slowly evolving thermal film and similar to the previously studied fast evolving tribofilms formed at high temperature, the tribofilm formed at low temperature did not appear to have an initial induction period, which is characterised mainly by the adsorption of the unreacted ZDDP to the steel surface without any decomposition to form phosphate glass. The induction period seems to be hastened by shear. Hence, the first apparent phase, i.e. stage (I) during the first 2.5 minutes, started with the fast consumption of the unreacted ZDDP to form phosphate glass. The consumption of ZDDP and formation of phosphates occurred at a fast rate of 0.8 eV/min. This is slower than the rate of 2.2 eV/min of the tribofilm formed at high temperature but still much faster than the rate of 0.15 ev/hr of the thermal film. This once more confirms that the ZDDP decomposition and tribofilm formation are thermally and mechanically assisted processes, which can be accelerated by both shear and heat. Therefore, the composition of the formed tribofilms at low temperature can take much longer time to evolve but eventually can approach the one of the tribo- or thermal films formed at high temperature [30].

As shearing continued, the decomposition of the unreacted ZDDP entered a new phase, i.e. stage (II) after the first 2.5 minutes. During this phase, a slow increase in the area of the unreacted ZDDP occurred at a rate of 0.05 eV/min accompanied by the slow decrease in the area of the phosphate peak at a similar

rate of 0.04 eV/min. This trend is in contrast to the trends observed in the case of the tribo- and thermal films formed at high temperature. One possible explanation for this can be related to the low tenacity of the expected minuscule amount of the formed phosphate glass at low temperature. Therefore, the low tenacious tribofilm can be removed easily, which exposes the steel surface underneath. The newly available steel surface can then be covered by more adsorbed ZDDP. Thus, the unreacted ZDDP area appears to increase as shearing continues.

6.3.3.2 Characterisation of S *k*-edge spectra

The evolution of the normalised S *k*-edge spectra after different shearing times is shown in Fig. 6.26. The clear change in the features observed in the S *k*-edge spectra indicates that the newly developed in-situ technique could successfully avoid various detrimental effects, especially the elastic and Compton scattering, on the acquired signal. This is evident in the overall high signal to noise ratio and the preservation of the peaks' heights.

The S *k*-edge spectra appeared to have three main and two secondary peaks, as listed in Section 6.3.2.1. The first main peak, (a), was observed at 2472.9 eV, which can be assigned to ZnS or alkyl sulphide [285]. The second main peak, (b), appeared at 2476.1 eV, which can be related to alkyl disulphide from the adsorbed unreacted ZDDP [288]. The third main peak, (c), appeared at 2481.9 eV, which can be attributed to $ZnSO_4$ [288] or $FeSO_4$ [286, 288].

Two other secondary peaks appeared after different shearing times. The first peak, (a'), was expected to appear in the pre-edge region at 2469.5 eV. The absence of this peak can be related to the absence of FeS or other iron sulphide or sulphate species from the tribofilm. The second secondary peak, (d), which was observed at 2498.2 eV, can be mainly related to the presence of sulphate species. This is evident from the absence of this peak from the unreacted ZDDP spectrum, i.e. before the tribotest has begun, and its absence from the spectra after short rubbing time during which plenty of the unreacted ZDDP is expected to still exist on the steel surface. As rubbing continued, more sulphate was formed, which resulted in the more distinctive appearance of peak (d).

The evolution of the S *k*-edge of the tribofilm formed at low temperature showed a similar trend to the one observed in the spectra of the tribo- and thermal films formed at high temperature. Initially, after shearing for a short period of time, e.g. < 5 minutes, the sulphur composing the tribofilm appeared mainly in the oxidised form of sulphate with only a small concentration of sulphur in the reduced sulphide form. However, after slightly longer shearing times, the

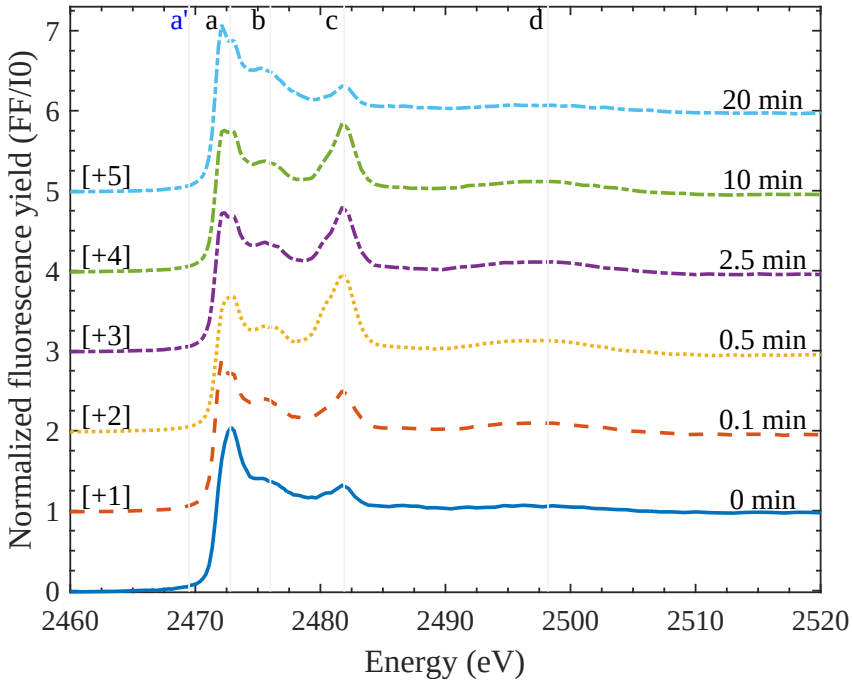

Fig. 6.18 Evolution of the normalised heights of peaks (a) and (b): sulphide and peak (c): sulphate at the S *k*-edge after different shearing times at 1.0 GPa and 25 °C. Each curve is vertically offset for clarity by adding a constant, as specified on each curve, relative to the first curve.

sulphate concentration decreased whereas the sulphide concentration increased, as indicated in the change of the heights of peaks (b) and (c). The sulphate formation is favoured in the beginning of the tribotest due to the surface smearing and wear during the initial running-in period, which can result in high temperature at the contacting asperities. As rubbing continues and the running-in period ends, the local temperature at the asperity-asperity contacts drops below the critical temperature needed for the sulphate formation and therefore the more stable ZnS is formed instead [118].

Using the fitting model described in Fig. 6.10, the qualitative changes in the XAS S *k*-edge spectra can be quantified by fitting the peaks of the sulphides, peaks (a) and (b), and sulphate, peak (c). Fig. 6.19 shows the evolution of the areas of these peaks after different shearing times. It can be clearly observed that during the initial stage of shearing, i.e. stage (I) during the first two minutes, the area of sulphate, peak (c), appeared to increase drastically over time at a rate of 3.3 eV/min. In contrast, the areas of sulphide, peak (a), and organic sulphide, peak (b), decreased over the same period at a rate of 2.3 eV/min and 1.3 eV/min, respectively.

After the first two minutes of shearing, the decomposition of the unreacted ZDDP entered a second phase, i.e. stage (II). During this phase, shearing caused

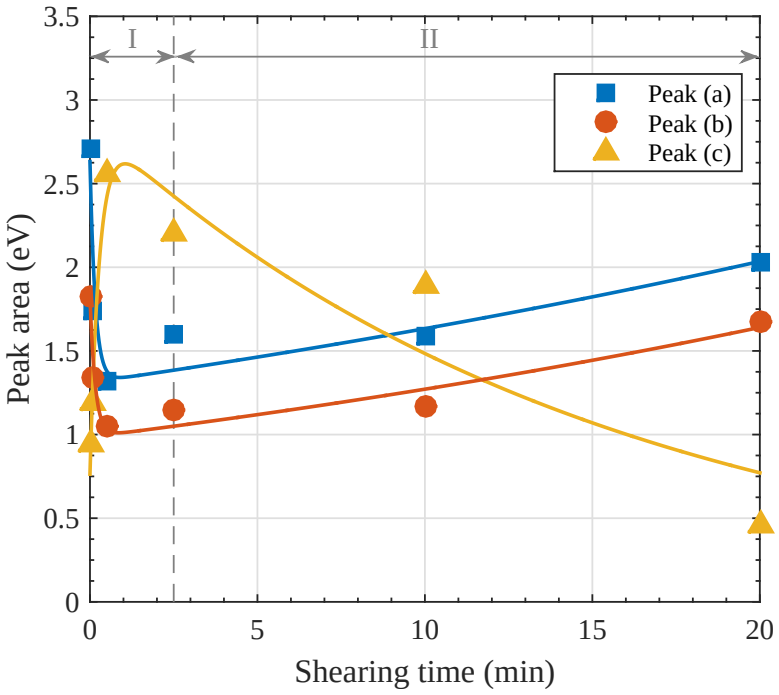

Fig. 6.19 Evolution of the normalised heights of peak (a), (b) and (c) of S *k*-edge of ZDDP tribofilms after different shearing times at 1.0 GPa and 25 °C.

the area of the sulphate peak to decrease gradually at a mean rate of 0.1 eV/hr. In contrast, shearing seemed to have an opposite effect on the areas of the sulphide peaks, which appeared to increase but with a smaller rate of 0.03 eV/min. Similar to the conclusion based on the P *k*-edge data, the mismatched rates can possibly indicate that at low temperature, a small volume of low tenacious tribofilm is formed. Thus, the tribofilm can be removed easily, as indicated by the matched signal of S *k*-edge after 20 minutes of shearing with the one before shearing started.

6.3.4 ZDDP tribofilms formed at 80°C and 1.0 GPa: DLC coated counter-surfaces

6.3.4.1 Characterisation of P *k*-edge spectra

The evolution of the P *k*-edge spectra inside the wear scar formed between DLC coated counter-surfaces is shown in Fig. 6.16. Similar to the thermal films and tribofilms formed at low and high temperatures on bare steel surfaces, as discussed in the previous sections, the P *k*-edge spectra of the tribofilm formed on DLC coated surfaces appeared to have four main peaks. The first one, peak (a), was observed at the low energy range at 2150.4 eV, which corresponds to unreacted ZDDP adsorbed to the DLC surface. The second peak (b) appeared at 2152.7 eV only after rubbing commenced. Thus, this peak can be assigned to zinc phosphate

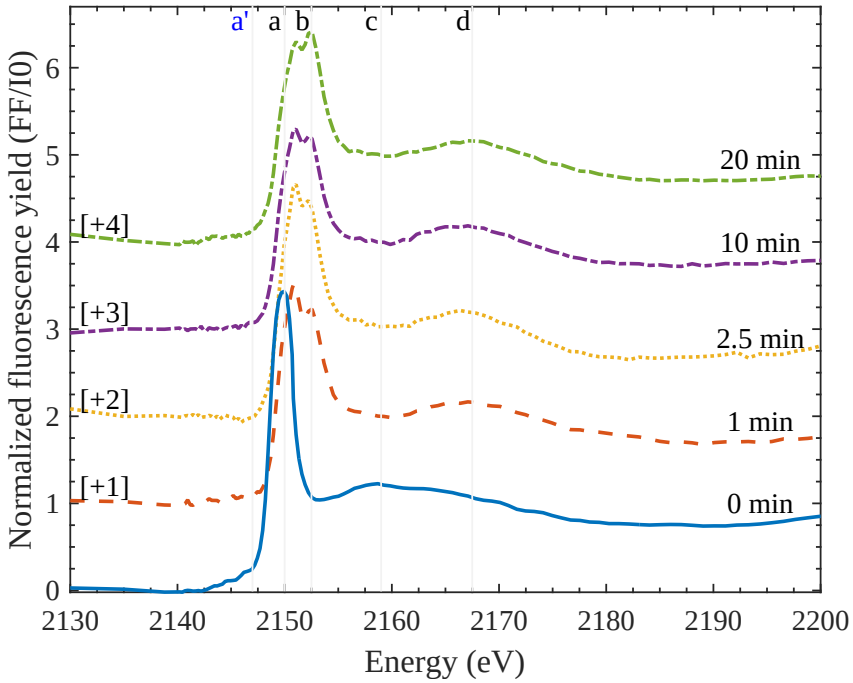

Fig. 6.20 Evolution of the ZDDP normalised fluorescence yield spectra of P *k*-edge after different shearing times using DLC coated counter-surfaces at 1.0 GPa and 80 °C. Each curve is vertically offset for clarity by adding a constant, as specified on each curve, relative to the first curve.

whether of short or long phosphate chains [162, 258, 288]. It is worth noting that the pre-edge peak (a') at 2148.0 eV, which is a fingerprint of iron, was absent as these are DLC coated counter-surfaces and no wear of the coating surface was observed during the tribotest. Thus, iron phosphate species cannot be formed in the tribofilm due to the absence of iron cations.

Additional two peaks, (c) and (d), appeared at 2160.0 eV and 2169.0 eV, respectively, in the high energy post-edge region, which can be related to the oxidation state and arrangements of the different elements within the phosphate glass structure composing the tribofilm [351]. Similar to the previously discussed tribo- or thermal films formed at high temperature, peak (c) corresponding to adsorbed unreacted ZDDP disappeared after shearing commenced. This suggests that the unreacted ZDDP was decomposed completely to form zinc phosphate glass covering the whole wear scar.

The quantitative changes in the areas of the peaks of the unreacted ZDDP and phosphate at the P *k*-edge can be found by fitting peaks (a) and (b) based on the fitting model described in Fig. 6.7. The fitting results are shown in Fig. 6.21 after different shearing times. Similar to the previously studied fast evolving tribofilms formed at high temperature on bare steel surfaces, shearing seemed to induce the decomposition of the unreacted ZDDP to form phosphate glass immediately after

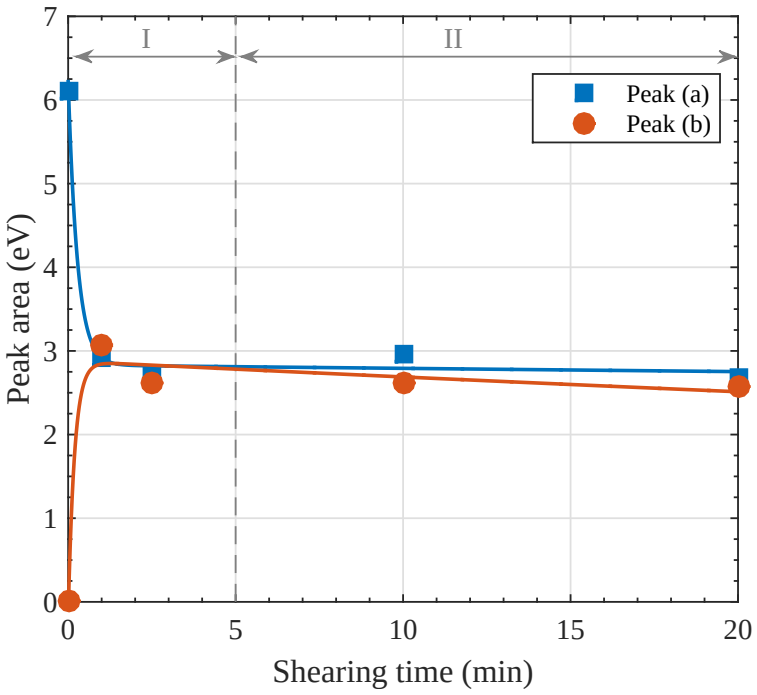

Fig. 6.21 Evolution of the normalised heights of peak (a): adsorbed ZDDP and peak (b): phosphate at the P *k*-edge of ZDDP tribofilms after different rubbing times using DLC coated counter-surfaces at 1.0 GPa and 80 °C.

the tribotest started without any observed induction period. The first apparent phase, i.e. stage (I) during the first few minutes of the tribotest, started with the fast decrease in the area of the unreacted ZDDP peak, i.e. marking the outset of the ZDDP decomposition, accompanied by the fast increase in the area of the phosphate peak, i.e. indicating the formation of zinc phosphate, at a fast rate of 3.2 eV/min. This is similar to the rate of 2.2 eV/min of the tribofilm formed on bare steel surfaces at high temperature but much faster than the rate of 0.15 ev/hr of the thermal film or the rate of 0.8 eV/min of the tribofilm formed at low temperature of 25 °C. These rates confirm that the ZDDP decomposition and tribofilm formation are thermally and mechanically assisted processes in which the kinetics can be greatly accelerated by either shear or heat.

After the first five minutes of shearing, the decomposition of the unreacted ZDDP entered a second phase, i.e. stage (II). During this phase, a negligible decrease occurred in the areas of the unreacted ZDDP and phosphate peaks. One possible explanation for this trend can be related to the low tenacity of the formed tribofilm on the DLC surface causing the tribofilm to be removed easily. However, at high temperature and under shear, the ZDDP decomposition to form phosphate glass is accelerated. Therefore, there will be a balance between the tribofilm formation and removal in such a way that no more phosphate glass is formed and the tribofilm thickness is kept relatively constant, which results in no apparent

change in the areas of the unreacted ZDDP and phosphate peaks. This is in line with several previous studies reported that the P-based additives such as ZDDP can react and form protective tribofilms on DLC coatings even without containing any doped cations [31, 32, 211–215]. In contrast, other studies found that no tribofilms can be formed on non-doped DLC coatings without metallic cations [216–221]. The main factor behind the wide disparity between the formation and absence of tribofilms on DLC coatings appears to be related to the tribofilm tenacity as discussed earlier. Several studies [31, 32, 211] have already suggested that the tribofilms formed on DLC-DLC contacting surfaces are less tenacious than the ones formed on steel surfaces. Furthermore, no iron was present in the formed tribofilms on DLC surfaces [211, 216], which suggests that the low tenacity to the surface can be related to the absence of mixed oxide/sulphide base layer. This layer seems to act as a glue joining the substrate with the subsequently formed phosphate layers composing the main bulk of the tribofilm. It follows that any formed tribofilms on DLC coatings, especially if non-doped, are weakly adhered leading to their effortless removal under rubbing once formed. The presence or absence of the sulphur-base layer will be examined in the subsequent section.

6.3.4.2 Characterisation of S *k*-edge spectra

The evolution of the normalised S *k*-edge spectra after different shearing times is shown in Fig. 6.26. The spectra appeared to have three main and two secondary peaks, as listed in Section 6.3.2.1.

The first main peak, (a) appeared at 2472.9 eV, which can be assigned to ZnS or alkyl sulphide [285]. The second main peak, (b), appeared at 2476.1 eV, which can be related to alkyl disulphide from the adsorbed ZDDP [288]. The third main peak, (c), was observed at 2481.9 eV, which can be attributed to $ZnSO_4$ [288] or $FeSO_4$ [286, 288].

Two other secondary peaks appeared at different shearing times. The first peak, (a'), is located in the pre-edge region at 2469.5 eV. The absence of this peak can be related to the absence of any iron-based sulphide or sulphate species. The second secondary peak, (d), which appeared at 2498.2 eV, can be mainly related to the presence of sulphate species. This is evident from the absence of the peak before shearing started in the unreacted ZDDP spectrum. As more sulphate is formed with progressive shearing, peak (d) started to appear and became visible just after the start of shearing.

The evolution of S *k*-edge of the tribofilm inside the wear scar showed a similar trend to the one observed in the spectra of the previously discussed tribo- and

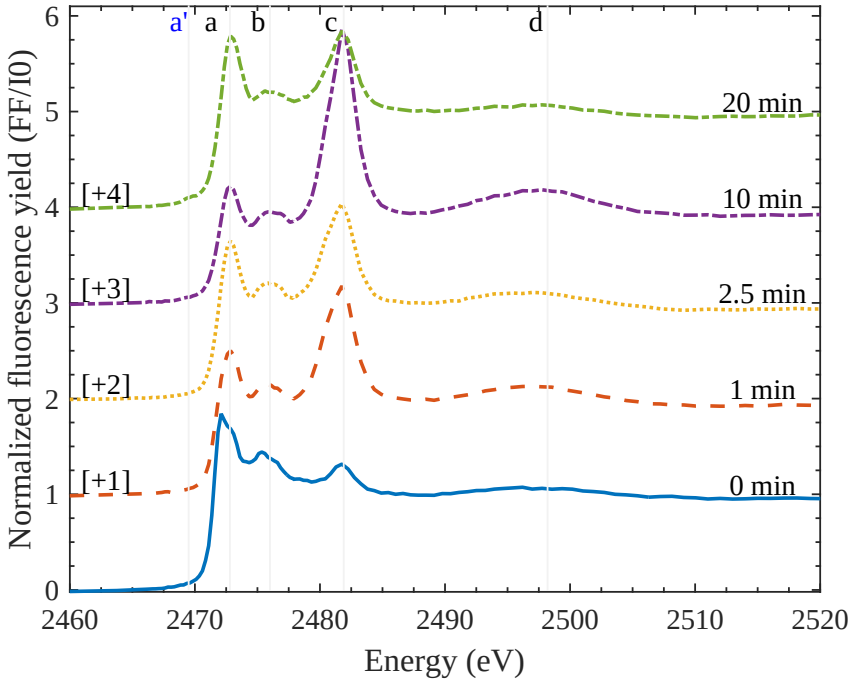

Fig. 6.22 Evolution of the ZDDP normalised fluorescence yield spectra of S k-edge after different shearing times at 1.0 GPa and 80 °C using DLC coated counter-surfaces. Each curve is vertically offset for clarity by adding a constant, as specified on each curve, relative to the first curve.

thermal films. Initially, after shearing for a short period of time, i.e. < 5 minutes, the sulphur composing the tribofilm appeared mainly in the oxidised sulphate form in addition to the reduced sulphide form. However, after longer shearing times, the sulphate concentration decreased whereas the sulphide concentration increased, as indicated in the change of the heights of peaks (a), (b) and (c).

The qualitative changes in the XAS S k-edge spectra can be quantified using the fitting model described in Fig. 6.10 to fit the peaks of the sulphides, peaks (a) and (b), and sulphate, peak (c). Fig. 6.23 shows the evolution of the areas of these peaks after different shearing times. During the first five minutes, i.e. stage (I), the area of sulphate, peak (c), appeared to increase drastically over time with a rate of 2.5 eV/min. In contrast, the areas of sulphide, peak (a), and organic sulphide, peak (b), decreased over the same period with a relatively smaller rate of 1.7 eV/min.

The progression of shearing, i.e. after the first five minutes, caused the decomposition of the unreacted ZDDP, adsorbed to the DLC surface, to enter a second phase, i.e. stage (II). During this phase, the area of the sulphate peak decreased gradually over shearing time with a mean rate of 0.36 eV/min. In contrast, the sulphide peaks showed an opposite trend of increasing in area, but with a much smaller rate of about 0.035 eV/min. The mismatch rates suggest

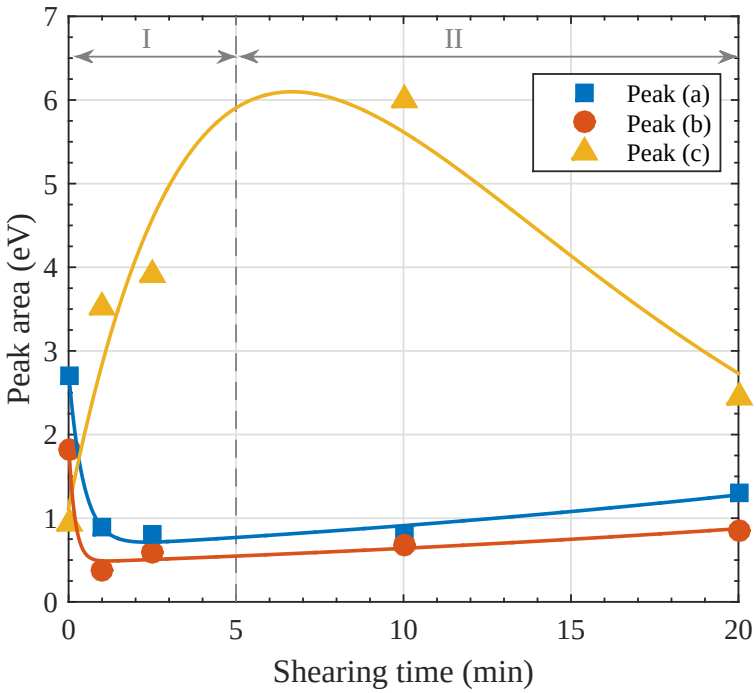

Fig. 6.23 Evolution of the normalised heights of peaks (a) and (b): sulphide and peak (c): sulphate at the S *k*-edge of ZDDP tribofilms after different shearing times at 1.0 GPa and 80 °C using DLC coated counter-surfaces

that the formed tribofilm on the DLC surface is of low tenacity, which results in the removal of the tribofilm instead of the consumption of the sulphate to form sulphide species. This added to the absence of iron confirms the observation discussed in the previous section that the low tenacity to the surface is related to the absence of mixed oxide/sulphide base layer that help bridge the substrate with the subsequently formed phosphate layers composing the main bulk of the tribofilm. The absence of this layer was also suggested by several previous studies [32, 211, 216].

6.3.5 ZDDP tribofilms formed at 80°C and 2.2 GPa

6.3.5.1 Characterisation of P *k*-edge spectra

The evolution of the P *k*-edge spectra of the tribofilm formed at high temperature and large contact pressure is shown in Fig. 6.24. The spectra appeared to have four main peaks, as listed in Table 6.2. The first one, peak (a), was observed at 2150.4 eV, which corresponds to unreacted ZDDP. The second peak (b) appeared at 2152.7 eV only after rubbing started, which can be assigned to zinc phosphate whether of short or long phosphate chains [162, 258, 288]. No pre-edge peak (a') appeared at 2148.0 eV, which suggests that iron-based phosphate glass might not

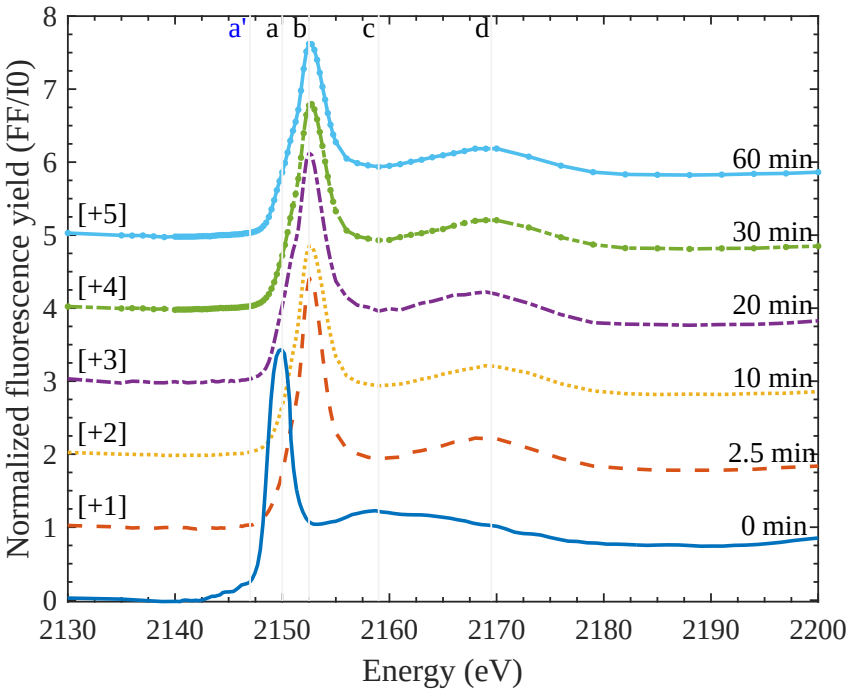

Fig. 6.24 Evolution of the ZDDP normalised fluorescence yield spectra of P k-edge after different shearing times at 2.2 GPa and 80 °C. Each curve is vertically offset for clarity by adding a constant, as specified on each curve, relative to the first curve.

be present in the tribofilm. Additional two peaks, (c) and (d), appeared at 2160.0 eV and 2169.0 eV, respectively. As stated before, these high energy post-edge peaks can be related to the oxidation state and arrangements of the different elements within the phosphate glass structure composing the tribofilm [351].

The evolution of the P k-edge spectra inside the wear scar suggests inconspicuous common changes over time as compared to the ones of the thermal films and tribofilms generated at low contact pressure of 1.0 GPa. For instance, from the inception of shearing, peak (a) appeared to be convoluted in peak (b) and existed as a shoulder, as compared to the case of the thermal film when this started to occur after 30 minutes of heating. In addition, peak (c) is absent and only peak (d) appears in the post-edge EXAFS region. The main reason behind this invariant trend can be explained as follows. As these experiments were not carried out at the critical glancing angle, the acquired XAS signal originates from not only the surface layer but also the bulk layers. Therefore, the common features of the spectra over shearing time indicate that the average composition of the tribofilm is unchanged. This can be mainly related to the nature of the ZDDP decomposition inside the wear scar under severe conditions of shear and heat. As the decomposition of the ZDDP additive is thermally activated and mechanically assisted process [30], this indicates that the ZDDP decomposition under harsh operating conditions will be faster as it will be accelerated by shear. For instance,

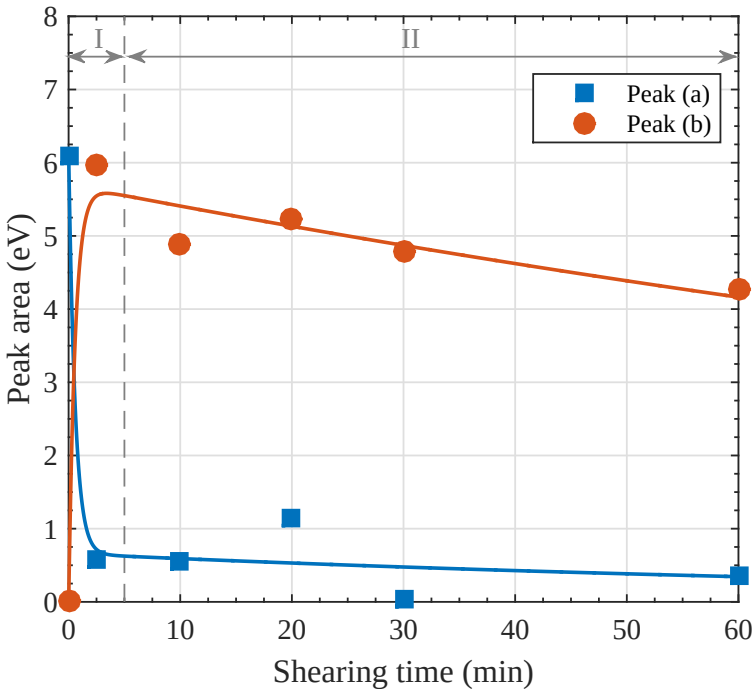

Fig. 6.25 Evolution of the normalised heights of peak (a): adsorbed ZDDP and peak (b): phosphate at the P *k*-edge of ZDDP tribofilms after different rubbing times at 2.2 GPa and 80 °C.

the steady-state composition of the tribofilm can be reached as early as shearing commences. However, the slowly evolving thermal film discussed before in section 6.3.1, took a much longer period, i.e. about 20 hours of heating, to reach the steady-state composition and to match the spectrum of the tribofilm after 2.5 minutes of shearing.

To get a better quantitative analysis, the fitting model described in Fig. 6.7 was used to find the areas of the unreacted ZDDP and phosphate peaks over shearing time. The results of this fitting are presented in Fig. 6.25. The areas of the peaks appear to undergo two distinctive phases. During the first phase, (I), the area of the unreacted ZDDP peak decreased sharply with a rate of about 5.5 eV/min whereas the area of the phosphate peak increased sharply with a similar rate. The results confirm that the contact pressure can accelerate the decomposition reaction of the ZDDP to a great extent, which is evident from the big jump in the area of the phosphate peak in the first couple of minutes after shearing started. Furthermore, the results suggest that the ZDDP molecules adsorb preferentially to the steel surface during the heating time and is ready to form the tribofilm immediately once shearing commences.

During the second phase, (II), after 5 minutes of rubbing, the area of the unreacted ZDDP peak appeared to be around 0.5 eV throughout the tribotest with a negligible decrease over time. Similarly, the area of the phosphate peak

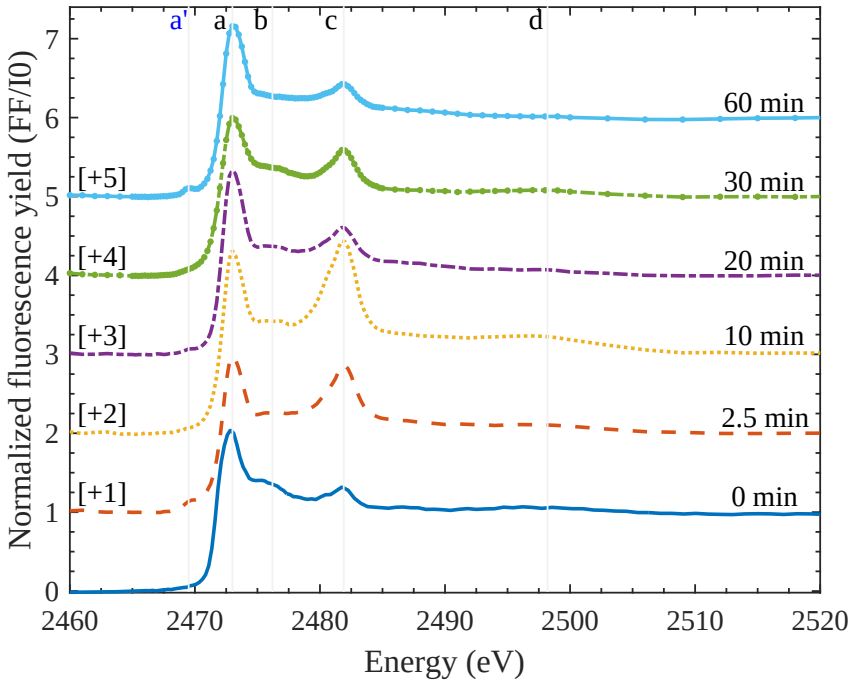

Fig. 6.26 Evolution of the ZDDP normalised fluorescence yield spectra of S *k*-edge after different shearing times at 2.2 GPa and 80 °C. Each curve is vertically offset for clarity by adding a constant, as specified on each curve, relative to the first curve.

appeared to be around 5.0 eV throughout the test with a mild decrease of 0.02 eV/min over shearing time. This decrease in the area of the phosphate peak can be related to the scission of long phosphate chains into shorter ones under the large contact pressure and to severe surface wear that can remove the long phosphate chains from the surface [186].

6.3.5.2 Characterisation of S *k*-edge spectra

The evolution of the normalised S *k*-edge spectra after different shearing times is shown in Fig. 6.26. The S *k*-edge spectra appeared to have three main and two secondary peaks, as listed in Section 6.3.2.1.

The first main peak, (a), appeared at 2472.9 eV, which can be assigned to ZnS or alkyl sulphide [285]. The second main peak, (b), appeared at 2476.1 eV, which can be related to alkyl disulphide from the adsorbed ZDDP [288]. The third main peak, (c), was observed at 2481.9 eV, which can be attributed to $ZnSO_4$ [288] or $FeSO_4$ [286, 288].

Two other secondary peaks appeared after different shearing times. The first peak, (a'), was expected in the pre-edge region at 2469.5 eV. The absence of this peak suggests the absence of iron-based sulphide or sulphate species from the tribofilm [288]. The second secondary peak, (d), which was observed at 2498.2

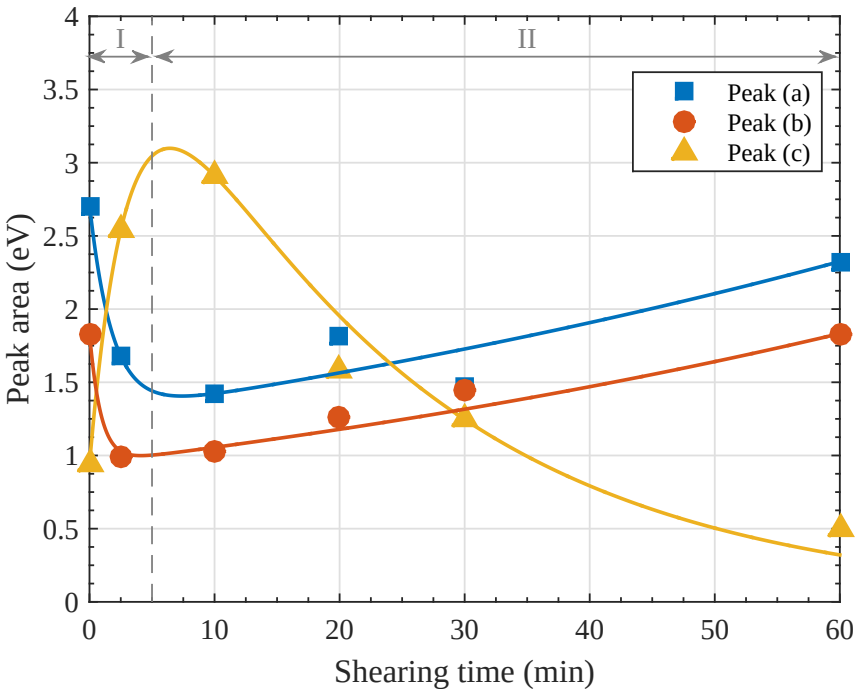

Fig. 6.27 Evolution of the normalised heights of peaks (a) and (b): sulphide and peak (c): sulphate at the S *k*-edge of ZDDP thermal film after different shearing times at 2.2 GPa and 80 °C.

eV, can be mainly related to the presence of sulphate species. The peak did not appear in the unreacted ZDDP or after short shearing time during which plenty of unreacted ZDDP molecules still adsorbed to steel surface. As more sulphate was formed during the progression of shearing, peak (d) emerged and became more visible. The link between the height of the sulphate peak (c) and the height of the high energy post-edge peak (d) can be clearly observed in the spectra evolution over shearing time.

In general, the evolution of the S *k*-edge spectra of the tribofilm inside the wear scar showed a similar trend to the one observed in the spectra of the tribo- and thermal films discussed before. Initially, after shearing for a short period of time, e.g. < 5 minutes, the sulphur composing the tribofilm appeared mainly in the sulphate form along with the sulphide form. However, after longer shearing times, the sulphate concentration decreased whereas the sulphide concentration increased, as indicated in the change of the heights of peak (a) and (c).

The qualitative changes in the XAS S *k*-edge spectra can be quantified by fitting the peaks of the sulphides, peaks (a) and (b), and sulphate, peak (c) using the fitting model presented in Fig. 6.10. Fig. 6.27 shows the evolution of the areas of these peaks after different shearing times. It can be clearly observed that during the initial stage of shearing, i.e. stage (I) during the first 5 minutes, the area of sulphate, peak (d), appeared to increase over time with a fast rate of 0.4

eV/min. In contrast, the areas of sulphide, peak (b), and organic sulphide, peak (c), appeared to decrease over the same period with a relatively similar rate of 0.3 eV/min.

As rubbing continued, i.e. after the first 5 minutes of shearing, the decomposition of the unreacted ZDDP adsorbed to the steel surface entered a second phase, i.e. stage (II). During this phase, the area of the sulphate peak (c) decreased gradually over shearing time with a mean rate of 0.055 eV/min. In contrast, the sulphide peaks (a) and (b) showed an opposite trend of increasing in area, but with a relatively similar rate of 0.035 eV/min. The comparable rates can possibly indicate a continuous consumption of the sulphate to form more stable sulphide species.

6.4 Overall comparison between ZDDP tribo- and thermal films

In the previous sections, each tribo- or thermal test was discussed individually. These tests were performed under different operating conditions of temperature, contact pressure and countersurfaces. To understand the effect of these conditions on the formed tribo- and thermal films, it is necessary to compare between the formed P- and S-species across the different tests.

Fig. 6.28 compares the normalised areas of the adsorbed ZDDP and phosphate peaks at the P *k*-edge of the ZDDP trio- and thermal films at the end of each test. The available data exhibit three distinctive features. First, as the operating conditions become harsher, i.e. higher temperature and contact pressure or just longer heating or shearing time, the area of peak (a) of adsorbed ZDDP decreases accompanied by a decrease in the area of the phosphate peak (b). Interestingly, this trend is similar to the evolution of the areas of the adsorbed ZDDP and phosphate peaks in any tribo- or thermal test. The significance of this observation is that it confirms that heat and shear role is just to accelerate the reaction kinetics of the additive decomposition but they do not affect the type of the formed species. For instance, observing the areas of the adsorbed ZDDP and phosphate peaks of the tribofilm formed under 2.2 GPa at 80 °C after 60 min and the ones of the thermal film formed under heating for 24 hours at 80 °C confirms that despite of the different kinetics governing the formation of these tribo- and thermal films, their final compositions appear to be similar.

Second, there is an upper limit for the area of the phosphate peak, which is reached after long rubbing or heating time. Beyond this point, either the

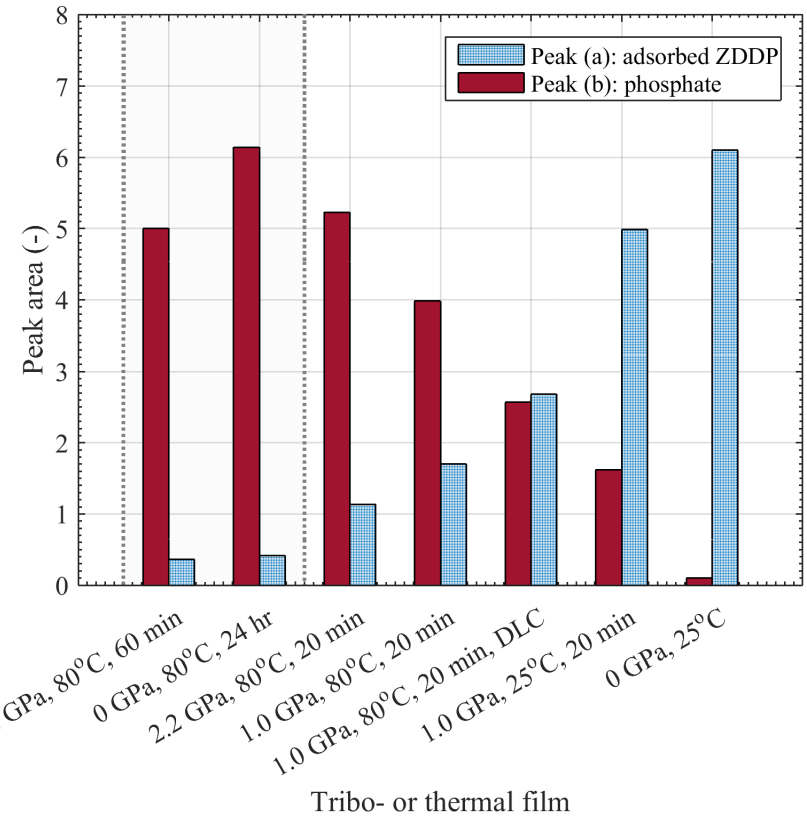

Fig. 6.28 Comparison between the normalised areas of the adsorbed additive and phosphate peaks at the P *k*-edge of the ZDDP tribo- and thermal films at the end of each test.

phosphate area reaches steady state or starts to decrease. This is in agreement with the findings of each test individually. The formed phosphate chains seem to reach a certain length, which can be shortened with the progression of heating or rubbing.

Third, there seems to be a trend that the larger the area of the phosphate peak, the smaller the area of the adsorbed ZDDP peak. As discussed before, this can be related to the availability of the substrate, whether bare or DLC coated steel surface. As more tribofilm volume is formed under shearing or heating, less substrate becomes available for the additive adsorption. This may indicate that the ZDDP molecules do not adsorb preferentially to the tribofilm and thus the detected signal comes mainly from the entrapped additive within the formed tribofilm itself and to a less extent from its upper surface.

Examining the sulphur-based species formed under the various tested operating conditions can provide a better understanding of the composition evolution of the ZDDP tribo- and thermal films. Fig. 6.29 compares the normalised areas of the sulphide and sulphate peaks at the S *k*-edge of the ZDDP films at the

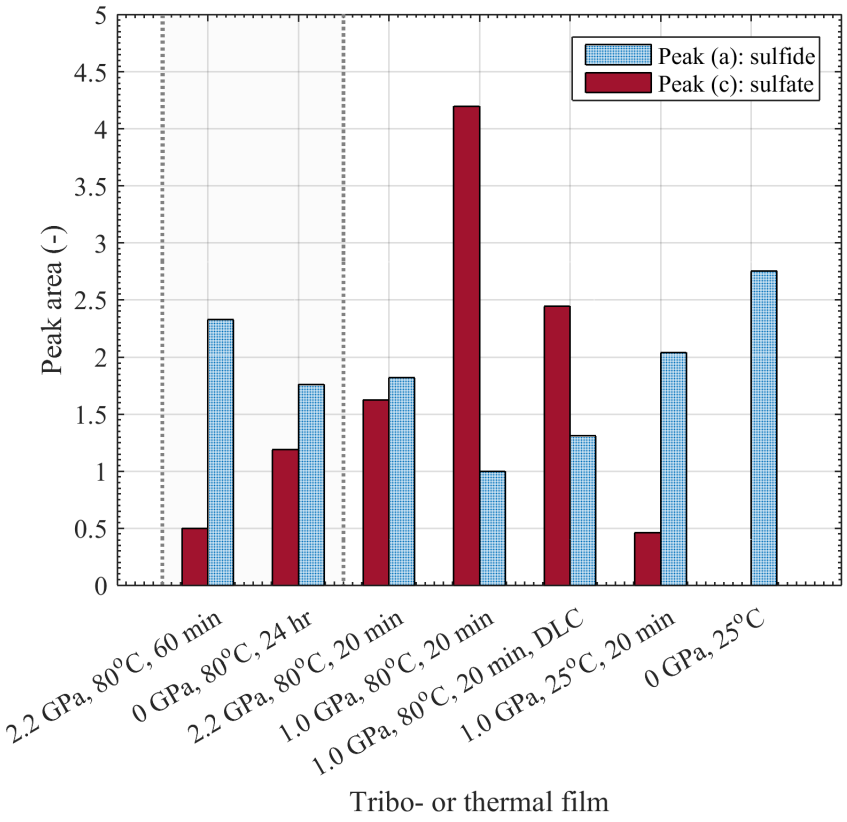

Fig. 6.29 Comparison between the normalised areas of the sulphide and sulphate peaks at the S k-edge of the ZDDP tribo- and thermal films at the end of each test.

end of each test. Similar to the P k-edge data, the available S data exhibit few distinctive features. First, as the temperature and contact pressure increase or just the heating or shearing time gets longer, the area of the sulphide peak initially decreased whereas the area of the sulphate peak increased. However, as the conditions become harsher the trend eventually reverses, i.e. sulphide increased and sulphate decreased. The overall trend across the various tribo- and thermal films is strikingly similar to the one observed in the evolution of the individual tribo- and thermal films, which confirms that the observed trend across the various tests is just related to the difference in the reaction kinetics. As throughout the ZDDP decomposition sulphur starts from unreacted ZDDP and ends with sulphide species, the apparent decrease and then increase in the sulphide area can be in part related to the fact that the initial sulphide area consists mainly of adsorbed ZDDP whereas the final area consists primarily of zinc sulphide and a small concentration of adsorbed ZDDP embedded within the tribofilm.

The second feature in the data is related to the transformation of sulphate as the operating conditions gets harsher. Under mild conditions, sulphate area starts

to increase, which reaches a peak value before starts to decrease to a minuscule value under harsher conditions or longer tests. These changes are mainly related to the potent effect of shear and heat, which can accelerate the decomposition of the adsorbed ZDDP.

6.5 XAS analysis of DDP-1 tribofilms

6.5.1 DDP-1 tribofilms formed at 80^{o}C and 1 GPa

In the following sections, the P k-edge spectra will be characterised first followed by the characterisation of the S k-edge spectra.

6.5.1.1 Characterisation of P k-edge spectra

The evolution of the P k-edge spectra inside the wear scar is shown in Fig. 6.30. Similar to the ZDDP trio- and thermal films discussed before, the P k-edge spectra of the DDP tribofilm have four main peaks. The first one, peak (a), was observed at 2150.2 eV, which corresponds to unreacted DDP adsorbed to the steel surface. This is evident from its distinctive appearance before shearing started. The second peak (b) started to appear at 2152.8 eV only after shearing commenced. This peak can be assigned to iron or zinc phosphate whether of short or long phosphate chains [162, 258, 288]. The presence of the pre-edge peak (a') at 2148.0 eV, which is a fingerprint of iron, cannot be confirmed for this dataset due to the convoluted noise in the spectra.

Additional two peaks, (c) and (d), were observed at 2160.0 eV and 2171.0 eV, respectively, in the post-edge region, which can be related to the oxidation state and arrangements of the different elements within the phosphate glass structure composing the tribofilm [351]. Similar to the previously discussed ZDDP tribo- and thermal films, peak (c) corresponding to adsorbed unreacted DDP disappeared shortly after shearing started.

The changes in the areas of the unreacted DDP and phosphate peaks at the P k-edge can be quantified by fitting these peaks using the fitting model presented in Fig. 6.7. The evolution of the areas of the fitted peaks is shown in Fig. 6.31 after different shearing times. Similar to the previously studied fast evolving ZDDP tribofilms formed at high temperature, the DDP tribofilm does not appear to have an initial induction period characterised by the adsorption of the unreacted DDP to the steel surface without the formation of phosphate glass. During the first minute of shearing, the first apparent phase, i.e. stage (I), started directly with

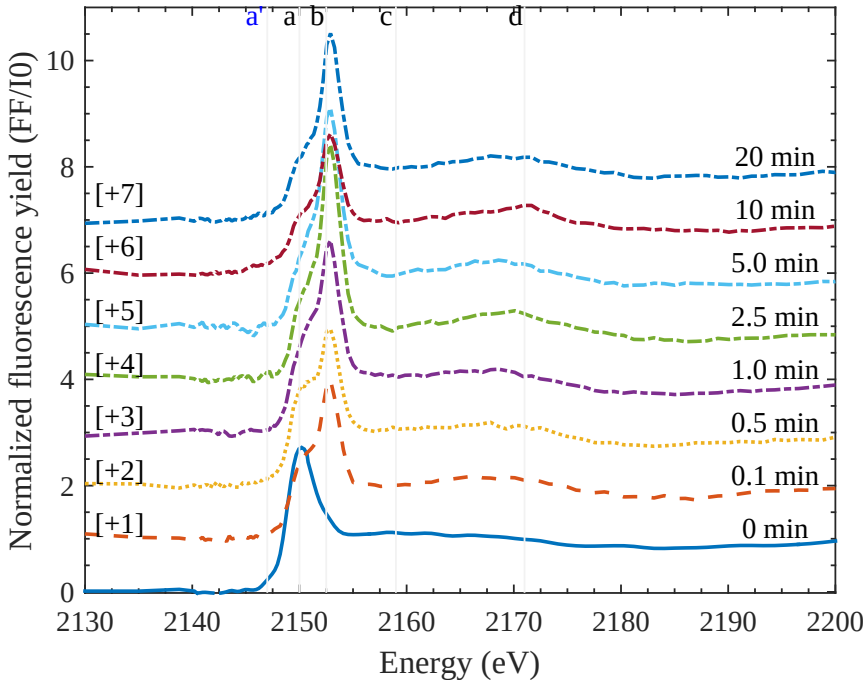

Fig. 6.30 Evolution of the DDP-1 normalised fluorescence yield spectra of P k-edge after different shearing times at 1.0 GPa and 80 ^{o}C. Each curve is vertically offset for clarity by adding a constant, as specified on each curve, relative to the first curve.

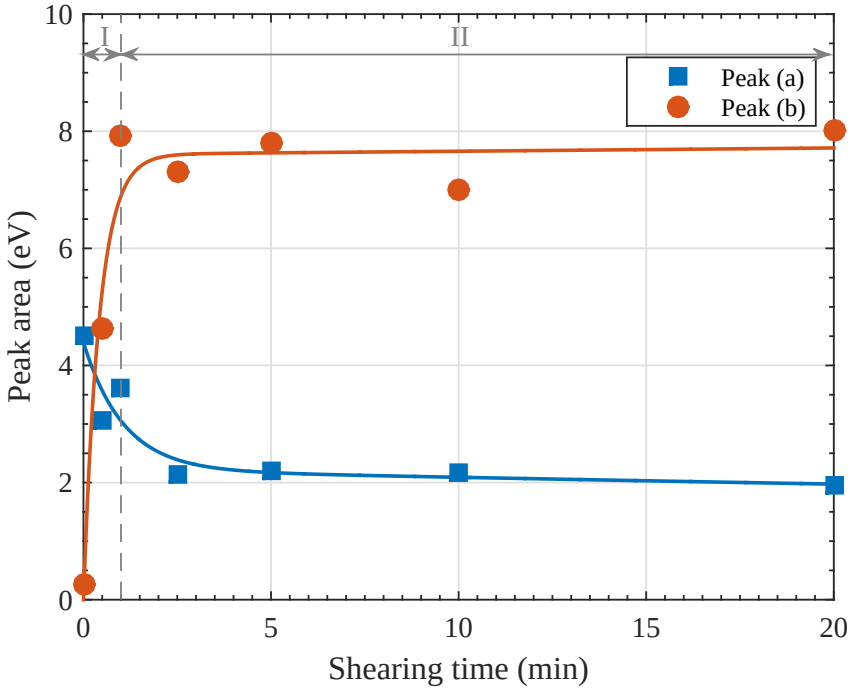

Fig. 6.31 Evolution of the normalised peak heights of unreacted DDP-1 and phosphate P k-edge of DDP-1 tribofilms after different rubbing times at 1.0 GPa and 80 ^{o}C

the fast decomposition of the unreacted DDP to form phosphate species. This is clear from the decrease in the area of the unreacted DDP peak at a rate of 0.9 eV/min accompanied by the fast increase in the area of the phosphate peak at a much faster rate of 7.5 eV/min.

After the first minute of shearing, a second phase, i.e. stage (II), of the decomposition of the DDP started. In this phase, a negligible change occurred in the areas of the unreacted DDP and phosphate peaks. One possible explanation for this observed trend can be related to the balance between the tribofilm formation and removal that keeps the phosphate glass composition and tribofilm thickness relatively constant during the tribotest period. Furthermore, this can also be related to the fact that contrary to the progressively evolving ZDDP tribofilms over rubbing time, the DDP tribofilms, in general, consist of short chains of iron polyphosphate undergoing minor changes over time [127, 136, 164, 179, 180]. This is primarily related to the rapid reaction of the DDP additive with the substrate covered with metal oxides, which induces a significant depolymerisation effect on the formed iron phosphate chains that ultimately limits their growth considerably [181].

6.5.1.2 Characterisation of S *k*-edge spectra

The evolution of the normalised S *k*-edge spectra after different shearing times is shown in Fig. 6.32. The spectra appeared to have three main and two secondary peaks.

The first main peak, (a), was observed at 2472.8 eV, which can be assigned to ZnS or alkyl sulphide [285]. The second main peak, (b), appeared at 2476.0 eV, which can be related to alkyl disulphide from the adsorbed DDP [288]. The third main peak, (c), appeared at 2481.9 eV, which can be attributed to $ZnSO_4$ [288] or $FeSO_4$ [286, 288].

The two other secondary peaks were observed after different shearing times. The first peak, (a'), was expected in the pre-edge region at 2469.5 eV. This peak is absent, which can be related to the absence of FeS or other iron-based sulphide or sulphate species in the formed tribofilm. The second secondary peak, (d), which appeared at 2498.2 eV, can be mainly related to the presence of sulphate species. This peak did not appear after short shearing times during which the sulphate peak was not very prominent as compared to the sulphide peak. As more sulphate was formed with progressive shearing, peak (e) started to appear more clearly.

The evolution of the S *k*-edge spectra of the tribofilm inside the wear scar showed a different trend from the one observed in the spectra of the ZDDP tribo-

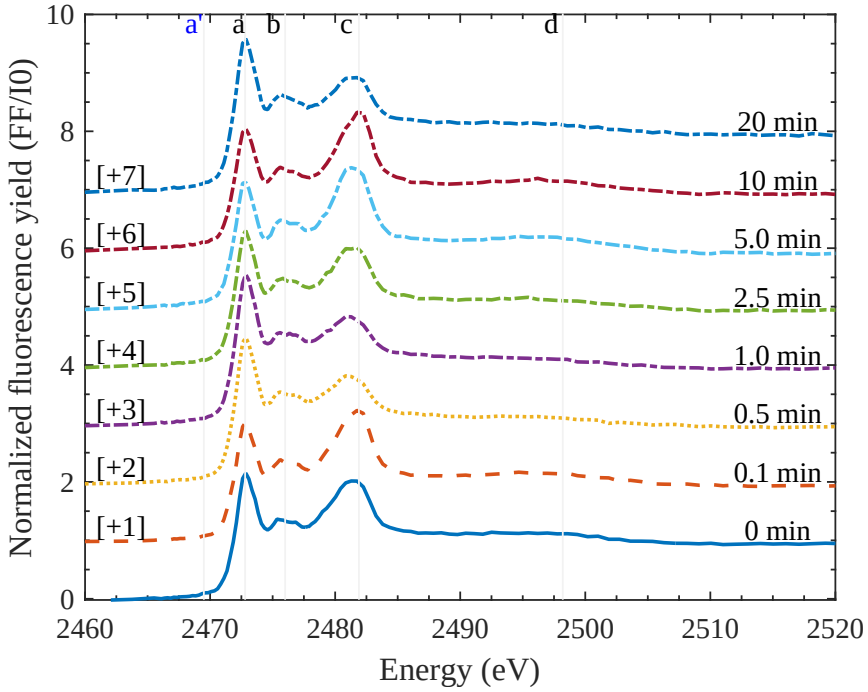

Fig. 6.32 Evolution of the DDP-1 normalised fluorescence yield spectra of S k-edge after different shearing times at 1.0 GPa and 80 ^{o}C. Each curve is vertically offset for clarity by adding a constant, as specified on each curve, relative to the first curve.

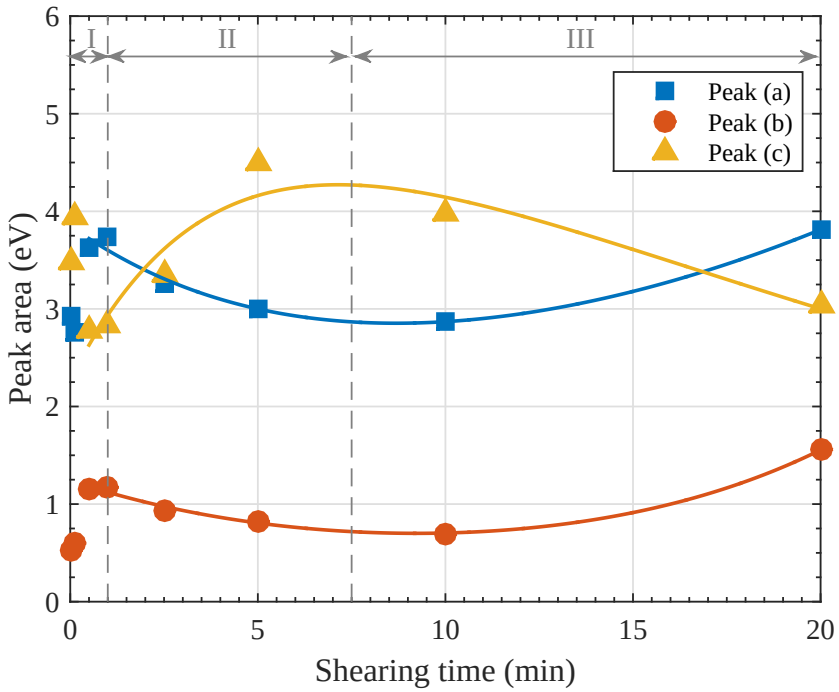

Fig. 6.33 Evolution of the normalised heights of peak (a), (b) and (c) of S k-edge of DDP-1 tribofilms after different shearing times at 1.0 GPa and 80 ^{o}C.

and thermal films. Initially, during phase (I) after shearing for a short period of time, the sulphate concentration decreased whereas the sulphide concentration increased, as indicated in the change of the heights of peaks (a), (b) and (c). With the progression of shearing, i.e. > 0.1 minutes, the height of the sulphate peak started to increase whereas the height of the sulphide peaks decreased. Opposite trends were observed after long rubbing times, i.e. > 7.5 minutes.

The qualitative changes in the XAS S k-edge spectra can be quantified using the fitting model presented in Fig. 6.10 to fit the peaks of the sulphides, peaks (a) and (b), and sulphate, peak (c). Fig. 6.33 shows the evolution of the areas of these peaks after different shearing times. It can be clearly observed that during the initial stage of shearing, i.e. stage (I) during the first minute, the area of sulphate, peak (d), appeared to decrease drastically over time with a rate of 1.9 eV/min. In contrast, the areas of sulphide, peak (b), and organic sulphide, peak (c), increased over the same period with a relatively similar rate of 1.7 eV/min.

With the progression of rubbing, the decomposition of the DDP entered a second phase, i.e. stage (II) after the first minute of shearing, in which the area of the sulphate peak increased gradually over heating time with a mean rate of 0.16 eV/min. In contrast, the sulphide peaks, (b) and (c), showed an opposite trend of decreasing in area, but with a smaller rate of 0.16 eV/min and 0.08 eV/min, respectively. The opposite trends can possibly indicate a continuous decomposition of the adsorbed unreacted DDP to form sulphate species. This is in agreement with the results of Kim et al. [136], which examined the decomposition of two different types of DDP additives. For one of the tested additives, both sulphides and sulphates were detected whereas for the other no sulphides were observed but only sulphates. The formation of sulphates species was related to the rapid reaction of the DDP with the substrate covered with oxides, which leads to the oxidation of the sulphur species into iron sulphate [182]. This was confirmed for both neutral and acidic DDPs [198].

As shearing continued, the decomposition of the DDP entered a third phase, i.e. stage (III) after the first 7.5 minutes of shearing. During this phase, the area of the sulphate peak decreased gradually over heating time with a mean rate of 0.1 eV/min. In contrast, the sulphide peaks showed an opposite trend of increasing in area, but with a relatively smaller rate of 0.06 eV/min. The comparable rates can possibly indicate a continuous consumption of the sulphate to form more stable sulphide species. This is in line with the results of Zhang et al. [164] suggesting that the DDP additive forms mainly FeS. The observed sulphides in the case of DDP, which is in contrast to the previously discussed studies suggesting the formation of final sulphates species, can be related to the

different operating conditions applied while generating the various tribofilms. For instance, previous studies [127, 181] showed that under high contact pressure, DDP tribo- or thermal films contain Fe sulphate near the steel surface whereas under less harsh conditions initially mixed iron sulphide, as FeS and FeS_2, and sulphate, as $FeSO_4$, are formed where the sulphides can oxidise over rubbing time yielding primarily sulphates at the end.

6.6 XAS analysis of DDP-2 tribofilms

6.6.1 DDP-2 tribofilms formed at 80^{o}C and 1 GPa

In the following sections, the P *k*-edge spectra will be characterised first followed by the characterisation of the S *k*-edge spectra.

6.6.1.1 Characterisation of P *k*-edge spectra

The evolution of the P *k*-edge spectra inside the wear scar is shown in Fig. 6.34. The P *k*-edge spectra of the DDP tribofilm have three main peaks. The first one, peak (a), appeared at the low energy range at 2150.0 eV, which corresponds to unreacted DDP adsorbed to the steel surface. The second peak (b) was observed at 2152.8 eV, which existed even before shearing commenced. Similar to the case of ZDDP and DDP-1 discussed before, this peak will be assigned to phosphate glass. Additional peak, (d), appears at 2169.5 eV in the high energy post-edge region. As this peak can be related to the oxidation state and arrangements of the different elements within the tribofilm [351], its unchanged energy indicates that no major changes occur to the phosphate species from the beginning to the end of the tribotest.

The previous observations can be confirmed by using the fitting model depicted in Fig. 6.7 to follow the changes in the areas of peaks (a) and (b) of the unreacted DDP and phosphate, respectively, at the P *k*-edge. The evolution of these areas is shown in Fig. 6.35 after different shearing times. The results indicate that in the very early stage, (I), of the tribotest, the phosphate peak (b) seems to increase swiftly over rubbing time. During the next stage (II), shearing seems to cause a negligible change in the areas of the unreacted DDP and phosphate peaks, which is followed by a mild decrease in the area of the phosphate peak during stage (III). The apparent quiescent nature of the spectra might be speculated to be a result of possibly ineffective decomposition nature of the additive under the applied operating conditions to form a protective tribofilm. However, as the additive

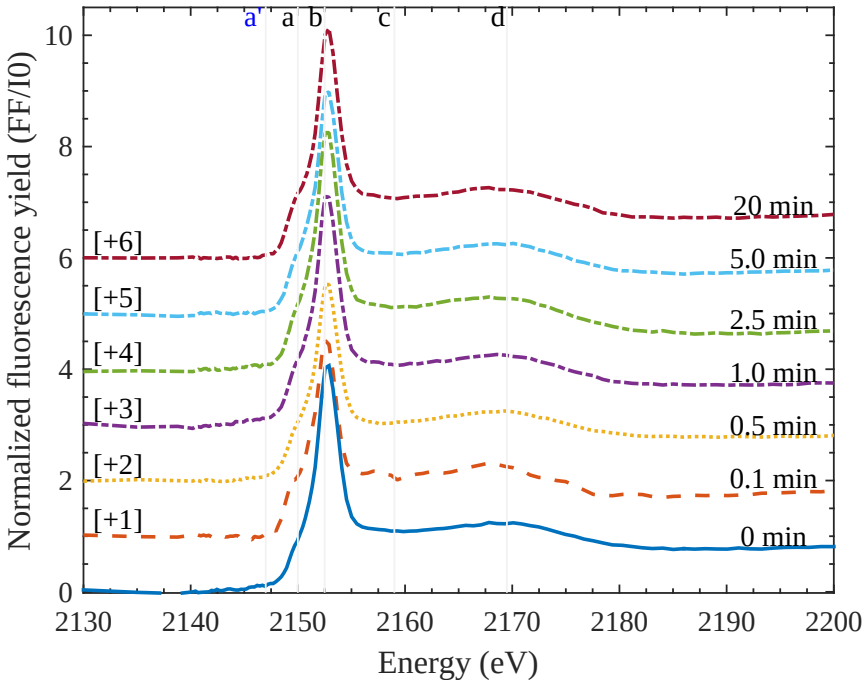

Fig. 6.34 Evolution of the DDP-2 normalised fluorescence yield spectra of P k-edge after different shearing times at 1.0 GPa and 80 ^{o}C. Each curve is vertically offset for clarity by adding a constant, as specified on each curve, relative to the first curve.

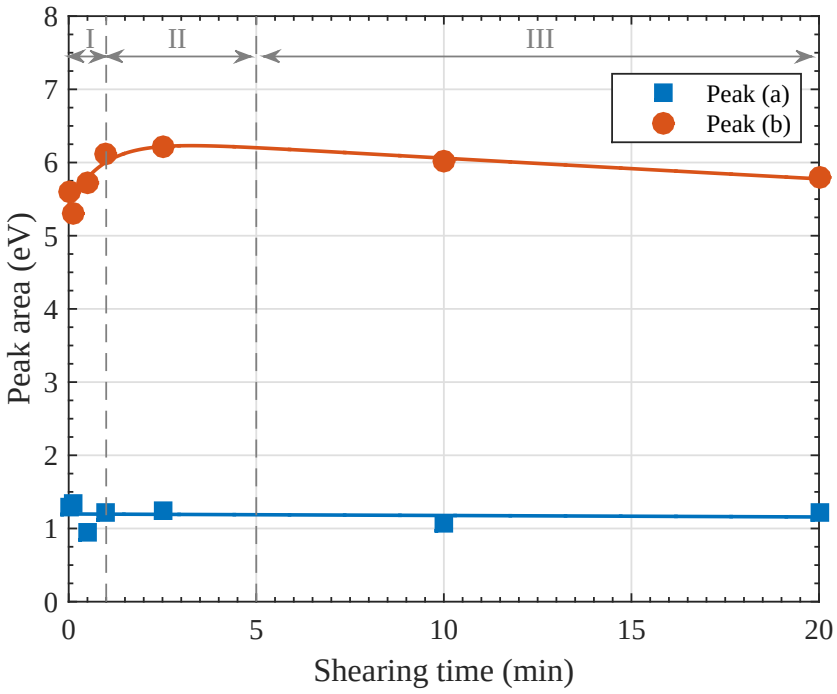

Fig. 6.35 Evolution of the normalised peak heights of unreacted DDP-2 and phosphate P k-edge of ZDDP tribofilms after different rubbing times at 1.0 GPa and 80 ^{o}C

provided a similar antiwear protection to the ZDDP additive, this possibility can be excluded. The other more plausible explanation to the observed trend can be related to the high reactivity of the additive, as suggested by the manufacturer, leading to the formation of ultra-thin protective P-rich film by just heating the oil even before any rubbing commences. This is supported based on the large similarity between the spectrum before rubbing, i.e. at 0 min, and the ones after rubbing.

6.6.1.2 Characterisation of S *k*-edge spectra

The evolution of the normalised S *k*-edge spectra after different shearing times is shown in Fig. 6.36. Similar to the previously discussed spectra of the ZDDP and DDP-1 tribofilms, the spectra of the DDP-2 tribofilm appeared to have three main and two secondary peaks.

The first main peak, (a), appeared at 2473.0 eV, which can be assigned to ZnS or alkyl sulphide [285]. The second main peak, (b), appeared at 2476.0 eV, which can be related to alkyl disulphide from the adsorbed ZDDP [288]. The third main peak, (c), was observed at 2481.5 eV, which can be attributed to $ZnSO_4$ [288] or $FeSO_4$ [286, 288].

Two other secondary peaks appeared after different shearing times. The first peak, (a'), was expected in the pre-edge region at 2469.5 eV. The absence of this peak suggests the absence of iron-based sulphide or sulphate species from the tribofilm [288]. The second secondary peak, (d), which was observed at 2498.2 eV, can be mainly related to the presence of sulphate species.

The evolution of S *k*-edge of the tribofilm inside the wear scar showed a different trend from the ones observed in the spectra of the ZDDP and DDP-1 tribofilms. Initially, after shearing for a short period of time, e.g. < 0.5 minutes, the sulphur composing the tribofilm appeared unchanged with rubbing and consisted of sulphur in the oxidised sulphate form and the reduced sulphide form. However, after slightly longer shearing times, the area of the sulphate peak (c) decreased whereas the areas of the sulphide peaks (a) and (b) were found to be invariant.

The qualitative changes in the XAS S *k*-edge spectra can be quantified by fitting the peaks of the sulphides, peaks (a) and (b), and sulphate, peak (c) using the fitting model described in Fig. 6.7. Fig. 6.37 shows the evolution of the areas of these peaks after different shearing times. During the first minute of shearing, i.e. stage (I), the area of sulphate, peak (d), appeared to decrease drastically over time with a rate of 3.3 eV/min. In contrast, the areas of sulphide, peak (b), and organic sulphide, peak (c), increased over the same period with a relatively

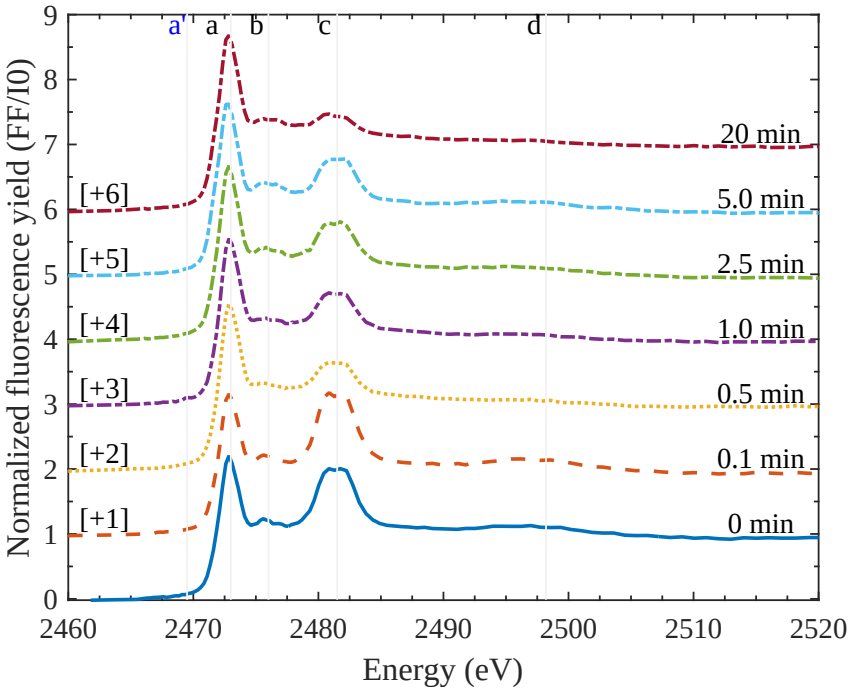

Fig. 6.36 Evolution of the DDP-2 normalised fluorescence yield spectra of S k-edge after different shearing times at 1.0 GPa and 80 ^{o}C. Each curve is vertically offset for clarity by adding a constant, as specified on each curve, relative to the first curve.

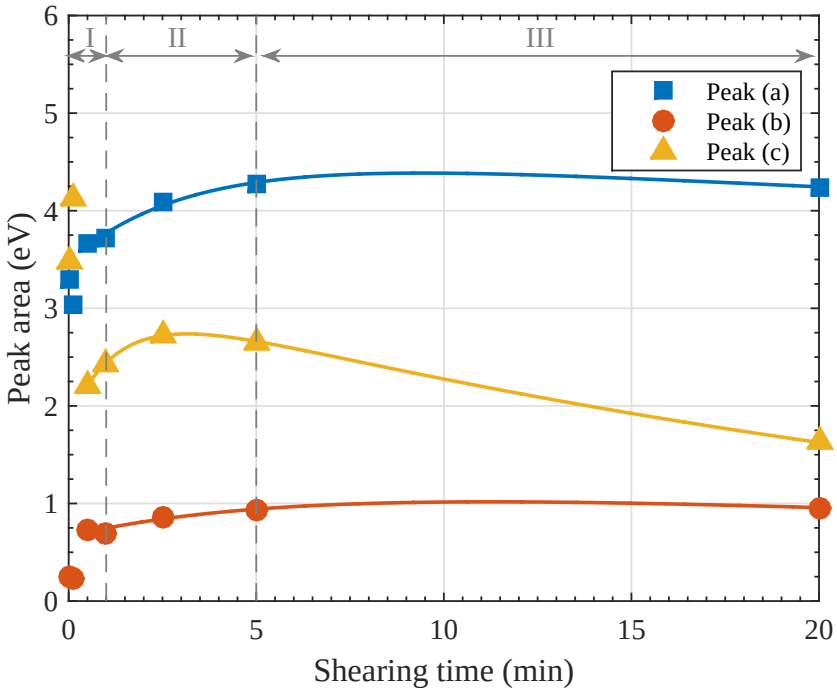

Fig. 6.37 Evolution of the normalised heights of peak (a), (b) and (c) of S k-edge of DDP-2 tribofilms after different shearing times at 1.0 GPa and 80 ^{o}C.

lower rate of 1.0 eV/min. With the progression of rubbing, the decomposition of the DDP entered a second phase, i.e. stage (II) during which the area of the sulphate peak increased gradually over time with a mean rate of 0.09 eV/min. Similarly, the sulphide peaks, (b) and (c), showed a similar trend of increasing in area, but with a rate of 0.14 and 0.05 eV/min, respectively. The similar low rates can possibly indicate a continuous adsorption of the unreacted DDP on the steel surface. After the first 7.5 minutes of shearing, the decomposition of the DDP additive entered a third phase, i.e. stage (III), during which the area of the sulphate peak decreased gradually over heating time with a mean rate of 0.07 eV/min. In contrast, the sulphide peaks showed a different trend of not changing in area over shearing time.

These results combined with the observations in the P k-edge spectra suggest that the complete decomposition of the DDP-2 additive occurred to form sulphate, sulphide and phosphate species even before shearing started. The initial changes in the sulphur, i.e. formation of sulphate and sulphide, are comparable to the evolution observed in the ZDDP tribo- and thermal films after long rubbing or heating times. This confirms the fast reactivity of the additive to form ultrathin protective tribofilms.

6.7 Summary and concluding remarks

A mini pin-on-disc tribotester was designed, which can be coupled with XAS to perform in-situ tribological tests at different contact pressures, temperatures and sliding speeds. Using this apparatus, it was possible to follow and examine the composition evolution over time of the tribo- and thermal films of different phosphorus based additives through the measurements of the P and S k-edge XAS spectra. The unique feature of this apparatus is that, for the first time, the composition of the tribo- and thermal films of various oil additives can be studied at ambient pressure in-situ without altering the sample condition.

The main in-situ XAS results can be summarised as follows:

- At the beginning of the tribo- or thermal test, the formed tribo- or thermal film consists of sulphur mainly in the form of sulphate with some disulphide, which progressively changes into mainly sulphide. Following this, the adsorbed additive starts to decompose completely to form phosphate species.

- The ZDDP decomposition process occurs as follows:

i. The unreacted ZDDP adsorbs to the substrate, whether a bare steel or DLC coated surface.

ii. The adsorbed molecules decompose partially by losing sulphur to form sulphate species. The sulphate formation is favoured in the beginning of the tribotest due to surface smearing and wear during the initial running-in period, which result in high temperature at the contacting asperities.

iii. The formed sulphate species are reduced to form sulphides. As rubbing continues and the running-in period ends, the local temperature at the asperity-asperity contacts drops below the critical temperature needed for the sulphate formation and therefore the more stable sulphide is formed instead.

iv. The adsorbed molecules decompose completely to form phosphate species in the form of layers of chains progressively increasing in length.

v. Any harsh conditions of high temperature and large contact pressure or even just long shearing or heating time can cleave the long phosphate chains into shorter ones.

vi. Once the phosphate-based tribofilm covers the substrate completely, the ZDDP molecules cannot adsorb preferentially to the tribo- or thermal film covering the substrate. The origin of the detected adsorbed molecules in the late stages of the test is mainly the trapped additive within the formed film, which occurs during the early stages of the test without any further replenishment.

- The DDP decomposition process is similar to the one of the ZDDP. This suggests that the zinc and iron cations can replace each other without much changes in the composition of the formed tribofilm except the chain length.

- The formed tribofilm on the DLC coated surfaces or at low temperature, i.e. 25 ^{o}C, is of small volume and low tenacity. The low tenacious tribofilm was related to the absence of mixed oxide/sulphide base layer. This layer seems to act as a glue joining the substrate with the subsequently formed phosphate layers composing the main bulk of the tribofilm.

The findings of this study widen the scope of the future investigations to study the reaction kinetics of different materials under shear and realistic test conditions. It also opens opportunities to study the evolution over time of various additives on different surfaces and their interaction under heat and shear.

To complement the work discussed in this chapter, the subsequent chapter will examine in-situ the reaction kinetics of the ZDDP, DDP-1 and DDP-2 additives on bare steel, DLC coated surfaces and various zinc and iron phosphate glasses using a newly developed high temperature AFM liquid cell. Furthermore, the evolution over time of the structure of the formed tribofilms will be studied in detail using the AFM under different operating conditions of temperature, contact pressure and sliding speed.

Chapter 7

Structure and rheology of ZDDP and DDP tribofilms using in-situ AFM

The ultra-thin protective tribofilms (< 200 nm) generated from P-based antiwear additives such as ZDDP and DDP long have been considered as rigid interfaces that act as a mechanical barrier [15], which helps protect the metal surface from severe wear. However, it was speculated that these films might also behave as molten glass [14] or viscous polymeric interface [36]. To better understand the origin of the superior antiwear properties of these films, a high temperature AFM liquid cell was designed and coupled with the atomic force microscope (AFM) to perform in-situ single asperity tribological and rheological tests at different contact pressures (2–7 GPa), temperatures (25–120 °C) and sliding speeds (50–450 μm/s). The chapter is divided into two main sections discussing the results of ZDDP and DDP additives, respectively. Each section presents and discusses different aspects related to the rheological and textural properties of the formed tribofilms including the local occupancy, durability, tenacity, flowability, growth hysteresis and formation kinetics.

7.1 Results of ZDDP tribofilms

7.1.1 Local occupancy of the tribofilm's pads

The origin of the patchy pad-like structure of the ZDDP tribofilms is still not well-understood. Various theories were proposed to explain the formation of such as a structure, which includes:

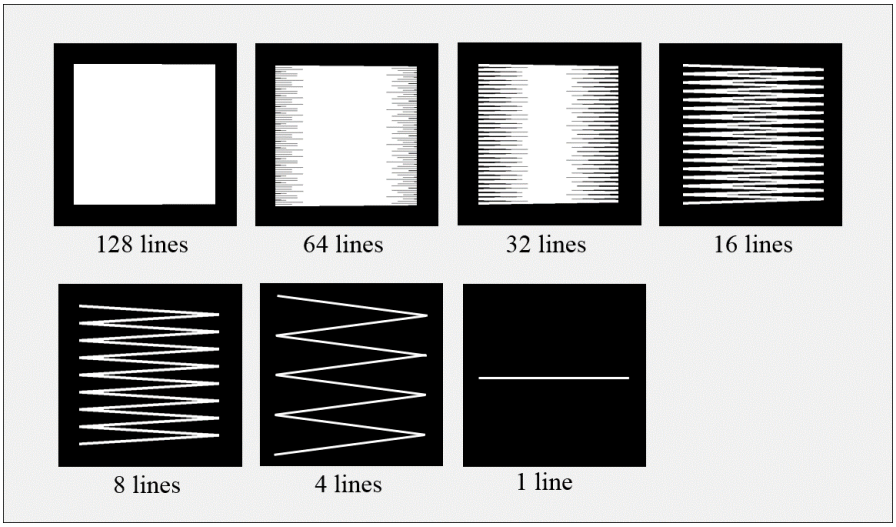

Fig. 7.1 Schematic of the different scan lines used to raster scanning a $5 \times 5\,\mu m^2$ area using the AFM tip during the in-situ tests to generate tribofilms.

- Glass flow and solidification [36, 248].
- Nucleation-growth due to load instability [167].
- Nucleation-growth due to surface defects [30].

A unique set of experiments are designed to examine the flowability and the nucleation-growth hypotheses of the ZDDP tribofilms pads as they are being formed. Fig. 7.1 shows a representation of this set in which the AFM tip is raster scanning across an area of $5\,\mu m \times 5\,\mu m$ at the same speed but following a different number of scanning lines, i.e. 128, 64, 32, 16, 8, 4 and 1 line.

7.1.1.1 Case I: 128 scanning lines

The evolution of the ZDDP tribofilm over sliding cycles using 128 scanning lines is shown in Fig. 7.2. It is evident that as the maximum space separating any two lines is less than 39 nm, which is less than the estimated diameter of the tip, i.e. 150 nm as discussed in appendix A, the formed tribofilm appeared as a continuous film without any distinctive lines. During the first stage of the in-situ tribotest, i.e. $<$ 2000 sliding cycles, two features appear in the structure of the formed tribofilm. The first feature is the accumulated tribofilm formed near the edges, which has larger thickness, i.e. nearly twice, than the one formed away from the edges. The reason for this enlarged thickness is related to the larger number of sliding cycles experienced near the edges due to the narrower gap between the adjacent scanning lines, as shown in 7.2a. Another possible reason can be related to the flowability of the tribofilm as the tip rasters the surface and pushes the

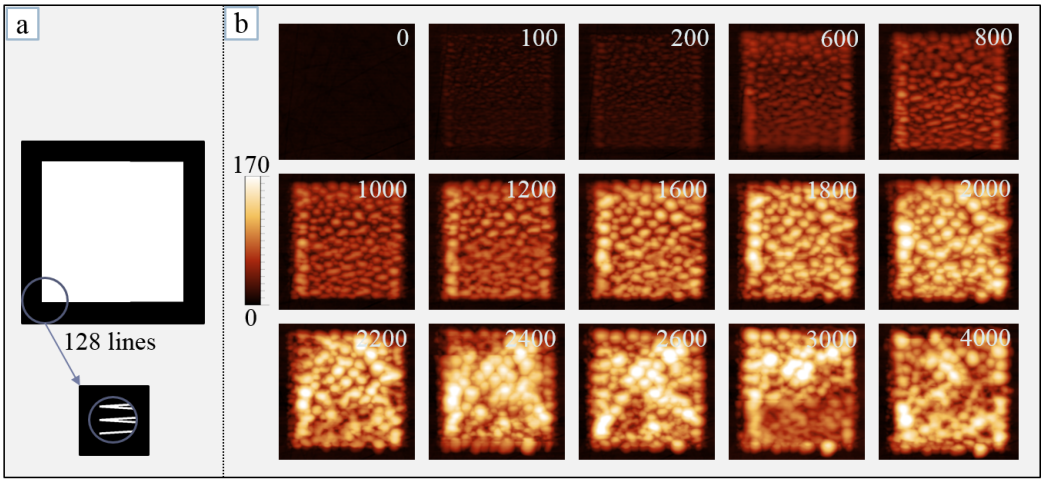

Fig. 7.2 In-situ ZDDP tribotest using the AFM liquid cell, where a) schematic of the 128 scan lines used to raster scanning a $5 \times 5\,\mu m^2$ area, and b) the generated tribofilm after different scanning cycles at 80 ^oC and 7.3 GPa. The scale bar is in nm.

tribofilm's pads to the sides. The second interesting feature during the first 2000 cycles of the tribofilm's formation is the distinctive arranged pads that are formed initially under the scanning lines of the tip. As rubbing continued, the size of the pads increased and they became less uniform than the ones formed during the beginning of the test. For instance, a comparison between the formed tribofilm after 800 and 2000 cycles confirms this observation.

The areas of small thickness away from the edges seem to increase in thickness until approaching the ones near the edges. This is an interesting observation because it is counterintuitive to what is generally expected to be a uniform formation as long as the initial conditions did not change. The abstruse behaviour might originate from the intrinsic limiting thickness of the tribofilm. This was related to the cushion effect of the thick tribofilm, which deforms easily leading to larger contact area and thus results in lower contact pressure and consequently low formation rate [30]. Another explanation is related to what appears as removal cycles followed the initial formation once the tribofilm reached a certain thickness. The removal cycles seem to be induced by the progressive shearing of the interface causing the weakly adhered top layers of the tribofilm to be removed or be reallocated within the central area of the evolving tribofilm. Following the changes between 2600, 3000 and 4000 cycles, reveals that the removal of the tribofilm occurs as follows. First, the tribofilm reaches a certain thickness. Second, a big part of the tribofilm having a large thickness is removed, as indicated in the gap after the 3000 cycle. Finally, a new cycle of formation starts, as indicated by the evolved structure of the tribofilm after the 4000 cycle as compared to its previously recorded state. These formation-removal cycles seem to be repetitive in nature.

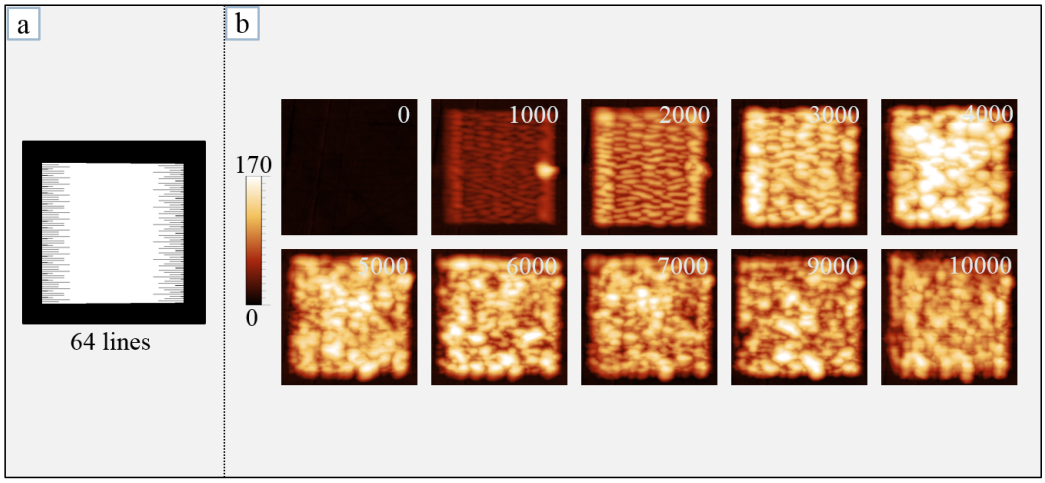

Fig. 7.3 In-situ ZDDP tribotest using the AFM liquid cell, where a) schematic of the 64 scan lines used to raster scanning a $5 \times 5\,\mu m^2$ area, and b) the generated tribofilm after different scanning cycles at 80 ^{o}C and 7.3 GPa. The scale bar is in nm.

7.1.1.2 Case II: 64 scanning lines

The evolution of the ZDDP tribofilm over sliding cycles using 64 scanning lines is shown in Fig. 7.3. In this case, the maximum space separating any two adjacent lines is less than 78 nm, which is less than the estimated diameter of the tip, i.e. 150 nm. Therefore, the formed tribofilm appeared as a continuous film without any distinctive lines. Similar to the case of the 128 lines, the tribofilm formed during the early stages of the tribotest has larger thickness near the edges than in the central areas. In these middle areas, the tribofilm is more uniform and consists of small thin pads elongated in the direction of rubbing. As rubbing cycles progressed, the pads thickness increased and the central areas appeared to have larger thickness than the ones near the edges. Following this, further rubbing seemed to cause severe mixing and distortion of the individual pads leading to wear and removal of parts of the tribofilm. All these features are akin to the ones observed previously in the case of 128 lines, which confirms that the tribofilm formation follows the same deterministic trend especially in the early stages of the tribotest but differences might arise as sliding cycles increase.

7.1.1.3 Case III: 32 scanning lines

In general, the evolution of the ZDDP tribofilm over sliding cycles for the case of 32 lines, as shown in Fig. 7.4, is similar to the cases of 128 and 64 scanning lines. The only difference occurs during the first 500 sliding cycles, which shows an apparent distinctive lines in the formed tribofilm. This can be related to the small tip diameter, i.e. less than 150 nm, compared to the maximum separation

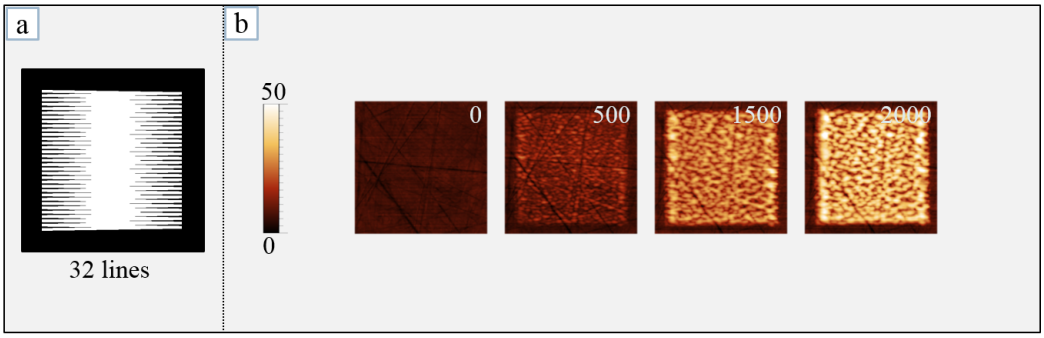

Fig. 7.4 In-situ ZDDP tribotest using the AFM liquid cell, where a) schematic of the 32 scan lines used to raster scanning a $5 \times 5\,\mu m^2$ area, and b) the generated tribofilm after different scanning cycles at 80 ^oC and 7.3 GPa. The scale bar is in nm.

distance between any two adjacent scanning lines, which is about 156 nm. Thus, it is expected to observe distinctive lines within the formed tribofilm following the scanning lines. As rubbing continued, these lines became less apparent and a continuous tribofilm was formed. The tribotest was stopped after 2000 cycles, but based on the available data and the previous discussion it is expected that the tribofilm will follow a similar trend to the ones in the case of 128 and 64 scanning lines.

7.1.1.4 Case VI: 16 scanning lines

The evolution of the structure of the ZDDP tribofilm during using 16 lines raster scanning an area of $5 \times 5\,\mu m^2$ is shown in Fig. 7.5. Unlike the case of scanning lines more than 32, the separation distance between any two adjacent lines in the case of 16 lines is about 312 nm, which is nearly twice the estimated diameter of the AFM tip. This is the reason of the appearance of clear distinctive lines during the early stages of the tribotest. However, similar to the previous cases of larger number of scanning lines, several common features appear in the case of 16 lines. The first feature is related to the thicker tribofilm formed near the edges as compared to the middle areas, which as discussed before can be related to the double rubbing action at these regions as the scanning lines get closer to each other and finally overlap when moving towards the edges.

The second feature is related to the uniform structure of the formed tribofilm during the early stages as compared to the final stages, which can be attributed to the wear action and the intrinsic deterministic nature of the tribofilm formation. As rubbing continues deviations and less uniform tribofilm are increasingly expected because of wear and smearing of the thicker areas of the tribofilm under shear. This is evident from the worn areas near the edges where the tribofilm was initially thicker. This is in line with the conclusions of Aktary et al. [167] that the ZDDP

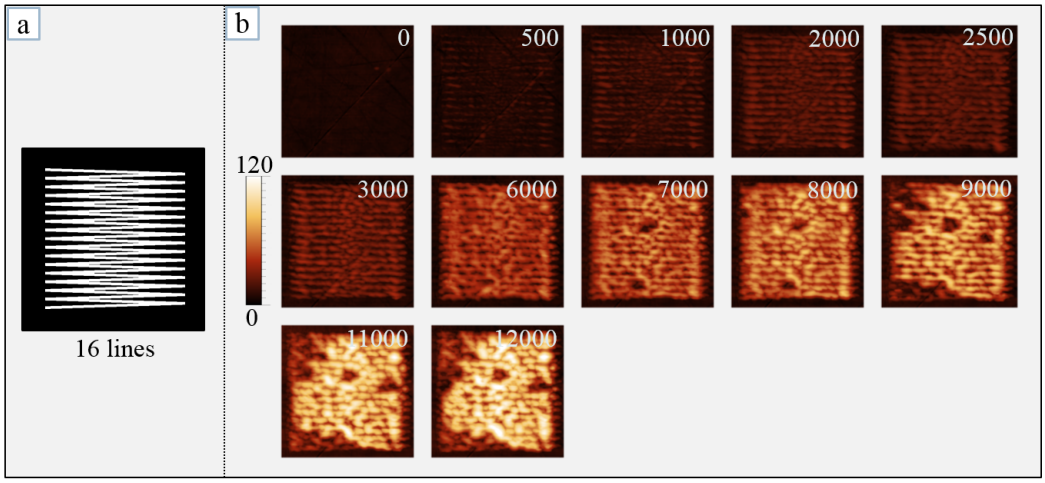

Fig. 7.5 In-situ ZDDP tribotest using the AFM liquid cell, where a) schematic of the 16 scan lines used to raster scanning a $5 \times 5\,\mu m^2$ area, and b) the generated tribofilm after different scanning cycles at 80 ^{o}C and 7.3 GPa. The scale bar is in nm.

tribofilm exhibits high plasticity suggesting a sacrificial nature of the tribofilm, which is continuously formed and removed at the interface. Conversely, Warren et al. [248] showed that the ridges of the tribofilm have great capacity of elastic deformation, which was also confirmed by the results of Graham et al. [249] and Ye et al. [253] that the ridges of ZDDP tribofilms can greatly resist plastic deformation. However, the high elastic modulus does not warrant high toughness and ductility for the large pads. The contrary might just be the case, i.e. the larger the thickness of the tribofilm the more its brittleness, as suggested by our results.

Another interesting feature is evident in the fact that the scanning lines become less visible as the tribofilm grows. Two factors can cause this behaviour to occur. First, rubbing might have pushed the worn parts of the tribofilm into the areas between the scanning lines. Second, the tribofilm itself might be soft and deformable. Thus, it is plausible that the interfacial shear stress and large contact pressure caused the thick soft areas of the tribofilm to flow and consequently cover the gaps between the adjacent scanning lines. This is in line with various previous reports [17, 36, 48] suggesting that the outer layers of the tribofilm are easily flowing viscous as opposed to the layers close to the metal surface, e.g. sulphides and phosphates, which are most likely elastic or elastoplastic solids of polymeric nature [151]. These bottom layers near the metal surface were suggested to have a viscosity around 10^8 Pa.s as opposed to 5.10^4 – 3.10^5 Pa.s for the top layer of alkyl phosphate [36].

To test the previous theories regarding the effect of the tribofilm's worn parts and flowability on the final structure of the tribofilm, it is necessary to vary

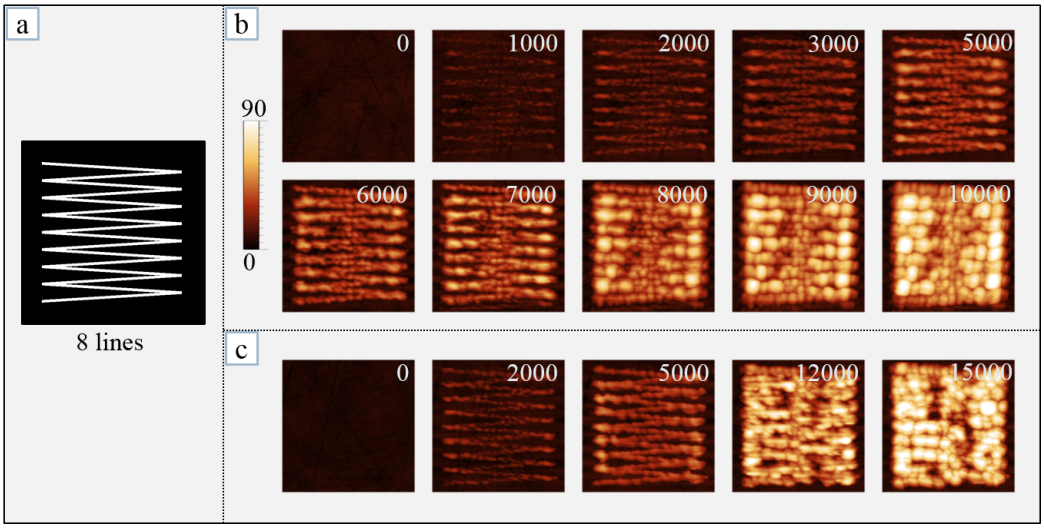

Fig. 7.6 In-situ ZDDP tribotest using the AFM liquid cell, where a) schematic of the 8 scan lines used to raster scanning a $5 \times 5\,\mu m^2$ area, b) the generated tribofilm after different scanning cycles at 80 ^{o}C and 7.3 GPa, and c) a repetition of the same test. The scale bar is in nm.

the local occupancy of the formed pads by decreasing the distance between the adjacent scanning lines. This will be discussed in detail in the subsequent sections.

7.1.1.5 Case V: 8 scanning lines

Fig. 7.6 shows the evolution of the structure of the ZDDP tribofilm during the in-situ tribotest using 8 scanning lines raster scanning an area of $5 \times 5\,\mu m^2$. In this case, the distance between the adjacent lines is about 625 nm, which is fourfold the diameter of the used AFM tip. This relation is confirmed by measuring the diameter of one line of the formed tribofilm after short rubbing cycles as compared to the distance between the lines.

The formed tribofilm showed similar features to the previously discussed cases of larger number of scanning lines. Initially, the edges of the formed tribofilm appears to be thicker than the areas in the middle. This continues to be the case until the end of test as shown in Fig. 7.6b. However, rubbing for larger number of cycles, as shown in Fig. 7.6c, shows that the tribofilm thickness becomes more uniform whether near or away from the edges. The findings also confirm that the gap between any two adjacent lines, nearly 625 nm, is completely filled with a tribofilm, despite the absence of any shearing occurring in these regions. Due to the large gap and the early coverage of these areas even before any significant wear occurs to the formed areas nearby, it is highly likely that the tribofilm in these un-sheared regions originates from the flow of the tribofilm from the sheared areas nearby.

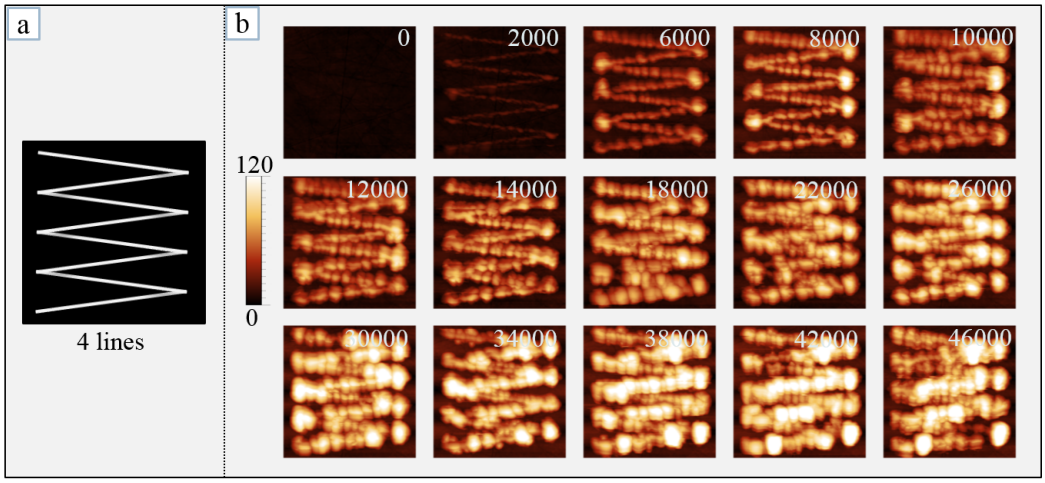

Fig. 7.7 In-situ ZDDP tribotest using the AFM liquid cell, where a) schematic of the 4 scan lines used to raster scanning a $5 \times 5\,\mu m^2$ area, and b) the generated tribofilm after different scanning cycles at 80 ^oC and 7.3 GPa. The scale bar is in nm.

7.1.1.6 Case VI: 4 scanning lines

To confirm the previous finding that the tribofilm can flow to cover wider areas than the sheared ones, the distance between any two adjacent scanning lines was further increased to about 1.25 μm. This was possible using 4 lines raster scanning an area of $5 \times 5\,\mu m^2$. Fig. 7.7 shows the evolution of the structure of the ZDDP tribofilm during the in-situ tribotest. The results reiterate the previous findings discussed in the previous section, that initially the tribofilm is formed under the scanning lines where the interface between the steel surface and the AFM tip experiences large shear stress and contact pressure. However, as shearing continued, the tribofilm starts to gradually fill the nearby areas. The structure of the tribofilm appears as if it flows from the areas of high contact pressure to spread to any available gap.

The finding confirms that contrary to the generally perceived conception that the tribofilm is rigid [14–18], the formed tribofilm behaves as a highly viscous material, which can deform and flow under shear. The significant implication of this finding is that for the first time it provides a novel mechanistic understanding for the excellent anti-wear properties of the ZDDP tribofilms. In addition of forming a mechanical barrier, the tribofilm can also deform and flow and thus mitigates the shear stress at the contacting asperities leading to less wear. Similar conclusion can also be inferred from the results of Pereira et al. [243] who showed that up to 200 ^oC the modulus of a mature tribofilm was nearly constant at around 100 GPa but dropped to about 70 GPa at 200 ^oC. The decrease in the modulus can indicate a compliant tribofilm that can be easily deformed especially at high temperature.

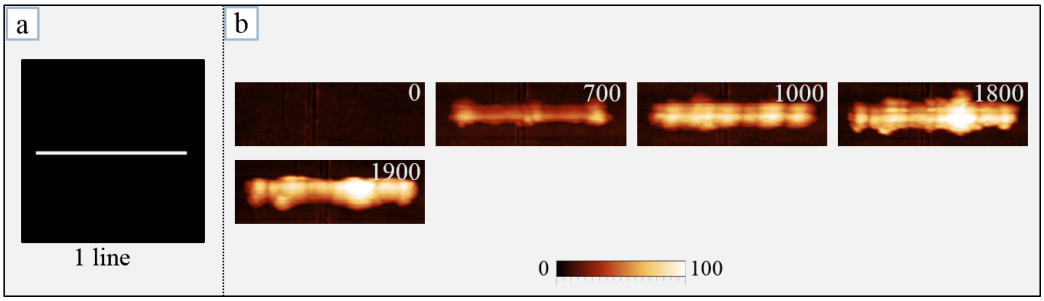

Fig. 7.8 In-situ ZDDP tribotest using the AFM liquid cell, where a) schematic of the single scan line used to raster scanning a $5 \times 5\,\mu m^2$ area, and b) the generated tribofilm after different scanning cycles at 80 ^oC and 7.3 GPa. The scale bar is in nm.

Apart from this, the thick areas within the tribofilm structure appears to be the first areas to be worn away. This is evident from observing that in the beginning of the test the edges of the lines are thicker than the ones in the middle. However, these areas are worn away quickly. Afterwards, the areas in the middle of the formed tribofilm start to grow in thickness before reaching a certain threshold after which removal occurs and then followed by another cycle of formation followed by removal and so forth.

7.1.1.7 Case VII: 1 scanning line

The flowability of the ZDDP tribofilm can be further confirmed by observing the evolution of the structure of the ZDDP tribofilm during the in-situ tribotest using a single scanning line of length of 5 μm, as shown in Fig. 7.8.

It is evident that the line thickness increases rapidly as rubbing cycles increase. This confirms that the tribofilm does not only form under the AFM tip but can also flow to the sides. Another observation is related to the uniformity of the formed line. The formed tribofilm appears less uniform along its length. One explanation for this behaviour can be related to the disruption caused by the reciprocating motion of the AFM tip over a very short period of time while the film is susceptible to deformation. This can also be related to load instability [167] as the AFM tip changes direction as well as to any surface heterogeneity [30].

7.1.2 Tribofilm durability and tenacity

Another way to examine the flowability of the tribofilm is by following the evolution of its structure over different levels of contact pressure. The idea behind this is that if the tribofilm truly flows then it should deform largely once under high contact pressure. To limit this effect to genuine flowability and avoid any formation during

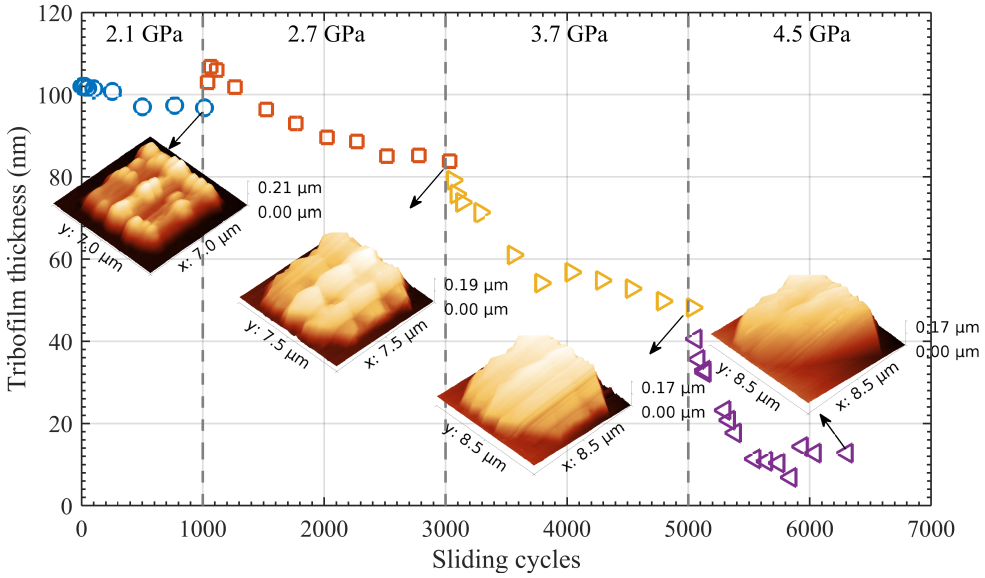

Fig. 7.9 Durability of mature ZDDP tribofilms measured by following the evolution of the tribofilm thickness after different sliding cycles at 25 ^{o}C under different contact pressures ranging from 2.1 to 4.5 GPa.

the process, these experiments were carried out at ambient temperature and in base oil without ZDDP additive. These same experiments will also be used to study the durability and tenacity of the ZDDP tribofilms.

Fig. 7.9 shows the evolution of the structure of a mature ZDDP tribofilm, i.e. formed initially at 80 ^{o}C and 4.5 GPa, when subjected to different levels of contact pressure while the AFM tip is raster scanning the surface. The data show that, initially when the tribofilm was subjected to a relatively small contact pressure of 2.1 GPa, a small decrease in the tribofilm thickness of about 5 nm was observed. This indicates that the mature tribofilm is largely tenacious and durable.

Once the contact pressure was increased to 2.7 GPa, a small recovery of 15 nm in the tribofilm thickness was observed. The exact source or mechanism of this recovery is not completely understood. We speculate that it could originate from the irreversible disruption of the local compactness of the interfacial layers of the tribofilm leading to an increase in the free volume within the phosphate glass. This necessary makes the tribofilm loose and more susceptible to wear, which is confirmed by the subsequent decrease in the tribofilm thickness over the sliding cycles until reaching a steady-state thickness of about 85 nm. Thus, the decompressing effect of contact pressure on mature tribofilms appears to be counter-productive compared to the case of immature tribofilms in which contact pressure acts to compact the loose top layers of the ZDDP decomposition products into solid polyphosphates [36].

As the contact pressure was increased to 3.7 GPa, a big drop in the tribofilm thickness was observed until it reached a steady-state thickness of 50 nm. When the contact pressure was further increased to 4.5 GPa, a large sudden decrease in the tribofilm thickness of more than 50 nm was observed until it reached steady-state thickness of 10 nm. Under this large contact pressure, a big part of the tribofilm was completely removed, which is unlike the layer-by-layer removal observed in the case of smaller contact pressures. The overall decrease in the tribofilm thickness is generally consistent with the statement that the larger the contact pressure the larger the removal rate of the tribofilm.

Another interesting observation in the evolution of the tribofilm structure is related to the increased flowability observed under the increasing contact pressures. For instance, when a small contact pressure was applied the tribofilm initially covered an area of $5 \times 5\,\mu m^2$. However, when the contact pressure was increased to 2.7 GPa, the covered area increased to about $6 \times 6\,\mu m^2$. The covered area increased further to $8 \times 8\,\mu m^2$ when the contact pressure was increased to 3.7 GPa. This tribofilm area stayed the same when the contact pressure increased further to 4.5 GPa.

The origin of this behaviour can be attributed to the squeezed flow effect of large contact pressures. The large pressures can deform the soft tribofilm between the contacting surfaces and squeeze it such that the film moves from the areas of high contact pressure towards the areas near the edges of low contact pressure in order to minimise the experienced shear stresses.

7.1.3 Tribofilm growth hysteresis

In the subsequent sections, the tribofilm growth hysteresis, i.e. repetitive behaviour of formation and removal, will be discussed in detail considering tribofilms formed under three different contact pressures, i.e. 2.7, 4.5 and 5.7 GPa.

7.1.3.1 Case I: growth at 2.7 GPa

Fig. 7.10 shows two repetitions of the thickness and topography evolution of the ZDDP tribofilm over sliding cycles. The tribofilm was formed at 80 ^oC and 2.7 GPa. The results indicate that below 10000 sliding cycles, the tribofilm thickness increased linearly. However, after this threshold, the thickness started to increase sharply with much faster kinetics. This is followed by a certain trend of tribofilm removal, which is evident from the decrease in the tribofilm thickness around 12000 sliding cycles. Following this removal phase, the tribofilm growth was minimal

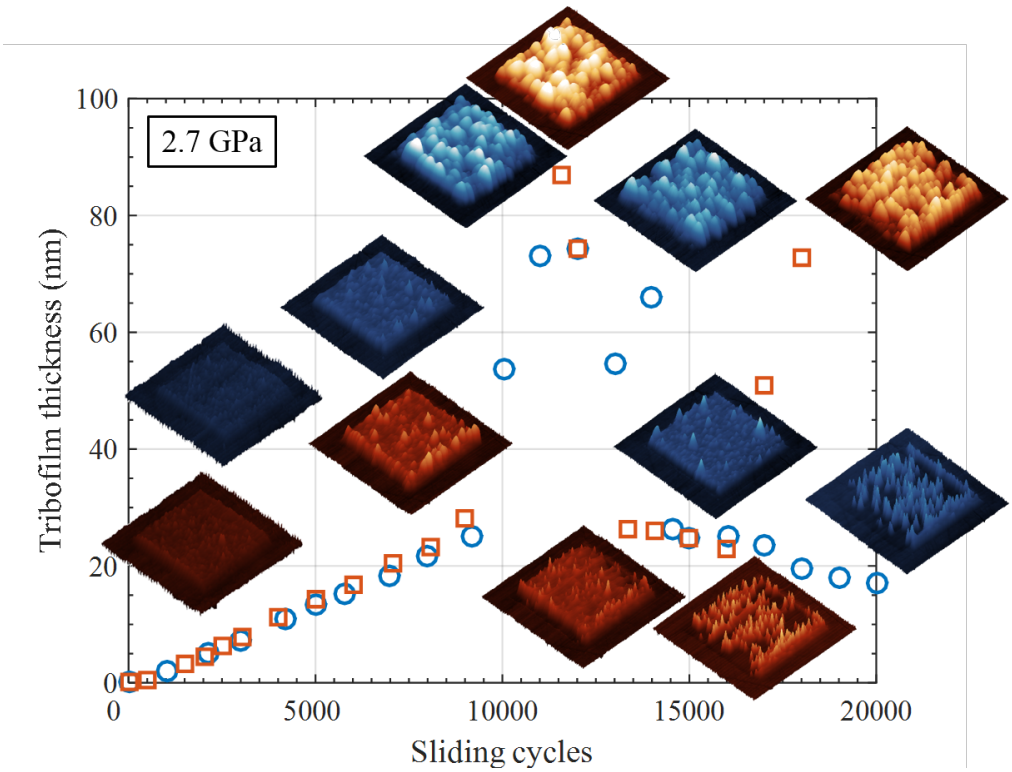

Fig. 7.10 Evolution of the ZDDP tribofilm thickness over time after two repetitions formed at 80 ^{o}C and 2.7 GPa.

in one repetition followed by a gradual decrease in thickness. However, in the second repetition, the tribofilm thickness started to increase sharply just after the precedent removal phase.

The data suggest that just before any growth phase of fast kinetics the structure of the tribofilm has a relatively high roughness. The rough surface contains various sharp protrusions, which might behave as seeds for the succeeding tribofilm layers to grow. Interestingly, after the first removal phase, the tribofilm surface also appears to be very rough, which helps accelerate the next fast formation phase. The fast growth can be a result of extra energy aroused from the dangling bonds from the preceding removal cycle. Every removal cycle seems to create more active sites with more energy available for the next succeeding growth cycle.

The above discussion indicates that the formation and removal cycles are repetitive in nature, i.e. the more the tribofilm removal, the rougher the surface and the more the energy available for the next formation phase and consequently the faster the tribofilm formation.

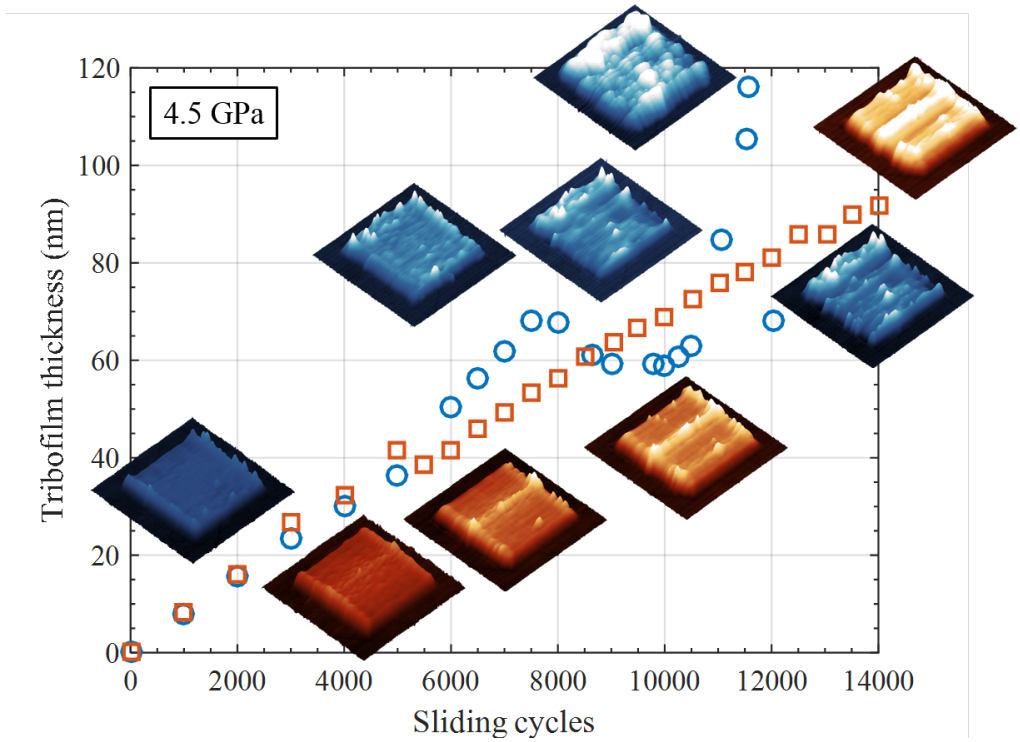

Fig. 7.11 Evolution of the ZDDP tribofilm thickness over time after two repetitions formed at 80 °C and 4.5 GPa.

7.1.3.2 Case II: growth at 4.5 GPa

Fig. 7.11 shows two repetitions of the evolution of the thickness and morphology of ZDDP tribofilms over sliding cycles formed at 80 °C and 4.5 GPa.

The first repetition (shown in red) indicates that the tribofilm formation was steady and relatively linear over the different sliding cycles. On the other hand, the second repetition (shown in blue) indicates that the tribofilm undergoes changes in its structure as it evolves over the sliding cycles. The first 5000 cycles appear to be similar to the first repetition as the thickness evolves linearly. After that, the thickness starts to increase with a much faster rate until reaching a maximum value of about 70 nm just before the 8000 cycle. As rubbing continued, layers of the tribofilm were worn away as indicated by the decrease in thickness. This is followed by an outburst of formation cycle in which the tribofilm thickness was doubled from 60 to 120 nm in less than 2000 cycles. This fast growth phase was followed by another removal phase of similar rate during which several layers of the tribofilm were worn away.

In order to understand the difference in behaviour between the two repetitions, one should examine the topography images showing the structure evolution of the tribofilm over the sliding cycles. The topography of the first repetition indicates that the formed tribofilm is smoother and more compact than the one formed

during the second repetition. It can be argued that the high roughness of the tribofilm in the second repetition is the main player inducing the fast formation and removal cycles. The rough peaks on the shearing surfaces can cleave some of the surface bonds and thus create more active sites and provide more energy for the succeeding formation outburst. The hastened formation produces thicker but less compact tribofilm layers that can be removed easily under shear. This is evident by noticing the striking similarity between the topography of the tribofilm just before and after the second fast formation cycle.

7.1.3.3 Case III: growth at 5.7 GPa

Fig. 7.12 shows two repetitions of the evolution the tribofilm thickness and topography formed at 80 ^{o}C and 5.7 GPa over sliding cycles.

The first repetition (shown in red) indicates that the tribofilm grows steadily following approximately a linear rate. However, the second repetition (shown in blue) indicates that the tribofilm grows linearly only during the first 4000 sliding cycles. After that, the tribofilm starts to grow logarithmically for 500 cycles. Following this, the growth of the tribofilm resumes to progress linearly for about 1000 cycles before a removal phase begins during which the thickness decreased logarithmically from 100 to 60 nm in less than 500 cycles. The removal phase was followed by another formation phase, which is characterised by a linear growth with a rate similar to the two preceding formation phases.

The difference in growth between the two repetitions is better understood by examining the topography evolution of the formed tribofilms. Around 4000 sliding cycles just before the logarithmic growth phase in the second repetition begins, the structure of the tribofilm of the second repetition seems to be rougher than the one of the first repetition. This confirms the observation of the previous tests at lower contact pressure, that the surface roughness can affect the growth kinetics by creating more surface energy and more active sites for the subsequent growth cycles.

On the other hand, the tribofilm formed in the first repetition appears to grow linearly for exceeding large sliding cycles, as shown in Fig. 7.13. The tribofilm formed in this case is argued to be more compact as it took more time to grow and thus steady local reconfigurations were available leading to better accommodation of the newly formed layers and thus high compactness. This is evident by observing that the tribofilm thickness reached about 320 nm without any apparent and distinctive removal phase.

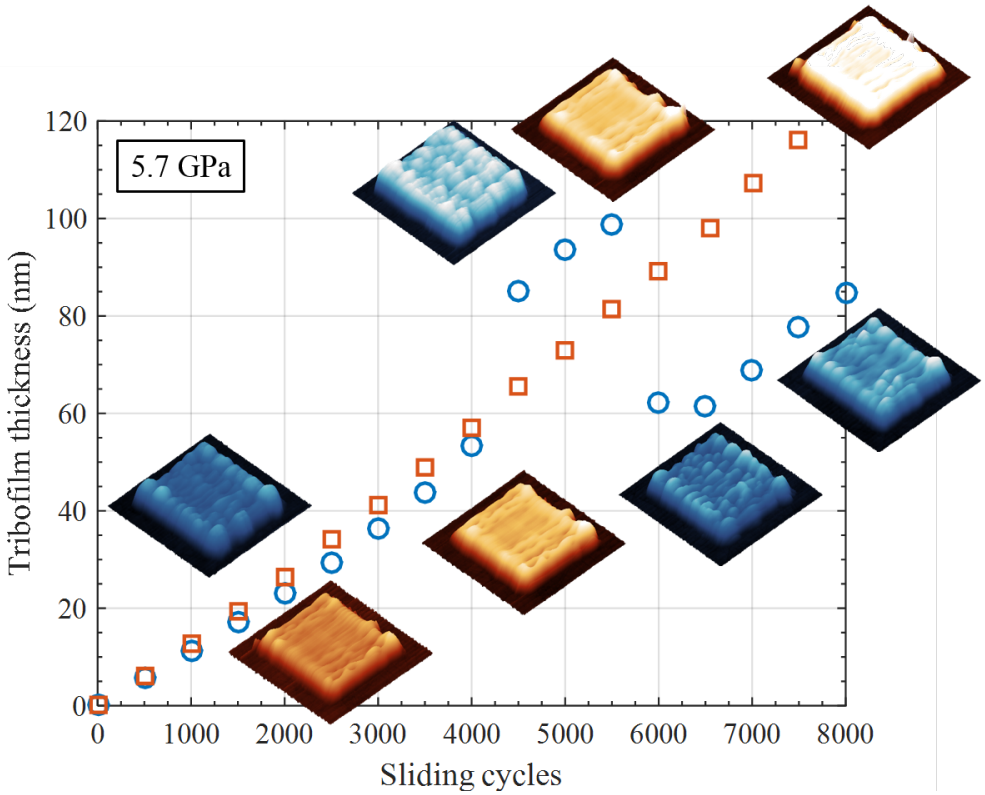

Fig. 7.12 Evolution of the ZDDP tribofilm thickness over time after two repetitions formed at 80 ^{o}C and 5.7 GPa.

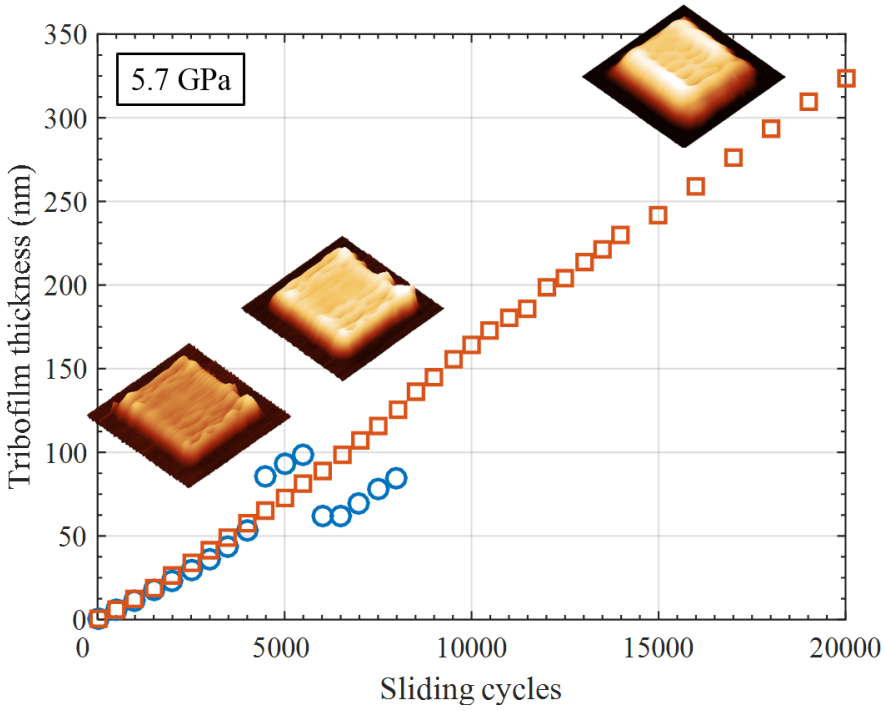

Fig. 7.13 Evolution of the ZDDP tribofilm thickness over time after two repetitions formed at 80 ^{o}C and 5.7 GPa.

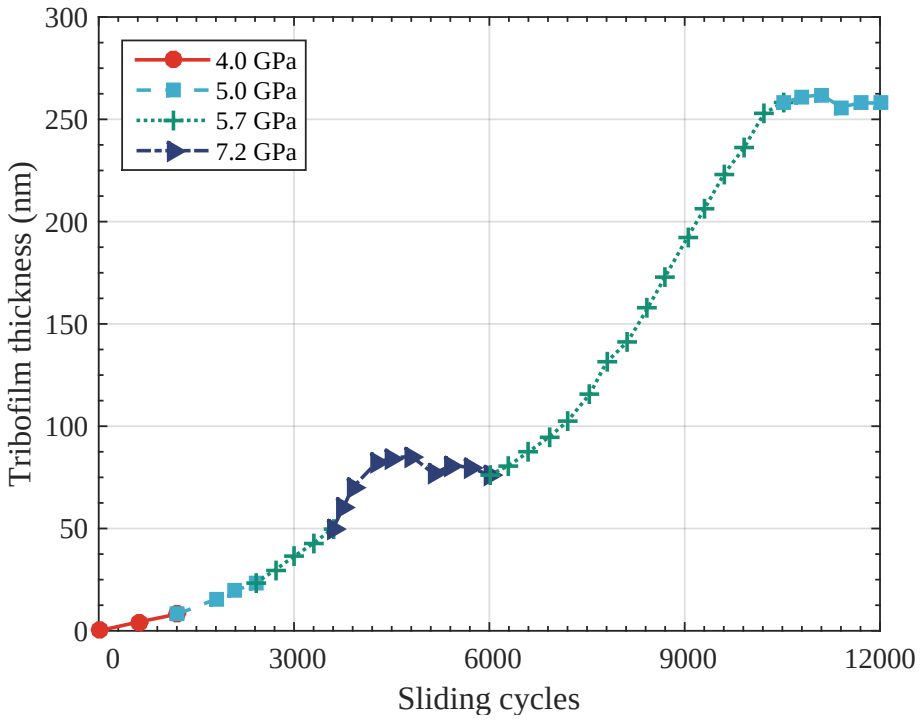

Fig. 7.14 Evolution of the ZDDP tribofilm thickness over sliding cycles at 80 ^{o}C while ramping the contact pressure from 4.0 to 7.2 GPa.

7.1.3.4 Comparison: growth at different contact pressures

The effect of contact pressure can be further examined by studying its effect on the same tribofilm as it forms. This gives a better understanding of the effect of not only the contact pressure but also the substrate and its hardness and elastic modulus on the tribofilm formation. Fig. 7.14 shows the evolution of the tribofilm thickness over different contact pressures ramped in the same in-situ tribotest. The data shows clearly the increase in the formation rate as the contact pressure increased. The growth rate over sliding cycles was the same whether the contact pressure was applied to steel surface directly or to a surface covered by a thin layer of tribofilm. The data provide several important conclusions.

The first important conclusion is that the substrate effective hardness and elastic modulus felt by the AFM tip are not altered due to the presence of the ultra-thin tribofilms of $<$ 100 nm thickness. If this was not the case, the tribofilm growth rate should have been reduced as the tribofilm grows because the increased deformation should have increased the contact area and thus decreased the effective contact pressure.

The second important conclusion is related to the pseudo steady-state thickness reached under 7.2 GPa of contact pressure. Under this pressure, it was expected that the tribofilm should grow in thickness but instead it reached a limited thickness

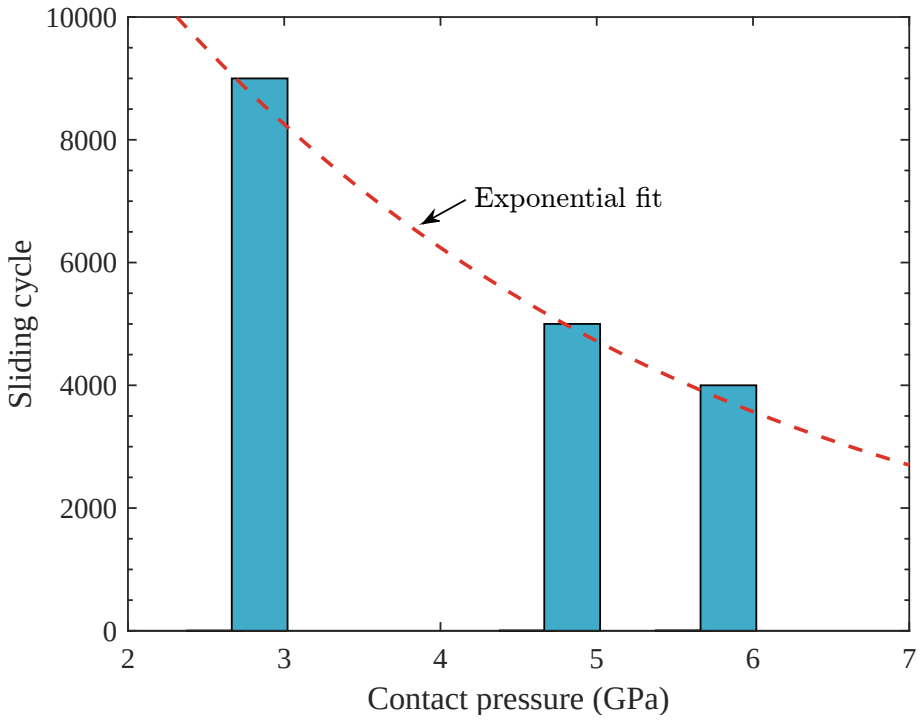

Fig. 7.15 Effect of contact pressure on the sliding cycles at which the tribofilm growth changes from linear to exponential.

after which no apparent growth was observed. The reason behind this steady-state condition can be related to the combined effect of the tribofilm flowability and the equilibrium between the tribofilm formation and removal. If removal was the only dominant process, then a sharp decrease in the tribofilm thickness, as observed in the previously discussed sections, should prevail. However, as the contact pressure is extremely severe, i.e. enough to wear the steel surface, the soft tribofilm can flow and be removed but at the same time the high stresses are enough to accelerate the decomposition process to a great extent as to counteract the thickness-reducing processes of flowability and wear.

The third important conclusion is related to the ability of the applied operating conditions to decompose the adsorbed ZDDP. It can be argued that the observed inability of the final contact pressure, i.e. 5.0 GPa applied at the end, to promote significant growth is related to the lack of adsorbed ZDDP molecules on the outer layers of the tribofilm as compared to the ones entrapped within the tribofilm. This implies that the ZDDP molecules cannot adsorb preferentially to the tribofilm surface as opposed to the steel surface. This is in line with the XANES results discussed in the previous chapter.

The contact pressure seems to affect the formation rate of the ZDDP tribofilm significantly. Fig. 7.15 provides a comparison between the numbers of sliding cycles required before the growth rate of the tribofilms, formed under different

contact pressures, to switch from slow to fast growth kinetics. The results showed that the increase in contact pressure reduces the needed cycles exponentially. For instance, at 2.7 GPa, 9000 cycles would be required as opposed to only 4000 cycles at 5.7 GPa. This indicates that the larger the contact pressure the faster the reaction kinetics of the ZDDP decomposition reactions.

The potent effect of contact pressure as well as temperature on the growth rate and reaction kinetics of the ZDDP tribofilms will be discussed in detail in the subsequent sections.

7.1.4 Tribofilm reaction kinetics

In this section, the effect of temperature, contact pressure and the synergy between them on the tribofilm formation kinetics will be studied in detail. This is important in order to develop a mechanistic understanding of the extent to which these operating conditions can affect the growth kinetics and thus the decomposition mechanism of the ZDDP.

7.1.4.1 Effect of contact pressure

Fig. 7.16 shows the evolution of the growth rate of the ZDDP tribofilm over different contact pressures at 80 ^{o}C. The data indicate that within the tested range of contact pressures, the tribofilm growth rate increases linearly with a rate of 0.027 nm/GPa.s. The only available data similar to this work are the ones of Gosvami et al. [30], which are plotted on the same Fig. 7.16 for comparison. The vertical shift is mainly related to the uncertainty in contact pressure, which can lead to a shift of the whole curve to the right or left. In agreement with our data, the previously reported data seem to follow a linear trend with a similar rate of 0.033 nm/GPa.s. It is worth mentioning that Gosvami et al. [30] suggested that their data follow three different phases, i.e. i) initial slow growth below 3.5 GPa, ii) exponential growth from about 3.5 to 5 GPa and iii) steady-state of formation and removal equilibrium at high contact pressures above 5.0 GPa.

To verify whether the tribofilm growth follows a linear or exponential growth, a wider range of contact pressures up to 7.0 GPa was tested at 80 ^{o}C and the results are shown in Fig. 7.17. The whole set of data appears to follow an exponential growth without any apparent phase during which steady-state thickness can be reached. This is contrary to the results of Gosvami et al. [30]. If their steady-state argument can be neglected then their whole set of data can also be fitted with a

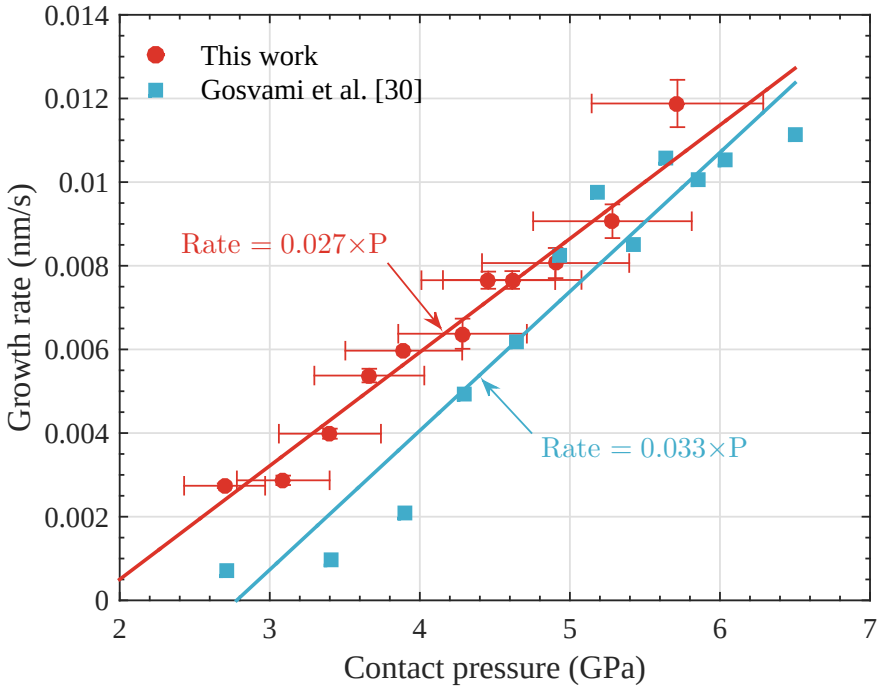

Fig. 7.16 Evolution of the growth rate of the ZDDP tribofilm formed at 80 °C over different contact pressures. The results of Gosvami et al. [30] were plotted for comparison.

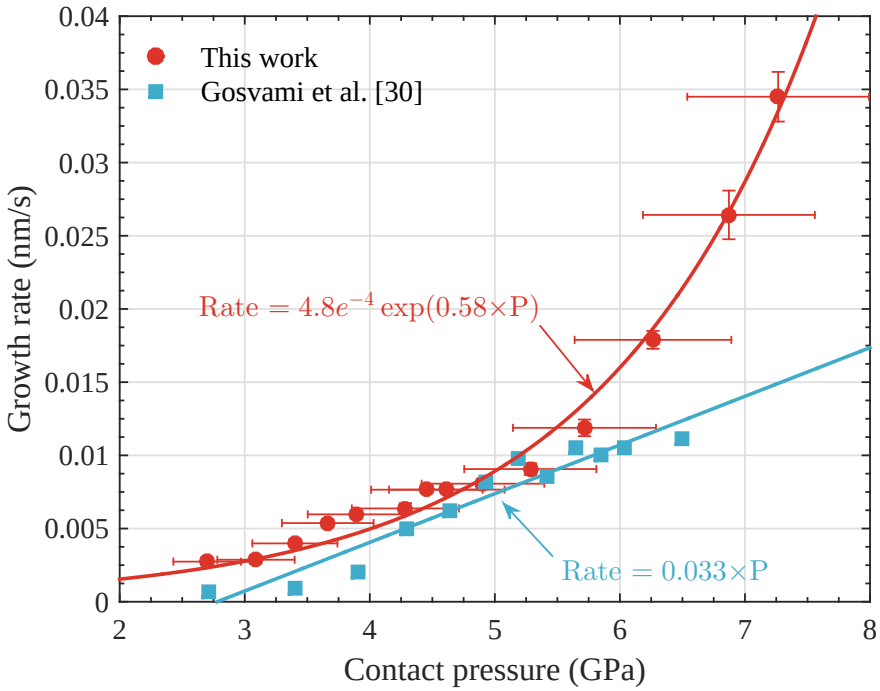

Fig. 7.17 Evolution of the growth rate of the ZDDP tribofilm formed at 80 °C over different contact pressures. The results of Gosvami et al. [30] were plotted for comparison.

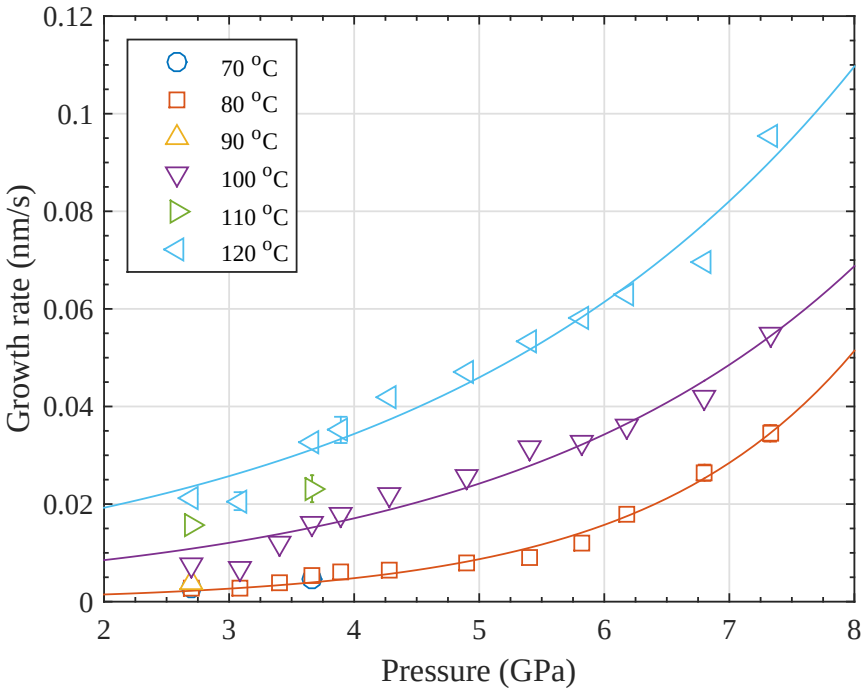

Fig. 7.18 Evolution of the growth rate of the ZDDP tribofilm over contact pressure formed at different temperatures.

single exponential growth model without the need to divide it into three phases as discussed before.

To confirm the validity of the single exponential fit, the data were repeated at various temperatures ranging from 70 to 120 °C. The evolution of the growth rate over contact pressure at the different tested temperatures is shown in Fig. 7.18. The results suggest that even at higher temperatures as high as 120 °C, the whole dataset can be fitted with one exponential fit. Furthermore, the data suggest that the higher the temperature the higher the increase in the growth rate which seems to follow exponential rate. The effect of temperature will be discussed in detail in the subsequent section.

7.1.4.2 Effect of temperature

Fig. 7.19 shows the evolution of the growth rate of ZDDP tribofilms over a wide range of temperatures, i.e. 70 to 120 °C, and contact pressures, i.e. 2.7 to 7.3 GPa. Similar to the growth rate evolution over contact pressure discussed in the previous section, the evolution over temperature appears to follow the same exponential trend.

The similar effect of temperature and contact pressure on the growth rate of the ZDDP tribofilms confirms their potent effect on the additive decomposition process [118, 350]. For instance, noticing the effect of increasing the contact

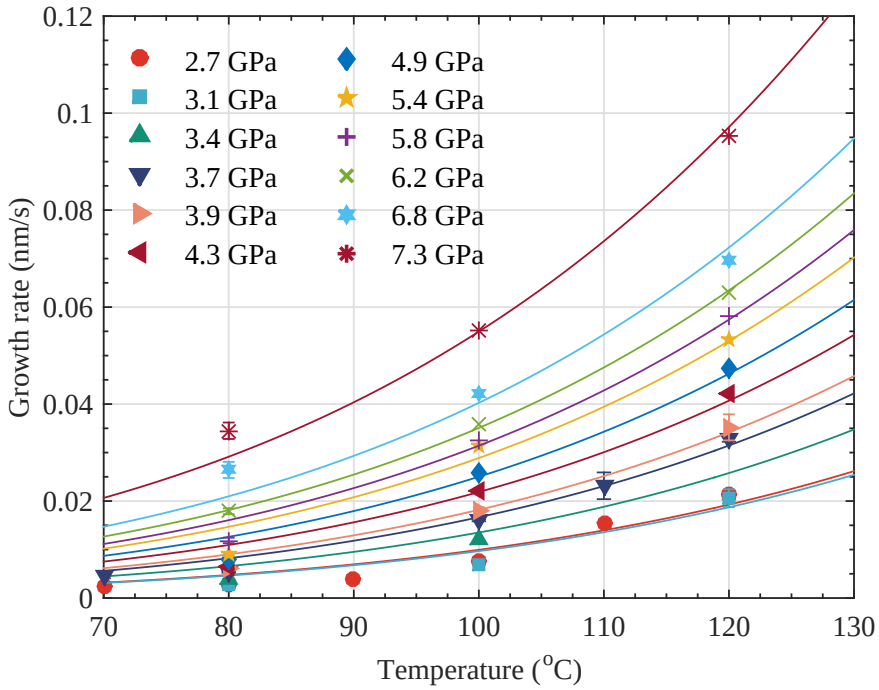

Fig. 7.19 Evolution of the growth rate of the ZDDP tribofilm over temperature formed under different contact pressures.

pressure or temperature on the formation rate suggests that the decomposition process of the ZDDP is thermally and mechanically assisted process, which can be activated by the availability of either shear or heat.

7.1.4.3 Combined effect of temperature and contact pressure

As discussed in the previous section, the decomposition reaction of ZDDP can be activated using heat and/or shear by means of contact pressure. The synergy of these two factors on the growth rate of the ZDDP tribofilm is demonstrated in Fig. 7.20. The exponential model described in Eq. (8.16), appears to fit the date extremely well.

The potent effect of either heat or shear on the decomposition reaction, can be confirmed by noticing that the growth rate can be increased tenfold from 0.002 nm/s, at 70 °C and 2.7 GPa, to about 0.02 nm/s by increasing either the temperature to 120 °C or the contact pressure to 7.0 GPa. Interestingly, the effect of temperature and contact pressure seems to be an additive effect as can be seen by the imaginary diagonal line in Fig. 7.20 between temperature and contact pressure manifested by the maximum growth rate when temperature and contact pressure are both maximum.

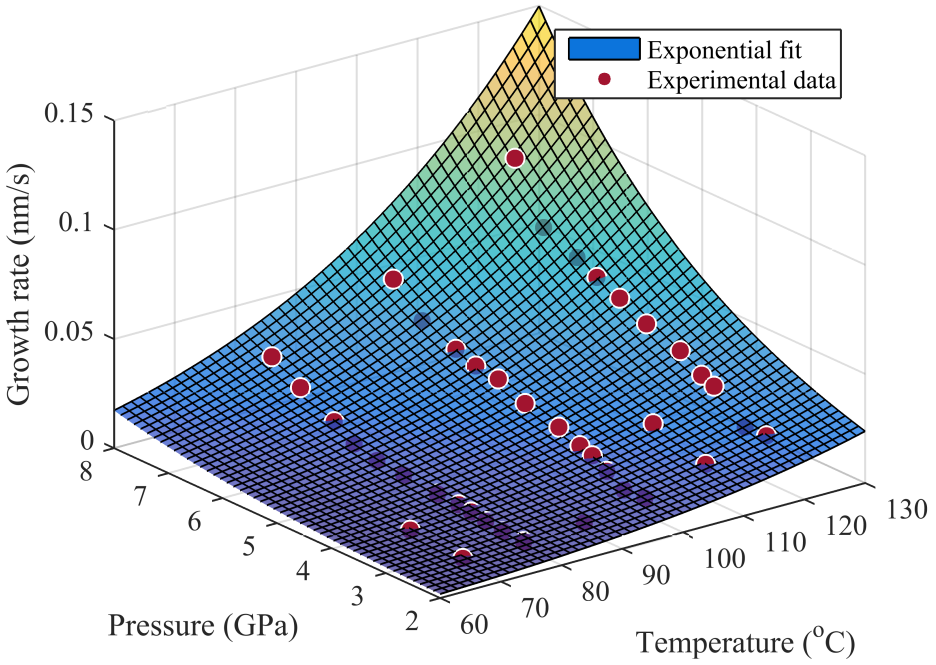

Fig. 7.20 Evolution of the growth rate of the ZDDP tribofilm formed under different contact pressures and temperatures. The 3D surface was generated using the chemo-mechanical Arrhenius-type model suggested by Gotsmann and Lantz [71].

7.1.5 Effect of substrate (H-DLC)

To study the effect of the substrate on the ZDDP tribofilm formation, in-situ tribotests were performed on non-doped (a-C:H) DLC coating and compared with the ones obtained using AISI 52100 bearing steel. This will help study the role of cations in the decomposition of the P-based antiwear additives and the formation of their tribofilms.

As expected, it was possible to form ZDDP tribofilms on bare steel surface under different operating conditions, which was discussed in detail in the previous sections. However, no apparent tribofilm formation was observed on the a-C:H coated steel surface, as shown in Fig. 7.21. This is in contrast with several previous studies reported that the P-based additives such as ZDDP or DDP can react and form protective tribofilms on DLC coatings even without containing any doped cations [31, 32, 211–215]. However, other studies, in line with our results, found that no tribofilms can be formed on non-doped DLC coatings without metallic cations [216–221]. The main factor behind the wide disparity between the formation and absence of tribofilms on DLC coatings appears to be related to the tribofilm tenacity. Several studies [31, 32, 211] showed that the tribofilms formed on DLC-DLC contacting surfaces are less tenacious than the ones formed on metal surfaces. Furthermore, no iron was present in the formed tribofilms on

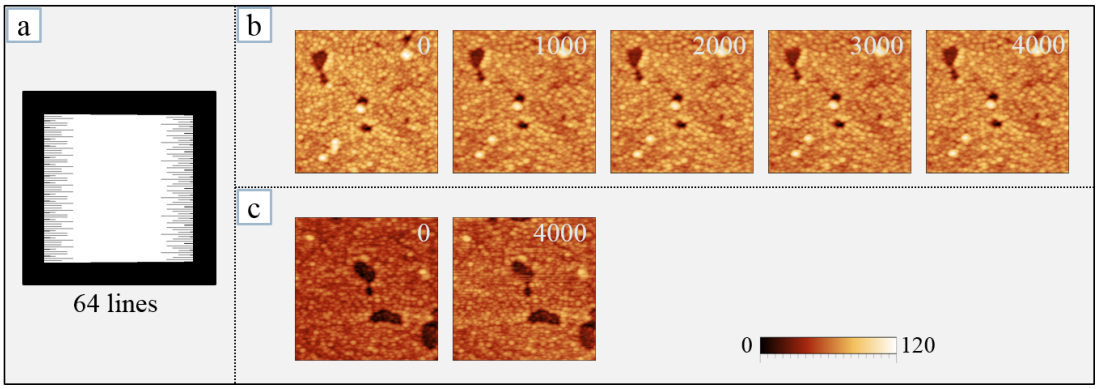

Fig. 7.21 In-situ ZDDP tribotest using the AFM liquid cell on H-DLC substrate, where a) schematic of the 64 scan lines used to raster scanning a $5 \times 5\,\mu m^2$ area, b) the substrate topography after different scanning cycles at 80 ^{o}C and 7.3 GPa, and c) the substrate topography after scanning at 120 ^{o}C and 7.3 GPa. The scale bar is in nm.

DLC surfaces [211, 216], which suggests that the low tenacity to the surface can be related to the absence of mixed oxide/sulphide base layer. This layer seems to act as a glue joining the substrate with the subsequently formed phosphate layers composing the main bulk of the tribofilm [36]. It follows that any formed tribofilms on DLC coatings, especially if non-doped, are weakly adhered leading to their effortless removal under rubbing once formed. Another explanation for the absence of formed tribofilms on DLC coatings was provided by Kalin and Vižintin [224] who suggested that the additive reaction with the substrate has different energy activation barriers depending on the surface whether doped or non-doped DLC or steel substrate. The difference in the activation barrier was attributed to the low thermal conductivity of the non-doped DLC (0.3 to 3.5 W/mK [353]) in comparison to steel (>50 W/mK [354]) or metal doped-DLC. The low conductivity of the non-doped DLC can lead to lower contact temperature that impedes or slows the additive decomposition and the tribofilm formation.

7.2 Results of DDP tribofilms

This section presents and discusses the main findings related to the DDP tribofilms including the local occupancy, durability, tenacity, flowability, growth hysteresis and formation kinetics.

7.2.1 Local occupancy of the tribofilm pads

In order to study the effect of the local occupancy of the neighbouring pads on the final structure of the tribofilm, several tribofilms were formed at varying

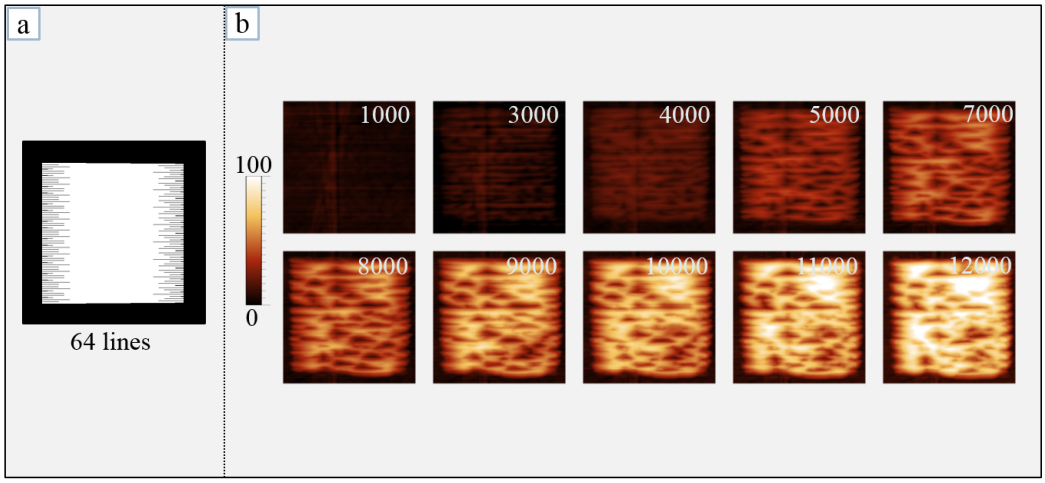

Fig. 7.22 In-situ DDP-1 tribotest using the AFM liquid cell, where a) schematic of the 64 scan lines used to raster scanning a $5 \times 5\,\mu m^2$ area, and b) the generated tribofilm after different scanning cycles at 80 ^{o}C and 4.8 GPa. The scale bar is in nm.

specific locations and their interaction was examined when the separation distance decreases or increases. For this purpose, five cases will be discussed, which are related to number of lines, i.e. 64, 16, 8, 4 and 1, used to raster scanning an area of $5\,\mu m \times 5\,\mu m$ on the steel surface at different contact pressures but at the same sliding speed, as depicted in Fig. 7.1. These are discussed in detail in the following sections.

7.2.1.1 Case I: 64 scanning lines

Fig. 7.22 shows the evolution of the structure of the DDP tribofilm formed using 64 lines raster scanning an area of $5 \times 5\,\mu m^2$ at 80 ^{o}C and 4.8 GPa. The maximum space separating any two adjacent scanning lines was less than 78 nm, which is less than the estimated diameter of the tip, i.e. 150 nm. Therefore, from the beginning of the tribotest, the formed tribofilm appeared as a continuous film without any distinctive lines. Contrary to the case of the ZDDP tribofilm, the DDP tribofilm formed during the early stage of the tribotest does not appear to have larger thickness near the edges as compared to the central region. In contrast, it appeared as a uniform film consisting of small thin pads elongated in the direction of shear.

As rubbing cycles progressed, further shearing does not seem to cause severe mixing and distortion to the individual pads, which leads to the preservation of the initial structure of the tribofilm despite the increase in thickness. All these features are different from the ones observed previously in the case of the ZDDP tribofilms. The reason behind this can be related to the type of the phosphate forming the main bulk of the tribofilm. In the case of the ZDDP, zinc phosphate

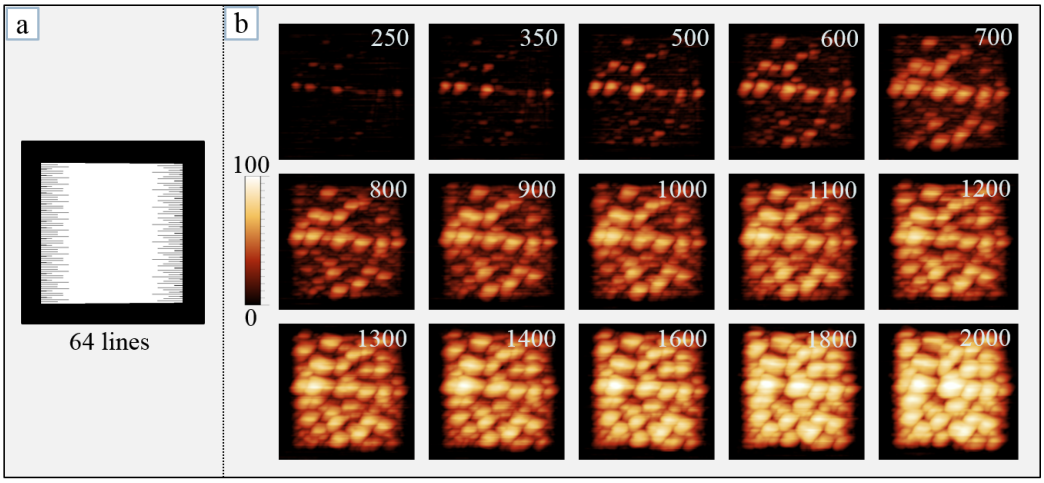

Fig. 7.23 In-situ DDP-1 tribotest using the AFM liquid cell, where a) schematic of the 64 scan lines used to raster scanning a $5 \times 5\,\mu m^2$ area, and b) the generated tribofilm after different scanning cycles at 80 ^{o}C and 5.6 GPa. The scale bar is in nm.

tribofilm is mainly formed as compared to the iron phosphate tribofilm in the case of DDP. Thus, the type of cations available during the decomposition of the additive seems to affect not only the composition but also the structure of the formed tribofilm. Furthermore, the reported DDP tribofilms were formed at smaller contact pressure than the ones of ZDDP, so this might have also affected the observed evolution in the structure.

To examine the effect of contact pressure, Fig. 7.23 shows the evolution of the DDP structure at 80 ^{o}C and 5.6 GPa. At this high contact pressure, the structure appears to be different from the previously discussed one at 4.8 GPa. Three main differences can be observed. First, the tribofilm grows at much faster rate, i.e. at least sixfold. Second, the tribofilm thickness is not uniform but depends mainly on the initially formed regions, which keep growing more than the rest of the tribofilm. These regions appear mainly in the middle of the tribofilm. Third, contrary to the thin largely elongated pads in the direction of shear formed at low contact pressure, high pressure caused the pads to be of wider breadth and less elongated. This can be related to the fast formation rate of the tribofilm at large contact pressure. In this case, the pads have neither enough time nor space to elongate over a large area. The local occupancy of the neighbouring pads appear to impede the growth of the pads laterally and thus forces them to immaturely grow vertically in thickness.

7.2.1.2 Case II: 16 scanning lines

Fig. 7.24 shows the evolution of the structure of the ZDDP tribofilm during the in-situ tribotest using 16 lines raster scanning an area of $5 \times 5\,\mu m^2$. The separation

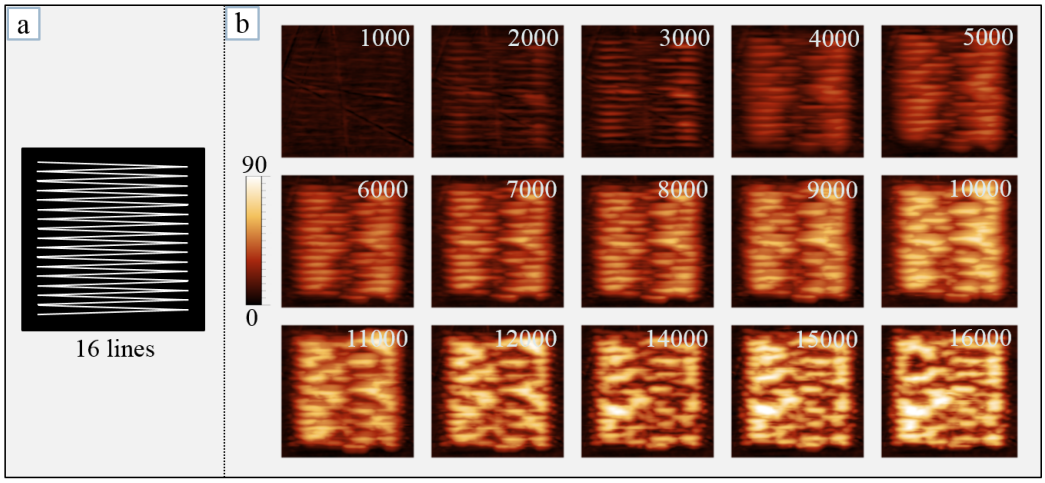

Fig. 7.24 In-situ DDP-1 tribotest using the AFM liquid cell, where a) schematic of the 16 scan lines used to raster scanning a $5 \times 5\,\mu m^2$ area, and b) the generated tribofilm after different scanning cycles at 80 ^{o}C and 4.8 GPa. The scale bar is in nm.

distance between any two adjacent lines is less than 312 nm, which is nearly twice the estimated diameter of the AFM tip. This resulted in the appearance of clear distinctive lines in the formed tribofilm during the early stages of the tribotest.

Several features appear in the formed DDP tribofilm. The first one is related to the thicker tribofilm formed near the edges as compared to the middle areas. The double rubbing action at these regions due to the overlapping scanning lines as they get closer to the edges is the main reason behind this phenomenon.

The second feature is related to the uniform structure of the formed tribofilm during the final stages. As rubbing continued, the areas in the middle of the tribofilm starts to form thicker tribofilm. However, contrary to the expected behaviour as in the case of ZDDP, the areas near the edges did not grow larger than the one in the middle despite being thicker in the beginning of the test. Wear and smearing of these thick areas of the tribofilm under shear might be responsible for this although there is a lack of evidence to support it. Another possible cause can be the flowability of the areas near the edges to the area in the middle, which is supported by the continuous elongation of these areas until they fill the whole region of the tribofilm. Finally, as shear progressed, the big elongated pads disintegrated into smaller ones.

Another interesting feature appears after long rubbing cycles, which is manifested in the disappearance of the scanning lines as the tribofilm grows resulting in a more uniform tribofilm similar to the one formed using larger number of scanning lines. Two factors can cause this behaviour. First, as indicated earlier the disintegration of the big elongated pads helps uniform the structure. Second, akin to the ZDDP, the DDP seems to form a highly viscous soft and deformable

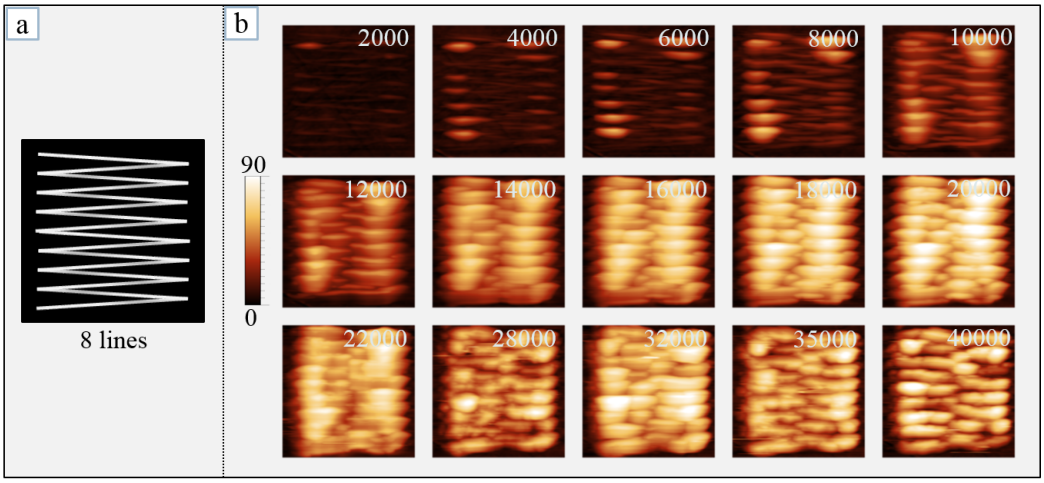

Fig. 7.25 In-situ DDP-1 tribotest using the AFM liquid cell, where a) schematic of the 8 scan lines used to raster scanning a $5 \times 5\,\mu m^2$ area, and b) the generated tribofilm after different scanning cycles at 80 ^oC and 4.8 GPa. The scale bar is in nm.

tribofilm that under shear or contact pressure can flow to cover the gaps between the adjacent scanning lines resulting in a more homogeneous tribofilm. This conjecture will be tested further by examining the tribofilm behaviour when the local occupancy of the scanning lines is increased to a larger separation distance.

7.2.1.3 Case III: 8 scanning lines

To test the previous theories regarding the tribofilm's flowability and its effect on the final structure, it is necessary to vary the local occupancy of the formed tribofilm's pads by increasing the distance between the adjacent scanning lines. Fig. 7.25 shows the evolution of the structure of the DDP tribofilm during the in-situ tribotest using 8 lines raster scanning an area of $5 \times 5\,\mu m^2$ at 80 ^oC and 4.8 GPa. In this case, the distance between the adjacent lines is about 625 nm, which is fourfold the estimated diameter of the used AFM tip. This relation can be confirmed by measuring the diameter of one of the lines of the formed tribofilm after short rubbing cycles and the distance between the lines.

Several features appear in the formed tribofilm, which are similar to the previously discussed tribofilms using larger number of scanning lines. Initially, the edges of the formed tribofilm appears to be thicker than the areas in the middle. However, as rubbing continued, the tribofilm thickness became more uniform near and away from the edges.

After 12000 cycles, the gap between any two adjacent lines, nearly 625 nm, appeared to be completely filled with a tribofilm. This is despite the absence of any shearing occurring in these regions. It is highly possible that the tribofilm

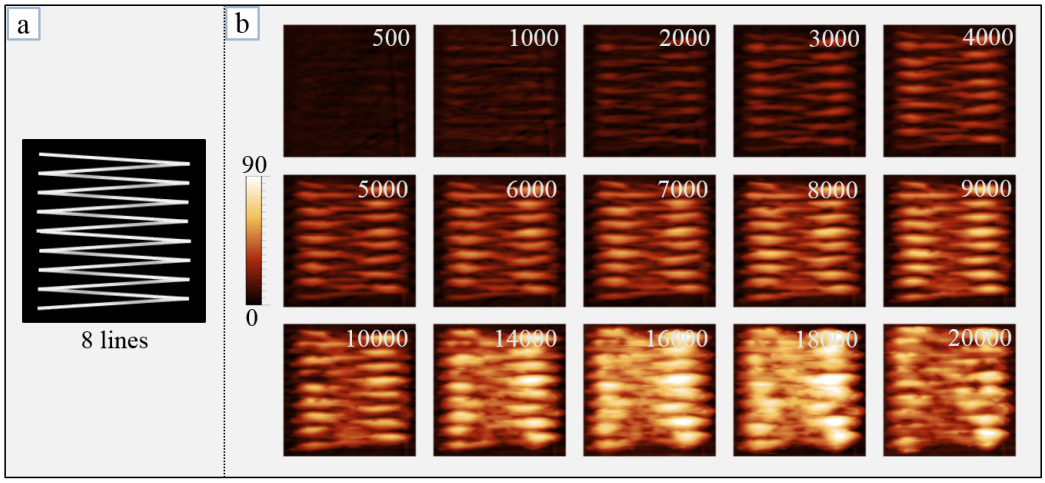

Fig. 7.26 In-situ DDP-1 tribotest using the AFM liquid cell, where a) schematic of the 8 scan lines used to raster scanning a $5 \times 5\,\mu m^2$ area, and b) the generated tribofilm after different scanning cycles at 80 ^{o}C and 5.6 GPa. The scale bar is in nm.

appearing in these un-sheared regions originated from the flow of the tribofilm of the sheared areas nearby. Similar conclusion can be observed when examining the evolution of the structure of DDP formed at higher contact pressure of 5.6 GPa, as shown in Fig. 7.26. These findings are also similar to the previous observations of the ZDDP tribofilms. Therefore, it can be argued that the P-based additives, whether ZDDP or DDP, can form soft deformable tribofilms, which can flow under the action of shear. The flowability of these tribofilms is expected to play a significant role in reducing the shear stresses between the shearing interfaces and thus mitigating wear.

7.2.1.4 Case IV: 4 scanning lines

To confirm the previous finding that the tribofilm can flow to cover wider areas than the sheared ones, the distance between any two adjacent scanning lines was further increased to about 1.25 μm. This was possible using 4 lines raster scanning an area of $5 \times 5\,\mu m^2$ at 80 ^{o}C and 4.8 GPa as shown in Fig. 7.27 and at 80 ^{o}C and 5.6 GPa as shown in Fig. 7.28. The results confirm the previously discussed observation that initially the tribofilm is only formed under the scanning lines where the interface between the steel surface and the AFM tip experiences large shear stress and contact pressure. However, as shearing continued, the tribofilm starts to fill the nearby areas gradually. The structure of the tribofilm appears as if it flows from the areas of high contact pressure to spread to any available gap, which is more evident in the long test carried out at the high contact pressure of 5.6 GPa shown in Fig. 7.28.

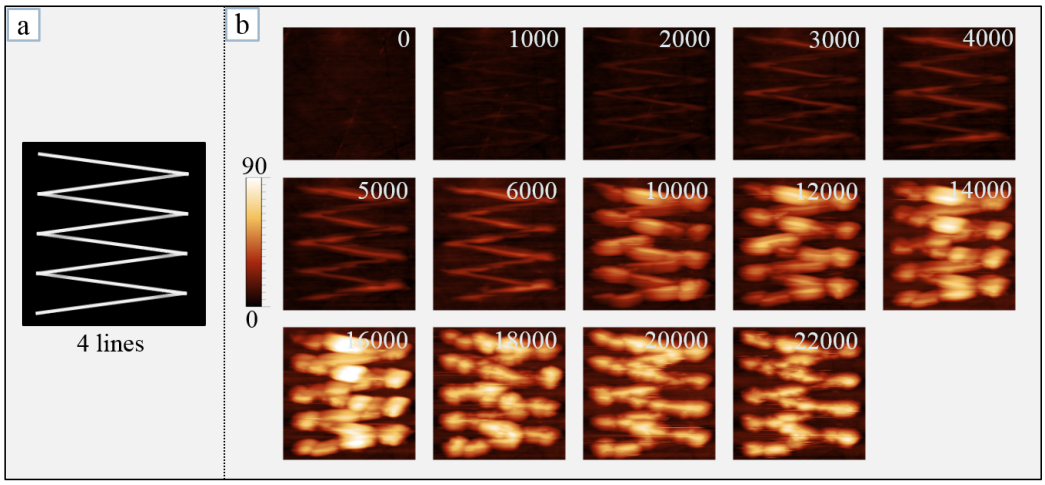

Fig. 7.27 In-situ DDP-1 tribotest using the AFM liquid cell, where a) schematic of the 4 scan lines used to raster scanning a $5 \times 5\,\mu m^2$ area, and b) the generated tribofilm after different scanning cycles at 80 ^{o}C and 4.8 GPa. The scale bar is in nm.

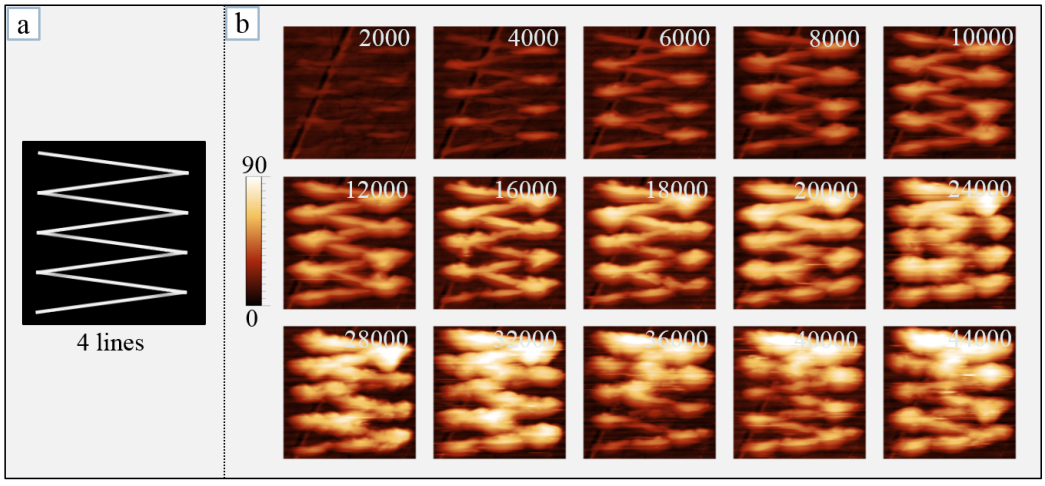

Fig. 7.28 In-situ DDP-1 tribotest using the AFM liquid cell, where a) schematic of the 4 scan lines used to raster scanning a $5 \times 5\,\mu m^2$ area, and b) the generated tribofilm after different scanning cycles at 80 ^{o}C and 5.6 GPa. The scale bar is in nm.

Similar to the case of ZDDP, the results of DDP confirm that contrary to the generally perceived conception that the P-based tribofilms are rigid interfaces acting as a mechanical barrier to protect against wear [14–18], the formed tribofilms appear to behave as a highly viscous material, which can deform and flow under shear. The significant importance of this finding is that for the first time it provides a new explanation for the excellent anti-wear properties of the P-based tribofilms. In addition to forming a mechanical barrier, the tribofilm can also deform and flow and thus mitigates the shear stress at the rubbing interfaces leading to less wear.

One difference between the DDP and ZDDP tribofilms is that in the case of the former, the thick areas formed near the edges due to the overlapping between the scanning lines do not appear to be worn away easily. This is evident from observing that in the beginning of the test the edges of the lines are thicker than the ones in the middle, which continue to be so for as long as the tribotest lasted. This suggests that the available cations during the additive decomposition can largely affect the structure, mechanical and rheological properties of the formed tribofilm. The results thus far indicate that the DDP tribofilm formed of mainly short iron phosphate is more tenacious and less flowable than the ZDDP tribofilm formed mainly of relatively long zinc phosphate chains.

7.2.1.5 Case V: 1 scanning line

The flowability of the ZDDP tribofilm can be further confirmed by observing the evolution of the structure of the DDP tribofilm during the in-situ tribotest using a single scanning line of length of 5 μm, as shown in Fig. 7.29 at 80 ^{o}C and 4.8 GPa.

The thickness and width of the formed tribofilm appears to increase rapidly as rubbing cycles increased. This confirms that the tribofilm does not only form under the AFM tip but can also flow to the sides. Another observation is related to the uniformity of the formed line. Similar to the ZDDP case, the formed DDP tribofilm appeared less uniform along its length. One explanation for this behaviour can be related to the disruption caused by the reciprocating motion of the AFM time over a very short period of time while the film is susceptible to deformation. Furthermore, this can also be related to load instability [167] as the AFM tip changes direction as well as to any surface heterogeneity [30].

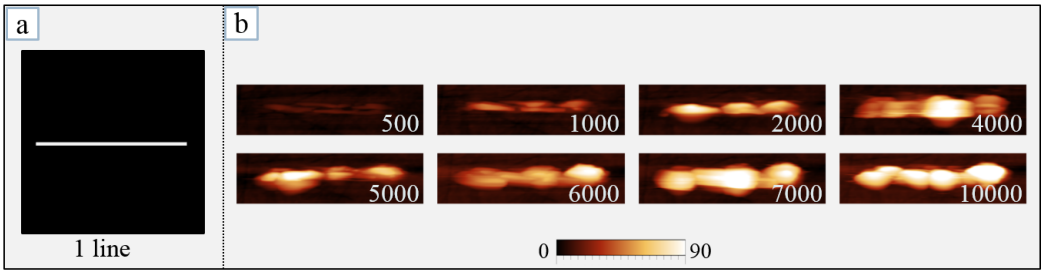

Fig. 7.29 In-situ DDP-1 tribotest using the AFM liquid cell, where a) schematic of the single scan line used to raster scanning a $5 \times 5\,\mu m^2$ area, and b) the generated tribofilm after different scanning cycles at 80 ^{o}C and 4.8 GPa. The scale bar is in nm.

7.2.2 Tribofilm durability and tenacity

To test the durability and tenacity of the DDP tribofilms, a mature tribofilm was subjected to different contact pressures and the evolution of its thickness was observed over the different sliding cycles as shown in Fig. 7.30. To avoid any formation in the process, the AFM tip was raster scanning the tribofilm at ambient temperature and in base oil without DDP additive. These same experiments can also be used to study the flowability of the tribofilm as the large applied shear stresses and pressures are expected to cause the tribofilm to flow.

The results show that initially when a relatively small contact pressure of 2.1 GPa was applied, a negligible change in the tribofilm thickness occurs. This indicates that under mild operating conditions the DDP tribofilm is largely tenacious and durable.

As the contact pressure was increased to 2.7 GPa, an instantaneous recovery of about 17 nm of the tribofilm thickness was observed. A similar behaviour was also observed in the case of the ZDDP. The source of this recovery might be related to the decompressing effect of contact pressure on mature tribofilms resulting from the irreversible disruption of the local compactness of the interfacial layers under pressure. Therefore, the free volume within the phosphate glass forming the tribofilm increases to a certain extent. These reconfigurations make the upper layers loose and more susceptible to wear. This can be confirmed by the subsequent decrease in the tribofilm thickness over the sliding cycles until reaching a steady-state thickness of about 118 nm.

As the contact pressure was subsequently increased to 3.7 GPa, a large instantaneous decrease in the thickness of more than 40 nm was observed. This is followed by a gradual decrease in the tribofilm thickness until it reached a steady-state thickness of 50 nm. Under this large contact pressure, a big part of

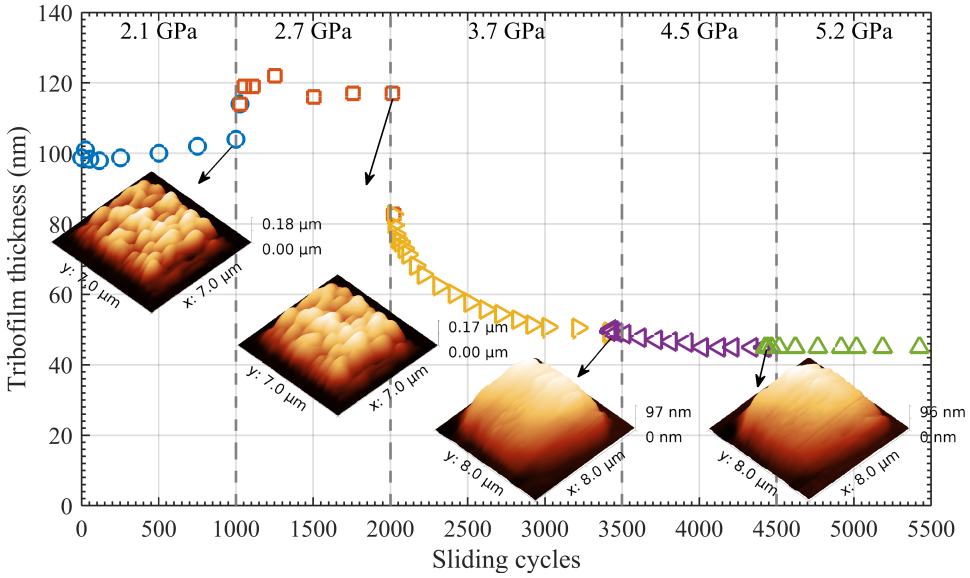

Fig. 7.30 Durability of mature DDP tribofilms measured by following the evolution of the tribofilm thickness after different sliding cycles at 25 ^{o}C under different contact pressures ranging from 2.1 to 5.2 GPa.

the tribofilm was completely removed, which is unlike the layer-by-layer removal observed in the case of smaller pressures.

When the contact pressure was further increased to 4.5 GPa, a small decrease in the tribofilm thickness of less than 8 nm was observed until it reached steady-state thickness of 42 nm. Another increase in the pressure to 5.2 GPa, did not cause any more removal of the tribofilm, which confirms the large tenacity and durability of the DDP tribofilm.

Another interesting observation in the structure evolution of the tribofilm is related to the flowability observed under the different contact pressures. For instance, when a small pressure was applied, the initial tribofilm area of $5 \times 5\,\mu m^2$ was preserved. However, when the contact pressure was increased to 2.7 GPa, the covered area increased to about $6 \times 6\,\mu m^2$. This area increased further to $7 \times 7\,\mu m^2$ when the pressure was increased to 3.7 GPa, which stayed the same when the pressure increased further to 4.5 and 5.2 GPa. The origin of this behaviour can be attributed to the large contact pressure that can deform the highly viscous and soft tribofilm and squeeze it such that the film moves from the areas of high contact pressure and large shear stresses towards the areas near the edges of low contact pressure in order to minimise the experienced shear stresses. The limited area reached at high contact pressures seemed to be related to two possible causes. First, the high tenacity of the more elastic than viscous sulphur-base layers [17, 36, 48] reduces the overall flowability. Second, the increased effect

of the hard substrate increases the effective viscosity of the remaining ultrathin tribofilm layers.

7.2.3 Effect of substrate

To study the effect of the substrate on the DDP tribofilm formation, in-situ tribotests were performed on various substrates including AISI 52100 bearing steel and different glasses of zinc-, iron- and mixed zinc-iron phosphates. This along with the different additives used, i.e. ZDDP and DDP, will also enable us to study the role of cations in the decomposition of the P-based antiwear additives and the formation of their tribofilms.

As expected, it was possible to form DDP tribofilms on a bare steel surface under different operating conditions, which was discussed in detail in the previous sections. It was also possible to form a tribofilm on the iron phosphate glass as shown in Fig. 7.31b using 64 lines raster scanning an area of $2 \times 2\,\mu m^2$ at 80 ^{o}C and 4.8 GPa. The structure of the formed tribofilm was similar to the ones generated on bare steel surfaces. This indicates that the availability of iron from the substrate, whether steel or iron phosphate, was enough to form a DDP tribofilm consisting mainly of iron phosphate. As the thermal conductivity of the phosphate bulk ranges from 0.2 to 2.3 W/mK [355] whereas for steel is about 50 W/mK [354], the ability to form a tribofilm on the phosphate glass contradicts the hypothesis of Kalin and Vižintin [224] that a substrate with a high thermal conductivity is required for the formation of P-based tribofilms. They based this argument on the observation that non-doped DLC coatings, which have low thermal conductivity, lacks the ability to form protective tribofilms in comparison to steel. This indicates that the other plausible reason is mainly related to the difference in tenacity as discussed earlier.

No tribofilm formation was possible on zinc and mixed zinc and iron phosphate glasses as shown in Figs. 7.31c and 7.31d. The inability to form a DDP tribofilm on these phosphate glasses is peculiar. The available zinc or zinc and iron cations were expected to be sufficient to induce the formation a tribofilm of zinc or iron phosphate. One possible explanation for this is related to our previous conclusion that the iron phosphate-based tribofilm is more tenacious than the zinc phosphate-based tribofilm. It follows that any formed phosphate-based tribofilm on the zinc or mixed zinc and iron glass could be too weakly adsorbed to withstand the applied shear stresses and thus is worn away at the moment being formed.

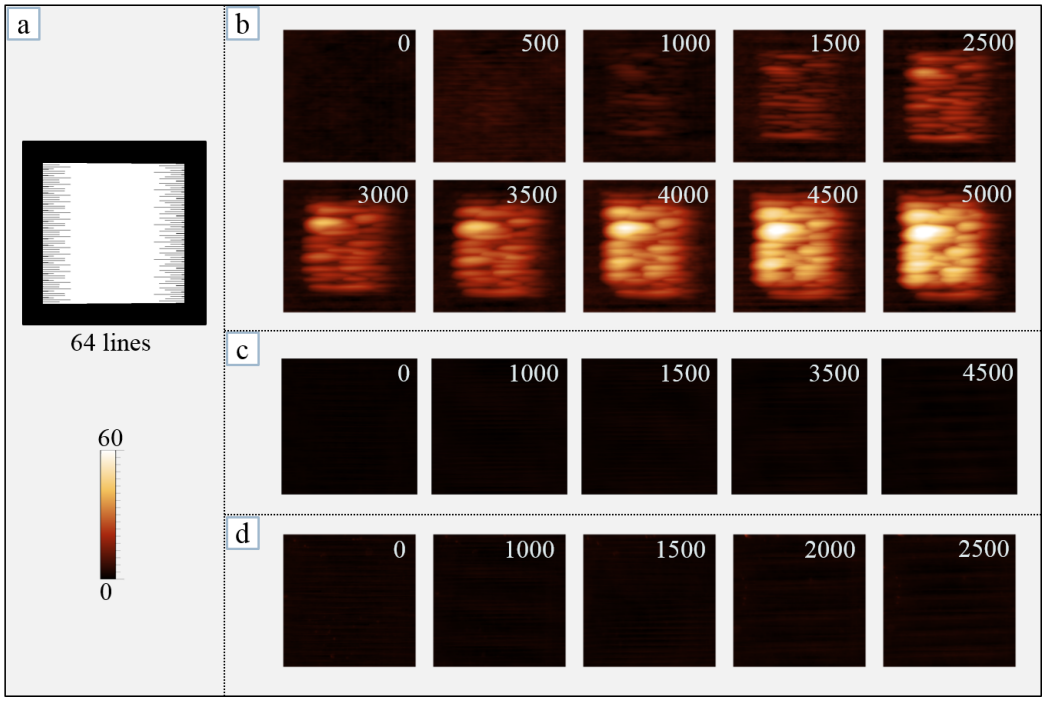

Fig. 7.31 Effect of substrate on the in-situ DDP-1 tribotest using the AFM liquid cell, where a) schematic of the 64 scan lines used to raster scanning a $2 \times 2\,\mu m^2$ area, b) the generated tribofilm on iron polyphosphate substrate, c) the generated tribofilm on zinc polyphosphate substrate, and d) the generated tribofilm on mixed zinc and iron polyphosphate substrate, after different scanning cycles. The scale bar is in nm.

7.2.4 Tribofilm growth hysteresis

Fig. 7.32 shows three repetitions of the thickness evolution over sliding cycles for DDP tribofilms formed at 80 ^oC and various contact pressures, i.e. 3.9, 4.3 and 5.2 GPa. The results show the clear potent effect of the contact pressure on increasing the growth rate. During the first 500 cycles, the formation rate increased from 0.005 nm/s at 3.9 GPa to about 0.018 nm/s at 5.2 GPa. For the following 1500 cycles, the latter increased to 0.043 nm/s until reaching steady state. This steady state was not observed at lower contact pressures as it seems to take longer sliding cycles than the ones reported in this work.

The exponential growth rate is in agreement our results of ZDDP tribofilm. However, they are in contrast with the results of Gosvami et al. [30] of the ZDDP tribofilm formation, which suggested a transition from linear to exponential growth rate over the sliding cycles.

It should be noted that in the case of DDP, the formed tribofilm did not show any removal as opposed to the case of ZDDP where the tribofilm formation was continuously interrupted by removal cycles. This can indicate that either the DDP

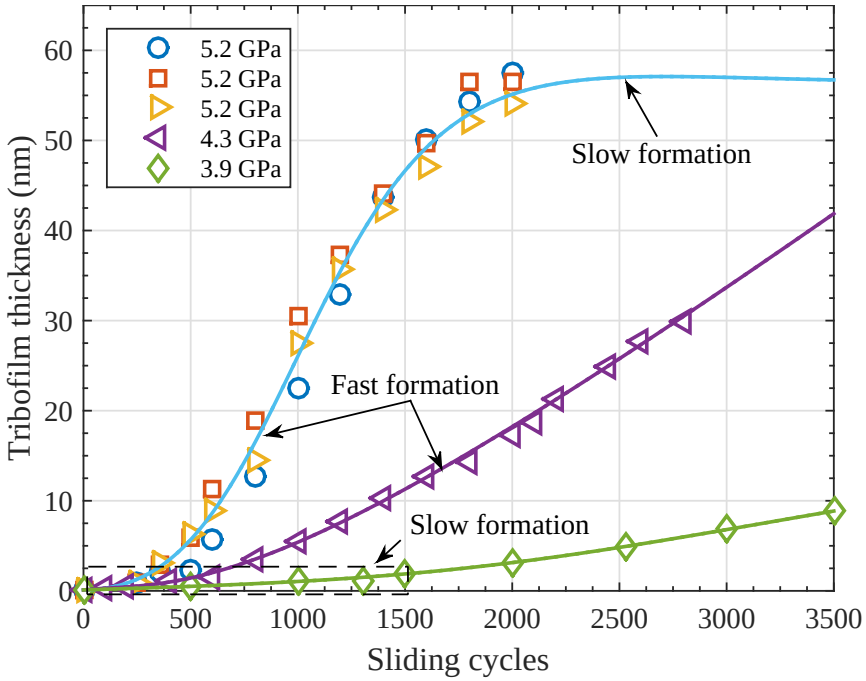

Fig. 7.32 Evolution of the tribofilm thickness over sliding cycles for DDP-1 tribofilms formed at 80 ^{o}C and different contact pressures.

tribofilm is more durable and tenacious than the ZDDP tribofilm or the removal cycles occurs primarily after the tribofilm reaches a certain large thickness.

7.2.5 Tribofilm reaction kinetics

In this section, the effect of temperature, contact pressure and the synergy between them on the reaction kinetics of DDP will be studied in detail. This is important to better understand the extent to which these operating conditions affect the decomposition mechanism of the DDP and the rate of formation of the generated tribofilm.

7.2.5.1 Effect of contact pressure

The evolution of the growth rate of the DDP tribofilm over different contact pressures is shown in Fig. 7.33. The data indicate that within the tested range of contact pressures, the tribofilm growth rate increases following a pattern of exponential growth. There are no data available in the literature regarding the change in growth rate of the DDP tribofilm over the contact pressure. However, the only similar data based on the ZDDP tribofilm were reported by Gosvami et al. [30], which in agreement with our data indicate an exponential change.

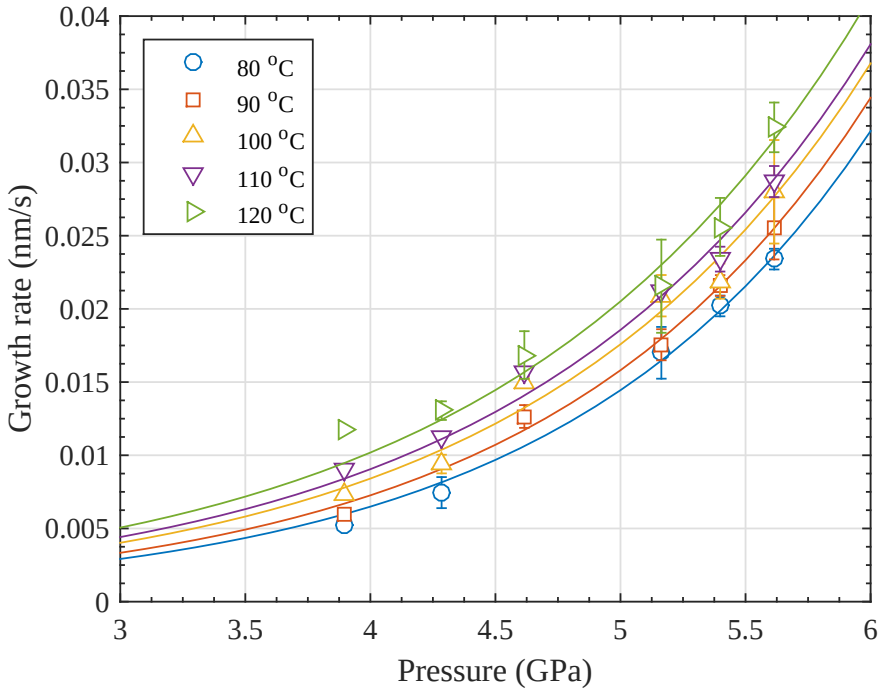

Fig. 7.33 Evolution of the growth rate of the DDP tribofilm over contact pressure formed at different temperatures.

To verify the exponential growth of the tribofilm, the tribotests were repeated at different temperatures ranging from 80 to 120 °C as shown in the same Fig. 7.33. The whole dataset appears to follow an exponential growth at all the tested temperatures. It is worth mentioning that no apparent phase indicates that the growth rate approaches a steady-state plateau. Furthermore, the data suggest that the higher the temperature, the higher the increase in the growth rate, which seems to follow exponential rate. This will be discussed in detail in the subsequent section.

7.2.5.2 Effect of temperature

The evolution of the growth rate of DDP tribofilms over a wide range of temperatures from 80 to 120 °C, and contact pressures from 3.9 to 5.6 GPa is shown in Fig. 7.34. Similar to the case of the evolution of the growth rate over contact pressure discussed in the previous section, the evolution over temperature appears to follow the same exponential model. However, it can be equally fitted using a linear growth model. The similar effect of temperature and contact pressure on the growth rate of the DDP tribofilm suggests, similar to ZDDP case, that they have a potent effect on increasing the additive decomposition process, which can be activated by the availability of either shear or heat.

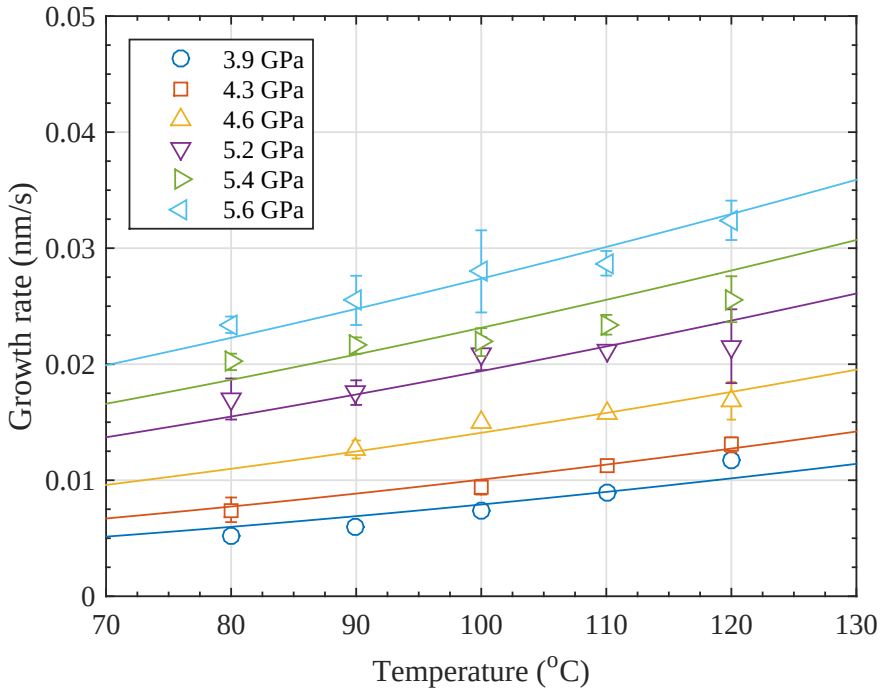

Fig. 7.34 Evolution of the growth rate of the ZDDP tribofilm over temperature formed under different contact pressures.

It is worth noting that the data seem to suggest that within the range of the tested conditions, the growth rate of the DDP tribofilm increases over the contact pressure more prominently than temperature. This implies that, above a certain threshold of temperature, shear stress alone is enough to cause a complete decomposition of the DDP additive to form a protective tribofilm. Increasing the temperature further does not have a potent effect as opposed to the case of ZDDP, which suggests different reaction pathways with different energy barriers.

7.2.5.3 Combined effect of temperature and contact pressure

As discussed in the previous section, the decomposition reaction of the DDP can be activated using heat and/or shear by means of contact pressure. The synergy of these two factors on the growth rate of the DDP tribofilms is demonstrated in Fig. 7.35. The exponential model described in Eq. (8.16) was used to fit the data.

Contrary to the case of the ZDDP additive, the effect of temperature and contact pressure does not appear to be additive. This is evident from the large increase in the growth rate with the contact pressure as compared to the mild increase with temperature. As discussed in the previous section, this indicates that above a certain threshold of temperature, shear stress alone is enough to cause a complete decomposition of the DDP additive to form a protective tribofilm. Beyond this threshold, temperature seems to have a mild effect on the growth rate.

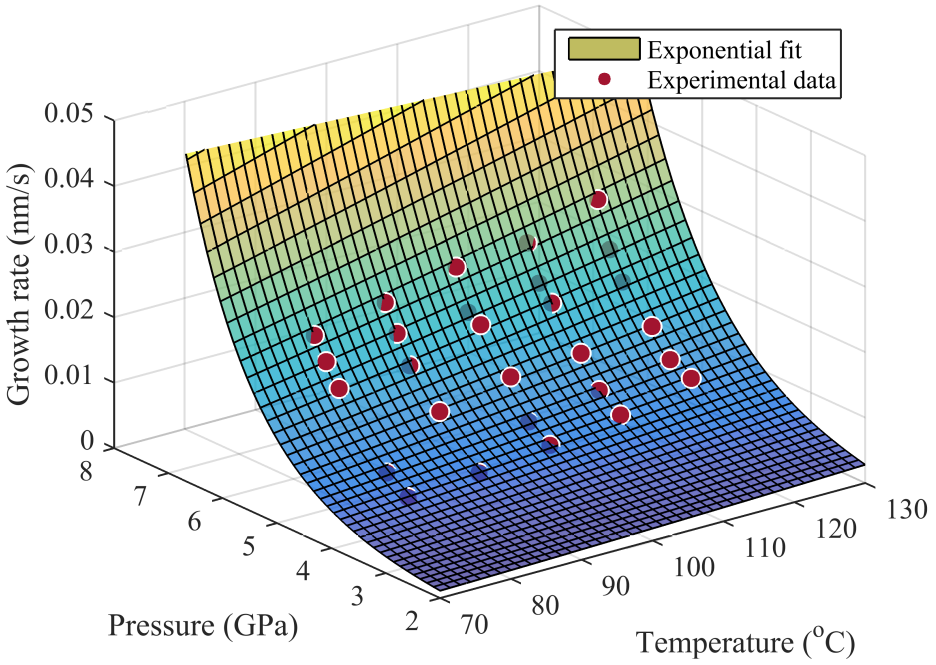

Fig. 7.35 Evolution of the growth rate of the DDP-1 tribofilm formed under different contact pressures and temperatures. The 3D surface was generated using the chemo-mechanical Arrhenius-type model suggested by Gotsmann and Lantz [71].

This indicates that the energy barrier of the DDP decomposition reactions can be lowered primarily using the effect of the contact pressure rather than temperature.

7.3 Summary

An AFM liquid cell was designed and coupled with the AFM to perform in-situ tribological tests at different contact pressures, temperatures and sliding speeds. Using this liquid cell, it was possible to follow and examine the evolution over time of the textural and rheological properties of the ZDDP and DDP tribofilms. Furthermore, it enabled us to study the formation kinetics of these P-based antiwear additives in-situ without altering the sample condition.

The main in-situ AFM results can be summarised as follows:

- Throughout the tribotests, formation-removal hysteresis behaviour is evident. This seems to be induced by the progressive shearing of the interface causing the weakly adhered top layers of the tribofilm to be removed or be reallocated within the central area of the evolving tribofilm.
- The tribofilm formation follows the same deterministic trend especially in the early stages of the tribotest but differences might arise as sliding cycles

increase due to severe mixing and distortion of the individual pads leading to wear and removal of parts of the tribofilm.

- The formed tribofilm during the early stages has a uniform structure as compared to the final stages, which can be attributed to the wear action and the intrinsic deterministic nature of the tribofilm formation.

- Contrary to the generally perceived conception that the P-based tribofilms are rigid, they were found to behave as a viscous polymer, which can deform and flow under shear. The origin of the this behaviour can be attributed to the large contact pressure that can deform the soft tribofilm and squeeze it such that the film moves from the areas of high contact pressure towards the areas near the edges of low contact pressure in order to minimise the experienced shear stresses. The significant implication of this finding is that for the first time it provides a new explanation for the excellent anti-wear properties of the P-based tribofilms. In addition of forming a mechanical barrier, these tribofilms can also deform and flow and thus help mitigate the shear stress at the contacting asperities leading to less wear.

- Once the mature tribofilm was subjected to shear in base oil under mild contact pressure, a small increase of the tribofilm thickness was observed instead of wear despite the low ambient temperature and absence of additive in the base oil. The source of this recovery is hypothesised to originate from the irreversible disruption of the local compactness of the interfacial layers of the tribofilm leading to an increase in the free volume within the phosphate glass forming the tribofilm. This necessary makes the tribofilm loose and more susceptible to wear, which is confirmed by the subsequent decrease in the tribofilm thickness over the sliding cycles until reaching a steady-state thickness.

- The formation and removal cycles appear to be repetitive in nature, i.e. the more the tribofilm is removed, the rougher surface is created, the more the energy available for the next formation phase and the more the tribofilm grows exponentially in the subsequent cycles.

- The high roughness of the tribofilm is the main player inducing the logarithmic formation and removal cycles. The rough peaks on the rubbing surfaces can cleave some of the interface bonds and thus creating more active sites and providing more energy for the succeeding formation outburst. The hastened formation produces thicker but less compact tribofilm layers that can be removed easily under shear.

- The P-based additives cannot adsorb preferentially to the formed tribofilm surface as opposed to the steel surface.
- The data suggest that temperature and contact pressure have a similar effect on the reaction kinetics of the P-based additives, i.e. the higher the temperature or pressure the higher the increase in the growth rate, which follows exponential rate. The similar effect of temperature and contact pressure on the growth rate confirms their potent effect on increasing the additive decomposition process, which can be activated by the availability of either shear or heat.
- For the ZDDP, the effect of temperature and contact pressure seems to have additive effect, e.g. the maximum growth rate occurs when temperature and contact pressure are both maximum. However, the formation rate of the DDP tribofilm increases over contact pressure more prominently than temperature. This implies that within the range of the tested conditions, above a certain threshold of temperature, shear stress alone is enough to cause a complete decomposition of the DDP additive to form a protective tribofilm. Increasing the temperature further does not have a potent effect as opposed to the case of ZDDP, which suggests different reaction pathways with different energy barriers.
- The iron phosphate-based tribofilm is more tenacious than the zinc phosphate-based tribofilm.
- The structure of the tribofilm formed on iron phosphate glass is similar to the one formed on bare steel surface. This indicates that the availability of iron from the substrate, whether steel or iron phosphate, is enough to form a DDP tribofilm consisting mainly of iron phosphate.

In the next chapter, the observations reported in the previous results chapters will be discussed in detail and compared with the available literature in order to develop a mechanistic understanding of the P-based additives' decomposition mechanisms and tribofilms formation.

Chapter 8

Overall discussion

This chapter summarises and discusses the most important findings presented throughout the thesis. The discussion will be centred on the data obtained using a combinatorial approach that aggregates evidence from multiple ex-situ and in-situ experimental techniques. The chapter is divided into ten sections. The first two discuss the decomposition mechanisms of ZDDP and DDP additives, respectively, and the composition of the formed antiwear tribofilms. Section three discusses the formation and removal mechanisms of the formed P-based triboreactive films. Section four to six discuss the effect of the sliding speed, temperature and counterbodies' material on the additives' decomposition mechanisms and formation of the antiwear films. Section seven and eight analyse the reaction kinetics, i.e. activation energy and reaction order, of the ZDDP and DDP additives, respectively. Section nine examines the flowability of the P-based tribofilms and their viscosity quantification. Finally, section ten summarises the main points discussed throughout the chapter.

8.1 ZDDP decomposition mechanisms

8.1.1 Induction period and base layer composition

The initial changes in the adsorbed ZDDP as revealed by XPS (Fig. 5.5) and XAS (Figs. 6.6 and 6.9) surface analyses and MTM-SLIM (Fig. 5.3), which show that sulphur species are formed first followed by phosphate species, suggest the presence of an initial induction period. The duration of this period can last for hours in the case of thermal films whereas it is shortened to only a couple of minutes in the case of tribofilms. This confirms the previous reports [30] that the ZDDP decomposition and tribofilm formation are thermally and mechanically

assisted processes, which can be largely accelerated by rubbing. Therefore, the composition of the thermal films can take much longer time to evolve but eventually can approach the one of the tribofilm [172].

The presence of the induction period has great implications. It has been long suggested that the ZDDP decomposition reaction is multistage, which involves initially the migration of the soft acid alkyl from the hard base oxygen atoms to the soft base sulphur atoms of thiophosphoryl (P=S) according to the following reaction [8]:

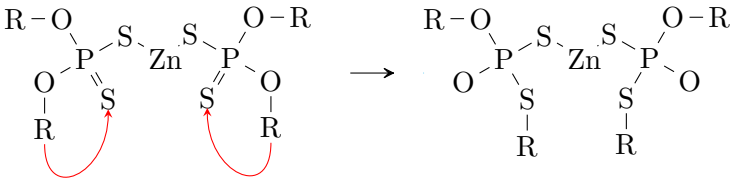

(8.1)

This reaction was also proposed to be followed by the formation of intermediate species before the formation of a phosphorus-rich film on the metal surface [7, 8]. Our results clearly support this hypothesis. The formation of sulphide and sulphate species before the formation of the phosphate-rich film indicates that these sulphur-based species are the main products of the intermediate reactions. These reactions appear to involve primarily the sulphur atoms in the adsorbed ZDDP molecules on the metal surface. This is in agreement with different previous studies [144, 202], which suggested that the formation of the tribofilm starts, even at low temperature, in the solution by forming a sulphur-rich layer deposited on the metal surface. In addition, several other studies proposed that Fe/Zn sulphides [17, 164, 190, 200, 277] and Fe/Zn sulphates [277] can be present at the metal surface. The formation of these species can be a result of the reaction of the adsorbed ZDDP with the hydroxyl (C-OH) and carboxyl (COOH) groups on the steel surface [118], which were identified in the XPS C1s signal (Fig. 5.5) and confirmed by other researchers [236]. The reaction of the adsorbed ZDDP with these groups on the surface can lead to the formation of zinc mercaptide $Zn(SR)_2$ and dithiophosphate PS_2O_2 tetrahedra fragments as intermediates according to the following reaction, which was initially proposed by Yin et al. [118]:

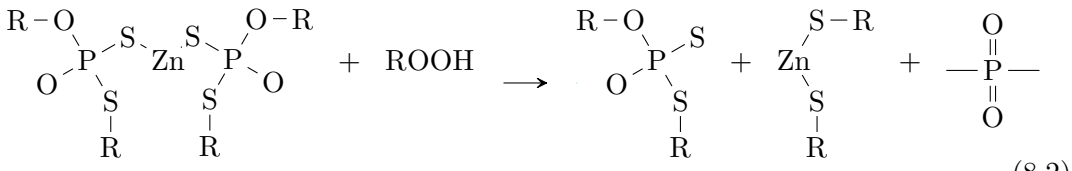

(8.2)

Originally this step was proposed to occur as a possible reaction with peroxides or oxygen. However, as our XAS experiments were conducted under a continuous helium environment, this excludes any role of oxygen originating from the ambient environment in this initial reaction. Nonetheless, dissolved oxygen in the oil can still be involved.

The XPS (Fig. 5.5) and XAS (Fig. 6.11) results indicate that initially sulphate and sulphides, linked to iron and zinc, are formed followed by the reduction of sulphate to sulphide. The results were not conclusive regarding whether these sulphur species are linked to iron or zinc. However, as iron fingerprint appeared in all XPS (Fig. 5.5) and TEM-EDX (Figs. 5.6 and 5.7) spectra of the layer near the steel surface but only in some of the XAS spectra, this indicates that the formed species most likely form patches rather than a continuous layer. In light of this, it is possible that the formed sulphide species originate from the loss of the alkyl groups and the elimination of sulphur from the initially formed zinc mercaptide under heat and chemical reaction with the nascent surface, according to the following reaction:

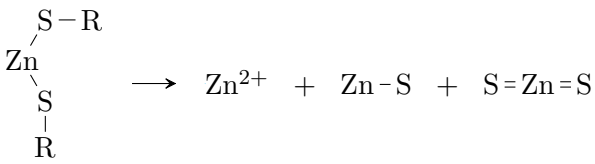

(8.3)

Subsequently, the ligand exchange between Zn^{2+} and Fe^{2+} cations can form FeS and possibly FeS_2 near the metal surface.

A redox reaction between the formed iron sulphides, oxygen and water near the substrate can lead to the generation of atomic hydrogen and the formation of iron(III) hydroxide and sulphate, according to the following reaction:

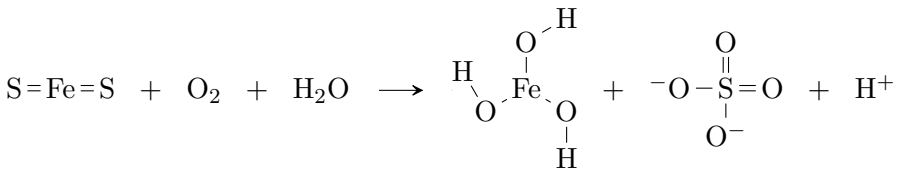

(8.4)

The formed sulphate can combine with the released Zn^{2+} cations from the ZDDP additive to form $ZnSO_4$, as follows:

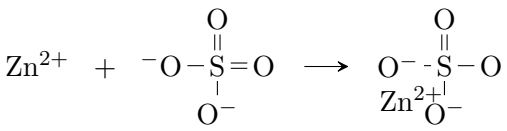

(8.5)

Ultimately, $Zn(SO)_4$ can be reduced into the more stable ZnS, according to the following reaction:

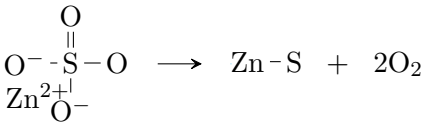

(8.6)

and the formed iron(III) hydroxide can decompose under high temperature and rubbing to form iron(III) oxide and water, as follows:

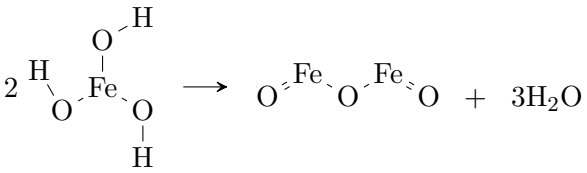

(8.7)

The formation of sulphide or sulphate species in the above reactions seems to be predetermined by the competition between the oxidation and sulphidation processes [356]. In the beginning of the tribotest, oxidation dominates due to the abundance of oxygen in the oil and the easy access to the unprotected oxidised steel surface. This leads to the formation of sulphate species. However, as heating and rubbing continue, sulphidation dominates and forms sulphides only. The formation of sulphides and the reduction of sulphates to sulphides continue until a patchy oxide-sulphide mixed base layer is formed, which is in line with our XAS, TEM-EDX and XPS results discussed before. The formation of this layer was also reported by several previous studies [19, 357–361].

The formed patchy base layer of isolated clusters of mainly sulphides, e.g. ZnS and FeS, on the metal surface, as schematically depicted in Fig. 8.1, can play different vital roles in the decomposition of ZDDP and its adsorption to the surface. Firstly, owing to their higher hardness than the metal oxides [357, 358], they can form a barrier to protect the steel surface from adhesive wear. Secondly, the clusters can act as a bridge or a binder between the subsequent decomposition products, e.g. zinc-polyphosphate, and the metal surface. FeS clusters can also transfer electrons, i.e. accepting and denoting. The ability to transfer electrons and their wide range of reduction potential, i.e. -0.6 V to +0.45 V [362], highlight their utility in the environment where redox reaction can take place. This means that although the metal surface can be covered completely by the tribofilm, redox reaction might continue even at a faster rate. The redox reaction can occur between different areas on the metal surface even if they are far apart through the electron

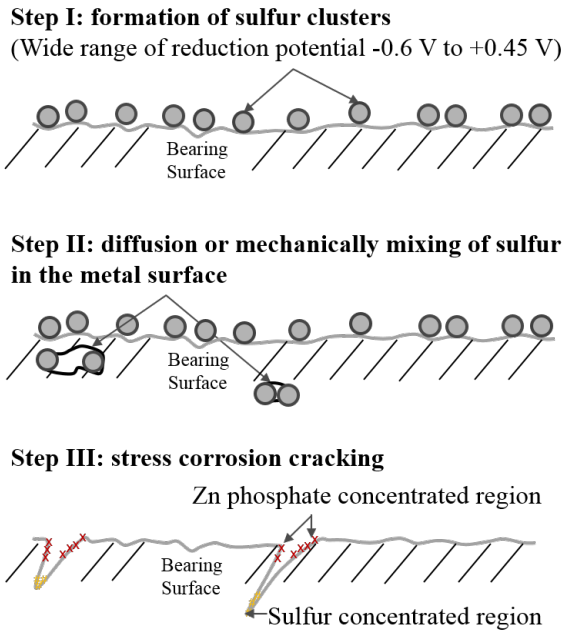

Fig. 8.1 Schematic of the formation of FeS clusters on the metal surface and the diffusion of S into steel, which induces stress corrosion cracking.

exchange via the FeS clusters. This mechanism can explain the increased rate of surface micropitting in rolling contacts lubricated with oils containing sulphur-based additives like ZDDP [236]. A fatigue initiated micropitting promoted by a localised micropitting corrosion on the steel surface seems plausible. Evidence for this mechanism can be found based on the observations of Jahanmir [357] that no sulphur is present in the centre of the pits whereas Martin [19] found that sulphur is present in the wear particles. This indicates that delamination removed the centre of the pit where sulphur is concentrated. The high concentration of sulphur in the centre indicates that sulphur is concentrated in the tip of the subsurface crack where fatigue starts. This suggests that delamination can also be assisted by a possible diffusion of sulphur into the iron grain boundaries and thus promoting fatigue [359].

8.1.2 Tribofilm composition

The XPS results (Fig. 5.5) indicate that iron is absent from the formed polyphosphates layers above the base layer, which agree with different previous studies [151, 157, 163, 164, 166, 168]. The only cation observed was Zn, which was assigned to ZnS and zinc phosphate throughout the bulk layers. The absence of FeS except possibly on the metal surface is in agreement with the results of Zhang et al. [164]. The authors observed the formation of both FeS and ZnS only in the beginning of the tribotest, i.e. after 10 s of rubbing, and ZnS only after

longer rubbing times. They related this behavior to the more favourable reaction to form ZnS. This was also explained by Martin [19] on the basis of the hard and soft acids and bases (HSAB) principle and suggested that FeS can be formed only under severe conditions. On the other hand, our TEM-EDX results (Figs. 5.6 and 5.7) indicate the presence of a minuscule amount of iron in the bulk layers, which is much smaller in concentration than the one found in the base layer near the steel surface. The presence of iron along with zinc in the bulk layers can indicate the presence of mixed Fe-Zn phosphate. This is in agreement with some previous studies [118, 183, 190], which proposed that a mixed Fe-Zn phosphate can form in the bulk. Nonetheless, Yin et al. [118] and later on Crobu et al. [183] have already indicated that the formation of these mixed phosphates of different cations requires much higher temperatures, i.e. above 1300 K, than the one of the oil, i.e. < 400 K, encountered during typical tribotests. Nonetheless, they suggested that the local flash temperature at the contacting sheared asperities can be higher and thus favours such a reaction. The maximum contact temperature T_c can be given using the following formula:

$$T_c = T_b + T_f \tag{8.8}$$

where T_b is the bulk temperature of the oil and T_f is the maximum flash temperature, which for circular contact with Peclet number of about 0.2 can be given as [3]:

$$T_f = 0.222 \frac{\mu U}{K} (p_y W)^{0.5} \tag{8.9}$$

where μ is the friction coefficient, U is the speed of the moving body in m/s, K is the thermal diffusivity in W/mK, p_y is the yield stress of the moving body in Pa, and W is the normal load in N. T_f can also be estimated using the simplified empirical model of Rabinowicz [363], as follows:

$$T_f \approx 100U(1 \pm 3) \tag{8.10}$$

Under the operating conditions of our tests where the sliding and rolling speeds are small, the two previous models are expected to give similar results [364]. It was found that the flash temperature using Eq. (8.9) is about 4.5 ^{o}C, whereas using Eq. (8.10) is about 3.5 ± 10 ^{o}C. Using the upper estimated value of $T_f = 13.5$ ^{o}C, the contact temperature will be less than 93.5 ^{o}C. This suggests that it is likely that no mixed Fe-Zn phosphate can be formed at this low temperature. Nevertheless, it is worth mentioning that the nascent surface due to wear might promote such a reaction. This can be demonstrated based on the observation that the reaction of the nascent surface with sulphur is 1000 times faster than in the

case of surface covered with oxide [361]. Furthermore, even if no mixed Fe-Zn phosphate are formed, the small Fe concentration detected by EDX but not XPS could mean than a small concentration of localised wear fragments is digested within the bulk layers. The digestion of such sharp wear particles is one of the known antiwear mechanisms of ZDDP to reduce abrasive wear [19, 21, 365]. This is further supported by the TEM-EDX results of Ito et al. [200], which similar to our results show that iron is mainly present near the metal surface and its concentration declines sharply just above the base layer where the main bulk of the tribofilm consisting of phosphate glass exists.

The XPS results indicate that initially short chain phosphates are formed followed by longer chains, which is evident from the evolution of BO/NBO, P/O and P/Zn ratios (Table 5.1 and Figs. 5.10 and 5.11). After few minutes of rubbing, the average ratio of Zn:P:O was 1:1:4, which suggests the formation of short chain phosphate of $ZnPO_4$. This can occur as a result of the reaction between the dissolved oxygen in the oil, the newly formed phosphate fragments, Eq. (8.2), and zinc cations, Eq. (8.3), as follows:

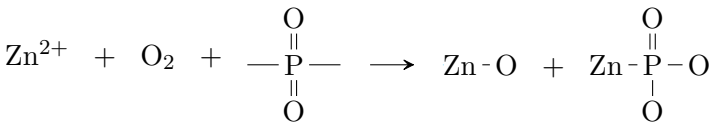

(8.11)

Subsequently, after long rubbing time, i.e. $>$ 20 min, the average ratio of Zn:P:O reached 4:5:10, which suggests the formation of long chain phosphates with a general formula ZnP_nO_{2n+1}. This can originate from the nucleophilic reaction of one hard acid tetravalent phosphorus O−P in one short phosphate segment with a hard base oxygen bonded to another phosphate segment O−P, as follows:

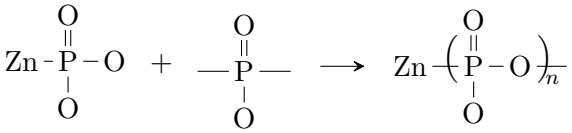

(8.12)

The formation of short chains in the base layer near the metal surface as compared to the long chains in the bulk is in agreement with several previous studies [194–197]. The trend can be related to the excess of metal oxides such as ZnO near the metal surface as compared to the bulk layers, which was verified experimentally using XPS (Figs. 5.8, 5.9, 5.12 and 5.13) and TEM-EDX (Figs. 5.6

and 5.7). Increasing the ZnO content hastens the fragmentation of any formed long phosphate chains, i.e. P−O−P, into shorter chains of P−O$^-$ and P=O. Subsequently, ZnO can compensate the negatively charged fragments by forming weak electrostatic interactions with their terminals [366], such as:

$$\text{P}-\text{O}-\text{P} + \text{ZnO} \longrightarrow \text{P}-\text{O}^- \cdots \text{Zn}^{2+} \cdots {}^-\text{O}-\text{P} \tag{8.13}$$

Other studies [186] attributed the reduced chain length near the metal surface to the shear stress between the contacting surfaces possibly cleaving the long phosphate chains into shorter ones and to severe surface wear that can remove the long phosphate chains from the surface. However, as our experiments were performed under nearly rolling conditions, i.e. 5% SRR, during which wear was insignificant (Fig. 5.4), this indicates that other factors than the shear stress could play a role. Apart from ZnO, various studies [19, 20, 183] suggested that in the presence of iron oxide or water any formed long phosphate chains are depolymerised into short ones of Fe-Zn phosphates. This can explain the short phosphate chains and large concentration of iron detected in the base layer near the metal surface compared to the long phosphate chains and small iron concentration in the bulk layer.

8.1.3 Effect of water

Water seems to affect the decomposition reaction of the ZDDP additive and its formed tribofilm selectively. For instance, in the presence of water in the oil, the XPS results indicate that the equilibrium concentrations of O (Fig. 5.14) and S (Fig. 5.15) are nearly unchanged. However, water decreases the equilibrium concentration of P (Fig. 5.16) and increases the one of Zn (Fig. 5.17) by about 38%. Furthermore, for all the components of the tribofilm, water appears to increase the reaction rate k substantially between 15–175%, which suggests that the decomposition reaction is faster. This is in line with the results of Rounds [169], which showed that water accelerates the rate of ZDDP decomposition and the formation of the tribofilm. In agreement with these findings, few studies suggested that the ZDDP decomposition is hydrolytic in nature, i.e. accelerated by water. For example, Spedding and Watkins [137] showed that in the absence of water, e.g. by heating the sample up to 100-170 ^{o}C in order to evaporate all water in addition to flooding the sample with dry nitrogen, the decomposition reaction was suppressed. In contrast, when the sample was flooded with water-saturated nitrogen, a rapid decomposition rate was observed. Nevertheless, it should be noted that when the tests were conducted at 200 ^{o}C, at which most of the water

should evaporate, the decomposition proceeded without any significant reduction in the reaction rate. Willermet et al. [24] argued that even a lower temperatures than 200 ^{o}C could not slow down the reaction rate, which challenges the premise of the hydrolytic decomposition mechanism.

The increased ZDDP decomposition rate in the oil containing water contradicts the widely perceived idea that water competes with the ZDDP molecules on the steel surface and thus decreases the decomposition rate [33, 236]. It also contradicts the observed delay in the growth of the tribofilm thickness shown in Fig. 5.3. To resolve this discrepancy, the effect of water on not only the tribofilm composition but also its thickness should be examined collectively rather than individually. Although Fig. 5.3 showed that water delays the growth of the tribofilm, the atomic concentration of O shown in Fig. 5.14, which initially consists of mainly metal oxides, decreases in the presence of water particularly during the running-in period. This may suggest that in the presence of water either less metal oxides are present on the steel surface, or a slightly thicker tribofilm is initially formed that masks the signal of the metal oxides. The latter seems more plausible as no change in the metal oxide concentration was observed in the absence or presence of water, whereas a decrease in the oxygen concentration by 5–7% was observed in the presence of water. In addition, the evolution of the tribofilm thickness shown in Fig. 5.3 indicates that in the early stage of the tribotest and in the presence of water the tribofilm is slightly thicker. Hence, it can be concluded that in the beginning of the running-in period, i.e. near the steel surface, water accelerates the decomposition of ZDDP and thus increases the thickness of its tribofilm, however, slightly.

The fast decomposition reaction in the presence of water leads to a faster reduction in the concentration of the decomposition products. This in turn leads to an early termination of the reactions forming the subsequent layers of the tribofilm, which is evident from the early approach to the steady state concentrations as indicated by the larger reaction rate k. Hence, water does not seem to hinder the formation of the early base layers on the steel surface nor the adsorption of ZDDP molecules. However, it can impede the formation of the subsequent layers possibly due to the lack of the available reactants.

8.1.3.1 Composition of base sulphur layer

The enhanced decomposition reaction in the presence of water discussed in the previous section can be related to possible changes on the steel surface induced by water. In the beginning of the tribotest, the steel surface was found to be

covered with hydroxyl (C−OH) and carboxyl (C=OOH) groups whether water was absent from or present in the oil (Fig. 5.5). Nevertheless, the presence of water was found to increase the abundance of these groups on the surface, which can affect the decomposition of ZDDP and its reaction with the steel surface. This is in accordance with the ZDDP decomposition reaction proposed by Yin et al. [118], which suggested that the COOH groups and possibly O_2 can react with the adsorbed ZDDP to form zinc phosphate and other sulphur species. Amongst the different sulphur species that can be formed on the steel surface, $FeSO_4$ was found to be formed initially. This is in agreement with several previous studies [33, 236, 367], which identified $FeSO_4$ after short rubbing time. However, these studies detected sulphate only in the presence of water whereas our results suggest that $FeSO_4$ can also be formed in the absence of water, which is in agreement with the results of Yin et al. [118]. Therefore, it seems that water can enhance the formation of sulphate as a result of the increased concentration of surface groups such as COOH.

The increased concentration of the sulphur species on the steel surface in the presence of water can explain the increased density of the surface micropits observed on the surface, which was also observed by Nedelcu et al. [236]. This can be due to a fatigue initiated micropitting promoted by a localised micropitting corrosion by sulphur on the steel surface.

8.1.3.2 Composition of phosphate bulk layers

Water appears to largely affect the concentrations of the P and Zn as shown in Figs. 5.16 and 5.17, which are the main elements forming the tribofilm's layers of zinc phosphate. In the presence of water, the formation of Zn was accelerated whereas P was decelerated. These changes can be explained by examining the progression of Δ, which is the difference in binding energy of Zn3s and P2p, over rubbing time as shown in Fig. 8.2. As Zn3s is largely insensitive to changes in the chain length of zinc phosphate [183, 191, 192], Δ can help determine the chemical changes associated with P while avoiding any uncertainties related to the calibration of the spectra [192]. In the absence of water, the binding energy increases in general with the continued rubbing. This indicates that a transformation occurs to the P species such as the polymerisation of the short phosphate chains to longer ones. However, in the presence of water, the binding energy during the running-in period appears to be constant. With the continued rubbing, a decline in the binding energy occurs suggesting that a depolymerisation reaction of the phosphate chains seemed to occur. This decrease in the binding energy in the presence of water appears to be the general trend over the different

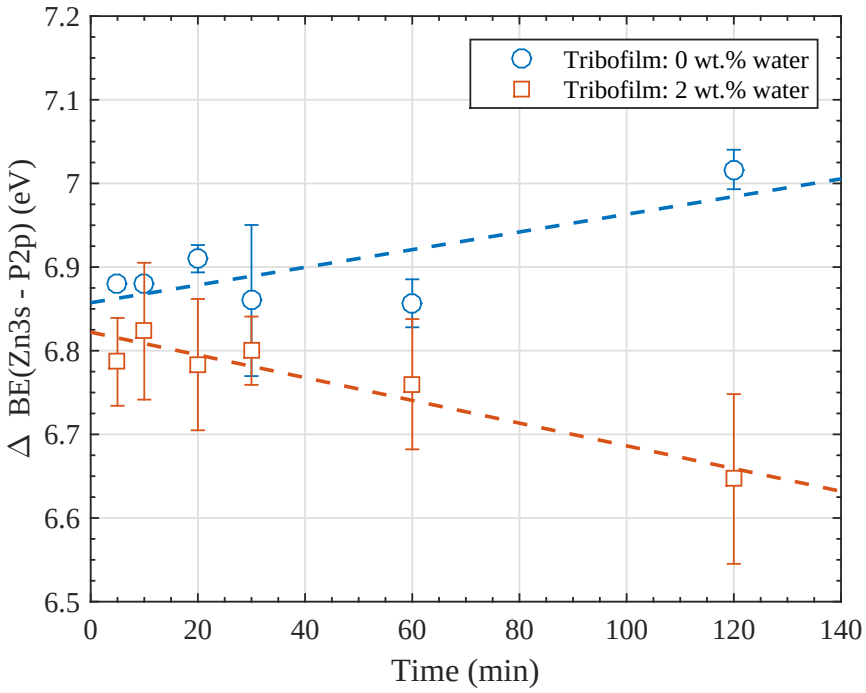

Fig. 8.2 Effect of water on the difference in binding energy between Zn3s and P2p of the top 5–7 nm of the tribofilm over rubbing time.

rubbing times. However, these results are in contrast with the results of Cen et al. [33] and Nedelcu et al. [236] who observed that the binding energy of P2p does not change in the presence of water, which suggested that water hinders the polymerisation of the short phosphate chains.

The transient behaviour observed in our results can be related to a combined effect of changes occurring in the tribofilm composition as well as to changes in the water concentration in the oil. Water initially hinders the transformation of P species during the running-in period. However, as water evaporates continuously from the oil (Fig. 5.2), polymerisation starts to occur. Nevertheless, the polymerisation reaction appears to terminate earlier than the case in which water in absent, as shown in Figs. 5.16 and 5.17. Furthermore, the presence of water seems to induce defects in the formed phosphate chains that make them more susceptible to breakage, i.e. water accelerates chains scission. This is evident from the fact that in the presence of water, the concentration of P never reaches the same terminal value as in the absence of water and nor does its binding energy. This indicates that water does not only retard the polymerisation reaction while it is present in the oil but it also changes the formed tribofilm even after it evaporates from the oil. Thus, the results suggest that the initial alteration of the tribofilm occurring due to the presence of water during the running-in period cannot be reversed even if water is removed from the oil in the subsequent stages. The most probable explanation for this could be related to the formation of a single or multiple bridges

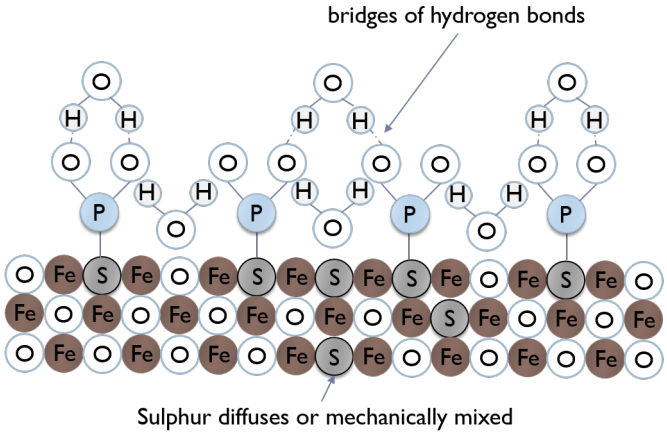

Fig. 8.3 Schematic of the caging effect of water on the initially formed phosphate species and the subsequent formation of a single and multiple bridges of hydrogen bonds between water molecules and PO_2^- groups of the decomposed ZDDP.

between water molecules and PO_2^- groups of the decomposed ZDDP, as shown in Fig. 8.3. This caging of the PO_2^- groups hinders their chemical reactivity greatly, which leads to the formation of short orthophosphate PO_4 segments. The short segments can be terminated easily by the available ZnO, which has higher concentration than if water is absent. The evaporation of water from the oil reduces the number of bridges between water molecules, PO_2^- groups and PO_4 segments, which results in the formation of longer phosphate chains. However, the increased concentration of Zn seems to oppose this effect by forming weak electrostatic interactions with the terminals of the short phosphate fragments to compensate their negative charge.

8.1.3.3 Length of phosphate chains

The polymerisation number n can be estimated by assuming that the zinc phosphate has the general formula $Zn_{n+2}[P_nO_{3n+1}]_2$ for odd n and $Zn_{(n+2)/2}P_nO_{3n+1}$ for even n [19]. In this case, n can be related to the ratio of bridging to non-bridging oxygen (BO/NBO) as follows [368]:

$$\mathrm{BO/NBO} = \frac{1}{2}\frac{n-1}{n+1} \tag{8.14}$$

However, as water can be present in the oil especially during the early stage of the tribotest, this ratio is likely to be prone to error. One way to check this is by calculating the BO/NBO ratio based on the difference in the binding energy Δ between XPS signals of Zn3s and P2p [192], as follows:

$$\Delta = \Delta_0 - \frac{3}{2}\frac{\mathrm{BO}}{\mathrm{NBO}} \tag{8.15}$$

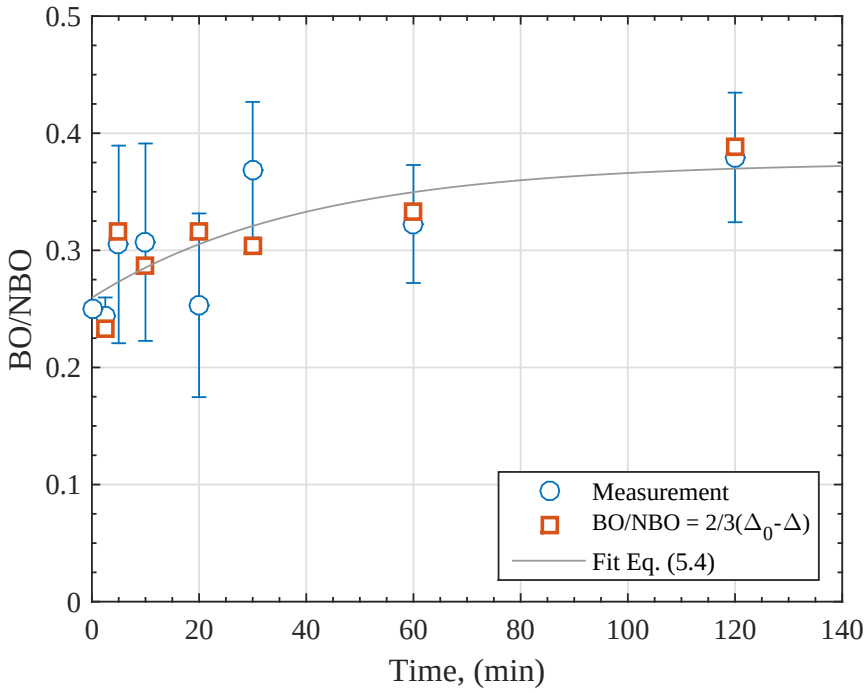

Fig. 8.4 Comparison between the measured and calculated polymerisation number n in the absence of water in the oil.

where Δ_0 is the binding energy difference in the case of short orthophosphate chains, i.e. at the limit of BO/NBO approaches zero, which can be taken as a free fitting parameter. Figs. 8.4 and 8.5 compares the BO/NBO estimated from direct fitting of O1s signal and using Eq. (8.15). The ratios estimated based on these methods appear to follow the same trend over time. Therefore, it is possible to use the latter method to check the accuracy of the O1s signal fitting. This should reduce the uncertainty associated with the fitting and thus improves the accuracy of the chain length identification.

More insight into the changes in the chain length due to the presence of water can be found by following the evolution of the BO/NBO ratio, Δ and n simultaneously over rubbing time. The effect of water on this evolution is shown in Fig. 8.6. The small range of Δ and its small values due to the presence of water confirm that water significantly hinders the growth of the phosphate chains. This also confirms the previously discussed two effects of water on the phosphate growth. Firstly, water can terminate the polymerisation reaction in the early stages of rubbing and hence the chain length does not grow. Secondly, water can result in weaker long chains that can be easily depolymerised into shorter ones. The trend of the chain length evolution suggests that the two mechanisms occur simultaneously.

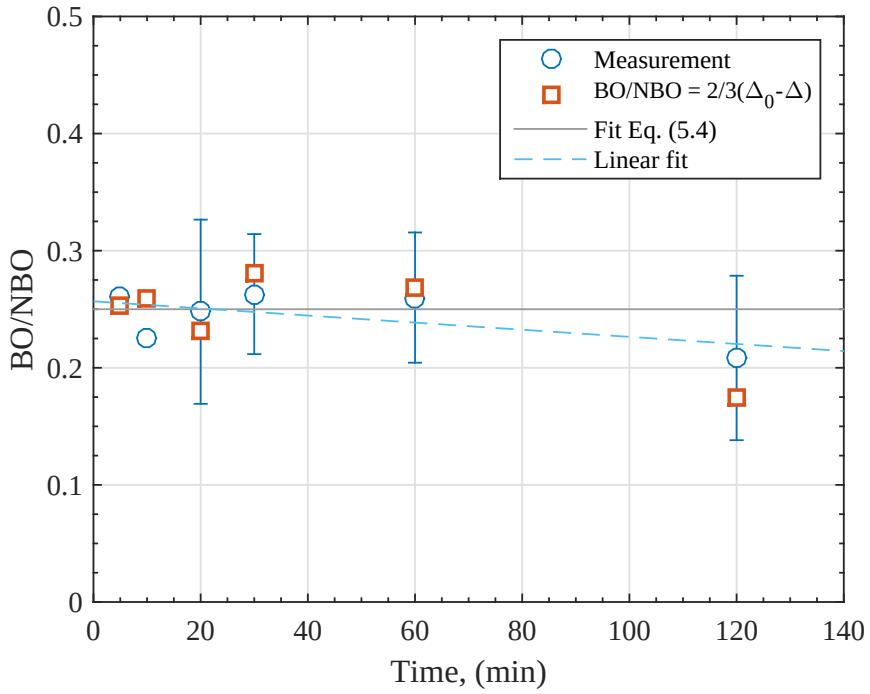

Fig. 8.5 Comparison between the measured and calculated polymerisation number n in the presence of water in the oil.

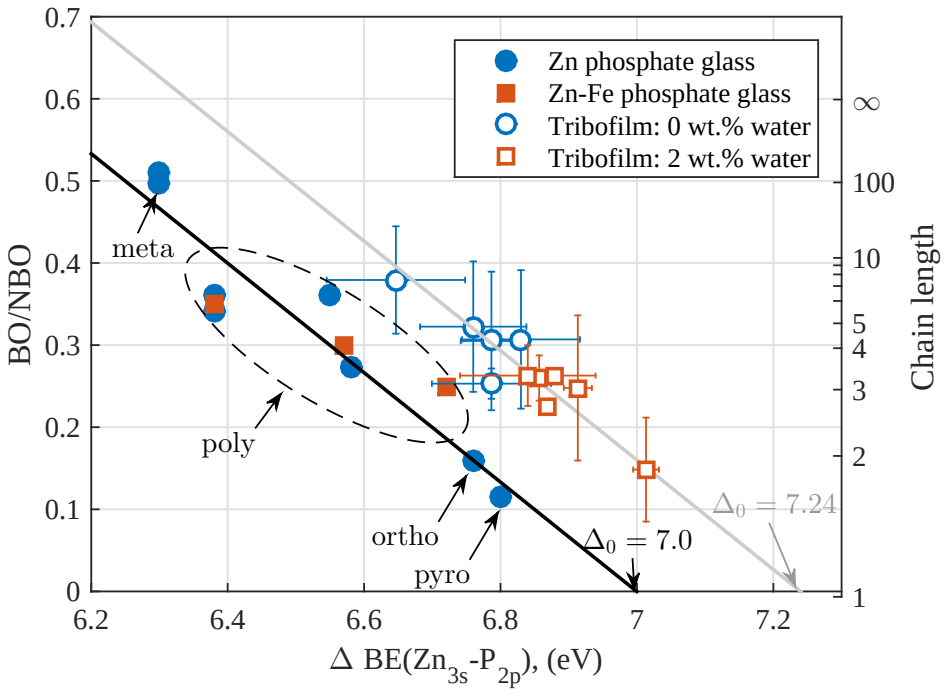

Fig. 8.6 Effect of water on the evolution of the BO/NBO ratio, binding energy difference Δ between Zn3s and P2p, and chain length n over rubbing time.

8.2 DDP decomposition mechanisms

The DDP additive decomposition process was found, in general, to be similar to the one of the ZDDP additive. The XAS results indicate that in the case of DDP-I (Figs. 6.32 and 6.33) or DDP-II (Figs. 6.36 and 6.37) additive a large formation of sulphates species occurs initially. This can be related to the rapid reaction of the DDP with the substrate covered with oxides, which leads to the oxidation of the sulphur species into iron sulphate [182]. This was confirmed previously for both neutral and acidic DDPs [198]. As rubbing progresses, a continuous consumption of the sulphate occurs to form more stable sulphide species. The formation of sulphides is in line with the results of Zhang et al. [164] suggesting that the DDP additive forms mainly FeS. The observed sulphides in the case of DDP, which is in contrast to the previously discussed studies suggesting final sulphates species, can be related to the different operating conditions used while generating the various tribofilms. For instance, previous studies [127, 181] showed that under high contact pressure, DDP tribo- or thermal films contain Fe sulphate near the steel surface whereas under less harsh conditions initially mixed iron sulphide, such as FeS and FeS_2, and sulphate, such as $FeSO_4$, are formed where the sulphides can oxidise over rubbing time yielding primarily sulphates at the end.

After the formation of the oxide-sulphide mixed layer, phosphate starts to form whether in the case of DDP-I (Figs. 6.30 and 6.31) or DDP-II (Figs. 6.34 and 6.35) additive. Over rubbing time, the composition of the DDP tribofilms shows minor changes, which seems to consist mainly of short chains of iron polyphosphate [127, 136, 164, 179, 180]. This is unlike the progressively evolving ZDDP tribofilms consisting of longer zinc polyphosphate chains. The short chains formed in the case of DDP can be primarily related to the rapid reaction of the DDP molecules with the substrate covered with iron oxides, which induces a significant depolymerisation effect on the formed iron phosphate chains that ultimately limits their growth considerably [181].

In summary, for the case of the DDP additive rubbed between uncoated bare steel surfaces, the results suggest that its decomposition reaction is similar to one of ZDDP and consists of multiple steps including the formation of several intermediates, as follows:

i. Prior to any tribofilm formation, the unreacted DDP adsorbs to the steel surface. The maximum adsorption occurs when the two sulphur atoms of every molecule are near the substrate.

ii. The adsorbed molecules decompose partially by losing sulphur, which is oxidised at once into sulphates due to its reaction with the oxides on the substrate or the dissolved oxygen and water in the oil. The sulphate formation is favoured in the beginning of the tribotest due to surface smearing and wear during the initial running-in period, which result in a sufficiently high temperature at the contacting asperities for the reaction to occur.

iii. As rubbing continues and the running-in period ends, the local temperature at the asperity-asperity contacts drops below the critical temperature needed for the sulphate formation and therefore the more stable sulphide is formed instead.

iv. The adsorbed molecules decompose completely to form phosphate species in the form of a two-dimensional network of short chain iron phosphate undergoing minor changes over time [127, 136, 164, 179, 180].

After this, a balance seems to occur between the tribofilm formation and removal that keeps the phosphate glass composition and tribofilm thickness relatively constant during the tribotest period.

8.3 Tribofilm formation/removal cycles

The formation of the main bulk of the P-based tribofilms, consisting of zinc-, iron-, or mixed zinc-iron-polyphosphates, was found to undergo several growth and removal cycles whether in the case of ZDDP (Figs. 7.10 to 7.12) or DDP additives (Figs. 7.22 to 7.28). Every removal cycle seems to leave a rough tribofilm surface. The rough surface contains various sharp protrusions, which might behave as seeds for the succeeding tribofilm layers to grow with much faster kinetics. The extra energy for this fast growth becomes available from the broken dangling bonds of undercoordinated atoms [369] and the creation of nascent surface of high reactivity from the preceding removal cycle [370]. If the tribofilm is always smooth, no hastened formation would occur and thus no removal (Fig. 7.13). That is because the hastened formation produces thicker but less compact tribofilm layers that can be removed easily under shear. However, steady formation results in a more compact tribofilm as it takes more time to grow and thus steady local reconfigurations are possible leading to better accommodation of the newly formed layers and thus high compactness. This was evidenced from the recovery of the tribofilm thickness when rubbed under high contact pressure in base oil without ZDDP (Fig. 7.9) or DDP additive (Fig. 7.30). The recovery can originate from

the irreversible disruption of the local compactness of the interfacial layers of the tribofilm leading to an increase in the free volume within the phosphate glass. This necessary makes the tribofilm loose and more susceptible to wear. Thus, the decompressing effect of contact pressure on mature tribofilms appears to be counter-productive compared to the case of immature tribofilms in which contact pressure acts to compact the loose top layers of the ZDDP or DDP decomposition products into solid polyphosphates [36].

8.4 Effect of countersurfaces

To study the effect of the substrate on the formation of ZDDP and DDP tribofilms, in-situ tribotests were performed on various substrates including AISI 52100 bearing steel, H-DLC coated surfaces and different glasses of zinc-, iron- and mixed zinc-iron phosphates. This along with the different additives used, i.e. ZDDP and DDP, will also enable us to study the role of cations in the decomposition of the P-based antiwear additives and the formation of their tribofilms.

8.4.1 ZDDP additive

The ZDDP additive can decompose easily to form tribofilms on bare steel surface under different operating conditions (Figs. 7.18 and 7.19). Similarly, in the case of the ZDDP additive being rubbed between counter-bodies coated with non-doped H-DLC, the XAS results (Figs. 6.20 and 6.21) showed that the additive seems to react with the coating to form a protective tribofilm. However, the in-situ AFM results (Fig. 7.21) showed that no apparent tribofilm was observed on the DLC coated steel surface.

The formation of a tribofilm on DLC coatings even without containing any doped cations as suggested by the XAS results is in line with several previous studies [31, 32, 211–215]. However, other studies found that no tribofilms can be formed on non-doped DLC coatings without metallic cations [216–221], which is in line with the in-situ AFM results. The main factor behind the wide disparity between the formation and absence of tribofilms on DLC coatings appears to be related to the tribofilm tenacity. In agreement with several previous studies [31, 32, 211], our XAS results suggest that the tribofilms formed on DLC-DLC contacting surfaces are less tenacious than the ones formed on steel surfaces. Such low tenacity causes the tribofilm to be removed easily. Furthermore, the absence of iron oxide in the formed tribofilms on DLC surfaces appears to greatly retard the consumption of the sulphate to form sulphide species (Figs. 6.22 and 6.23).

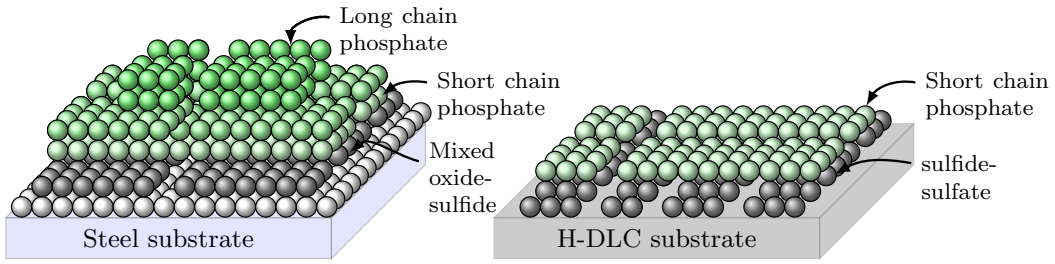

Fig. 8.7 Schematic of the tribofilms formed on bare steel (left) and DLC coated surfaces (right).

This suggests that the low tenacity to the surface can be related to the absence of a mixed oxide/sulphide base layer. This layer seems to act as a glue joining the substrate with the subsequently formed phosphate layers composing the main bulk of the tribofilm. It follows that any formed tribofilm on DLC coatings, especially if non-doped, is likely to be weakly adhered leading to its effortless removal under rubbing once formed. The structure of the formed tribofilm on the DLC coating in comparison to the one formed on bare steel surfaces is shown in Fig. 8.7.

Another explanation for the absence of formed tribofilms on DLC coatings was provided by Kalin and Vižintin [224] who suggested that the additive reaction with the substrate has different energy activation barriers depending on the surface whether doped or non-doped DLC or steel substrate. The difference in the activation barrier was attributed to the low thermal conductivity of the non-doped DLC (0.3 to 3.5 W/mK [353]) in comparison to steel (>50 W/mK [354]) or metal doped-DLC. The low conductivity of the non-doped DLC can lead to lower contact temperature that impedes or slows the additive decomposition and the tribofilm formation.

8.4.2 DDP additive

As expected, it was possible to form DDP tribofilms on bare steel surface under different operating conditions (Figs. 7.33 and 7.34). It was also possible to form a tribofilm on the iron phosphate glass (Fig. 7.31b) at high temperature and contact pressure. The structure of the formed tribofilm was similar to the ones generated on bare steel surfaces. This indicates that the availability of iron from the substrate, whether steel or iron phosphate, was enough to form a DDP tribofilm consisting mainly of iron phosphate. As the thermal conductivity of the phosphate bulk ranges from 0.2 to 2.3 W/mK [355] whereas for steel is about 50 W/mK [354], the ability to form a tribofilm on the phosphate glass contradicts the hypothesis of Kalin and Vižintin [224] that a substrate with a high thermal

conductivity is required for the formation of P-based tribofilms. They based this argument on the observation that non-doped DLC coatings, which have low thermal conductivity, lacks the ability to form protective tribofilms in comparison to steel. This indicates that the other plausible reason is mainly related to the difference in tenacity as discussed earlier.

No tribofilm formation was possible on zinc and mixed zinc and iron phosphate glasses (Figs. 7.31c and 7.31d). The inability to form a DDP tribofilm on these glasses is peculiar. The available zinc or zinc and iron cations were expected to be sufficient to induce the formation a tribofilm of zinc or iron phosphate. One possible explanation for this is related to our previous conclusion that the iron phosphate-based tribofilm is more tenacious than the zinc phosphate-based tribofilm. It follows that any formed phosphate-based tribofilm on the zinc or mixed zinc and iron glass could be too weakly adsorbed to withstand the applied shear stresses and thus is worn away at the moment being formed.

8.5 Effect of sliding speed

The changes in the growth rate of the ZDDP at 80 ^{o}C and 7.2 GPa as a function of the scanning speed and sliding time per cycle are shown in Fig. 8.8 during the in-situ AFM tribotests. The results show that the speed does impact the reaction kinetics. However, the apparent increase in the formation rate over speed is primarily related to the decreased sliding time per cycle, as shown on the same Fig. 8.8 rather than a genuine effect of the speed or shear rate. This is further confirmed in the inset of Fig. 8.8, which shows that if the growth rate is measured per cycle instead of per time, the speed has a negligible effect on the kinetics. This is somewhat expected as Clasen et al. [311] using the micro-gap rheometer showed that the shear stress in the boundary lubrication regime is independent of the shear rate and depends only on the friction coefficient, which is constant in this regime, and the applied normal force on the contacting asperities, which was constant during the in-situ tribotests at the various tested speeds. This is also in line with the results of Shimizu and Spikes [245] that in the mixed sliding and rolling condition, the formation rate of the ZDDP tribofilm is less sensitive to the exact SRR, which indicates that shear stress rather than the rate is the controlling parameter. However, they interpreted the data as the rubbing time is far more important than the sliding distance.

Our data seem to suggest that in the boundary lubrication regime the growth rate is less sensitive to the sliding speed and is only dependent on the sliding cycles.

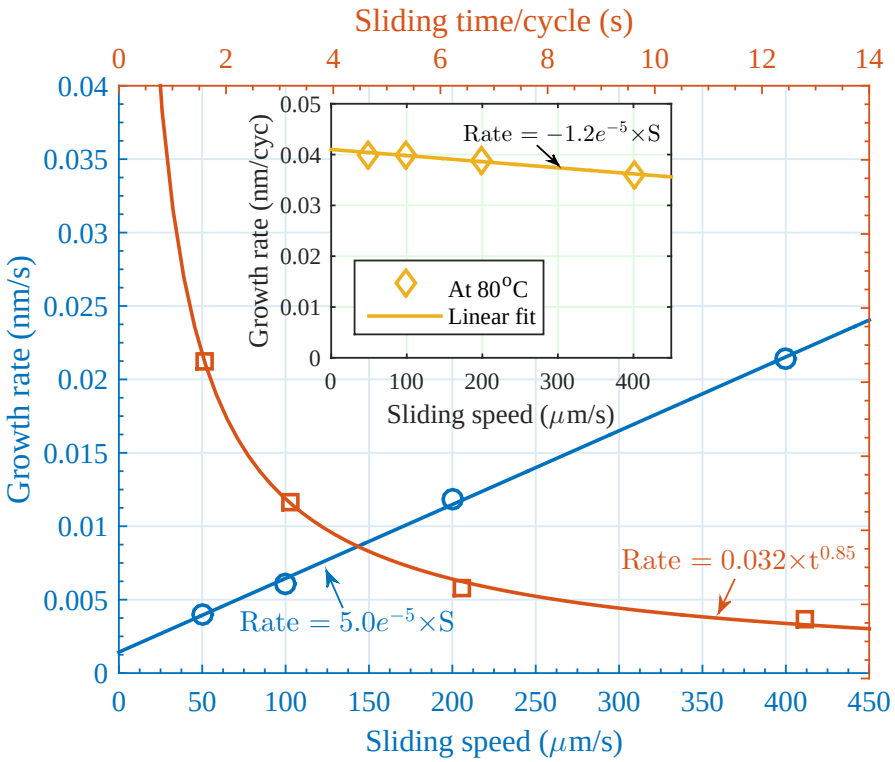

Fig. 8.8 Evolution of the growth rate of the ZDDP tribofilm formed at 80 ^{o}C and 7.2 GPa over different sliding speeds.

This is an interesting result as it indicates that the growth occurs accumulatively in a layer-by-layer fashion, i.e. every rubbing cycle regardless of its timing adds one layer of a certain thickness depending on the other operating conditions of temperature and contact pressure.

Similar conclusion can also be drawn for the case of DDP additive based on the growth pattern of its tribofilm (Figs. 7.25 to 7.28) that initially the edges of the formed tribofilm appears to be thicker than the areas in the middle. The thick areas near the edges appear to be formed due to the overlapping between the scanning lines, which results in larger effective sliding cycles than the case away from the edges.

8.6 Effect of temperature and contact pressure

The decomposition reaction of ZDDP was found to be activated using heat and/or shear at high contact pressure (Fig. 8.9a). The synergy between these two factors appears to have an additive effect on the growth rate of the ZDDP tribofilm, i.e. the growth rate increases equally with temperature or contact pressure.

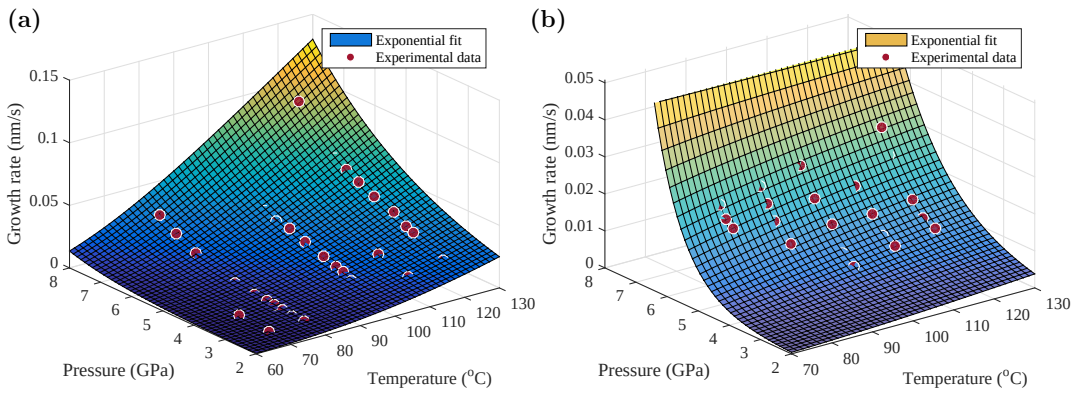

Fig. 8.9 Evolution of the growth rate of (a) ZDDP and (b) DDP-1 tribofilms formed under different contact pressures and temperatures. The 3D surfaces were generated using the chemo-mechanical Arrhenius-type model suggested by Gotsmann and Lantz [71].

However, for the case of the DDP additive, contact pressure causes much larger increase in the growth rate in comparison with the mild increase caused by temperature (Fig. 8.9b). Thus, it appears that above a certain threshold of temperature, shear stress alone is enough to cause a complete decomposition of the DDP additive to form a protective tribofilm. Beyond this threshold, temperature seems to have a minor effect on the growth rate. The trend indicates that the energy barrier of the DDP decomposition reactions can be lowered primarily using the potent effect of the contact pressure rather than temperature.

The reaction kinetics and activation energies of the decomposition reactions of the ZDDP and DDP additives will be discussed in detail in the subsequent section.

8.7 Reaction kinetics of ZDDP tribofilms

8.7.1 Activation energy

Based on how the decomposition reaction of the ZDDP additive behaves under temperature and contact pressure (Figs. 7.20 and 8.9a), it can be considered to follow the chemo-mechanical Arrhenius-type model suggested by Gotsmann and Lantz [71] and discussed in detail in section 2.1.2: Eqs. (2.9) and (2.10), which reads:

$$k\left(T,P\right)=A\left[\exp\left(-\frac{E_a\left(P\right)}{k_{\mathrm{B}}T}\right)\right] \tag{8.16}$$

where A is the pre-exponential constant in the Arrhenius equation depending on the attempt frequency that is of the same order as the atomic vibration and the lattice parameter, k_{B} is the Boltzmann constant, T is the absolute temperature and E_a is the activation energy, which considering the second-order effects of the shear stress on the shape of the energy profile, can be given by [143]:

$$E_a\left(P\right) = E_0 - \mu P A_r \Delta x + \frac{\mu^2 P^2 A_r^2}{2}\left(\xi_{\mathrm{I}} - \xi_{\mathrm{T}}\right) \tag{8.17}$$

where E_0 is the nominal activation energy at no applied contact pressure, P, μ is the friction coefficient, A_r is the reactant area at which the contact pressure is applied, Δx is the activation length from the reactant state at $x = 0$ to the transition state along the reaction coordinate, ξ_I and ξ_T are the curvature values of the initial and transition states along the reaction coordinate, which can be given as follows:

$$\xi_{\mathrm{I}} = \frac{2\Delta x^2}{E_0 \pi^2}\left(\frac{1+r}{1-r}\right)^2 \tag{8.18}$$

and

$$\xi_{\mathrm{T}} = -\frac{2\Delta x^2}{E_0 \pi^2}\left(\frac{1-r}{1+r}\right)^2 \tag{8.19}$$

where $|r| \leq 1$ is the potential shape parameter, e.g. $r = 0$ represents a gradual transition from the reactant to the transition state whereas $r = 1$ represents a sharp step like transition [371]. This parameter is not known although a priori assumptions can be made. For instance, previous experimental results [30, 142] suggested that the contact pressure reduces the nominal activation energy of the ZDDP decomposition reaction linearly, which indicates that within the experimental certainties: $r < 0.7$ [143]. It follows that the higher order quadratic term of Eq. (8.17), which consists of small quantities multiplied and all raised to the power of two, is likely to be negligible.

To fit Eqs. (8.16) and (8.17) to the experimental data, we need to make few assumptions. First, the pre-exponential factor, A, can be assumed to represent the frequency at which the reactant molecules cross the energy barrier into the transition state along the reaction coordinate. Considering that the distance from the reactant to the transition state is Δx and the molecules speed to be equally given by:

$$\nu = \sqrt{\frac{8k_{\mathrm{B}}T}{\pi\mu}} \tag{8.20}$$

where μ is the effective mass, then the molecule frequency can be given by:

$$f_{\mathrm{a}} = \alpha\frac{\nu}{\Delta x} = \alpha\sqrt{\frac{8k_{\mathrm{B}}T}{\pi\mu}}/\Delta x \tag{8.21}$$

where α is a correction factor for the uncertainties related to the determination of both ν and Δx, which can be limited to $\pm 10\%$ of the nominal frequency value. The above relation is consistent with the oscillation frequency of the bond that is broken from the reactant, which is of the order:

$$f_{\mathrm{a}} \approx \frac{k_{\mathrm{B}}T}{h} \approx 10^{13}\,\mathrm{s}^{-1} \tag{8.22}$$

where h is the Plank constant.

The second assumption is related to the adsorption of the ZDDP molecules to the metal surface. This can be assumed to occur with a maximum coverage when the ZDDP molecule is flat on the surface, which means that the four sulphur atoms lay near the surface. Thus, considering the standard structure of the ZDDP with average bond length of 2 Å [372, 373], it follows that the effective area A_r can be taken as 0.94 nm^2 per ZDDP molecule [199]. A similar value of 1 nm^2 was suggested by Zhang and Spikes [142] and also supported by our ex-situ surface analysis and the results of several previous studies [200–202, 238], which indicated that the concentration of sulphur chemisorption products are higher on the steel surface as compared to the bulk of the tribofilm. This suggests that the ZDDP decomposition starts with the four sulphur atoms near the surface, which is consistent with our proposed assumption.

The third assumption is related to the friction coefficient μ, which can be taken as 0.1 such that it matches the average in-situ and ex-situ values obtained of ZDDP tribofilms.

The fit of Eqs. (8.16) and (8.17) to the experimental data starts with three fitting parameters, i.e. α, E_0 and Δx while ignoring the second quadratic term of Eq. (8.16). This is necessary for two reasons. First, in order to accurately estimate Δx and second, to be able to assess the significance of the quadratic term when compared to the results without including it. The fitting results are shown in Fig. 7.20. Same fit was obtained with and without the quadratic term, which indicates that the ZDDP decomposition reaction has the familiar Sine-Gordon

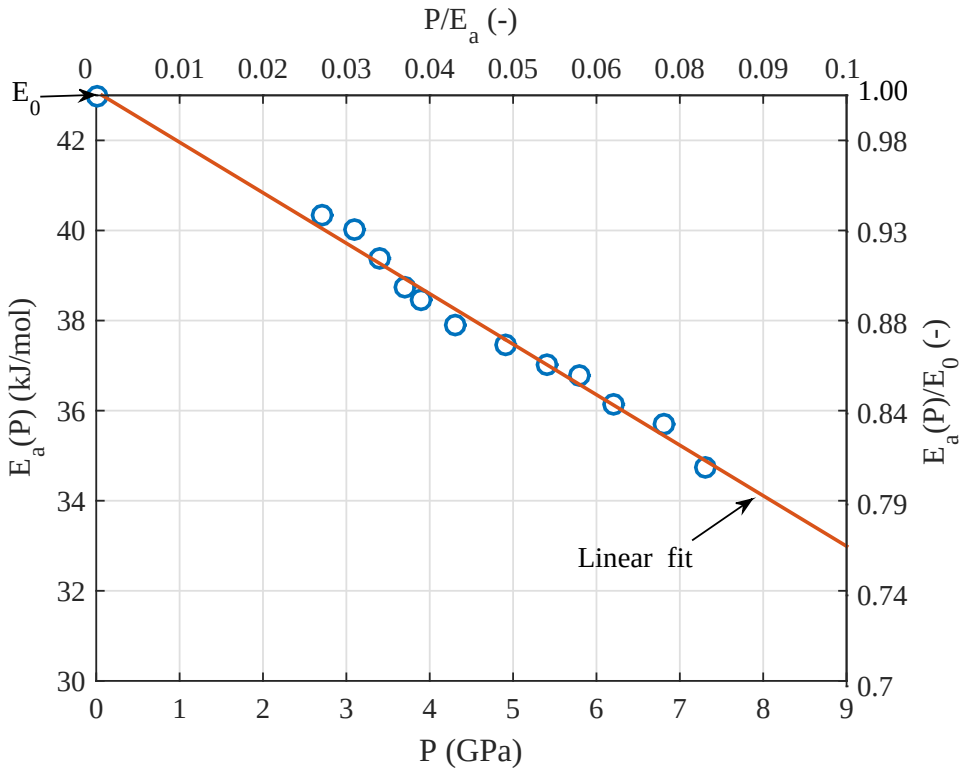

Fig. 8.10 Evolution of activation energy E_a of the growth of the ZDDP tribofilms over contact pressure.

(SG) potential rather than a step-like potential. This is confirmed by noticing the linear decrease of the activation energy E_0 over the contact pressure even when extrapolated to zero pressure, as shown in Fig. 8.10. Such a behaviour suggests a small $r \to 0$, which is also suggested by the numerical results of Tysoe, e.g. see Fig. 5 in [143].

The correction factor α for the uncertainties related to the determination of the attempt frequency, f_a, was found to be unity for all the rate results over the entire tested range of pressure and temperature. The results showed that the attempt frequency $f_a = 10^{13}\,s^{-1}$, which as suggested before is consistent with the oscillation frequency of the bond that is broken from the reactant. The value is also in agreement with the previously reported data related to ZDDP [30].

The activation energy values ranging from 43 to 35 kJ/mol are consistent with the recent results of Gosvami et al. [30] of similar in-situ AFM tribotests and the results of Zhang and Spikes [142] of the ZDDP additive decomposing in viscous fluids using shear only and assuming no direct asperity-asperity contacts.

The activation length was found to be about 0.2 Å, which is consistent with the ZDDP results of Gosvami et al. [30] of 0.35 Å and other previously reported data in the literature for other materials but using a similar model [374, 375]. The reported values are feasible for the fitted atom-by-atom decomposition model

that implies the activation lengths to be less than the length of the bond to be broken. On the other hand, the ZDDP results of Zhang and Spikes [142] suggested activation length of about 1.8 Å, which is of a relative order to the average bond length of 2 Å found in the ZDDP molecule [372, 373].

Several factors might have contributed to this discrepancy. First, the different operating conditions between our single asperity AFM tribotests in the boundary lubrication regime and the conventional experiments of Zhang and Spikes in the elasto-hydrodynamic lubrication (EHL) regime.

Second, the limited range of contact pressures used to fit the data of Zhang and Spikes, which can result in misleading results by not capturing the complete but part of the formation trend.

Third, the original chemo-mechanical Arrhenius-type model suggested by Gotsmann and Lantz [71] is typically applied when the shear stress is taken to act on the bonds directly. However, the way the model implemented here is by taking the average shear stress to be equal to the applied contact pressure multiplied by the friction coefficient. The oversimplification of the complex flow within the contact can bring large errors in estimating the activation energy and its length. It is worth noting that Zhang and Spikes assumed that no direct contact exists between the sliding counterbodies as their experiments were conducted in the EHL regime. However, they considered the shear stress in a similar way to our treatment. Again, this is an overestimation rather than actual consideration.

Fourth, for the used Arrhenius kinetics model, the applied force is expected to weaken the bonds more as the force quiescent time increases due to the sharp decrease in the lifetime of the bond τ by several orders of magnitude [374], i.e. $F \propto 1/\tau$. This indicates that the applied force has a time dependent effect, which can induce outburst of bonds' rupture and therefore making the formation/removal rate constant k time dependent. However, despite its potential large impact, this effect has not been taken into account in the available experimental data related to the ZDDP additive. Nonetheless, it is worth noting that Tysoe [143] proposed a model to account for the velocity effect on the tribochemical reaction. The model was based on assuming that the energy barrier is time dependent and convoluted in the sliding velocity, thus the reaction rate can be found as follows:

$$\ln k\left(\nu\right) = \ln k_0 + \frac{\Delta x}{k_\mathrm{B}T}\left[\frac{2F^*}{\pi} + \frac{2k_\mathrm{B}T}{a}\ln\left(\frac{\nu}{aP}\right) - \frac{2}{a}\Delta E \ln\left(\frac{t_\mathrm{c}\nu}{a}\right)\right] \tag{8.23}$$

where k_0 is the thermal reaction rate, ν is the sliding velocity, t_c is some characteristic time such that $t_c\nu/a \gg 1$, P is a factor related to the sliding transition over the energy barrier, ΔE is the change in the initial potential minimum due to sliding, $F^* = \pi E_0/a \gg F$ is the maximum force that can cause spontaneous sliding, E_0 and a are the height and periodicity of the energy potential. The terms inside the square brackets represent the applied force. Therefore, the model requires two fitting steps; one for the force to find the unknown parameters: F^*, a, P, and t_c and the other is for the whole rate equation in order to find the unknown Δx. As the applied force does not appear explicitly, the model is of less use due to the convoluted effect of the force and sliding velocity. Furthermore, in the case the change in the energy minimum, ΔE, is smaller than the thermal energy, $k_B T$, which is expected to be almost always the case, the model predicts that increasing the sliding velocity would result in increasing the reaction rate. This is because the original formulation was designed to accommodate the observation that at small sliding speeds, where slip-stick friction occurs, increasing the speed results in a logarithmic increase in the atomic lateral force, i.e. atomic friction, leading to lower activation energy barrier [62, 376–378]. However, this does not hold true for micro- and macroscopic friction at high sliding speeds like the one used during the in-situ AFM tribotests. Furthermore, Eq. (8.23) is in contrast with the above discussion that the longer the force is applied the weaker the bonds and thus the larger the reaction rate. A more appropriate treatment would rely on the reduction caused on the activation energy as the force is applied, which can be assumed a monotonically increasing time dependent effect. Thus, the external force terms in Eq. (8.17) can be modified, as follows:

$$E_a\left(P\right) = E_0 + \left[\mu P A_r \Delta x + \frac{\mu^2 P^2 A_r^2}{2}\left(\xi_I - \xi_T\right)\right]\left(1 + \sqrt{\frac{\Delta x}{\nu t_c}}\right) \tag{8.24}$$

Fitting this equation is straightforward and based on the speed of 400 μm/s, it yields insignificant contribution of speed to the applied force, i.e the last term $\ll 1$. This is consistent with our results discussed in section 8.5 that the scanning speed per se does not impact the growth rate.

Fifth, under certain harsh conditions of high temperature and contact pressure, the severity at the contacting interface causes distortion to the structure of the transition state, i.e. the shape of the energy potential [62, 376, 377]. As the decomposition reaction is endothermic, Hammond's postulate [379], which describes the structure of the transition state along the reaction coordinate, suggests that the energy of the transition state would be closer to that of the

products than that of the reactants. In this case, the harsh conditions might alter this state such that the energy minimum in the reactants state to the transition state along the reaction coordinate becomes smaller with possible alteration to the relative energy difference as well [143]. Nonetheless, it is worth noting that this effect is not probable within our in-situ tested conditions as the contact pressure is not large enough to cause any alteration to the structure of the energy potential. Furthermore, if any alteration occurs, the activation length is expected to be elongated rather than shortened.

Sixth, the possible different types of the ZDDP additives, e.g. primary, secondary or a mixture of the two among others, used in the two cases though not expected to have any significant effect.

8.7.2 Reaction order

To find the order of the ZDDP decomposition reaction to form a protective tribofilm on the shearing interfaces, the following equation for the nth order reaction rate can be used [30]:

$$\frac{1}{[V]^{n-1}} = \frac{1}{[V_0]^{n-1}} - (n-1)\,kt \tag{8.25}$$

where n is the reaction order, k is the reaction constant, V_0 and V are the tribofilm volumes at the beginning of the tribotest and at any time t, respectively. The initial volume of the tribofilm, V_0, can be taken as zero.

It should be noted that the above equation is suitable to estimate the reaction order only in the case of considering the changes of the reactants, i.e. additive concentration, or the products, i.e. the formed species of the tribofilm presumably phosphate species. As this information cannot be assessed during the AFM in-situ tribotests, the volume of the products will be considered instead of the concentration. This is a rough estimation but still feasible under the assumption that the thicker the tribofilm the larger the phosphate concentration, as verified and discussed in detail in chapter 5.

As discussed in section 7.1.4.1, the tribofilm formation follows a single exponential rate (Figs. 7.16 to 7.20) as opposed to the suggestion of Gosvami et al. [30] that it undergoes two distinctive phases starting from a slow linear growth phase followed by a fast logarithmic phase. For comparison purposes, our data will be fitted assuming two phases in order to have a parallel comparison with the available data in the literature. This would not affect the conclusions as the first

linear fit can always be ignored and the second exponential fit be extended to the whole dataset.

The reaction order was estimated by fitting Eq. (8.25) to the growth evolution data obtained at three different contact pressures, i.e. 2.7, 4.5, and 5.7 GPa, as shown in Figs. 7.10 to 7.12. The fitting results indicate that, regardless of the applied contact pressure, the slow linear phase of the tribofilm formation follows a zero reaction order with $n = 0.073 \pm 0.10$. On the other hand, the fitting results indicate that, regardless of the applied contact pressure, the fast logarithmic growth phase of the tribofilm follows approximately first order reaction kinetics with $n = 0.71 \pm 0.14$. As mentioned earlier, the entire dataset can be fitted using first order kinetics without the need of the initial zero order rate. This is in line with several previous reports suggesting a first order reaction kinetics for the decomposition of materials of similar functional groups found in ZDDP, e.g. dimethyl and diethyl disulphide [279] and other groups under shear [280, 281]. The reaction order can be taken as a measure for the decomposition efficiency to form the bulk of the tribofilm, i.e. sulphides and phosphates. The slightly lower order than unity indicates that the ZDDP decomposition process include few side and intermediate reactions that consume part of the available ZDDP molecules to form species other than sulphides and phosphates, i.e. possibly volatile products.

The zero order of the slow initial reaction is in agreement with the in-situ AFM results reported by Gosvami et al. [30], which suggested that the ZDDP decomposes initially with a zero reaction rate $n = 0.12 \pm 0.11$. Furthermore, their results indicated that as rubbing continued the reaction rate becomes $n = 0.22 \pm 0.02$, which suggests more complex reaction pathways during the decomposition of the ZDDP. This is in contrast with our first order kinetics for the fast logarithmic growth phase. It is also in contrast with our XPS ex-situ surface analysis, which indicated that the ZDDP decomposition and the phosphate-rich tribofilm's formation and growth follow first order reaction kinetics.

8.8 Reaction kinetics of DDP tribofilms

8.8.1 Activation energy

Based on how the decomposition reaction of the DDP additive behaves under temperature and contact pressure (Figs. 7.35 and 8.9b), it can be considered to follow the chemo-mechanical Arrhenius-type model suggested by Gotsmann and Lantz [71] and discussed in detail in section 8.7.1:Eq. (8.16) and section 2.1.2:

Eqs. (2.9) and (2.10). The potential shape parameter, r, was found to be similar to the case of ZDDP, i.e. $r \ll 1$, representing a gradual transition from the reactants to the transition state [371]. This indicates that the higher order quadratic term of Eq. (8.17), which is used to correct for the shape changes of the potential energy due to shear, is negligible.

Similar to the case of the ZDDP additive, the fit of Eqs. (8.16) and (8.17) to the experimental data requires few assumptions, which can be briefly summarized as follows:

- The pre-exponential factor, A, can be assumed to represent the frequency at which the reactant molecules cross the energy barrier into the transition state along the reaction coordinate. This will be calculated using Eq. (8.21).
- The DDP molecules adsorb to the metal in such a way that they are flat on the surface. Therefore, considering the standard structure of DDP with average bold length of 2 Å, it follows that the effective area A_r can be taken 0.5 nm^2 per DDP molecule, i.e. half the one of the ZDDP.
- The friction coefficient, μ, can be taken as 0.1 such that it matches the in-situ and ex-situ value obtained for DDP tribofilms.

The fit of Eqs. (8.16) and (8.17) to the experimental data starts with two fitting parameters, which is similar to the ZDDP case achieved by assuming that the second quadratic term of Eq. (8.16) is negligible. The fitting results are shown in Fig. 7.20. The same fit was obtained with and without the quadratic term, which indicates that similar to the ZDDP, the DDP decomposition reaction has the familiar Sine-Gordon (SG) potential rather than a step-like potential. This is confirmed by noticing the sharp linear decrease of the activation energy E_0 over the contact pressure even when extrapolated to zero pressure, as shown in Fig. 8.10. As suggested by the numerical results of Tysoe, e.g. see Fig. 5 in [143], this suggests a small $r \to 0$.

The correction factor α for the uncertainties related to the determination of the attempt frequency, f_a, was found to be in the range of 0.01 to 1.0 for all the rate results over the entire tested range of pressure and temperature. The main deviation from unity originates from the mild rate increase over temperature as compared to contact pressure. Similar deviation was also found by Gosvami et al. [30]. This results in an attempt frequency $f_a = 10^{10}\,s^{-1}$. The lower end was adopted in order to fit the entire range of data with a single value.

The activation energy values ranges from about 10 to 25 kJ/mol, which are nearly half the value found for the ZDDP additive discussed in section 8.7.1.

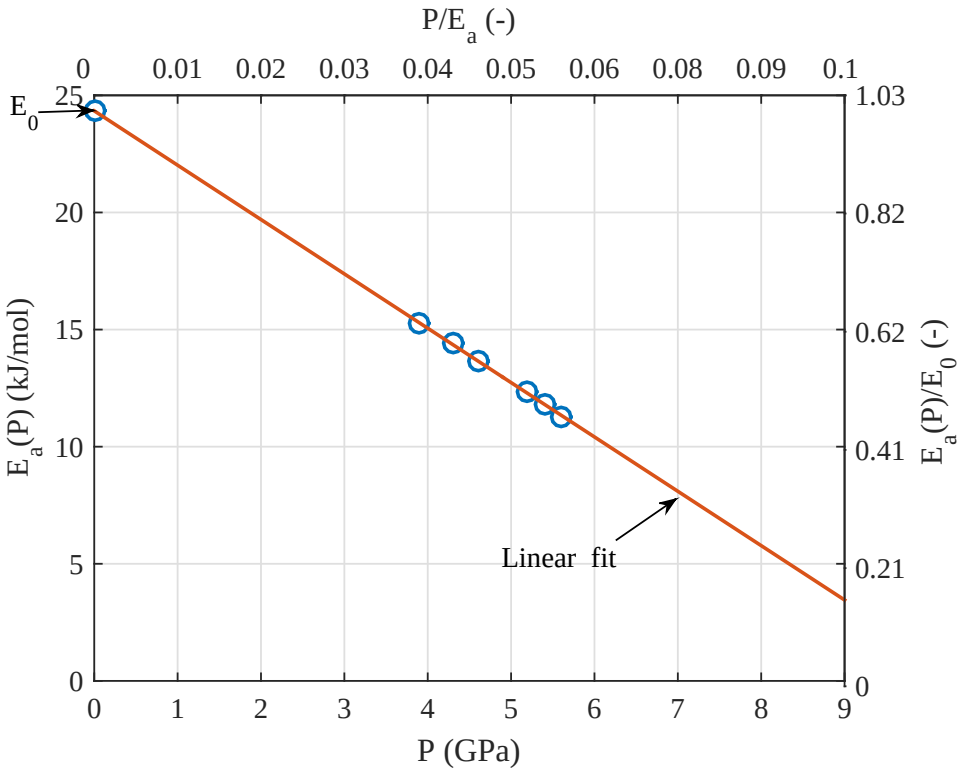

Fig. 8.11 Evolution of activation energy E_a of the growth of the DDP tribofilms over contact pressure.

Interestingly, the relatively small energy barrier, E_0 appears to be more susceptible to contact pressure than the larger barrier found for ZDDP. This suggests that the lack of zinc cations within the DDP molecules results in weaker overall bonds as opposed to the ZDDP molecules. Nonetheless, this does not warrant a faster reaction rate as it can be significantly affected by the activation length, which constitutes the rate-force dependency.

The activation length in the case of DDP was found to be about 0.8 Å, which is nearly fivefold the one found in the case of ZDDP. However, the reported values are feasible for the fitted atom-by-atom decomposition model that implies the activation lengths to be less than the length of the bond to be broken. It is also, in general, consistent with the available tribochemical results in the literature, e.g. 0.35 Å for the ZDDP [30]. The larger activation length in the case of DDP indicates that the decomposition rate is more sensitive to external force, which is manifested in the large slope of 2.3 kJ/GPa.mol of E_a versus P shown in Fig. 8.11 as compared to the 1.12 kJ/GPa.mol of ZDDP shown in Fig. 8.11.

It is worth mentioning that as the DDP atoms are more susceptible to shear, it follows that they might be more susceptible to shear rate as opposed to the case of the less sensitive ZDDP. For the used Arrhenius kinetics model, the applied force is expected to weaken the bonds more as the force quiescent time increases due to

the sharp decrease in the lifetime of the bond τ by several orders of magnitude [374]. This indicates that the applied force has a time dependent effect, which makes the formation rate constant k time dependent. However, this effect cannot be verified using the proposed Eq. (8.24) because all the DDP experiments were performed under the same sliding speed.

8.8.2 Reaction order

The formation rate of the DDP tribofilm over time can be fitted using Eq. (8.25) in order to find the order of the DDP decomposition reaction. Although the tribofilm formation occurs over a single distinctive logarithmic phase (Figs. 7.33 to 7.35), Eq. (8.25) was fitted assuming two phases, i.e. initial slow linear growth phase that accelerate into a fast logarithmic phase, in order to have a parallel comparison with the available literature [30]. This would not affect the conclusions as the first linear fit can always be ignored and the second exponential fit be extended to the whole dataset.

The fitting results indicate that, regardless of the applied contact pressure, the slow linear phase of the tribofilm formation follows a zero reaction order with $n = 0.047 \pm 0.01$. On the other hand, the fast logarithmic growth phase of the tribofilm follows a more complex reaction kinetics with $n = 0.52 \pm 0.07$.

The zero order of the slow initial reaction is in agreement with the in-situ AFM results regarding ZDDP tribofilms as well as the previously reported data of ZDDP [30]. However, the fractional logarithmic rate is lower than the one found for the case of ZDDP, i.e. 0.77. The reaction order can be taken as a measure for the decomposition efficiency to form the bulk of the tribofilm, i.e. sulphides and phosphates. The low order indicates that the DDP decomposition process include more side and intermediate reactions of possibly volatile products that consume part of the available DDP molecules to form species other than sulphides and phosphates.

8.9 Flowability of P-based tribofilms

The rheological properties of the ultra-thin P-based tribofilms, whether ZDDP or DDP, were quantified using a set of novel creep and squeeze flow experiments. The two methods are discussed in detail in the following sections.

8.9.1 Viscosity quantification using creep

In the creep experiments, a fixed stress is applied and the resulting deformation is observed. The performed AFM experiments described in Figs. 7.2 to 7.8 can be considered as creep experiments. In those experiments, the AFM tip applies a constant stress via contact pressure on a certain initial area of the formed film, which undergoes deformation and flowability in the lateral direction. The shear stress σ can be estimated to be dependent on the friction coefficient μ and contact pressure P, i.e. $\sigma = \mu P$, assuming the two are constant. The strain $\gamma(t)$ can be obtained by normalising the area evolution of the film $\mathrm{A}(t)$ by its initial area $\mathrm{A}(0)$ under the AFM tip, i.e. $\gamma(t) = \mathrm{A}(t)/\mathrm{A}(0)$. The creep compliance $J(t)$ can then be found be dividing the strain by the applied stress, i.e. $J(t) = \gamma(t)/\sigma$. In the limit of linear viscoelasticity, the creep compliance, can be defined as [77]:

$$J(t) = J_0 + J_R\psi(t) + \frac{1}{\eta_0}t \tag{8.26}$$

where J_0 is the instantaneous creep compliance, J_R is the total recoverable compliance, and $\psi(t)$ is the delayed elasticity function which is zero at time zero and one for $t \longrightarrow \infty$. Considering the ZDDP triboreactive films are viscous instead of viscoelastic, only the last term of the above equation is of importance.

Figure 8.12 shows the evolution of the creep compliance over time for different ZDDP films formed at 80 °C and 4.5 GPa using different scanning lines, i.e. 8, 4 and 1. In order to obtain these results several considerations were taken into account. First, the flowability was considered to occur in the direction across the formed film as well as in the direction along the action of shear. Second, the film growth (formation and removal) and flowability were supposed to occur simultaneously, which were readily decoupled as the growth occurs only in the vertical direction whereas flowability in the lateral direction. In the case of a big removal event occurs such that the covered area with the film decreases, this is registered as a sharp drop in the followed film creep compliance, as identified in Fig. 8.12. Third, the geometry of the tip-substrate counterbodies can be simplified to a plate-plate geometry without a direct contact between them but separated by the film. This is especially true for worn tips and for films of thickness larger than the substrate roughness, i.e. > 10 nm. Fourth, in the limiting case of small gaps, viscosity is not affected by the shear rate but solely by the shear stress [311].

The compliance evolution over time (Fig. 8.12) indicates two creep regimes. Initially, the film experienced a primary fast linear creep followed by a secondary slower linear creep. The Newtonian viscosity, i.e. the inverse slope of the compli-

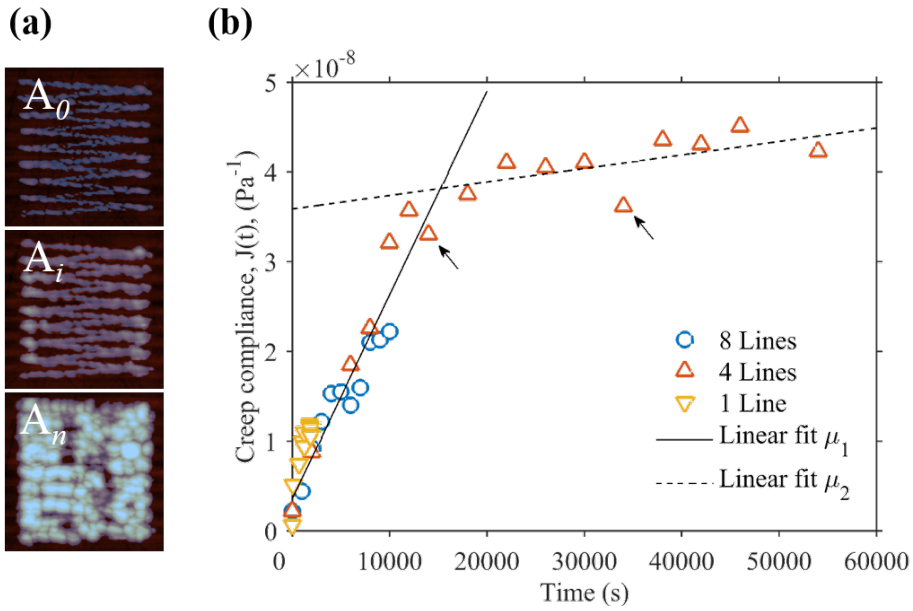

Fig. 8.12 Viscosity quantification of triboreactive ZDDP films using creep method. a, Sample of masked images used to calculate the area evolution of the formed films. b, Evolution of the creep compliance, $J(t)$, over time for different ZDDP films formed at 80 °C and 4.5 GPa using different scanning lines, i.e. 8, 4 and 1. Arrows indicate instances of film removal.

ance versus time as suggested by Eq. (8.26), was estimated based on the two creep regimes. The primary creep suggests a viscosity of about 4×10^{11} Pa.s as opposed to 7×10^{12} Pa.s for the secondary regime. These results are comparable to the bulk viscosity of various metallic glasses near and above their glassy transition temperature, i.e. $T_g > 350$ °C, as reported in the literature using bulk rheometry [380–384]. The close viscosities between the ZDDP film and metallic glasses confirm that the final structure of the film is merely a final solidified image of what once was hot, flowing and molten phosphate glass. For the first time, this evidences how rubbing can accelerate the formation of a highly viscous amorphous phosphate glass that helps protect contacting surfaces from excessive wear.

For the case of DDP, the compliance evolution over time (Figs. 8.13 and 8.14) is similar to the one observed for ZDDP. Initially, the tribofilm seems to undergo fast linear deformation, which is followed by an eventual slower deformation. The initial fast flow period suggests a viscosity of about 5-7 $\times 10^{11}$ Pa.s as compared to 9×10^{12} Pa.s for the slow flow in the terminal period. The range of these values is strikingly similar to the case of ZDDP tribofilms and comparable to the viscosity of various metallic glasses near and above their glassy transition temperature, as reported in the literature using bulk rheometry [380–384]. The close viscosities between the DDP and ZDDP tribofilms on the one hand and the metallic glasses around their glassy transition temperatures on the other hand confirm that the

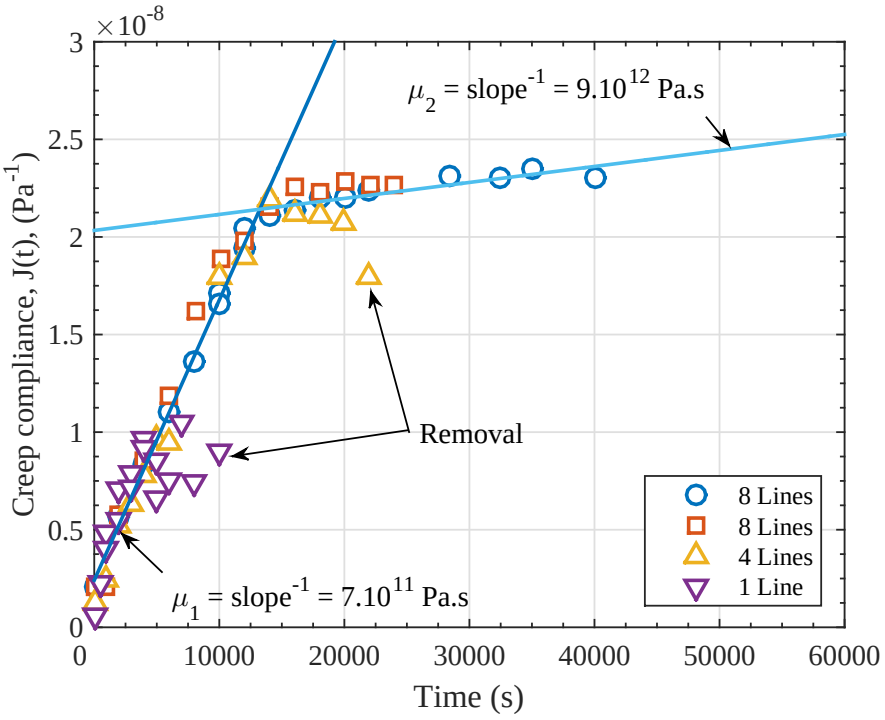

Fig. 8.13 Evolution of the creep compliance, $J(t)$, over time for different ZDDP tribofilms formed at 80 ^{o}C and 4.8 GPa using different scanning lines, i.e. 8, 4 and 1.

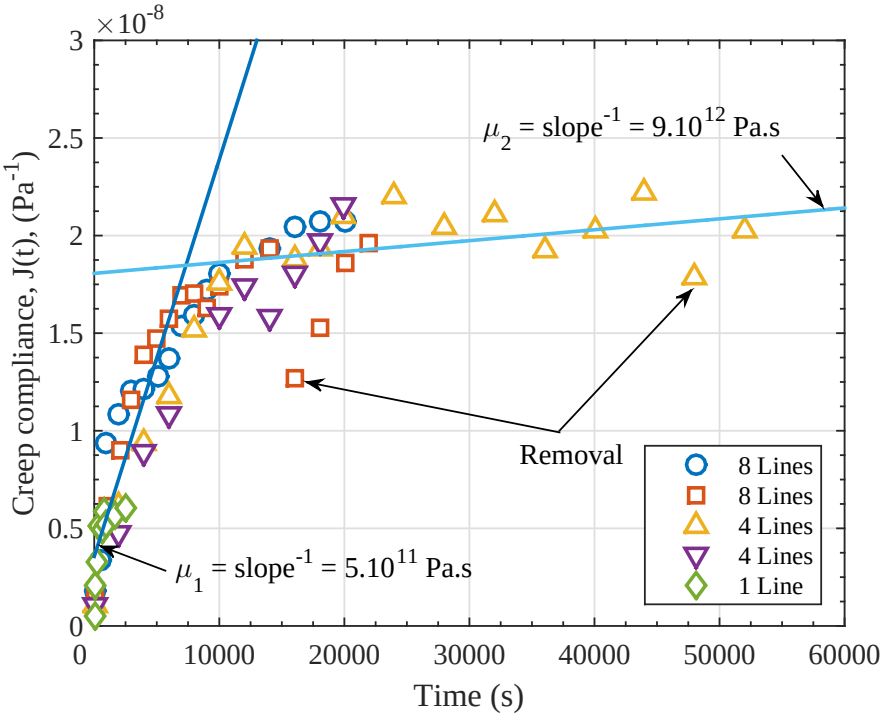

Fig. 8.14 Evolution of the creep compliance, $J(t)$, over time for different DDP tribofilms formed at 80 ^{o}C and 5.6 GPa using different scanning lines, i.e. 8, 4 and 1.

final structure of the tribofilm of mainly phosphates is just a final solidified image of the once hot, flowing and molten glass.

8.9.2 Viscosity quantification using squeeze-flow

Quantifying the viscosity using squeeze flow analysis is based on squeezing the triboreactive film between two parallel plates, as depicted in Fig. 8.15a. To limit this effect to genuine flowability and avoid any formation, the experiments were carried out ex-situ at ambient temperature in base oil without ZDDP reactive additive after the film was formed (Fig. 8.15b). The results show that when a small contact pressure was applied the film initially covered an area of $5\times5\,\mu m^2$. However, when the contact pressure was increased to 2.7 GPa and subsequently to 3.7 GPa, the covered area increased to about $6\times6\,\mu m^2$ and $7\times7\,\mu m^2$, respectively. Further increase of contact pressure to 4.5 GPa did not seem to have any significant effect on the film area, which can be a result of wear that reduces the area proportionally to the increase caused by the squeeze flow (Fig. 8.15c). The removal amount can be readily quantified and decoupled from the true flowability by observing the changes in the film thickness, area and volume (Fig. 8.15b-c). In case of flow without wear, the film volume should be preserved but as its area spreads the thickness decreases. However, in case of flow accompanied by wear, the volume can decrease because of removal of parts of the film. This reduction can be subtracted from the apparent film volume to obtain its evolution due to flowability only. Counterintuitive to this behaviour, a small recovery in the film volume was observed when the contact pressure was increased from 2.1 to 2.7 GPa. The source of this recovery might be related to irreversible disruption of the local compactness of the interfacial layers of the film leading to an increase in the free volume within the phosphate glass. This makes the film loose and more susceptible to wear, which is confirmed by the subsequent decrease in the film volume over the sliding cycles.

The Newtonian viscosity, μ, of the triboreactive films can be quantified by following the gap evolution $H(t)$, i.e. the film thickness while it is squeezed, as follows [312]:

$$H(t) = H_0 \left(1 + \frac{8H_0^2 F_0 t}{3\pi\mu R_0^4}\right)^{-1/4} \tag{8.27}$$

where H_0 is the initial film thickness just before applying load F_0, $H(t)$ is the film thickness over time and R_0 is the initial radius of the squeezed film, which can be taken as the tip radius. The experimental data discussed before in Fig. 7.9b-c can

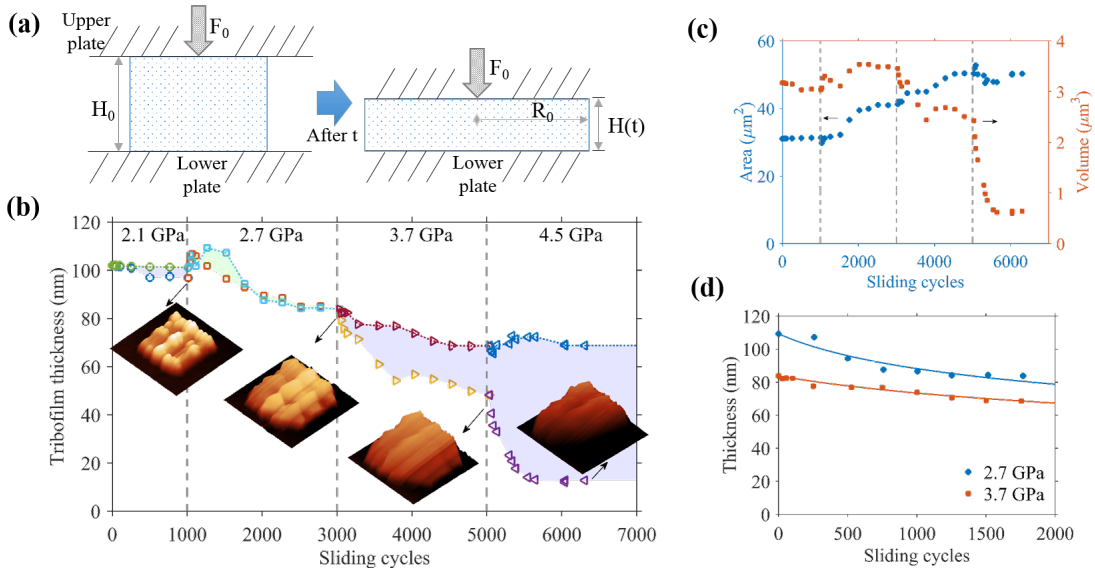

Fig. 8.15 Viscosity quantification of triboreactive ZDDP films using squeeze-flow method. a, Schematic of the squeeze flow between two parallel plates assuming constant volume just before applying the constant load (left) and after a certain squeeze time (right). b, Evolution of the total film thickness (symbols) and film thickness without wear (symbols and dashed line) after different sliding cycles at 25 °C under different contact pressures ranging from 2.1 to 4.5 GPa. Green areas indicate increase in film thickness whereas blue areas indicate film removal. The AFM images are $8.5 \times 8.5\,\mu m^2$ with colour ranges from 0-180 nm. c, Analysis of the film volume and area. d, Fit of the thickness at 2.7 and 3.7 GPa.

be fitted using the above equation to obtain the film viscosity, which is the only unknown. The result of this fitting is shown in Fig. 8.15d, which shows that in average the Newtonian viscosity of the film is about 2×10^{11} Pa.s.

The viscosity values based on either creep or squeeze flow experiments are larger than the reported values in literature [36] for ZDDP films, i.e. 10^8 Pa.s. These values are two to three decades lower than the ones estimated in this study. Several factors might be responsible for this discrepancy. First, Bec et al. [36] did not actually measure the viscosity of the film layers but instead they related it to the measured elastic modulus. Thus, it was more of a numerical estimation than an experimental quantification. Second, there is a significant difference between the experimental methods used in this study as compared to the previous ones. The current study implemented two novel methods based on the AFM with tip radius less than 80 nm whereas the previous study of Bec et al. [36] used the surface-force apparatus with a sphere of radius < 2.125 mm. The large difference in the probe size indicates that the viscosity values reported in the previous studies were averaged over a large area of the film whereas the current ones are of localised area within the film. As the film typically consists of ridges and troughs of heterogeneous mechanical properties as well as varied

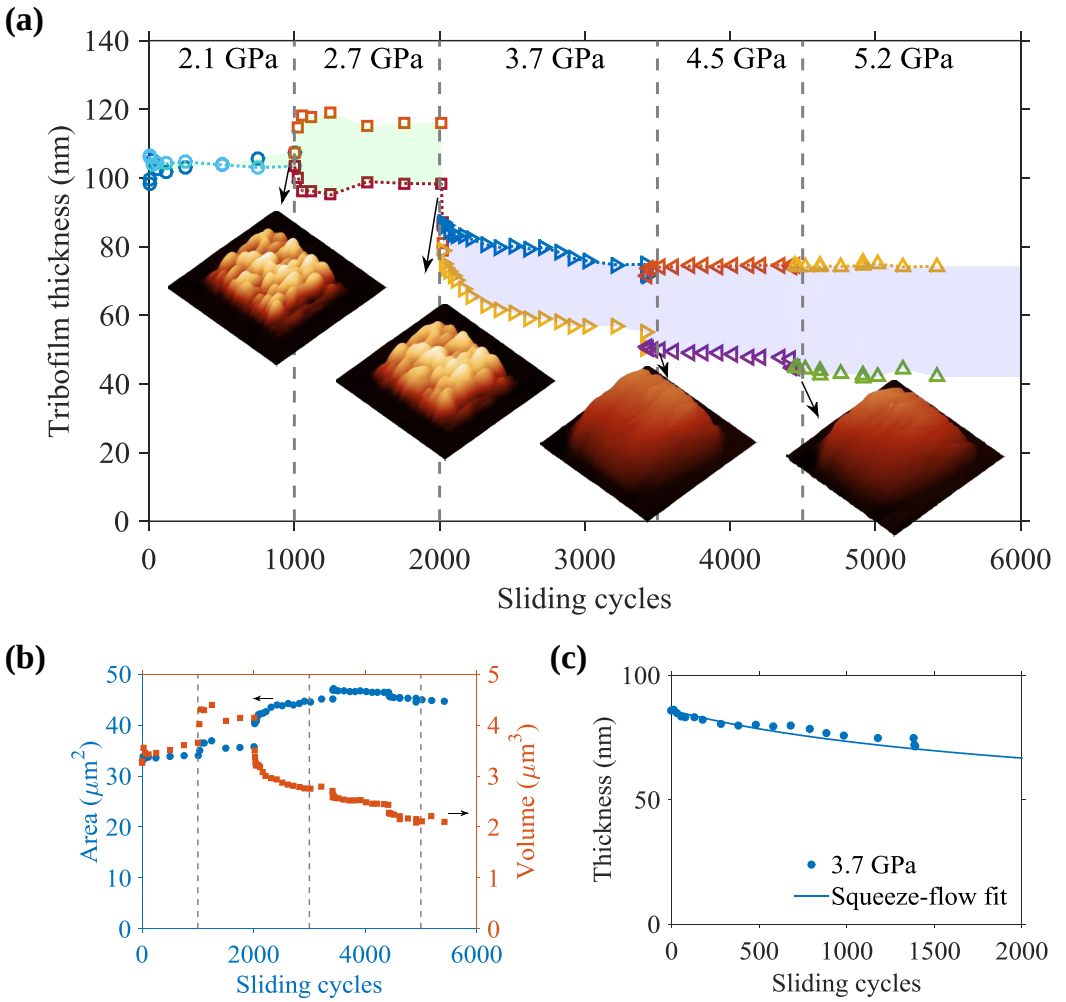

Fig. 8.16 Viscosity quantification of triboreactive DDP-1 films using squeeze-flow method. a, Evolution of the total film thickness (symbols) and film thickness without wear (symbols and dashed line) after different sliding cycles at 25 °C under different contact pressures ranging from 2.1 to 5.2 GPa. Green areas indicate increase in film thickness whereas blue areas indicate film removal. The AFM images are $8.5 \times 8.5\,\mu m^2$ with colour ranges from 0-180 nm. b, Analysis of the film volume and area. c, Fit of the thickness at 3.7 GPa.

thickness and composition (Table 3.3 and Figs. 3.10 and 3.11), it follows that the averaged properties measured by a large probe can be different from the local ones measured by a significantly smaller probe.

For the case of DDP additive, similar to the previously discussed creep analysis, the squeeze flow experiments show that in average the Newtonian viscosity of the DDP tribofilms ranges from 9×10^{10} to 6×10^{11} Pa.s (Fig. 8.16). These are similar to the values obtained using the creep experiments discussed above. Thus, the two independent methods, i.e. creep and squeeze flow, suggest unambiguously that under rubbing the formed tribofilm of amorphous phosphate behaves as a molten glass despite the relatively low temperature of the oil of 80 °C. This suggests that one of the antiwear mechanisms of the P-based additives is to form a highly

viscous glass on the contacting surfaces that helps reduce wear and mitigates contact stresses.

8.10 Summary

The generation of ZDDP triboreactive films is a complex multistage process [7]. As demonstrated in Fig. 8.17, it starts with the self- and trans-alkylation of the ZDDP additive in the oil (Fig. 8.17a), which involve the migration of alkyl groups from the O to S atoms [8]. The additive then adsorbs to the steel substrate as linkage isomer (LI-ZDDP) [28]. In case of shearing the countersurfaces at high temperature and contact pressure, two phenomena are accelerated. First, iron cations are released from the steel substrate. Second, the adsorbed ZDDP molecules undergo a partial decomposition into zinc and iron sulphate followed by sulphide species. Heat causes sulphur to diffuse into the steel whereas shear assists the formation of a mixed oxide-sulphide base layer of isolated clusters (Fig. 8.17b). The base layer acts as a glue providing excellent tenacity between the steel surface and subsequently formed layers of amorphous iron and zinc polyphosphate chains of increasing length towards the film's surface (Fig. 8.17c). These layers mark the final decomposition stage of ZDDP molecules.

The DDP decomposition process is similar to the one of the ZDDP. This suggests that the zinc and iron cations can replace each other without much changes in the composition of the formed tribofilm.

The resulting amorphous polyphosphate forms a unique antiwear structure of growing thickness and patchiness over sliding cycles (Fig. 8.17d). The antiwear protection of such evolving structure has been attributed to its rigid sacrificial nature [14–18] and its ability to digest the sharp worn particles [19–21]. These mechanisms are either mechanical or chemical in nature. However, our results indicate that the good antiwear properties might have a rheological origin, which can greatly influence friction, lubrication and adhesion properties of any tribological surface. For instance, the outer layers were found viscous with a viscosity in the order $10^{11} - 10^{12}$ Pa.s. The top viscous layer can explain the patchy pad-like structure of the film (Fig. 8.17d) as a final solidified image of the once hot flowing glass. The ridges of this glass are formed due to asperity-asperity contact whereas the troughs originate from the flow of some material from the regions of ridges to troughs. This suggests that the superior antiwear properties of P-based tribofilms originate from their intrinsic rheological properties that allow them to flow while formed, which was clear from their ability to maintain local order on the nanoscale

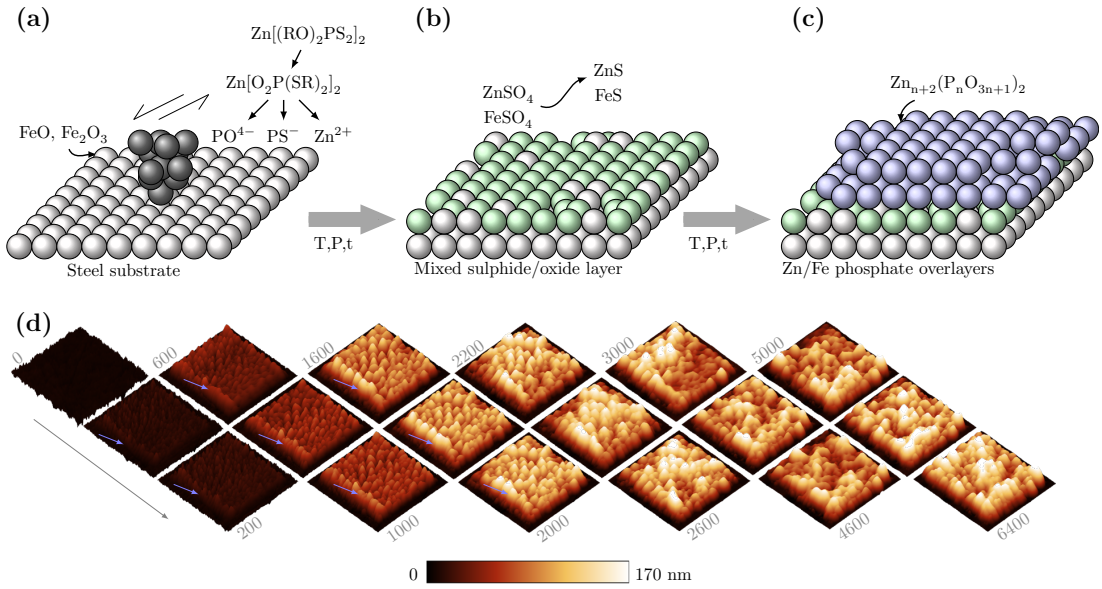

Fig. 8.17 In-situ generation of ultrathin ZDDP triboreactive films. a, Schematic illustration of AFM Si tip raster scanning steel substrate submersed in PAO oil containing ZDDP additive at high temperature and contact pressure. b, Formation of mixed oxide-sulphide base layer on the steel substrate. c, Formation of iron and zinc polyphosphate on the sulphur-oxide base layer. d, In-situ evolution of the structure of the ZDDP film formed at 80 °C and 7.3 GPa.

through the motion, rearrangement and local reconfiguration of single and multiple patches of the formed tribofilm at the interface. This seems to effectively mitigate the smearing and wearing of the contacting asperities resulting in less wear. The findings of this study open future opportunities for quantitatively analysing the interfacial rheology and reaction kinetics governing a broad range of additives and substrates, which can help build mechanistic models capable of better predicting wear.

Chapter 9

Conclusions, recommendations and outlook

9.1 Conclusions

9.1.1 Developed techniques

- A mini pin-on-disc tribotester was designed, which can be coupled with XAS to perform in-situ tribological tests at different levels of contact pressure (1.0 - 3.0precursors GPa), temperature (25 - 120 °C) and sliding speed (30 - 3000 rpm or 0.15 - 15 m/s). Using this apparatus, it was possible to follow and examine the composition evolution over time of the tribo- and thermal films of different phosphorus based additives through the measurements of the P and S k-edge XAS spectra. The unique feature of this apparatus is that, for the first time, the composition of the tribo- and thermal films of various oil additives can be studied at ambient pressure in-situ without altering the sample condition.

- An AFM liquid cell was designed and coupled with the AFM to perform in-situ tribological tests at different contact pressures (2–7 GPa), temperatures (25–120 °C) and sliding speeds (50–450 μm/s). Using this liquid cell, it was possible to follow and examine the evolution over time of the textural and rheological properties of the ZDDP and DDP tribofilms. Furthermore, it enabled us to study the formation kinetics of these P-based antiwear additives in-situ without altering the sample condition.

9.1.2 Additive decomposition and tribofilm composition

- At the beginning of the tribo- or thermal test, the formed tribo- or thermal film consists of sulphur mainly in the form of sulphate with some disulphide, which progressively changes into mainly sulphide. Following this, the adsorbed additive starts to decompose completely to form phosphate species.
- The ZDDP decomposition process occurs as follows:
  i. The unreacted ZDDP adsorbs to the substrate, whether a bare steel or DLC coated surface.
  ii. The adsorbed molecules decompose partially by losing sulphur to form sulphate species. The sulphate formation is favoured in the beginning of the tribotest due to surface smearing and wear during the initial running-in period, which results in high temperature at the contacting asperities.
  iii. The formed sulphate species are reduced to form sulphides. As rubbing continues and the running-in period ends, the local temperature at the asperity-asperity contacts drops below the critical temperature needed for the sulphate formation and therefore the more stable sulphide is formed instead.
  iv. The adsorbed molecules decompose completely to form phosphate species in the form of a two-dimensional network of chains progressively increasing in length.
  v. Any harsh conditions of high temperature and large contact pressure or even just long shearing or heating time can cleave the long phosphate chains into shorter ones.
  vi. Once the phosphate-based tribofilm covers the substrate completely, the ZDDP molecules cannot adsorb preferentially to the tribo- or thermal film covering the substrate. The origin of the detected adsorbed molecules in the late stages of the test is mainly the trapped additive within the formed film, which occurs during the early stages of the test without any further replenishment.
- The DDP decomposition process is similar to the one of the ZDDP. This suggests that the zinc and iron cations can replace each other without much changes in the composition of the formed tribofilm.

- The formed tribofilm on the DLC coated surface or at low temperature, i.e. 25 ^{o}C, is of small volume and low tenacity. The low tenacious tribofilm was related to the absence of mixed oxide/sulphide base layer. This layer seems to act as a glue joining the substrate with the subsequently formed phosphate layers composing the main bulk of the tribofilm.

- Sulphide clusters formed on the metal surface can have a vital role in the redox reactions occurring on the surface as they work as tunnels for electron exchange. This can explain the increase in the micropitting even after short tribological tests in contacts lubricated with oils containing ZDDP additive.

9.1.3 Effect of water

- Water can change the composition of the different layers forming the tribofilm depending on their proximity to the metal surface. In the base layer near the surface, the presence of water in the oil increased the atomic concentration of S whereas it did not affect the concentrations of P and Zn. However, in the subsequent layers near the tribofilm surface water decreased the equilibrium concentration of P and increased the Zn concentration by about 30%.

- The effect of water on the concentrations of the decomposition products can vary between a small short-term effect limited to the running-in period, such as in the case of O and S, and a large long-term effect such as in the case of P and Zn.

- Water does not hinder the formation of the early base layers on the metal surface nor the adsorption of ZDDP molecules. However, it was found that water can impede the polymerisation reaction in the subsequent layers, which resulted in the formation of short zinc phosphate chains.

- The above effect of water was related to the formation of a single or multiple bridges between water molecules and PO_2^- groups of the decomposed ZDDP. This caging effect can suppress the chemical reactivity of the PO_2^- groups to a great extent, which in turn can hinder their polymerisation into long phosphate chains.

- The initial alteration of the tribofilm occurring due to the presence of water during the running-in period cannot be reversed even if water is removed from the oil in the subsequent stages.

9.1.4 Tribological properties of the formed tribofilms

- The different kinetics that govern the evolution of friction and tribofilm growth indicate that the changes in the friction force are not only a function of the tribofilm thickness but also the composition. By comparing the friction coefficient and the tribofilm morphology, we have shown that the increased friction due to the presence of ZDDP tribofilm can be related to the interactions between the phosphate chains covering the two contacting surfaces. The longer the rubbing time, the longer the phosphate chains and the stronger the interactions are.

- The initial transient changes in the friction coefficient during the running-in period was related to two possible mechanisms. The first one was related to the local arrangements of the long phosphate chains, which after reaching a certain threshold of length can form an ordered structure in the direction of shear. The second mechanism was related to the changes in the local compactness of the interfacial layers of the tribofilm during the test.

9.1.5 Reaction kinetics

- The shear stress in the boundary lubrication regime is independent of the shear rate and depends only on the friction coefficient.

- The growth rate is independent of the sliding speed and is only dependent on the scanning cycles. This indicates that the growth occurs accumulatively in a layer-by-layer fashion, i.e. every rubbing cycle regardless of its timing adding one layer of a certain thickness depending on the other operating conditions of temperature and contact pressure.

- The formation of sulphur species first followed by phosphate species, suggests the presence of an initial induction period. The duration of this period can last for hours in the case of thermal films whereas it is shortened to only a couple of minutes in the case of tribofilms.

- The precursors' reaction kinetics of the sulphur base layer seem to evolve nearly instantly, however the formation of zinc phosphate has a transient burst phase near the metal surface followed by a slow phase until asymptotically approaching steady state. Based on the observed growth trend of the ZDDP decomposition components, the polymerisation reaction of the phosphate chains was suggested to follow a first-order reaction kinetics.

However, the DDP appears to follow more complex reaction pathways with a fractional kinetics order of 0.52 ± 0.07.

- The data suggest that temperature and contact pressure have a similar effect on the reaction kinetics of the P-based additives, i.e. the higher the temperature or pressure the higher the increase in the growth rate, which follows exponential rate. The similar effect of temperature and contact pressure on the growth rate confirms their potent effect on accelerating the additive decomposition process, which can be activated by the availability of either shear or heat.

- For the ZDDP, the effect of temperature and contact pressure seems to have an additive effect, e.g. the maximum growth rate occurs when temperature and contact pressure are both maximum. However, the formation rate of the DDP tribofilm increases over contact pressure more prominently than temperature. This implies that within the range of the tested conditions, above a certain threshold of temperature, shear stress alone is enough to cause a complete decomposition of the DDP additive to form a protective tribofilm. Increasing the temperature further does not have a potent effect as opposed to the case of ZDDP, which suggests different reaction pathways with different energy barriers.

- The activation energy of the ZDDP ranges from about 35 to 43 kJ/mol, which is nearly twice the value found for the DDP additive ranging from 10 to 25 kJ/mol. The relatively small energy barrier of the DDP decomposition makes it more susceptible to contact pressure than the larger barrier found for ZDDP. This suggests that the lack of zinc cations within the DDP molecules results in weaker but more flexible overall bonds as opposed to the ZDDP molecules.

9.1.6 Tribofilm structure and properties

- Throughout the tribotests, a general behaviour of formation-removal hysteresis is evident. This seems to be induced by the progressive shearing of the interface causing the weakly adhered top layers of the tribofilm to be removed or be reallocated within the central area of the evolving tribofilm.

- The formation and removal cycles appear to be repetitive in nature, i.e. the more the tribofilm is removed, the rougher surface is created, the more the energy available for the next formation phase and the more the tribofilm grows exponentially in the subsequent cycles.

- The high roughness of the tribofilm is the main player inducing the logarithmic formation and removal cycles. The rough peaks on the shearing surfaces can cleave some of the interface bonds and thus creating more active sites and providing more energy for the succeeding formation outburst. The hastened formation produces thicker but less compact tribofilm layers that can be removed easily under shear.

- The tribofilm formation follows the same deterministic trend especially in the early stages of the tribotest but differences might arise as sliding cycles increase due to severe mixing and distortion of the individual pads leading to wear and removal of parts of the tribofilm.

- The formed tribofilm during the early stages has a uniform structure as compared to the final stages, which can be attributed to the wear action and the intrinsic deterministic nature of the tribofilm formation. As sliding cycles increase, differences might arise due to severe mixing and distortion of the individual pads leading to wear and removal of parts of the tribofilm.

- Contrary to the generally perceived conception that the P-based tribofilms are rigid, they were found to behave as a viscous polymer, which can deform and flow under shear. The origin of this behaviour can be attributed to the large contact pressure that can deform the soft tribofilm and squeeze it such that the film moves from the areas of high contact pressure towards the areas near the edges of low contact pressure in order to minimise the experienced shear stresses. The significant implication of this finding is that for the first time it provides a new explanation for the excellent anti-wear properties of the P-based tribofilms. In addition of forming a mechanical barrier, these tribofilms can also deform and flow and thus help mitigate the shear stress at the contacting asperities leading to less wear.

- Once the mature tribofilm was subjected to shear in base oil under mild contact pressure, a small increase of the tribofilm thickness was observed instead of wear despite the low ambient temperature and absence of additive in the base oil. The source of this recovery is hypothesised to originate from the irreversible disruption of the local compactness of the interfacial layers of the tribofilm leading to an increase in the free volume within the phosphate glass forming the tribofilm. This necessary makes the tribofilm loose and more susceptible to wear, which is confirmed by the subsequent decrease in the tribofilm thickness over the sliding cycles until reaching a steady-state thickness.

- The P-based additives cannot adsorb preferentially to the formed tribofilm surface as opposed to the steel surface.
- The iron phosphate-based tribofilm is more tenacious than the zinc phosphate-based tribofilm.
- The structure of the tribofilm formed on iron phosphate glass is similar to the one formed on bare steel surface. This indicates that the availability of iron from the substrate, whether steel or iron phosphate, is enough to form a DDP tribofilm consisting mainly of iron phosphate.

9.2 Limitations and recommendations

The study presented novel methodologies that enabled us to study the antiwear tribofilms like never before. However, despite all the advantages of the newly developed techniques, they suffer some inevitable limitations, as summarised below:

- **Interruption of shearing while acquiring the in-situ data**
  During the acquisition of the XAS spectra, shearing was stopped but the temperature control was maintained. Although for real in-situ experiments the test conditions should not be altered, stopping shearing during the spectra acquisition was performed in order to obtain time-resolved XRF maps both inside and outside the wear scar before collecting the XAS signal. This is a first step towards a complete in-situ technique by acquiring the signal while the disc is rotating, which is planned for the next beam time.
- **Use of helium atmosphere during the in-situ XAS experiments**
  All the XAS experiment were performed under helium atmosphere instead of ambient condition like the one typically encountered during the tribological testing. This was needed to be able to collect the data without the need for high vacuum. Helium was selected for many reasons. The low atomic number helium reduces absorption of low-energy phosphorus and sulphur fluorescence signals. In addition, owing to its unique characteristics of being colourless, odourless, non-toxic and non-flammable gas it can be used at ambient and high temperatures without health risks. Furthermore, helium is an inert gas and thus it is not expected to interact or react with the metal surface or the oil and its additives. The helium environment also helps exclude water contamination, which originates from the humidity carried by the ambient air, from affecting the chemical reactions under study. Although

this is different from the real testing conditions that are affected by the presence of oxygen and water, it helps understand the fundamental reactions with less complexity by excluding these factors. The initial theory regarding the decomposition mechanisms of ZDDP suggests that they can be thermal [137, 144], thermo-oxidative [28, 118], hydrolytic [137] or hybrid. Focusing our attention on one mechanism only, i.e. thermal, helps understanding the extent of contribution of the other mechanisms by comparing our results with the ones reported in the literature under more realistic conditions.

Limited signals to P and S k-edge

Because of the use of helium environment and hard x-ray incident beam, the XAS could not detect the L-edges of various elements of interest, e.g. S, P, Zn and Fe. The ability to acquire spectra other than P and S k-edges, would provide us with unprecedented complete information regarding the formed species as they evolve over time. This information can help us solve the over 70 years question concerning the different theories proposed to explain the decomposition reactions of P-based antiwear additives to form protective tribofilms covering the contacting surfaces. The implications of this are of great extent as finally we will be able to replace the harmful ZDDP additive with an environmentally friendly one that does not degrade the catalyst performance of the catalytic converter in the vehicle's exhaust system and thus help reduce harmful emissions.

- **Use of vertical-horizontal incident-detector geometry instead of horizontal-horizontal one**

  The vertical geometry of the detector relative to the surface can have a detrimental effect on the acquired signal especially for thick and concentrated samples. It can increase the elastic and Compton scattering by at least one order of magnitude, which can result in an overall decrease in the signal to noise ratio and deterioration of the peaks heights [317]. However, although the vertical geometry worsens the inevitable attenuation of the signal amplitude, it has a negligible effect on the energy shifts. Thus, for comparing the positions of different peaks under the same conditions, the vertical measurement geometry is sufficient. The ability to observe and distinguish different features in the P and S k-edge spectra during the tribo- and thermal tests demonstrates the feasibility of the newly developed in-situ technique to unravel more information than what is currently possible using ex-situ techniques. Furthermore, the clear and strong peaks indicate that the detrimental scattering effect due to the vertical geometry of the detector discussed above is minimum. However, the use of vertical geometry did

not allow the mapping of the tribofilm along its thickness as the technique becomes surface insensitive. For the future experiments we plan to use the horizontal geometry instead. It is more technically demanding than the vertical one but the advantage of getting depth profiles is worth overcoming the difficulties.

- **Bulk instead of surface-sensitive information using the in-situ XAS**
  In the FY mode applied during the current in-situ XAS, the x-ray beam can easily penetrate the formed tribofilm, which has a few tens of nanometres thickness. Thus, the technique is mostly considered surface insensitive. However, the surface sensitivity can be largely increased by aligning the sample below the critical glancing angle relative to the incident beam. This results in a total external reflection with an evanescent wave interacting with only a few nanometres, i.e. less than 10 nm, of the surface layers and decaying exponentially with the penetration depth. The ability to obtain the reflectance angle in routine way would enable the analysis of tribofilms with different depth sensitivity. We currently run small angle XAS analysis of tribofilms which is very helpful in obtaining the overall film chemical structures, but the ability to control the depth sensitivity would enable accessing the chemical structure of different layers of the film.

- **Long acquisition time of XAS and XRF maps**
  This is an inherent limitation of I-18 synchrotron beam. However, an upgrade is taking place this year and the coming ones. For instance, the new upgrade this year have cut the deadtime in raster maps scans down from ca 10 s to 2 s per row, and the scientist at Diamond stated that this should be 1 s in a few months. The ability to acquire XAS spectra faster than currently possible, would enable us to study the transient chemical reactions much closer to the real time. This is essential in understanding the intermediate reactions and their kinetics and their effect on the formation of the protective antiwear tribofilms.

  Large XAS beam size
  The ability to use a smaller beam size with higher detection sensitivity, than currently possible, would enable us use a smaller size in-situ rig with smaller and more realistic wear scar while using less amount of oil.

- **Uncertainty of contact pressure and other parameters of AFM in-situ tribotests**
  Several experimental variables might cause propagation of uncertainty in

any in-situ AFM measurement. These can include the temperature at the interface between the AFM tip and substrate, which is taken as the temperature of the oil that submerges the tip and substrate. Other uncertainties might also arise from the difficulties in determining the real contact area, the exact applied normal force and subsequently the exact contact pressure forcing the counter-surfaces together during rubbing. The uncertainty in any of these parameters stems from not only one but typically a couple of experimental parameters that define them. In the current work we performed a detailed analysis regarding the sources and causes of uncertainty in the in-situ AFM measurements and the resulting effects on the measurable parameters (Appendix A). The overall uncertainty in the contact pressure ranges from 9.0 to 13.7%.

In order to improve the uncertainty in the future work, probing the sample properties using large beads, e.g. 5 μm, seems better than using the sharp AFM tip. The large bead makes larger contact area than the traditional AFM tip, which reduces the contact pressure and thus preserves the sample from wear. In addition, using a spherical bead gives a well-defined contact area, which in the case of the AFM tip is hard to determine. The limitation of using beads, however, is the lengthy waiting period before any tribofilm is detected in addition to the reduction in the lateral resolution. As we aim at studying the morphology evolution of the tribofilms, a high lateral resolution is required, which might deem the option of using colloidal cantilevers with beads inadequate for the purpose.

- **Lack of mechanical information data besides the in-situ composition and textural data**

  The developed experimental techniques in the current work can only perform tribological tests while coupled to other techniques to perform surface analysis. In order to obtain a mechanical characterisation of the formed tribofilm an embedded or coupled nanoindentation is needed. This can be feasible by reducing the size of the currently developed pin-on-disc further.

  Nonetheless, even for the ex-situ mechanical data of P-based tribofilms available in the literature, there is wide range of values in the reported indentation modulus (Table 3.3). This disparity can be related to the extent of the additive decomposition to form polyphosphates [89] in addition to the intrinsic uncertainties associated with probing such ultra-thin heterogeneous films using any indentation technique.

  Furthermore, the ZDDP and DDP antiwear films have rich mechanical properties, which can be affected by the decomposition mechanism, load

and temperature. In addition, the mechanical properties might also be affected by the rheological properties of the tribofilm. For instance, in case of the tribofilm is viscoelastic then its mechanical response can look similar to the plastic behaviour of a compliant material. Moreover, a viscoelastic tribofilm may suggest that its mechanical properties are rate dependent. Hence, the history and rate of measurement can play a major role in the measured properties. Therefore, studying the rheological properties of the antiwear tribofilm is necessary to give insight into its mechanical as well as tribological properties.

- **Different sliding motion during the ex-situ and in-situ experiments**
  The developed techniques in this work perform tribotests under pure sliding only. In order to be able to generate tribofilms under more realistic conditions of sliding and rolling, the developed rigs should be minimised in size while adding another motor to control the rotation of the ball. We are in the process of implementing this upgrade.

9.3 Closing statement

The newly developed techniques enabled us to study the tribochemical processes in real time and under realistic conditions using synchrotron X-ray absorption spectroscopy (XAS) and mapping the transient tribological and rheological properties using atomic force microscopy (AFM) in a way that is currently not possible. The novel developed techniques can provide significant insights into the reaction kinetics of the formation and removal mechanisms of ultra-thin tribofilms. This ultimately will improve the predictability and accuracy of the currently used friction and wear models and provide promising results to develop new mechanistic models.

References

[1] D Tabor. The contribution of a physicist to tribology. *Industrial Lubrication and Tribology*, 19(7):274–275, 1967.

[2] P. Jost. Lubrication (Tribology) – A report on the present position and industry's needs, 1966.

[3] Gwidon Stachowiak and Andrew W Batchelor. *Engineering tribology*. Butterworth-Heinemann, 2013.

[4] K Carnes. The ten greatest events in tribology history. *TRIBOLOGY & LUBRICATION TECHNOLOGY*, 61(6):38–47, JUN 2005. ISSN 0024-7154.

[5] A. Stevenson. *Oxford Dictionary of English*. Oxford Dictionary of English. Oxford University Press, 2010. ISBN 9780199571123.

[6] J.H. Mackle. Lubricating oil, 17 Jul 1928. US Patent 1,677,244.

[7] H. Spikes. The History and Mechanisms of ZDDP. *Tribology Letters*, 17(3): 469–489, October 2004. ISSN 1023-8883. doi: 10.1023/B:TRIL.0000044495.26882.b5.

[8] RB Jones and RC Coy. The chemistry of the thermal degradation of zinc dialkyldithiophosphate additives. *Asle Transactions*, 24(1):91–97, 1981.

[9] Kenneth Holmberg, Peter Andersson, and Ali Erdemir. Global energy consumption due to friction in passenger cars. *Tribology International*, 47: 221–234, 2012.

[10] Udo D Schwarz. Tracking antiwear film formation. *Science*, 348(6230):40–41, 2015.

[11] B. Bhushan. *Micro/Nanotribology and Its Applications*. Nato Science Series E:. Springer Netherlands, 2012. ISBN 9789401156462.

[12] Si-wei Zhang. Green tribology: Fundamentals and future development. *Friction*, 1(2):186–194, 2013.

[13] Tasuku Onodera, Yusuke Morita, Ai Suzuki, Michihisa Koyama, Hideyuki Tsuboi, Nozomu Hatakeyama, Akira Endou, Hiromitsu Takaba, Momoji Kubo, Fabrice Dassenoy, et al. A computational chemistry study on friction of h-MoS_2. Part I. Mechanism of single sheet lubrication. *The Journal of Physical Chemistry B*, 113(52):16526–16536, 2009.

[14] R.C. Watkins. The antiwear mechanism of zddp's. part {II}. *Tribology International*, 15(1):13 – 15, 1982. ISSN 0301-679X. doi: http://dx.doi.org/10.1016/0301-679X(82)90102-5.

[15] Fred G Rounds. Effects of additives on the friction of steel on steel i. surface topography and film composition studies. *ASLE TRANSACTIONS*, 7(1): 11–23, 1964.

[16] W.A. Glaeser, D. Baer, and M. Engelhardt. In situ wear experiments in the scanning auger spectrometer. *Wear*, 162–164, Part A(0):132 – 138, 1993. ISSN 0043-1648. doi: http://dx.doi.org/10.1016/0043-1648(93)90494-7. Wear of Materials: Proceedings of the 9th International Conference.

[17] JC Bell, KM Delargy, and AM Seeney. Paper ix (ii) the removal of substrate material through thick zinc dithiophosphate anti-wear films. *Tribology series*, 21:387–396, 1992.

[18] JM Palacios. Thickness and chemical composition of films formed by antimony dithiocarbamate and zinc dithiophosphate. *Tribology international*, 19(1):35–39, 1986.

[19] Jean Michel Martin. Antiwear mechanisms of zinc dithiophosphate: a chemical hardness approach. *Tribology letters*, 6(1):1–8, 1999.

[20] Jean Michel Martin, Carol Grossiord, Thierry Le Mogne, Sandrine Bec, and André Tonck. The two-layer structure of zndtp tribofilms: Part i: Aes, xps and xanes analyses. *Tribology international*, 34(8):523–530, 2001.

[21] MJMJL Belin, JM Martin, and JL Mansot. Role of iron in the amorphization process in friction-induced phosphate glasses. *Tribology Transactions*, 32(3): 410–413, 1989.

[22] J. J. Habeeb and W. H. Stover. The role of hydroperoxides in engine wear and the effect of zinc dialkyldithiophosphates. *A S L E Transactions*, 30(4): 419–426, 1986. doi: 10.1080/05698198708981775.

[23] Fred Rounds. Effects of hydroperoxides on wear as measured in four-ball wear tests. *Tribology transactions*, 36(2):297–303, 1993.

[24] PA Willermet, DP Dailey, RO Carter, PJ Schmitz, and W Zhu. Mechanism of formation of antiwear films from zinc dialkyldithiophosphates. *Tribology International*, 28(3):177–187, 1995.

[25] Jonas Andersson, Matilda Antonsson, Lisa Eurenius, Eva Olsson, and Magnus Skoglundh. Deactivation of diesel oxidation catalysts: Vehicle-and synthetic aging correlations. *Applied Catalysis B: Environmental*, 72(1): 71–81, 2007.

[26] C Larese, F Cabello Galisteo, M López Granados, R Mariscal, JLG Fierro, M Furió, and R Fernández Ruiz. Deactivation of real three way catalysts by cepo 4 formation. *Applied Catalysis B: Environmental*, 40(4):305–317, 2003.

[27] S. Bec, a. Tonck, J. M. Georges, and G. W. Roper. Synergistic Effects of MoDTC and ZDTP on Frictional Behaviour of Tribofilms at the Nanometer Scale. *Tribology Letters*, 17(4):797–809, November 2004. ISSN 1023-8883. doi: 10.1007/s11249-004-8088-7.

[28] Marina L Suominen Fuller, Masoud Kasrai, G Michael Bancroft, Kim Fyfe, and Kim H Tan. Solution decomposition of zinc dialkyl dithiophosphate and its effect on antiwear and thermal film formation studied by x-ray absorption spectroscopy. *Tribology international*, 31(10):627–644, 1998.

[29] M. a. Nicholls, P. R. Norton, G. M. Bancroft, M. Kasrai, G. De. Stasio, and L. M. Wiese. Spatially resolved nanoscale chemical and mechanical characterization of ZDDP antiwear films on aluminum-silicon alloys under cylinder/bore wear conditions. *Tribology Letters*, 18(3):261–278, March 2005. ISSN 1023-8883. doi: 10.1007/s11249-004-2752-9.

[30] NN Gosvami, JA Bares, F Mangolini, AR Konicek, DG Yablon, and RW Carpick. Mechanisms of antiwear tribofilm growth revealed in situ by single-asperity sliding contacts. *Science*, 348(6230):102–106, 2015.

[31] Sébastien Equey, Sigfried Roos, Ulrich Mueller, Roland Hauert, Nicholas D Spencer, and Rowena Crockett. Reactions of zinc-free anti-wear additives in dlc/dlc and steel/steel contacts. *Tribology International*, 41(11):1090–1096, 2008.

[32] Balasubramaniam Vengudusamy, Jonathan H Green, Gordon D Lamb, and Hugh A Spikes. Tribological properties of tribofilms formed from zddp in dlc/dlc and dlc/steel contacts. *Tribology International*, 44(2):165–174, 2011.

[33] Hui Cen, Ardian Morina, Anne Neville, Rihard Pasaribu, and Ileana Nedelcu. Effect of water on zddp anti-wear performance and related tribochemistry in lubricated steel/steel pure sliding contacts. *Tribology International*, 56: 47–57, 2012.

[34] P.A. Willermet, D.P. Dailey, R.O. Carter III, P.J. Schmitz, W. Zhu, J.C. Bell, and D. Park. The composition of lubricant-derived surface layers formed in a lubricated cam/tappet contact ii. effects of adding overbased detergent and dispersant to a simple {ZDTP} solution. *Tribology International*, 28(3):163–175, 1995. ISSN 0301-679X. doi: http://dx.doi.org/10.1016/0301-679X(95)98964-F.

[35] Graham C Smith. Evaluation of a simple correction for the hydrocarbon contamination layer in quantitative surface analysis by xps. *Journal of electron spectroscopy and related phenomena*, 148(1):21–28, 2005.

[36] SAJMRCJC Bec, André Tonck, Jean-Marie Georges, RC Coy, JC Bell, and GW Roper. Relationship between mechanical properties and structures of zinc dithiophosphate anti–wear films. In *Proceedings of the Royal Society of London A: Mathematical, Physical and Engineering Sciences*, volume 455, pages 4181–4203. The Royal Society, 1999.

[37] Matthew C Friedenberg and C Mathew Mate. Dynamic viscoelastic properties of liquid polymer films studied by atomic force microscopy. *Langmuir*, 12(25):6138–6142, 1996.

[38] Sung-H Choa, Kenneth C Ludema, Gregg E Potter, Benjamin M Dekoven, Ted A Morgan, and Kishore K Kar. A model of the dynamics of boundary film formation. *Wear*, 177(1):33–45, 1994.

[39] Donald H Buckley. *Surface effects in adhesion, friction, wear, and lubrication*, volume 5. Elsevier, 1981.

[40] Jiping Ye, Makoto Kano, and Yoshiteru Yasuda. Friction property study of the surface of zddp and modtc antiwear additive films using afm/lfm and force curve methods. *Tribotest*, 9(1):13–21, 2002.

[41] Izabela Szlufarska, Michael Chandross, and Robert W Carpick. Recent advances in single-asperity nanotribology. *Journal of Physics D: Applied Physics*, 41(12):123001, 2008.

[42] Bharat Bhushan. *Introduction to tribology*. John Wiley & Sons, 2013.

[43] RW Carpick, Q Dai, DF Ogletree, and M Salmeron. Friction force microscopy investigations of potassium halide surfaces in ultrahigh vacuum: structure, friction and surface modification. *Tribology Letters*, 5(1):91–102, 1998.

[44] RW Carpick, M Enachescu, DF Ogletree, and M Salmeron. Making, breaking and sliding of nanometer-scale contacts. In *MRS Proceedings*, volume 539, page 93. Cambridge Univ Press, 1998.

[45] RW Carpick, N Agrait, DF Ogletree, and M Salmeron. Variation of the interfacial shear strength and adhesion of a nanometer-sized contact. *Langmuir*, 12(13):3334–3340, 1996.

[46] Robert W Carpick and Miquel Salmeron. Scratching the surface: fundamental investigations of tribology with atomic force microscopy. *Chemical Reviews*, 97(4):1163–1194, 1997.

[47] Ang Li, Shivaprakash N Ramakrishna, Prathima C Nalam, Edmondo M Benetti, and Nicholas D Spencer. Stratified polymer grafts: Synthesis and characterization of layered 'brush' and 'gel' structures. *Advanced Materials Interfaces*, 1(1):1300007, 2014.

[48] AJ Pidduck and GC Smith. Scanning probe microscopy of automotive anti-wear films. *Wear*, 212(2):254–264, 1997.

[49] Vladimir V Tsukruk, Valery N Bliznyuk, John Hazel, Dale Visser, and Mark P Everson. Organic molecular films under shear forces: fluid and solid langmuir monolayers. *Langmuir*, 12(20):4840–4849, 1996.

[50] Hisae Yoshizawa, You Lung Chen, and Jacob Israelachvili. Fundamental mechanisms of interfacial friction. 1. relation between adhesion and friction. *The Journal of Physical Chemistry*, 97(16):4128–4140, 1993.

[51] E Meyer, R_ Overney, D Brodbeck, L Howald, R Lüthi, J Frommer, and H-J Güntherodt. Friction and wear of langmuir-blodgett films observed by friction force microscopy. *Physical review letters*, 69(12):1777, 1992.

[52] C Mathew Mate, Gary M McClelland, Ragnar Erlandsson, and Shirley Chiang. Atomic-scale friction of a tungsten tip on a graphite surface. *Physical Review Letters*, 59(17):1942, 1987.

[53] F.P. Bowden and D. Tabor. *The Friction and Lubrication of Solids*. Number pt. 1 in International series of monographs on physics. Clarendon Press, 1954.

[54] Erin E Flater, Jeffrey R VanLangendon, Erik H Wilson, K Sridharan, and Robert W Carpick. Frictional and adhesive properties of diamond-like carbon/silicon nitride nanocontacts. In *Proc. Society for Experimental Mechanics Annual Conf.(Milwaukee, WI)*, volume 42, 2002.

[55] Marius Enachescu, RJA Van Den Oetelaar, RW Carpick, DF Ogletree, CFJ Flipse, and M Salmeron. Observation of proportionality between friction and contact area at the nanometer scale. *Tribology Letters*, 7(2-3):73–78, 1999.

[56] AR Burns, JE Houston, RW Carpick, and TA Michalske. Friction and molecular deformation in the tensile regime. *Physical review letters*, 82(6): 1181, 1999.

[57] AR Burns, JE Houston, RW Carpick, and TA Michalske. Molecular level friction as revealed with a novel scanning probe. *Langmuir*, 15(8):2922–2930, 1999.

[58] M Enachescu, RJA Van Den Oetelaar, Robert W Carpick, DF Ogletree, CFJ Flipse, and Miguel Salmeron. Atomic force microscopy study of an ideally hard contact: the diamond (111)/tungsten carbide interface. *Physical review letters*, 81(9):1877, 1998.

[59] Robert W Carpick, DF Ogletree, and Miguel Salmeron. Lateral stiffness: a new nanomechanical measurement for the determination of shear strengths with friction force microscopy. *Applied Physics Letters*, 70(12):1548–1550, 1997.

[60] Robert W Carpick, N Agrait, DF Ogletree, and Miguel Salmeron. Measurement of interfacial shear (friction) with an ultrahigh vacuum atomic force microscope. *Journal of Vacuum Science & Technology B*, 14(2):1289–1295, 1996.

[61] MJ Starr, E David Reedy, Alex D Corwin, Robert W Carpick, and Erin E Flater. Contact mechanics description of inelastic displacement response of a nano-positioning device. In *MEMS, NANO and Smart Systems, 2005. Proceedings. 2005 International Conference on*, pages 421–422. IEEE, 2005.

[62] E Gnecco, R Bennewitz, T Gyalog, Ch Loppacher, M Bammerlin, E Meyer, and H-J Güntherodt. Velocity dependence of atomic friction. *Physical Review Letters*, 84(6):1172, 2000.

[63] Yihan Liu, D Fennell Evans, Qun Song, and David W Grainger. Structure and frictional properties of self-assembled surfactant monolayers. *Langmuir*, 12(5):1235–1244, 1996.

[64] IL Singer. Friction and energy dissipation at the atomic scale: A review. *Journal of Vacuum Science & Technology A*, 12(5):2605–2616, 1994.

[65] Vahid Vahdat, Kathleen E Ryan, Pamela L Keating, Yijie Jiang, Shashishekar P Adiga, J David Schall, Kevin T Turner, Judith A Harrison, and Robert W Carpick. Atomic-scale wear of amorphous hydrogenated carbon during intermittent contact: A combined study using experiment, simulation, and theory. *ACS nano*, 8(7):7027–7040, 2014.

[66] Vahid Vahdat, David S Grierson, Kevin T Turner, and Robert W Carpick. Mechanics of interaction and atomic-scale wear of amplitude modulation atomic force microscopy probes. *ACS nano*, 7(4):3221–3235, 2013.

[67] JeFoa Archard. Contact and rubbing of flat surfaces. *Journal of applied physics*, 24(8):981–988, 1953.

[68] DA Rigney. Some thoughts on sliding wear. *Wear*, 152(1):187–192, 1992.

[69] John M Thompson and Mary Kathryn Thompson. A proposal for the calculation of wear. In *Proceedings of the 2006 International ANSYS Users Conference & Exhibition, Pittsburgh*, 2006.

[70] HC Meng and KC Ludema. Wear models and predictive equations: their form and content. *Wear*, 181:443–457, 1995.

[71] Bernd Gotsmann and Mark A Lantz. Atomistic wear in a single asperity sliding contact. *Physical review letters*, 101(12):125501, 2008.

[72] Tevis DB Jacobs and Robert W Carpick. Nanoscale wear as a stress-assisted chemical reaction. *Nature nanotechnology*, 8(2):108–112, 2013.

[73] Tevis DB Jacobs, Bernd Gotsmann, Mark A Lantz, and Robert W Carpick. On the application of transition state theory to atomic-scale wear. *Tribology letters*, 39(3):257–271, 2010.

[74] Lihui Weng, Xuming Chen, and Weiliam Chen. Rheological characterization of in situ crosslinkable hydrogels formulated from oxidized dextran and n-carboxyethyl chitosan. *Biomacromolecules*, 8(4):1109–1115, 2007. doi: 10.1021/bm0610065.

[75] J.M. Krishnan, A. Deshpande, and P.B.S. Kumar. *Rheology of Complex Fluids*. Springer, 2010. ISBN 9781441964939.

[76] A. Rao. *Rheology of Fluid and Semisolid Foods: Principles and Applications*. Food Engineering Series. Springer, 2007. ISBN 9780387709291.

[77] Christopher W Macosko and Ronald G Larson. Rheology: principles, measurements, and applications. 1994.

[78] M. Kraft, J. Meissner, and J. Kaschta. Linear viscoelastic characterization of polymer melts with long relaxation times. *Macromolecules*, 32(3):751–757, 1999. doi: 10.1021/ma980730f.

[79] Chunxia He, Paula Wood-Adams, and John M. Dealy. Broad frequency range characterization of molten polymers. *Journal of Rheology*, 48(4): 711–724, 2004. doi: 10.1122/1.1763943.

[80] J. Cochrane, G. Harrison, J. Lamb, and D.W. Phillips. Creep, creep recovery and dynamic mechanical measurements of a poly(propylene glycol) oligomer. *Polymer*, 21(7):837–844, 1980. ISSN 0032-3861. doi: 10.1016/0032-3861(80)90306-7.

[81] Faith A Morrison. *Understanding rheology*. Oxford University Press, 2001.

[82] Giovanni Astarita and Giuseppe Marrucci. *Principles of non-Newtonian fluid mechanics*, volume 28. McGraw-Hill New York, 1974.

[83] Hans-Jürgen Butt, Brunero Cappella, and Michael Kappl. Force measurements with the atomic force microscope: Technique, interpretation and applications. *Surface science reports*, 59(1):1–152, 2005.

[84] Warren Carl Oliver and George Mathews Pharr. An improved technique for determining hardness and elastic modulus using load and displacement sensing indentation experiments. *Journal of materials research*, 7(06):1564–1583, 1992.

[85] Kevin D. Costa. Single-Cell Elastography: Probing for Disease with the Atomic Force Microscope. *Disease Markers*, 19(2-3):139–154, 2004. ISSN 0278-0240. doi: 10.1155/2004/482680.

[86] Heinrich Hertz. Über die berührung fester elastischer körper. 1882.

[87] KL Johnson, K Kendall, and AD Roberts. Surface energy and the contact of elastic solids. In *Proceedings of the Royal Society of London A: Mathematical, Physical and Engineering Sciences*, volume 324, pages 301–313. The Royal Society, 1971.

[88] Boris V Derjaguin, Vladimir M Muller, and Yu P Toporov. Effect of contact deformations on the adhesion of particles. *Journal of Colloid and interface science*, 53(2):314–326, 1975.

[89] M.a. Nicholls, P.R. Norton, G.M. Bancroft, M. Kasrai, T. Do, B.H. Frazer, and G. De Stasio. Nanometer Scale Chemomechanical Characterization of Antiwear Films. *Tribology Letters*, 17(2):205–216, August 2004. ISSN 1023-8883. doi: 10.1023/B:TRIL.0000032447.32442.6a.

[90] Brunero Cappella and Giovanni Dietler. Force-distance curves by atomic force microscopy. *Surface science reports*, 34(1):1–104, 1999.

[91] S. Bec, a. Tonck, and J. L. Loubet. A simple guide to determine elastic properties of films on substrate from nanoindentation experiments. *Philosophical Magazine*, 86(33-35):5347–5358, November 2006. ISSN 1478-6435. doi: 10.1080/14786430600660856.

[92] Antoine Perriot and Etienne Barthel. Elastic contact to a coated half-space: Effective elastic modulus and real penetration. *Journal of Materials Research*, 19(02):600–608, 2004.

[93] Gao Huajian, Chiu Cheng-Hsin, and Lee Jin. Elastic contact versus indentation modeling of multi-layered materials. *International Journal of Solids and Structures*, 29(20):2471–2492, 1992.

[94] Andrei Rar, H Song, and GM Pharr. Assessment of new relation for the elastic compliance of a film-substrate system. In *MRS Proceedings*, volume 695, pages L10–10. Cambridge Univ Press, 2001.

[95] Kathleen E Ryan, Pamela L Keating, Tevis DB Jacobs, David S Grierson, Kevin T Turner, Robert W Carpick, and Judith A Harrison. Simulated adhesion between realistic hydrocarbon materials: Effects of composition, roughness, and contact point. *Langmuir*, 30(8):2028–2037, 2014.

[96] Tevis DB Jacobs, Kathleen E Ryan, Pamela L Keating, David S Grierson, Joel A Lefever, Kevin T Turner, Judith A Harrison, and Robert W Carpick. The effect of atomic-scale roughness on the adhesion of nanoscale asperities: A combined simulation and experimental investigation. *Tribology Letters*, 50(1):81–93, 2013.

[97] Robert J Good and LA Girifalco. A theory for estimation of surface and interfacial energies. iii. estimation of surface energies of solids from contact angle data. *The Journal of Physical Chemistry*, 64(5):561–565, 1960.

[98] R. Mahaffy, C. Shih, F. MacKintosh, and J. Käs. Scanning Probe-Based Frequency-Dependent Microrheology of Polymer Gels and Biological Cells. *Physical Review Letters*, 85(4):880–883, July 2000. ISSN 0031-9007. doi: 10.1103/PhysRevLett.85.880.

[99] E A-Hassan, W F Heinz, M D Antonik, N P D'Costa, S Nageswaran, C a Schoenenberger, and J H Hoh. Relative microelastic mapping of living cells by atomic force microscopy. *Biophysical journal*, 74(3):1564–78, March 1998. ISSN 0006-3495. doi: 10.1016/S0006-3495(98)77868-3.

[100] Daniel Maugis. Adhesion of spheres: the jkr-dmt transition using a dugdale model. *Journal of Colloid and Interface Science*, 150(1):243–269, 1992.

[101] D Tabor. Surface forces and surface interactions. *Journal of colloid and interface science*, 58(1):2–13, 1977.

[102] JA Greenwood. Adhesion of elastic spheres. *Proceedings of the Royal Society of London. Series A: Mathematical, Physical and Engineering Sciences*, 453 (1961):1277–1297, 1997.

[103] Andrew Fogden and Lee R White. Contact elasticity in the presence of capillary condensation: I. the nonadhesive hertz problem. *Journal of Colloid and Interface Science*, 138(2):414–430, 1990.

[104] Ian N Sneddon. The relation between load and penetration in the axisymmetric boussinesq problem for a punch of arbitrary profile. *International Journal of Engineering Science*, 3(1):47–57, 1965.

[105] JB Wachtman Jr, WE Tefft, DG Lam Jr, and CS Apstein. Exponential temperature dependence of young's modulus for several oxides. *Physical review*, 122(6):1754, 1961.

[106] Orson L Anderson. Derivation of wachtman's equation for the temperature dependence of elastic moduli of oxide compounds. *Physical Review*, 144(2): 553, 1966.

[107] Vivekananda P Adiga, Sampath Suresh, Arindom Datta, John A Carlisle, and Robert W Carpick. Thermomechanical stability of ultrananocrystalline diamond. *Journal of Applied Physics*, 111(5):054913, 2012.

[108] BJ Briscoe and DCB Evans. The shear properties of langmuir-blodgett layers. *Proceedings of the Royal Society of London. A. Mathematical and Physical Sciences*, 380(1779):389–407, 1982.

[109] Yi Sang, Martin Dubé, and Martin Grant. Thermal effects on atomic friction. *Physical review letters*, 87(17):174301, 2001.

[110] TJ Young, MA Monclus, TL Burnett, WR Broughton, SL Ogin, and PA Smith. The use of the peakforcetm quantitative nanomechanical mapping afm-based method for high-resolution young's modulus measurement of polymers. *Measurement Science and Technology*, 22(12):125703, 2011.

[111] Matthew S Marcus, MA Eriksson, Darryl Y Sasaki, and Robert W Carpick. In-plane contributions to phase contrast in intermittent contact atomic force microscopy. *Ultramicroscopy*, 97(1):145–150, 2003.

[112] Matthew S Marcus, Robert W Carpick, Darryl Y Sasaki, and Mark A Eriksson. Material anisotropy revealed by phase contrast in intermittent contact atomic force microscopy. *Physical review letters*, 88(22):226103, 2002.

[113] MR VanLandingham, SH McKnight, GR Palmese, JR Elings, X Huang, TA Bogetti, RF Eduljee, and JW Gillespie Jr. Nanoscale indentation of polymer systems using the atomic force microscope. *The Journal of adhesion*, 64(1-4):31–59, 1997.

[114] Michelle L Oyen and Robert F Cook. A practical guide for analysis of nanoindentation data. *Journal of the mechanical behavior of biomedical materials*, 2(4):396–407, 2009.

[115] William D Nix. Mechanical properties of thin films. *Metallurgical transactions A*, 20(11):2217–2245, 1989.

[116] Warren C Oliver and Georges M Pharr. Measurement of hardness and elastic modulus by instrumented indentation: Advances in understanding and refinements to methodology. *Journal of materials research*, 19(01):3–20, 2004.

[117] S Bec, A Tonck, J-M Georges, E Georges, and J-L Loubet. Improvements in the indentation method with a surface force apparatus. *Philosophical magazine A*, 74(5):1061–1072, 1996.

[118] Zhanfeng Yin, Masoud Kasrai, Marina Fuller, G Michael Bancroft, Kim Fyfe, and Kim H Tan. Application of soft x-ray absorption spectroscopy in chemical characterization of antiwear films generated by zddp part i: the effects of physical parameters. *Wear*, 202(2):172–191, 1997.

[119] GM Bancroft, M Kasrai, M Fuller, Z Yin, K Fyfe, and KH Tan. Mechanisms of tribochemical film formation: stabilityof tribo-and thermally-generated ZDDP films. *Tribology Letters*, 3:47–51, 1997.

[120] MN Webster and CJJ Norbart. An experimental investigation of micropitting using a roller disk machine. *Tribology Transactions*, 38(4):883–893, 1995.

[121] C Benyajati, AV Olver, and CJ Hamer. An experimental study of micropitting, using a new miniature test-rig. *Tribology Series*, 43:601–610, 2003.

[122] V Brizmer, HR Pasaribu, and Guillermo E Morales-Espejel. Micropitting performance of oil additives in lubricated rolling contacts. *Tribology Transactions*, 56(5):739–748, 2013.

[123] Emmanuel Lainé, AV Olver, and TA Beveridge. Effect of lubricants on micropitting and wear. *Tribology International*, 41(11):1049–1055, 2008.

[124] BoHoon Kim, Ramoun Mourhatch, and Pranesh B Aswath. Properties of tribofilms formed with ashless dithiophosphate and zinc dialkyl dithiophosphate under extreme pressure conditions. *Wear*, 268(3):579–591, 2010.

[125] Xisheng Fu, Weimin Liu, and Qunji Xue. The application research on series of ashless p-containing ep and aw additives. *Industrial lubrication and tribology*, 57(2):80–83, 2005.

[126] RAKDKASMM Sarin, AK Gupta, DK Tuli, AS Verma, MM Rai, and AK Bhatnagar. Synthesis and performance evaluation of o, o-dialkylphosphorodithioic disulphides as potential antiwear, extreme-pressure and antioxidant additives. *Tribology international*, 26(6):389–394, 1993.

[127] MN Najman, M Kasrai, and GM Bancroft. Chemistry of antiwear films from ashless thiophosphate oil additives. *Tribology Letters*, 17(2):217–229, 2004.

[128] Z Zhang, ES Yamaguchi, M Kasrai, and GM Bancroft. Tribofilms generated from ZDDP and DDP on steel surfaces: Part 1, growth, wear and morphology. *Tribology Letters*, 19(3):211–220, 2005.

[129] Allyson M. Barnes, Keith D. Bartle, and Vincent R.a. Thibon. A review of zinc dialkyldithiophosphates (ZDDPS): characterisation and role in the lubricating oil. *Tribology International*, 34(6):389–395, June 2001. ISSN 0301679X. doi: 10.1016/S0301-679X(01)00028-7.

[130] Mark a. Nicholls, Than Do, Peter R. Norton, Masoud Kasrai, and G.Michael Bancroft. Review of the lubrication of metallic surfaces by zinc dialkyl-dithiophosphates. *Tribology International*, 38(1):15–39, January 2005. ISSN 0301679X. doi: 10.1016/j.triboint.2004.05.009.

[131] DR Armstrong, ES Ferrari, KJ Roberts, and D Adams. An examination of the reactivity of zinc di-alkyl-di-thiophosphate in relation to its use as an anti-wear and anti-corrosion additive in lubricating oils. *Wear*, 217(2): 276–287, 1998.

[132] Leslie R Rudnick. *Lubricant additives: chemistry and applications*. CRC Press, 2009.

[133] Philip G Harrison and Thakor Kikabhai. Proton and phosphorus-31 nuclear magnetic resonance study of zinc (ii) o, o'-dialkyl dithiophosphates in solution. *Journal of the Chemical Society, Dalton Transactions*, (4):807–814, 1987.

[134] Zenon Pawlak. *Tribochemistry of lubricating oils*, volume 45. Elsevier, 2003.

[135] D. R. Armstrong, E. S. Ferrari, K. J. Roberts, and D. Adams. An investigation into the molecular stability of zinc di-alkyl-di-thiophosphates (zddps) in relation to their use as anti-wear and anti-corrosion additives in lubricating oils. *Wear*, 208(1-2):138–146, 1997.

[136] BoHoon Kim, Vinay Sharma, and Pranesh B Aswath. Chemical and mechanistic interpretation of thermal films formed by dithiophosphates using xanes. *Tribology International*, 114:15–26, 2017.

[137] H. Spedding and R.C. Watkins. The antiwear mechanism of zddp's. part i. *Tribology International*, 15(1):9 – 12, 1982. ISSN 0301-679X. doi: http://dx.doi.org/10.1016/0301-679X(82)90101-3.

[138] THOMAS H Handley and JOHN A Dean. O, o'-dialkyl phosphorodithioic acids as extractants for metals. *Analytical Chemistry*, 34(10):1312–1315, 1962.

[139] Nicholas E Gallopoulos. Thermal decomposition of metal dialkyldithiophosphate oil blends. *ASLE TRANSACTIONS*, 7(1):55–63, 1964.

[140] PA Willermet, LR Mahoney, and CM Bishop. Lubricant degradation and wear iii. antioxidant reactions and wear behavior of a zinc dialkyldithiophosphate in a fully formulated lubricant. *ASLE TRANSACTIONS*, 23(3): 225–231, 1980.

[141] A Neville, A Morina, T Haque, and M Voong. Compatibility between tribological surfaces and lubricant additives–how friction and wear reduction can be controlled by surface/lube synergies. *Tribology International*, 40(10): 1680–1695, 2007.

[142] Jie Zhang and Hugh Spikes. On the mechanism of zddp antiwear film formation. *Tribology Letters*, 63(2):1–15, 2016.

[143] Wilfred Tysoe. On stress-induced tribochemical reaction rates. *Tribology Letters*, 65(2):48, 2017.

[144] FT Barcroft, RJ Bird, JF Hutton, and D Park. The mechanism of action of zinc thiophosphates as extreme pressure agents. *Wear*, 77(3):355–384, 1982.

[145] H. So, Y.C. Lin, Gibbs G.S. Huang, and Terny S.T. Chang. Antiwear mechanism of zinc dialkyl dithiophosphates added to a paraffinic oil in the boundary lubrication condition. *Wear*, 166(1):17 – 26, 1993. ISSN 0043-1648. doi: http://dx.doi.org/10.1016/0043-1648(93)90274-P.

[146] Albert Molina. Isolation and chemical characterization of a zinc dialkyldithiophosphate-derived antiwear agent. *ASLE transactions*, 30(4): 479–485, 1986.

[147] Dmitry Shakhvorostov, Martin H Müser, Yang Song, and Peter R Norton. Smart materials behavior in phosphates: Role of hydroxyl groups and relevance to antiwear films. *The Journal of chemical physics*, 131(4):044704, 2009.

[148] I-Ming Feng. Pyrolysis of zinc dialkyl phosphorodithioate and boundary lubrication. *Wear*, 3(4):309–311, 1960. ISSN 0043-1648. doi: http://dx.doi.org/10.1016/0043-1648(60)90295-7.

[149] I-Ming Feng, Warren L Perilstein, and Martin R Adams. Solid film deposition and non-sacrificial boundary lubrication. *ASLE transactions*, 6(1):60–66, 1963.

[150] RC Coy and RB Jones. The thermal degradation and ep performance of zinc dialkyldithiophosphate additives in white oil. *ASLE transactions*, 24 (1):77–90, 1981.

[151] RJ Bird and GD Galvin. The application of photoelectron spectroscopy to the study of ep films on lubricated surfaces. *Wear*, 37(1):143–167, 1976.

[152] Ralph G Pearson. Hard and soft acids and bases. *Journal of the American Chemical Society*, 85(22):3533–3539, 1963.

[153] Ralph G Pearson and Jon Songstad. Application of the principle of hard and soft acids and bases to organic chemistry. *Journal of the American Chemical Society*, 89(8):1827–1836, 1967.

[154] Ralph G Pearson. Hard and soft acids and bases, hsab, part 1: Fundamental principles. *Journal of Chemical Education*, 45(9):581, 1968.

[155] Ralph G Pearson. Hard and soft acids and bases, hsab, part ii: Underlying theories. *Journal of Chemical Education*, 45(10):643, 1968.

[156] Ralph G Pearson. Recent advances in the concept of hard and soft acids and bases. *Journal of Chemical Education*, 64(7):561, 1987.

[157] P.A. Willermet, R.O. Carter III, and E.N. Boulos. Lubricant-derived tribochemical films–an infra-red spectroscopic study. *Tribology International*, 25(6):371 – 380, 1992. ISSN 0301-679X. doi: http://dx.doi.org/10.1016/0301-679X(92)90074-W.

[158] AJ Burn. The mechanism of the antioxidant action of zinc dialkyl dithiophosphates. *Tetrahedron*, 22(7):2153–2161, 1966.

[159] JA Howard, Y Ohkatsu, JHB Chenier, and KU Ingold. Metal complexes as antioxidants. i. the reaction of zinc dialkyldithiophosphates and related compounds with peroxy radicals. *Canadian Journal of Chemistry*, 51(10): 1543–1553, 1973.

[160] Jean-Michel Martin, Carol Grossiord, Thierry Le Mogne, and Jinichi Igarashi. Transfer films and friction under boundary lubrication. *Wear*, 245(1-2):107–115, October 2000. ISSN 00431648. doi: 10.1016/S0043-1648(00)00471-3.

[161] Zhanfeng Yin, M. Kasrai, G.M. Bancroft, K. Fyfe, M.L. Colaianni, and K.H. Tan. Application of soft x-ray absorption spectroscopy in chemical characterization of antiwear films generated by {ZDDP} part ii: the effect of detergents and dispersants. *Wear*, 202(2):192 – 201, 1997. ISSN 0043-1648. doi: http://dx.doi.org/10.1016/S0043-1648(96)07273-0.

[162] Ardian Morina, Hongyuan Zhao, and J Fred W Mosselmans. In-situ reflection-xanes study of zddp and modtc lubricant films formed on steel and diamond like carbon (dlc) surfaces. *Applied Surface Science*, 297:167–175, 2014.

[163] M Nicholls, MN Najman, Z Zhang, M Kasrai, PR Norton, and PUPA Gilbert. The contribution of xanes spectroscopy to tribology. *Canadian journal of chemistry*, 85(10):816–830, 2007.

[164] Z Zhang, ES Yamaguchi, M Kasrai, GM Bancroft, X Liu, and ME Fleet. Tribofilms generated from zddp and ddp on steel surfaces: Part 2, chemistry. *Tribology Letters*, 19(3):221–229, 2005.

[165] J.S. Sheasby, T.A. Caughlin, A.G. Blahey, and K.F. Laycock. A reciprocating wear test for evaluating boundary lubrication. *Tribology International*, 23 (5):301 – 307, 1990. ISSN 0301-679X. doi: http://dx.doi.org/10.1016/0301-679X(90)90003-8.

[166] PA Willermet, JM Pieprzak, DP Dailey, RO Carter, NE Lindsay, LP Haack, et al. The composition of surface layers formed in a lubricated cam/tappet contact. *Journal of Tribology*, 113(1):38–47, 1991.

[167] Mirwais Aktary, MT McDermott, and GA McAlpine. Morphology and nanomechanical properties of ZDDP antiwear films as a function of tribological contact time. *Tribology letters*, 12(3):155–162, 2002.

[168] N.E. Lindsay, R.O. Carter III, P.J. Schmitz, L.P. Haack, R.E. Chase, J.E. deVries, and P.A. Willermet. Characterization of films formed at a lubricated cam/tappet contact. *Spectrochimica Acta Part A: Molecular Spectroscopy*, 49(13–14):2057 – 2070, 1993. ISSN 0584-8539. doi: http://dx.doi.org/10.1016/S0584-8539(09)91015-7.

[169] Fred G. Rounds. Some factors affecting the decomposition of three commercial zinc organodithiophosphates. *A S L E Transactions*, 18(2):79–89, 1975. doi: 10.1080/05698197508982749.

[170] Ralph McClintock. Effect of lubricants on rear axle pinion bearing break-in. *ASLE transactions*, 6(2):154–160, 1963.

[171] J.S. Sheasby, T.A. Caughlin, and J.J. Habeeb. Observation of the antiwear activity of zinc dialkyldithiophosphate additives. *Wear*, 150(1–2):247 – 257, 1991. ISSN 0043-1648. doi: http://dx.doi.org/10.1016/0043-1648(91)90320-T.

[172] MMMZRWGMMEK Kasrai, M Puller, M Scaini, Z Yin, RW Brunner, GM Bancroft, ME Fleet, K Fyfe, and KH Tan. Study of tribochemical film formation using x-ray absorption and photoelectron spectroscopies. *Tribology Series*, 30:659–669, 1995.

[173] EH Loeser, RC Wiquist, and SB Twiss. Cam and tappet lubrication. iv–radioactive study of sulfur in the ep film. *ASLE Transactions*, 2(2):199–207, 1959.

[174] Jiping Ye, Sawa Araki, Makoto Kano, and Yoshiteru Yasuda. Nanometer-scale Mechanical/Structural Properties of Molybdenum Dithiocarbamate and Zinc Dialkylsithiophosphate Tribofilms and Friction Reduction Mechanism. *Japanese Journal of Applied Physics*, 44(7B):5358–5361, July 2005. ISSN 0021-4922. doi: 10.1143/JJAP.44.5358.

[175] Marina Fuller, Zhanfeng Yin, Masoud Kasrai, G.Michael Bancroft, Elaine S. Yamaguchi, P.Ray Ryason, Pierre A. Willermet, and Kim H. Tan. Chemical characterization of tribochemical and thermal films generated from neutral and basic {ZDDPs} using x-ray absorption spectroscopy. *Tribology International*, 30(4):305 – 315, 1997. ISSN 0301-679X. doi: http://dx.doi.org/10.1016/S0301-679X(96)00059-X.

[176] MLS Fuller and LR Fernandez. The use of X-ray absorption spectroscopy for monitoring the thickness of antiwear films from ZDDP. *Tribology Letters*, 8:187–192, 2000.

[177] Mark a. Nicholls, G. Michael Bancroft, Peter R. Norton, Masoud Kasrai, Gelsomina De Stasio, Bradley H. Frazer, and Lisa M. Wiese. Chemomechanical Properties of Antiwear Films Using X-ray Absorption Microscopy and Nanoindentation Techniques. *Tribology Letters*, 17(2):245–259, August 2004. ISSN 1023-8883. doi: 10.1023/B:TRIL.0000032451.97552.3d.

[178] JM Martin, M Belin, JL Mansot, H Dexpert, and P Lagarde. Friction-induced amorphization with zddp – an exafs study. *ASLE transactions*, 29 (4):523–531, 1986.

[179] MN Najman, M Kasrai, GM Bancroft, and A Miller. Study of the chemistry of films generated from phosphate ester additives on 52100 steel using X-ray absorption spectroscopy. *Tribology Letters*, 13(3):209–218, 2002.

[180] MN Najman, M Kasrai, GM Bancroft, BH Frazer, and G De Stasio. The correlation of microchemical properties to antiwear (AW) performance in ashless thiophosphate oil additives. *Tribology Letters*, 17(4):811–822, 2004.

[181] Z Zhang, M Najman, M Kasrai, GM Bancroft, and ES Yamaguchi. Study of interaction of ep and aw additives with dispersants using xanes. *Tribology Letters*, 18(1):43–51, 2005.

[182] MN Najman, M Kasrai, and GM Bancroft. Investigating binary oil additive systems containing p and s using x-ray absorption near-edge structure spectroscopy. *Wear*, 257(1):32–40, 2004.

[183] Maura Crobu, Antonella Rossi, Filippo Mangolini, and Nicholas D Spencer. Tribochemistry of bulk zinc metaphosphate glasses. *Tribology letters*, 39(2): 121–134, 2010.

[184] Roman Heuberger, Antonella Rossi, and Nicholas D. Spencer. XPS study of the influence of temperature on ZnDTP tribofilm composition. *Tribology Letters*, 25(3):185–196, November 2006. ISSN 1023-8883. doi: 10.1007/s11249-006-9166-9.

[185] Roman Heuberger, Antonella Rossi, and ND Spencer. Reactivity of alkylated phosphorothionates with steel: a tribological and surface analytical study. *Lubrication Science*, (January):79–102, 2008. doi: 10.1002/ls.

[186] Roman Heuberger, Antonella Rossi, and Nicholas D Spencer. Pressure dependence of zndtp tribochemical film formation: a combinatorial approach. *Tribology Letters*, 28(2):209–222, 2007.

[187] John R Van Wazer and Karl A Holst. Structure and properties of the condensed phosphates. i. some general considerations about phosphoric acids. *J. Am. Chem. Soc*, 72(2):639–644, 1950.

[188] John R Van Wazer. Structure and properties of the condensed phosphates. iii. solubility fractionation and other solubility studies. *Journal of the American Chemical Society*, 72(2):647–655, 1950.

[189] C Minfray, JM Martin, Claude Esnouf, T Le Mogne, R Kersting, and B Hagenhoff. A multi-technique approach of tribofilm characterisation. *Thin Solid Films*, 447:272–277, 2004.

[190] Roman Heuberger, Antonella Rossi, and Nicholas D Spencer. Xps study of the influence of temperature on zndtp tribofilm composition. *Tribology Letters*, 25(3):185–196, 2007.

[191] Maura Crobu, Antonella Rossi, and Nicholas D Spencer. Effect of chain-length and countersurface on the tribochemistry of bulk zinc polyphosphate glasses. *Tribology Letters*, 48(3):393–406, 2012.

[192] Maura Crobu, Antonella Rossi, Filippo Mangolini, and Nicholas D Spencer. Chain-length-identification strategy in zinc polyphosphate glasses by means of xps and tof-sims. *Analytical and bioanalytical chemistry*, 403(5):1415–1432, 2012.

[193] Eric Liu and Sylvain D Kouame. An xps study on the composition of zinc dialkyl dithiophosphate tribofilms and their effect on camshaft lobe wear. *Tribology Transactions*, 57(1):18–27, 2014.

[194] EC Onyiriuka. Zinc phosphate glass surfaces studied by xps. *Journal of non-crystalline solids*, 163(3):268–273, 1993.

[195] JW Wiench, M Pruski, B Tischendorf, JU Otaigbe, and BC Sales. Structural studies of zinc polyphosphate glasses by nuclear magnetic resonance. *Journal of Non-Crystalline Solids*, 263:101–110, 2000.

[196] B Tischendorf, JU Otaigbe, JW Wiench, M Pruski, and BC Sales. A study of short and intermediate range order in zinc phosphate glasses. *Journal of non-crystalline solids*, 282(2):147–158, 2001.

[197] G Walter, U Hoppe, J Vogel, G Carl, and P Hartmann. The structure of zinc polyphosphate glass studied by diffraction methods and 31 p nmr. *Journal of non-crystalline solids*, 333(3):252–262, 2004.

[198] Morey Najman, Masoud Kasrai, G. Michael Bancroft, and Ross Davidson. Combination of ashless antiwear additives with metallic detergents: interactions with neutral and overbased calcium sulfonates. *Tribology International*, 39(4):342–355, April 2006. ISSN 0301679X. doi: 10.1016/j.triboint.2005.02.014.

[199] B Dacre and CH Bovington. The effect of metal composition on the adsorption of zinc di-isopropyldithiophosphate. *ASLE TRANSACTIONS*, 26(3): 333–343, 1983.

[200] Kosuke Ito, Jean-Michel Martin, Clotilde Minfray, and Koji Kato. Low-friction tribofilm formed by the reaction of zddp on iron oxide. *Tribology international*, 39(12):1538–1544, 2006.

[201] K Ito, JM Martin, C Minfray, and K Kato. Formation mechanism of a low friction zddp tribofilm on iron oxide. *Tribology transactions*, 50(2):211–216, 2007.

[202] S Plaza. The adsorption of zinc dibutyldithiophosphates on iron and iron oxide powders. *ASLE transactions*, 30(2):233–240, 1987.

[203] Masatoshi Watanabe, Minoru Sakuma, Takeshi Inaba, and Yasutaka Iguchi. Formation and oxidation of sulfides on pure iron and iron oxides. *Materials Transactions, JIM*, 41(7):865–872, 2000.

[204] Yue-Rong Li, Gavin Pereira, Masoud Kasrai, and Peter R. Norton. The Effect of Steel Hardness on the Performance of ZDDP Antiwear Films: A Multi-Technique Approach. *Tribology Letters*, 29(3):201–211, January 2008. ISSN 1023-8883. doi: 10.1007/s11249-008-9297-2.

[205] JS Sheasby, TA Caughlin, and WA Mackwood. The effect of steel hardness on the performance of antiwear additives. *Wear*, 201(1-2):209–216, 1996.

[206] Ali Erdemir and Christophe Donnet. Tribology of diamond-like carbon films: recent progress and future prospects. *Journal of Physics D: Applied Physics*, 39(18):R311, 2006.

[207] Igor Velkavrh, Mitjan Kalin, and Jozef Vizintin. The performance and mechanisms of dlc-coated surfaces in contact with steel in boundary-lubrication conditions: a review. *Strojniški vestnik*, 54(3):189–206, 2008.

[208] M Kalin, I Velkavrh, J Vižintin, and L Ožbolt. Review of boundary lubrication mechanisms of dlc coatings used in mechanical applications. *Meccanica*, 43(6):623–637, 2008.

[209] Dewan M Nuruzzaman, Mohammad A Chowdhury, Akira Nakajima, Mohammad L Rahaman, and Syed M I Karim. Friction and wear of diamond like carbon (dlc) coatings-a review. *Recent Patents on Mechanical Engineering*, 4(1):55–78, 2011.

[210] Rehan Zahid, Masjuki Bin Haji Hassan, Mahendra Varman, Riaz Ahmad Mufti, Md Abul Kalam, Nurin Wahidah Binti Mohd Zulkifli, and Mubashir Gulzar. A review on effects of lubricant formulations on tribological performance and boundary lubrication mechanisms of non-doped dlc/dlc contacts. *Critical Reviews in Solid State and Materials Sciences*, pages 1–28, 2016.

[211] Sébastien Equey, Sigfried Roos, Ulrich Mueller, Roland Hauert, Nicholas D Spencer, and Rowena Crockett. Tribofilm formation from zndtp on diamond-like carbon. *Wear*, 264(3):316–321, 2008.

[212] Ksenija Topolovec-Miklozic, Frances Lockwood, and Hugh Spikes. Behaviour of boundary lubricating additives on dlc coatings. *Wear*, 265(11):1893–1901, 2008.

[213] M Kalin, E Roman, L Ožbolt, and J Vižintin. Metal-doped (ti, wc) diamond-like-carbon coatings: reactions with extreme-pressure oil additives under tribological and static conditions. *Thin Solid Films*, 518(15):4336–4344, 2010.

[214] Mitjan Kalin, E Roman, and Jože Vižintin. The effect of temperature on the tribological mechanisms and reactivity of hydrogenated, amorphous diamond-like carbon coatings under oil-lubricated conditions. *Thin Solid Films*, 515(7):3644–3652, 2007.

[215] S Akbari, J Kovač, and M Kalin. Effect of zddp concentration on the thermal film formation on steel, hydrogenated non-doped and si-doped dlc. *Applied Surface Science*, 383:191–199, 2016.

[216] T Haque, A Morina, A Neville, R Kapadia, and S Arrowsmith. Non-ferrous coating/lubricant interactions in tribological contacts: assessment of tribofilms. *Tribology International*, 40(10):1603–1612, 2007.

[217] Bojan Podgornik, Staffan Jacobson, and Sture Hogmark. Dlc coating of boundary lubricated components–advantages of coating one of the contact surfaces rather than both or none. *Tribology International*, 36(11):843–849, 2003.

[218] B Podgornik, J Vižintin, Staffan Jacobson, and Sture Hogmark. Tribological behaviour of wc/c coatings operating under different lubrication regimes. *Surface and Coatings Technology*, 177:558–565, 2004.

[219] Bojan Podgornik and Jože Vižintin. Tribological reactions between oil additives and dlc coatings for automotive applications. *Surface and Coatings Technology*, 200(5):1982–1989, 2005.

[220] MI de Barros' Bouchet, JM Martin, T Le-Mogne, and B Vacher. Boundary lubrication mechanisms of carbon coatings by modtc and zddp additives. *Tribology International*, 38(3):257–264, 2005.

[221] Masahito Ban, Makoto Ryoji, Sadao Fujii, and Junzo Fujioka. Tribological characteristics of si-containing diamond-like carbon films under oil-lubrication. *Wear*, 253(3):331–338, 2002.

[222] Bojan Podgornik, Staffan Jacobson, and Sture Hogmark. Influence of ep additive concentration on the tribological behaviour of dlc-coated steel surfaces. *Surface and Coatings Technology*, 191(2):357–366, 2005.

[223] M Kalin, J Vižintin, J Barriga, K Vercammen, K van Acker, and A Arnšek. The effect of doping elements and oil additives on the tribological performance of boundary-lubricated dlc/dlc contacts. *Tribology Letters*, 17(4): 679–688, 2004.

[224] Mitjan Kalin and Jože Vižintin. Differences in the tribological mechanisms when using non-doped, metal-doped (ti, wc), and non-metal-doped (si) diamond-like carbon against steel under boundary lubrication, with and without oil additives. *Thin solid films*, 515(4):2734–2747, 2006.

[225] T Haque, A Morina, and A Neville. Tribological performance evaluation of a hydrogenated diamond-like carbon coating in sliding/rolling contact–effect of lubricant additives. *Proceedings of the Institution of Mechanical Engineers, Part J: Journal of Engineering Tribology*, 225(6):393–405, 2011.

[226] Liuquan Yang, Anne Neville, Alisdair Brown, Paul Ransom, and Ardian Morina. Effect of lubricant additives on the wdlc coating structure when tested in boundary lubrication regime. *Tribology Letters*, 57(2):14, 2015.

[227] C Donnet and A Grill. Friction control of diamond-like carbon coatings. *Surface and Coatings Technology*, 94:456–462, 1997.

[228] Mitjan Kalin, Said Jahanmir, and Goran Dražič. Wear mechanisms of glass-infiltrated alumina sliding against alumina in water. *Journal of the American Ceramic Society*, 88(2):346–352, 2005.

[229] L Lazzarotto, L Dubar, A Dubois, P Ravassard, and J Oudin. Three selection criteria for the cold metal forming lubricating oils containing extreme pressure agents. *Journal of Materials Processing Technology*, 80: 245–250, 1998.

[230] Aldara Naveira-Suarez, Agnieszka Tomala, Mattias Grahn, Maurizio Zaccheddu, Rihard Pasaribu, and Roland Larsson. The influence of base oil polarity and slide–roll ratio on additive-derived reaction layer formation. *Proceedings of the Institution of Mechanical Engineers, Part J: Journal of Engineering Tribology*, pages 565–576, 2011.

[231] Agnieszka Tomala, Aldara Naveira-Suarez, Ilse C Gebeshuber, and Rihard Pasaribu. Effect of base oil polarity on micro and nanofriction behaviour of base oil+ zddp solutions. *Tribology-Materials, Surfaces & Interfaces*, 3(4): 182–188, 2009.

[232] A Naveira Suarez, Mattias Grahn, Rihard Pasaribu, and Roland Larsson. The influence of base oil polarity on the tribological performance of zinc dialkyl dithiophospate additives. *Tribology International*, 43(12):2268–2278, 2010.

[233] Prasenjit Kar, Pranay Asthana, and Hong Liang. Formation and characterization of tribofilms. *Journal of tribology*, 130(4):042301, 2008.

[234] Ichiro Minami, Keiji Hirao, Michimasa Memita, and Shigeyuki Mori. Investigation of anti-wear additives for low viscous synthetic esters: Hydroxyalkyl phosphonates. *Tribology international*, 40(4):626–631, 2007.

[235] I. Minami and S. Mori. Anti-wear additives for ester oils. *Journal of Synthetic Lubrication*, 22(2):105–121, 2005.

[236] I Nedelcu, E Piras, A Rossi, and HR Pasaribu. Xps analysis on the influence of water on the evolution of zinc dialkyldithiophosphate–derived reaction layer in lubricated rolling contacts. *Surface and Interface Analysis*, 44(8): 1219–1224, 2012.

[237] ES Ferrari, KJ Roberts, and D Adams. A multi-edge x-ray absorption spectroscopy study of the reactivity of zinc di-alkyl-di-thiophosphates (zddps) anti-wear additives:: 1. an examination of representative model compounds. *Wear*, 236(1):246–258, 1999.

[238] ES Ferrari, KJ Roberts, M Sansone, and D Adams. A multi-edge x-ray absorption spectroscopy study of the reactivity of zinc di-alkyl-di-thiophosphates anti-wear additives: 2. in situ studies of steel/oil interfaces. *Wear*, 236(1):259–275, 1999.

[239] CH Bovington and B Dacre. The adsorption and reaction of decomposition products of zinc di-isopropyldiophosphate on steel. *ASLE transactions*, 27 (3):252–258, 1984.

[240] Ali Ghanbarzadeh, Pourya Parsaeian, Ardian Morina, Mark CT Wilson, Marcel CP van Eijk, Ileana Nedelcu, Duncan Dowson, and Anne Neville. A semi-deterministic wear model considering the effect of zinc dialkyl dithiophosphate tribofilm. *Tribology Letters*, 61(1):12, 2016.

[241] Pourya Parsaeian, Ali Ghanbarzadeh, Mark Wilson, Marcel CP Van Eijk, Ileana Nedelcu, Duncan Dowson, Anne Neville, and Ardian Morina. An experimental and analytical study of the effect of water and its tribochemistry on the tribocorrosive wear of boundary lubricated systems with zddp-containing oil. *Wear*, 358:23–31, 2016.

[242] Pourya Parsaeian, Ali Ghanbarzadeh, Marcel CP Van Eijk, Ileana Nedelcu, Ardian Morina, and Anne Neville. Study of the interfacial mechanism of zddp tribofilm in humid environment and its effect on tribochemical wear; part ii: Numerical. *Tribology International*, 107:33–38, 2017.

[243] Gavin Pereira, David Munoz-Paniagua, Andreas Lachenwitzer, Masoud Kasrai, Peter R Norton, T Weston Capehart, Thomas A Perry, and Yang-Tse Cheng. A variable temperature mechanical analysis of zddp-derived antiwear films formed on 52100 steel. *Wear*, 262(3):461–470, 2007.

[244] Hongbing Ji, Mark A Nicholls, Peter R Norton, Masoud Kasrai, T Weston Capehart, Thomas A Perry, and Yang-Tse Cheng. Zinc-dialkyldithiophosphate antiwear films: dependence on contact pressure and sliding speed. *Wear*, 258(5):789–799, 2005.

[245] Yasunori Shimizu and Hugh A Spikes. The influence of slide–roll ratio on zddp tribofilm formation. *Tribology Letters*, 64(2):19, 2016.

[246] PME Cann, GJ Johnston, and HA Spikes. Formation of thick films by phosphorus-based anti-wear additives. pages 543–554. Mechanical Engineering Publ Ltd, 1987.

[247] H. So and Y.C. Lin. The theory of antiwear for {ZDDP} at elevated temperature in boundary lubrication condition. *Wear*, 177(2):105 – 115, 1994. ISSN 0043-1648. doi: http://dx.doi.org/10.1016/0043-1648(94)90236-4.

[248] OL Warren, JF Graham, PR Norton, JE Houston, and TA Michalske. Nanomechanical properties of films derived from zinc dialkyldithiophosphate. *Tribology Letters*, 4(2):189–198, 1998.

[249] JF Graham, C McCague, and PR Norton. Topography and nanomechanical properties of tribochemical films derived from zinc dialkyl and diaryl dithiophosphates. *Tribology letters*, 6:149–157, 1999.

[250] L Taylor, A Dratva, and HA Spikes. Friction and wear behavior of zinc dialkyldithiophosphate additive. *Tribology transactions*, 43(3):469–479, 2000.

[251] Mirwais Aktary, Mark T. McDermott, and Jeff Torkelson. Morphological evolution of films formed from thermooxidative decomposition of {ZDDP}. *Wear*, 247(2):172 – 179, 2001. ISSN 0043-1648. doi: http://dx.doi.org/10.1016/S0043-1648(00)00525-1.

[252] GW Canning, ML Suominen Fuller, GM Bancroft, M Kasrai, JN Cutler, G De Stasio, and B Gilbert. Spectromicroscopy of tribological films from engine oil additives. part i. films from zddp's. *Tribology letters*, 6(3-4): 159–169, 1999.

[253] Jiping Ye, Makoto Kano, and Yoshiteru Yasuda. Evaluation of local mechanical properties in depth in MoDTC/ZDDP and ZDDP tribochemical reacted films using nanoindentation. *Tribology Letters*, 13(1):41–47, 2002.

[254] Jiping Ye, M Kano, and Y Yasuda. Evaluation of nanoscale friction depth distribution in ZDDP and MoDTC tribochemical reacted films using a nanoscratch method. *Tribology Letters*, 16(February):107–112, 2004.

[255] Jiping Ye, Makoto Kano, and Yoshiteru Yasuda. Determination of nanostructures and mechanical properties on the surface of molybdenum dithiocarbamate and zinc dialkyl-dithiophosphate tribochemical reacted films using atomic force microscope phase imaging technique. *Journal of applied physics*, 93(9):5113–5117, 2003.

[256] Ksenija Topolovec Miklozic, Jocelyn Graham, and Hugh Spikes. Chemical and physical analysis of reaction films formed by molybdenum dialkyldithiocarbamate friction modifier additive using raman and atomic force microscopy. *Tribology Letters*, 11(2):71–81, 2001.

[257] Chau Chang Chou and Jen Fin Lin. A new approach to the effect of ep additive and surface roughness on the pitting fatigue of a line-contact system. *Journal of tribology*, 124(2):245–258, 2002.

[258] Mark A Nicholls, Than Do, Peter R Norton, G Michael Bancroft, Masoud Kasrai, T Weston Capehart, Yang-Tse Cheng, and Thomas Perry. Chemical and mechanical properties of zddp antiwear films on steel and thermal spray coatings studied by xanes spectroscopy and nanoindentation techniques. *Tribology Letters*, 15(3):241–248, 2003.

[259] Pourya Parsaeian, Ali Ghanbarzadeh, Marcel CP Van Eijk, Ileana Nedelcu, Anne Neville, and Ardian Morina. A new insight into the interfacial mechanisms of the tribofilm formed by zinc dialkyl dithiophosphate. *Applied Surface Science*, 403:472–486, 2017.

[260] Jean-Marie Georges, André Tonck, Stéphane Poletti, Elaine S Yamaguchi, and PR Ryason. Film thickness and mechanical properties of adsorbed neutral and basic zinc diisobutyl dithiophosphates. *Tribology transactions*, 41(4):543–553, 1998.

[261] I Neitzel, V Mochalin, JA Bares, RW Carpick, A Erdemir, and Y Gogotsi. Tribological properties of nanodiamond-epoxy composites. *Tribology Letters*, 47(2):195–202, 2012.

[262] L. J. Taylor and H. A. Spikes. Friction-enhancing properties of zddp antiwear additive: Part i–friction and morphology of zddp reaction films. *Tribology Transactions*, 46(3):303–309, 2003. doi: 10.1080/10402000308982630.

[263] D Mazuyer, A Tonck, S Bec, JL Loubet, and JM Georges. Nanoscale surface rheology in tribology. *Tribology Series*, pages 273–282, 2001.

[264] Jean-Marie Georges, André Tonck, Jean-Luc Loubet, Denis Mazuyer, Etienne Georges, and François Sidoroff. Rheology and friction of compressed polymer layers adsorbed on solid surfaces. *Journal de Physique II*, 6(1): 57–76, 1996.

[265] Qunyang Li, Changgu Lee, Robert W Carpick, and James Hone. Substrate effect on thickness-dependent friction on graphene. *physica status solidi (b)*, 247(11-12):2909–2914, 2010.

[266] Changgu Lee, Xiaoding Wei, Qunyang Li, Robert Carpick, Jeffrey W Kysar, and James Hone. Elastic and frictional properties of graphene. *physica status solidi (b)*, 246(11-12):2562–2567, 2009.

[267] Changgu Lee, Qunyang Li, William Kalb, Xin-Zhou Liu, Helmuth Berger, Robert W Carpick, and James Hone. Frictional characteristics of atomically thin sheets. *Science*, 328(5974):76–80, 2010.

[268] J Gansheimer. On the lubricating properties of mixtures of mineral oil with certain inorganic phosphates, hydroxides, and sulfides. *Asle TRANSACTIONS*, 15(3):201–206, 1972.

[269] Dieter Landolt and Stefano Mischler. *Tribocorrosion of passive metals and coatings*. Elsevier, 2011.

[270] Michael Duncanson. Detecting and controlling water in oil. In *Proceedings of Noria Lubrication Excellence 2005 Conference April 25-29, San Antonio, Texas*, 2005.

[271] Alan C Eachus. The trouble with water. *Tribology & lubrication technology*, 61(10):32–38, 2005.

[272] PE Sheehan. The wear kinetics of nacl under dry nitrogen and at low humidities. *Chemical physics letters*, 410(1):151–155, 2005.

[273] Pourya Parsaeian, Marcel CP Van Eijk, Ileana Nedelcu, Anne Neville, and Ardian Morina. Study of the interfacial mechanism of zddp tribofilm in humid environment and its effect on tribochemical wear; part i: Experimental. *Tribology International*, 107:135–143, 2017.

[274] Owen D Faut and Donald R Wheeler. On the mechanism of lubrication by tricresylphosphate (tcp) – the coefficient of friction as a function of temperature for tcp on m-50 steel. *ASLE TRANSACTIONS*, 26(3):344–350, 1983.

[275] W. A. WEYL. Phosphate glasses. *Chemical & Engineering News Archive*, 27(15):1048–1049, 1949. doi: 10.1021/cen-v027n015.p1048.

[276] Zenon Pawlak, Vladis Kosse, Adekunle Oloyede, Teresa Rauckyte, Andrzej Kopkowski, Douglas J Hargreaves, Raghuvir B Pai, and David Macintosh. The antiwear effectiveness of micellar zinc phosphates and copper oxide through friction-induced cross-linking. 2006.

[277] Ramoun Mourhatch and Pranesh B Aswath. Tribological behavior and nature of tribofilms generated from fluorinated zddp in comparison to zddp under extreme pressure conditions–part 1: Structure and chemistry of tribofilms. *Tribology International*, 44(3):187–200, 2011.

[278] S Hofmann. Sputter depth profile analysis of interfaces. *Reports on Progress in Physics*, 61(7):827, 1998.

[279] Heather Adams, Brendan P Miller, Peter V Kotvis, Octavio J Furlong, Ashlie Martini, and Wilfred T Tysoe. In situ measurements of boundary film formation pathways and kinetics: dimethyl and diethyl disulfide on copper. *Tribology Letters*, 62(1):12, 2016.

[280] Jonathan R Felts, Andrew J Oyer, Sandra C Hernández, Keith E Whitener Jr, Jeremy T Robinson, Scott G Walton, and Paul E Sheehan. Direct mechanochemical cleavage of functional groups from graphene. *Nature communications*, 6:6467, 2015.

[281] Heather L Adams, Michael T Garvey, Uma Shantini Ramasamy, Zhijiang Ye, Ashlie Martini, and Wilfred T Tysoe. Shear-induced mechanochemistry: pushing molecules around. *The Journal of Physical Chemistry C*, 119(13): 7115–7123, 2015.

[282] S Berkani, F Dassenoy, C Minfray, M Belin, B Vacher, JM Martin, H Cardon, G Montagnac, and B Reynard. Model formation of ZDDP tribofilm from a mixture of zinc metaphosphate and goethite. *Tribology International*, 79: 197–203, 2014.

[283] Sophia Berkani, Fabrice Dassenoy, Clotilde Minfray, Jean-Michel Martin, Herve Cardon, Gilles Montagnac, and Bruno Reynard. Structural Changes in Tribo-Stressed Zinc Polyphosphates. *Tribology Letters*, 51(3):489–498, July 2013. ISSN 1023-8883. doi: 10.1007/s11249-013-0188-9.

[284] Yue-Rong Li, Gavin Pereira, Andreas Lachenwitzer, Masoud Kasrai, and Peter R Norton. Studies on ZDDP thermal film formation by XANES spectroscopy, atomic force microscopy, FIB/SEM and 31P NMR. *Tribology Letters*, 29(1):11–22, 2008.

[285] Karine Masenelli-Varlot, M Kasrai, GM Bancroft, G De Stasio, B Gilbert, ES Yamaguchi, and PR Ryason. Spatial distribution of the chemical species generated under rubbing from ZDDP and dispersed potassium triborate. *Tribology Letters*, 14(3):157–166, 2003.

[286] MN Najman, M Kasrai, and GM Bancroft. X-ray absorption spectroscopy and atomic force microscopy of films generated from organosulfur extreme-pressure (EP) oil additives. *Tribology Letters*, 14(4):225–235, 2003.

[287] Marina Fuller, Masoud Kasraia, John S Sheasby, G Michael Bancroft, Kim Fyfe, and Kim H Tan. X-ray absorption spectroscopy of antiwear films on aluminum alloys generated from zinc dialkyldithiophosphate. *Tribology Letters*, 1(4):367–378, 1995.

[288] ZMGMES Zhang, M Kasrai, GM Bancroft, and ES Yamaguchi. Study of the interaction of ZDDP and dispersants using X-ray absorption near edge structure spectroscopy – Part 1: Thermal chemical reactions. *Tribology Letters*, 15(4):377–384, 2003.

[289] Gelsomina De Stasio, M Capozi, GF Lorusso, PA Baudat, TC Droubay, P Perfetti, G Margaritondo, and BP Tonner. MEPHISTO: Performance tests of a novel synchrotron imaging photoelectron spectromicroscope. *Review of scientific instruments*, 69(5):2062–2066, 1998.

[290] C Donnet, JM Martin, J Fontaine, JC Sánchez-López, C Quirós, E Elizalde, JM Sanz, TC Rojas, and A Fernández. The role of CN chemical bonding on the tribological behaviour of CN_x coatings. *Surface and Coatings Technology*, 120:594–600, 1999.

[291] C Donnet, J Fontaine, A Grill, and T Le Mogne. The role of hydrogen on the friction mechanism of diamond-like carbon films. *Tribology Letters*, 9 (3-4):137–142, 2001.

[292] M. Gauvin, F. Dassenoy, C. Minfray, J. M. Martin, G. Montagnac, and B. Reynard. Zinc phosphate chain length study under high hydrostatic pressure by Raman spectroscopy. *Journal of Applied Physics*, 101(6):063505, 2007. ISSN 00218979. doi: 10.1063/1.2710431.

[293] Federica M Piras, Antonella Rossi, and Nicholas D Spencer. Combined in situ (ATR FT-IR) and ex situ (XPS) study of the ZnDTP-iron surface interaction. *Tribology Letters*, 15(3):181–191, 2003.

[294] A Rossi, M Eglin, FM Piras, K Matsumoto, and ND Spencer. Surface analytical studies of surface-additive interactions, by means of in situ and combinatorial approaches. *Wear*, 256(6):578–584, 2004.

[295] George Socrates. *Infrared and Raman characteristic group frequencies: Tables and charts*. John Wiley & Sons, 2004.

[296] Katrin Kneipp, Harald Kneipp, Irving Itzkan, Ramachandra R Dasari, and Michael S Feld. Surface-enhanced Raman scattering and biophysics. *Journal of Physics: Condensed Matter*, 14(18):R597, 2002.

[297] Federica M Piras, Antonella Rossi, and Nicholas D Spencer. Growth of tribological films: In situ characterization based on attenuated total reflection infrared spectroscopy. *Langmuir*, 18(17):6606–6613, 2002.

[298] TL Reitz, PL Lee, KF Czaplewski, JC Lang, KE Popp, and HH Kung. Time-resolved XANES investigation of CuO/ZnO in the oxidative methanol reforming reaction. *Journal of catalysis*, 199(2):193–201, 2001.

[299] Marco Maria Günter, Thorsten Ressler, Rolf E Jentoft, and Bettina Bems. Redox behavior of copper oxide/zinc oxide catalysts in the steam reforming of methanol studied by in situ X-ray diffraction and absorption spectroscopy. *Journal of Catalysis*, 203(1):133–149, 2001.

[300] Won-Sub Yoon, Clare P Grey, Mahalingam Balasubramanian, Xiao-Qing Yang, and James McBreen. In situ X-ray absorption spectroscopic study on $LiNi_{0.5}Mn_{0.5}O_2$ cathode material during electrochemical cycling. *Chemistry of materials*, 15(16):3161–3169, 2003.

[301] YW Tsai, BJ Hwang, G Ceder, HS Sheu, DG Liu, and JF Lee. In-situ X-ray absorption spectroscopic study on variation of electronic transitions and local structure of $LiNi_{1/3}Co_{1/3}Mn_{1/3}O_2$ cathode material during electrochemical cycling. *Chemistry of materials*, 17(12):3191–3199, 2005.

[302] Feng Zhou, Yongmin Liang, and Weimin Liu. Ionic liquid lubricants: designed chemistry for engineering applications. *Chemical Society Reviews*, 38 (9):2590–2599, 2009.

[303] PM Cann, HA Spikes, and J Hutchinson. The development of a spacer layer imaging method (slim) for mapping elastohydrodynamic contacts. *Tribology Transactions*, 39(4):915–921, 1996.

[304] Joe Kaperick. Elbow grease: The work behind the art. *TRIBOLOGY & LUBRICATION TECHNOLOGY*, 68(11):36–38, 2012.

[305] Ian M Hutchings. Tribology: friction and wear of engineering materials. 1992.

[306] TE Tallian. On competing failure modes in rolling contact. *ASLE TRANSACTIONS*, 10(4):418–439, 1967.

[307] B.J. Hamrock, D. Dowson, L.R. Center, and U.S.N.A.S.A.S.T.I. Office. *Minimum film thickness in elliptical contacts for different regimes of fluid-film lubrication*. National Aeronautics and Space Administration, Scientific and Technical Information Office, 1978.

[308] Benjamin a Smith, Barbara Tolloczko, James G Martin, and Peter Grütter. Probing the viscoelastic behavior of cultured airway smooth muscle cells with atomic force microscopy: stiffening induced by contractile agonist. *Biophysical journal*, 88(4):2994–3007, April 2005. ISSN 0006-3495. doi: 10.1529/biophysj.104.046649.

[309] B Ravel and M Newville. ATHENA and ARTEMIS: interactive graphical data analysis using IFEFFIT. *Physica Scripta*, 2005(T115):1007, 2005.

[310] Bede Pittenger, Natalia Erina, and Chanmin Su. Quantitative mechanical property mapping at the nanoscale with peakforce qnm. *Application Note Veeco Instruments Inc*, 2010.

[311] Christian Clasen, H Pirouz Kavehpour, and Gareth H McKinley. Bridging tribology and microrheology of thin films. *Appl. Rheol*, 20(4):196, 2010.

[312] Jan Engmann, Colin Servais, and Adam S Burbidge. Squeeze flow theory and applications to rheometry: a review. *Journal of non-newtonian fluid mechanics*, 132(1):1–27, 2005.

[313] Franck Rose, Na Wang, Robert Smith, Qi-Fan Xiao, Hiroshi Inaba, Toru Matsumura, Yoko Saito, Hiroyuki Matsumoto, Qing Dai, Bruno Marchon, et al. Complete characterization by raman spectroscopy of the structural properties of thin hydrogenated diamond-like carbon films exposed to rapid thermal annealing. *Journal of Applied Physics*, 116(12):123516, 2014.

[314] Michael Eglin, Antonella Rossi, and Nicholas D Spencer. X-ray photoelectron spectroscopy analysis of tribostressed samples in the presence of zndtp: a combinatorial approach. *Tribology Letters*, 15(3):199–209, 2003.

[315] EE Khawaja, SMA Durrani, FF Al-Adel, MA Salim, and M Sakhawat Hussain. X-ray photoelectron spectroscopy and fourier transform-infrared studies of transition metal phosphate glasses. *Journal of materials science*, 30(1):225–234, 1995.

[316] J Frederick W Mosselmans, Paul D Quinn, Andrew J Dent, Stuart A Cavill, Sofia Diaz Moreno, Andrew Peach, Peter J Leicester, Stephen J Keylock, Simon R Gregory, Kirk D Atkinson, et al. I18 – the microfocus spectroscopy beamline at the Diamond Light Source. *Journal of synchrotron radiation*, 16(6):818–824, 2009.

[317] Gangadhar Das, MK Tiwari, AK Singh, and Haranath Ghosh. Effect of synchrotron polarization on grazing incidence X-ray fluorescence analysis. *Journal of Analytical Atomic Spectrometry*, 29(12):2405–2413, 2014.

[318] Reinhold Klockenkämper and Alex von Bohlen. *Total-reflection X-ray Fluorescence Analysis and Related Methods*. John Wiley & Sons, 2014.

[319] G Walter, G Goerigk, and C Rüssel. The structure of phosphate glass evidenced by small angle X-ray scattering. *Journal of non-crystalline solids*, 352(38):4051–4061, 2006.

[320] John H Hubbell and Stephen M Seltzer. Tables of X-ray mass attenuation coefficients and mass energy-absorption coefficients 1 kev to 20 MeV for elements Z= 1 to 92 and 48 additional substances of dosimetric interest. Technical report, National Inst. of Standards and Technology-PL, Gaithersburg, MD (United States). Ionizing Radiation Div., 1995.

[321] Juliane Benedet, Jonathan H Green, Gordon D Lamb, and Hugh A Spikes. Spurious mild wear measurement using white light interference microscopy in the presence of antiwear films. *Tribology Transactions*, 52(6):841–846, 2009.

[322] Ksenija Topolovec-Miklozic, T Reg Forbus, and Hugh A Spikes. Film thickness and roughness of zddp antiwear films. *Tribology Letters*, 26(2): 161–171, 2007.

[323] JK Lancaster. A review of the influence of environmental humidity and water on friction, lubrication and wear. *Tribology International*, 23(6):371–389, 1990.

[324] Asako Koike and Makoto Yoneya. Chain length effects on frictional behavior of confined ultrathin films of linear alkanes under shear. *The Journal of Physical Chemistry B*, 102(19):3669–3675, 1998.

[325] Richard K Brow, David R Tallant, Sharon T Myers, and Carol C Phifer. The short-range structure of zinc polyphosphate glass. *Journal of Non-Crystalline Solids*, 191(1):45–55, 1995.

[326] HS Liu, TS Chin, and SW Yung. Ftir and xps studies of low-melting pbo-zno-p 2 o 2 glasses. *Materials chemistry and physics*, 50(1):1–10, 1997.

[327] PY Shih, SW Yung, and TS Chin. Ftir and xps studies of p 2 o 5–na 2 o–cuo glasses. *Journal of non-crystalline solids*, 244(2):211–222, 1999.

[328] M Eglin, A Rossi, and ND Spencer. Additive-surface interaction in boundary lubrication: a combinatorial approach. *Tribology Series*, 40:49–57, 2002.

[329] Richard K Brow. An xps study of oxygen bonding in zinc phosphate and zinc borophosphate glasses. *Journal of non-crystalline solids*, 194(3):267–273, 1996.

[330] Alexandrine Flambard, Jean-Jacques Videau, Laurent Delevoye, Thierry Cardinal, Christine Labrugère, CA Rivero, Michel Couzi, and Lionel Montagne. Structure and nonlinear optical properties of sodium–niobium phosphate glasses. *Journal of Non-Crystalline Solids*, 354(30):3540–3547, 2008.

[331] MA Salim, GD Khattak, PS Fodor, and LE Wenger. X-ray photoelectron spectroscopy (xps) and magnetization studies of iron–vanadium phosphate glasses. *Journal of non-crystalline solids*, 289(1):185–195, 2001.

[332] C Minfray, JM Martin, MI De Barros, T Le Mogne, R Kersting, and B Hagenhoff. Chemistry of zddp tribofilm by tof-sims. *Tribology Letters*, 17 (3):351–357, 2004.

[333] D Brion. Etude par spectroscopie de photoelectrons de la degradation superficielle de fes 2, cufes 2, zns et pbs a l'air et dans l'eau. *Applications of Surface Science*, 5(2):133–152, 1980.

[334] KONNO H., SASAKI K., TSUNEKAWA M., TAKAMORI T., and FURUICHI R. X-ray photoelectron spectroscopic analysis of surface products on pyrite formed by bacterial leaching. *Bunseki Kagaku*, 40(11):609–616, 1991.

[335] Ph De Donato, C Mustin, R_ Benoit, and R_ Erre. Spatial distribution of iron and sulphur species on the surface of pyrite. *Applied Surface Science*, 68(1):81–93, 1993.

[336] BrJ Lindberg, K Hamrin, G Johansson, U Gelius, A Fahlman, C Nordling, and K Siegbahn. Molecular spectroscopy by means of esca ii. sulfur compounds. correlation of electron binding energy with structure. *Physica Scripta*, 1(5-6):286, 1970.

[337] Ranjani V Siriwardane, James A Poston Jr, Edward P Fisher, Ming-Shing Shen, and Angela L Miltz. Decomposition of the sulfates of copper, iron (ii), iron (iii), nickel, and zinc: Xps, sem, drifts, xrd, and tga study. *Applied surface science*, 152(3):219–236, 1999.

[338] NS McIntyre and DG Zetaruk. X-ray photoelectron spectroscopic studies of iron oxides. *Analytical Chemistry*, 49(11):1521–1529, 1977.

[339] M Descostes, F Mercier, N Thromat, C Beaucaire, and M Gautier-Soyer. Use of xps in the determination of chemical environment and oxidation state of iron and sulfur samples: constitution of a data basis in binding energies for fe and s reference compounds and applications to the evidence of surface species of an oxidized pyrite in a carbonate medium. *Applied Surface Science*, 165(4):288–302, 2000.

[340] JC Carver, GK Schweitzer, and Thomas A Carlson. Use of x-ray photoelectron spectroscopy to study bonding in cr, mn, fe, and co compounds. *The Journal of Chemical Physics*, 57(2):973–982, 1972.

[341] Xiao-hong Guan, Guang-hao Chen, and Chii Shang. Atr-ftir and xps study on the structure of complexes formed upon the adsorption of simple organic acids on aluminum hydroxide. *Journal of Environmental Sciences*, 19(4): 438–443, 2007.

[342] Sang Woo Han, Sang Woo Joo, Tai Hwan Ha, Yunsoo Kim, and Kwan Kim. Adsorption characteristics of anthraquinone-2-carboxylic acid on gold. *The Journal of Physical Chemistry B*, 104(50):11987–11995, 2000.

[343] John J Friel and Charles E Lyman. Tutorial review: X-ray mapping in electron-beam instruments. *Microscopy and Microanalysis*, 12(1):2–25, 2006.

[344] Li-Shin Chang, Yi-Chun Lin, Ching-Yi Su, Hung-Chun Wu, and Jing-Pin Pan. Effect of c60 ion sputtering on the compositional depth profiling in xps for li (ni, co, mn) o 2 electrodes. *Applied Surface Science*, 258(3):1279–1281, 2011.

[345] Jill Sundberg, Rebecka Lindblad, Mihaela Gorgoi, Håkan Rensmo, Ulf Jansson, and Andreas Lindblad. Understanding the effects of sputter damage in w–s thin films by haxpes. *Applied Surface Science*, 305:203–213, 2014.

[346] LE Rumaner, T Tazawa, and FS Ohuchi. Compositional change of (0001) ws2 surfaces induced by ion beam bombardment with energies between 100 and 1500 ev. *Journal of Vacuum Science & Technology A*, 12(4):2451–2456, 1994.

[347] MA Baker, R Gilmore, C Lenardi, and W Gissler. Xps investigation of preferential sputtering of s from mos 2 and determination of mos x stoichiometry from mo and s peak positions. *Applied surface science*, 150 (1):255–262, 1999.

[348] JC Bernede. About the preferential sputtering of chalcogen from transition metal dichalcogenide compounds and the determination of compound stoichiometry from xps peak positions. *Applied surface science*, 171(1):15–20, 2001.

[349] Lisa J Taylor and Hugh A Spikes. Friction-enhancing properties of zddp antiwear additive: part ii– influence of zddp reaction films on ehd lubrication. *Tribology transactions*, 46(3):310–314, 2003.

[350] Nitya Nand Gosvami, Prathima C Nalam, Annemarie L Exarhos, Qizhan Tam, James M Kikkawa, and Robert W Carpick. Direct torsional actuation of microcantilevers using magnetic excitation. *Applied Physics Letters*, 105 (9):093101, 2014.

[351] Ellery D Ingall, Jay A Brandes, Julia M Diaz, Martin D de Jonge, David Paterson, Ian McNulty, W Crawford Elliott, and Paul Northrup. Phosphorus k-edge XANES spectroscopy of mineral standards. *Journal of synchrotron radiation*, 18(2):189–197, 2011.

[352] A. Dorgham, A. Neville, K. Ignatyev, F. Mosselmans, and A. Morina. An in situ synchrotron xas methodology for surface analysis under high temperature, pressure, and shear. *Review of Scientific Instruments*, 88(1): 015101, 2017. doi: 10.1063/1.4973354.

[353] M Shamsa, WL Liu, AA Balandin, C Casiraghi, WI Milne, and AC Ferrari. Thermal conductivity of diamond-like carbon films. *Applied Physics Letters*, 89(16):161921, 2006.

[354] RW Powell, Cho Yen Ho, and Peter Edward Liley. Thermal conductivity of selected materials. Technical report, NATIONAL STANDARD REFERENCE DATA SYSTEM, 1966.

[355] RG Craig and FA Peyton. Thermal conductivity of tooth structure, dental cements, and amalgam. *Journal of Dental Research*, 40(3):411–418, 1961.

[356] AW Batchelor and GW Stachowiak. Some kinetic aspects of extreme pressure lubrication. *Wear*, 108(2):185–199, 1986.

[357] Said Jahanmir. Wear reduction and surface layer formation by a zddp additive. *Journal of tribology*, 109(4):577–586, 1987.

[358] Bernard A Baldwin. Relationship between surface composition and wear: an x-ray photoelectron spectroscopic study of surfaces tested with organosulfur compounds. *ASLE transactions*, 19(4):335–344, 1976.

[359] BA Baldwin. Wear mitigation by antiwear additives in simulated valve train wear. *Asle Transactions*, 26(1):37–47, 1983.

[360] Toshio Sakurai and Kachio Sato. Study of corrosivity and correlation between chemical reactivity and load-carrying capacity of oils containing extreme pressure agents. *ASLE TRANSACTIONS*, 9(1):77–87, 1966.

[361] AW Batchelor, A Cameron, and H Okabe. An apparatus to investigate sulfur reactions on nascent steel surfaces. *ASLE transactions*, 28(4):467–474, 1985.

[362] Francesco Capozzi, Stefano Ciurli, and Claudio Luchinat. Coordination sphere versus protein environment as determinants of electronic and functional properties of iron-sulfur proteins. In *Metal Sites in Proteins and Models Redox Centres*, pages 127–160. Springer, 1998.

[363] Ernest Rabinowicz. Friction and wear of materials. 1965.

[364] P.J. Blau. *Friction Science and Technology: From Concepts to Applications, Second Edition*. Mechanical Engineering. CRC Press, 2008. ISBN 9781420054101.

[365] JM Martin, Carol Grossiord, and Thierry Le Mogne. The two-layer structure of Zndtp tribofilms: Part I: AES, XPS and XANES analyses. *Tribology ...*, 34:523–530, 2001.

[366] Mattias Edén. Nmr studies of oxide-based glasses. *Annual Reports Section" C"(Physical Chemistry)*, 108(1):177–221, 2012.

[367] Haibing Ma, Jing Li, Huan Chen, Guangzhi Zuo, Yi Yu, Tianhui Ren, and Yidong Zhao. Xps and xanes characteristics of tribofilms and thermal films generated by two p-and/or s-containing additives in water-based lubricant. *Tribology international*, 42(6):940–945, 2009.

[368] BC Sales, JU Otaigbe, GH Beall, LA Boatner, and JO Ramey. Structure of zinc polyphosphate glasses. *Journal of non-crystalline solids*, 226(3): 287–293, 1998.

[369] Richard Tran, Zihan Xu, Donald Winston Balachandran Radhakrishnan, Wenhao Sun, Kristin A Persson, and Shyue Ping Ong. Surface energies of elemental crystals. *Scientific data*, 3:160080, 2016.

[370] Stephen M Hsu and Richard S Gates. Effect of materials on tribochemical reactions between hydrocarbons and surfaces. *Journal of Physics D: Applied Physics*, 39(15):3128, 2006.

[371] M Remoissenet and M Peyrard. A new simple model of a kink bearing hamiltonian. *Journal of Physics C: Solid State Physics*, 14(18):L481, 1981.

[372] TETSUZU Ito, TOSHIO Igarashi, and HITOSI Hagihara. The crystal structure of metal diethyldithiophosphates. i. zinc diethyldithiophosphate. *Acta Crystallographica Section B: Structural Crystallography and Crystal Chemistry*, 25(11):2303–2309, 1969.

[373] Nicholas J Mosey and Tom K Woo. Finite temperature structure and dynamics of zinc dialkyldithiophosphate wear inhibitors: a density functional theory and ab initio molecular dynamics study. *The Journal of Physical Chemistry A*, 107(25):5058–5070, 2003.

[374] Martin K Beyer. The mechanical strength of a covalent bond calculated by density functional theory. *The Journal of Chemical Physics*, 112(17): 7307–7312, 2000.

[375] Insun Park, David Shirvanyants, Alper Nese, Krzysztof Matyjaszewski, Michael Rubinstein, and Sergei S Sheiko. Spontaneous and specific activation of chemical bonds in macromolecular fluids. *Journal of the American Chemical Society*, 132(35):12487–12491, 2010.

[376] Xin-Z Liu, Zhijiang Ye, Yalin Dong, Philip Egberts, Robert W Carpick, and Ashlie Martini. Dynamics of atomic stick-slip friction examined with atomic force microscopy and atomistic simulations at overlapping speeds. *Physical review letters*, 114(14):146102, 2015.

[377] Qunyang Li, Yalin Dong, Danny Perez, Ashlie Martini, and Robert W Carpick. Speed dependence of atomic stick-slip friction in optimally matched experiments and molecular dynamics simulations. *Physical review letters*, 106(12):126101, 2011.

[378] Peter Reimann and Mykhaylo Evstigneev. Nonmonotonic velocity dependence of atomic friction. *Physical review letters*, 93(23):230802, 2004.

[379] George S Hammond. A correlation of reaction rates. *Journal of the American Chemical Society*, 77(2):334–338, 1955.

[380] William L Johnson. Bulk glass-forming metallic alloys: Science and technology. *MRS bulletin*, 24(10):42–56, 1999.

[381] Wei-Hua Wang, Chuang Dong, and CH Shek. Bulk metallic glasses. *Materials Science and Engineering: R: Reports*, 44(2):45–89, 2004.

[382] TA Waniuk, R Busch, A Masuhr, and WL Johnson. Equilibrium viscosity of the zr 41.2 ti 13.8 cu 12.5 ni 10 be 22.5 bulk metallic glass-forming liquid and viscous flow during relaxation, phase separation, and primary crystallization. *Acta Materialia*, 46(15):5229–5236, 1998.

[383] E Bakke, R Busch, and WL Johnson. The viscosity of the zr46. 75ti8. 25cu7. 5ni10be27. 5 bulk metallic glass forming alloy in the supercooled liquid. *Applied Physics Letters*, 67(22):3260–3262, 1995.

[384] R Busch, E Bakke, and WL Johnson. Viscosity of the supercooled liquid and relaxation at the glass transition of the zr 46.75 ti 8.25 cu 7.5 ni 10 be 27.5 bulk metallic glass forming alloy. *Acta Materialia*, 46(13):4725–4732, 1998.

[385] Ben Ohler. Practical advice on the determination of cantilever spring constants. Technical Report AN94–RevA0, Veeco Instruments, Inc., 2007.

[386] Johann Mertens, Eric Finot, Thomas Thundat, Arnaud Fabre, Marie-Hélène Nadal, Vincent Eyraud, and Eric Bourillot. Effects of temperature and pressure on microcantilever resonance response. *Ultramicroscopy*, 97(1): 119–126, 2003.

[387] Louis A Girifalco. *Statistical mechanics of solids*, volume 58. OUP USA, 2003.

[388] YP Varshni. Temperature dependence of the elastic constants. *Physical Review B*, 2(10):3952, 1970.

[389] H Ledbetter. Relationship between bulk-modulus temperature dependence and thermal expansivity. *physica status solidi (b)*, 181(1):81–85, 1994.

[390] WB Gauster. Low-temperature grüneisen parameters for silicon and aluminum. *Physical Review B*, 4(4):1288, 1971.

[391] American National Standards Institute and American Society of Mechanical Engineers. *Power Piping: ASME Code for Pressure Piping, B31 : an American National Standard*. ASME B31.1-1995. ASME, 1995.

[392] Thomas R Albrecht, Shinya Akamine, TE Carver, and Calvin F Quate. Microfabrication of cantilever styli for the atomic force microscope. *Journal of Vacuum Science & Technology A: Vacuum, Surfaces, and Films*, 8(4): 3386–3396, 1990.

[393] H-J Butt and Manfred Jaschke. Calculation of thermal noise in atomic force microscopy. *Nanotechnology*, 6(1):1, 1995.

[394] NA Burnham, Xinyong Chen, CS Hodges, GA Matei, EJ Thoreson, CJ Roberts, MC Davies, and SJB Tendler. Comparison of calibration methods for atomic-force microscopy cantilevers. *Nanotechnology*, 14(1):1, 2002.

[395] Jeffrey L Hutter and John Bechhoefer. Calibration of atomic-force microscope tips. *Review of Scientific Instruments*, 64(7):1868–1873, 1993.

[396] Bruker Corporation. *NanoScope 8.15 Software User Guide*, 2013. Analysis Functions: Tip Qualification.

[397] Jingjing Liu, Jacob K Notbohm, Robert W Carpick, and Kevin T Turner. Method for characterizing nanoscale wear of atomic force microscope tips. *ACS nano*, 4(7):3763–3772, 2010.

Appendix A

AFM experimental uncertainty analysis

A.1 Uncertainty propagation

The uncertainty in the measurement of any variable, say x, is a means to estimate how far the measured value deviates from the true value of the variable. The uncertainty can be expressed in various ways, which includes:

- The absolute error, which is defined as:

$$\Delta x = |x - x_{\mathrm{a}}| \tag{A.1}$$

  where x is the true value and x_{a} is the approximated or observed value.

- The relative error, which is defined as:

$$\frac{\Delta x}{x} = \left|\frac{x - x_{\mathrm{a}}}{x}\right| \tag{A.2}$$

  where this definition is subjected to the conditions that $x \neq 0$ and $x \gg |x - x_a|$, otherwise some other suitable normalizing quantity, e.g. x_a or $x + x_a$, should be used in the denominator instead of x.

- The percent error, which is equal to the relative error multiplied by 100%.

- The standard deviation, which is defined as:

$$\sigma = \sqrt{\sum_{i=1}^{N} p_i \left(x_i - \mu\right)^2} \tag{A.3}$$

where N is the number of observations, p_i is the probability of observation x_i and μ is the average value of all the observations, i.e. $\mu = \sum_{i=1}^{N} p_i x_i$. In the case that all the observations have equal probability, then $p_i = 1/N$.

The previous quantities are useful to estimate the uncertainty of a single experimental variable. In addition, they are useful in the case of measuring multiple variables, e.g. x, y, z,..., and calculating the error in the resulting function, $f(x, y, z, ...)$. However, if this function is not defined or there is experimental difficulty in testing all the variables affecting the function f, then the error propagation approach is the best tool to estimate uncertainty.

Assuming a function $f(x, y, z, ...)$ consists of a combination of independent variables, x, y, z, ..., then the standard deviation, σ_f, of the function can be related to the individual standard deviations, σ_x, σ_y, σ_z, ..., of the variables as follows:

$$\sigma_f = \sqrt{\left(\frac{\partial f}{\partial x}\right)^2 \sigma_x^2 + \left(\frac{\partial f}{\partial y}\right)^2 \sigma_y^2 + \left(\frac{\partial f}{\partial z}\right)^2 \sigma_z^2 + ...} \tag{A.4}$$

which for the general case of a function f of multiplied or divided variables in the form $f = dx^a y^b z^c$, can be further simplified to the following form:

$$\sigma_f = |f| \sqrt{\left(a\frac{\sigma_x}{x}\right)^2 + \left(b\frac{\sigma_y}{y}\right)^2 + \left(c\frac{\sigma_z}{z}\right)^2 + ...} \tag{A.5}$$

The variance of the function is defined as the square of its standard deviation, i.e. σ_f^2. Two important notes regarding the above equation are noteworthy. First, it represents a simplified relation based on a first-order Taylor series expansion, which indicates that the function is linearly approximated within a certain interval. This means that it is only valid for small errors, especially as compared to the partial derivatives. Second, it neglects any correlations between the variables and the errors. In the case of a strong correlation between the measured variables, the following linear approximation can be used to relate the absolute error in the function to the ones of the individual correlated variables:

$$\Delta f = \left(\frac{\partial f}{\partial x}\right) \Delta x + \left(\frac{\partial f}{\partial y}\right) \Delta y + \left(\frac{\partial f}{\partial z}\right) \Delta z + ... \tag{A.6}$$

This equation can be utilized as follows. First, the partial derivatives are calculated. Second, the calculated terms are inserted and the left and right hand sides of the equation are squared. The correlated terms, e.g. $\Delta x \Delta y$, should be taken

into account in the case of correlated variables. The variance can be taken as $\sigma_f^2 = \Delta^2 f$ and the standard deviation, σ_f, as the square root of the equation.

A.2 Sources of uncertainty in the in-situ AFM measurements

Several experimental variables might cause propagation of uncertainty in any in-situ AFM measurement. These can include the temperature at the interface between the AFM tip and substrate, which is taken as the temperature of the oil that submerges the tip and substrate. Other uncertainties might also arise from the difficulties in determining the real contact area, the exact applied normal force and subsequently the exact contact pressure forcing the counter-surfaces together during rubbing. The uncertainty in any of these parameters stems from not only one but typically a couple of experimental parameters that define them.

In the following sections, a detailed analysis will be presented regarding the sources and causes of uncertainty in the in-situ AFM measurements and the resulting effects on the measurable parameters.

A.2.1 Source I: temperature

The oil submerging the AFM tip and substrate was heated using two cartridge heaters inserted inside the liquid cell as shown in Fig. 4.6 at a distance 3 cm apart. As discussed in section 4.2.1.2, the two heaters were needed in order to assure the temperature homogeneity and thus avoid any microflow due to any local thermal variations within the oil. To further minimize this effect, the oil volume was limited to less than 3 ml.

The temperature of the cartridge heaters was controlled using a PID controller (Watlow, UK) using a closed loop algorithm with two k-type thermocouples integrated within the heaters. The accuracy and repetition of the system were better than $\pm 1.1\,^{o}$C. This results in a percent error of 1.6 to 0.9% depending on the setpoint, which ranges from 70 to 120 ^{o}C, respectively. To further check the calibration of the cartridge heaters, their values (when soaked in oil) were compared with the ones obtained from an external thermometer and multimeter and the accuracy was better than 1.0 ^{o}C.

The in-situ tests were performed after the liquid cell reaches thermal equilibrium. The equilibrium steady-state takes typically 15 min, as shown in Fig. A.1

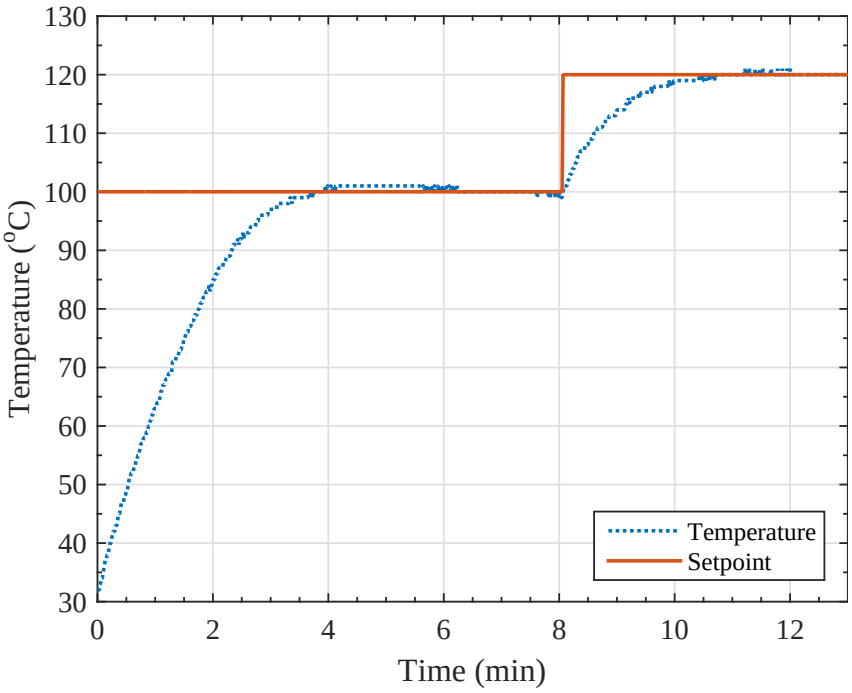

Fig. A.1 Ramp of the set versus actual temperature as read from the cartridge heaters' controller of the in-house developed AFM liquid cell.

of the evolution of temperature over time. Nevertheless, in order to assure the thermal equilibrium, a minimum of 30 additional minutes were allowed before the start of the in-situ tests.

A.2.2 Source II: normal force

The uncertainly of the applied force, F, can be estimated by examining the individual parameters constituting the force, which can be associated as follows:

$$F = s_p d_s k \tag{A.7}$$

where s_p is the setpoint of the applied force in V, d_s is the deflection sensitivity of the AFM cantilever in nm/V, and k is the spring constant of the cantilever in N/m. The outcome of the equation is the applied force, F, in nN.

The uncertainties of all the input parameters can contribute to the uncertainty of the output force. Therefore, the individual uncertainty of each variable will be estimated and discussed in detail first then the error will be propagated to estimate the uncertainty in the composed normal force.

A.2.2.1 Source II-i: force setpoint

The uncertainty of the setpoint of the applied force is primarily limited to the measured voltage response of the AFM's Position Sensitive Detector (PSD). The uncertainty of the used PSD in Bruker's Dimension Icon AFM was estimated to be better than 3% [385]. Therefore, the uncertainty of the setpoint of the applied force will be taken as 3%.

A.2.2.2 Source II-ii: deflection sensitivity

As discussed in detail in section 4.2.1.2, the deflection sensitivity is mainly dictated by the geometry of the AFM cantilever, i.e. its length and thickness. However, as these cannot be measured accurately enough without the use of advanced electron microscopes, the deflection sensitivity is typically determined by obtaining force curves as shown in Fig. A.5. The method generally assumes that the cantilever is linearly deformed if pressed on an infinitely hard substrate, and hence a linear relation will be obtained between the measured voltage response of the AFM's PSD and the cantilever deflection. Therefore, similar to the uncertainty of the setpoint, the error in the deflection sensitivity can be partly related to the accuracy of the AFM's PSD, which is about 3%. In addition to that, the accuracy limit of the Z Position Sensor can add to the overall uncertainty of the cantilever deflection. For the closed loop control system of the Bruker's dimension icon AFM, the Z Position Sensor has a noise level lower than 0.2 nm. Thus, for a cantilever of a typical deflection sensitivity around 100 nm/V, the uncertainty due to the Z positioning system is about 0.2%. Applying the uncertainty propagation approach, the uncertainty of the deflection sensitivity can be estimated assuming that the affecting variables, i.e. PSD and Z-sensor voltages are uncorrelated, as follows:

$$\sigma_{d_s} = |d_s| \sqrt{\left(\frac{\sigma_{V_{\mathrm{PSD}}}}{V_{\mathrm{PSD}}}\right)^2 + \left(\frac{\sigma_{V_{\mathrm{Z}}}}{V_{\mathrm{Z}}}\right)^2 + \ldots} \tag{A.8}$$

where $\sigma_{V_{\mathrm{PSD}}}/V_{\mathrm{PSD}} < 3.0\%$ and $\sigma_{V_{\mathrm{Z}}}/V_{\mathrm{Z}} < 0.2\%$. This results in $\sigma_{d_s}/d_s < 3.0\%$. This good accuracy of the deflection sensitivity is also accompanied by a good repetition achieved during its calibration procedure, which is always repeated more than 6 times on various locations of hard sapphire standard calibration substrate. Fig. A.2 further confirms that during the entire in-situ experiment the value remain constant over the long rubbing cycles with a minor variation less than 5%.

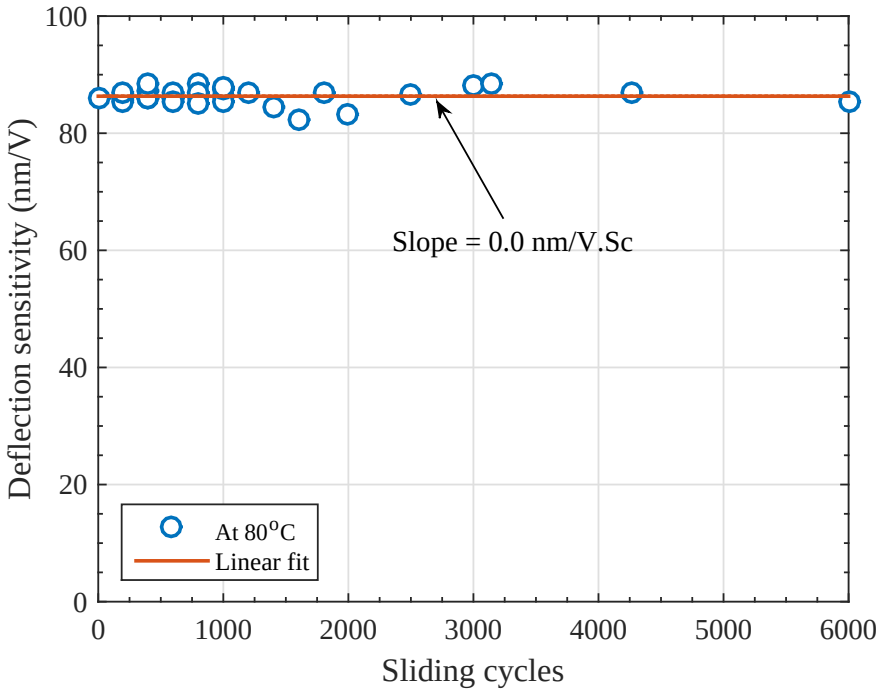

Fig. A.2 Evolution of the deflection sensitivity of one RTespa AFM cantilever (Bruker, USA) over sliding cycles measured at 80 ^{o}C during one of the in-situ tribotests.

It should be noted that the above analysis is valid under ambient temperature whereas heat might affect the geometry of the cantilever and consequently its deflection calibration. For instance, the coefficient of thermal expansion of a standard Si cantilever is about 2.6×10^{-6} /^{o}C, which can elongate the typically used RTESPA-300 (Bruker®, USA) cantilever of a nominal length 125 μm by about 12 nm over the maximum temperature of 120 ^{o}C used in the in-situ tests. However, as the backside of the cantilever is coated with a thin layer of nominally 40 nm of reflective aluminium to improve laser signal, temperature might induce extra deflection, i.e. bending, due to the different thermal expansions on the coated and uncoated sides [386]. Nonetheless, we always assume zero deformation before the start of the tribotest, so this bending effect is not expected to have any significant impact.

On the other hand, apart from the probe geometry, temperature can affect the mechanical properties of the cantilever, e.g. its Young's modulus, and consequently its deflection. The origin of this effect is the increase in the length of the bonds during the thermal expansion. The elongated bonds are weaker causing reduction in the microscopic holding force, which is the origin of the macroscopic elastic modulus. Wachtman et al. followed by Anderson [105, 106] proposed that the Young's modulus depends on temperature according to the relation:

$$E(T) = E(0) - BT\exp\left(\frac{-T_0}{T}\right) \tag{A.9}$$

where $E(0)$ is the Young's modulus at temperature of 0 K and B is a constant related to Grüneisen parameter γ and Debye temperature Θ_D, which is given by:

$$\Theta_D = \frac{\hbar\nu_D}{k}\left(\frac{6\pi^2 N}{V_0}\right)^{\frac{1}{3}} \tag{A.10}$$

where ν_D is Debye velocity, k is Boltzmann's constant, N is Avogadro's number, $\hbar$ is the reduced Planck constant ($\hbar = h/2\pi$) and V_0 is the atomic volume at 0 K. The B constant depends strongly on the heat capacity of the material, which in turn depends on the Grüneisen parameter and Debye energy. In the limit of $T \ll \Theta_\mathrm{D}$, an identical expression for the change of heat capacity with temperature can be used for the dependency of the elastic modulus on temperature, as follows [387]:

$$E(T) = E(0) - \frac{9\,(1-2\nu)\,\pi^4 R\Theta_D\gamma\,(3\gamma-1)}{5V_0}\left(\frac{T}{\Theta_D}\right)^4 \tag{A.11}$$

were ν is the Poisson's ratio. An additional factor of $3\,(1-2\nu)$ was multiplied to the original equation in order to explicitly account for the effect of the Poisson's ratio on the elastic modulus [107].

Another expression for $E(T)$ was proposed by Varshni [388] using Einstein oscillator expression, as follows:

$$E(T) = E(0) - \frac{3\,(1-2\nu)\,s}{\left(\exp\left(\frac{\Theta}{T}\right)-1\right)} \tag{A.12}$$

where Θ is the effective Einstein temperature and s is a parameter related to the contribution of zero point vibration energy to elastic stiffness, which can be given by [389]:

$$s = \frac{3R\gamma\,(\gamma+1)\,\Theta_\mathrm{D}}{V_0} \tag{A.13}$$

We attempted to examine the predictions of the two models of $E(T)$ considering the cantilevers used in the AFM in-situ tests. As discussed before and shown in the inset of Fig. A.3, these cantilevers consist of a composite structure of thick silicon layer overlaid with a thin layer of aluminum. We estimated the average of any physical property (P) of the composite structure, e.g. E, ν, γ, V_0 and Θ_D,

Table A.1 Fitting parameters for the Einstein oscillator and Debye-Grüneisen models for Si and Al [390].

Parameter	Si cantilever	Al coating
E (GPa)	150	70
ν (-)	0.25	0.33
γ (-)	0.5	2.0
V_0 (cm^3/mol)	12	10
Θ_D (K)	645	428

to be a combination of the properties of the materials of the cantilever and its coating, where their contribution is weighted by the layer thickness, as follows:

$$P = P_{Si} + \frac{d_{Al}}{d_{Si}} P_{Al} \tag{A.14}$$

The fitting parameters of the two models are listed in Table A.1. Using these parameters, the change in the elastic modulus over temperature is shown in Fig. A.3. The results indicate that the two models give similar prediction at low temperature, below 300 K, but start to deviate at higher temperature. Nonetheless, the two models, in general, predict a mild decrease in the elastic modulus over temperature. The Einstein oscillator model predicts a decrease of 0.004 GPa/K, whereas the Debye-Grüneisen model suggests a decrease of about 0.02 GPa/K. These predictions are not far from the reported values of the change in the elastic modulus over temperature for various metals (see ASME B31.1-1995 [391]), which ranges from 0.023 GPa/K for Al to 0.047 GPa/K for steel. It follows that within the temperature range of the AFM in-situ tests, the decrease predicted by the two models is insignificant, i.e. $\ll 1\%$, which matches the mild decrease in the deflection sensitivity observed over temperature, as shown in Fig. A.4 for two different Si cantilevers.

One final remark on the effect of temperature is that it could cause an extra deformation of the piezoelectric elements of the cantilever holder. However, as our Dimension Icon AFM implements a closed loop algorithm to control the scanning head, this should not have any significant impact.

A.2.2.3 Source II-iii: spring constant

The uncertainty in the spring constant originates from the difficulties in accurately determining the cantilever elastic modulus (E) and its geometry, i.e. thickness (t), width(w) and length(L). Based on Euler-Bernoulli beam theory, the spring constant can be approximated as follows [392]:

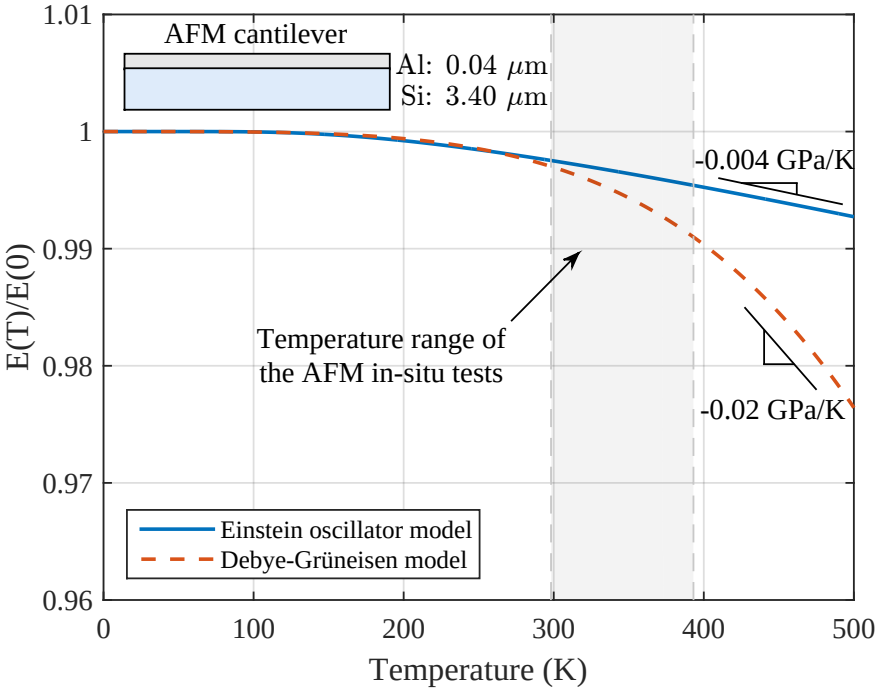

Fig. A.3 Prediction of the evolution of the normalized elastic modulus of one RTespa AFM cantilever (Bruker, USA) over temperature using both the Einstein oscillator and Debye-Grüneisen models.

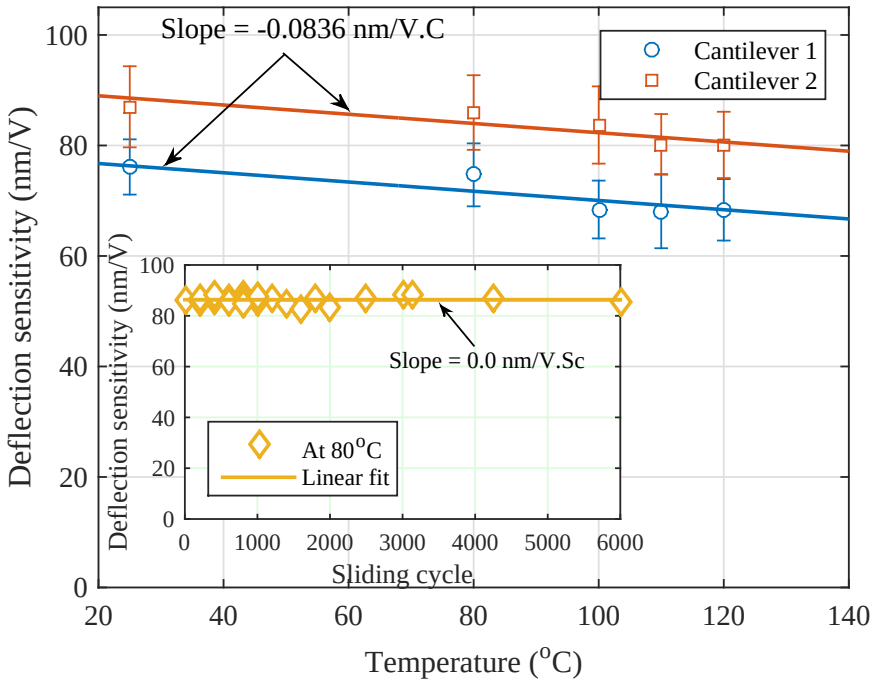

Fig. A.4 Evolution of the deflection sensitivity of two RTespa AFM cantilevers (Bruker, USA) over temperature. The inset of the figure shows the evolution of the deflection sensitivity over sliding cycles measured at 80 ^{o}C during one of the in-situ tribotests.

$$k = \frac{Ewt^3}{4L^3} \tag{A.15}$$

where other exact formulas are discussed in detail elsewhere [83].

For soft cantilevers, i.e. compliant and flexible of small spring constant, the thermal noise of the cantilever at rest can be measured and modelled as a simple harmonic oscillator to obtain the spring constant as follows:

$$k = \frac{k_{\mathrm{B}}T}{\langle z^2 \rangle} \tag{A.16}$$

where k_{B} is Boltzmann constant (1.38×10^{-23} J/K), T is the absolute temperature in K and z is the vertical deflection of the cantilever in m. A correction is needed for the above equation as the cantilever does not behave as ideal spring. This deviation causes its oscillation modes and their energies to differ from that of a simple harmonic oscillator. Thus, the vibration modes, α_i, of the cantilever should be taken into account in order to adjust the thermal noise in the above equation, which can be accounted for as follows [393]:

$$k = \frac{12 k_{\mathrm{B}}T}{\alpha_i^4 \langle z^2 \rangle} \tag{A.17}$$

Considering only the first fundamental and most prominent vibration mode, $\alpha_1 = 1.8751$ [393], for the typically used rectangular cantilevers in our in-situ tests, the above equation can be simplified to:

$$k = 0.971 \frac{k_{\mathrm{B}}T}{\langle z^2 \rangle} \tag{A.18}$$

Furthermore, the typical AFM relies on the optical lever technique, discussed in detail in section 4.2.1.2, to measure the inclination of the cantilever, $\mathrm{d}z(L)/\mathrm{d}(x)$, rather than its deflection $z(L)$. In this case, Butt and Jaschke [393] found that the vibration modes, α_i, of the cantilever affect the measured thermal noise and consequently the spring constant as follows:

$$k = \frac{16 k_{\mathrm{B}}T}{3\alpha_i^2 \langle z^2 \rangle} \left[\frac{\sin \alpha_i \sinh \alpha_i}{\sin \alpha_i + \sinh \alpha_i} \right]^2 \tag{A.19}$$

Again, considering only the first and most prominent vibration mode, $\alpha_1 = 1.8751$, for rectangular cantilevers, the above equation can be simplified to:

$$k = 0.817 \frac{k_{\mathrm{B}}T}{\langle z^2 \rangle} \tag{A.20}$$

To sum up, it is worth noting that the purpose of Eqs. (A.18) and (A.20) is to correct for the effect of the vibration modes of the cantilever on its deflection response. The first equation is used if the cantilever's deflection is measured directly, e.g. using interferometer, whereas the second equation is used when the deflection is measured indirectly, e.g. using the optical lever technique. It is possible to combine Eqs. (A.18) and (A.20), as follows:

$$k = 0.971 \frac{k_{\mathrm{B}} T}{\chi^2 \langle z^2 \rangle} \tag{A.21}$$

where $\chi = 1.09$ produces Eq. (A.18).

Applying the uncertainty propagation approach, the uncertainty of the spring constant can be calculated assuming that the affecting variables, i.e. temperature and deflection sensitivity, are uncorrelated, as follows:

$$\sigma_k = |k| \sqrt{\left(\frac{\sigma_T}{T}\right)^2 + \left(2\frac{\sigma_{d_s}}{d_s}\right)^2 + \ldots} \tag{A.22}$$

where $\sigma_T/T < 1.6\%$ and $\sigma_{d_s}/d_s < 3\%$, as discussed earlier. This results in $\sigma_k/k < 6.2\%$. However, as $\langle z^2 \rangle$ in the above equation is expected to be very minute, the thermal noise technique typically gives best results with good certainty for soft compliant cantilevers, i.e. for $k \ll 20$ N/m. On the other hand, for the stiff cantilevers of 40 N/m used in our in-situ experiments the uncertainty of the spring constant using the thermal noise method is expected to be at least threefold, i.e. $\sim 20\%$, larger than the one predicted by the uncertainty propagation analysis [394]. The origin of the underestimation is the exclusion of the goodness of the fit of the thermal noise signal to the harmonic oscillator model. That is to say, the uncertainty is mainly dominated by the signal to noise ratio of the acquired thermal noise signal, which is required to be well above the combined noise background from all external sources and deflection measurement itself [395].

Despite its lack of accuracy, the thermal noise method gives good repetition better than 5%. Furthermore, in order to assure the same results across the experiments, whenever the cantilever was changed and before performing new in-situ experiments few repetitions of the previously performed experiments using the previous cantilevers were made. Although this practice does not improve the accuracy but it definitely assures the repeatability of the results.

It is worth noting that the above discussion is related to calibrating the cantilever at ambient condition in air. If the same calibration is intended to be made in the high viscous oil at high temperature, large variations might occur

due to i) hydrodynamic drag changing the effective mass of the cantilever, ii) micro-flow within the oil and iii) thermal variations in the oil larger than the thermal noise signal, i.e. $\Delta T \gg \langle z^2 \rangle$. This variability will cautiously be considered by taking the high end of the uncertainty of the spring constant, i.e. 20%, in the subsequent uncertainty propagation calculations used to estimate the error in the normal force.

A.2.2.4 Uncertainty propagation of the normal force

Based on the discussion presented in the previous sections regarding the various variables affecting the normal force, i.e. force setpoint, deflection sensitivity, and spring constant, and assuming they are uncorrelated, the uncertainty in the normal force can be estimated using the uncertainty propagation approach, as follows:

$$\sigma_F = |F| \sqrt{\left(\frac{\sigma_{s_p}}{s_p}\right)^2 + \left(\frac{\sigma_{d_s}}{d_s}\right)^2 + \left(\frac{\sigma_k}{k}\right)^2 + \ldots} \tag{A.23}$$

where $\sigma_{s_p}/s_p = 3.0\%$, $\sigma_{d_s}/d_s = 5.0\%$ and $5.0\% < \sigma_k/k < 20.0\%$. This results in an estimated relative error in the applied force, $(\sigma_F/|F|)$, ranges from 6.5% to 20.5%, depending on the used uncertainty of the spring constant whether 5% or 20%, respectively.

It should be noted that although the previous analysis assumes uncorrelated variables, the accurate representation would suggest otherwise. The uncertainties of the setpoint of the applied force, deflection sensitivity and spring constant are definitely correlated. This becomes evident by noticing that the spring constant calculation using the thermal noise method, i.e. Eq. (A.21), relies on the cantilever deflection, which in turn relies to the PSD response affecting the setpoint. However, the exact relation between the three variables is not known. In addition, as no large deviation was observed across the repeated in-situ experiments using different cantilevers, thus, in order to simplify the calculations, a good estimate can be achieved by assuming that the input variables are uncorrelated and considering, as stated earlier, a wide range of uncertainty for one variable, i.e. the spring constant, $5\% < k < 20\%$.

A.2.3 Source III: contact area

The actual contact area is different from the nominal area calculated from the probe geometry and indentation depth. The only feasible way to estimate the real contact area is by using one of the available models. However, these models are

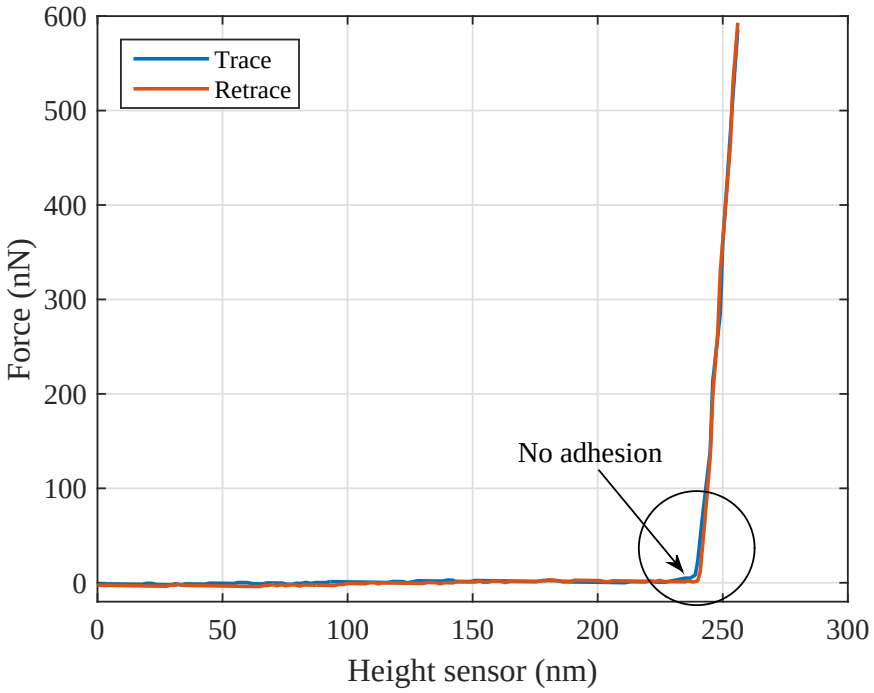

Fig. A.5 Force-displacement curves (trace and retrace) obtained with one RTespa AFM cantilever (Bruker, USA) of nominal spring constant 40 N/m showing that the tip-sample interaction lacks any adhesion force.

empirical and prone to error. Thus, the uncertainty analysis will not focus on the goodness of the model per se but the direct error brought by the uncertainty of the experimental input parameters of the model.

The real contact area can be estimated using one of the most used elastic deformation models such as Hertz [86], Johnson–Kendall–Roberts (JKR) [87], and Derjaguin–Muller–Toporov (DMT) [88], which were discussed in detail in section 2.3. The former two models are extensions to the latter to account for the adhesion force between the probe and substrate. However, for a Si tip probing a steel substrate, the adhesion force was found negligible as validated based on the force-distance curves of which one example is shown in Fig. A.5. This justifies the use of Hertz model to estimate the contact area.

Using Hertz model, the contact radius a for the case of a spherical probe of radius R exerting a normal force F on a flat surface that causes a sample indentation δ, can be given as follows:

$$a = \left(\frac{R_r F}{E_r}\right)^{1/3} \tag{A.24}$$

where R_r is the reduced radius of curvature of the two contacting surfaces and E_r is the reduced elastic modulus, which is defined as:

$$\frac{1}{E_r} = \frac{3}{4}\left(\frac{1-\nu_1^2}{E_1} + \frac{1-\nu_2^2}{E_2}\right) \tag{A.25}$$

where ν is the Poisson's ratio and the subscripts 1 and 2 refer to the sample and indenter, respectively.

The above discussion indicates that the main uncertainties in finding the real contact area arise from the error in determining or measuring the tip radius, applied force and reduced elastic modulus. In the subsequent sections, the sources of uncertainty associated with each of these parameters will be discussed in detail first individually followed by the uncertainty propagation analysis in order to estimate the overall uncertainty in the contact area.

A.2.3.1 Source III-i: AFM tip radius

Despite the numerous advantages of the AFM, it has some limitations as well. One of these limitations is mainly related to the continuous wear of the AFM tip during imaging, which could lead to changing the scanning parameters or obtaining erroneous information about the scanned surface. For instance, Vahdat et al. [66] showed that the wear of the tip causes larger deviations of the average normal stress over the scanning cycles than the ones observed in the case of the constant parabolic shape of the tip that is typically assumed. Furthermore, the worn tip can give misleading flattened topography images. Fig. A.6 shows AFM topography images of a Ti substrate of large roughness after different sliding distances. The captured topography was largely affected by the normal load applied during scanning. The flattening of the rough features under the high contact pressure is mainly related to the large increase in the tip radius due to its progressive wear over sliding distance. The large tip overestimates any feature of a size below the tip diameter, as shown in Fig. A.7.

To quantify the flattening effect of the tip size on the features of the captured images, Figs. A.8 and A.9 show the evolution of the measured surface properties based on the arithmetic average (Ra), Root Mean Square (Rms) and maximum (Rmax) roughness of the surface, as a function of the sliding distance. These statistical properties appear to be affected only slightly in the case of sliding under the adhesion force only. In contrast, when the applied load was increased to $>$ 100 nN, a reduction by 30-40% was observed in the first 100 mm of the sliding distance, which is in agreement with the observed increase in the tip radius shown in Fig. A.11.

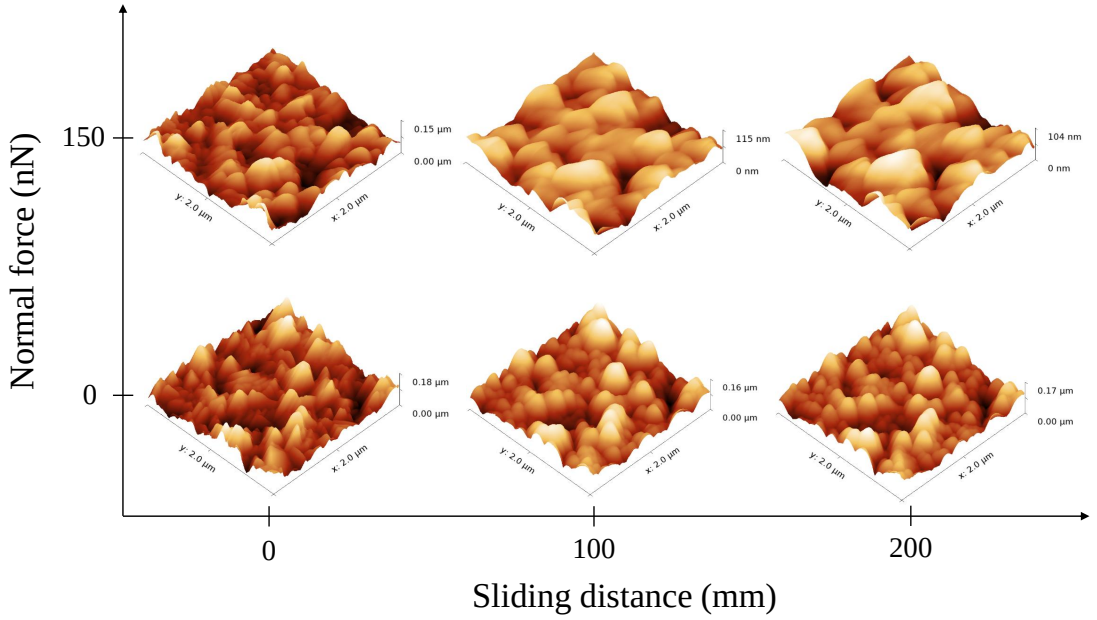

Fig. A.6 Evolution of the AFM topography images over sliding distance of rough Ti substrate used for tip estimation under small adhesion force versus large contact force.

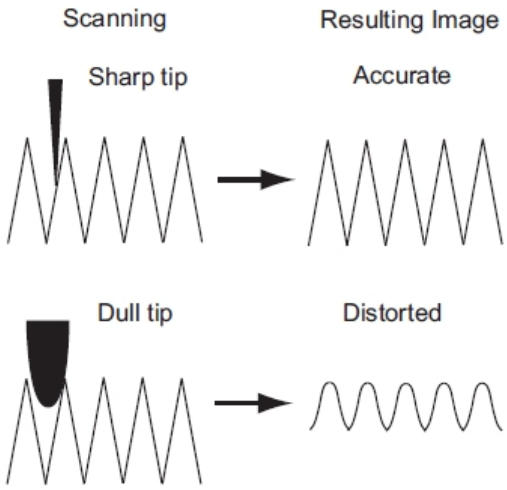

Fig. A.7 Schematic of the effect of scanning using sharp versus worn tips on the resulting AFM topography images [396].

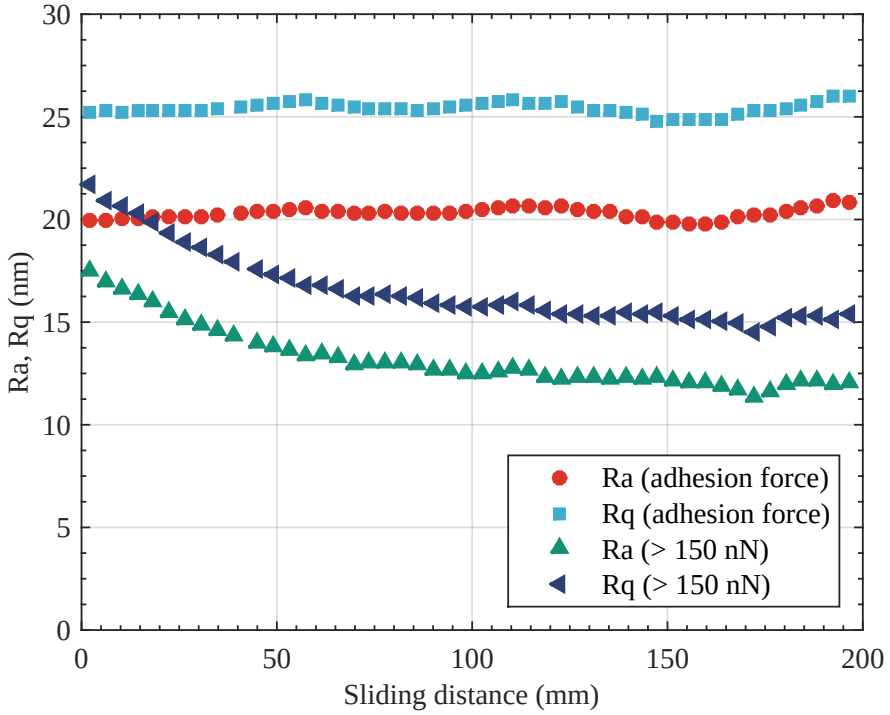

Fig. A.8 Evolution of the estimated R_a and R_q over sliding distance under small adhesion force versus large contact force.

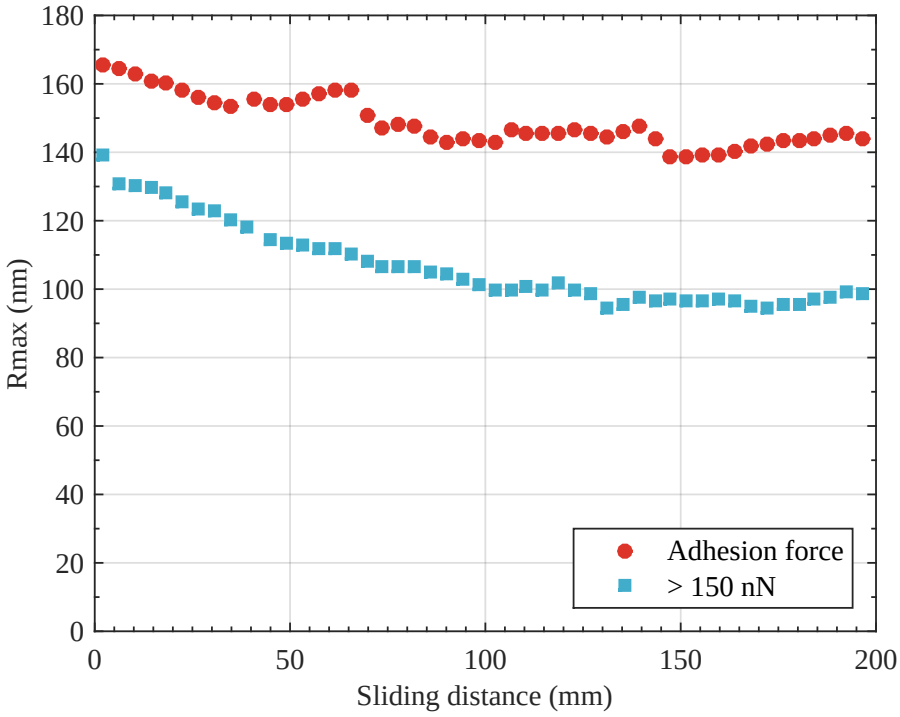

Fig. A.9 Evolution of the estimated R_{max} over sliding distance under small adhesion force versus large contact force.

One possible solution to the uncertainty in the tip size is by replacing the tip with a fresh one before every in-situ test. However, changing the tip is not the best strategy since big variations of geometry or mechanical properties exist between the different tips. Furthermore, this will increase the importance of the other uncertainties related to the cantilever calibration, e.g. deflection sensitivity and spring constant. Another solution to avoid this problem is by SEM imaging the tip before and after the test. However, this solution is not practical in the case of long tests that necessitate a continuous monitoring of the wear of the AFM tip during the test.

The best solution to tackle the uncertainty of the size of the AFM tip was discussed by Liu et al. [397] who reported a method for calculating the wear of the AFM tip through the estimation of the tip shape as it scans sharp features. The idea is based on the fact that the tip cannot discern features less than the diameter of the tip as shown in Fig. A.10. Thus, by imaging extremely sharp features using a worn tip, the obtained images will be of that of the tip diameter itself rather than the shape of the features. The blind reconstruction of the tip shape using this method was compared with the one using TEM imaging and good agreement between them was found [397]. However, it is worth noting that under few special circumstances, the method can fail to estimate the tip shape accurately. For instance, as shown in Fig. A.10, imaging a flattened surface using a sharp tip causes the estimated tip shape to be mistaken for that of the true surface features. To avoid this problem, only substrates of sharp features should be used to estimate the tip shape, which inevitably can result in more tip wear.

To test the validity of this method, Fig. A.11 shows the evolution of the tip radius over 200 mm of sliding distance under two different loads using a standard Ti substrate of high roughness. The first chosen load was only due to adhesion force without any normal load applied whereas the second load was set at > 100 nN to represent a large normal force that could be applied during the in-situ AFM experiments. The results indicate that the tip initially has a radius of about 15 nm, which is close to its nominal value of 8 nm. The slight deviation can be related to the wear of the tip occurring during the tip engagement with the surface and during the calibration of the cantilever deflection sensitivity. The evolution of the tip size indicates that even after the first few millimetres of sliding, higher normal load leads to more wear of the tip, which is expected. Furthermore, the results indicate that the majority of wear occurs during the first 50 mm of sliding distance. The tip wear appears to follow a logarithmic trend until the tip radius reaches a steady state value after a sliding distance depending on the applied load, e.g. 25 mm in the case of adhesion force and 50 mm in the case of large contact

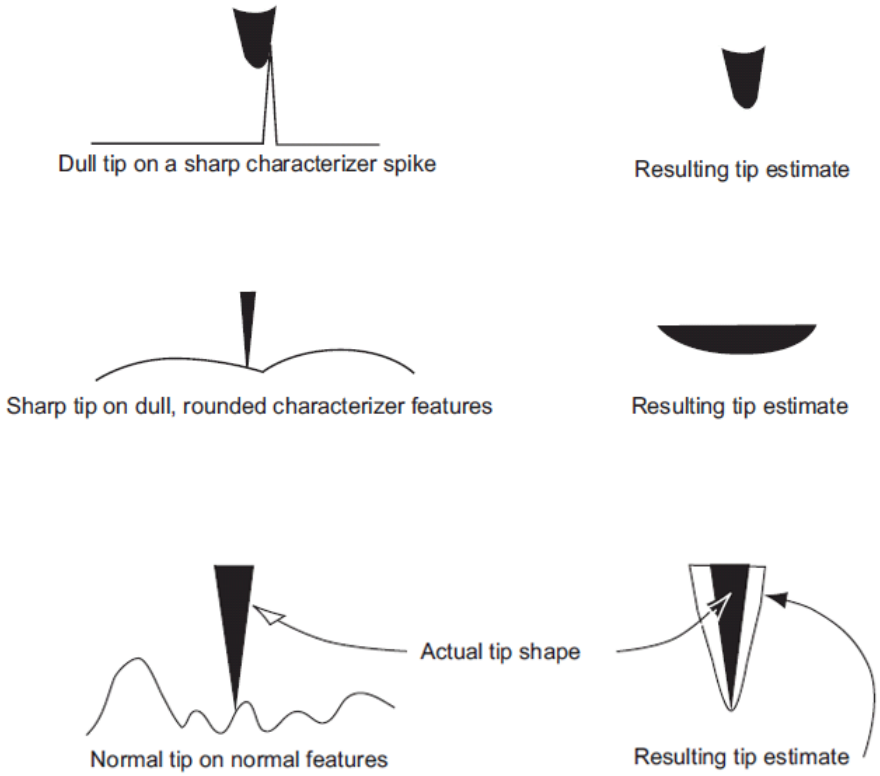

Fig. A.10 Schematic of the effect of scanning sharp, rounded and normal features using sharp and worn tips on the resulting tip estimate [396].

force. This trend in agreement with the wear models described in section 2.1.2 and the results of Gotsmann and Lantz [71] and Liu et al. [397].

The uncertainty of the tip radius, R, as shown in Fig. A.11 based on the tip estimation method, is approximately 10%. This value is further confirmed by observing the width of the tribofilm formed under the tip using few scanning lines after small rubbing cycles, e.g. as shown in Figs. 7.6 to 7.8.

A.2.3.2 Source III-ii: reduced elastic modulus

The elastic modulus cannot be measured accurately enough for ultra-thin tribofilms due to the large substrate effect. Furthermore, the used probe, tribofilm and substrate form a sandwich structure that cannot be solved without knowing the exact thickness, modulus and Poisson's ratio of its various elements. Therefore, we can only rely on the scattered and sometimes controversial available data in the literature related to the reduced elastic modulus of the ZDDP tribofilm. For instance, a number of studies [29, 30, 174, 177, 248, 249, 253, 254] reported that the mechanical properties of the tribofilms, e.g. modulus and hardness, are thickness dependent, i.e. the larger the thickness the lower the hardness

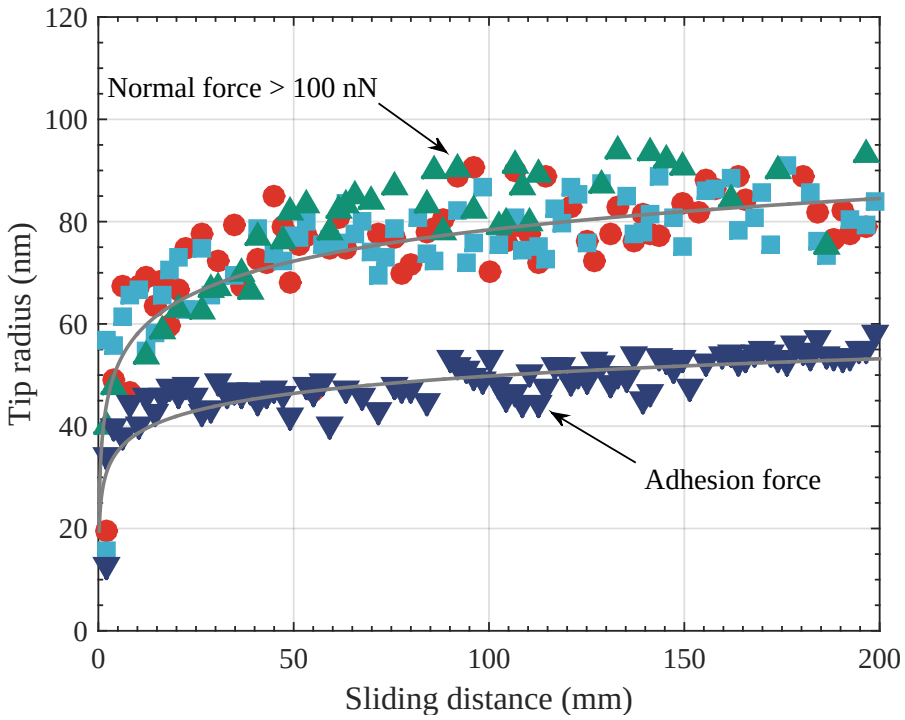

Fig. A.11 Evolution of the estimated AFM tip radius over sliding distance under small adhesion force versus large contact force.

and modulus. On the other hand, few other studies [167] found that the elastic modulus and hardness of the tribofilm are independent of thickness and rubbing time. This was explained by pointing out that the majority of the bulk material of the tribofilm at any time consists mainly of short chain polyphosphates. Therefore, the nanomechanical properties are predetermined by the properties of this bulk material. However, Nicolls et al. [29] reported that the large pads of the tribofilm consist mainly of long chain polyphosphates whereas small pads and troughs consist of short chain phosphates. Graham et al. [249] showed that the large pads have great elastic response. The indentation modulus was about 180-250 GPa at the centre of the pad compared with 50-110 GPa at the edge. Nicolls et al. [177] found that the indentation modulus was 120 GPa at the centre of the pad compared with 90 GPa at the edge. In a later study, Nicolls et al. [29] reported indentation modulus of 80 GPa for the large pads but could not measure the modulus of small pads due to the effect of the substrate on the indentation measurements of these thin regions. This wide range of values of the reported indentation modulus was related to the extent of ZDDP decomposition to form polyphosphates [89].

Considering that the tribofilm is formed of small and large pads and assuming they are of equal proportions, the widely scattered data discussed above and

summarized in Table 3.3 in section 3.5.2, indicate an average reduced modulus of 80 GPa with a large uncertainty < 20 %.

It is worth noting that temperature as discussed in section A.2.2.2 will have a negligible effect on the reduced elastic modulus within the temperature range of 25-120 ^{o}C used during the in-situ tests.

A.2.3.3 Source III-iii: contact force

As discussed in detail in section A.2.2.4, the estimated relative error in the applied force, $(\sigma_F/|F|)$, ranges from 6.5 to 20.5%, depending on the used uncertainty in the spring constant whether 5% or 20%, respectively.

A.2.3.4 Uncertainty propagation of the contact area

Based on the discussion in the previous sections regarding the various variables affecting the contact area, i.e. the tip radius, applied force and reduced elastic modulus, and assuming they are uncorrelated, the uncertainty in the contact area can be estimated using the uncertainty propagation approach, as follows:

$$\sigma_a = \frac{|a|}{3}\sqrt{\left(\frac{\sigma_{R_r}}{R_r}\right)^2 + \left(\frac{\sigma_F}{F}\right)^2 + \left(\frac{\sigma_{E_r}}{E_r}\right)^2 + ...} \tag{A.26}$$

where $\sigma_{R_r}/R_r = 10.0\%$, $6.5\% < \sigma_F/F < 20.5\%$ and $\sigma_{E_r}/E_r < 20.0\%$. This results in an estimated relative error in the contact area, $(\sigma_a/|a|)$, ranges from 7.5 to 10.0%, depending on the used uncertainty in the contact force whether 6.5 or 20.5%, respectively.

A.2.4 Source VI: contact pressure

Assuming that the AFM end tip area is circular, the contact pressure applied during the in-situ AFM tests can be given by:

$$P = \frac{F}{\pi a^2} \tag{A.27}$$

where F is the applied normal force and a is the real contact area. In this case, the uncertainty in determining the contact pressure is originated from the uncertainties related to the measurements of F and a.

Due to the strong correlation between the contact area and contact force, the uncertainty of the contact pressure will be estimated using Eq. (A.6) instead of

Eq. (A.5) in order to account for the correlations between the variables. This results in the following relation:

$$\sigma_P = |P| \sqrt{\left(\frac{\sigma_F}{F}\right)^2 + 4\left(\frac{\sigma_a}{a}\right)^2 - 4\left(\frac{\sigma_F}{F}\right)\left(\frac{\sigma_a}{a}\right) + ...} \tag{A.28}$$

where we assumed that the covariance between the contact force and the contact area can be decoupled to the multiplication of the two individual standard deviations, i.e. the square root of the variance of the two. This is true given that an increasing linear relationship, i.e. a perfect correlation, exists between the two variables, which can be asserted from Eq. (A.24) under the condition of large F.

Plugging these uncertainties into Eq. (A.28), results in an estimated relative error in the applied contact pressure, $(\sigma_P/|P|)$, ranges from 9.0 to 13.7%, depending on the used uncertainty in the contact force whether 6.5 or 20.5%, respectively. The main reason for the low error is that the contact pressure results from a division between the force and contact area. Therefore, there is a negative term due to their perfect correlation resulting in a error cancellation and huge decrease in the overall estimated error value. Gosvami et al. [30] used a flat value of 10% for their similar in-situ AFM measurements, which is close the mean estimated value of our uncertainty propagation analysis.

A.2.5 Source V: scanning speed

Our data seem to suggest that the growth rate is less sensitive to the sliding speed and is only dependent on the scanning cycles. This is an interesting result as it indicates that the growth occurs accumulatively in a layer-by-layer fashion, i.e. every rubbing cycle regardless of its timing adds one layer of a certain thickness depending on the other operating conditions of temperature and contact pressure.

As the scanning speed per se does not impact the growth rate, its uncertainty will not be estimated. In all the experimental work discussed in the subsequent sections, a single scanning speed of 200 μm/s was used throughout the in-situ tests.

Appendix B

Characterization of synthesized polyphosphate glasses

B.1 Surface analysis of polyphosphate glasses

B.1.1 XPS degradation analysis

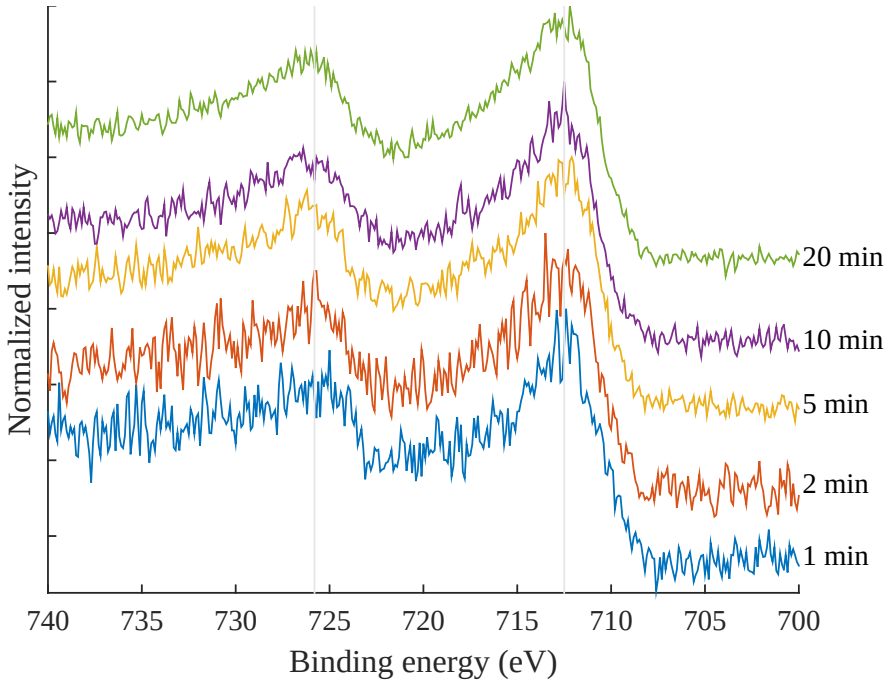

Fig. B.1 XPS degradation analysis after different acquisition time of the Fe 2p signal of iron poly (0.33) phosphate glass.

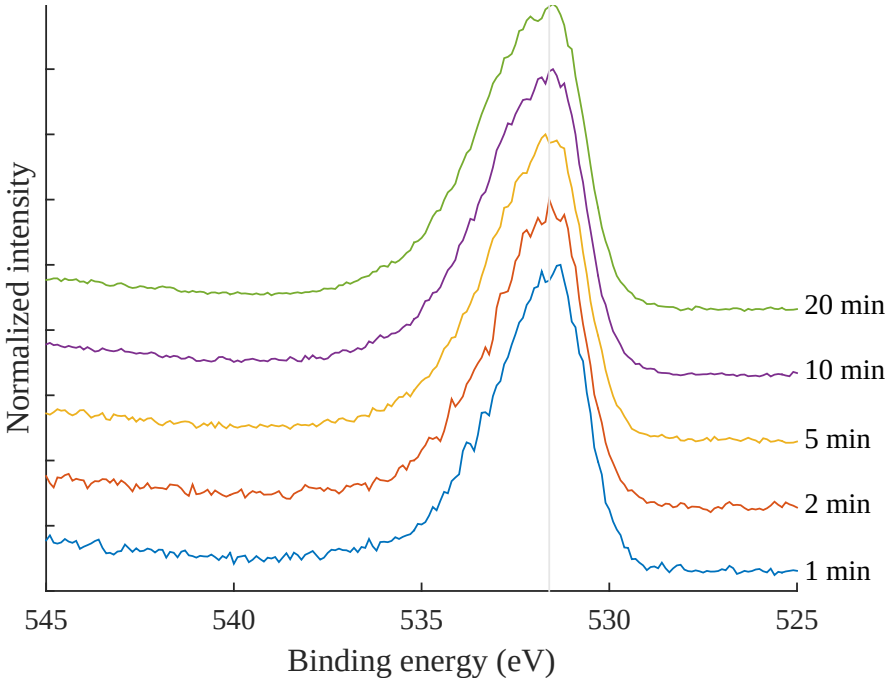

Fig. B.2 XPS degradation analysis after different acquisition time of the O 1s signal of iron poly (0.33) phosphate glass.

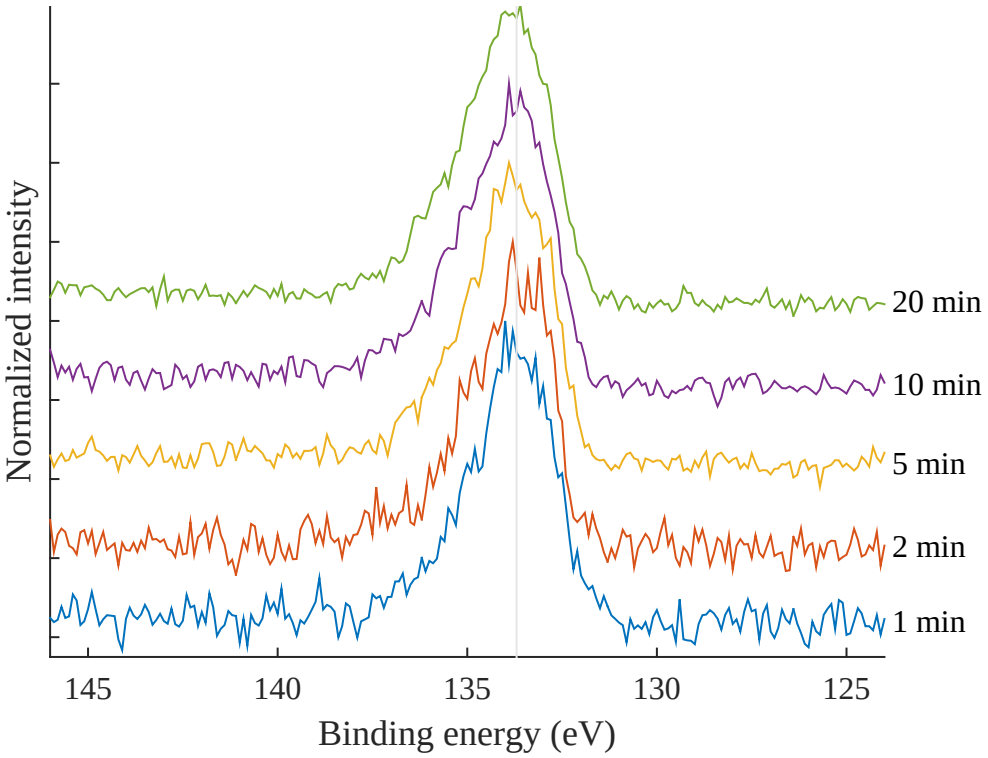

Fig. B.3 XPS degradation analysis after different acquisition time of the P 2p signal of iron poly (0.33) phosphate glass.

B.1.2 XPS quantification of zinc phosphate glass

Table B.1 XPS vs batch composition for zinc phosphate glasses.

Zn Glass	Method	Zn [at.%]	P [at.%]	O [at.%]	Error [%]
meta-phosphate	XPS	9.4	23.9	66.7	7.6
	Batch	11.1	22.2	66.7	
poly-phosphate	XPS	13.7	21.0	65.3	0.6
	Batch	13.7	20.7	65.5	
pyro-phosphate	XPS	17.6	19.2	63.2	3.7
	Batch	18.4	18.1	63.6	
ortho-phosphate	XPS	22.3	16.9	60.7	4.9
	Batch	23.1	15.4	61.5	

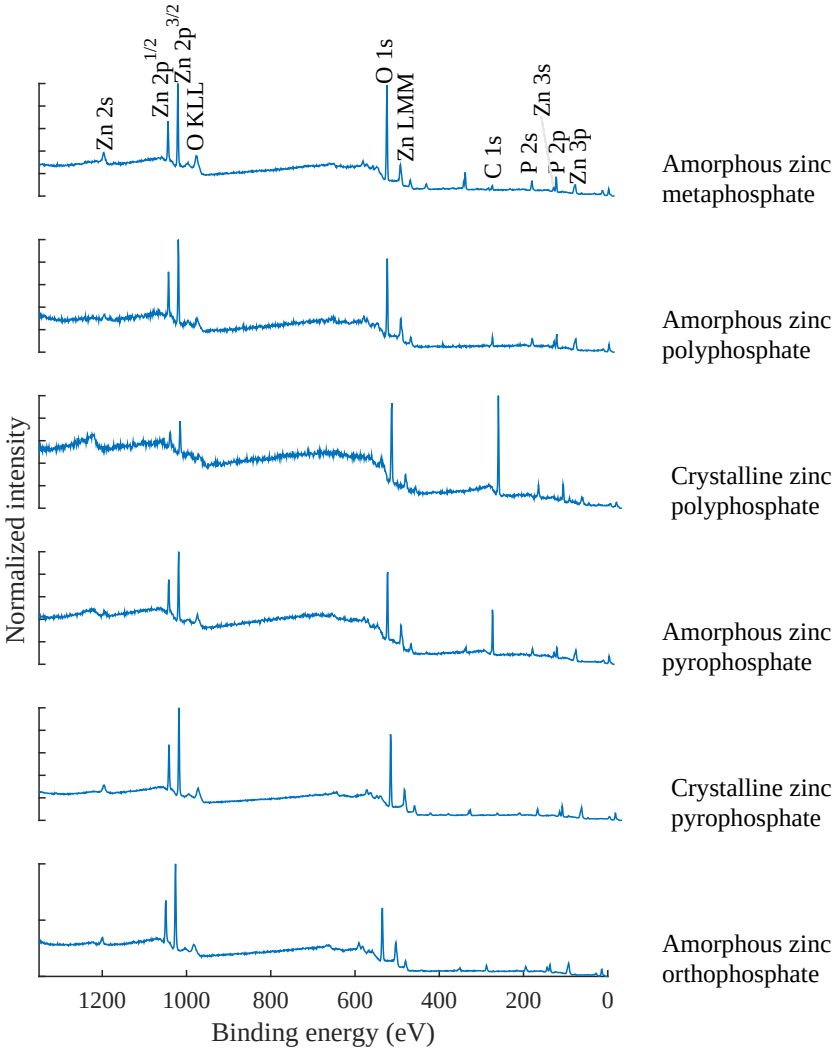

Fig. B.4 XPS survey spectra of various zinc phosphate glasses.

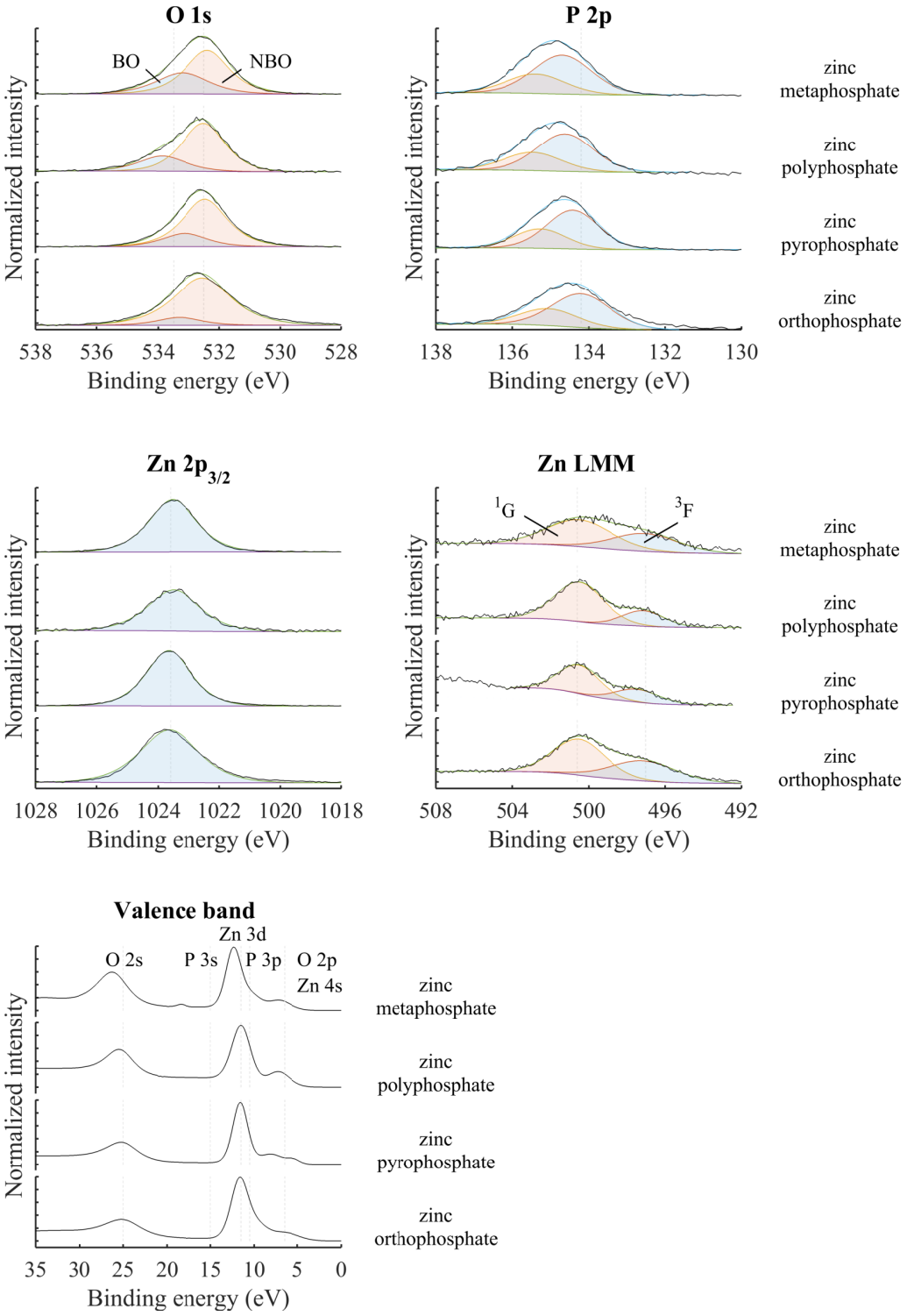

Fig. B.5 XPS high resolution spectra of various zinc phosphate glasses.

B.1.3 XPS quantification of iron phosphate glass

Table B.2 XPS vs batch composition for iron phosphate glasses.

Fe Glass	Method	Fe [at.%]	P [at.%]	O [at.%]	Error [%]
$poly_{33}$-phosphate	XPS	6.1	19.2	74.7	12.4
	Batch	7.7	23.1	69.2	
$poly_{50}$-phosphate	XPS	6.8	22.6	70.6	5.0
	Batch	10.4	21.1	68.5	
$poly_{67}$-phosphate	XPS	10.2	17.8	72.0	7.2
	Batch	12.9	19.4	67.7	
$poly_{100}$-phosphate	XPS	10.1	14.9	75.1	11.7
	Batch	16.7	16.7	66.7	

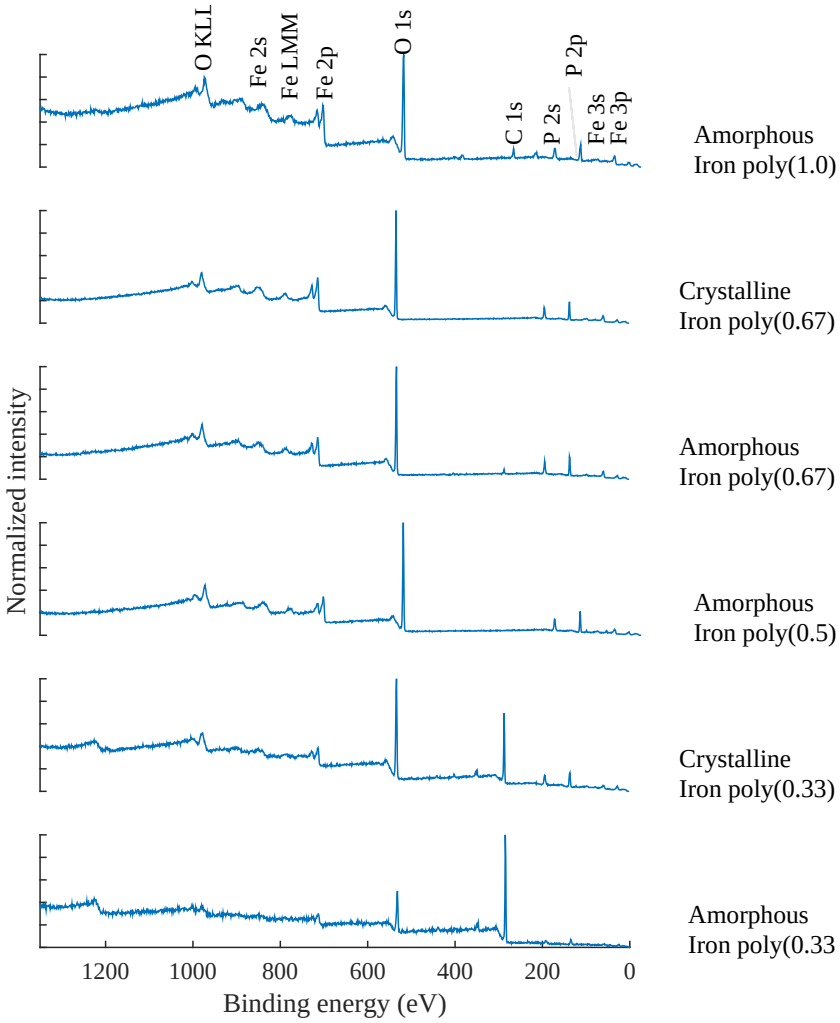

Fig. B.6 XPS survey spectra of various iron phosphate glasses.

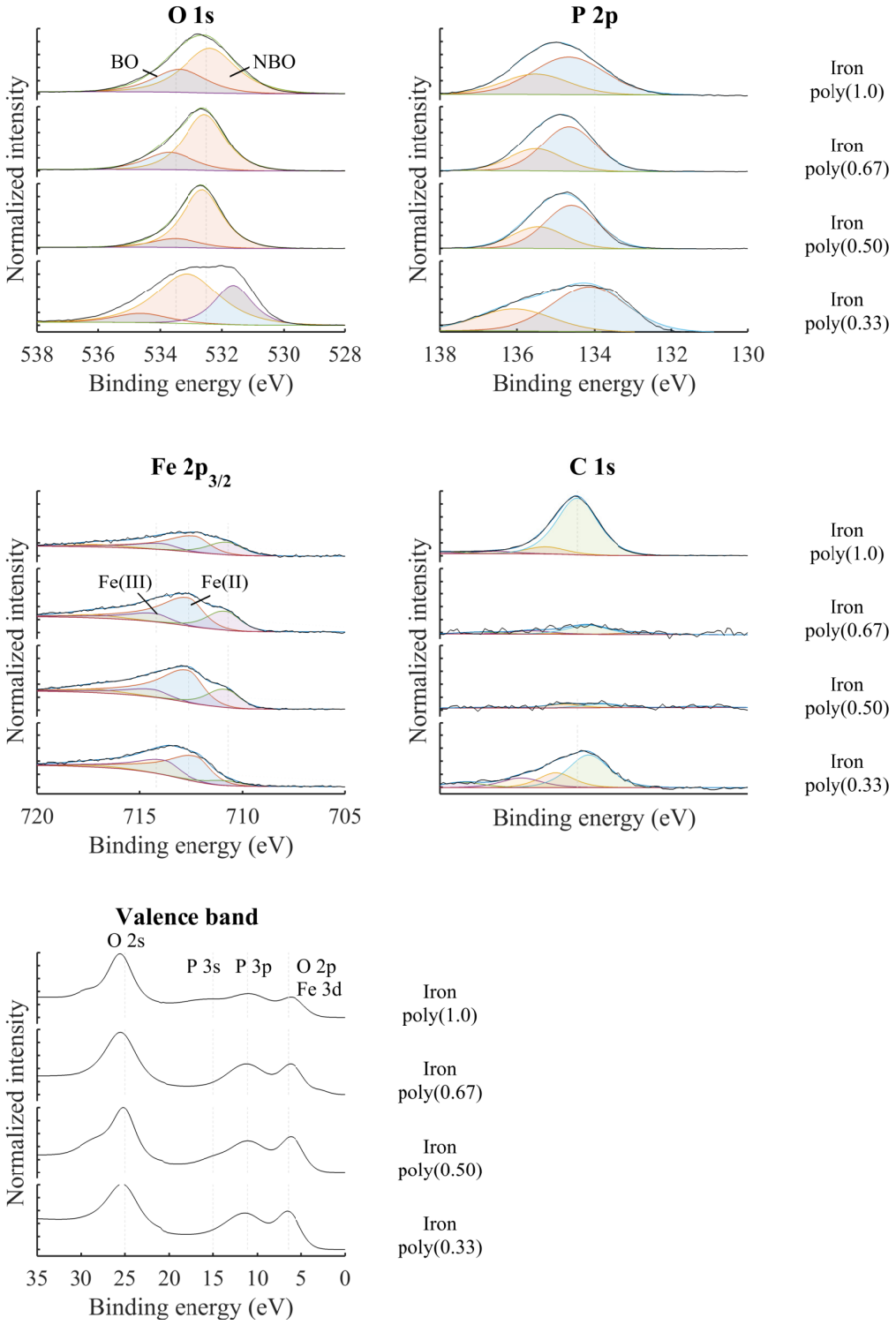

Fig. B.7 XPS high resolution spectra of various iron phosphate glasses.

B.1.4 XPS quantification of mixed phosphate glass

Table B.3 XPS vs batch composition for mixed zinc-iron phosphate glasses.

Zn-Fe Glass	Method	Zn [at.%]	Fe [at.%]	P [at.%]	O [at.%]	Error [%]
zn_{25}-Fe_{75}	XPS	8.2	1.0	25.5	65.3	6.5
	Batch	8.2	2.9	21.8	67.1	
zn_{50}-Fe_{50}	XPS	3.9	3.7	14.4	78.1	16.8
	Batch	3.9	5.5	22.4	68.2	
zn_{75}-Fe_{25}	XPS	2.6	4.5	27.7	65.2	11.4
	Batch	2.6	7.9	21.4	68.0	

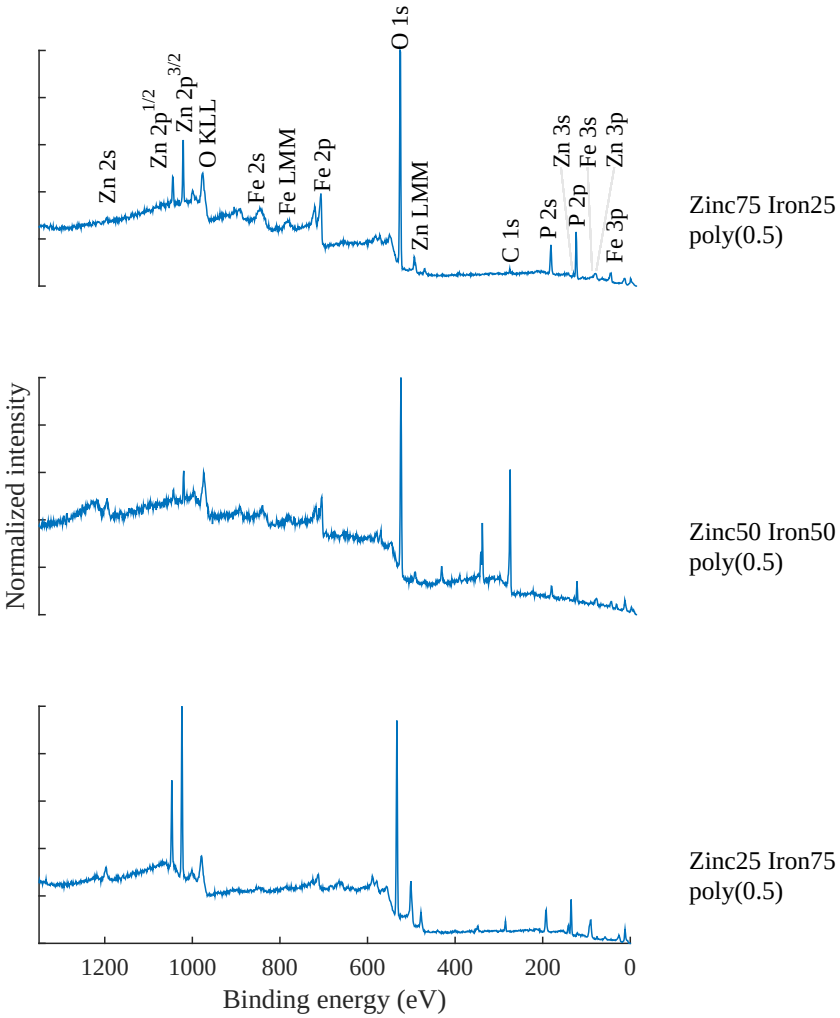

Fig. B.8 XPS survey spectra of various mixed zinc-iron phosphate glasses.

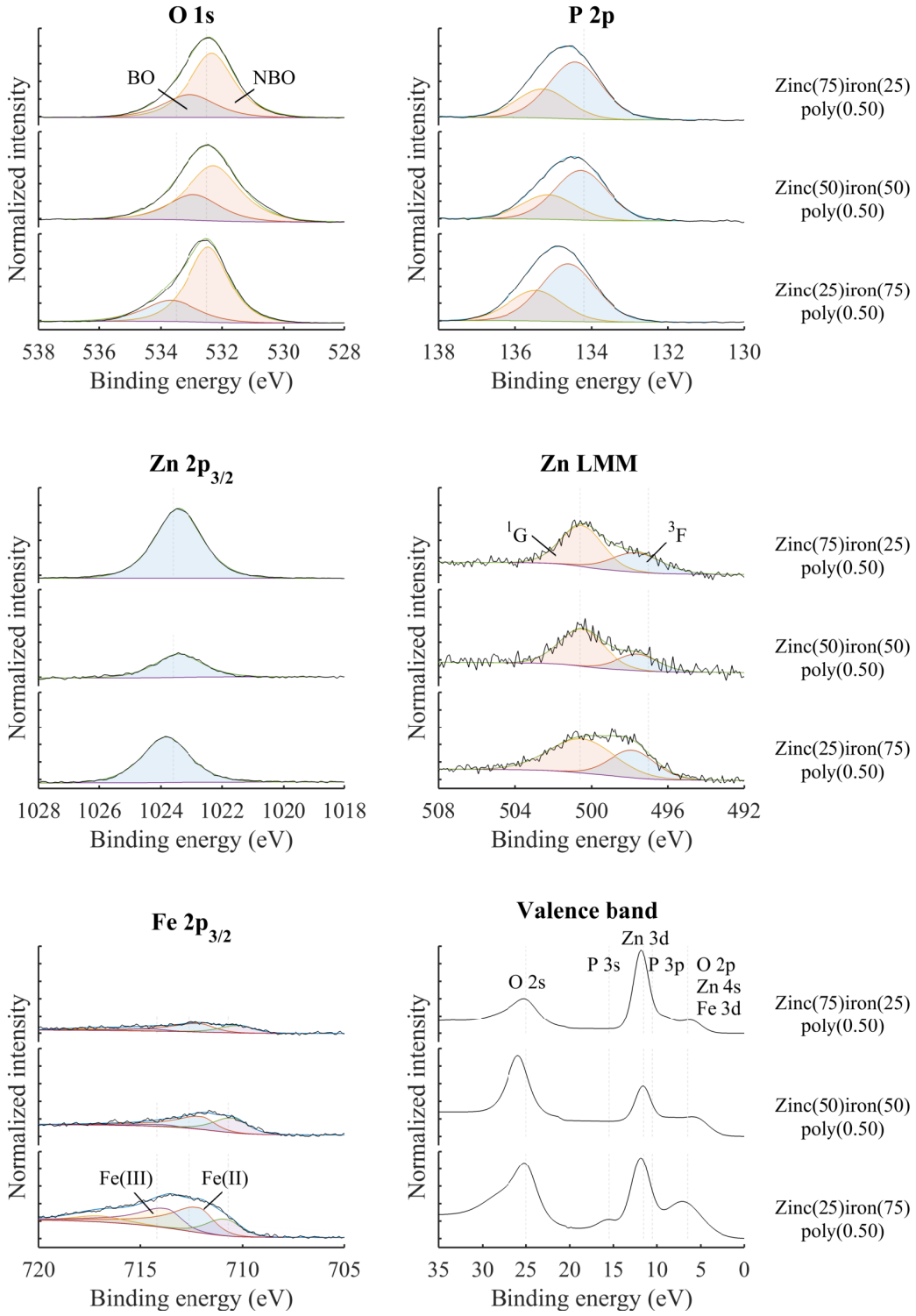

Fig. B.9 XPS high resolution spectra of various mixed zinc-iron phosphate glasses.

B.1.5 Comparison between different glasses

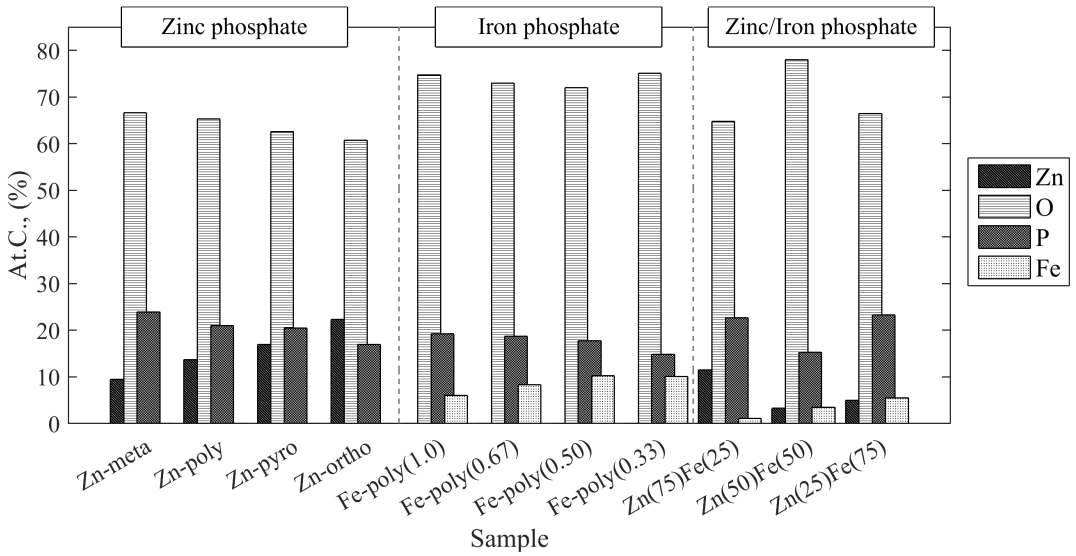

Fig. B.10 Comparison between the XPS composition of various zinc, iron and mixed zinc-iron phosphate glasses.

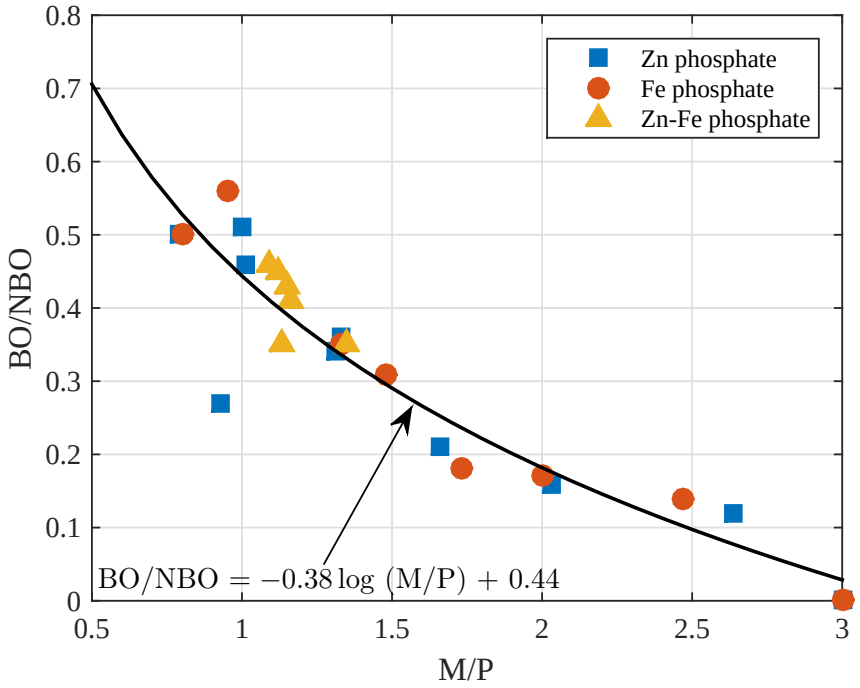

Fig. B.11 BO/NBO ratio vs M/P ratio of various zinc, iron and mixed zinc-iron phosphate glasses.

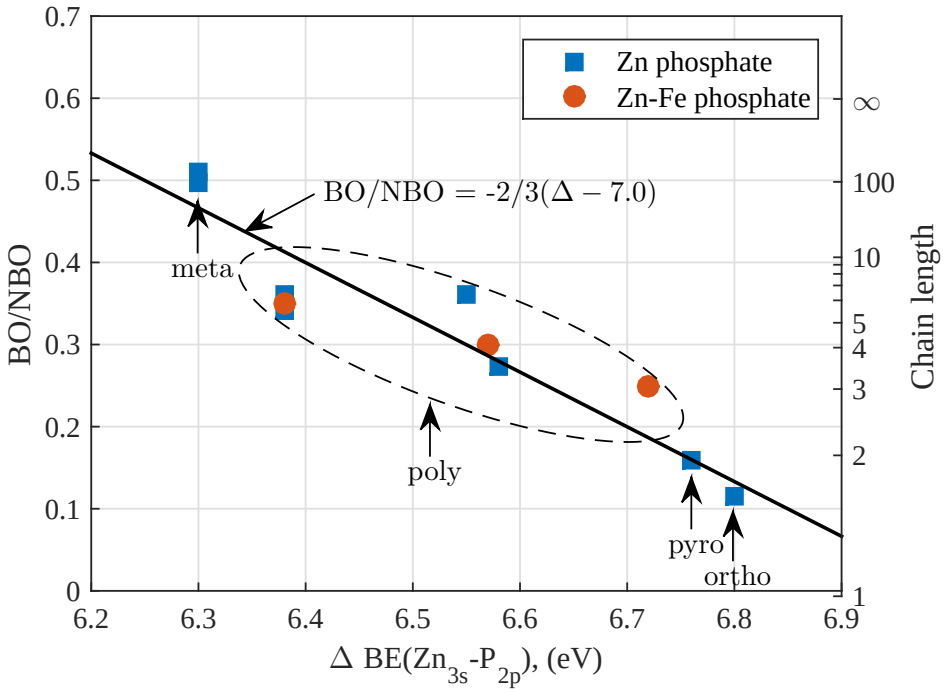

Fig. B.12 BO/NBO ratio vs the difference in binding energy between Zn 3s and P 2p of various zinc and mixed zinc-iron phosphate glasses.

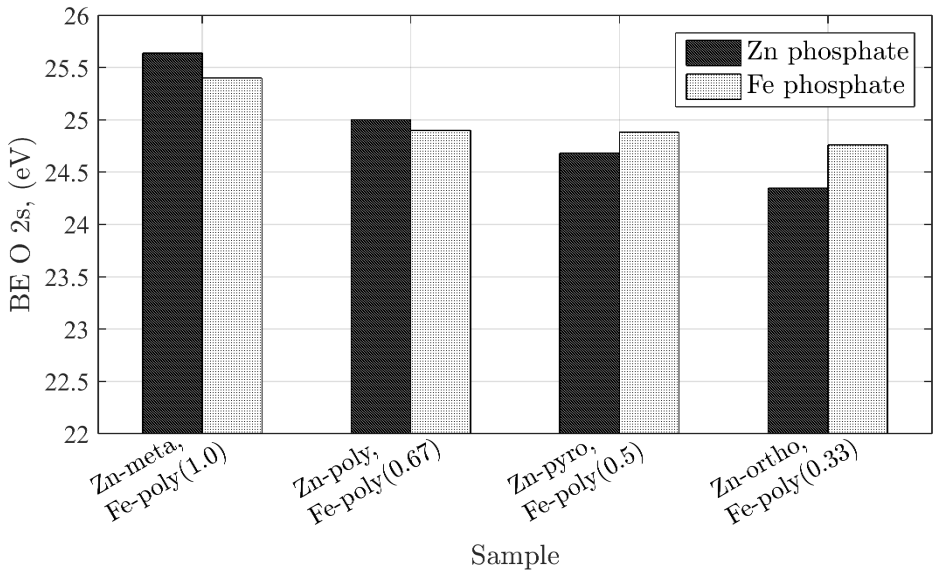

Fig. B.13 Binding energy of O 2s signal of various zinc and iron phosphate glasses.